TECHNICAL UNIVERSITY OF MUNICH

Department of Chemistry

Conventional and Microwave-Assisted Solvothermal Synthesis, Characterization, and Optimization of the High-Voltage Cathode Material $LiCoPO_4$ for Lithium-Ion Batteries

Jennifer Ludwig

Dissertation

2017

TECHNISCHE UNIVERSITÄT MÜNCHEN
Fachgebiet Synthese und Charakterisierung innovativer Materialien

Conventional and Microwave-Assisted Solvothermal Synthesis, Characterization, and Optimization of the High-Voltage Cathode Material $LiCoPO_4$ for Lithium-Ion Batteries

Jennifer Ludwig

Vollständiger Abdruck der von der Fakultät für Chemie der Technischen Universität München zur Erlangung des akademischen Grades eines

Doktors der Naturwissenschaften (Dr. rer. nat.)

genehmigten Dissertation.

Vorsitzender: Prof. Dr. Michael Groll

Prüfer der Dissertation:

1. Prof. Dr. Tom Nilges
2. Prof. Dr. Hubert A. Gasteiger
3. Prof. Dr. Richard Weihrich (schriftliche Beurteilung)
   Prof. Dr. Richard Fischer (mündliche Prüfung)

Die Dissertation wurde am 12.07.2017 bei der Technischen Universität München eingereicht und durch die Fakultät für Chemie am 19.09.2017 angenommen.

Science is organized knowledge. Wisdom is organized life.

Immanuel Kant

Danksagung

Mein besonderer Dank gilt meinem Doktorvater

Prof. Dr. Tom Nilges

für die interessante Themenstellung, die umfangreiche Unterstützung, das entgegengebrachte Vertrauen, Wohlwollen und wissenschaftliche Freiheit (bis hin zur Bierothermalsynthese), ohne die das Gelingen dieser Arbeit und mein Auslandsaufenthalt am Lawrence Berkeley National Laboratory in dieser Form nicht möglich gewesen wären.

Danken möchte ich darüber hinaus:

- der **BMW Group** für die finanzielle Unterstützung und fruchtbare Zusammenarbeit im PhosphoLiCat-Projekt, in dessen Kontext diese Arbeit entstanden ist. Ein großes Dankeschön geht insbesondere an **Dr. Christoph Stinner** für viele konstruktive Beiträge sowie seine stete Diskussions- und Hilfsbereitschaft.

- **Prof. Dr. Hubert A. Gasteiger** vom Lehrstuhl für Technische Elektrochemie für die exzellente Zusammenarbeit im Rahmen unserer Kooperation und einen schier unermüdlichen Strom an Kaffee und Schokolade, ohne den wir so manches Projektmeeting nur halb so gut überstanden hätten. Ich danke dir für viele ungewöhnliche Fragestellungen und Anregungen sowie die Kontaktherstellung zu Marca!

- allen weiteren Beteiligten am PhosphoLiCat-Projekt für die konstruktive Zusammenarbeit. Mein besonderer Dank geht an **Dr. Cyril Marino** und **Dominik Haering** für zahlreiche elektrochemische, BET- und TGA/DSC-Messungen sowie an **Carlos Alarcón-Suesca** für die gute Zusammenarbeit bei der Betreuung der Mikrowelle und den *Cmcm*-Publikationen.

- **Prof. Dr. Janós Mink** der Hungarian Academy of Sciences für Raman-Messungen, **Dr. Stephan Geprägs** vom Walther-Meißner-Institut für SQUID-Messungen, **Dr. Inés Puente Orench** vom Institut Laue-Langevin und **Carlos Alarcón-Suesca** für Neutronenbeugungs-Experimente, **Pankaj Madhikar** für TGA/DSC-Messungen, dem mikroanalytischem Labor, insbesondere **Ulrike Ammari**, für Elementaranalysen, **Dr. Marianne Hanzlik** für TEM/SAED-Aufnahmen und **Katia Rodewald** für diverse REM-Messungen.

- meinen Forschungspraktikanten **Patrick Bretzler, Christoph Denk, Felix Kaiser, Gergana Nenova** und **Daniel Pritzl** für das rege Interesse, die gute Zusammenarbeit und die Unterstützung meiner Arbeit durch ihre hervorragenden Beiträge.

- meinen Laborkollegen **Sarah-Jane Chripunow** und **Dr. Michael Hörmannsdorfer** für die positive und kurzweilige Arbeitsatmosphäre. Danke für die musikalischen Thementage (Nyan Cat!) und die kulinarische Versorgung mit Kuchen!

- **Dr. Marca M. Doeff**. Thank you so much for having me at the Lawrence Berkeley National Laboratory and being the best host one could possibly imagine. Thanks for helping me with the organization of my research stay, for always lending an ear, fruitful discussions, and your valuable feedback on my manuscripts.

- my colleagues at LBNL for their warm welcome and for sharing their knowledge about electrochemistry: **Dr. Chixia Tian, Edgar Olivera, Dr. Guoying Chen, Dr. Saravanan Kuppan, Dr. Wei Tong, Dr. Jing Xu, Dr. Alpesh Shukla**, and **Yuyi Li**. I miss you guys!

- **Dr. Dennis Nordlund** from the Stanford Synchrotron Radiation Lightsource for numerous XAS measurements, further insights into the analysis of XAS data and fruitful discussions.

- **Prof. Dr. Richard W. Fischer** von MuniCat und der Clariant für seine stete Hilfsbereitschaft und umfassende Unterstützung mit Rat und Tat.

- **Lucia Weissenborn** und **Manuela Donaubauer** für ihre Unterstützung bei organisatorischen Angelegenheiten.

- **allen Kollegen der Arbeitsgruppen Nilges, Fässler und Gasteiger** für ihre stete Hilfsbereitschaft, die gute Zusammenarbeit und eine schöne gemeinsame Zeit!

- **allen weiteren Mitarbeitern der Fakultät für Chemie der Technischen Universität München**, die ebenfalls zum Gelingen dieser Arbeit beigetragen haben.

- dem **Max Weber-Programm Bayern**, dem **Fonds der Chemischen Industrie** und der **TUM Graduate School** für die großzügige finanzielle und ideelle Unterstützung meines Bachelor- und Masterstudiums, meiner Promotion sowie meines Auslandsaufenthaltes.

- insbesondere **meinen Freunden** und **meiner Familie** für bedingungslosen Rückhalt, ein stets offenes Ohr für Anliegen jeglicher Art und ihre fortwährende Unterstützung.

Abstract

In order to increase the energy density of lithium-ion batteries and to meet future demands for instance in the field of electric mobility, cathode materials with higher voltage and capacity than current materials are needed. With a theoretical capacity of 167 $mAh \cdot g^{-1}$ and energy density of 802 $Wh \cdot kg^{-1}$, one promising candidate is the high-voltage (4.8 V) cathode material *Pnma*-$LiCoPO_4$, which belongs to the group of phospho-olivines $LiMPO_4$ (*M* = Fe, Mn, Co, Ni). Successful deployment of the material, however, remains challenging due to its intrinsically low and one-dimensional ([010] direction) electrical and ionic conductivities, resulting in unsatisfactory electrochemical performances. One approach to optimize the performance is particle size and morphology control, which can be accomplished by kinetically controlled soft-chemical synthesis methods such as the solvothermal technique. A simple process towards high-performance *Pnma*-$LiCoPO_4$ and a thorough understanding of the relationship between synthesis parameters and material properties are still lacking despite the recent advance.

In this work, a simple and fast (t = 30 min), low-temperature (T = 250 °C) microwave-assisted solvothermal (MWST) synthesis process using a binary water/ethylene glycol (EG) solvent mixture is presented, which delivers submicron *Pnma*-$LiCoPO_4$ particles with a hexagonal platelet morphology in a single step. The particles demonstrate a discharge capacity of 137 $mAh \cdot g^{-1}$ (0.1 C; energy density: 658 $Wh \cdot kg^{-1}$) and a cycle life of over 100 cycles, which represents a significant increase in performance over previous results. Being very flexible with regard to the synthesis design, the novel MWST process can be further modified to precisely control the particle size and shape. The size of the platelets can be reduced from the micron- to the nano-range by increasing the concentration of the EG co-solvent, and hence, the viscosity of the solvent blend. The morphology, on the other hand, can be tuned to square, rhombic, and hexagonal platelet shapes by varying the type of co-solvent, using an array of polyols such as di-, tri-, tetra-, and polyethylene glycol (DEG, TEG, TTEG, PEG) as well as benzyl alcohol (BA). Owing to the soft template effect of all co-solvents (*i.e.*, the selective adsorption on (010) crystal faces), the MWST process exclusively delivers particles with reduced dimensions along the preferred [010] direction, and hence, shortened Li diffusion pathways. As a result of these tuned crystal orientations, all materials deliver cutting-edge electrochemical performances. Notably, in contrast to conventional synthesis techniques, no further post-processing steps like high-temperature annealing or carbon coating are required. The best performance was achieved for micron-sized square platelets produced from a TEG co-solvent with a capacity of

141 mAh·g^{-1} at 0.1 C, corresponding to a gravimetric energy density of 677 Wh·kg^{-1}. This represents the best performance reported for an unprocessed, uncoated *Pnma*-$LiCoPO_4$ material to date. In contrast to the literature, the findings further suggest that because of increased side reactions of nano-sized materials with the electrolyte at high potential, a medium particle size range represents the optimum for the high-voltage cathode material *Pnma*-$LiCoPO_4$.

Another focus was set on metastable cobalt phosphates, which are accessible by a variety of wet-chemical (hydro- and solvothermal, polyol) synthesis approaches. A thorough characterization allowed fundamental insights into the complex structural chemistry and structure–property relationships of this class of materials, which are crucial for further developments in the field. Compared to the thermodynamically stable olivine *Pnma*-$LiCoPO_4$, its metastable *Pna*2_1 and *Cmcm* modifications have not been studied as comprehensively. A redetermination of the crystal structures revealed that both phases are non-stoichiometric and exhibit disorder or vacancies in the cation substructures. This also provides an explanation for the poor electrochemical performance of the materials. Temperature-dependent *in situ* X-ray powder diffraction experiments demonstrated that both polymorphs transform to *Pnma*-$LiCoPO_4$ at elevated temperatures (T ~500–600 °C). Interestingly, *Pna*2_1-$LiCoPO_4$, which has hitherto been considered a low-temperature modification only, was found to re-emerge as a stable high-temperature phase at T > 700–800 °C in both cases. Moreover, X-ray absorption spectra of both phases and the magnetic properties of *Cmcm*-$LiCoPO_4$ were reported for the first time.

Furthermore, two new mixed-valent Co(II,III) phases are presented. The trigonal *P*31*m*-type framework $Co_{11}Li[(OH)_5O][(PO_3OH)(PO_4)_5]$ was identified as a key competing phase in the hydrothermal synthesis of *Pnma*-$LiCoPO_4$. The first Li-deficient structural derivative of *Cmcm*-$LiCoPO_4$ with the nominal composition $Li_{0.5-\delta}CoPO_4$ represents the first partially delithiated derivative of the entire $LiCoPO_4$ family that can be obtained by a direct (bottom-up) polyol synthesis rather than common (electro)chemical delithiation (top-down) techniques. The Co oxidation states of both heterovalent Co(II,III) phases were quantified using X-ray absorption spectroscopy. Owing to the intrinsic instability of Co^{3+} and driven by redox reactions, both compounds exhibit complex, multi-step thermal decomposition mechanisms with oxygen release, which were elaborated in detail with the help of *ex* and *in situ* techniques. The interesting properties suggest that these materials are of potential interest for catalytic applications.

Zusammenfassung

Um die Energiedichte von Lithium-Ionen-Batterien zu erhöhen und zukünftigen Anforderungen gerecht zu werden, insbesondere auf dem Gebiet der Elektromobilität, werden leistungsfähigere Kathodenmaterialien benötigt. Mit einer theoretischen Kapazität von 167 $mAh \cdot g^{-1}$ und einer Energiedichte von 802 $Wh \cdot kg^{-1}$ wird dem Hochvolt-Kathodenmaterial (4.8 V) *Pnma*-$LiCoPO_4$ aus der Gruppe der Phosphoolivine $LiMPO_4$ (*M* = Fe, Mn, Co, Ni) vielversprechendes Potential zugeschrieben. Die praktische Anwendung des Materials stellt jedoch angesichts der geringen, eindimensionalen ([010]-Richtung) elektrischen und ionischen Leitfähigkeiten sowie der damit verbundenen geringen elektrochemischen Performance eine Herausforderung dar. Eine Möglichkeit zur Performancesteigerung bildet die gezielte Partikelgrößen- und Morphologiekontrolle, die mittels kinetisch kontrollierter nasschemischer Synthesemethoden wie der Solvothermaltechnik erreicht werden kann. Die Entwicklung eines einfachen, einstufigen Solvothermalverfahrens zur Darstellung von hochleistungsfähigem *Pnma*-$LiCoPO_4$ war bislang noch nicht gelungen. Darüber hinaus fehlte ein tiefergehendes Verständnis des Zusammenhangs zwischen Syntheseparametern und Materialeigenschaften.

Diese Arbeit beschreibt einen einfachen und schnellen (t = 30 min), einstufigen Mikrowellen-assistierten Solvothermalprozess, welcher bei niedriger Temperatur (T = 250 °C) und unter Einsatz eines binären Wasser/Ethylenglycol (EG)-Lösemittelsystems hexagonal geformte, mikropartikuläre *Pnma*-$LiCoPO_4$-Plättchen liefert. Mit einer Entladekapazität von 137 $mAh \cdot g^{-1}$ (0.1 C; Energiedichte: 658 $Wh \cdot kg^{-1}$) sowie einer Zyklenstabilität von über 100 Zyklen wurde mit diesem Material eine deutliche Steigerung der elektrochemischen Performance erzielt. Aufgrund der Flexibilität des neuartigen Prozesses im Hinblick auf das Synthesedesign ist durch gezielte Wahl der Reaktionsparameter zudem eine präzise Kontrolle der Partikelgröße und -morphologie möglich. So kann durch Erhöhung der EG-Konzentration und somit der Viskosität des Lösemittelgemischs eine Partikelgrößenreduktion vom Mikrometer- in den Nanometerbereich erzielt werden. Eine Steuerung der Partikelform hin zu quadratischen, rhombischen und hexagonalen Plättchen wird hingegen durch Variation des Co-Solvens erreicht, wobei diverse Polyole wie Di-, Tri-, Tetra- und Polyethylenglycol (DEG, TEG, TTEG, PEG) und Benzylalkohol (BA) zum Einsatz kommen. Aufgrund des sog. Soft-Templat-Effekts dieser Lösemittel (d. h. der selektiven Adsorption auf (010)-Kristalloberflächen) weisen sämtliche Partikel reduzierte Dimensionen und somit verbesserte Li-Transporteigenschaften entlang [010] auf. Folglich zeigen alle Materialien eine außergewöhnlich gute elektrochemische Perfor-

mance. Hervorzuheben ist, dass im Gegensatz zu konventionellen Synthesemethoden keine zusätzliche Materialprozessierung (z. B. durch nachträgliches Tempern bei hoher Temperatur oder Kohlenstoff-Coating) erforderlich ist. Mit 141 $mAh \cdot g^{-1}$ bei 0.1 C, entsprechend einer gravimetrischen Energiedichte von 677 $Wh \cdot kg^{-1}$, erzielen quadratische Mikroplättchen, hergestellt mittels des Co-Solvens TEG, die höchste bislang erreichte Performance für unprozessiertes *Pnma*-$LiCoPO_4$. Im Kontrast zur Literatur zeigen die Ergebnisse ferner, dass angesichts ausgeprägter Nebenreaktionen von Nanomaterialien mit dem Elektrolyten bei hohen Spannungen ein mittlerer Partikelgrößenbereich zu bevorzugen ist.

Ein weiterer Schwerpunkt dieser Arbeit lag auf metastabilen Cobaltphosphaten, die über eine Reihe nasschemischer Syntheseverfahren (hydro- und solvothermal, polyolbasiert) hergestellt werden können. Deren sorgfältige Charakterisierung ermöglichte umfassende Einblicke in die komplexe Strukturchemie und die Struktur-Eigenschafts-Beziehungen dieser Materialklasse, die für Weiterentwicklungen auf diesem Gebiet essentiell sind. Im Vergleich zum thermodynamisch stabilen *Pnma*-$LiCoPO_4$ wurde der Charakterisierung der *Pna*2_1- und *Cmcm*-$LiCoPO_4$-Polymorphe bislang weniger Beachtung geschenkt. So zeigte die Neubestimmung der Kristallstrukturen von *Pna*2_1- und *Cmcm*-$LiCoPO_4$, dass es sich um nicht-stöchiometrische Verbindungen handelt, deren Kationenteilstrukturen durch Fehlordnung oder Vakanzen charakterisiert sind. Dies bietet einen Erklärungsansatz für die schlechte elektrochemische Performance beider Materialien. Temperaturabhängige *in situ* Röntgenpulverdiffraktometrie-Experimente zeigten, dass sich beide Polymorphe bei ~500–600 °C zu *Pnma*-$LiCoPO_4$ umwandeln. In beiden Fällen wurde bei weiterer Temperaturerhöhung (T > 700–800 °C) *Pna*2_1-$LiCoPO_4$ als Hochtemperaturphase erhalten, das bis dato lediglich als Tieftemperaturmodifikation beschrieben wurde. Des Weiteren wurden Röntgenabsorptionsspektren beider Polymorphe sowie magnetische Eigenschaften von *Cmcm*-$LiCoPO_4$ erstmals untersucht.

Darüber hinaus gelang die Darstellung zweier neuer, gemischtvalenter Co(II,III)-Phasen. Zum einen wurde $Co_{11}Li[(OH)_5O][(PO_3OH)(PO_4)_5]$ als wichtiges Konkurrenzprodukt bei der Hydrothermalsynthese von *Pnma*-$LiCoPO_4$ identifiziert. Zum anderen stellt die Li-defizitäre Variante von *Cmcm*-$LiCoPO_4$ mit der nominellen Zusammensetzung $Li_{0.5-\delta}CoPO_4$ die erste delithiierte Phase der $LiCoPO_4$-Strukturfamilie dar, die im Gegensatz zu gängigen (elektro-) chemischen Delithiierungsverfahren (top-down) direkt über einen einfachen Polyolprozess (bottom-up) zugänglich ist. Die Oxidationszustände beider heterovalenter Phasen wurden mittels Röntgenabsorptionsspektroskopie quantifiziert. Bedingt durch die intrinsische Instabilität der enthaltenen Co^{3+}-Ionen zeigen beide Verbindungen komplexe, mehrstufige Zersetzungsmechanismen, denen Redoxprozesse zugrunde liegen und die mittels diverser *ex* sowie *in situ* Methoden aufgeklärt werden konnten. Aufgrund ihrer interessanten Materialeigenschaften sind beide Phasen ferner für katalytische Anwendungen von potentiellem Interesse.

List of Abbreviations

AAS	atomic absorption spectroscopy
AC	alternating current
AEY	Auger electron yield
APCU	automatic pressure control unit
arb. unit	arbitrary unit
ATR	attenuated total reflection
BA	benzyl alcohol
BET	Brunauer–Emmett–Teller (surface area)
c	concentration ($mol \cdot L^{-1}$)
CCCV	constant-current, constant-voltage
CCD	charge-coupled device
CCDC	Cambridge Crystallographic Data Centre
CIF	crystallographic information file
CN	coordination number
const.	constant
CSD	crystal structure depot
CTAB	cetyltrimethylammonium bromide
d	diameter (mm), interatomic distance (Å)
DC	direct current
DEC	diethyl carbonate
DEG	diethylene glycol
DFT	density functional theory
DMC	dimethyl carbonate
DSC	differential scanning calorimetry
E	potential (V)
EC	ethylene carbonate
EDS	energy-dispersive X-ray spectroscopy
EG	ethylene glycol
endo	endothermic
exo	exothermic
exp.	experimental
FC	field-cooled

FEC	fluoroethylene carbonate
FTIR	Fourier-transform infrared spectroscopy
FWHM	full width at half maximum
FY	fluorescence yield
GB	gentle beam
θ	diffraction angle (°)
HMD	hexamethylenediamine
HMT	hexamethylenetetraamine
HPHT	high-pressure high-temperature
HR	high-resolution
HS	high-spin
HT	hydrothermal
ICSD	Inorganic Crystal Structure Database
IR	infrared
IUCr	International Union of Crystallography
λ	wavelength (nm)
LCP	lithium cobalt phosphate, $LiCoPO_4$
LEI	lower secondary electron image
LFP	lithium iron phosphate, $LiFePO_4$
LIB(s)	lithium-ion battery (batteries)
LiBOB	lithium bis(oxalato)borate
LMP	lithium manganese phosphate, $LiMnPO_4$
LNP	lithium nickel phosphate, $LiNiPO_4$
LR	low-resolution
LS	low-spin
μ	magnetic moment (μ_B)
m	mass (g)
M	molar mass ($g \cdot mol^{-1}$), transition metal (Fe, Mn, Co, Ni)
MWHT	microwave-assisted hydrothermal
MWST	microwave-assisted solvothermal
n	moles (mol)
NMC	lithium nickel manganese cobalt oxide (*e.g.* $LiNi_{1/3}Mn_{1/3}Co_{1/3}O_2$)
NMP	*N*-methyl-2-pyrrolidone
NMR	nuclear magnetic resonance
no.	number
occ.	occupancy
OEC	oxygen-evolving catalyst

O_h	octahedral symmetry
p	pressure (bar)
P	power (W)
PE	polyethylene
PEG	polyethylene glycol
pH	potential of hydrogen, *pondus Hydrogenii*
Ph. Eur.	*Pharmacopoeia Europaea*
PND	powder neutron diffraction
PO	polyol
PP	polypropylene
ppb	parts per billion
PPG	polypropylene glycol
PSD	position-sensitive detector
PTFE	polytetrafluoroethylene
PVDF	polyvinylidene difluoride
PVP	polyvinylpyrrolidone
PXRD	powder X-ray diffraction
ρ	density ($g \cdot cm^{-3}$), resistivity ($M\Omega \cdot cm$)
R	reliability factor
ref.	reference
rpm	revolutions per minute
RT	room temperature (25 °C)
S	specific surface area ($m^2 \cdot g^{-1}$)
SAED	selected area electron diffraction
SCF	supercritical fluid
SDBS	sodium dodecylbenzenesulfonate
SEM	scanning electron microscopy
SG	sol–gel
s.o.f.	site occupancy factor
SP	spray pyrolysis
SQUID	superconducting quantum interference device
SS	solid-state
ST	solvothermal
t	time (min)
T	temperature (°C, K)
T_d	tetrahedral symmetry
TEG	triethylene glycol

TEM	transmission electron microscopy
TEY	total electron yield
TFM	perfluoro(propyl vinyl ether)-modified polytetrafluoroethylene
TGA	thermogravimetric analysis
theor.	theoretical
TMB	trimethylboroxine
TOC	total organic carbon
TTEG	tetraethylene glycol
U_{iso}	isotropic thermal displacement parameter (Å^2)
UV	ultraviolet
V	volume (mL), cell volume (Å^3)
v:*v*	volume per volume
vol%	volume percent
w:*w*	weight per weight
wt%	weight percent
χ^2	goodness of fit
XAS	X-ray absorption spectroscopy
YAG	yttrium aluminum garnet, $Y_3Al_5O_{12}$
Z	number of units per formula unit
ZFC	zero-field-cooled

Table of Contents

Note

This dissertation is written as a publication-based thesis, which includes six articles published in international, peer-reviewed journals and – in the case of unpublished work – a manuscript submitted for publication.

The content is organized as follows:

- **Chapter 1:** Introduction focusing on the theoretical background, a review of the state of the art and the relevant literature.
- **Chapter 2:** Scope and outline of this work.
- **Chapter 3:** Experimental part providing details on the synthesis and characterization methods. Contributions from co-workers and co-authors are explicitly stated therein.
- **Chapter 4:** The results of this thesis are presented on the basis of short summaries of the publications and manuscripts embedded in Chapter 6, highlighting the individual author contributions. The results are further discussed in context of the literature.
- **Chapter 5:** Overall conclusions and outlook.
- **Chapter 6:** Publications and manuscripts. This part includes a complete list of the bibliographic data of the publications, reprints of the six articles published in peer-reviewed journals, and one manuscript submitted for publication. Each publication or manuscript is followed by its respective supporting materials.

Chapter 1 and parts of Chapter 4 will be published as a separate review article after the submission of this thesis.

Chapter 1
Introduction

1.1 Phospho-Olivines Li*M*PO_4 (*M* = Fe, Mn, Co, Ni) as Cathode Materials for Lithium-Ion Batteries

In light of global warming and the depletion of fossil fuel resources, the transition to sustainable energy production and storage is a fundamental challenge of this century.[1] One important aspect of this transition is turning from vehicles driven by combustion engines to electric vehicles powered by lithium-ion batteries (LIBs).[1-2] However, to meet the requirements for electric vehicles, the energy density of LIBs needs to be increased.[3-5] While the performance of LIBs depends on both the active materials and the electrolyte, the cathode material remains the main determinant of energy density.[2-4, 6-7] Therefore, great research effort has been directed in the last decades towards developing new cathode materials with higher operating voltage, capacity and hence, higher energy density but also lower cost and better safety characteristics than current materials such as $LiCoO_2$.[7-12]

Since the pioneering work of Padhi and co-workers[13] in 1997, phospho-olivines, *i.e.* materials isostructural to olivine Mg_2SiO_4[14] (space group: *Pnma*) and the composition Li*M*PO_4 (*M* = Fe, Mn, Co, Ni), have been receiving considerable attention as cathode materials due to their high specific capacities (~170 $mAh \cdot g^{-1}$), thermal stability, low cost, and environmental friendliness.[5-6, 15-21] The orthorhombic olivine structure is presented in Figure 1.1. It is based on a distorted hexagonal close-packed (*hcp*) oxygen array, in which Li and the transition metal *M* occupy half of the octahedral voids ([LiO_6] and [*M*O_6] units, coordination number (CN) = 6) and P one eighth of the tetrahedral voids ([PO_4]).[17, 22] The [*M*O_6] octahedra form layers in the *bc* plane, which are built from corner-shared zigzag chains. The layers are cross-linked by [PO_4] tetrahedra, creating a three-dimensional network. The Li ions are located in one-dimensional channels along the [010] and [001] directions. However, theoretical studies suggest that Li diffusion is only promoted along [010] since the activation energy is significantly lower along this pathway.[23-26] As a result of these one-dimensional Li migration paths and the separation between the [*M*O_6] and [PO_4] units in the structure, all the olivines generally exhibit poor electronic and ionic conductivities.[21, 23, 27-28] On the other hand, the highly covalent P–O bonds in the form of [PO_4] units prevent oxygen release from the charged olivines upon heating, which makes them intrinsically more thermally stable and thus safer compared to oxides.[21, 29-30]

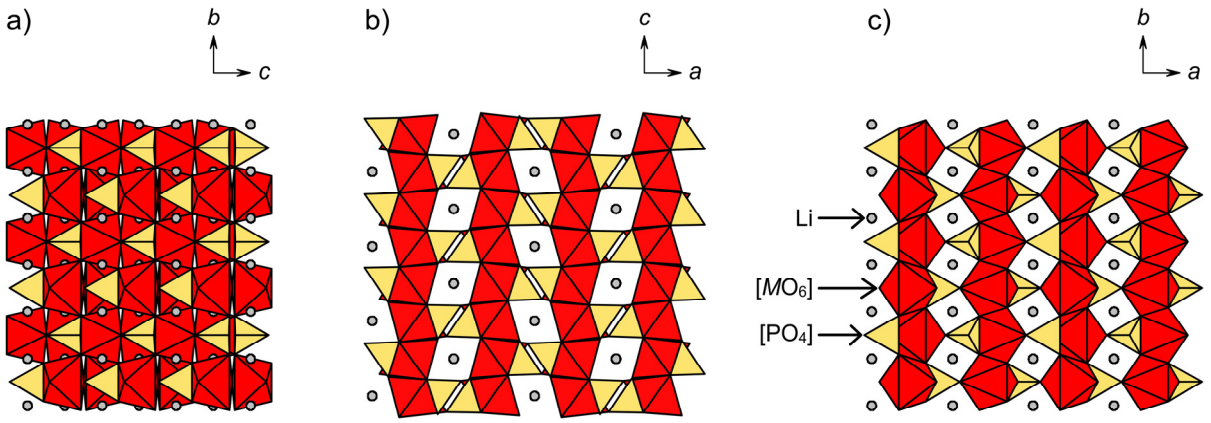

Figure 1.1 Polyhedral representation of the crystal structure of *Pnma*-Li*M*PO_4 (*M* = Fe, Mn, Co, Ni; *Z* = 4) viewed along the three crystallographic axes: (a) [100], (b) [010], and (c) [001]. The structure features chains of [CoO_6] octahedra (red), which form layers in the *bc* plane that are cross-linked by [PO_4] tetrahedra (yellow). The octahedrally coordinated Li ions (grey, CN = 6) are located in channels of the three-dimensional network along [010] and [001] yet Li migration is only promoted along the [010] direction (see text). The figure was adapted from reference [31], Copyright (2016), with permission from Elsevier B.V.

Within the olivine group, $LiFePO_4$ (short: LFP) by far represents the most widely investigated compound (07/2017: ~7400 publications in SciFinder)[32] and is now a fully developed material that is already in commercial use.[21, 33-36] $LiFePO_4$ operates at a flat voltage of 3.45 V *versus* Li/Li^+,[13] which is compatible with commercially available electrolytes. In the last decade, research efforts have increasingly been focusing on the isostructural $LiMnPO_4$ (LMP), $LiCoPO_4$ (LCP), and $LiNiPO_4$ (LNP) phospho-olivines. These compounds allow a significant increase in energy densities compared to $LiFePO_4$ because of their higher operating voltages *vs.* Li/Li^+ (Mn^{2+}/Mn^{3+}: 4.1 V,[13] Co^{2+}/Co^{3+}: 4.8 V,[37] Ni^{2+}/Ni^{3+}: 5.1 V[38], *cf.* Table 1.1).[11, 19, 21, 39-40] However, the redox potential of $LiNiPO_4$ is far above the stability limit of common electrolytes (~4.5 V)[41-46] and as a result, its electrochemical activation remains challenging.[15, 38, 47-49] Therefore $LiCoPO_4$, which shows the second highest operating voltage of the olivine family and a high specific energy of 802 $Wh \cdot kg^{-1}$, currently represents the most promising olivine candidate for high-energy-density LIBs.[7, 15, 17, 19, 21, 44, 50]

Table 1.1 Comparison of the electrochemical properties of the phospho-olivines Li*M*PO_4 (*M* = Fe, Mn, Co, Ni).

Li*M*PO_4	$LiFePO_4$	$LiMnPO_4$	$LiCoPO_4$	$LiNiPO_4$
Potential *vs.* Li/Li^+ (V)	3.45[13]	4.1[13]	4.8[37]	5.1[38]
Theoretical capacity ($mAh \cdot g^{-1}$)	170	171	167	167
Theoretical energy density ($Wh \cdot kg^{-1}$)	587	701	802	852

1.2 The Olivine-Type High-Voltage Cathode Material *Pnma*-$LiCoPO_4$

1.2.1 Electrochemical Properties

The electrochemical activity of *Pnma*-$LiCoPO_4$ was first reported in 2000 by Amine *et al.*,[37] who demonstrated that Li can be reversibly extracted at an average voltage of 4.8 V. The phase transitions occurring upon lithium insertion–extraction of *Pnma*-$LiCoPO_4$ have been investigated by a large number of groups, with Ehrenberg and co-workers taking a leading role.[51-59] In contrast to $LiFePO_4$, which exhibits a one-step two-phase mechanism with the end members $LiFePO_4$ and $FePO_4$ (*cf.* Scheme 1.1, Equation I),[60-62] the delithiation of $LiCoPO_4$ occurs in two distinct reaction steps *via* a Li_xCoPO_4 intermediate (Scheme 1.1, Equation IIa, b).[52, 55] The two-step mechanism is reflected by two oxidation peaks (~4.8 V and ~4.9 V *vs.* Li/Li^+) and two reduction peaks (~4.7 V and ~4.8 V *vs.* Li/Li^+) in cyclic voltammetry plots as well as two corresponding plateaus during galvanostatic charge–discharge.[51-52, 55]

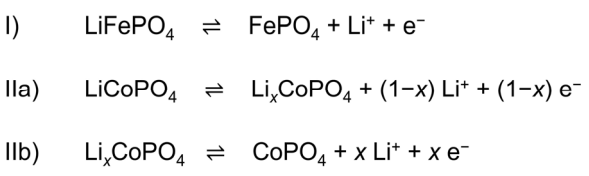

Scheme 1.1 Reactions occurring upon Li insertion–extraction of olivine-type $LiFePO_4$ (I) and $LiCoPO_4$ (IIa, b).

The composition (Li content *x*) of the intermediate phase Li_xCoPO_4, however, is still under investigation and debated in the literature. Earlier investigations suggested *x* to be 0.7[55] and 0.6[63] based on X-ray, neutron, and synchrotron diffraction studies, whereas a later report[64] stated a Li_xCoPO_4 (x = 0.20–0.45) composition. Recently, the lithiation state of the intermediate was determined to be $Li_{2/3}CoPO_4$ by three independent studies[56-58] using *ex situ* ^7Li and ^{31}P NMR (nuclear magnetic resonance), *in situ* synchrotron diffraction and XAS (X-ray absorption spectroscopy) as well as first-principles DFT (density functional theory) calculations. Notably, the use of inert gas atmospheres and/or *in situ* techniques is crucial for these studies because the completely delithiated phase $CoPO_4$ has been shown to be unstable and undergo amorphization when exposed to air or moisture.[51, 55, 63, 65] Furthermore, as opposed to the assumption that charged (delithiated) olivines are thermally stable because of the strong covalent P–O bonds (*cf.* Chapter 1.1), thermal instability has been reported for charged $LiCoPO_4$ electrodes. According to Bramnik *et al.*,[66] both lithium-poor, Co^{3+}-containing phases

$CoPO_4$ and Li_xCoPO_4 decompose rapidly at temperatures of 100–200 °C, leading to gas evolution and the formation of $Co_2P_2O_7$ and $LiCoPO_4$ (only in the case of $x > 0$ in Li_xCoPO_4). In contrast, Theil *et al.*[67] claimed that the phase with higher Li content Li_xCoPO_4 is thermally stable up to 550 °C and that the thermal instability of charged $LiCoPO_4$ electrodes is only because of the instability of the $CoPO_4$ phase. To date, both Li-deficient phases have exclusively been accessible by electrochemical or chemical Li extraction from olivine-type $LiCoPO_4$ in a top-down process.[52, 63, 65-67] A direct bottom-up synthesis route to these phases is unknown.

Despite these fundamental findings, the electrochemical performance of *Pnma*-$LiCoPO_4$ in cells is generally unsatisfactory and characterized by low capacities, poor rate performance, and serious capacity fading after only a few cycles.[7, 12, 15, 17, 21, 44, 68] The main issues hindering its practical use as a cathode material are its intrinsically low electronic ($< 10^{-9}$ Sm·cm^{-1})[27, 69-71] and ionic ($< 10^{-8}$ Sm·cm^{-1})[23, 27, 71-74] conductivities, the latter being related to the one-dimensional ([010] direction) Li transport channels as discussed in Chapter 1.1. While these features limit its capacity especially at high C rates, the poor cycle life is related to parasitic degradation reactions at the interface of the electrode and the electrolyte since the working potential of $LiCoPO_4$ (4.8 V[37]) exceeds the stability limit of standard carbonate-based electrolytes (~4.5 V).[41-46, 75-76] The decomposition products of the electrolyte form resistive films on the particle surfaces, which block Li re-intercalation on discharge.[77] As shown by Aurbach and co-workers,[75, 78] the capacity fading in $LiPF_6$-containing electrolytes is due to a nucleophilic attack of F^- anions on the P atoms of the delithiated $CoPO_4$ phase, resulting in a break-up of the P–O bonds in the $[PO_4]$ units to form $LiPO_2F_2$, and a progressive structural degradation of $LiCoPO_4$. In addition to these extrinsic causes, recently, advanced microscopic methods allowed the identification of antisite (exchange) defect formation in $LiCoPO_4$ upon charging as an intrinsic reason for capacity fading.[79-81] The occupation of Li sites in the crystal structure by Co ions (12% after the 1st cycle) blocks the one-dimensional Li diffusion pathways, reducing Li mobility and impeding Li reinsertion upon discharge, and as a result, significantly lowers the performance. The defect concentration progresses upon cycling, and reaches 24% after only 30 cycles.[80] Interestingly, Co–Li antisite defects were not only observed in cycled materials, but also in as-synthesized *Pnma*-$LiCoPO_4$ crystals,[82] which in agreement with similar studies on $LiFePO_4$[83-87] might explain the generally poor performance of materials produced at low temperatures.

In order to improve the electrochemical performance of *Pnma*-$LiCoPO_4$, tremendous research efforts have been made in recent years. In particular, three strategies have been used extensively: (1) surface modification (*e.g.* coating with conductive carbon),[44, 70, 88-96] (2) metal doping or substitution[26, 69, 71-72, 97-108], and (3) particle size reduction.[19, 109-114] While coating the particles with a thin, often amorphous layer of carbon (*ex* or *in situ*) helps to overcome the limitation of low electrical conductivity, the coat is also believed to reduce the

activation energy for Li^+ transfer across the electrode–electrolyte interface.[21] Doping and substitution (*e.g.* with Fe, Mn, Ni, Cr, V, Y) aim at improving both the electrical conductivity and Li-ion diffusivity by modifying the band structure[24, 26] but also at stabilizing the delithiated olivine phases.[102] Decreasing the particle dimensions allows a more effective electrode–electrolyte contact area and reduces the length of the Li migration paths inside the particles, which results in a higher capacity at high C rates and therefore a larger power density.[21]

The simplest and by far most common method to realize these optimization strategies is by conventional solid-state (SS) synthesis,[52, 70, 90, 101, 115-123] which typically involves high-temperature annealing (T = 800–900 °C, 'hard chemistry') and additional ball milling steps to reduce the particle size in a so-called top-down process. However, the high consumption of energy by these steps makes this approach economically unviable. Furthermore, the particles are often inhomogeneous in size and shape and tend to form agglomerates.[44] In contrast to this thermodynamically controlled solid-state approach, kinetically controlled wet-chemical methods are of greater interest because of lower synthesis temperatures ('soft chemistry') and the option to modify the particle size and morphology in a bottom-up process. The kinetically controlled approach includes a variety of techniques, such as sol–gel (SG),[63, 74, 88, 124-134] co-precipitation,[72, 135-137] spray pyrolysis (SP),[109-110, 138-139] polyol (PO),[92, 95, 140-142] conventional hydrothermal (HT)[96, 143-151] and solvothermal (ST)[58, 148, 151-155] synthesis, microwave-assisted hydrothermal (MWHT)[91, 156-157] and solvothermal (MWST)[108, 158-161] synthesis, as well as supercritical fluid (SCF) processes.[56, 112, 114, 162-164] However, most of these methods still require long reaction times, and controlling the shape and size of the particles has proven challenging. Furthermore, additional post-heating steps are needed, the only exception being the HT, ST, SCF, MWHT, and MWST techniques, which have been reported to deliver $LiCoPO_4$ in a single synthesis step. This makes these approaches particularly appealing for the economical large-scale production of *Pnma*-$LiCoPO_4$. The theoretical background and the state of the art in the HT, ST, SCF, MWHT, and MWST synthesis of *Pnma*-$LiCoPO_4$ are outlined in the following.

1.2.2 Hydrothermal (HT), Solvothermal (ST), Supercritical Fluid (SCF), Microwave-Assisted Hydrothermal (MWHT), and Microwave-Assisted Solvothermal (MWST) Synthesis

(a) Theoretical Background

Hydro- and solvothermal processes are heterogeneous chemical reactions, which are performed in a closed system (*i.e.*, a hermetically sealed reaction container such as an autoclave; experimental details see Chapter 3.1.2) above the boiling point T_b of a solvent and the

ambient pressure of 1 bar but typically below its critical point (*i.e.*, under subcritical conditions).[165-166] The corresponding temperature and pressure ranges ($T_b < T < T_c$, $p_b = 1$ bar < $p < p_c$) in a *T*–*p* phase diagram of an arbitrary solvent are highlighted in grey in Figure 1.2. The processes are classified on basis of the solvent used. Reactions in water, mimicking geological phenomena in the Earth's crust, are called hydrothermal (HT) syntheses.[165-167] Reactions using non-aqueous, primarily organic solvents (*e.g.* alcohols, hydrocarbons, liquid CO_2, H_2S or NH_3), on the other hand, are grouped under the general term solvothermal (ST) synthesis.[165-168] As evident from the vapor pressure curve (Figure 1.2), under these subcritical conditions (*e.g.* for water: $T_c > T > T_b = 100$ °C), the solvent is in equilibrium with its vapor, and an autogenous pressure is developed that increases with temperature. It is worth noting that in addition to the temperature, also the filling degree of the vessel will affect the pressure.[165-166]

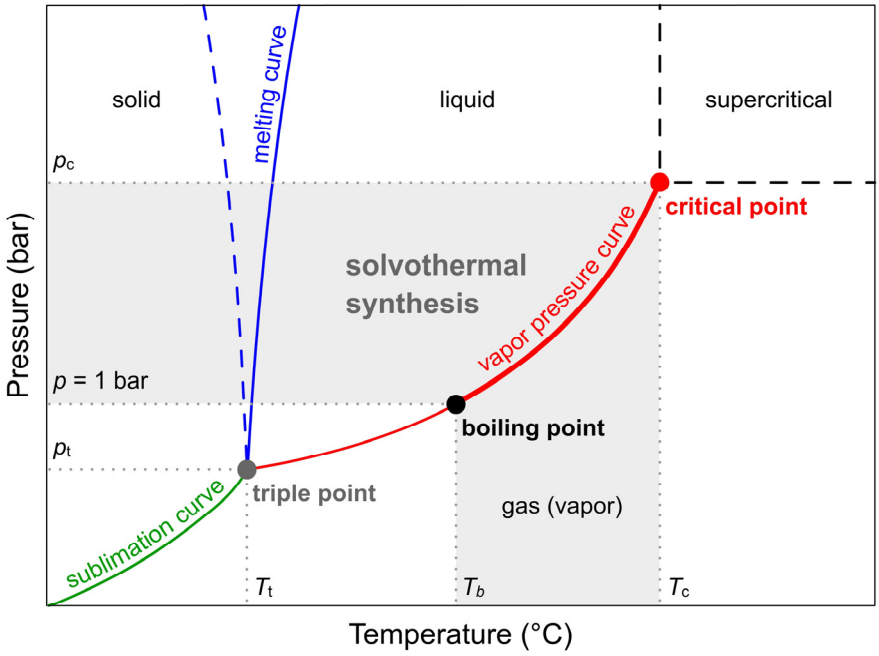

Figure 1.2 Schematic *T*–*p* phase diagram of an arbitrary solvent. The pressure and temperature range between the boiling point T_b (p = 1 bar) and critical point (T_c, p_c) applied for hydrothermal (HT) and solvothermal (ST) syntheses, at which the liquid solvent is in equilibrium with its vapor, is highlighted in light grey. Supercritical fluid (SCF) processes are performed at temperatures and pressures above the critical point ($T > T_c$ and $p > p_c$), where liquid and gas phases are indistinguishable. The sublimation curve is displayed in green, the vapor pressure curve in red, and the melting curve in blue. The melting curve of water, which shows an anomaly, is indicated by a dotted blue line. The triple point marks conditions (T_t, p_t) at which the three different phases (solid, liquid, and gas) coexist. The figure was created and modified using reference [169] as a template.

When the temperature and pressure exceed those of the critical point (*i.e.*, $T > T_c$, $p > p_c$; *e.g.* for water: $T_c = 374$ °C, $p_c = 217.6$ bar),[170] representing the terminus of the vapor–liquid coexistence curve, the solvent undergoes a phase transition to form a supercritical

fluid.[171-174] Accordingly, reactions performed under these supercritical conditions are referred to as supercritical fluid (SCF) processes, with the most extensively used solvents being supercritical CO_2, water, and ethanol.[171, 173, 175-177] In the supercritical region, there is no liquid–gas phase boundary and the liquid and gas phases become indistinguishable. The SCF exhibits both properties of a liquid and a gas, in particular a gas-like diffusivity, low viscosity, and a density closer to that of a liquid.[171, 174, 178] In general, the solubilities of the reactants and the mobility of dissolved ions and molecules are increased with increasing temperature, which helps to reduce transport limitations in the synthesis.[179] The physico-chemical properties of the supercritical fluid (such as density, viscosity, dielectric constant, diffusivity, and surface tension) can be fine-tuned by controlling the pressure and temperature of the system, affecting the reactant solubilities and ion mobilities, which can be utilized to control reaction kinetics or the crystal growth to obtain desired dimensions and morphologies.[165, 174-175, 178] Similar but less pronounced effects are observed under subcritical conditions and therefore also play a role in conventional HT and ST syntheses.[165-166, 176]

The main advantage of the HT/ST techniques over conventional solid-state and other wet-chemical methods that feature high-temperature calcination steps, are the relatively low process temperatures and short reaction times. This makes it a cost-effective and environmentally benign ('green chemistry') option.[180-181] Furthermore, the process is rather simple, easily scalable and hence, compatible with industrial manufacturing.[181] In fact, hydrothermal synthesis is well-established for the large-scale production of zeolites, quartz crystals, and nanomaterials.[165, 182] SCF processes, on the other hand, are less common since they require high temperatures (T ~400 °C) and expensive reactors that can withstand the extremely high pressures (typically p ~400 bar; pressure limit of conventional autoclaves: 200 bar, *cf.* Chapter 3.1.2).[174, 183] As solvothermal syntheses are kinetically controlled reactions, the technique further allows isolation of new materials that are not accessible by high-temperature approaches, for example metastable phases and compounds with less common valence states.[165, 168, 180] With regard to functional materials, the option to control and tailor the desired material properties (crystal size, shape, and orientation) by modifying the synthesis conditions is of particular interest.[181]

There are also a few disadvantages to ST processes, such as the need for expensive equipment (stainless-steel autoclaves) and possible safety issues because of the high pressures involved, particularly with regard to SCF processes.[181] Furthermore, the reaction vessels being 'black box' systems, it is difficult to study the reactions *in situ* or to predict their outcome.[165-166, 181] The main drawback of the technique, however, is that it relies on convective heating (*i.e.* the autoclaves are heated by an external heating block), which causes sharp thermal gradients and thus, non-uniform reaction conditions in the vessels.[158, 184-185] As a result, the produced materials often exhibit inhomogeneous particle size distributions and

morphologies. In addition, from a practical point of view, the processes are often limited by slow reaction kinetics and therefore, rather long reaction times of several hours up to weeks are required.[184]

A solution to the limitations of conventional solvothermal processes is offered by using the state-of-the-art microwave technique. While microwave-assisted hydrothermal (MWHT) or solvothermal (MWST) processes underlie the same principles as the conventional ones, they use dielectric heating by microwave irradiation (typical frequency: 2.45 GHz) instead of convective heating.[184-185] Since the energy is selectively transferred to microwave-absorbing materials, thermal gradients inside the reaction vessels are significantly reduced.[158, 184-185] The method therefore ensures uniform nucleation conditions and allows reproducible fabrication of highly crystalline materials with narrow particle size distributions and homogeneous morphologies.[158, 185] Furthermore, because of increased reaction rates, the synthesis time can be reduced to only a few minutes, which offers considerable energy and cost savings.[91, 185] Taking these and the general advantages of the solvothermal technique into account, the MWST technique is therefore particularly appealing for large-scale industrial manufacturing.[158, 184-185]

(b) State of the Art in the Synthesis of Pnma-$LiCoPO_4$

Given the numerous benefits of these various techniques, they are considered a viable approach for the production of active materials.[166-167, 174, 176] Research in the broad field of solvothermal synthesis (HT, ST, SCF, MWHT, MWST) of *Pnma*-$LiCoPO_4$ has been ongoing since the first report of a hydrothermal (HT) synthesis by Huang *et al.*[143] in 2005. Although the process was further developed, in particular by Chen *et al.*[144-145], it was not before 2009 that a HT *Pnma*-$LiCoPO_4$ material was first electrochemically characterized by Zhao and coworkers.[146] The performance of the material that consisted of large, irregular agglomerates (dimensions: ~10–40 µm) of micron-sized primary particles (~1.0 µm × 1.0 µm × 2.0 µm), however, was poor. A capacity of only 15 $mAh \cdot g^{-1}$ was reached at 0.1 C rate (corresponding to ~9% of the theoretical capacity of 167 $mAh \cdot g^{-1}$),[146] which was drastically lower than state-of-the-art capacities of materials produced by solid-state (SS) synthesis (~120–125 $mAh \cdot g^{-1}$, *i.e.* ~72–75%, reached by *e.g.* Lloris,[115] Nakayama,[118] and Wolfenstine[70]). Since then, a number of groups have been working on the optimization of the HT process but also the development of alternative solvothermal (ST), supercritical fluid (SCF), and microwave-assisted (MWHT, MWST) procedures to improve the performance of the material.

The initial discharge capacities reached at 0.1 C between 2009 and 2017 for uncoated *Pnma*-$LiCoPO_4$ as well as carbon-coated *Pnma*-$LiCoPO_4$/C materials produced by the HT, ST, SCF, MWHT, and MWST techniques are compiled in Figure 1.3 (for a detailed listing of the synthesis conditions, particle sizes, morphologies, and performances reported in the years

2009–2016, please refer to the supporting materials of Chapter 6.2). In order to assess the values in this comparison, a discharge capacity of 125 $mAh \cdot g^{-1}$, corresponding to 75% of the theoretical capacity of $LiCoPO_4$ (167 $mAh \cdot g^{-1}$), is deemed a reasonable performance since this is competitive with state-of-the-art values (~120–125 $mAh \cdot g^{-1}$, *i.e.* 72–75%)[70, 115, 118] reached for materials produced by conventional solid-state synthesis. However, it is important to note that the electrode composition (*w*(active material):*w*(conductive carbon):*w*(binder)), cell design, test protocol (potential window, C rate, CV step, etc.) as well as post-processing of the material affect the performance. Furthermore, while uncoated *Pnma*-$LiCoPO_4$ samples reflect the intrinsic performance of the material, coated *Pnma*-$LiCoPO_4$/C samples may show a better performance, in particular at higher C rates. Hence, the values are comparable to a limited extent only.[186]

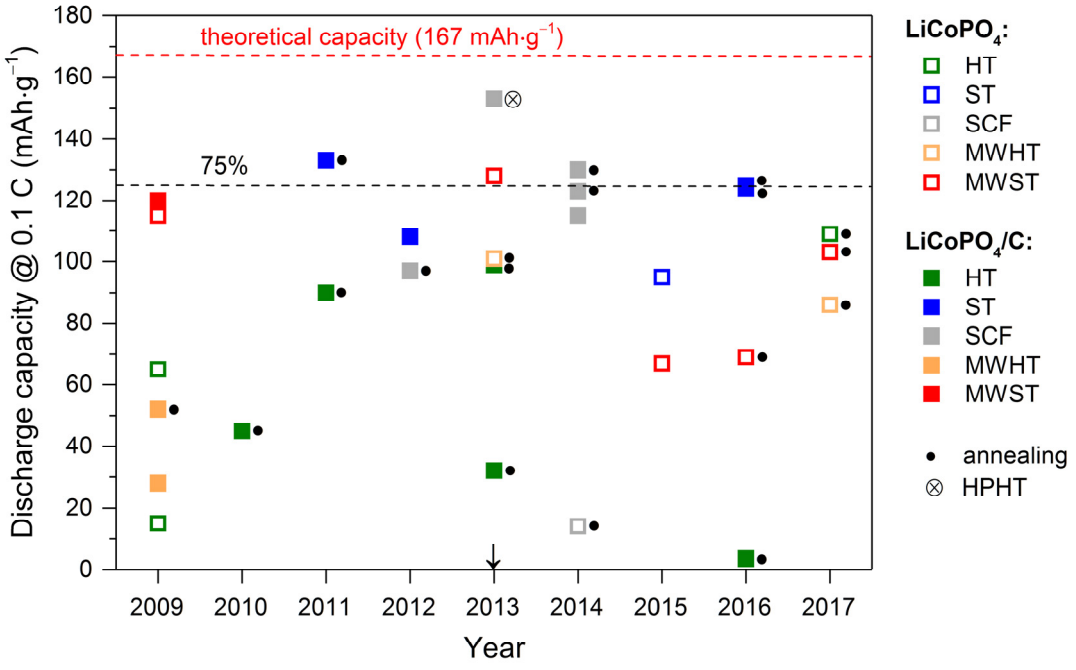

Figure 1.3 Comparison of the initial discharge capacities at 0.1 C reported between 2009 and 2017 for uncoated, pure *Pnma*-$LiCoPO_4$ (□) and carbon-coated *Pnma*-$LiCoPO_4$/C (■) materials synthesized *via* hydrothermal (HT),[96, 146-148, 150-151] solvothermal (ST),[58, 148, 151, 153-154] supercritical fluid (SCF)[56, 112, 114, 162-164] as well as microwave-assisted hydrothermal (MWHT)[91, 156, 187] and solvothermal (MWST)[108, 158-161] procedures. The year 2013, marking the start of this work, is indicated by an arrow (↓). Dots (●) right to the symbols mark materials that underwent additional post heat treatments at high temperatures. The highest capacity of 153 $mAh \cdot g^{-1}$ was reached in 2013 for *Pnma*-$LiCoPO_4$/C nanosheets prepared by a complex high-pressure high-temperature (HPHT) supercritical fluid process (⊗).[114] It is evident that a good performance above 125 $mAh \cdot g^{-1}$, corresponding to 75% (dashed black line) of the theoretical capacity of 167 $mAh \cdot g^{-1}$ of *Pnma*-$LiCoPO_4$ (represented by a dashed red line), is exclusively realized by using SCF, ST or MWST synthesis procedures in combination with post-processing of the material (carbon coating, annealing). The only exception is the MWST process, for which high capacities were reached without additional treatment. The figure was modified and updated on basis of the references [186] and [31] with permission from The Royal Society of Chemistry and Elsevier B.V.

As evident from Figure 1.3, the HT synthesis is the most widely used technique yet the materials generally exhibit the poorest performances. While Zhao *et al.*[146] showed that the initially reported performance of 15 mAh·g^{-1} can be improved to 65 mAh·g^{-1} by using PVP (polyvinylpyrrolidone) as a dispersant in the HT process, the most common optimization strategies are additional post-calcinations at high temperatures (T ~900 °C) in combination with conductive carbon coatings to give *Pnma*-$LiCoPO_4$/C.[96, 147-148, 150-151] The use of post-synthetic thermal treatments serves three purposes: (1) the conversion of carbon precursors to electrically conductive C-coatings,[89, 145, 188] (2) the reduction of Co–Li antisite defects that block the Li diffusion pathways (*cf.* Chapter 1.2.1) and are more likely to appear in materials synthesized at low temperature,[83, 189] and (3) the conversion of metastable intermediates to *Pnma*-$LiCoPO_4$.[156, 190] In fact, only very few reports[143-146, 149] demonstrated the formation of *Pnma*-$LiCoPO_4$ in a single step (notably, with the exception of ref. [146], the obtained materials were not electrochemically characterized). On the other hand, the use of microwave-assisted hydrothermal (MWHT) technique allows a fast one-step synthesis.[91] Although most procedures do not require C-coatings to deliver a performance comparable to the best post-heated, carbon-coated *Pnma*-$LiCoPO_4$/C HT materials (~100 mAh·g^{-1}, *cf.* Figure 1.3),[96, 150] they mostly involve post-annealing steps as well.[91, 156, 187] Hence, the MWHT technique does not constitute a substantial improvement over the HT approach. Taking into account the inferior performance and the requirement of material post-processing, HT and MWHT processes are rather unattractive for the production of high-performance active materials. The main issue of these techniques is that the use of water as a solvent lacks the option of controlling the particle size and shape, resulting in the formation of large, micron-sized particles with irregular shapes and size distributions, and the tendency to form agglomerates, all of which are detrimental to the performance.[146-147, 186]

The development of processes using solvents other than water, *i.e.* solvothermal (ST), supercritical fluid (SCF) and microwave-assisted solvothermal (MWST) techniques, paved the way for improvements (*cf.* Figure 1.3). Because organic solvents reportedly show properties of a soft template[148, 191-192] or capping agent,[181, 185, 193-195] they promote the formation of well-dispersed particles with desired sizes, shapes, and orientations which can have beneficial effects on the electrochemical properties. It should be emphasized that before the start of this work in 2013, there have been only four reports on these three techniques. Murugan and co-workers[158] described the first MWST process, which delivered nano-thumblike particles (dimensions: ~200 nm × 80 nm) with capacities of 115 mAh·g^{-1} ($LiCoPO_4$) and 120 mAh·g^{-1} ($LiCoPO_4$/C), from a tetraethylene glycol (TTEG) solvent. Using a ST process with a mixed water/benzyl alcohol solvent and glucose as carbon precursor, Wang *et al.*[148] synthesized hierarchically structured, hedgehog-like $LiCoPO_4$/C microspheres (~2–3 µm) with nanorod-like primary particles (~35–50 nm × 1 µm) that showed a capacity of 133 mAh·g^{-1} after high-

temperature calcination. Li *et al.,*[153] on the other hand, obtained aggregates (~2–3 µm) of irregular, C-coated $LiCoPO_4$/C particles (~200 nm) with 108 $mAh \cdot g^{-1}$ from ST synthesis. The first SCF process was reported by Devaraju and co-workers.[112] With the help of an oleylamine surfactant, platelets with dimensions of ~100–200 nm × 50–250 nm × 5–15 nm were produced in supercritical ethanol, which achieved ~97 $mAh \cdot g^{-1}$ after ball milling, C-coating, and post-heating. Since 2013, a variety of particle shapes could be realized with the ST, SCF, and MWST techniques, specifically rods,[160, 162] spindles,[151] platelets,[154-155, 162] disks,[163] and sheets.[114, 163] However, a large number of studies[56, 58, 108, 151, 159, 162, 164] also reported the formation of crystals with irregular or undefined shapes and sizes and hence, inferior electrochemical performance, which reflects the ongoing difficulties with particle size and morphology control in such processes. In fact, in the period of 2014–2017, in parallel to this work, no improvement in performance could be reached for any of the three methods (*cf.* Figure 1.3).

In general, three trends could the observed for the synthesis of particles with desired properties. MWST syntheses were exclusively based on pure tetraethylene glycol (TTEG) as a solvent (common synthesis conditions: T = 240–300 °C, t = 15–30 min), predominantly delivering rod- or thumb-shaped particles in a single step without post-annealing.[108, 158-161] Surprisingly, the best performance of a MWST material (128 $mAh \cdot g^{-1}$) was reached for irregularly shaped, uncoated *Pnma*-$LiCoPO_4$ particles of ~0.2–1 µm in size.[159] In ST synthesis on the other hand, the use of binary solvent systems combining water and an organic solvent (in specific benzyl alcohol,[148] ethylene glycol,[151, 154-155] and diethylene glycol[58]; conditions: T = 180–240 °C, t = 5–100 h) has recently become very popular. The solvent blend is supposed to be beneficial for effectively regulating the morphology due to the soft template effect[148, 191-192] of the organic component, and also promotes the complete dissolution of the starting materials with the help of the aqueous phase.[186] Despite the fact that different shapes (platelets, spindles; sizes around 0.5–1 µm)[151, 154-155] could be realized, the initial performance of Wang *et al.*[148] in 2011 (133 $mAh \cdot g^{-1}$) could not be improved. Moreover, good performances were still only reached with the help of post-annealing and C-coatings.[58, 151] Since Li mobility in the olivine structure is one-dimensional along the [010] direction (*cf.* Chapter 1.1), reducing the Li diffusion pathways along this direction is considered a viable approach to improve the electrochemical performance. Hence, there has been enormous interest in synthesizing nanostructured materials with the [010] axis along the shortest dimension of the crystallites. With the exception of [010]-oriented nanocrystals synthesized by a PVP-supported ST process, which unfortunately were not characterized electrochemically,[152] this was exclusively accomplished by SCF methods performed in supercritical ethanol (T = 380–400 °C, t = 6–60 min, p = 400 bar) as shown in a number of studies by Truong and Devaraju.[112, 162-164] In these processes, the crystal shape and orientation was tailored with the help of surfactants, structure directing or capping agents such as oleylamine,[112] benzylamine,[163] hexamethylene-

diamine (HMD) or hexamethylenetetraamine (HMT).[162] As expected, the resulting unique nanoplatelets (lateral dimensions: ~200–800 nm, thickness: ~50 nm) with shortened Li migration pathways showed generally high performances with capacities in the range of 97–130 mAh·g^{-1}. However, as in the case of ST materials, post-calcinations and C-coating were required to reach such performances.

With an initial discharge capacity of 153 mAh·g^{-1} and a remarkable capacity retention of 88% after 50 cycles, the best performance reported to date for any *Pnma*-$LiCoPO_4$-type material was reached in 2013 by Rui and co-workers[114] for carbon-coated $LiCoPO_4$/C nanosheets with lateral dimensions of ~500 nm and a thickness of only 4.6 nm in the [010] direction. The high-pressure high-temperature (HPHT) supercritical fluid (SCF) process used to produce these nanosheets applied a different synthetic strategy to reduce the particle dimension along [010] than the aforementioned conventional SCF procedures.[112, 162-164] Instead of using an additive in a one-pot synthesis, the novel process was based on a liquid-phase exfoliation approach combined with a high-pressure high-temperature (HPHT) SCF lithiation process. In detail, bulk $NH_4CoPO_4 \cdot H_2O$ was produced in a solid-state reaction using polyethylene glycol (PEG) as a surfactant (t = 60 h), followed by swelling (t = 12 h) and ultrasonic exfoliation (t = 3 d) in a formamide solution. The as-obtained $NH_4CoPO_4 \cdot H_2O$ precursor nanosheets were dispersed in ethanol with the help of PVP and then converted with lithium acetate to $LiCoPO_4$/C nanosheets by a HPHT SCF lithiation in supercritical ethanol (T = 400 °C, p = 100 bar, t = 2 h). Despite the impressive performance of the material, the complex process, however, cannot be regarded feasible from a practical or economical perspective. The long synthesis time (total: > 1 week), many recovering steps in between the individual process steps, specialized equipment (autoclaves suitable for high pressures and temperature, *e.g.* using graphite gaskets), the toxic chemicals (formamide) and the extremely small yield (< 10 mg) preclude easy scale-up and industrial applicability.

In summary, materials produced from hydrothermal techniques (HT, MWHT) generally deliver inferior performance due to the lack of morphology and particle size control. Techniques using solvents other than water (ST, MWST, SCF) are more promising due to the possibility of producing particles with defined sizes and shapes, and in selected cases have been shown to deliver materials with reasonable electrochemical performances higher than 75% (*i.e.*, 125 mAh·g^{-1}) of the theoretical capacity of $LiCoPO_4$ (*cf.* Figure 1.3). In particular, particles with reduced dimensions along the [010] direction of the Li migration pathways such as sheets and platelets have demonstrated superior electrochemical properties. These anisotropic crystal shapes, however, are predominantly accessible by SCF methods that involve rather harsh synthesis conditions (T = 400 °C, p = 400 bar) that are undesirable with regard to safety and cost. The best performance to date (153 mAh·g^{-1}, corresponding to 92% of the theoretical capacity of $LiCoPO_4$) has been reached in 2013 for [010]-oriented $LiCoPO_4$/C nanosheets

produced by a complex, multistep high-pressure high-temperature SCF process[114] that lacks industrial applicability due to reasons discussed before. A simpler and faster synthetic approach with milder reaction conditions (pressure, temperature) towards *Pnma*-$LiCoPO_4$ particles with reduced [010] dimensions that is compatible with large-scale industrial manufacturing is yet to be fully developed. Moreover, despite the advances in morphological tuning, the majority of ST and SCF processes still require additional post-calcinations at temperatures as high as 900 °C and/or carbon coating of the materials to reach high capacities. The only exception is the MWST approach for which an as-prepared (*i.e.* no annealing or coating) *Pnma*-$LiCoPO_4$ material has demonstrated a good performance of 128 $mAh \cdot g^{-1}$ (77% of the theoretical capacity),[159] which is comparable with post-heated, carbon-coated *Pnma*-$LiCoPO_4$/C materials produced by ST and conventional SCF methods (*cf.* Figure 1.3). Since C-coatings cause a significant decrease in practical energy density, only active materials with low carbon contents or better, without carbon, and thus higher energies will be competitive as cathode materials for future Li-ion batteries, in particular with regard to electric mobility applications.[195] Therefore, the rather simple one-step MWST technique, which is also appealing because of short reaction times and low synthesis temperatures, is probably the most promising approach for producing high-performance *Pnma*-$LiCoPO_4$. However, despite the advantages of the MWST technique compared to HT, ST, and SCF methods, the number of reports is still very limited. Hence, the MWST approach represents the least developed and investigated out of the field but shows large potential for improvements. While different solvent systems have been shown to tune the morphology in ST synthesis,[58, 148, 151, 154-155] MWST procedures have so far only been based on TTEG as a solvent, invariably producing thumb- or rod-like morphologies. Furthermore, as opposed to very few reports[151, 155] on ST syntheses, the relationship between the synthesis conditions, crystal properties, and the electrochemical performance has not been investigated for the MWST technique except for the pH value.[159] As a result, the systematic implementation of particle size, morphology, and orientation tuning approaches for improving the electrochemical performance of *Pnma*-$LiCoPO_4$ are still overdue. Rather than a phenomenological description of the structure–morphology–performance relationship as shown in previous studies,[158-159] only a fundamental and thorough understanding of the crystal growth conditions and the effects on the material properties will allow further developments in the field.

1.3 Metastable, Non-Olivine $LiCoPO_4$ Polymorphs

1.3.1 Overview and Comparison with Olivine-Type *Pnma*-$LiCoPO_4$

In addition to the thermodynamically stable olivine *Pnma*-$LiCoPO_4$, two other, non-olivine $LiCoPO_4$ polymorphs have been reported that are metastable and belong to the space groups *Pna*2_1 and *Cmcm*, respectively. Whereas the majority of studies has been focused on the olivine phase due its high potential as a cathode material, the *Pna*2_1 and *Cmcm* modifications, which were discovered about half a century later, have been considerably less investigated. The current state of research on the three $LiCoPO_4$ polymorphs (*Pnma*, *Pna*2_1, and *Cmcm*) is compiled in Table 1.2.

Whereas *Pnma*-$LiCoPO_4$ is accessible by a plethora of different synthesis techniques (see also Chapter 1.2.1), its metastable modifications can be almost exclusively obtained by kinetically controlled low-temperature techniques, namely microwave-assisted hydrothermal (MWHT) and solvothermal (MWST) synthesis.[160, 196] The only exception is *Cmcm*-$LiCoPO_4$ for which until very recently only a high-pressure high-temperature (HPHT) solid-state (SS) route (T = 900 °C, p > 6 GPa)[197] was known. Due to the limited amount of synthesis pathways, approaches to tailor the crystal properties have not been thoroughly investigated.

As discussed in Chapter 1.1, *Pnma*-$LiCoPO_4$ adopts the Mg_2SiO_4 (olivine) structure type,[14] which features $[CoO_6]$ octahedra, $[PO_4]$ tetrahedra, and Li ions in octahedral (CN = 6) voids (see also Chapter 1.1, Figure 1.1).[13] In the denser Na_2CrO_4-type[198-199] high-pressure modification *Cmcm*-$LiCoPO_4$ (*cf.* cell volumes V in Table 1.2), the CN of the Li ions is reduced to 4 ($[LiO_4]$ units), whereas the arrangement of the $[CoO_6]$ and $[PO_4]$ units is changed (for details see Chapter 1.3.3, Figure 1.5).[197] The *Pna*2_1-$LiCoPO_4$ framework (δ_1-$LiZnPO_4$ structure type),[200] which is the least dense structure, shows an exclusively tetrahedral coordination with $[CoO_4]$ and $[PO_4]$ units, and Li ions occupy tetrahedral voids (CN = 4; see also Chapter 1.3.2, Figure 1.4).[196] Notably, while all transition-metal homologues with *Pnma* and *Cmcm* structures exist[13, 201] in the Li*M*PO_4 (*M* = Fe, Mn, Co, Ni) family, with the Mn- and Co-based *Cmcm* phases having been discovered very recently,[160, 202], *Pna*2_1-$LiCoPO_4$ to date is the only known representative of the δ_1-$LiZnPO_4$ structure type.

As a result of the different crystal structures and building blocks, the three polymorphs exhibit different material properties. While the *Pnma* and *Cmcm* phases exhibit a purple[119] to violet[203] or pink color,[160] *Pna*2_1-$LiCoPO_4$ is dark blue[196] (for images of the powders refer to Chapter 4, Figures 4.1, 4.6, and 4.8). The variation in color can be explained by the occurrence of the tetrahedral (T_d) $[CoO_4]$ units in the *Pna*2_1 structure as opposed to the octahedral (O_h) $[CoO_6]$ units in the *Pnma* and *Cmcm* phases.[204] Since the crystal field splitting energy in a T_d

field Δ_t is significantly smaller than in a O_h field ($\Delta_t \approx 4/9\ \Delta_o$),[205] the energy of the photons absorbed by *Pna*2_1-$LiCoPO_4$ will be lower than in the case of *Pnma*- and *Cmcm*-$LiCoPO_4$ (*e.g.* orange light *vs.* green light), whereas higher-energy wavelengths (*e.g.* blue light *vs.* red light) are transmitted. As a result, the materials will show different colors.

Also the electrochemical potential of the Co^{2+}/Co^{3+} redox couple *versus* Li/Li^+ is affected by the different bonding environments of the cobalt ions in the structures. Whereas the lowest redox potential (4.3 V)[160] is observed for *Cmcm*-$LiCoPO_4$, *Pna*2_1-$LiCoPO_4$ exhibits the highest potential (5.0 V)[160, 196] of the $LiCoPO_4$ family and hence, the highest theoretical energy density (835 $Wh \cdot kg^{-1}$). However, as opposed to the olivine, for which a maximum practical capacity of 153 $mAh \cdot g^{-1}$ (corresponding to 92% of the theoretical capacity of 167 $mAh \cdot g^{-1}$) could be realized for an optimized material,[114] first reports on the electrochemical performance of the metastable *Pna*2_1 and *Cmcm* polymorphs were disappointing and maximum capacities of only 33 $mAh \cdot g^{-1}$ and 6 $mAh \cdot g^{-1}$ (*i.e.* 20% and 4% of the theoretical capacity) could be reached, respectively.[160] Notably, the number of reports is extremely limited, and to date, no attempt was made to optimize the performance of these materials using modification strategies similar to the olivine (*i.e.* size and morphology tuning, conductive coatings, doping; *cf.* Chapter 1.2.1).

Whereas the magnetic properties of the olivine *Pnma*-$LiCoPO_4$ have been explored in a vast number of studies[206-214], considerably less is known about the magnetic features of *Pna*2_1-$LiCoPO_4$.[196, 213] The magnetic properties of the *Cmcm* phase have not been investigated. Both the *Pnma* and *Pna*2_1 polymorphs show an antiferromagnetic order below the Néel temperature T_N, with T_N being significantly lower for *Pna*2_1-$LiCoPO_4$ (11 K or 7 K)[196, 213] compared to the olivine (21.6 K),[215-216] which demonstrates the close relationship between structural and magnetic features. The magnetic moments μ_{eff} of both compounds exceed the spin-only value of 3.87 μ_B expected for high-spin (HS) Co^{2+} ($3d^7$ configuration),[196, 213] indicating non-negligible orbital contributions.[213]

Olivine-type *Pnma*-$LiCoPO_4$ is reportedly thermally stable up to 900 °C.[143, 145] The metastable *Pna*2_1 and *Cmcm* phases, on the other hand, undergo irreversible transformations to the olivine structure upon heating, suggesting that *Pnma*-$LiCoPO_4$ corresponds to the thermodynamic ground state of that compound. While the transition temperature of *Pna*2_1-$LiCoPO_4$ is considerably lower than that of *Cmcm*-$LiCoPO_4$ (T ~425 °C),[160] different temperatures have been reported (T ~221 °C and ~340 °C).[160, 196] Furthermore, for both polymorphs, the information on the enthalpy of this transformation is either lacking or contradictory.

In the following chapters, the synthesis pathways, crystal structures, and material properties (electrochemical, magnetic, and thermal) of *Pna*2_1- and *Cmcm*-$LiCoPO_4$ are discussed in detail.

Table 1.2 Comparison of the synthesis methods and material properties of the three reported $LiCoPO_4$ polymorphs.[a]

Polymorph	***Pnma*-$LiCoPO_4$**	***Cmcm*-$LiCoPO_4$**	***Pna*2$_1$-$LiCoPO_4$** [b]
Year of first report	1965[217]	2009[197]	2013[196]
Color	violet[203]/purple[119]	light pink[160]	blue[196]
Synthesis methods	SS,[51, 119, 123] SG,[124, 126-127] SP,[109, 139] PO,[92, 141] HT,[143-144, 146, 150] ST,[148, 154] SCF,[112, 114, 164] MWHT,[91] MWST[158-159]	HPHT SS[197], MWST[161]	MWHT[196], MWST[160]
Crystal structure			
Structure type	Mg_2SiO_4[14]	Na_2CrO_4[198-199]	δ_1-$LiZnPO_4$[200]
Building blocks	[LiO_6], [CoO_6], [PO_4]	[LiO_4], [CoO_6], [PO_4]	[LiO_4], [CoO_4], [PO_4]
a (Å)	10.2057(1)	5.423(1)	10.023(8)
b (Å)	5.9228(1)	8.161(1)	4.963(4)
c (Å)	4.7009(1)	6.222(0) [c]	6.724(7)
V (Å^3)	284.15 [d, 218]	275.40 [d, 160]	334.569 [d, 196]
Electrochemical properties			
Potential *vs.* Li/Li^+ (V)	4.8[37]	4.3[160]	5.0[160, 196]
Theor. capacity (mAh·g^{-1})	167	167	167
Exp. capacity (mAh·g^{-1})	153[114]	6[160]	33[160]
Theor. energy density (Wh·kg^{-1})	802	718	835
Magnetic properties			
T_N (K)	21.6[215-216]	– [e]	11[196]/7[213]
μ_{eff} (μ_B)	5.1[213]	– [e]	4.4[196, 213]
Thermal stability	stable up to *T* = 900 °C[143, 145]	transition to *Pnma*-$LiCoPO_4$ at *T* ~425 °C (– [e])[160]	transition to *Pnma*-$LiCoPO_4$ at *T* = 221 °C (exo)[196]/ *T* = 340 °C (endo)[160]

[a] Abbreviations: endo, endothermic; exp., experimental; exo, exothermic; HPHT, high-pressure high-temperature; HT, hydrothermal; MWHT, microwave-assisted hydrothermal; MWST, microwave-assisted solvothermal; PO, polyol; SCF, supercritical fluid, SG, sol-gel; SP, spray pyrolysis; SS, solid-state; ST, solvothermal; theor., theoretical. [b] Note that the structure was originally reported in space group *Pn*2$_1$*a*. For consistency reasons, the standard setting *Pna*2$_1$ is used in this work. [c] Standard deviation of 0 reported. [d] Standard deviations not reported. [e] Not reported.

1.3.2 Tetrahedrally Coordinated *Pna*2_1-$LiCoPO_4$

The *Pna*2_1-$LiCoPO_4$ modification, which adopts the exclusively tetrahedrally coordinated δ_1-$LiZnPO_4$ structure type,[200], to date represents the only known phase with tetrahedrally coordinated Co^{2+} ions other than $Li_4Co(PO_4)_2$ (space group: *P*2_1/*a*).[219] The phase was theoretically predicted in 2009 by Hautier and co-workers[40] based on high-throughput *ab initio* DFT calculations on phosphate cathodes. Surprisingly, the *Pna*2_1-$LiCoPO_4$ structure was predicted to be significantly more stable than the *Pnma*-$LiCoPO_4$ olivine structure, whereas the Fe and Mn structures were computed to be slightly less stable than the corresponding olivines.[40] In fact, *Pna*2_1-$LiCoPO_4$ to date is the only representative of the Li*M*PO_4 (*M* = Fe, Mn, Co, Ni) family that adopts the δ_1-$LiZnPO_4$ structure.

Its first experimental evidence was provided in 2013 by Jähne *et al*.[196] In 2015, it was revisited by Kreder and co-workers.[160] (Note that the structures were reported in *Pn*2_1*a*, a non-standard setting of the space group *Pna*2_1. For consistency reasons, the structure is referred to as *Pna*2_1-$LiCoPO_4$ using the conventional setting throughout this work.) Both groups described microwave-assisted procedures (MWHT and MWST synthesis) towards the phase, in both cases using acetates as starting materials and alkaline conditions.[160, 196] The MWHT process by Jähne[196] delivered micrometer-sized (~10 µm) crystals with an octahedra-like morphology, whereas the MWST process by Kreder[160] in a tetraethylene glycol (TTEG) solvent produced nanorods (~200 nm × 1 µm), demonstrating that the product morphology is influenced by the synthesis conditions. The formation of *Pna*2_1-$LiCoPO_4$ in the MWHT process[196] was found to compete with olivine-structured *Pnma*-$LiCoPO_4$,[218] $Co_2(OH)PO_4$,[220] and Li_3PO_4,[221] the key parameters being the synthesis temperature, pH, and precursor concentration.[196] As a result, the synthesis parameter region where pure *Pna*2_1-$LiCoPO_4$ can be obtained was found to be rather small, the optimum being reached at *T* = 220 °C, pH = 9.0, and $c(Co^{2+})$ = 0.04 mol/L. The MWST process, on the other hand, allows the production of all three $LiCoPO_4$ modifications by varying the synthesis conditions, the critical parameters being the water content of the solvent and the absence or presence of ammonium hydroxide. While the conditions necessary to obtain the *Pnma* and *Cmcm* polymorphs were examined in detail (see Chapter 1.3.3), the formation mechanism of *Pna*2_1-$LiCoPO_4$ has not been discussed.

Unlike the *Pnma* and *Cmcm* polymorphs that feature $[CoO_6]$ octahedra and $[PO_4]$ tetrahedra as building units, the three-dimensional *Pna*2_1-$LiCoPO_4$ network is built from chains of corner-sharing $[CoO_4]$ and $[PO_4]$ tetrahedra (Figure 1.4).[196] The Li^+ ions occupy tetrahedrally coordinated interstitial positions ($[LiO_4]$ units, CN = 4) of the framework. In contrast to the olivine-type *Pnma* structure, which features Li channels along [010] and [001] (*cf.* Chapter 1.1, Figure 1.1), no direct Li channels are found in *Pna*2_1-$LiCoPO_4$. As shown in

Figure 1.4c, possible tunnels are blocked by [CoO_4] tetrahedra along [001]. Along the [100] direction (Figure 1.4a), zig-zag-like channels are observed with Li–Li distances of *d*(Li–Li) = 5.047 Å. Distorted six-ring channels of alternating [CoO_4] and [PO_4] units with Li ions in the resulting voids are observed along [010] (Figure 1.4b). Although these channels offer direct connections between the Li ions, the Li pathways are still very long (*d*(Li–Li) = 4.963 Å). Due to the fact that the Li–Li distances along both the [100] and [001] directions are rather large (*i.e.*, approximately doubled compared to the olivine structure), these channels cannot be considered as suitable Li migration pathways. As a result, the activation energy for Li transport along these paths will be very high and *vice versa*, the ionic and electrical conductivities very low.[160, 196]

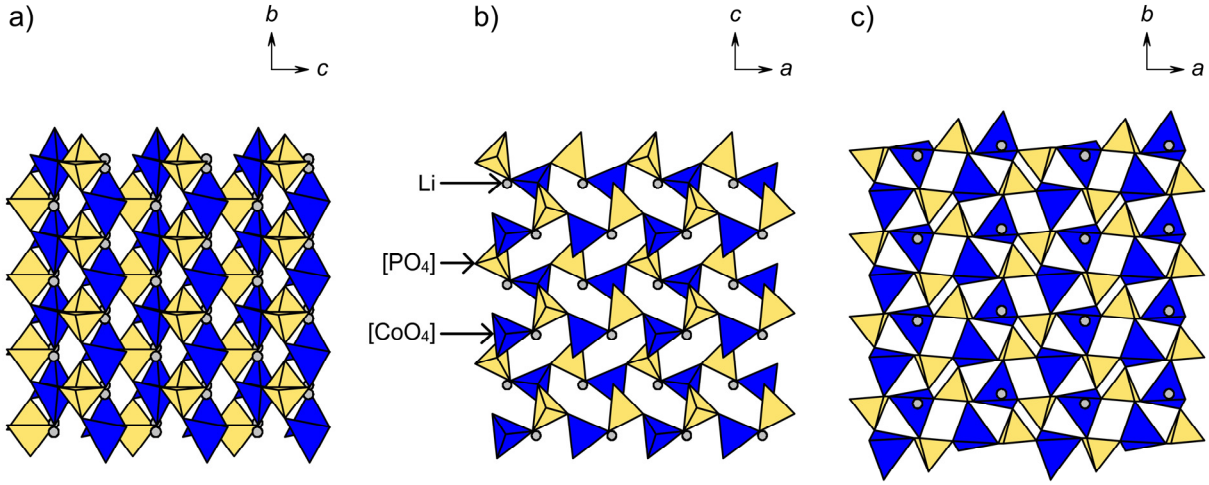

Figure 1.4 Polyhedral representation of the crystal structure of *Pna*2_1-$LiCoPO_4$ (*Z* = 4) viewed along the three crystallographic axes: (a) [100], (b) [010], and (c) [001]. The three-dimensional framework is built from chains of corner-sharing [CoO_4] (blue) and [PO_4] (yellow) tetrahedra with Li ions (grey) occupying tetrahedral sites (CN = 4). The structure does not feature direct channels for Li migration because of long Li–Li distances (see text). The figure was adapted from reference [222], Copyright (2017), with permission from Elsevier Inc.

Regarding the crystal structure, there are some issues that remain unresolved. As already mentioned, the structure was solved using the space group *Pn*2_1*a*,[160, 196] a non-standard setting of the space group *Pna*2_1. Due to the fact that the structure contains only T_d building blocks, it was referred to as $LiCoPO_4^{tetra}$.[196] Because of this notation, the structure was mistakenly described as being a tetragonal $LiCoPO_4$ modification in most reports[156, 196, 213] despite the space group *Pna*2_1 being associated with an orthorhombic crystal system. Although elemental analysis suggested a stoichiometric composition of the material with a molar ratio of *n*(Li):*n*(Co):*n*(P) ~1:1:1, this was not reflected in the structure solution by Jähne *et al.*[196]. In fact, a site occupancy factor (*s.o.f.*) of 122% was refined for the Li position. The point that this population is not reasonable from a physical standpoint and thus indicated a higher degree of

electron density on this site was not addressed. The refinement of Kreder *et al.*[160], on the other hand, assumed a fully populated Li site (*s.o.f.* = 100%) yet the reliability factors were rather high (*e.g.* R_{wp} = 31.4%, χ^2 = 1.78). Taking these flaws into account, a correct structure solution for *Pna*2_1-$LiCoPO_4$ is yet to be presented.

The redox potential of 4.95 V *vs.* Li/Li^+ for *Pna*2_1-$LiCoPO_4$, and accordingly also the energy density of 835 $Wh \cdot kg^{-1}$ are the highest of the three $LiCoPO_4$ modifications.[160, 196] The cyclic voltammogram showed a single redox peak, indicating that the compound is delithiated in a single step with no intermediate phases involved.[196] The electrochemical performance, however, was found to be poor and initial discharge capacities of only 27 $mAh \cdot g^{-1}$ [196] and 33 $mAh \cdot g^{-1}$ [160] were reached (corresponding to 16% and 20% of the theoretical value of 167 $mAh \cdot g^{-1}$), which faded quickly upon cycling. The poor performance was suggested to be related to similar issues as with the olivine, such as electrolyte decomposition at high voltage (> 4.5 V, *cf.* also Chapter 1.2.1),[55, 88] metal dissolution[223-224] and structural degradation[78] due to HF formation from residual water in the sample.[196] In addition to these extrinsic factors, a number of intrinsic reasons were discussed. In addition to the kinetic limitation caused by the poor electrical and ionic conductivities, possible volumetric changes upon cycling and the metastable nature of the material might represent an issue which leads to phase transitions or amorphization.[196] In order to tackle these limitations, particle size control, post-processing of the material (*e.g.* by carbon coating), and the use of electrolytes suitable for the potential window were suggested.[160, 196] However, to date, no attempts have been made to optimize the performance using these approaches or to investigate the reasons for the poor electrochemical performance from a fundamental point of view.

Magnetic measurements indicated a paramagnetic Curie–Weiss-like behavior at high temperatures, and a long-range antiferromagnetic order below a temperature of T_N = 11 K,[196] which was re-determined to be at 7 K in a later study.[213] The effective magnetic moment μ_{eff} is 4.4 μ_B, which exceeds the expected spin-only value of 3.87 μ_B for high-spin Co^{2+} ($3d^7$, S = ⅔). ^7Li and ^{31}P NMR spin lattice relaxation experiments further revealed that the exchange interactions between the Co^{2+} spins are significantly smaller in *Pna*2_1-$LiCoPO_4$ than in the *Pnma* structure. The different spin dynamics were correlated with a strong geometrical spin frustration due to the corner-shared $[CoO_4]$–$[PO_4]$ geometry, which may result in incommensurate magnetic ordering.[213]

Studies on the thermal stability of *Pna*2_1-$LiCoPO_4$ showed that the compound irreversibly transforms to the olivine-type *Pnma*-$LiCoPO_4$ phase at elevated temperatures.[160, 196] In contrast to the findings by Hautier *et al.*,[40] which based on DFT simulations suggested a higher stability of the *Pna*2_1 phase compared to the *Pnma* one, this indicates that *Pna*2_1-$LiCoPO_4$ exhibits a metastable character and that the olivine-type *Pnma*-$LiCoPO_4$ is the thermodynamically more stable polymorph. Interestingly, different phase transition temperatures were

reported for *Pna*2$_1$-$LiCoPO_4$ upon heating under an inert argon atmosphere. Jähne *et al.*[196] showed that the transformation occurs in a pronounced exothermic process at 221 °C (total weight loss: < 1 wt%), which was supported by TGA/DSC and combined *ex situ* annealing and PXRD experiments. Because of the broad DSC signal width of ~50 °C and the fact that the transition was incomplete when the powder was heated to 220 °C, it was suggested[196] that the phase transition is possibly affected by the crystallographic domain or particle size but no further studies were conducted to provide evidence for this assumption. Contrary to that, Kreder *et al.*[160] on the basis of TGA/DSC data claimed that the phase transition occurs at 340 °C and is endothermic. The discrepancy with the Jähne study[196] was not addressed and no PXRD data of the post-TGA/DSC material were provided. Since the *Pna*2$_1$–*Pnma* phase transformation can be used to produce hierarchically structured, electrochemically active olivine-type *Pnma*-$LiCoPO_4$ materials in a two-step process by post-annealing of *Pna*2$_1$-$LiCoPO_4$ as an intermediate as shown in another report,[156] a fundamental and thorough understanding of the transition process and an explanation for these contradictory findings will be crucial in order to further explore this synthesis route.

1.3.3 High-Pressure *Cmcm*-$LiCoPO_4$

Although *Cmcm*-$LiCoPO_4$ was first reported four years earlier than *Pna*2$_1$-$LiCoPO_4$ (2009) by Amador and co-workers,[197] it represents the least investigated polymorph of the $LiCoPO_4$ family. This is probably related to the fact that it was only accessible through an experimentally complicated high-pressure high-temperature (HPHT) synthesis route, treating olivine-type *Pnma*-$LiCoPO_4$ at a temperature of 900 °C and pressures above 6 GPa in a Walker-type multianvil module.[197, 225] An alternative low-temperature (T = 260 °C) microwave-assisted solvothermal (MWST) pathway towards *Cmcm*-$LiCoPO_4$ particles with a nanosheet-like morphology (dimensions: 1−3 µm × 200 nm × 50 nm) was described recently by Kreder *et al*.[160] Based on the same MWST process used for the synthesis of *Pna*2$_1$-$LiCoPO_4$ in a TTEG (tetraethylene glycol) solvent (*cf.* Chapter 1.3.2), the formation of the *Pnma* and *Cmcm* polymorphs was found to be highly sensitive towards the water content of the solvent. Since 2 vol% H_2O in the TTEG solvent already resulted in 22 wt% *Pnma*-$LiCoPO_4$ in the product, the formation of pure (> 99 wt%) *Cmcm*-$LiCoPO_4$ required the use of anhydrous phosphoric acid and freshly dried TTEG. Interestingly, by modifying the reaction parameters (type and amount of precursor, synthesis temperature and time), the MWST process can also be used to produce the isostructural Fe-, Mn-, and Ni-based *Cmcm* phases.[202]

Similarly to *Pnma*-$LiCoPO_4$, the structure of *Cmcm*-$LiCoPO_4$ features octahedral [CoO_6] and tetrahedral [PO_4] building blocks (Figure 1.5). The Li^+ ions are located on tetra-

hedral sites and form $[LiO_4]$ units (as opposed to $[LiO_6]$ units in the *Pnma* structure). As illustrated in Figure 1.5a, the $[CoO_6]$ octahedra are connected to $[CoO_6]_\infty$ strands *via* shared edges, which run along the [001] direction.[197, 201] The $[CoO_6]_\infty$ rows are further cross-linked along [100] by alternating pairs of edge-sharing $[PO_4]$ and $[LiO_4]$ tetrahedra, forming layers of the composition $([CoO_6][LiO_4][PO_4])_\infty$ in the *ac* plane (one such layer is displayed in Figure 1.5b). These layers are in turn stacked along the [010] direction in the sequence AB (as indicated by black and grey boxes in Figure 1.5a and c) with a displacement of *a*/2 *via* apical oxygen atoms of the $[CoO_6]$ units. As a result, a three-dimensional framework is formed. Although Li channels seem to be running along [100] (Fig. 2a), the tetrahedral Li sites can be considered isolated since the Li–Li distances are very long (> 5 Å),[226] which is in fact even larger than in *Pna*2_1-$LiCoPO_4$ (*cf.* Chapter 1.3.2). Analogous to the *Pna*2_1 structure, Li mobility along this path will thus be hindered.[197, 201] It is worth mentioning that although elemental analysis of the material indicated a surplus of lithium and a deficit in cobalt (molar ratio *n*(Li):*n*(Co):*n*(P) = 1.04:0.96:1.00), the material was considered to be stoichiometric.[160] Therefore, the occupancy factors of the Li and Co sites were kept fixed at 100% in the Rietveld refinement. The rather high reliability factors of R_{wp} = 21.9% and χ^2 = 1.71, however, suggest that the structure is not sufficiently described by this solution.

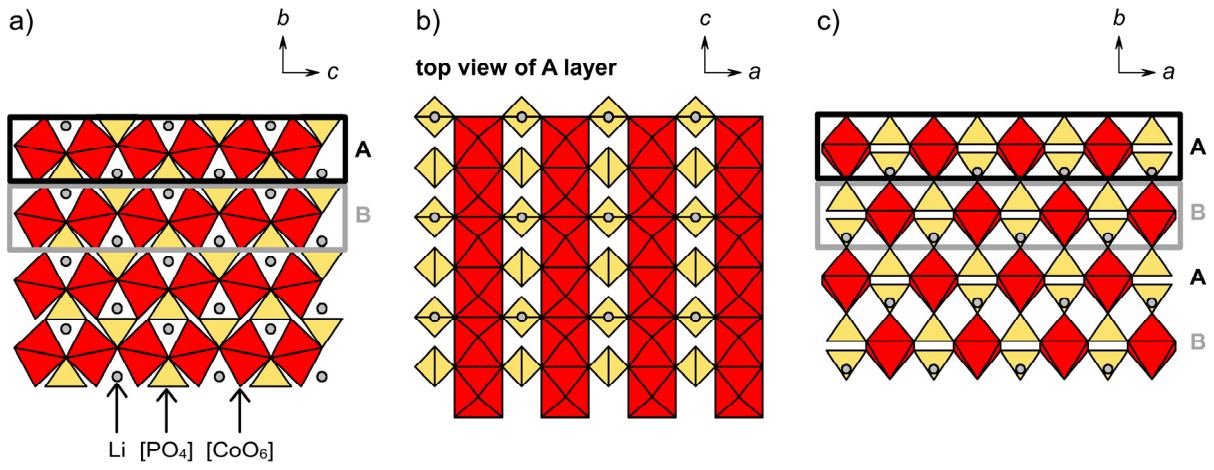

Figure 1.5 Polyhedral representation of the crystal structure of *Cmcm*-$LiCoPO_4$ (Z = 4) viewed along the three crystallographic axes: (a) [100], (b) [010] (showing one A layer as indicated by the black boxes in a and c), and (c) [001]. $[CoO_6]$ octahedra are displayed in red, $[PO_4]$ tetrahedra in yellow, and tetrahedrally coordinated Li ions (CN = 4) in grey. The structure is built from $([CoO_6][LiO_4][PO_4])_\infty$ layers in the *ac* plane (b), which are stacked along [010] in the sequence AB (a, c). The Li sites are isolated because of large Li–Li distances along [010], as a result of which the Li migration is hindered (see text). The figure was adapted from reference [226]. – Published by The Royal Society of Chemistry.

Cmcm-$LiCoPO_4$ shows a single redox peak at ~4.3 V *vs.* Li/Li^+,[160] which is the lowest redox potential of all $LiCoPO_4$ polymorphs. As a result, the theoretical energy density of

718 $Wh \cdot kg^{-1}$ is also the lowest of the $LiCoPO_4$ family. An extremely low discharge capacity of 6 $mAh \cdot g^{-1}$ (corresponding to merely ~4% of the theoretical capacity of 167 $mAh \cdot g^{-1}$) has been reported, which was attributed to the poor conductivity of the material.[160] It was suggested that the poor performance might be improved by applying material modification strategies similar to those used for *Pnma*-type $LiCoPO_4$, such as conductive coatings or ball milling.[160]

Notably, the magnetic properties of *Cmcm*-$LiCoPO_4$ have not been investigated. This is surprising since cobalt-based compounds in general exhibit interesting magnetic features as is true for the *Pnma* and *Pna*2_1 polymorphs (*cf.* Chapter 1.3.1, Table 1.2 and Chapter 1.3.2).

The investigation of the thermal stability up to 500 °C under an Ar stream using TGA/DSC revealed an endothermic event at ~400 °C, which was accompanied by a small mass loss of ~0.5 wt% that remained unexplained.[160] No further signals were observed. The *ex situ* PXRD analysis of samples annealed at different temperatures (T = 400–625 °C, increment step: 25 °C, argon stream) led to the conclusion that *Cmcm*-$LiCoPO_4$ is metastable and starts to transform to the *Pnma* phase around 425 °C, with the transformation not being completed before 600 °C. Unfortunately, no PXRD data were provided in the report[160] to further substantiate these findings. Furthermore, the design of the study did not allow to gain information about the high-temperature behavior (T > 625 °C) of the phase or possible phase transitions upon cooling.

1.4 References

[1] Poizot, P.; Dolhem, F., Clean energy new deal for a sustainable world: from non-CO_2 generating energy sources to greener electrochemical storage devices. *Energy Environ. Sci.* **2011,** *4*, 2003–2019.

[2] Hayner, C. M.; Zhao, X.; Kung, H. H., Materials for rechargeable lithium-ion batteries. *Annu. Rev. Chem. Biomol. Eng.* **2012,** *3*, 445–471.

[3] Etacheri, V.; Marom, R.; Elazari, R.; Salitra, G.; Aurbach, D., Challenges in the development of advanced Li-ion batteries: a review. *Energy Environ. Sci.* **2011,** *4*, 3243–3262.

[4] Xu, B.; Qian, D.; Wang, Z.; Meng, Y. S., Recent progress in cathode materials research for advanced lithium ion batteries. *Mater. Sci. Eng. R. Rep.* **2012,** *73*, 51–65.

[5] Doeff, M. M., Battery Cathodes. In *Batteries for Sustainability: Selected Entries from the Encyclopedia of Sustainability Science and Technology*, Brodd, R. J., Ed. Springer New York: New York, NY, USA, **2013;** pp 5–49.

[6] Whittingham, M. S., Lithium Batteries and Cathode Materials. *Chem. Rev.* **2004,** *104*, 4271–4301.

[7] Hu, M.; Pang, X.; Zhou, Z., Recent progress in high-voltage lithium ion batteries. *J. Power Sources* **2013,** *237*, 229–242.

[8] Okada, S., Analytical studies of new 5V class cathode materials for Li-ion batteries. *Kyushu Daigaku Chuo Bunseki Senta Hokoku* **2004,** *22*, 2–12.

[9] Ellis, B. L.; Lee, K. T.; Nazar, L. F., Positive Electrode Materials for Li-Ion and Li-Batteries. *Chem. Mater.* **2010,** *22*, 691–714.

[10] Gong, Z.; Yang, Y., Recent advances in the research of polyanion-type cathode materials for Li-ion batteries. *Energy Environ. Sci.* **2011,** *4*, 3223–3242.

[11] Kraytsberg, A.; Ein-Eli, Y., Higher, stronger, better... A review of 5 volt cathode materials for advanced lithium-ion batteries. *Adv. Energy Mater.* **2012,** *2*, 922–939.

[12] Julien, C. M.; Mauger, A.; Zaghib, K.; Liu, D., High Voltage Cathode Materials. In *Rechargeable Batteries: Materials, Technologies and New Trends*, Zhang, Z.; Zhang, S. S., Eds. Springer International Publishing: Cham, Switzerland, **2015;** pp 477–509.

[13] Padhi, A. K.; Nanjundaswamy, K. S.; Goodenough, J. B., Phospho-olivines as Positive-Electrode Materials for Rechargeable Lithium Batteries. *J. Electrochem. Soc.* **1997,** *144*, 1188–1194.

[14] Bragg, W. L.; Brown, G. B., The structure of olivine $(Mg,Fe)_2SiO_4$. *Z. Kristallogr., Kristallgeom., Kristallphys., Kristallchem.* **1926,** *63*, 538–556.

[15] Okada, S.; Sawa, S.; Egashira, M.; Yamaki, J.; Tabuchi, M.; Kageyama, H.; Konishi, T.; Yoshino, A., Cathode properties of phospho-olivine Li*M*PO_4 for lithium secondary batteries. *J. Power Sources* **2001,** *97–98*, 430–432.

[16] Thackeray, M., Lithium-ion batteries: An unexpected conductor. *Nat. Mater.* **2002,** *1*, 81–82.

[17] Yamada, A.; Hosoya, M.; Chung, S.-C.; Kudo, Y.; Hinokuma, K.; Liu, K.-Y.; Nishi, Y., Olivine-type cathodes, achievements and problems. *J. Power Sources* **2003,** *119–121*, 232–238.

[18] Wang, Y.; He, P.; Zhou, H., Olivine $LiFePO_4$: development and future. *Energy Environ. Sci.* **2011,** *4*, 805–817.

[19] Zaghib, K.; Guerfi, A.; Hovington, P.; Vijh, A.; Trudeau, M.; Mauger, A.; Goodenough, J. B.; Julien, C. M., Review and analysis of nanostructured olivine-based lithium recheargeable batteries: Status and trends. *J. Power Sources* **2013,** *232*, 357–369.

[20] Masquelier, C.; Croguennec, L., Polyanionic (phosphates, silicates, sulfates) frameworks as electrode materials for rechargeable Li (or Na) batteries. *Chem. Rev.* **2013,** *113*, 6552–6591.

[21] Zaghib, K.; Mauger, A.; Julien, C. M., Olivine-Based Cathode Materials. In *Rechargeable Batteries: Materials, Technologies and New Trends*, Zhang, Z.; Zhang, S. S., Eds. Springer International Publishing: Cham, Switzerland, **2015;** pp 25–65.

[22] Kubel, F., Crystal-Structure of Lithium Cobalt Double Orthophosphate, $LiCoPO_4$. *Z. Kristallogr.* **1994,** *209*, 755.

[23] Morgan, D.; Van der Ven, A.; Ceder, G., Li Conductivity in Li_xMPO_4 (*M* = Mn, Fe, Co, Ni) Olivine Materials. *Electrochem. Solid-State Lett.* **2003,** *7*, A30–A32.

[24] Islam, M. S.; Driscoll, D. J.; Fisher, C. A. J.; Slater, P. R., Atomic-Scale Investigation of Defects, Dopants, and Lithium Transport in the $LiFePO_4$ Olivine-Type Battery Material. *Chem. Mater.* **2005,** *17*, 5085–5092.

[25] Nishimura, S.-I.; Kobayashi, G.; Ohoyama, K.; Kanno, R.; Yashima, M.; Yamada, A., Experimental visualization of lithium diffusion in Li_xFePO_4. *Nat. Mater.* **2008,** *7*, 707–711.

[26] Fisher, C. A. J.; Hart, P. V. M.; Islam, M. S., Lithium Battery Materials $LiMPO_4$ (*M* = Mn, Fe, Co, and Ni): Insights into Defect Association, Transport Mechanisms, and Doping Behavior. *Chem. Mater.* **2008,** *20*, 5907–5915.

[27] Rissouli, K.; Benkhouja, K.; Ramos-Barrado, J. R.; Julien, C., Electrical conductivity in lithium orthophosphates. *Mater. Sci. Eng., B* **2003,** *B98*, 185–189.

[28] Delacourt, C.; Laffont, L.; Bouchet, R.; Wurm, C.; Leriche, J. B.; Morcrette, M.; Tarascon, J. M.; Masquelier, C., Toward understanding of electrical limitations (electronic, ionic) in $LiMPO_4$ (*M* = Fe, Mn) electrode materials. *J. Electrochem. Soc.* **2005,** *152*, A913–A921.

[29] Andersson, A. S.; Thomas, J. O.; Kalska, B.; Haggstrom, L., Thermal stability of $LiFePO_4$-based cathodes. *Electrochem. Solid-State Lett.* **2000,** *3*, 66–68.

[30] Martha, S. K.; Haik, O.; Zinigrad, E.; Exnar, I.; Drezen, T.; Miners, J. H.; Aurbach, D., On the Thermal Stability of Olivine Cathode Materials for Lithium-Ion Batteries. *J. Electrochem. Soc.* **2011,** *158*, A1115–A1122.

[31] Ludwig, J.; Marino, C.; Haering, D.; Stinner, C.; Gasteiger, H. A.; Nilges, T., Morphology-controlled microwave-assisted solvothermal synthesis of high-performance $LiCoPO_4$ as a high-voltage cathode material for Li-ion batteries. *J. Power Sources* **2017,** *342*, 214–223.

[32] *SciFinder® A CAS Solution*. Chemical Abstracts Service: Columbus, OH, USA, **2017** (http://www.cas.org/products/scifinder).

[33] Zhang, W.-J., Structure and performance of $LiFePO_4$ cathode materials: A review. *J. Power Sources* **2011,** *196*, 2962–2970.

[34] Park, O. K.; Cho, Y.; Lee, S.; Yoo, H.-C.; Song, H.-K.; Cho, J., Who will drive electric vehicles, olivine or spinel? *Energy Environ. Sci.* **2011,** *4*, 1621–1633.

[35] Julien, C. M.; Zaghib, K.; Mauger, A.; Goult, H., Enhanced electrochemical properties of $LiFePO_4$ as positive electrode of Li-ion batteries for HEV application. *Adv. Chem. Eng. Sci.* **2012,** *2*, 321–329.

[36] Wang, G.; Chen, L.; Mathur, G. N.; Varadan, V. K., Lithium iron phosphates as cathode materials in lithium ion batteries for electric vehicles. *Proc. SPIE* **2012,** *8344*, 83440L/1–83440L/8.

[37] Amine, K.; Yasuda, H.; Yamachi, M., Olivine $LiCoPO_4$ as 4.8 V electrode material for lithium batteries. *Electrochem. Solid-State Lett.* **2000,** *3*, 178–179.

[38] Wolfenstine, J.; Allen, J., Ni^{3+}/Ni^{2+} redox potential in $LiNiPO_4$. *J. Power Sources* **2005,** *142*, 389–390.

[39] Howard, W. F.; Spotnitz, R. M., Theoretical evaluation of high-energy lithium metal phosphate cathode materials in Li-ion batteries. *J. Power Sources* **2007,** *165*, 887–891.

[40] Hautier, G.; Jain, A.; Ong, S. P.; Kang, B.; Moore, C.; Doe, R.; Ceder, G., Phosphates as Lithium-Ion Battery Cathodes: An Evaluation Based on High-Throughput *ab Initio* Calculations. *Chem. Mater.* **2011,** *23*, 3495–3508.

[41] Hayashi, K.; Nemoto, Y.; Tobishima, S.-I.; Yamaki, J.-I., Mixed solvent electrolyte for high voltage lithium metal secondary cells. *Electrochim. Acta* **1999,** *44*, 2337–2344.

[42] Egashira, M.; Takahashi, H.; Okada, S.; Yamaki, J.-I., Measurement of the electrochemical oxidation of organic electrolytes used in lithium batteries by microelectrode. *J. Power Sources* **2001,** *92*, 267–271.

[43] Xu, K., Nonaqueous Liquid Electrolytes for Lithium-Based Rechargeable Batteries. *Chem. Rev.* **2004,** *104*, 4303–4418.

[44] Brutti, S.; Panero, S., Recent advances in the development of $LiCoPO_4$ as high voltage cathode material for Li-ion batteries. *ACS Symp. Ser.* **2013,** *1140*, 67–99.

[45] Xu, K., Electrolytes and Interphases in Li-Ion Batteries and Beyond. *Chem. Rev.* **2014,** *114*, 11503–11618.

[46] Hu, L.; Zhang, S. S.; Zhang, Z., Electrolytes for Lithium and Lithium-Ion Batteries. In *Rechargeable Batteries: Materials, Technologies and New Trends*, Zhang, Z.; Zhang, S. S., Eds. Springer International Publishing: Cham, Switzerland, **2015;** pp 231–261.

[47] Wolfenstine, J.; Allen, J., $LiNi_xCo_{1-x}PO_4$ ($0 < x < 1$) cathodes. *Proc. Power Sources Conf.* **2004,** *41st*, 383–385.

[48] Dimesso, L.; Spanheimer, C.; Jaegermann, W., Investigation on graphitic carbon foams – $LiNi_yPO_4$ (y = 0.8–1.0) composites. *Solid State Sci.* **2012,** *14*, 1372–1377.

[49] Rommel, S. M.; Schall, N.; Bruenig, C.; Weihrich, R., Challenges in the synthesis of high voltage electrode materials for lithium-ion batteries: a review on $LiNiPO_4$. *Monatsh. Chem.* **2014,** *145*, 385–404.

[50] Julien, C. M.; Mauger, A., Review of 5-V electrodes for Li-ion batteries: status and trends. *Ionics* **2013,** *19*, 951–988.

[51] Bramnik, N. N.; Bramnik, K. G.; Buhrmester, T.; Baehtz, C.; Ehrenberg, H.; Fuess, H., Electrochemical and structural study of $LiCoPO_4$-based electrodes. *J. Solid State Electrochem.* **2004,** *8*, 558–564.

[52] Bramnik, N. N.; Bramnik, K. G.; Baehtz, C.; Ehrenberg, H., Study of the effect of different synthesis routes on Li extraction-insertion from $LiCoPO_4$. *J. Power Sources* **2005,** *145*, 74–81.

[53] Nakayama, M.; Goto, S.; Uchimoto, Y.; Wakihara, M.; Kitajima, Y.; Miyanaga, T.; Watanabe, I., X-ray absorption spectroscopic study on the electronic structure of $Li_{1-x}CoPO_4$ electrodes as 4.8 V positive electrodes for rechargeable lithium ion batteries. *J. Phys. Chem. B* **2005,** *109*, 11197–11203.

[54] Wolfenstine, J.; Foster, D.; Allen, J.; Behl, W.; Walker, C., Conductivity of $Li_{1-x}Cr_xCoPO_4$, $LiCo_{1-x}Cu_xPO_4$ and $Li_{1-x}CoPO_4$. *Proc. Power Sources Conf.* **2006,** *42nd*, 233–235.

[55] Bramnik, N. N.; Nikolowski, K.; Baehtz, C.; Bramnik, K. G.; Ehrenberg, H., Phase Transitions Occurring upon Lithium Insertion–Extraction of $LiCoPO_4$. *Chem. Mater.* **2007,** *19*, 908–915.

[56] Kaus, M.; Issac, I.; Heinzmann, R.; Doyle, S.; Mangold, S.; Hahn, H.; Chakravadhanula, V. S. K.; Kuebel, C.; Ehrenberg, H.; Indris, S., Electrochemical Delithiation/Relithiation of $LiCoPO_4$: A Two-Step Reaction Mechanism Investigated by *in Situ* X-ray Diffraction, *in Situ* X-ray Absorption Spectroscopy, and *ex Situ* $^7Li/^{31}P$ NMR Spectroscopy. *J. Phys. Chem. C* **2014,** *118*, 17279–17290.

[57] Strobridge, F. C.; Clement, R. J.; Leskes, M.; Middlemiss, D. S.; Borkiewicz, O. J.; Wiaderek, K. M.; Chapman, K. W.; Chupas, P. J.; Grey, C. P., Identifying the Structure of the Intermediate, $Li_{2/3}CoPO_4$, Formed during Electrochemical Cycling of $LiCoPO_4$. *Chem. Mater.* **2014,** *26*, 6193–6205.

[58] Palmer, M. G.; Frith, J. T.; Hector, A. L.; Lodge, A. W.; Owen, J. R.; Nicklin, C.; Rawle, J., *In situ* phase behaviour of a high capacity $LiCoPO_4$ electrode during constant or pulsed charge of a lithium cell. *Chem. Commun.* **2016,** *52*, 14169–14172.

[59] Strobridge, F. C.; Liu, H.; Leskes, M.; Borkiewicz, O. J.; Wiaderek, K. M.; Chupas, P. J.; Chapman, K. W.; Grey, C. P., Unraveling the Complex Delithiation Mechanisms of Olivine-Type Cathode Materials, $LiFe_xCo_{1-x}PO_4$. *Chem. Mater.* **2016,** *28*, 3676–3690.

[60] Srinivasan, V.; Newman, J., Discharge Model for the Lithium Iron-Phosphate Electrode. *J. Electrochem. Soc.* **2004,** *151*, A1517–A1529.

[61] Yamada, A.; Koizumi, H.; Sonoyama, N.; Kanno, R., Phase change in Li_xFePO_4. *Electrochem. Solid-State Lett.* **2005,** *8*, A409–A413.

[62] Ramana, C. V.; Mauger, A.; Gendron, F.; Julien, C. M.; Zaghib, K., Study of the Li-insertion/extraction process in $LiFePO_4/FePO_4$. *J. Power Sources* **2009,** *187*, 555–564.

[63] Ehrenberg, H.; Bramnik, N. N.; Senyshyn, A.; Fuess, H., Crystal and magnetic structures of electrochemically delithiated $Li_{1-x}CoPO_4$ phases. *Solid State Sci.* **2009,** *11*, 18–23.

[64] Ju, H.; Wu, J.; Xu, Y., Lithium ion intercalation mechanism for $LiCoPO_4$ electrode. *Int. J. Energy Environ. Eng.* **2013,** *4*, 22, 6 pp.

[65] Wolfenstine, J.; Poese, B.; Allen, J. L., Chemical oxidation of $LiCoPO_4$. *J. Power Sources* **2004,** *138*, 281–282.

[66] Bramnik, N. N.; Nikolowski, K.; Trots, D. M.; Ehrenberg, H., Thermal stability of $LiCoPO_4$ cathodes. *Electrochem. Solid-State Lett.* **2008,** *11*, A89–A93.

[67] Theil, S.; Fleischhammer, M.; Axmann, P.; Wohlfahrt-Mehrens, M., Experimental investigations on the electrochemical and thermal behaviour of $LiCoPO_4$-based cathode. *J. Power Sources* **2013,** *222*, 72–78.

[68] Gong, X.-p.; Zou, Q.-f.; Wang, L., Research progress in $LiCoPO_4$ as high voltage cathode for Li-ion battery. *Dianchi Gongye* **2014,** *19*, 148–152.

[69] Wolfenstine, J., Electrical conductivity of doped $LiCoPO_4$. *J. Power Sources* **2006,** *158*, 1431–1435.

[70] Wolfenstine, J.; Read, J.; Allen, J. L., Effect of carbon on the electronic conductivity and discharge capacity of $LiCoPO_4$. *J. Power Sources* **2007,** *163*, 1070–1073.

[71] Allen, J. L.; Thompson, T.; Sakamoto, J.; Becker, C. R.; Jow, T. R.; Wolfenstine, J., Transport properties of $LiCoPO_4$ and Fe-substituted $LiCoPO_4$. *J. Power Sources* **2014,** *254*, 204–208.

[72] Shanmukaraj, D.; Murugan, R., Synthesis and characterization of $LiNi_yCo_{1-y}PO_4$ (y = 0 - 1) cathode materials for lithium secondary batteries. *Ionics* **2004,** *10*, 88–92.

[73] Prabu, M.; Selvasekarapandian, S.; Kulkarni, A. R.; Karthikeyan, S.; Hirankumar, G.; Sanjeeviraja, C., Ionic transport properties of $LiCoPO_4$ cathode material. *Solid State Sci.* **2011,** *13*, 1714–1718.

[74] Prabu, M.; Selvasekarapandian, S.; Reddy, M. V.; Chowdari, B. V. R., Impedance studies on the 5-V cathode material, $LiCoPO_4$. *J. Solid State Electrochem.* **2012,** *16*, 1833–1839.

[75] Markevich, E.; Sharabi, R.; Gottlieb, H.; Borgel, V.; Fridman, K.; Salitra, G.; Aurbach, D.; Semrau, G.; Schmidt, M. A.; Schall, N.; Bruenig, C., Reasons for capacity fading of $LiCoPO_4$ cathodes in $LiPF_6$ containing electrolyte solutions. *Electrochem. Commun.* **2012,** *15*, 22–25.

[76] Fukutsuka, T.; Nakagawa, T.; Miyazaki, K.; Abe, T., Electrochemical properties of $LiCoPO_4$-thin film electrodes in LiF-based electrolyte solution with anion receptors. *J. Power Sources* **2016,** *306*, 753–757.

[77] Aurbach, D.; Markovsky, B.; Salitra, G.; Markevich, E.; Talyossef, Y.; Koltypin, M.; Nazar, L.; Ellis, B.; Kovacheva, D., Review on electrode-electrolyte solution interactions, related to cathode materials for Li-ion batteries. *J. Power Sources* **2007,** *165*, 491–499.

[78] Sharabi, R.; Markevich, E.; Borgel, V.; Salitra, G.; Gershinsky, G.; Aurbach, D.; Semrau, G.; Schmidt, M. A.; Schall, N.; Stinner, C., Raman study of structural stability of $LiCoPO_4$ cathodes in $LiPF_6$ containing electrolytes. *J. Power Sources* **2012,** *203*, 109–114.

[79] Truong, Q. D.; Devaraju, M. K.; Sasaki, Y.; Hyodo, H.; Tomai, T.; Honma, I., Relocation of cobalt ions in electrochemically delithiated $LiCoPO_4$ cathode materials. *Chem. Mater.* **2014,** *26*, 2770–2773.

[80] Boulineau, A.; Gutel, T., Revealing Electrochemically Induced Antisite Defects in $LiCoPO_4$: Evolution upon Cycling. *Chem. Mater.* **2015,** *27*, 802–807.

[81] Ikuhara, Y. H.; Gao, X.; Fisher, C. A. J.; Kuwabara, A.; Moriwake, H.; Kohama, K.; Iba, H.; Ikuhara, Y., Atomic level changes during capacity fade in highly oriented thin films of cathode material $LiCoPO_4$. *J. Mater. Chem. A* **2017,** *5*, 9329–9338.

[82] Devaraju, M. K.; Truong, Q. D.; Tomai, T.; Hyodo, H.; Sasaki, Y.; Honma, I., Antisite defects in $LiCoPO_4$ nanocrystals synthesized *via* a supercritical fluid process. *RSC Adv.* **2014,** *4*, 52410–52414.

[83] Chen, J.; Graetz, J., Study of Antisite Defects in Hydrothermally Prepared $LiFePO_4$ by in Situ X-ray Diffraction. *ACS Appl. Mater. Interfaces* **2011,** *3*, 1380–1384.

[84] Qin, X.; Wang, J.; Xie, J.; Li, F.; Wen, L.; Wang, X., Hydrothermally synthesized $LiFePO_4$ crystals with enhanced electrochemical properties: simultaneous suppression of crystal growth along [010] and antisite defect formation. *Phys. Chem. Chem. Phys.* **2012,** *14*, 2669–2677.

[85] Jensen, K. M. O.; Christensen, M.; Gunnlaugsson, H. P.; Lock, N.; Boejesen, E. D.; Proffen, T.; Iversen, B. B., Defects in Hydrothermally Synthesized $LiFePO_4$ and $LiFe_{1-x}Mn_xPO_4$ Cathode Materials. *Chem. Mater.* **2013,** *25*, 2282–2290.

[86] Jensen, K. M. Ø.; Gunnlaugsson, H. P.; Christensen, M.; Iversen, B. B., Moessbauer spectroscopy study of defects in hydrothermally synthesized $LiFePO_4$ cathode material. *Hyperfine Interact.* **2014,** *226*, 73–78.

[87] Chen, J.; Whittingham, M. S., Hydrothermal synthesis of lithium iron phosphate. *Electrochem. Commun.* **2006,** *8*, 855–858.

[88] Yang, J.; Xu, J. J., Synthesis and Characterization of Carbon-Coated Lithium Transition Metal Phosphates Li*M*PO_4 (*M* = Fe, Mn, Co, Ni) Prepared via a Nonaqueous Sol-Gel Route. *J. Electrochem. Soc.* **2006,** *153*, A716–A723.

[89] Doeff, M. M.; Wilcox, J. D.; Kostecki, R.; Lau, G. Y. Formation of structured carbon films on electrode material particles used for the manufacture of secondary lithium batteries. WO2008088573A1, **2008**.

[90] Jin, B.; Gu, H.-B.; Kim, K.-W., Effect of different conductive additives on charge/discharge properties of $LiCoPO_4$/Li batteries. *J. Solid State Electrochem.* **2008,** *12*, 105–111.

[91] Murugan, A. V.; Muraliganth, T.; Manthiram, A., One-Pot Microwave-Hydrothermal Synthesis and Characterization of Carbon-Coated Li*M*PO_4 (*M* = Mn, Fe, and Co) Cathodes. *J. Electrochem. Soc.* **2009,** *156*, A79–A83.

[92] Kumar, P. R.; Venkateswarlu, M.; Misra, M.; Mohanty, A. K.; Satyanayana, N., Synthesis, characterization and electrical properties of carbon coated $LiCoPO_4$ nanoparticles. *J. Nanosci. Nanotechnol.* **2011,** *11*, 3314–3322.

[93] Markevich, E.; Sharabi, R.; Haik, O.; Borgel, V.; Salitra, G.; Aurbach, D.; Semrau, G.; Schmidt, M. A.; Schall, N.; Stinner, C., Raman spectroscopy of carbon-coated $LiCoPO_4$ and $LiFePO_4$ olivines. *J. Power Sources* **2011,** *196*, 6433–6439.

[94] Li, H.; Zhou, H., Enhancing the performances of Li-ion batteries by carbon-coating: present and future. *Chem. Commun.* **2012,** *48*, 1201–1217.

[95] Kumar, P. R.; Madhusudhanrao, V.; Nageswararao, B.; Venkateswarlu, M.; Satyanarayana, N., Enhanced electrochemical performance of carbon-coated Li*M*PO_4 (*M* = Co and Ni) nanoparticles as cathodes for high-voltage lithium-ion battery. *J. Solid State Electrochem.* **2016,** *20*, 1855–1863.

[96] Maeyoshi, Y.; Miyamoto, S.; Noda, Y.; Munakata, H.; Kanamura, K., Effect of organic additives on characteristics of carbon-coated $LiCoPO_4$ synthesized by hydrothermal method. *J. Power Sources* **2017,** *337*, 92–99.

[97] Chung, S.-Y.; Bloking, J. T.; Chiang, Y.-M., Electronically conductive phospho-olivines as lithium storage electrodes. *Nat. Mater.* **2002,** *1*, 123–128.

[98] Kishore, M. V. V. M. S.; Varadaraju, U. V., Influence of isovalent ion substitution on the electrochemical performance of $LiCoPO_4$. *Mater. Res. Bull.* **2005,** *40*, 1705–1712.

[99] Han, D.-W.; Kang, Y.-M.; Yin, R.-Z.; Song, M.-S.; Kwon, H.-S., Effects of Fe doping on the electrochemical performance of $LiCoPO_4$/C composites for high power-density cathode materials. *Electrochem. Commun.* **2009,** *11*, 137–140.

[100] Wang, F.; Yang, J.; NuLi, Y.; Wang, J., Highly promoted electrochemical performance of 5 V $LiCoPO_4$ cathode material by addition of vanadium. *J. Power Sources* **2010,** *195*, 6884–6887.

[101] Allen, J. L.; Jow, T. R.; Wolfenstine, J., Improved cycle life of Fe-substituted $LiCoPO_4$. *J. Power Sources* **2011,** *196*, 8656–8661.

[102] Kang, Y.-M.; Kim, Y.-I.; Oh, M.-W.; Yin, R.-Z.; Lee, Y.; Han, D.-W.; Kwon, H.-S.; Kim, J. H.; Ramanath, G., Structurally stabilized olivine lithium phosphate cathodes with enhanced electrochemical properties through Fe doping. *Energy Environ. Sci.* **2011,** *4*, 4978–4983.

[103] Minakshi, M.; Kandhasamy, S., Utilizing active multiple dopants (Co and Ni) in olivine $LiMnPO_4$. *Curr. Opin. Solid State Mater. Sci.* **2012,** *16*, 163–167.

[104] Li, H.; Wang, Y.; Yang, X.; Liu, L.; Chen, L.; Wei, J., Improved electrochemical performance of 5 V $LiCoPO_4$ cathode materials via yttrium doping. *Solid State Ionics* **2014,** *255*, 84–88.

[105] Di Lecce, D.; Manzi, J.; Vitucci, F. M.; De Bonis, A.; Panero, S.; Brutti, S., Effect of the iron doping in $LiCoPO_4$ cathode materials for lithium cells. *Electrochim. Acta* **2015,** *185*, 17–27.

[106] Rommel, S. M.; Rothballer, J.; Schall, N.; Bruenig, C.; Weihrich, R., Characterization of the carbon-coated $LiNi_{1-y}Co_yPO_4$ solid solution synthesized by a non-aqueous sol-gel route. *Ionics* **2015,** *21*, 325–333.

[107] Allen, J. L.; Allen, J. L.; Thompson, T.; Delp, S. A.; Wolfenstine, J.; Jow, T. R., Cr and Si Substituted-$LiCo_{0.9}Fe_{0.1}PO_4$: Structure, full and half Li-ion cell performance. *J. Power Sources* **2016,** *327*, 229–234.

[108] Kreder, K. J.; Assat, G.; Manthiram, A., Aliovalent Substitution of V^{3+} for Co^{2+} in $LiCoPO_4$ by a Low-Temperature Microwave-Assisted Solvothermal Process. *Chem. Mater.* **2016,** *28*, 1847–1853.

[109] Liu, J.; Conry, T. E.; Song, X.; Yang, L.; Doeff, M. M.; Richardson, T. J., Spherical nanoporous $LiCoPO_4$/C composites as high performance cathode materials for rechargeable lithium-ion batteries. *J. Mater. Chem.* **2011,** *21*, 9984–9987.

[110] Doan, T. N. L.; Taniguchi, I., Preparation of $LiCoPO_4$/C nanocomposite cathode of lithium batteries with high rate performance. *J. Power Sources* **2011,** *196*, 5679–5684.

[111] Brutti, S.; Reale, P.; Piciollo, E.; Gentili, V.; Bruce, P. G.; Scrosati, B.; Panero, S., Nanosized advanced materials for application in lithium-ion batteries. *Prepr. Symp. - Am. Chem. Soc., Div. Fuel Chem.* **2012,** *57*, 737–739.

[112] Devaraju, M. K.; Rangappa, D.; Honma, I., Controlled synthesis of plate-like $LiCoPO_4$ nanoparticles via supercritical method and their electrode property. *Electrochim. Acta* **2012,** *85*, 548–553.

[113] Dimesso, L.; Foerster, C.; Jaegermann, W.; Khanderi, J. P.; Tempel, H.; Popp, A.; Engstler, J.; Schneider, J. J.; Sarapulova, A.; Mikhailova, D.; Schmitt, L. A.; Oswald, S.; Ehrenberg, H., Developments in nanostructured Li*M*PO_4 (*M* = Fe, Co, Ni, Mn) composites based on three dimensional carbon architecture. *Chem. Soc. Rev.* **2012,** *41*, 5068–5080.

[114] Rui, X.; Zhao, X.; Lu, Z.; Tan, H.; Sim, D.; Hng, H. H.; Yazami, R.; Lim, T. M.; Yan, Q., Olivine-Type Nanosheets for Lithium Ion Battery Cathodes. *ACS Nano* **2013,** *7*, 5637–5646.

[115] Lloris, J. M.; Perez, V. C.; Tirado, J. L., Improvement of the electrochemical performance of $LiCoPO_4$ 5 V material using a novel synthesis. *Electrochem. Solid-State Lett.* **2002,** *5*, A234–A237.

[116] Piana, M.; Arrabito, M.; Bodoardo, S.; D'Epifanio, A.; Satolli, D.; Croce, F.; Scrosati, B., Characterization of phospho-olivines as materials for Li-ion cell cathodes. *Ionics* **2002,** *8*, 17–26.

[117] Okada, S.; Ueno, M.; Uebou, Y.; Yamaki, J., Structure and cathode properties of $LiCoPO_4$ and Li_2CoPO_4F for high-voltage Li-ion batteries. In *Intelec'03: Powering the Broadband Network, Proceedings*, **2003;** pp 66–71.

[118] Nakayama, M.; Goto, S.; Uchimoto, Y.; Wakihara, M.; Kitajima, Y., Changes in Electronic Structure between Cobalt and Oxide Ions of Lithium Cobalt Phosphate as 4.8-V Positive Electrode Material. *Chem. Mater.* **2004,** *16*, 3399–3401.

[119] Wolfenstine, J.; Lee, U.; Poese, B.; Allen, J. L., Effect of oxygen partial pressure on the discharge capacity of $LiCoPO_4$. *J. Power Sources* **2005,** *144*, 226–230.

[120] Rabanal, M. E.; Gutierrez, M. C.; Garcia-Alvarado, F.; Gonzalo, E. C.; Arroyo-de Dompablo, M. E., Improved electrode characteristics of olivine-$LiCoPO_4$ processed by high energy milling. *J. Power Sources* **2006,** *160*, 523–528.

[121] Allen, J. L.; Jow, T. R.; Wolfenstine, J. In *Preparation and properties of lithium cobalt phosphate for lithium-ion batteries*, American Chemical Society: 2009; pp INOR–665.

[122] Jang, I. C.; Lim, H. H.; Lee, S. B.; Karthikeyan, K.; Aravindan, V.; Kang, K. S.; Yoon, W. S.; Cho, W. I.; Lee, Y. S., Preparation of $LiCoPO_4$ and $LiFePO_4$ coated $LiCoPO_4$ with improved battery performance. *J. Alloys Compd.* **2010,** *497*, 321–324.

[123] Yang, S. M. G.; Aravindan, V.; Cho, W. I.; Chang, D. R.; Kim, H. S.; Lee, Y. S., Realizing the performance of $LiCoPO_4$ cathodes by Fe substitution with off-stoichiometry. *J. Electrochem. Soc.* **2012,** *159*, A1013–A1018.

[124] Gangulibabu; Bhuvaneswari, D.; Kalaiselvi, N.; Jayaprakash, N.; Periasamy, P., CAM sol-gel synthesized Li*M*PO_4 (*M* = Co, Ni) cathodes for rechargeable lithium batteries. *J. Sol-Gel Sci. Technol.* **2009,** *49*, 137–144.

[125] Zhang, Y.; Sun, C. S.; Zhou, Z., Sol-gel preparation and electrochemical performances of $LiFe_{1/3}Mn_{1/3}Co_{1/3}PO_4$/C composites with core-shell nanostructure. *Electrochem. Commun.* **2009,** *11*, 1183–1186.

[126] Bhuwaneswari, M. S.; Dimesso, L.; Jaegermann, W., Preparation of $LiCoPO_4$ powders and films via sol-gel. *J. Sol-Gel Sci. Technol.* **2010,** *56*, 320–326.

[127] Poovizhi, P. N.; Selladurai, S., Study of pristine and carbon-coated $LiCoPO_4$ olivine material synthesized by modified sol-gel method. *Ionics* **2011,** *17*, 13–19.

[128] Kim, E. J.; Xu, H. Y.; Lim, J. S.; Kang, J. W.; Gim, J. H.; Mathew, V.; Kim, J., Impact of glucose on the electrochemical performance of nano-$LiCoPO_4$ cathode for Li-ion batteries. *J. Solid State Electrochem.* **2012,** *16*, 149–155.

[129] Ni, J.; Wang, H.; Gao, L.; Lu, L., A high-performance $LiCoPO_4$/C core/shell composite for Li-ion batteries. *Electrochim. Acta* **2012,** *70*, 349–354.

[130] Dimesso, L.; Cherkashinin, G.; Spanheimer, C.; Jaegermann, W., Preparation and characterization of carbon foams-$LiCoPO_4$ composites. *J. Alloys Compd.* **2012,** *516*, 119–125.

[131] Dimesso, L.; Jacke, S.; Spanheimer, C.; Jaegermann, W., Investigation on $LiCoPO_4$ powders as cathode materials annealed under different atmospheres. *J. Solid State Electrochem.* **2012,** *16*, 911–919.

[132] Sarapulova, A.; Mikhailova, D.; Schmitt, L. A.; Oswald, S.; Bramnik, N.; Ehrenberg, H., Disordered carbon nanofibers/$LiCoPO_4$ composites as cathode materials for lithium ion batteries. *J. Sol-Gel Sci. Technol.* **2012,** *62*, 98–110.

[133] Du, C. Q.; Tang, Z. Y.; Wu, J. W.; Tang, H. Q.; Zhang, X. H., A three volt lithium ion battery with $LiCoPO_4$ and zero-strain $Li_4Ti_5O_{12}$ as insertion material. *Electrochim. Acta* **2014,** *125*, 58–64.

[134] Kim, K.; Kim, J.-K., Comparison of structural characteristics and electrochemical properties of Li*M*PO_4 (*M* = Fe, Mn, and Co) olivine compounds. *Mater. Lett.* **2016,** *176*, 244–247.

[135] Delacourt, C.; Wurm, C.; Reale, P.; Morcrette, M.; Masquelier, C., Low temperature preparation of optimized phosphates for Li-battery applications. *Solid State Ionics* **2004,** *173*, 113–118.

[136] Wu, Y.; Li, C.; Yu, Z.; Zhou, K.; Ma, X.; Wang, P. Manufacturing of Li(MnFeCo)PO_4 cathode material by coprecipitation. CN104900873A, **2015**.

[137] Choi, D.; Li, X.; Henderson, W. A.; Huang, Q.; Nune, S. K.; Lemmon, J. P.; Sprenkle, V. L., $LiCoPO_4$ cathode from a $CoHPO_4 \cdot xH_2O$ nanoplate precursor for high voltage Li-ion batteries. *Heliyon* **2016,** *2*, e00081.

[138] Taniguchi, I.; Doan, T. N. L.; Shao, B., Synthesis and electrochemical characterization of $LiCo_xMn_{1-x}PO_4$/C nanocomposites. *Electrochim. Acta* **2011,** *56*, 7680–7685.

[139] Doan, T. N. L.; Taniguchi, I., Effect of spray pyrolysis temperature on physical and electrochemical properties of $LiCoPO_4$/C nanocomposites. *Powder Technol.* **2012,** *217*, 574–580.

[140] Vasanthi, R.; Kalpana, D.; Renganathan, N. G., Olivine-type nanoparticle for hybrid supercapacitors. *J. Solid State Electrochem.* **2008,** *12*, 961–969.

[141] Wang, F.; Yang, J., Synthesis and electrochemical performance of nano $LiCoPO_4$ by polyol method. *Dianhuaxue* **2013,** *19*, 585–589.

[142] Padmanathan, N.; Selladurai, S., Polyol mediated synthesis and microstructural features of polycrystalline Li*M*PO_4 (*M* = Mn and Co) olivine phosphates for lithium batteries. *Asian J. Chem.* **2013,** *25*, 9605–9609.

[143] Huang, X.; Ma, J.; Wu, P.; Hu, Y.; Dai, J.; Zhu, Z.; Chen, H.; Wang, H., Hydrothermal synthesis of $LiCoPO_4$ cathode materials for rechargeable lithium-ion batteries. *Mater. Lett.* **2005,** *59*, 578–582.

[144] Chen, J.; Wang, S.; Whittingham, M. S., Hydrothermal synthesis of cathode materials. *J. Power Sources* **2007,** *174*, 442–448.

[145] Chen, J.; Vacchio, M. J.; Wang, S.; Chernova, N.; Zavalij, P. Y.; Whittingham, M. S., The hydrothermal synthesis and characterization of olivines and related compounds for electrochemical applications. *Solid State Ion.* **2008,** *178*, 1676–1693.

[146] Zhao, Y.; Wang, S.; Zhao, C.; Xia, D., Synthesis and electrochemical performance of $LiCoPO_4$ micron-rods by dispersant-aided hydrothermal method for lithium ion batteries. *Rare Met.* **2009,** *28*, 117–121.

[147] Kotobuki, M.; Mizuno, Y.; Munakata, H.; Kanamura, K., Electrochemical properties of hydrothermally synthesized $LiCoPO_4$ as a high voltage cathode material for lithium secondary battery. *Phosphorus Res. Bull.* **2010,** *24*, 12–15.

[148] Wang, F.; Yang, J.; Nuli, Y.; Wang, J., Novel hedgehog-like 5 V $LiCoPO_4$ positive electrode material for rechargeable lithium battery. *J. Power Sources* **2011,** *196*, 4806–4810.

[149] Recham, N.; Oro-Sole, J.; Djellab, K.; Palacin, M. R.; Masquelier, C.; Tarascon, J. M., Hydrothermal synthesis, silver decoration and electrochemistry of Li*M*PO_4 (*M* = Fe, Mn, and Co) single crystals. *Solid State Ionics* **2012,** *220*, 47–52.

[150] Kotobuki, M., Hydrothermal synthesis of carbon-coated $LiCoPO_4$ cathode material from various Co sources. *Int. J. Energy Environ. Eng.* **2013,** *4*, 25–32.

[151] Wu, B.; Xu, H.; Mu, D.; Shi, L.; Jiang, B.; Gai, L.; Wang, L.; Liu, Q.; Ben, L.; Wu, F., Controlled solvothermal synthesis and electrochemical performance of $LiCoPO_4$ submicron single crystals as a cathode material for lithium ion batteries. *J. Power Sources* **2016,** *304*, 181–188.

[152] Su, J.; Wei, B.-Q.; Rong, J.-P.; Yin, W.-Y.; Ye, Z.-X.; Tian, X.-Q.; Ren, L.; Cao, M.-H.; Hu, C.-W., A general solution-chemistry route to the synthesis Li*M*PO_4 (*M* = Mn, Fe, and Co) nanocrystals with [010] orientation for lithium ion batteries. *J. Solid State Chem.* **2011,** *184*, 2909–2919.

[153] Li, M., Solvothermal synthesis of $LiCo_{1-x}Mn_xPO_4$/C cathode materials for lithium-ion batteries. *Ionics* **2012,** *18*, 507–512.

[154] Brutti, S.; Manzi, J.; De Bonis, A.; Di Lecce, D.; Vitucci, F.; Paolone, A.; Trequattrini, F.; Panero, S., Controlled synthesis of $LiCoPO_4$ by a solvo-thermal method at 220 °C. *Mater. Lett.* **2015,** *145*, 324–327.

[155] Manzi, J.; Curcio, M.; Brutti, S., Structural and morphological tuning of $LiCoPO_4$ materials synthesized by solvo-thermal methods for Li-cell applications. *Nanomaterials* **2015,** *5*, 2212–2230.

[156] Neef, C.; Meyer, H.-P.; Klingeler, R., Morphology-controlled two-step synthesis and electrochemical studies on hierarchically structured $LiCoPO_4$. *Solid State Sci.* **2015,** *48*, 270–277.

[157] Örnek, A., A new and effective approach to 4.8 V cathode synthesis with superior electrochemical qualities for lithium-ion applications. *J. Alloys Compd.* **2017,** *710*, 809–818.

[158] Murugan, A. V.; Muraliganth, T.; Ferreira, P. J.; Manthiram, A., Dimensionally Modulated, Single-Crystalline Li*M*PO_4 (*M* = Mn, Fe, Co, and Ni) with Nano-Thumblike Shapes for High-Power Energy Storage. *Inorg. Chem.* **2009,** *48*, 946–952.

[159] Rogers, R. E.; Clarke, G. M.; Matthew, O. N.; Ganter, M. J.; DiLeo, R. A.; Staub, J. W.; Forney, M. W.; Landi, B. J., Impact of microwave synthesis conditions on the rechargeable capacity of $LiCoPO_4$ for lithium ion batteries. *J. Appl. Electrochem.* **2013,** *43*, 271–278.

[160] Kreder, K. J.; Assat, G.; Manthiram, A., Microwave-Assisted Solvothermal Synthesis of Three Polymorphs of $LiCoPO_4$ and Their Electrochemical Properties. *Chem. Mater.* **2015,** *27*, 5543–5549.

[161] Kreder, K. J.; Manthiram, A., Vanadium-Substituted $LiCoPO_4$ Core with a Monolithic $LiFePO_4$ Shell for High-Voltage Lithium-Ion Batteries. *ACS Energy Lett.* **2017,** *2*, 64–69.

[162] Truong, Q. D.; Devaraju, M. K.; Ganbe, Y.; Tomai, T.; Honma, I., Controlling the shape of $LiCoPO_4$ nanocrystals by supercritical fluid process for enhanced energy storage properties. *Sci. Rep.* **2014,** *4*, 3975.

[163] Truong, Q. D.; Devaraju, M. K.; Honma, I., Benzylamine-directed growth of olivine-type $LiMPO_4$ nanoplates by a supercritical ethanol process for lithium-ion batteries. *J. Mater. Chem. A* **2014,** *2*, 17400–17407.

[164] Devaraju, M. K.; Truong, Q. D.; Hyodo, H.; Tomai, T.; Honma, I., Supercritical fluid synthesis of $LiCoPO_4$ nanoparticles and their application to lithium ion battery. *Inorganics* **2014,** *2*, 233–247.

[165] Rabenau, A., The role of hydrothermal synthesis in preparative chemistry. *Angew. Chem.* **1985,** *97*, 1017–1032.

[166] Walton, R. I., Subcritical solvothermal synthesis of condensed inorganic materials. *Chem. Soc. Rev.* **2002,** *31*, 230–238.

[167] Yoshimura, M.; Byrappa, K., Hydrothermal processing of materials: past, present and future. *J. Mater. Sci.* **2008,** *43*, 2085–2103.

[168] Demazeau, G., Solvothermal processes: a route to the stabilization of new materials. *J. Mater. Chem.* **1999,** *9*, 15–18.

[169] *Phase diagram*. Wikimedia Commons: **2008** (https://commons.wikimedia.org/wiki/File:Phase-diag2.svg).

[170] Reid, R. C.; Prausnitz, J. M.; Sherwood, T. K., *The Properties of Gases and Liquids. 3rd Ed*. McGraw-Hill: **1977;** p 688 pp.

[171] Savage, P. E.; Gopalan, S.; Mizan, T. I.; Martino, C. J.; Brock, E. E., Reactions at supercritical conditions: applications and fundamentals. *AIChE J.* **1995,** *41*, 1723–1778.

[172] Adschiri, T.; Hakuta, Y.; Arai, K., Hydrothermal Synthesis of Metal Oxide Fine Particles at Supercritical Conditions. *Ind. Eng. Chem. Res.* **2000,** *39*, 4901–4907.

[173] Byrappa, K.; Ohara, S.; Adschiri, T., Nanoparticles synthesis using supercritical fluid technology - towards biomedical applications. *Adv. Drug Delivery Rev.* **2008,** *60*, 299–327.

[174] Devaraju, M. K.; Truong, Q. D.; Tomai, T.; Honma, I., Supercritical fluid methods for synthesizing cathode materials towards lithium ion battery applications. *RSC Adv.* **2014,** *4*, 27452–27470.

[175] Aymonier, C.; Erriguible, A.; Marre, S.; Serani, A.; Cansell, F., Processes using supercritical fluids: a sustainable approach for the design of functional nanomaterials. *Int. J. Chem. React. Eng.* **2007,** *5*, A77.

[176] Byrappa, K.; Adschiri, T., Hydrothermal technology for nanotechnology. *Prog. Cryst. Growth Charact. Mater.* **2007,** *53*, 117–166.

[177] Priamo, W. L.; Dalmolin, I.; Boschetto, D. L.; Mezzomo, N.; Ferreira, S. R. S.; Oliveira, J. V., Micronization processes by supercritical fluid technologies: a short review on process design (2008–2012). *Acta Sci., Technol.* **2013,** *35*, 695–709.

[178] Cansell, F.; Aymonier, C., Design of functional nanostructured materials using supercritical fluids. *J. Supercrit. Fluids* **2009,** *47*, 508–516.

[179] Brennecke, J. F.; Eckert, C. A., Phase equilibria for supercritical fluid process design. *AIChE J.* **1989,** *35*, 1409–1427.

[180] Feng, S.; Xu, R., New Materials in Hydrothermal Synthesis. *Acc. Chem. Res.* **2001,** *34*, 239–247.

[181] Devaraju, M. K.; Honma, I., Hydrothermal and solvothermal process towards development of Li*M*PO_4 (*M* = Fe, Mn) nanomaterials for lithium-ion batteries. *Adv. Energy Mater.* **2012,** *2*, 284–297.

[182] Cundy, C. S.; Cox, P. A., The Hydrothermal Synthesis of Zeolites: History and Development from the Earliest Days to the Present Time. *Chem. Rev.* **2003,** *103*, 663–702.

[183] Sasikala, S. P.; Aymonier, C.; Poulin, P., Advances in Subcritical Hydro-/Solvothermal Processing of Graphene Materials. *Adv. Mater.* **2017,** *29*, 1605473.

[184] Gerbec, J. A.; Magana, D.; Washington, A.; Strouse, G. F., Microwave-Enhanced Reaction Rates for Nanoparticle Synthesis. *J. Am. Chem. Soc.* **2005,** *127*, 15791–15800.

[185] Bilecka, I.; Niederberger, M., Microwave chemistry for inorganic nanomaterials synthesis. *Nanoscale* **2010,** *2*, 1358–1374.

[186] Ludwig, J.; Marino, C.; Haering, D.; Stinner, C.; Nordlund, D.; Doeff, M. M.; Gasteiger, H. A.; Nilges, T., Facile, ethylene glycol-promoted microwave-assisted solvothermal synthesis of high-performance $LiCoPO_4$ as a high-voltage cathode material for lithium-ion batteries. *RSC Adv.* **2016,** *6*, 82984–82994.

[187] Örnek, A., An impressive approach to solving the ongoing stability problems of $LiCoPO_4$ cathode: Nickel oxide surface modification with excellent core-shell principle. *J. Power Sources* **2017,** *356*, 1–11.

[188] Doeff, M. M.; Hu, Y.; McLarnon, F.; Kostecki, R., Effect of Surface Carbon Structure on the Electrochemical Performance of $LiFePO_4$. *Electrochem. Solid-State Lett.* **2003,** *6*, A207–A209.

[189] Chung, S.-Y.; Choi, S.-Y.; Yamamoto, T.; Ikuhara, Y., Atomic-Scale Visualization of Antisite Defects in $LiFePO_4$. *Phys. Rev. Lett.* **2008,** *100*, 125502/1–125502/4.

[190] Ludwig, J., Synthesis and Characterization of Phospho-olivines. Master's thesis, Technical University of Munich, Department of Chemistry, Garching, Germany, **2012**.

[191] Zhang, X.; Ai, Z.; Jia, F.; Zhang, L., Generalized One-Pot Synthesis, Characterization, and Photocatalytic Activity of Hierarchical BiO*X* (*X* = Cl, Br, I) Nanoplate Microspheres. *The Journal of Physical Chemistry C* **2008,** *112*, 747–753.

[192] Wu, M.; Wang, Z. H.; Yuan, L. X.; Zhang, W. X.; Hu, X. L.; Huang, Y. H., Morphology-controllable solvothermal synthesis of nanoscale $LiFePO_4$ in a binary solvent. *Chin. Sci. Bull.* **2012,** *57*, 4170–4175.

[193] Feldmann, C., Polyol-mediated synthesis of nanoscale functional materials. *Solid State Sci.* **2005,** *7*, 868–873.

[194] Ghoshal, T.; Kar, S.; Chaudhuri, S., ZnO Doughnuts: Controlled Synthesis, Growth Mechanism, and Optical Properties. *Cryst. Growth Des.* **2007,** *7*, 136–141.

[195] Hong, Y.; Tang, Z.; Wang, S.; Quan, W.; Zhang, Z., High-performance $LiMnPO_4$ nanorods synthesized *via* a facile EG-assisted solvothermal approach. *J. Mater. Chem. A* **2015,** *3*, 10267–10274.

[196] Jähne, C.; Neef, C.; Koo, C.; Meyer, H.-P.; Klingeler, R., A new $LiCoPO_4$ polymorph *via* low temperature synthesis. *J. Mater. Chem. A* **2013,** *1*, 2856–2862.

[197] Amador, U.; Gallardo-Amores, J. M.; Heymann, G.; Huppertz, H.; Moran, E.; Arroyo-de Dompablo, M. E., High pressure polymorphs of $LiCoPO_4$ and $LiCoAsO_4$. *Solid State Sci.* **2009,** *11*, 343–348.

[198] Miller, J. J., The crystal structure of anhydrous sodium chromate, Na_2CrO_4. *Z. Kristallogr., Kristallgeom., Kristallphys., Kristallchem.* **1936,** *94*, 131–136.

[199] Niggli, A., The space group of Na_2CrO_4. *Acta Crystallogr.* **1954,** *7*, 776.

[200] Jensen, T. R.; Norby, P.; Stein, P. C.; Bell, A. M. T., Preparation, structure determination and thermal transformation of a new lithium zinc phosphate, δ_1-$LiZnPO_4$. *J. Solid State Chem.* **1995,** *117*, 39–47.

[201] Garcia-Moreno, O.; Alvarez-Vega, M.; Garcia-Alvarado, F.; Garcia-Jaca, J.; Gallardo-Amores, J. M.; Sanjuan, M. L.; Amador, U., Influence of the structure on the electrochemical performance of lithium transition metal phosphates as cathodic materials in rechargeable lithium batteries: a new high-pressure form of Li*M*PO_4 (*M* = Fe and Ni). *Chem. Mater.* **2001,** *13*, 1570–1576.

[202] Assat, G.; Manthiram, A., Rapid Microwave-Assisted Solvothermal Synthesis of Non-Olivine *Cmcm* Polymorphs of Li*M*PO_4 (*M* = Mn, Fe, Co, and Ni) at Low Temperature and Pressure. *Inorg. Chem.* **2015,** *54*, 10015–10022.

[203] Ito, S.; Kubo, Y.; Kuwahara, T., Hydrothermal synthesis of cobalt lithium phosphate ($CoLiPO_4$) pigment from cobalt phosphate [$Co_3(PO_4)_{2.8}H_2O$] and lithium phosphate (Li_3PO_4) as starting materials. *Shikizai Kyokaishi* **1978,** *51*, 70–74.

[204] Ludwig, J.; Haering, D.; Doeff, M. M.; Nilges, T., Particle size-controllable microwave-assisted solvothermal synthesis of the high-voltage cathode material $LiCoPO_4$ using water/ethylene glycol solvent blends. *Solid State Sci.* **2017,** *65*, 100–109.

[205] A. F. Holleman; E. Wiberg; Wiberg, N., Grundlagen der Komplexchemie. In *Lehrbuch der Anorganischen Chemie*, 102nd ed.; Walter de Gruyter: Berlin, Germany, **2007;** p 1360.

[206] Santoro, R. P.; Segal, D. J.; Newnham, R. E., Magnetic properties of $LiCoPO_4$ and $LiNiPO_4$. *Phys. Chem. Solids* **1966,** *27*, 1192–1193.

[207] Creer, J. G.; Troup, G. J., Magnetic susceptibility of $LiFePO_4$ and $LiCoPO_4$. *Phys. Lett. A* **1970,** *32*, 439–440.

[208] Vaknin, D.; Zarestky, J. L.; Rivera, J.-P.; Schmid, H., Antiferromagnetism in $LiCoPO_4$ and $LiNiPO_4$. *NATO Sci. Ser., II* **2004,** *164*, 203–218.

[209] Kharchenko, N. F.; Khrustalev, V. M.; Savitskii, V. N., Magnetic field induced spin reorientation in the strongly anisotropic antiferromagnetic crystal $LiCoPO_4$. *Low Temp. Phys.* **2010,** *36*, 558–564.

[210] Baker, P. J.; Franke, I.; Pratt, F. L.; Lancaster, T.; Prabhakaran, D.; Hayes, W.; Blundell, S. J., Probing magnetic order in $LiMPO_4$ (*M* = Ni, Co, Fe) and lithium diffusion in Li_xFePO_4. *Phys. Rev. B: Condens. Matter Mater. Phys.* **2011,** *84*, 174403/1–174403/8.

[211] Szewczyk, A.; Gutowska, M. U.; Wieckowski, J.; Wisniewski, A.; Puzniak, R.; Diduszko, R.; Kharchenko, Y.; Kharchenko, M. F.; Schmid, H., Phase transitions in single-crystalline magnetoelectric $LiCoPO_4$. *Phys. Rev. B: Condens. Matter Mater. Phys.* **2011,** *84*, 104419/1–104419/8.

[212] Singh, V.; Gershinsky, Y.; Kosa, M.; Dixit, M.; Zitoun, D.; Major, D. T., Magnetism in olivine-type $LiCo_{1-x}Fe_xPO_4$ cathode materials: bridging theory and experiment. *Phys. Chem. Chem. Phys.* **2015,** *17*, 31202–31215.

[213] Baek, S. H.; Klingeler, R.; Neef, C.; Koo, C.; Buechner, B.; Grafe, H. J., Unusual spin fluctuations and magnetic frustration in olivine and non-olivine $LiCoPO_4$ detected by ^{31}P and ^{7}Li nuclear magnetic resonance. *Phys. Rev. B: Condens. Matter Mater. Phys.* **2014,** *89*, 134424/1–134424/6.

[214] Khrustalyov, V. M.; Savytsky, V. M.; Kharchenko, M. F., Magnetoelectric effect in antiferromagnetic $LiCoPO_4$ in pulsed magnetic fields. *Low Temp. Phys.* **2016,** *42*, 280–285.

[215] Kharchenko, N. F.; Kharchenko, Y. N.; Szymczak, R.; Baran, M.; Schmid, H., Weak ferromagnetism in the antiferromagnetic magnetoelectric crystal $LiCoPO_4$. *Low Temp. Phys.* **2001,** *27*, 895–898.

[216] Rivera, J. P., The linear magnetoelectric effect in $LiCoPO_4$ revisited. *Ferroelectrics* **1994,** *161*, 147–164.

[217] Newnham, R. E.; Redman, M. J., Crystallographic data for $LiMgPO_4$, $LiCoPO_4$, and $LiNiPO_4$. *J. Am. Ceram. Soc.* **1965,** *48*, 547.

[218] Koleva, V.; Zhecheva, E.; Stoyanova, R., Ordered Olivine-Type Lithium-Cobalt and Lithium-Nickel Phosphates Prepared by a New Precursor Method. *Eur. J. Inorg. Chem.* **2010**, 4091–4099.

[219] Glaum, R.; Gerber, K.; Schulz-Dobrick, M.; Herklotz, M.; Scheiba, F.; Ehrenberg, H., Synthesis, structures and properties of the new lithium cobalt(II) phosphate $Li_4Co(PO_4)_2$. *J. Solid State Chem.* **2012,** *188*, 26–31.

[220] Harrison, W. T. A.; Vaughey, J. T.; Dussack, L. L.; Jacobson, A. J.; Martin, T. E.; Stucky, G. D., Two new adamite-type phases, $Co_2(OH)PO_4$ and $Zn_2(OH)PO_4$: structure-directing effect of organic additives. *J. Solid State Chem.* **1995,** *114*, 151–158.

[221] Zemann, J., The crystal structure of lithium phosphate, Li_3PO_4. *Acta Crystallogr.* **1960,** *13*, 863–867.

[222] Ludwig, J.; Nordlund, D.; Doeff, M. M.; Nilges, T., Synthesis and characterization of metastable, 20 nm-sized *Pna*2_1-$LiCoPO_4$ nanospheres. *J. Solid State Chem.* **2017,** *248*, 9–17.

[223] Kawamura, T.; Okada, S.; Yamaki, J.-i., Decomposition reaction of $LiPF_6$-based electrolytes for lithium ion cells. *J. Power Sources* **2006,** *156*, 547–554.

[224] Oh, S.-M.; Myung, S.-T.; Sun, Y.-K., Olivine $LiCoPO_4$-carbon composite showing high rechargeable capacity. *J. Mater. Chem.* **2012,** *22*, 14932–14937.

[225] Huppertz, H., Multianvil high-pressure / high-temperature synthesis in solid state chemistry. *Z. Kristallogr.* **2004,** *219*, 330–338.

[226] Ludwig, J.; Alarcón-Suesca, C.; Geprägs, S.; Nordlund, D.; Doeff, M. M.; Puente Orench, I.; Nilges, T., Direct synthesis and characterization of mixed-valent $Li_{0.5-\delta}CoPO_4$, a Li-deficient derivative of the *Cmcm* polymorph of $LiCoPO_4$. *RSC Adv.* **2017,** *7*, 28069–28081.

Chapter 2
Scope and Outline

As described in Chapter 1.3, $LiCoPO_4$ exists in three orthorhombic modifications that belong to the space groups *Pnma*, *Pna*2_1, and *Cmcm*. While the thermodynamically stable *Pnma*-$LiCoPO_4$ is considered a promising high-voltage cathode material for lithium-ion batteries and represents the most widely investigated polymorph, comparably little is known about the metastable *Pna*2_1- and *Cmcm*-$LiCoPO_4$ phases. In two parts, this work focuses on all three $LiCoPO_4$ polymorphs as well as two new metastable phases, which are outlined as follows.

(I) Microwave-Assisted Solvothermal (MWST) Synthesis and Optimization of Pnma-$LiCoPO_4$ as a High-Voltage Cathode Material for Lithium-Ion Batteries

- Development of a simple, fast MWST process for the synthesis of *Pnma*-$LiCoPO_4$
- Optimization of the performance by particle size and morphology control

Because of its high theoretical capacity (167 $mAh \cdot g^{-1}$) and operating potential (4.8 V *vs.* Li/Li^+), olivine-type *Pnma*-$LiCoPO_4$ offers the potential to significantly increase the energy density (802 $Wh \cdot kg^{-1}$) of lithium-ion batteries. Major obstacles that limit its electrochemical performance, however, are its low and anisotropic (transport along the [010] direction) electronic and ionic conductivities. A promising approach to tackle this issue is to tailor the crystal properties (size, shape, and orientation), which can be realized by kinetically controlled synthesis methods. As pointed out in Chapter 1.2.2, to date, the only such technique that delivered a high-capacity *Pnma*-$LiCoPO_4$ material (> 75% of the theoretical capacity, *i.e.* > 125 $mAh \cdot g^{-1}$) in a simple process without any additional carbon coating or annealing steps is the microwave-assisted solvothermal (MWST) synthesis. Despite the recent progress and the numerous advantages of the MWST technique compared to other wet-chemical procedures, the number of reports is still very limited. A deeper understanding of the relationship between the synthesis parameters and material properties, and the systematic exploration of particle size- and morphology-tuning approaches are long overdue.

Therefore, a facile and rapid one-step MWST process using a binary water/ethylene glycol (EG) solvent mixture towards high-performance *Pnma*-$LiCoPO_4$ particles with tailored crystal properties was developed (Chapter 4.1.1). To further improve the performance, the

process was then adapted to implement particle size and morphology control. For that purpose, the composition of the H_2O/EG solvent blend (Chapter 4.1.2) and the type of co-solvent (Chapter 4.1.3) were varied. The obtained materials were comprehensively characterized using powder X-ray diffraction (PXRD), elemental and surface area analysis, scanning and transmission electron microscopy (SEM/TEM), selected area electron diffraction (SAED), and galvanostatic cycling. This thorough analysis allowed to gain fundamental insights into the influence of the synthesis conditions on the material microstructure and electrochemical performance, which is crucial for further developments in the field. With the help of spectroscopic methods, thermogravimetry/differential scanning calorimetry (TGA/DSC) and temperature-dependent *in situ* PXRD studies, it was possible to identify an amorphous secondary phase in the *Pnma*-$LiCoPO_4$ material. In contrast to previous reports on its high thermal stability, the studies further revealed a high-temperature phase transition of *Pnma*-$LiCoPO_4$.

(II) Metastable Lithium Cobalt Phosphates

- Metastable $LiCoPO_4$ polymorphs: *Pna*2_1-$LiCoPO_4$ and *Cmcm*-$LiCoPO_4$
- Novel, mixed-valent Co(II,III) phases: *Cmcm*-$Li_{0.5-\delta}CoPO_4$ and $Co_{11}Li[(OH)_5O][(PO_3OH)(PO_4)_5]$

Despite the recent advance on the *Pna*2_1- and *Cmcm*-$LiCoPO_4$ polymorphs as reviewed in the Chapters 1.3.2 and 1.3.3, fundamental questions and issues have not or only sparsely been addressed prior to this work. Given the small number of studies and the metastability of the phases, their synthetic accessibility is still very limited and complex procedures are required. Other important open issues are the correct determination of the compositions and crystal structures as well as the unclear thermal behavior of these phases. While reports on the thermal stability of *Pna*2_1-$LiCoPO_4$ are contradictory, the high-temperature behavior of *Cmcm*-$LiCoPO_4$ as well as its magnetic properties are unknown. Furthermore, no attempt was made to elucidate the reasons for the poor electrochemical performance of these polymorphs or to improve it (*e.g.* by using particle size and morphology tuning approaches similar to *Pnma*-$LiCoPO_4$).

This work presents alternative and simple synthesis pathways towards *Pna*2_1- and *Cmcm*-$LiCoPO_4$, using conventional and microwave-assisted solvothermal as well as polyol techniques (Chapters 4.2.2 and 4.2.3). The formation mechanisms as well as structural and morphological tuning options were explored, which has only barely been touched in previous reports. X-ray and neutron powder diffraction (PXRD, PND) studies supported by elemental analysis allowed a fundamental revision of the crystal structures, which helped to identify the intrinsic causes of the poor electrochemical performance. Further analysis using SEM, infrared

(IR), and X-ray absorption spectroscopy (XAS) as well as electrochemical and magnetic measurements provided further insights into the structure–property relationships of these materials. A thorough investigation of the thermal properties of *Pna*2_1- and *Cmcm*-$LiCoPO_4$ using TGA/DSC, *ex* and *in situ* PXRD studies finally gave clarity to the issue of thermal stabilities and sheds light on the contradictory findings of previous studies. The significant role of *Pna*2_1-$LiCoPO_4$ in the high-temperature regime was revealed, which gives new impulses to critically review the thermodynamic relation of all three $LiCoPO_4$ polymorphs.

The application of kinetically controlled synthesis procedures also provided a pathway towards two new lithium cobalt phosphate phases. *Cmcm*-$Li_{0.5-\delta}CoPO_4$, the first Li-deficient structural derivative of *Cmcm*-$LiCoPO_4$, could be prepared by a simple bottom-up polyol approach as opposed to common top-down (electro)chemical delithiation techniques (Chapter 4.2.4). Furthermore, the trigonal framework compound $Co_{11}Li[(OH)_5O][(PO_3OH)(PO_4)_5]$ was identified as a key competing phase in the hydrothermal synthesis of *Pnma*-$LiCoPO_4$ (Chapter 4.2.1). The phases were thoroughly characterized by PXRD (and PND), elemental analysis, SEM, IR spectroscopy, and magnetic measurements. The Co oxidation state of both mixed-valent Co(II,III) phases was quantified with the help of XAS, which in combination with a comprehensive thermal analysis allowed the elucidation of the complex, multi-step thermal decomposition mechanisms. In this regard, this work makes an important contribution and opens up further perspectives towards new materials and applications in this field of research.

Chapter 3
Experimental Methods

3.1 Starting Materials and Synthesis Equipment

3.1.1 Reactants and Solvents

Table 3.1 lists all starting materials, solvents, and additives used for the syntheses with their respective specifications. All chemicals were used as received from the supplier without further purification.

Ultrapure type 1 water (ρ = 18.2 MΩ·cm at T = 25 °C; TOC (total organic carbon) ≤ 5 ppb) for synthesis and washing purposes was produced from tap water using a Direct-Q 3 UV water purification system (MERCK MILLIPORE) with an integrated dual wavelength UV lamp (λ = 185/254 nm) for photo-oxidation of organic contaminants.[1] For solvothermal syntheses, a variety of polyol (co-)solvents with multiple hydroxyl groups were used, including ethylene glycol (EG), diethylene glycol (DEG), triethylene glycol (TEG), tetraethylene glycol (TTEG), and polyethylene glycol 400 (PEG; $\overline{M}_w$ = 380–420 g·mol^{-1}). In addition, benzyl alcohol (BA) was explored as an alternative solvent. The structural formulas of the organic solvents are compiled in Figure 3.1.

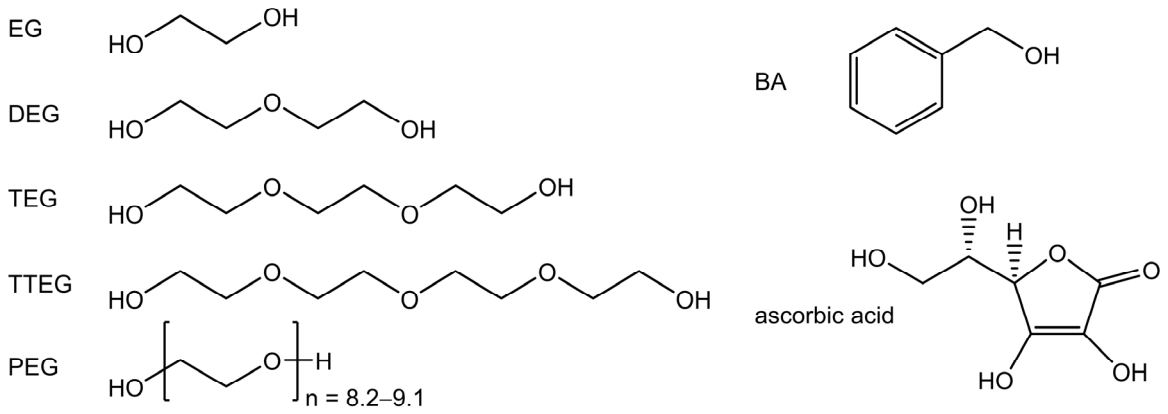

Figure 3.1 Structural formulas of the solvents ethylene glycol (EG), diethylene glycol (DEG), triethylene glycol (TEG), tetraethylene glycol (TTEG), polyethylene glycol 400 (PEG), and benzyl alcohol (BA) as well as the additive L(+)-ascorbic acid (vitamin C) that served as a reducing agent.

Table 3.1 Specifications of all reactants, solvents, and additives used for the syntheses.

Compound	Sum Formula	Shape	Supplier	Purity
Lithium acetate	$LiCH_3COO$	powder	ChemPur	99+%
Lithium dihydrogen phosphate	LiH_2PO_4	powder	Sigma Aldrich	99%
Lithium hydroxide monohydrate	$LiOH \cdot H_2O$	powder	Bernd Kraft	≥ 99.0%
Cobalt acetate tetrahydrate	$Co(CH_3COO)_2 \cdot 4\ H_2O$	powder	Merck	99.99%
			Alfa Aesar	98%
Cobalt sulfate heptahydrate	$CoSO_4 \cdot 7\ H_2O$	powder	ChemPur	99%
Cobalt oxalate dihydrate	$CoC_2O_4 \cdot 2\ H_2O$	powder	Alfa Aesar	98%
Diammonium hydrogen phosphate	$(NH_4)_2HPO_4$	powder	Merck Emsure	≥ 99.0%
Phosphoric acid	H_3PO_4	85 wt% solution	AppliChem	*Ph. Eur.*
Water (deionized)	H_2O	liquid	Merck Millipore water purification system (from tab)	type 1 (18.2 MΩ·cm, TOC ≤ 5 ppb)
Ethylene glycol (EG)	$HOCH_2CH_2OH$	liquid	VWR Analar Normapur	99.9%
Diethylene glycol (DEG)	$HO(CH_2CH_2O)_2H$	liquid	Merck	≥ 99.0%
Triethylene glycol (TEG)	$HO(CH_2CH_2O)_3H$	liquid	Merck	≥ 99.0%
Tetraethylene glycol (TTEG)	$HO(CH_2CH_2O)_4H$	liquid	Merck	≥ 99.0%
			Merck	≥ 98%
Polyethylene glycol 400 (PEG; $\bar{M}_w$ = 380–420 g·mol^{-1})	$HO(CH_2CH_2O)_nH$ (n = 8.2–9.1)	liquid	Merck	for synthesis
Benzyl alcohol (BA)	C_7H_8O	liquid	AppliChem Panreac	≥ 99.5%
Ethanol (absolute)	CH_3CH_2OH	liquid	VWR Analar Normapur	99.95%
Hydrochloric acid	HCl	37 wt% solution	Merck Emsure	*Ph. Eur.*, for analysis
L(+)-ascorbic acid	$C_6H_8O_6$	powder	Alfa Aesar	99+%

Solvent volumes were measured with the help of a volume-adjustable, piston-operated 10 mL single-channel pipette (BRAND Transferpette S, volume range: V = 1,000–10,000 µL, increment: ΔV = 10 µL, error: ≤ ± 0.6%) equipped with a hydrophobic PE (polyethylene) filter as a safeguard against liquid entering the pipette. For the exact dosage of smaller reagent quantities, *e.g.* of phosphoric acid, a 200 µL pipette (BRAND Transferpette S, volume range: V = 20–200 µL, increment: ΔV = 0.2 µL, error: ≤ ± 0.6%) was used. Due to the high viscosity of most liquids, an adequate waiting time was required to achieve the specified accuracies.[2]

In order to control the reaction steps or, where applicable, to adjust the pH values of the reaction mixtures (*e.g.* by using hydrochloric acid, *cf.* Chapter 3.2.4), pH values were determined using non-bleeding pH-indicator test strips (MERCK MColorpHast, pH range: 2.0–9.0, pH graduation: 0.5 or MERCK MColorpHast, pH range: 1–14, pH graduation: 1.0).

The precipitates obtained after the reactions were washed thoroughly with deionized (*i.e.* ultrapure type 1) water and absolute ethanol in order to remove possible side products and/or organic residues and decomposition products from the solvents and ascorbic acid (vitamin C; structural formula see Figure 3.1). The latter was used as a reductive additive to prevent the oxidation of Co^{2+} to Co^{3+} in solution (*cf.* Chapter 3.2.1).

3.1.2 Pressure Digestion System

The hydrothermal (HT) and solvothermal (ST) syntheses were performed using a pressure digestion system (digestec, BERGHOF) equipped with teflon-lined DAB-2 stainless steel pressure vessels (316 Ti, *i.e.* titanium-stabilized CrNiMo stainless steel; V = 50 mL). The system can be operated at a maximum temperature T_{max} of 250 °C and a pressure p_{max} of up to 200 bar.[3] The schematic construction of a DAB-2 pressure vessel (or autoclave) is shown in Figure 3.2a. The pressure vessel is equipped with a TFM–PTFE insert (perfluoro(propyl vinyl ether)-modified polytetrafluoroethylene, Teflon, Hostaflon, V_{max} = 50 mL) with a V-sealing cap. The cylindric body is closed by a base plate at the bottom, and a bayonet quick closure with a hexagon head bolt and a spring at the top. A pressure cover with a rupture disk (p_{max} = 200 bar) is implemented as a safeguard against overpressure. The vessels are opened and closed with the help of a mounting station, which essentially consists of a mounting plate and a torque wrench (closing force: 25 Nm; *cf.* Figure 3.2b). For the synthesis, the vessels are heated externally with a DAH-412 heating block (capacity: 12 vessels), and a programmable BTC-3000 temperature control unit with a NiCr-Ni temperature probe (Figure 3.2c). The vessels are naturally cooled down to room temperature after the synthesis. Note that it is not possible to stir the reaction mixtures during the synthesis due to the setup. Moreover, there is no option to monitor the internal vessel temperature.

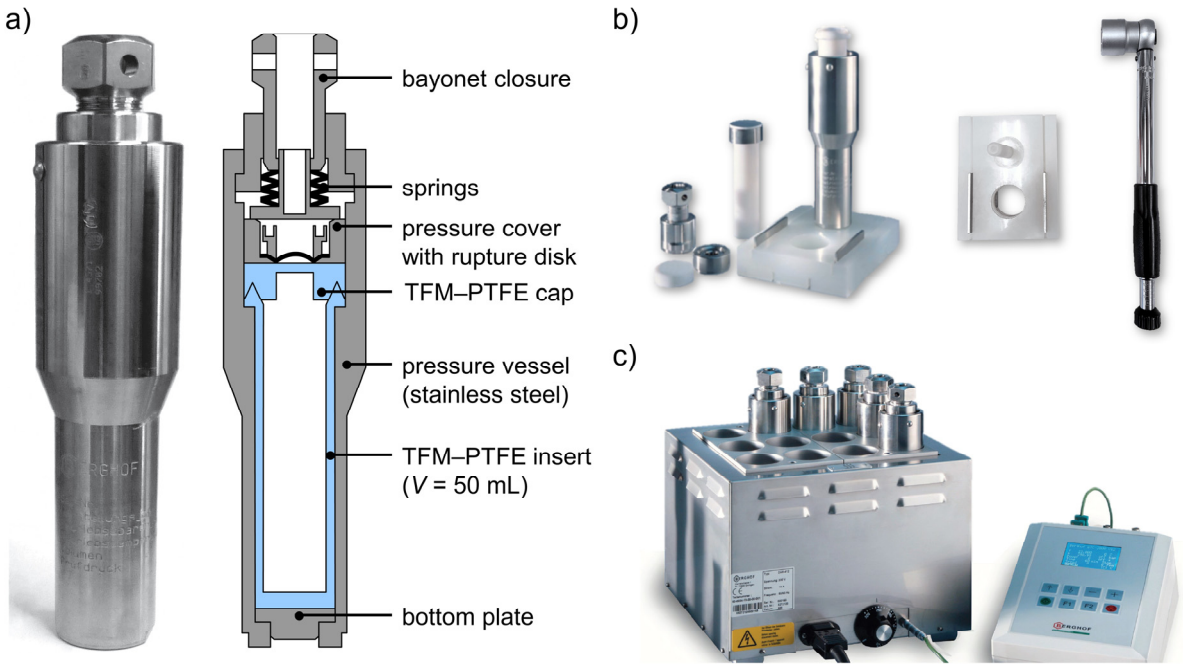

Figure 3.2 BERGHOF digestec pressure digestion system used for hydro- (HT) and solvothermal (ST) syntheses. (a) Schematic construction of a DAB-2 pressure vessel (V = 50 mL, p_{max} = 200 bar), (b) mounting station including a mounting plate and torque wrench to open and close the vessels, and (c) DAH-412 heating block and BTC-3000 temperature control unit. The schematic drawing in (a) and graphic (c) were modified on the basis of reference [4].

3.1.3 Microwave Synthesis System

An Ethos One microwave synthesis system (MLS; maximum power: 1200 W, frequency: 2.45 GHz) was used for the microwave-assisted solvothermal (MWST) syntheses. Since the minimum synthesis temperature to obtain *Pnma*-$LiCoPO_4$ was found to be comparably high in previous experiments (T ~220 °C),[5] the high-pressure high-temperature MR-8 HT monobloc rotor system (T_{max} = 300 °C, p_{max} = 75 bar)[6] was used for the experiments (Figure 3.3d). The rotor has positions for eight reaction containers (HTV-75, V = 75 mL) and an external explosion protection. The design of a HTV-75 high-pressure vessel assembly (normal vessel *vs.* reference vessel with a temperature probe placed inside a thermowell) is indicated in Figure 3.3a–c. The inner TFM–PTFE vessel is enclosed by a ceramic high-pressure jacket with a spherical bottom cap that is additionally surrounded by a fiber-reinforced plastic protection shield with cooling fins. The vessel is sealed with a TFM cover, which is equipped with an automatic pressure control unit (APCU) and a pressure release valve. Unlike the pressure digestion system (Chapter 3.1.2), the microwave system features a built-in stirring unit that ensures continuous homogenization of the reaction mixture during the synthesis using common magnetic stir bars.

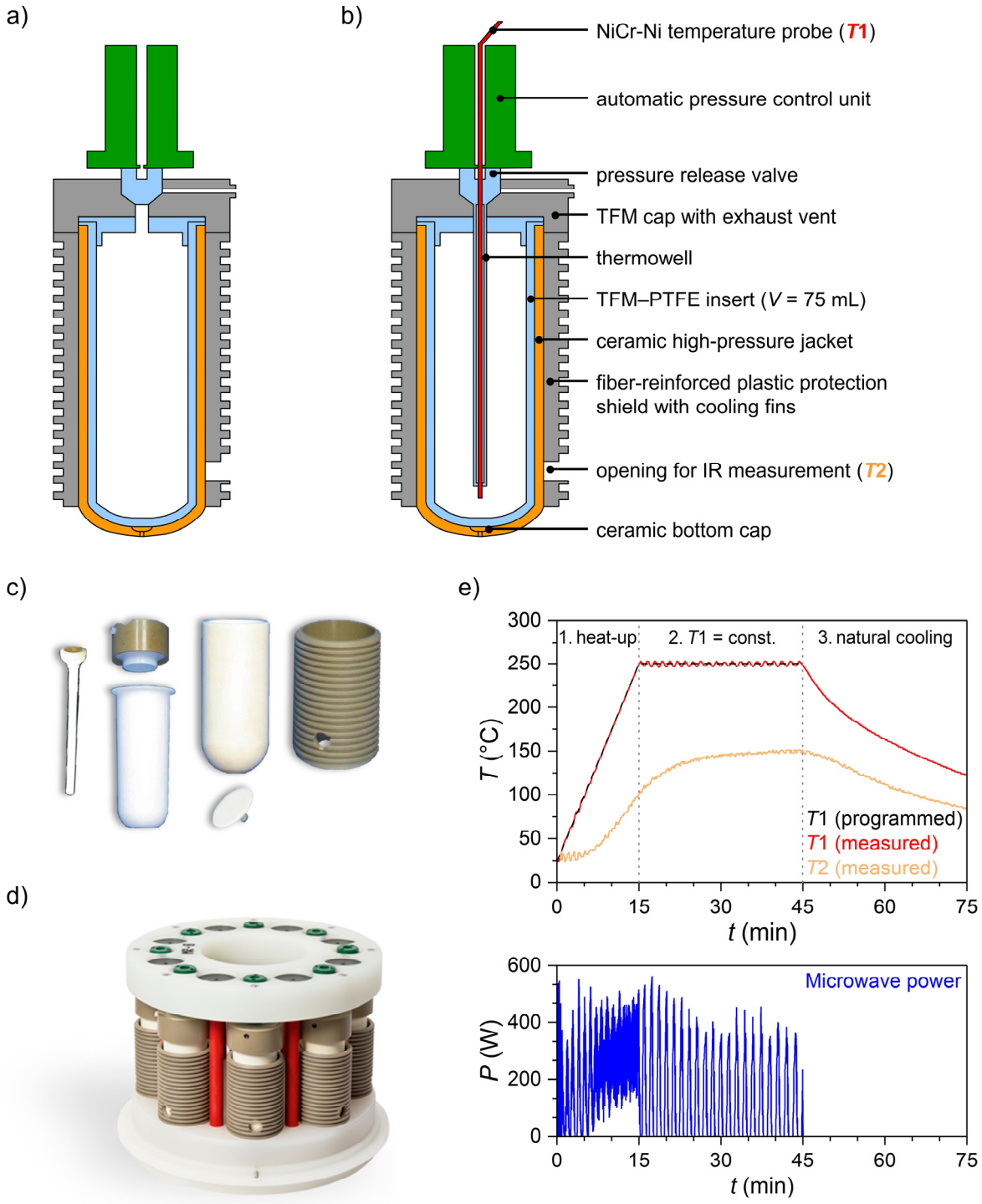

Figure 3.3 Ethos One microwave synthesis system (MLS; maximum power: 1200 W, frequency: 2.45 GHz) used for the microwave-assisted solvothermal (MWST) syntheses. (a) Schematic construction of a HTV-75 high-pressure vessel (V = 75 mL, p_{max} = 160 bar) compared to (b) a reference vessel with an ATC-CE-400 temperature probe placed inside a thermowell. (c) shows the parts of the vessel assembly and (d) the MR-8 HT high-pressure high-temperature monobloc rotor system. An exemplary measurement log demonstrating the programmed temperature profile (1. heat-up phase to $T1$ = 250 °C within 15 min, 2. $T1$ = 250 °C = const. for 30 min, 3. natural cooling to room temperature), the measured internal ($T1$) and external ($T2$) temperatures as well as the irradiated microwave power (P) is displayed in (e). The small oscillations of $T1$ from the target temperature can be related with the irradiation of individual microwave pulses. The drawings in (a, b) were created and modified using reference [6] as a template.

The easyCONTROL-640 software package[7] allows programming of the reaction temperature, reaction time, and stirring speed. The automatic temperature control unit (T660, MLS) ensures continuous on-line monitoring of the internal temperature (*T*1) of the reference vessel *via* an ATC-CE-400 temperature probe (NiCr-Ni thermocouple) placed inside a thermowell. The set internal temperature profile was followed automatically by regulating the irradiated microwave power. Additionally, the external temperature (*T*2) of the ceramic jackets of all vessels was monitored by an IR-TC infrared sensor *via* openings in the explosion protection of the rotor and the plastic protection shield of the containers (Figure 3.3a, b). To ensure safe operation of the device, *T*2 should not exceed 180 °C. An exemplary measurement log demonstrating the programmed temperature profile (1. heat-up phase to *T*1 = 250 °C within 15 min, 2. *T*1 = 250 °C = constant for 30 min, 3. natural cooling to room temperature), the measured internal and external temperatures *T*1 and *T*2 as well as the irradiated microwave power is presented in Figure 3.3e. It can be derived that there is little deviation of the actual from the ideal temperature program, ensuring appropriate temperature control and reproducibility of the experiments. The small oscillations of *T*1 from the target temperature can be explained by the irradiation of individual microwave pulses.

3.2 Synthesis

3.2.1 Standard Microwave-Assisted Solvothermal (MWST) Synthesis of *Pnma*-$LiCoPO_4$

Taking a synthesis process for the production of $LiMn_{0.7}Fe_{0.3}PO_4$ nanorods from the literature[8] as a starting point, a novel microwave-assisted solvothermal (MWST) process for the synthesis of *Pnma*-$LiCoPO_4$ was developed. In order to produce phase pure olivine-type $LiCoPO_4$, the process was optimized in the precursor system $LiOH \cdot H_2O$ – $CoSO_4 \cdot 7\ H_2O$ – H_3PO_4 with respect to a number of reaction parameters, such as reaction time and temperature, power of the microwave irradiation, stirring speed during the synthesis, pH value of the reaction mixture, the application of reducing agents as well as the concentration, molar *n*(Li):*n*(Co):*n*(P) ratio, and mixing sequence of the starting materials. For these investigations, which are not included in this work, only one synthesis parameter was changed while keeping all other reaction conditions constant in order to be able to evaluate the effect of the individual parameter. Since an aqueous component in the solvent was found to be crucial to obtain *Pnma*-$LiCoPO_4$ (possibly related to the increased vapor pressure during the synthesis) and a polyol-type co-solvent proved to be necessary to allow for a defined particle morphology (due to its soft template effect[9-10]) and reasonable electrochemical performance, 30 mL of a binary 1:1 (*v*:*v*, by volume) water/ethylene glycol (EG) solvent blend with 50 vol% H_2O and 50 vol% EG were used for the investigations. The sum of these efforts resulted in a standardized basic MWST process towards *Pnma*-$LiCoPO_4$ particles with a hexagonal platelet morphology (Chapter 4.1.1), which is described in the following and shown in Scheme 3.1 and Figure 3.4, respectively. The process served as a starting point for the further optimization of the *Pnma*-$LiCoPO_4$ material from an electrochemical point of view by tuning the size (Chapter 3.2.2) and morphology (Chapter 3.2.3) of the particles. It was also used for the production of nanoparticles of the metastable *Pna*2_1-$LiCoPO_4$ polymorph (Chapter 3.2.5).

$$3\ LiOH \cdot H_2O + CoSO_4 \cdot 7\ H_2O + H_3PO_4 \xrightarrow[\text{ascorbic acid}\ (H_2O/EG = 1:1)]{T = 250\ °C,\ t = 30\ min;\ P = 600\ W} \textit{Pnma}\text{-}LiCoPO_4 + Li_2SO_4 \cdot H_2O + 12\ H_2O$$

Scheme 3.1 Reaction scheme of the microwave-assisted solvothermal (MWST) standard process for the synthesis of *Pnma*-$LiCoPO_4$ particles with a hexagonal platelet morphology using a binary 1:1 (*v*:*v*) water/ethylene glycol (EG) solvent mixture. Note that the two additional equivalents of $LiOH \cdot H_2O$ are required to bind the sulfate ions to form stoichiometric amounts of water-soluble $Li_2SO_4 \cdot H_2O$ as a side product.

The MWST standard process produces *Pnma*-$LiCoPO_4$ in a single step without further post-heat treatment at a moderate temperature of 250 °C and a short reaction time of only 30 min, using 30 mL of a binary 1:1 (*v*:*v*) water/ethylene glycol (EG) mixture as a solvent (Scheme 3.1). The molar ratio *n*(Li):*n*(Co):*n*(P) of the starting materials $LiOH \cdot H_2O$, $CoSO_4 \cdot 7\ H_2O$, and H_3PO_4 was 3:1:1, with the two additional equivalents of Li being required to bind the SO_4^{2-} ions as $Li_2SO_4 \cdot H_2O$ in a stoichiometric reaction. The highly water-soluble[11-12] lithium sulfate side phase was subsequently removed by washing (for further discussions on the Li_2SO_4 phase, please refer to the respective publication and supporting materials in Chapter 6.2). Furthermore, ascorbic acid was used as reducing agent to prevent the oxidation of Co^{2+} to Co^{3+} in the aqueous solvent phase.[13-14]

In the first step of the process (Figure 3.4), 22.5 mmol $LiOH \cdot H_2O$ were dissolved in 15 mL deionized water. Then, 7.5 mmol H_3PO_4 (85 wt% solution) were added dropwise under stirring to the clear solution with pH = 14, which produced a white suspension of Li_3PO_4 with pH = 10.5. Subsequently, 15 mL ethylene glycol, 7.5 mmol $CoSO_4 \cdot 7\ H_2O$ and 0.075 g ascorbic acid were added in this sequence. The resulting blue-violet gel (pH = 5.5), which consists of a mixture of $Co_3(PO_4)_2 \cdot 8\ H_2O$, $Li_2SO_4 \cdot H_2O$, and Li_3PO_4 according to further studies not included in this work, was homogenized for 20 min and then transferred into a 75 mL capacity TFM–PTFE vessel (HTV-75). The solvothermal reaction was performed using the Ethos One microwave synthesis system equipped with the MR-8 HT monobloc rotor as described in Chapter 3.1.3. The sample temperature (*T*1) was ramped to 250 °C within 15 min and kept at 250 °C for 30 min under stirring (speed setting: 50%), with a maximum microwave power of P_{max} = 600 W being applied (*cf.* also Figure 3.3e, Chapter 3.1.3). After natural cooling to room temperature (RT), the violet precipitate was separated from the mother solution (pH = 5.0) by suction filtration, and washed five times with 50 mL deionized water and one time with 50 mL absolute ethanol in order to remove the lithium sulfate side product and organic residues of the EG co-solvent, the ascorbic acid additive, and their decomposition products. The light pink powder (see bottom left of Figure 3.4 or Figure 4.1, Chapter 4.1.1) was finally dried in air at 150 °C overnight.

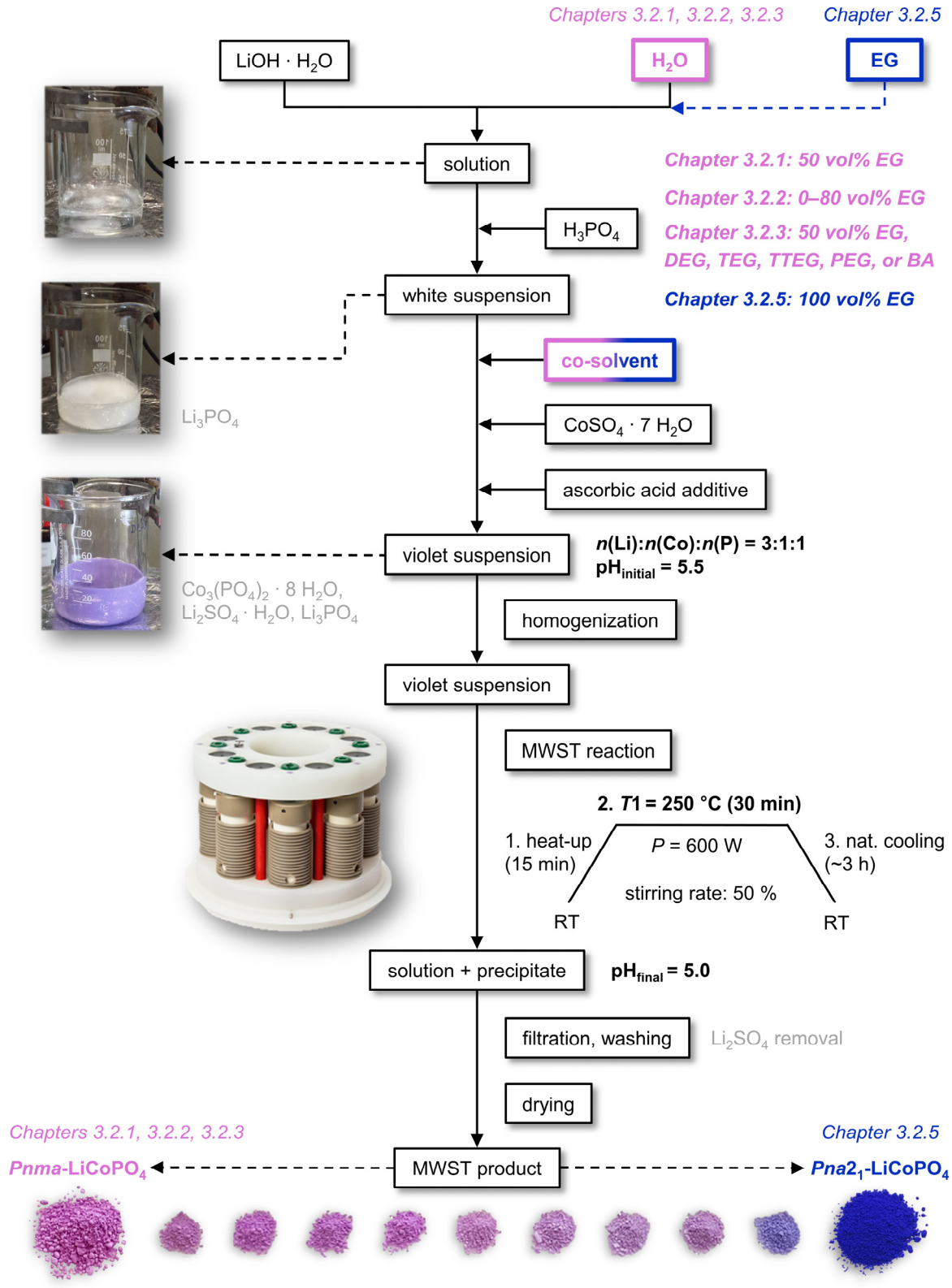

Figure 3.4 Flow chart demonstrating the microwave-assisted solvothermal (MWST) process. The standard synthesis of *Pnma*-$LiCoPO_4$ (Chapter 3.2.1) was based on a binary solvent blend of water and ethylene glycol (EG) as a co-solvent (50 vol%). It was further modified for tuning the size (variation of the EG content between 0 and 80 vol%; Chapter 3.2.2) and morphology (variation of the type of co-solvent, 50 vol%: DEG, diethylene glycol; TEG, triethylene glycol; TTEG, tetraethylene glycol; PEG, polyethylene glycol; BA, benzyl alcohol; Chapter 3.2.3) of the *Pnma*-$LiCoPO_4$ particles. *Pna*2_1-$LiCoPO_4$ was obtained by using a pure (100 vol%) EG solvent (Chapter 3.2.5).

3.2.2 Microwave-Assisted Solvothermal (MWST) Synthesis of Size-Controlled *Pnma*-$LiCoPO_4$ Particles

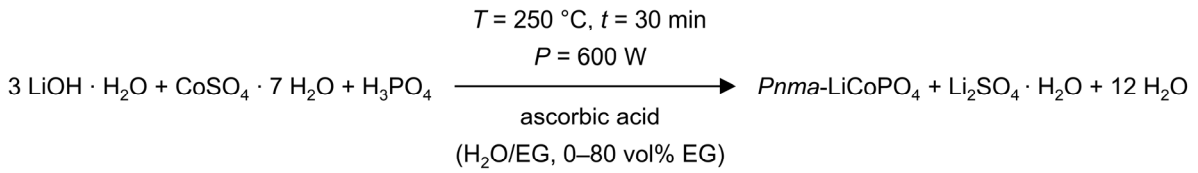

Scheme 3.2 Reaction scheme of the microwave-assisted solvothermal (MWST) process for the synthesis of size-tuned *Pnma*-$LiCoPO_4$ particles by using ethylene glycol (EG) concentrations of 0–80 vol% (increment step: 10 vol%) in the binary water/ethylene glycol solvent blend.

Size-tuned *Pnma*-$LiCoPO_4$ particles (Chapter 4.1.2) were obtained using the standard MWST process described in Chapter 3.2.1 by altering the ethylene glycol (EG) concentration of the binary H_2O/EG solvent mixture between 0 vol% EG (*i.e.* using pure water in a microwave-assisted hydrothermal (MWHT) process) and 80 vol% EG with an increment step of 10 vol% (Scheme 3.2). All other parameters were kept constant in order to ensure reliable and comparable results. To further investigate the influence of the solvent composition on the particle size, the viscosities of the respective solvent mixtures were determined by rheometry (for details refer to Chapter 3.3.7). The *Pnma*-$LiCoPO_4$ (LCP) samples were denoted by the amount of EG in vol% used in the solvent blend, *i.e.* LCP-0, LCP-10, (…), and LCP-80, respectively. The pink color of the powders became lighter and more bluish going from LCP-0 to LCP-80 (*cf.* bottom of Figure 3.4 or the respective publication in Chapter 6.3), which can be explained by a reduction of the particle size.[15] Note that at EG concentrations of 90 vol%, a mixture of the *Pnma*- and *Pna*2_1-$LiCoPO_4$ polymorphs was obtained. The synthesis in pure (100 vol%) EG yielded single-phase *Pna*2_1-$LiCoPO_4$, which was investigated in another study (see Chapter 3.2.5).

3.2.3 Microwave-Assisted Solvothermal (MWST) Synthesis of Morphology-Controlled *Pnma*-$LiCoPO_4$ Particles

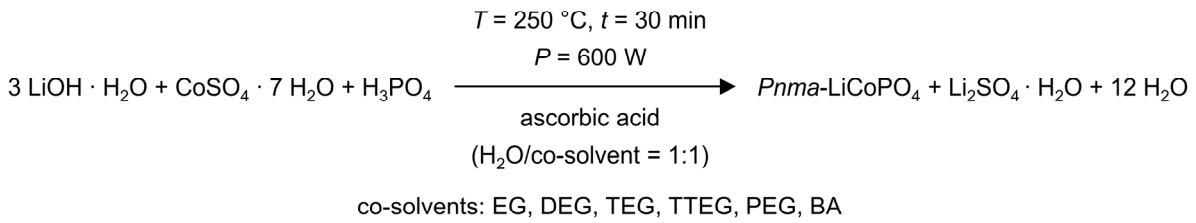

Scheme 3.3 Reaction scheme of the microwave-assisted solvothermal (MWST) process for the synthesis of morphology-tuned *Pnma*-$LiCoPO_4$ particles by using various co-solvents in a binary (1:1, *v*:*v*) mixture with water. Specifically, 50 vol% ethylene glycol (EG), diethylene glycol (DEG), triethylene glycol (TEG), tetraethylene glycol (TTEG), polyethylene glycol 400 (PEG), or benzyl alcohol (BA) were employed as co-solvents.

For the production of *Pnma*-$LiCoPO_4$ particles with tuned morphologies (Chapter 4.1.3), the standard MWST process (see Chapter 3.2.1 and Figure 3.4) was altered by using a number of different 1:1 (*v*:*v*) binary solvent blends (Scheme 3.3). The mixtures were composed of deionized water (50 vol%) and the following polyol-type co-solvents (50 vol%) that feature different amounts of hydroxyl groups (for the structural formulas, please refer to Chapter 3.1.1, Figure 3.1): ethylene glycol (EG), diethylene glycol (DEG) triethylene glycol (TEG), tetraethylene glycol (TTEG), polyethylene glycol 400 (PEG), and benzyl alcohol (BA). In order to ensure that only the effect of the co-solvent was evaluated, all other reaction conditions were kept constant. The corresponding *Pnma*-$LiCoPO_4$ (LCP) samples were denoted by the co-solvent used as follows: LCP-EG, LCP-DEG, LCP-TEG, LCP-TTEG, LCP-PEG, and LCP-BA. The color of the powders ranged from light pink (LCP-TTEG) to dark violet (LCP-PEG; *cf.* Figure 4.3, Chapter 4.1.3), which was related to particle size effects with the color becoming darker and more intense for bigger crystallites.[16]

3.2.4 Hydrothermal (HT) Synthesis of $Co_{11}Li[(OH)_5O][(PO_3OH)(PO_4)_5]$

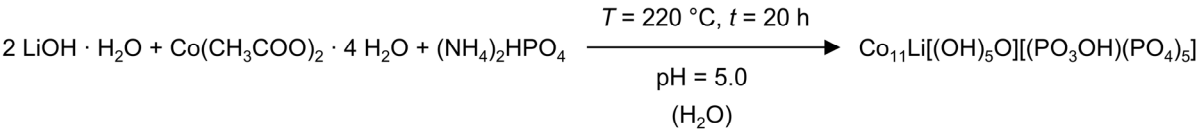

Scheme 3.4 Reaction scheme of the hydrothermal (HT) process towards $Co_{11}Li[(OH)_5O][(PO_3OH)(PO_4)_5]$. Because the pH-dependent formation of other phases such as $Co_3(OH)_2(PO_3OH)_2$ and *Pnma*-$LiCoPO_4$ competes in the process, adjusting the pH value of the reaction mixture to a value of 5.0 by adding HCl is crucial to obtain a single-phase material. Since the starting materials are not quantitatively incorporated in the phase in stoichiometric amounts, it is not possible to provide the exact molar ratios of the precursors and theoretical side products of the process. To keep the scheme simple, the nominal molar amount of the starting materials (*n*(Li):*n*(Co):*n*(P) molar ratio of 2:1:1) that was employed is provided, and possible side products have been omitted.

$Co_{11}Li[(OH)_5O][(PO_3OH)(PO_4)_5]$ (Chapter 4.2.1) was prepared by hydrothermal synthesis using the pressure digestion system described in Chapter 3.1.2 and $LiOH \cdot H_2O$, $Co(CH_3COO)_2 \cdot 4\ H_2O$, and $(NH_4)_2HPO_4$ in a molar ratio of *n*(Li):*n*(Co):*n*(P) = 2:1:1 as starting materials (Scheme 3.4). First, 1.50 mmol $Co(CH_3COO)_2 \cdot 4\ H_2O$ and $(NH_4)_2HPO_4$ each were dissolved in 20 mL deionized water, forming a pink solution with pH = 5.5. A solution of 3.00 mmol $LiOH \cdot H_2O$ in 10 mL water was then added dropwise to the first solution under continuous stirring. The pH value of the resulting purple suspension with pH = 10.0 was further lowered to 5.0 by adding hydrochloric acid (37 wt% solution). Since investigations on the influence of the pH value of the precursor mixture showed that the phase formation is highly pH-sensitive and competes with other phases such as $Co_3(OH)_2(PO_3OH)_2$ (at pH = 3.0–4.5) and *Pnma*-$LiCoPO_4$ (at pH = 8.0; for specific details refer to Chapter 6.5), adjusting the pH to a value of 5.0 proved to be a crucial step to obtain single-phase $Co_{11}Li[(OH)_5O][(PO_3OH)(PO_4)_5]$. The mixture was homogenized, transferred to a teflon-lined stainless steel pressure vessel, and sealed quickly. The vessel was heated to 220 °C within 2 h and kept at that temperature for a period of 20 h. After natural cooling to ambient temperature, the violet crystals (*cf.* Figure 4.5, Chapter 4.2.1) were separated from the mother solution (pH = 5.0) by suction filtration, and washed five times with 25 mL deionized water and 25 mL absolute ethanol. The powder was dried in air at 150 °C for 12 h.

3.2.5 Microwave-Assisted Solvothermal (MWST) Synthesis of Nano-Sized *Pna*2$_1$-LiCoPO$_4$ Particles

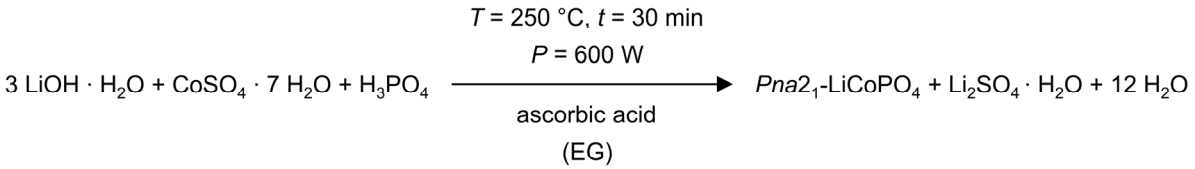

Scheme 3.5 Reaction scheme of the microwave-assisted solvothermal (MWST) process used for the synthesis of nano-sized *Pna*2$_1$-LiCoPO$_4$ particles by using pure (100 vol%) ethylene glycol (EG) as a solvent.

*Pna*2$_1$-LiCoPO$_4$ nanoparticles (Chapter 4.2.2) were obtained from a modified microwave-assisted solvothermal (MWST) process as described in Chapter 3.2.1, using 30 mL of pure ethylene glycol (EG; *i.e.* 100 vol%) as a solvent instead of an aqueous binary solvent mixture (Scheme 3.5). All other synthesis parameters and steps remained unchanged. The precipitate exhibited an intense dark blue color as demonstrated at the bottom right of Figure 3.4, Chapter 3.2.1 and in Figure 4.6, Chapter 4.2.2.

3.2.6 Solvothermal (ST) Synthesis of *Cmcm*-LiCoPO$_4$

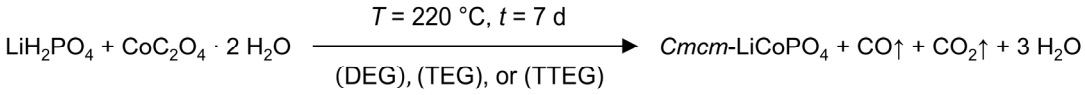

Scheme 3.6 Reaction scheme of the solvothermal (ST) process used to synthesize *Cmcm*-LiCoPO$_4$. The process can be performed using different polyol-type solvents, specifically diethylene glycol (DEG), triethylene glycol (TEG), or tetraethylene glycol (TTEG). The release of CO and CO_2 gas is the result of the decomposition of oxalic acid, which is obtained as an intermediate in the process. Minor amounts of Li_3PO_4 and *Pnma*-LiCoPO$_4$ are obtained as side phases (not shown in the scheme for simplicity).

The solvothermal (ST) synthesis of *Cmcm*-type LiCoPO$_4$ (Chapter 4.2.3) was carried out using the pressure digestion system described in Chapter 3.1.2. 9.00 mmol of LiH_2PO_4 and $CoC_2O_4 \cdot 2\ H_2O$ each, corresponding to a molar ratio of *n*(Li):*n*(Co):*n*(P) = 1:1:1, were dissolved in 9 mL of a polyol-type solvent, such as diethylene glycol (DEG), triethylene glycol (TEG), or tetraethylene glycol (TTEG; *cf.* Scheme 3.6). The resulting light pink suspensions (pH = 4.5) were homogenized for 20 min and transferred to teflon-lined stainless steel pressure vessels. The temperature was ramped to 220 °C within 2 h and held for 7 d, followed

by natural cooling to ambient temperature. The resulting light pink precipitates were separated from the solution (pH = 4.5) by filtration, washed four times with 10 mL deionized water and 10 mL absolute ethanol, and subsequently dried at 130 °C for 12 h under air. It is worth noting that in all cases, Li_3PO_4 and *Pnma*-$LiCoPO_4$ were obtained as side phases (see Chapter 6.7 for further details). Since the sample obtained from DEG contained the least amount of impurities, it was used for further characterization in Chapter 4.2.3 and the publication in Chapter 6.7 (denoted as LCP-*Cmcm* (ST)). It was compared with a single-phase *Cmcm*-$LiCoPO_4$ material, which was exclusively accessible by a polyol process (denoted as LCP-*Cmcm* (PO)) as described in Chapter 3.2.7.

3.2.7 Polyol (PO) Synthesis of *Cmcm*-$Li_{1-\gamma}CoPO_4$ and *Cmcm*-$Li_{0.5-\delta}CoPO_4$

a)

$$3\ LiCH_3COO + Co(CH_3COO)_2 \cdot 4\ H_2O + 10\ H_3PO_4 \xrightarrow[(TTEG)]{T = 200\ °C,\ t = 14\ h} Cmcm\text{-}Li_{1-\gamma}CoPO_4$$

b)

$$LiCH_3COO + Co(CH_3COO)_2 \cdot 4\ H_2O + 10\ H_3PO_4 \xrightarrow[(TTEG)]{T = 185\ °C,\ t = 14\ h} Cmcm\text{-}Li_{0.5-\delta}CoPO_4$$

Scheme 3.7 Reaction scheme of the polyol (PO) process towards *Cmcm*-type $LiCoPO_4$ phases with varied lithium contents by using different *n*(Li):*n*(Co):*n*(P) molar ratios of the starting materials. (a) *Cmcm*-$Li_{1-\gamma}CoPO_4$ (referred to as *Cmcm*-$LiCoPO_4$ with $\gamma = 0$ in Chapter 4.2.3 and as *Cmcm*-$Li_{1-\gamma}CoPO_4$ in Chapter 4.2.4 to reflect the sub-stoichiometry) can be obtained from a *n*(Li):*n*(Co):*n*(P) ratio of 3:1:10. (b) Li-deficient *Cmcm*-$Li_{0.5-\delta}CoPO_4$ is produced by employing a reduced amount of lithium acetate precursor, corresponding to *n*(Li):*n*(Co):*n*(P) = 1:1:10. Note that since the starting materials are not used in stoichiometric amounts (*cf.* excess of $LiCH_3COO$ and H_3PO_4), it is not possible to predict the theoretical side products of the process. Hence, no side products are provided in the scheme.

Cmcm-type $LiCoPO_4$ phases with varied Li contents, specifically *Cmcm*-$Li_{1-\gamma}CoPO_4$ (referred to as *Cmcm*-$LiCoPO_4$ with $\gamma = 0$ in Chapter 4.2.3 and as *Cmcm*-$Li_{1-\gamma}CoPO_4$ in Chapter 4.2.4, reflecting the sub-stoichiometry of the material) and *Cmcm*-$Li_{0.5-\delta}CoPO_4$ (Chapter 4.2.4) were obtained from polyol synthesis. The synthesis was performed by Carlos Alarcón-Suesca at the Professorship of Synthesis and Characterization of Innovative Materials, TECHNICAL UNIVERSITY OF MUNICH, Garching, Germany. $LiCH_3COO$, $Co(CH_3COO)_2 \cdot 4\ H_2O$, and H_3PO_4 were used as starting materials in different *n*(Li):*n*(Co):*n*(P) molar ratios to adjust the Li content of the product, and tetraethylene glycol (TTEG) was applied as solvent. *Cmcm*-$Li_{1-\gamma}CoPO_4$ was obtained by using the starting materials in a molar ratio of

n(Li):*n*(Co):*n*(P) = 3:1:10 (Scheme 3.7a), whereas *Cmcm*-$Li_{0.5-\delta}CoPO_4$ was synthesized from a modified process with *n*(Li):*n*(Co):*n*(P) = 1:1:10 (Scheme 3.7b), and one equivalent corresponding to 7.42 mmol in both cases. (At this point, it is noteworthy that the molar amounts of the precursors and Li contents of the produced materials are not correlated linearly.) First, H_3PO_4 was added dropwise to a solution of $Co(CH_3COO)_2 \cdot 4\ H_2O$ in 125 mL TTEG to produce a pink solution. A second solution of $LiCH_3COO$ in 75 mL TTEG was then added dropwise to the first solution under stirring. The resulting blue-violet mixtures were refluxed at 200 °C (*Cmcm*-$Li_{1-\gamma}CoPO_4$) respective 185 °C (*Cmcm*-$Li_{0.5-\delta}CoPO_4$) for 14 h in a three-neck round-bottom flask. After cooling to room temperature, the precipitates were recovered by centrifugation (1500 rpm, 20 min, three times) and washed with absolute ethanol between the centrifugation steps. The light pink powders (*cf.* Figure 4.8, Chapter 4.2.4) were finally recovered by filtration, washed with acetone, and dried at 100 °C for 14 h under air.

3.3 Characterization

3.3.1 Powder X-ray Diffraction (PXRD) and Rietveld Refinements

Powder X-ray diffraction (PXRD) data were collected on a STOE STADI P diffractometer equipped with a Ge(111) monochromator for Mo $K_{\alpha1}$ radiation (λ = 0.70930 Å) and a DECTRIS MYTHEN DCS 1K silicon solid-state detector. The powders were ground in an agate mortar and sealed in 0.5 mm borosilicate glass capillaries (HILGENBERG, glass type no. 50, length: 80 mm, wall thickness: 0.01 mm). The measurements were performed in Debye-Scherrer geometry in a 2θ range of 3–60° (PSD (position sensitive detector) step: 0.015°; time/step: 30 s, three ranges, total measurement time: 12 h),

Raw data were handled with the STOE WINXPOW software package,[17] and calibrated using an external Si standard (a = 5.43088 Å) to ensure the comparability of all cell parameters. For the phase identification, the Search/Match routine of WINXPOW as well as the crystallographic databases ICSD (INORGANIC CRYSTAL STRUCTURE DATABASE, implemented in the FINDIT program)[18] and PEARSON'S CRYSTAL DATA[19] were used.

Rietveld refinements were performed with the JANA 2006 software package[20], using the following structures as starting models: olivine-type $LiCoPO_4$ (space group: *Pnma*, ICSD no. 247497)[21] for *Pnma*-$LiCoPO_4$ (Chapters 4.1.1–4.1.3), and the isostructural phases satterlyite $Fe_{9.24}Mg_{2.76}(OH,O)_6(PO_3OH)(PO_4)_5$ (space group: $P31m$, ICSD no. 94842)[22] for $Co_{11}Li[(OH)_5O][(PO_3OH)(PO_4)_5]$ (Chapter 4.2.1), δ_1-$LiZnPO_4$ (space group: $Pna2_1$, ICSD no. 79537)[23] for $Pna2_1$-$LiCoPO_4$ (Chapter 4.2.2), and high-pressure $LiNiPO_4$ (space group: *Cmcm*, ICSD no. 97767)[24] for *Cmcm*-type $Li_{1-\gamma}CoPO_4$ ($LiCoPO_4$) and $Li_{0.5-\delta}CoPO_4$ (Chapters 4.2.3 and 4.2.4), respectively. The background profile, which can be attributed to the capillaries used for the measurements rather than to amorphous portions of the materials according to our studies[13] (see also Chapter 6.2), was fitted with a Chebyshev polynomial function with 35 coefficients. A pseudo-Voigt profile function was used for peak shape modeling, and peak asymmetry was corrected by the axial divergence model described by Finger *et al.*[25] using empirically determined starting values of the parameters S/L (−0.011) and H/L (0.06). No correction for preferred orientation was applied. Absorption correction was performed with the help of the Cromer–Liberman algorithm[26] based on an estimated packing fraction of ~0.6 of the powder in the capillary. The refinement of general atomic positions and isotropic thermal displacement parameters of Co, P, and O was performed without restrictions. The Li positions and thermal displacement parameters were kept fixed since they cannot be deduced by means of X-ray diffraction because of the low atomic scattering factor of lithium. In some cases, the site occupancy factors of the Li and Co sites (Chapter 4.2.4) or a slightly disordered Li/Co

distribution (Chapters 4.2.1 and 4.2.2) were tentatively refined. The positional atomic parameters were then standardized using the Structure Tidy routine[27] implemented in the PLATON software package[28] where applicable. Finally, the Berar's factor was applied to all refined parameters in order to obtain more realistic standard uncertainties.[29] Further details on the individual refinement strategies are provided in the respective publications in Chapter 6.

Crystallographic information files (CIF) obtained from the structure refinements were prepared for deposition with journals as well as the ICSD (INORGANIC CRYSTAL STRUCTURE DATABASE) and CCDC (CAMBRIDGE CRYSTALLOGRAPHIC DATA CENTRE) databases using the publCIF[30] or enCIFer[31] editors, and subsequently validated using the checkCIF[32] utility provided by the IUCr (INTERNATIONAL UNION OF CRYSTALLOGRAPHY). Graphical crystal structure representations were drawn using the DIAMOND 3.2d software[33] and further enhanced with COREL DRAW X3.[34]

3.3.2 Powder Neutron Diffraction (PND)

In order to refine the Li positions and occupancy factors in the *Cmcm*-type structures $Li_{1-\gamma}CoPO_4$ and $Li_{0.5-\delta}CoPO_4$ (*cf.* Chapters 4.2.4 and 6.8), powder neutron diffraction (PND) experiments were performed by Dr. Inés Puente Orench and Carlos Alarcón-Suesca at the INSTITUT LAUE-LANGEVIN (ILL, Grenoble, France). The patterns were collected on the D2B diffractometer (λ = 1.5942 Å) at 23 °C in a 2θ range of 5–160° (measurement time: 4 h). Rietveld refinements of the data were performed using the FULLPROF program[35] using the structures obtained from PXRD experiments as starting models. A pseudo-Voigt function was used for peak fitting, and the instrumental contribution to the peak broadening was determined with the help of an instrument resolution function based on the refinement of a $Na_2Ca_3Al_2F_{14}$ standard. The wavelength was refined using a silicon standard.

3.3.3 Elemental Analysis

Elemental analysis was provided by the Microanalytical Laboratory of the TECHNICAL UNIVERSITY OF MUNICH (Garching, Germany). The Li and Co contents of the materials were determined by atomic absorption spectroscopy (AAS, VARIAN AA280FS sequential spectrometer), and the P contents by photometry (SHIMADZU UV-160 photometer). Prior to the measurements, the materials were dissolved using common sample digestion procedures (*e.g.* using strong acids). The C, H, N, and S contents were measured by combustion analysis with the help of a HEKATECH Euro EA CHNSO instrument. The typical measurement errors were as follows: Li ± 0.2 wt%; Co ± 1 wt%; P ± 0.3 wt%; and C, H, N, S ± 0.3 wt% each.

3.3.4 Scanning Electron Microscopy (SEM) and Energy-Dispersive X-ray Spectroscopy (EDS)

A JEOL JSM-7500F scanning electron microscope (SEM) was used to determine the morphology of the particles. The device was typically operated at an accelerating voltage of 1 kV and a working distance of 8 mm, using either the LEI (lower secondary electron image) detector or the GB (gentle beam) mode to prevent charging effects due to the low conductivity of the materials. Semi-quantitative energy-dispersive X-ray spectroscopy (EDS), including element mapping and point analyses, was performed with a NORAN S1X system (THERMO ELECTRON CORPORATION, model 6714A01SUS-SN; accelerating voltage: 15 kV, probe current: 20 µA). For both measurements, the powders were mounted on an aluminum stub using double-sided graphite tape. The measurements were either performed by Katia Rodewald at the WACKER-Chair of Macromolecular Chemistry of the TECHNICAL UNIVERSITY OF MUNICH (Garching, Germany) or by Jennifer Ludwig at the Energy Storage and Distributed Resources Division of the LAWRENCE BERKELEY NATIONAL LABORATORY (Berkeley, CA, USA).

3.3.5 Transmission Electron Microscopy (TEM) and Selected Area Electron Diffraction (SAED)

Transmission electron microscopy (TEM) and selected area electron diffraction (SAED) were performed by Dr. Marianne Hanzlik at the Associate Professorship of Electron Microscopy, TECHNICAL UNIVERSITY OF MUNICH (Garching, Germany). The images were collected on a JEOL JEM-2010 electron microscope at 160 kV (LaB_6 cathode, max. resolution: 0.2 nm). For the measurements, specimens of approximately 1 mg were dispersed in 1.5 µL absolute ethanol with the help of an ultrasonic bath (VWR, model: USC 300T). In order to avoid sedimentation of samples containing micron-sized particles, the dispersions were then quickly dropped onto either 200 or 300 mesh carbon film and dried. Magnetite was used as a reference material for the SAED patterns, which were analyzed with the help of the CRYSTALMAKER 2.5.5 software[36] provided by the LAWRENCE BERKELEY NATIONAL LABORATORY (Berkeley, CA, USA).

3.3.6 Brunauer–Emmett–Teller (BET) Surface Area Analysis

The specific surface areas *S* of the powders were determined by the Brunauer–Emmett–Teller (BET) method using nitrogen physisorption on a QUANTACHROME Autosorb iQ device (number of measurement points: 11). Prior to the measurements, the samples were

degassed under vacuum for 12 h at 150 °C. The measurements were performed by Dominik Haering at the Chair of Technical Electrochemistry, TECHNICAL UNIVERSITY OF MUNICH (Garching, Germany).

Based on the assumption that all particles are spherical, non-porous, and do not form agglomerates, the diameter d (m) of the particles can be estimated on basis of the measured specific surface area S ($m^2 \cdot kg^{-1}$) and the material density ρ ($kg \cdot m^{-3}$) using Equation 3.1:

Equation 3.1

$$d = \frac{6}{S \cdot \rho}$$

3.3.7 Rheometry

The dynamic viscosities of pure water, ethylene glycol (Chapter 4.2.2) as well as water/ethylene glycol (EG) solvent mixtures containing 10–90 vol% EG (*v*:*v*; increment step: 10 vol%, Chapter 4.1.2) at T = 25 °C were determined in parallel plate–plate geometry (PP-50 plate, diameter: 49.991 mm, gap: 0.250 mm) using an ANTON PAAR MCR 302 Modular Compact Rheometer provided by the Chair of Technical Electrochemistry, TECHNICAL UNIVERSITY OF MUNICH (Garching, Germany). For the measurements, 10 mL of the solvent blends were prepared by mixing the appropriate solvent volumes, which were measured with the help of a piston-operated pipette (BRAND Transferpette S, V = 1,000–10,000 µL, error: ≤ ± 0.6%). Per solvent mixture, six measurements were performed in a shear rate range of 1–120 s^{-1} (no. of measurement points: 40, time/measurement: 10.2 s) using a sample volume of approximately 0.5 mL. The average viscosities were determined at a shear rate of 100 s^{-1}.

3.3.8 Thermogravimetric Analysis (TGA) and Differential Scanning Calorimetry (DSC)

The thermal stability of the materials in a temperature range of 30–900 °C was assessed by simultaneous thermogravimetric analysis (TGA) and differential scanning calorimetry (DSC) using a METTLER TOLEDO TGA/DSC 1 STAR system. Due to the simultaneous setup, only the heating cycle could be monitored. A specimen weight of ~5 mg was placed inside an alumina crucible, and the experiments were run at heating rate of 10 °C·min^{-1}. The measurements were performed under to different atmospheres, an argon (10 mL·min^{-1}) as well as a synthetic air stream (10 mL·min^{-1}), respectively. The measurements were performed by Dominik Haering and Pankaj Madhikar at the Chair of Technical Electrochemistry, TECHNICAL UNIVERSITY OF MUNICH (Garching, Germany).

3.3.9 Temperature-Dependent *In Situ* Powder X-ray Diffraction (PXRD)

The thermal stability of some materials was further investigated by temperature-controlled *in situ* powder X-ray diffraction experiments. The studies were either performed in Debye-Scherrer (Chapter 4.2.3, publication see Chapter 6.7) or Bragg-Brentano geometry (Chapters 4.1.1, 4.2.2, and 4.2.4; for publications see Chapters 6.2, 6.6, and 6.8).

Transmission measurements were carried out by Dr. Wilhelm Klein (Chair of Inorganic Chemistry with Focus on Novel Materials, TECHNICAL UNIVERSITY OF MUNICH, Garching, Germany) on a STOE STADI P diffractometer (Cu K_α radiation, Ge(111) monochromator, λ = 1.540598 Å) equipped with a DECTRIS MYTHEN 1K OEM silicon solid-state detector. The sample was sealed inside a quartz capillary and measured between 19° and 38° 2θ in a temperature range of 20–800 °C (heating rate: 10 °C·min^{-1}, increment step: 25 °C). In temperature regions where phase transitions were expected on the basis of TGA/DSC measurements, the heating rates were decreased to 2 °C·min^{-1} for a more precise monitoring. For further details on the temperature program, please refer to the publication in Chapter 6.7.

Alternatively, a PANALYTICAL X'Pert Pro diffractometer in Bragg-Brentano geometry (Cu K_α radiation) equipped with an XCELERATOR detector, an ANTON PARR HTK-1200 hot stage, and a TCU 1000N temperature controller was available at the LAWRENCE BERKELEY NATIONAL LABORATORY (Berkeley, CA, USA). The materials were prepared on a corundum flatplate sample holder and heated up to 900 °C (heating rate: 5 °C·min^{-1}, increment step: 100 °C) under air or alternatively, an argon atmosphere. Each temperature was held for 5 min before starting the data collection. The data were collected in a 2θ range of 15–70° (step: 0.022°), with the time per step and total measurement time being increased by a factor of ~2 for measurements under Ar because the signal-to-noise ratio was significantly lower in that case (air: 209.5 s/step, total measurement time: 145.5 h; Ar: 400 s/step, total measurement time: 277 h).

3.3.10 Fourier-Transform Infrared (FTIR) and Raman Spectroscopy

Fourier-transform infrared (FTIR) spectra of the powder samples were collected in a wavenumber range of 400–4000 cm^{-1} using either a VARIAN 670 IR (under ambient atmosphere; provided by the Associate Professorship of Molecular Catalysis, TECHNICAL UNIVERSITY OF MUNICH, Garching, Germany) or a Spectrum Two PERKIN ELMER FTIR spectrometer (placed inside an argon-filled glovebox, MBRAUN; provided by the Chair of Technical Electrochemistry, TECHNICAL UNIVERSITY OF MUNICH, Garching, Germany). Both spectrometers were equipped with a diamond ATR (attenuated total reflection) stage.

Raman spectra were recorded by Prof. Dr. Janós Mink at the HUNGARIAN ACADEMY OF SCIENCES (Budapest, Hungary). The measurements were performed on a LABRAM HR 800 spectrometer in a wavenumber range of 50–1300 cm^{-1}. The device was equipped with a 800 mm focal length spectrograph and a cooled (T = −70 °C), back-thinned CCD (charge-coupled device) detector (pixel size: 26 µm × 26 µm). The samples were excited by an air-cooled doubled Nd:YAG laser (λ = 532 nm), and several input laser powers of 0.056 mW, 0.56 mW, and 5.6 mW were applied.

3.3.11 X-ray Absorption Spectroscopy (XAS)

Co $L_{2,3}$-edge soft X-ray absorption spectroscopy (XAS) was performed by Dr. Dennis Nordlund at beamline 8-2 of the STANFORD SYNCHROTRON RADIATION LIGHTSOURCE (SSRL, Menlo Park, CA, USA). The samples were attached to an aluminum sample holder using double-sided conductive carbon tape for the measurements. The incident beam was monochromatized using a spherical grating monochromator with 1100 mm^{-1} ruling and 40 mm exit and entrance slits, providing an intermediate resolution of 0.3 eV in a 1 mm^2 beam spot size.[13] The Co $L_{2,3}$-edge μ(E) spectra were acquired at ambient temperature under ultrahigh vacuum (10^{-9} Torr) in the Auger electron yield (AEY), total electron yield (TEY), and fluorescence yield (FY) modes, corresponding to probing depths of 1–2 nm, 2–5 nm, and 50–100 nm, respectively.[37] AEY was collected from a double-pass cylindrical mirror analyzer at a pass energy of 200 eV, TEY was observed through the drain current without bias, and FY was collected from a silicon diode (IRD AXUV-100) mounted at a higher glancing angle in order to reduce saturation effects.

Data handling was performed using the PYMCA 5.1.1 software.[38] The individual spectra were merged and normalized to the incident photon flux. The energy was then aligned to a common energy scale as reported by Hibberd and co-workers,[39] followed by a linear background subtraction. For better comparability, the intensity of all spectra was further normalized to a maximum value of 1. CoO and Co_3O_4 powders were used as reference materials for visual comparison with the XAS spectra of the Co(II) compounds *Pnma*- and *Pna*2_1-$LiCoPO_4$ (Chapters 4.1.1 and 4.2.2, for details refer to the publications in the Chapters 6.2 and 6.6). In the case of the heterovalent Co(II,III) phases $Co_{11}Li[(OH)_5O][(PO_3OH)(PO_4)_5]$ and *Cmcm*-$Li_{0.5-\delta}CoPO_4$ (Chapters 4.2.1 and 4.2.4, publications see Chapters 6.5 and 6.8), data fitting was performed on a small energy region across the L_3 edge (774–784 eV) in order to quantify the formal oxidation state of the Co ions, using reference spectra[39-40] of octahedrally coordinated (O_h, CN = 6) high-spin Co^{2+} as well as low- and high-spin Co^{3+} ions.

3.3.12 Magnetic Measurements (SQUID)

DC magnetization measurements were performed by Dr. Viktor Hlukhyy (Chair of Inorganic Chemistry with Focus on New Materials, TECHNICAL UNIVERSITY OF MUNICH, Garching, Germany) and Dr. Stephan Geprägs (WALTHER MEISSNER INSTITUTE, Garching, Germany) using either a QUANTUM DESIGN MPMS XL5 (Chapter 4.2.3) or XL7 (Chapters 4.2.1 and 4.2.4) superconducting quantum interference device (SQUID) magnetometer. The samples were placed inside calibrated gelatin capsules held at the center of a drinking straw for the measurements. Temperature-dependent measurements were performed in a temperature range of T = 2–300 K in the zero-field-cooled (ZFC) and field-cooled (FC) modes. Magnetic hysteresis curves were collected at various temperatures by measuring the magnetization as a function of the applied field strength. For specific experimental details, please refer to the individual publications in the Chapters 6.5, 6.7, and 6.8.

3.3.13 Electrochemical Characterization

The electrochemical properties of the $LiCoPO_4$ cathode materials were evaluated using either SWAGELOK (Chapters 4.1.1–4.1.3, for further experimental details see publications in Chapters 6.2–6.4; performed by Dr. Cyril Marino and Dominik Haering at the Chair of Technical Electrochemistry, TECHNICAL UNIVERSITY OF MUNICH, Garching, Germany) or CR2032 coin-type cells (Chapters 4.2.2 and 4.2.4, publications see Chapters 6.6 and 6.8; performed by Jennifer Ludwig at the Electrochemical Technologies Group, Energy Storage and Distributed Resources Division, LAWRENCE BERKELEY NATIONAL LABORATORY, Berkeley, CA, USA). In both cases, the electrodes with typical loadings of 4–5 $mg \cdot cm^{-2}$ were composed of 80 wt% of the as-prepared active material, 10 wt% conductive carbon (Super C65) and 10 wt% polyvinylidene difluoride (PVDF) binder. In order to gain more reliable data and to derive standard deviations, two cells were cycled for each material. Differences regarding the electrode preparation and battery testing protocols are described in the following.

(a) Swagelok Cells

80 wt% $LiCoPO_4$, 10 wt% carbon Super C65 (Timcal) and 10 wt% PVDF binder (Kynar HSV 900, ARKEMA; structural formula see Figure 3.5c) were mixed with *N*-methyl-2-pyrrolidone (NMP, SIGMA ALDRICH; formula see Figure 3.5c) using a planetary centrifugal vacuum mixer (THINKY) at 2000 rpm for 20 min. The resulting ink was cast onto aluminum foil (15 µm, MTI) and then dried at 55 °C for 3–4 h. Circular electrodes with a diameter of d = 10 mm were

punched out, pressed two times at 250 MPa for 1 min using a KBr press (PERKINELMER), and dried for 2 h at 120 °C under vacuum (BÜCHI B-585 glass oven).

The SWAGELOK cells composed of the $LiCoPO_4$ cathode, pure Li foil (ROCKWOOD LITHIUM, 450 µm, battery grade, > 99.8%) as anode, two glass fiber separators (VWR, 691, 250 µm) and 80 µL electrolyte (1 M $LiPF_6$ in ethylene carbonate (EC)/dimethyl carbonate (DMC); 1:1 (*w*:*w*, by weight), MERCK, LP30; structural formulas see Figure 3.5c) were assembled in an Ar-filled glove box (MBRAUN; < 0.1 ppm H_2O, < 0.1 ppm O_2). Charge–discharge cycling was carried out galvanostatically (using either a BIOLOGIC or MACCOR galvanostat) between 3.5 V and 5.2 V for 3 cycles each at 0.1 C, 0.2 C, 0.5 C, 1 C, and 2 C in order to test the C rate capability, which was followed by 15 cycles at 0.5 C to evaluate the cycle life. Charges were performed in CCCV (constant-current, constant-voltage) mode with the potentiostatic step limited by a current of C/20. Current densities and specific capacities were calculated using the weight of $LiCoPO_4$ active material in the electrodes, with the weight of a minor lithium sulfate impurity being neglected because it only accounted for less than 5 wt% and further experiments[13] (see also supporting materials of Chapter 6.2) had shown that it does not affect the electrochemical performance.

(b) Coin Cells

An overview over the electrode preparation process and cell assembly of the coin cells is presented in Figure 3.5a. The cathode slurries were prepared by thoroughly mixing 80 wt% of the active material, 10 wt% carbon Super C65 (TIMCAL), and 10 wt% PVDF (SOLVAY) with NMP in an agate mortar (structural formulas *cf.* Figure 3.5c). The slurries were spread on carbon-coated Al current collectors (COVERIS ADVANCED COATINGS) with the help of a doctor-blade coater. The electrode sheets were dried at 120 °C for 5 h in a vacuum oven (THERMO SCIENTIFIC), calendered (INTERNATIONAL ROLLING MILLS device), and then vacuum dried a second time for 12 h at 120 °C before being transferred into an Ar-filled glove-box (VAC, < 0.1 ppm H_2O, < 0.1 ppm O_2). The CR2032 coin-type cells (details on the coin cell parts see Figure 3.5b) were assembled using the circular cathode (d = 14.3 mm), a Li foil anode (ALFA AESAR, 0.75 mm, 99.9%, metals basis), a microporous monolayer PP membrane separator (CELGARD 2400, 25 µm, polypropylene), and 1 M $LiPF_6$ dissolved in ethylene carbonate (EC)/diethyl carbonate (DEC) in a ratio of 1:1 (*v*:*v*, by volume) as electrolyte (DAIKIN; structural formulas see Figure 3.5c). Galvanostatic cycling was performed on a BIOLOGIC VMP3 multichannel galvanostat in a potential window of 3.0–5.2 V at C rates of 0.1 C, 0.2 C, 0.5 C, and 1 C for three cycles each, followed by 20 cycles at 0.1 C. Current densities and specific capacities were calculated on basis of the weight of active material in the electrode.

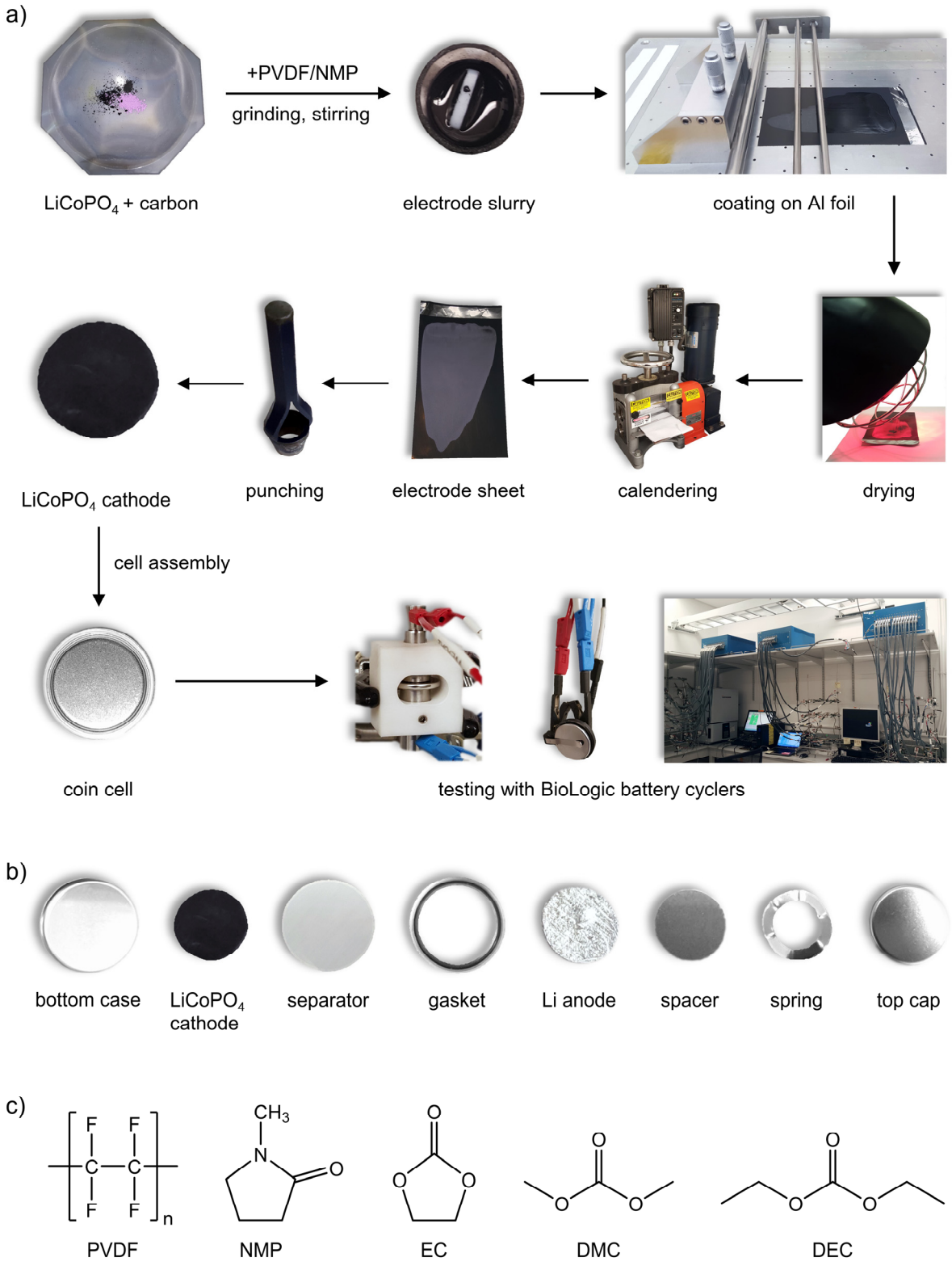

Figure 3.5 (a) Overview over the electrode and cell preparation process using coin cells, (b) components of CR2032 coin cells, and (c) structural formulas of the PVDF (polyvinylidene difluoride) binder, the NMP (*N*-methyl-2-pyrrolidone) solvent as well as the EC (ethylene carbonate), DMC (dimethyl carbonate), and DEC (diethyl carbonate) electrolytes.

3.4 References

[1] *Direct-Q® 3, 5, 8 Water Purification Systems*. Millipore Corporation: Billerica, MA, USA, **2011** (www.millipore.com/directq358).

[2] *SciFinder® A CAS Solution*. Chemical Abstracts Service: Columbus, OH, USA, **2017** (http://www.cas.org/products/scifinder).

[3] *digestec™ Berghof Druckaufschlusssystem DAB-2 und DAB-3 Anwenderhandbuch V. 1.0*. BERGHOF Products + Instruments GmbH: Eningen, Germany, **2012**.

[4] *Berghof Homepage. Laborgeräte - Aufschlusstechnik - Druckaufschluss. Übersicht: Druckaufschluss-Systeme für den geschlossenen Säureaufschluss*. BERGHOF Products + Instruments GmbH: Eningen, Germany, **2017** (http://www.berghof-instruments.com/laborgeraete/aufschlusstechnik/druckaufschluss/uebersicht/).

[5] Ludwig, J., Synthesis and Characterization of Phospho-olivines. Master's thesis, Technical University of Munich, Department of Chemistry, Garching, Germany, **2012**.

[6] *Bedienungsanleitung Monoblockrotor MR-8 HT*. MLS GmbH Mikrowellen-Laborsysteme: Leutkirch, Germany, **2009**.

[7] *Bedienungsanleitung Mikrowellensystem START 1500*. MLS GmbH Mikrowellen-Laborsysteme: Leutkirch, Germany, **2009**.

[8] Liang, H.; Zhang, L., High-energy-density $LiMn_{0.7}Fe_{0.3}PO_4$ nanorods synthesized by microwave-assisted solvothermal method. *Russ. J. Electrochem.* **2014,** *50*, 297–300.

[9] Kuppan, S.; Balaya, P.; Reddy, M. V.; Chowdari, B. V. R.; Vittal, J. J., Morphology controlled synthesis of $LiFePO_4$/C nanoplates for Li-ion batteries. *Energy Environ. Sci.* **2010,** *3*, 457–464.

[10] Song, J.; Wang, L.; Shao, G.; Shi, M.; Ma, Z.; Wang, G.; Song, W.; Liu, S.; Wang, C., Controllable synthesis, morphology evolution and electrochemical properties of $LiFePO_4$ cathode materials for Li-ion batteries. *Phys. Chem. Chem. Phys.* **2014,** *16*, 7728–7733.

[11] Friend, J. A. N., The hydrates of lithium sulfate and their solubility in water between −16° and +103°. *J. Chem. Soc.* **1929**, 2330–2333.

[12] Linke, W. F.; Seidell, A., *Solubilities of Inorganic and Metal Organic Compounds Vol. II. 4th ed*. Am. Chem. Soc.: **1966;** p 1941 pp.

[13] Ludwig, J.; Marino, C.; Haering, D.; Stinner, C.; Nordlund, D.; Doeff, M. M.; Gasteiger, H. A.; Nilges, T., Facile, ethylene glycol-promoted microwave-assisted solvothermal synthesis of high-performance $LiCoPO_4$ as a high-voltage cathode material for lithium-ion batteries. *RSC Adv.* **2016,** *6*, 82984–82994.

[14] Chen, J.; Wang, S.; Whittingham, M. S., Hydrothermal synthesis of cathode materials. *J. Power Sources* **2007,** *174*, 442–448.

[15] Ludwig, J.; Haering, D.; Doeff, M. M.; Nilges, T., Particle size-controllable microwave-assisted solvothermal synthesis of the high-voltage cathode material $LiCoPO_4$ using water/ethylene glycol solvent blends. *Solid State Sci.* **2017,** *65*, 100–109.

[16] Ludwig, J.; Marino, C.; Haering, D.; Stinner, C.; Gasteiger, H. A.; Nilges, T., Morphology-controlled microwave-assisted solvothermal synthesis of high-performance $LiCoPO_4$ as a high-voltage cathode material for Li-ion batteries. *J. Power Sources* **2017,** *342*, 214–223.

[17] *WinXPOW (Version 3.0.2.1)*. STOE & CIE GmbH: Darmstadt, Germany, **2009**.

[18] *FindIt - ICSD (Inorganic Crystal Structure Database), Version 1.9.3*. Fachinformationszentrum (FIZ) Karlsruhe, Germany, **2013**.

[19] P. Villars; Cenzual, K., *Pearson's Crystal Data: Crystal Structure Database for Inorganic Compounds, Release 2008/9 (Version 1.2)*. ASM International, Materials Park, OH, USA, **2008**.

[20] Petricek, V.; Dusek, M.; Palatinus, L., Crystallographic Computing System JANA2006: General features. *Z. Kristallogr. - Cryst. Mater.* **2014,** *229*, 345–352.

[21] Koleva, V.; Zhecheva, E.; Stoyanova, R., Ordered Olivine-Type Lithium-Cobalt and Lithium-Nickel Phosphates Prepared by a New Precursor Method. *Eur. J. Inorg. Chem.* **2010**, 4091–4099.

[22] Kolitsch, U.; Andrut, M.; Giester, G., Satterlyite, $(Fe,Mg)_{12}(PO_3OH)(PO_4)_5(OH,O)_6$: crystal structure and infrared absorption spectra. *Eur. J. Mineral.* **2002,** *14*, 127–133.

[23] Jensen, T. R.; Norby, P.; Stein, P. C.; Bell, A. M. T., Preparation, structure determination and thermal transformation of a new lithium zinc phosphate, δ_1-$LiZnPO_4$. *J. Solid State Chem.* **1995,** *117*, 39–47.

[24] Garcia-Moreno, O.; Alvarez-Vega, M.; Garcia-Alvarado, F.; Garcia-Jaca, J.; Gallardo-Amores, J. M.; Sanjuan, M. L.; Amador, U., Influence of the structure on the electrochemical performance of lithium transition metal phosphates as cathodic materials in rechargeable lithium batteries: a new high-pressure form of Li*M*PO_4 (*M* = Fe and Ni). *Chem. Mater.* **2001,** *13*, 1570–1576.

[25] Finger, L. W.; Cox, D. E.; Jephcoat, A. P., A correction for powder diffraction peak asymmetry due to axial divergence. *J. Appl. Crystallogr.* **1994,** *27*, 892–900.

[26] Cromer, D. T.; Liberman, D. A., Anomalous dispersion calculations near to and on the long-wavelength side of an absorption edge. *Acta Crystallogr., Sect. A* **1981,** *A37*, 267–268.

[27] Gelato, L. M.; Parthe, E., STRUCTURE TIDY - a computer program to standardize crystal structure data. *J. Appl. Cryst.* **1987,** *20*, 139–143.

[28] Spek, A. L., Structure validation in chemical crystallography. *Acta Crystallogr., Sect. D: Biol. Crystallogr.* **2009,** *65*, 148–155.

[29] Berar, J. F.; Lelann, P., E.S.D.'s and estimated probable error obtained in Rietveld refinements with local correlations. *J. Appl. Crystallogr.* **1991,** *24*, 1–5.

[30] Westrip, S. P., publCIF: software for editing, validating and formatting crystallographic information files. *J. Appl. Crystallogr.* **2010,** *43*, 920–925.

[31] Allen, F. H.; Johnson, O.; Shields, G. P.; Smith, B. R.; Towler, M., CIF applications. XV. enCIFer: a program for viewing, editing and visualizing CIFs. *J. Appl. Crystallogr.* **2004,** *37*, 335–338.

[32] *checkCIF*. International Union of Crystallography (IUCr): Chester, England **2017** (http://checkcif.iucr.org/).

[33] Brandenburg, K., *Diamond V3.2d, Crystal Impact Gbr*. Bonn, Germany, **2009**.

[34] *CorelDRAW Graphics Suite X3 (Version 13.0.0.576)*. Corel Corporation: Ottawa, Canada, **2005**.

[35] Rodriguez-Carvajal, J., Recent advances in magnetic structure determination by neutron powder diffraction. *Physica B* **1993,** *192*, 55–69.

[36] Palmer, D. C., *CrystalMaker (Version 2.5.5)*. CrystalMaker Software Ltd: Begbroke, England, **2012**.

[37] Lin, F.; Nordlund, D.; Markus, I. M.; Weng, T.-C.; Xin, H. L.; Doeff, M. M., Profiling the nanoscale gradient in stoichiometric layered cathode particles for lithium-ion batteries. *Energ. Environ. Sci.* **2014,** *7*, 3077–3085.

[38] Solé, V. A.; Papillon, E.; Cotte, M.; Walter, P.; Susini, J., A multiplatform code for the analysis of energy-dispersive X-ray fluorescence spectra. *Spectrochim. Acta B* **2007,** *62*, 63–68.

[39] Hibberd, A. M.; Doan, H. Q.; Glass, E. N.; de Groot, F. M. F.; Hill, C. L.; Cuk, T., Co Polyoxometalates and a Co_3O_4 Thin Film Investigated by L-Edge X-ray Absorption Spectroscopy. *J. Phys. Chem. C* **2015,** *119*, 4173–4179.

[40] Hu, Z.; Wu, H.; Haverkort, M. W.; Hsieh, H. H.; Lin, H. J.; Lorenz, T.; Baier, J.; Reichl, A.; Bonn, I.; Felser, C.; Tanaka, A.; Chen, C. T.; Tjeng, L. H., Different Look at the Spin State of Co^{3+} Ions in a CoO_5 Pyramidal Coordination. *Phys. Rev. Lett.* **2004,** *92*, 207402/1–207402/4.

Chapter 4
Results and Discussion

4.1 Microwave-Assisted Solvothermal (MWST) Synthesis and Optimization of *Pnma*-$LiCoPO_4$ as a High-Voltage Cathode Material for Lithium-Ion Batteries

Low capacities, low rate capabilities, and fast capacity fading generally characterize the electrochemical performance of the olivine-structured high-voltage cathode material *Pnma*-$LiCoPO_4$.[1-5] In addition to the limited stability of standard electrolytes at the operating potential of 4.8 V *vs.* Li/Li^+,[6-7] the low electrical[8-9] and ionic[10-12] conductivities as well as the anisotropic nature of the Li-ion transport ([010] direction) in the crystal structure[13-14] remain major obstacles to its successful utilization (*cf.* Chapter 1.2.1).

As discussed in Chapter 1.2.2, one promising approach to improve its electrochemical performance is by controlling the size, shape, and orientation (in particular, reducing the particle dimensions along [010]) of the crystals, which can be accomplished by kinetically controlled synthesis procedures.[15] In the case of hydrothermal (HT) or solvothermal (ST) synthesis methods, however, only a few reports[16-19] indicate the direct formation of *Pnma*-$LiCoPO_4$ in a single step and the materials demonstrated inferior electrochemical performance. Capacities above 125 $mAh \cdot g^{-1}$ (*i.e.*, > 75% of the theoretical capacity) have exclusively been achievable by post-processing of the HT or ST materials (*e.g.* carbon coating, high-temperature annealing)[17, 20-21] or complex procedures such as the high-pressure high-temperature (HPHT) supercritical fluid (SCF) process described by Rui and co-workers.[22] To date, the only pathway reported to deliver high-performance *Pnma*-$LiCoPO_4$ in a single step at low temperature is the microwave-assisted solvothermal (MWST) technique.[23-24] The MWST technique being comparably new in the field of *Pnma*-$LiCoPO_4$ research and the number of reports being very limited, a thorough understanding of the process and the implementation of particle size- and morphology-tuning approaches are still lacking despite the recent advance.

Therefore, a simple and rapid (30 min) one-step MWST process towards high-performance *Pnma*-$LiCoPO_4$ using a binary 1:1 (*v*:*v*) water/ethylene glycol (EG) solvent and low temperatures (250 °C) was developed (Chapter 4.1.1). Based on the novel process, the effects of the EG concentration in the binary solvent mixture (Chapter 4.1.2) as well as six different

polyol-type co-solvents (Chapter 4.1.3) on the particle size and morphology were investigated. The specific focus was directed towards understanding the relationship between the synthesis conditions, material microstructure, and electrochemical performance, which has hitherto not or only barely been touched upon in the literature. For that matter, the as-prepared *Pnma*-$LiCoPO_4$ materials were comprehensively characterized using powder X-ray diffraction (PXRD), elemental analysis, scanning electron microscopy (SEM), transmission electron microscopy (TEM) and selected area electron diffraction (SAED), Brunauer–Emmett–Teller (BET) surface area analysis, and electrochemical measurements. In addition, the material obtained from the standard process (Chapter 4.1.1) was analyzed by infrared (IR), Raman, and X-ray absorption (XAS) spectroscopy as well as thermogravimetric analysis and differential scanning calorimetry (TGA/DSC) in combination with temperature-dependent *in situ* PXRD studies, which allowed the identification of an amorphous side product of the process.

4.1.1 Summary: Facile, Ethylene Glycol-Promoted Microwave-Assisted Solvothermal Synthesis of High-Performance $LiCoPO_4$ as a High-Voltage Cathode Material for Lithium-Ion Batteries

Jennifer Ludwig, Cyril Marino, Dominik Haering, Christoph Stinner, Dennis Nordlund, Marca M. Doeff, Hubert A. Gasteiger, and Tom Nilges

RSC Adv. **2016,** *6*, 82984–82994. see Chapter 6.2
DOI: 10.1039/c6ra19767a

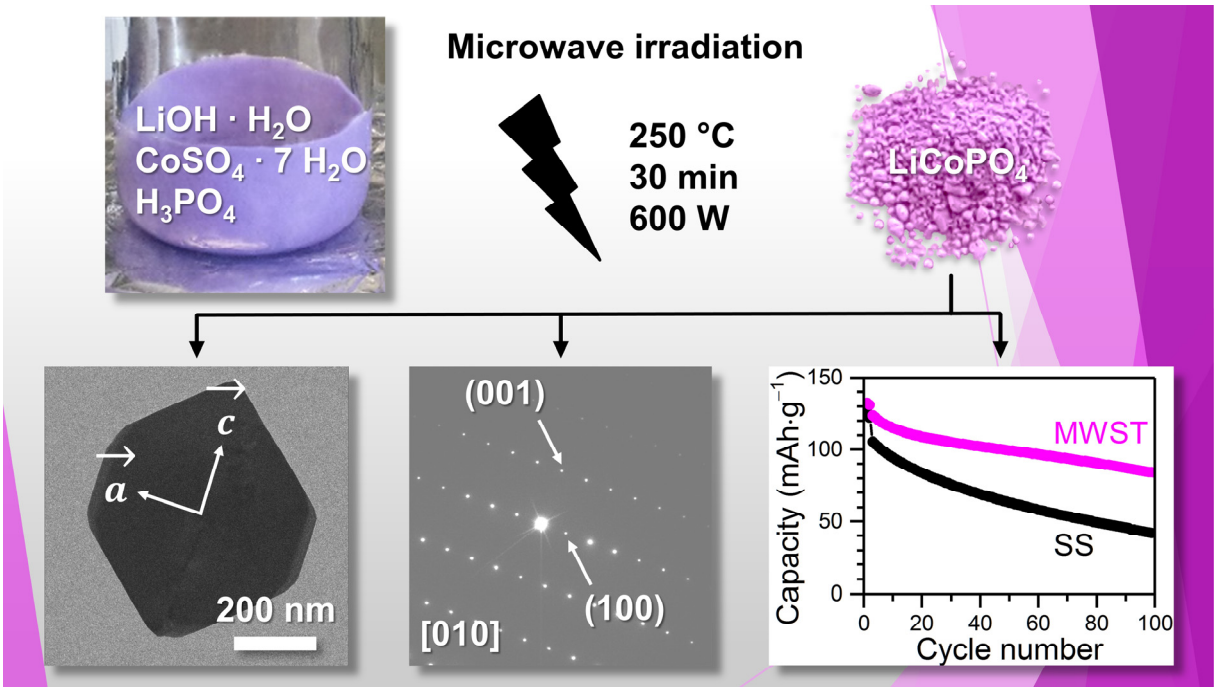

Figure 4.1 Hexagonal platelets of *Pnma*-$LiCoPO_4$ with tuned crystal orientations (smallest dimension along the [010] direction; bottom left and center) and excellent electrochemical performance (initial discharge capacity of 137 $mAh \cdot g^{-1}$ at 0.1 C; bottom right) were prepared by a simple and rapid (30 min) one-step microwave-assisted solvothermal (MWST) process at low temperature (250 °C, top). The electrochemical performance (cycle life) of the MWST material is significantly improved compared to a benchmark material obtained from conventional solid-state (SS) synthesis (bottom right). The graphic was adapted from reference [25] with permission from The Royal Society of Chemistry.

Starting from the precursors $LiOH \cdot H_2O$, $CoSO_4 \cdot 7\ H_2O$, and H_3PO_4, a simple and fast (30 min) one-step microwave-assisted solvothermal (MWST) process at low temperature (250 °C) for the synthesis of olivine-type *Pnma*-$LiCoPO_4$ particles was developed (*cf.* Figure 4.1, top and Chapter 3.2.1 for experimental details). With the help of a binary 1:1 (*v*:*v*) water/ethylene glycol (EG) solvent mixture, the technique directly delivers high-performance

Pnma-$LiCoPO_4$ particles with a defined hexagonal platelet-like morphology and tuned crystal orientations without requiring the use of additional templates. Furthermore, as opposed to most conventional hydrothermal or solvothermal techniques,[20-21, 26-27] the procedure does not include any further post-processing steps such as high-temperature annealing or carbon coating. The as-prepared light pink material (*cf.* Figure 4.1, top right) was thoroughly characterized, and the relationship between the synthesis conditions, material microstructure, and electrochemical performance was investigated.

PXRD experiments showed that highly crystalline, olivine-type *Pnma*-$LiCoPO_4$ was formed directly in one step from the MWST process. Elemental analysis indicated an excess of Li (~0.3 wt%, *i.e.* a deviation from the ideal *n*(Li):*n*(Co):*n*(P) = 1:1:1 composition) and significant amounts of sulfur (~1.5 wt%), which could be related to the presence of traces (< 5 wt%) of amorphous lithium sulfate, which is formed as a side product of the reaction (see also Scheme 3.1, Chapter 3.2.1) and undetectable by PXRD. The presence of Li_2SO_4 was confirmed by a combined TGA/DSC and temperature-dependent *in situ* PXRD approach, which showed that the amorphous phase can be crystallized upon heating. Interestingly, the study also suggested that olivine-type *Pnma*-$LiCoPO_4$ partially transforms to the metastable *Pna*2_1-$LiCoPO_4$ modification[28-29] at high temperatures (T > 800 °C), which contrasts previous reports[16, 30] on the high thermal stability of *Pnma*-$LiCoPO_4$. It was further shown that the highly water-soluble[31-32] Li_2SO_4 phase forms inclusions inside the *Pnma*-$LiCoPO_4$ particles that cannot be removed despite intensive washing. Furthermore, the Co $L_{2,3}$-edge X-ray absorption spectrum of *Pnma*-$LiCoPO_4$ was presented for the first time and confirmed the presence of octahedrally coordinated Co^{2+} ions in the structure. The Co oxidation state was found to be consistently +II from the surface to the bulk, indicating that the synthesis conditions (ascorbic acid and EG co-solvent acting as reducing agents)[30, 33] are effectively preventing the oxidation of Co^{2+} to Co^{3+} in the aqueous solution.

SEM and TEM/SAED studies revealed that the hexagonal platelets exhibit dimensions of 700–800 nm × 400–600 nm in the (010) plane and a thickness of 100–220 nm along [010] (*cf.* Figure 4.1, bottom), which is the direction of the lithium diffusion pathways in the olivine crystal structure. The observed particle size range was consistent with the specific surface area of ~6 $m^2 \cdot g^{-1}$. Based on the results, it could be inferred that the EG co-solvent plays a key role in promoting the growth of crystals with anisotropic shapes and uniform particle size distributions. Whereas the size-regulating effect could be attributed to the increased viscosity of the binary H_2O/EG solvent compared to pure water (see also Chapter 4.1.2), the tuned morphologies and crystal orientations were attributed to the soft template effect[33-34] of the EG co-solvent. EG molecules specifically adsorb on (010) crystal faces, dramatically decreasing the surface energies and hence, inhibit the crystal growth along the [010] direction. As a result, platelet-like particles with reduced dimensions along the *b* direction are formed in the process.

Due to the favorable crystal orientations with shortened Li-ion migration pathways along [010], the hexagonal platelets exhibited excellent electrochemical properties, which were tested alongside a benchmark material (spherical nanoparticles with 50–60 nm in diameter)[35] obtained from conventional high-temperature solid-state (SS) synthesis with additional ball milling for particle size reduction. At a rate of 0.1 C, an initial discharge capacity of 137 $mAh \cdot g^{-1}$ was reached for the MWST material (corresponding to a specific energy of 658 $Wh \cdot kg^{-1}$ based on its capacity and voltage), whereas only 125 $mAh \cdot g^{-1}$ was obtained for the SS one. In fact, the capacity reached for the microwave material represents one of the best values reported for *Pnma*-$LiCoPO_4$ to date. Furthermore, the material shows a high rate capability and cycle life: at 2 C, a capacity of 98 $mAh \cdot g^{-1}$ (SS: 87 $mAh \cdot g^{-1}$) was still reached whereas after 100 cycles at 0.5 C, 68% of the initial capacity was retained compared to only 38% for the SS material (*cf.* Figure 4.1, bottom right). This is remarkable since the material was tested using a standard electrolyte system (EC/DMC) and reasonably high active material loadings (4–5 $mg \cdot cm^{-2}$), and did not undergo additional post-processing (high-temperature annealing or carbon coating) to improve the performance. A possible effect of the amorphous Li_2SO_4 impurity on the electrochemical properties could be ruled out by additional studies showing that similar samples with increased Li_2SO_4 contents deliver comparable performances (for further details, please refer to the supporting materials of Chapter 6.2). Hence, the influence of this electrochemically inactive side phase was neglected in further studies. The promising results of this study and the advantages of the state-of-the-art microwave synthesis technique triggered a number of subsequent investigations to elucidate whether the electrochemical performance of *Pnma*-$LiCoPO_4$ could be further improved (see Chapters 4.1.2 and 4.1.3).

Author contributions: J. Ludwig conceived and designed this work, and carried out the synthesis and material characterization (*in* and *ex situ* PXRD, IR) under the supervision of T. Nilges and M. M. Doeff. The electrochemical measurements were performed by C. Marino and D. Haering. TGA/DSC and BET were measured by D. Haering, and XAS by D. Nordlund, respectively. J. Ludwig interpreted the data and wrote the manuscript with the help of C. Marino for the electrochemical part. All authors read and approved the final version of the manuscript.

4.1.2 Summary: Particle Size-Controllable Microwave-Assisted Solvothermal Synthesis of the High-Voltage Cathode Material $LiCoPO_4$ Using Water/Ethylene Glycol Solvent Blends

Jennifer Ludwig, Dominik Haering, Marca M. Doeff, and Tom Nilges

Solid State Sci. **2017,** *65*, 100–109.
DOI: 10.1016/j.solidstatesciences.2017.01.009

see Chapter 6.3

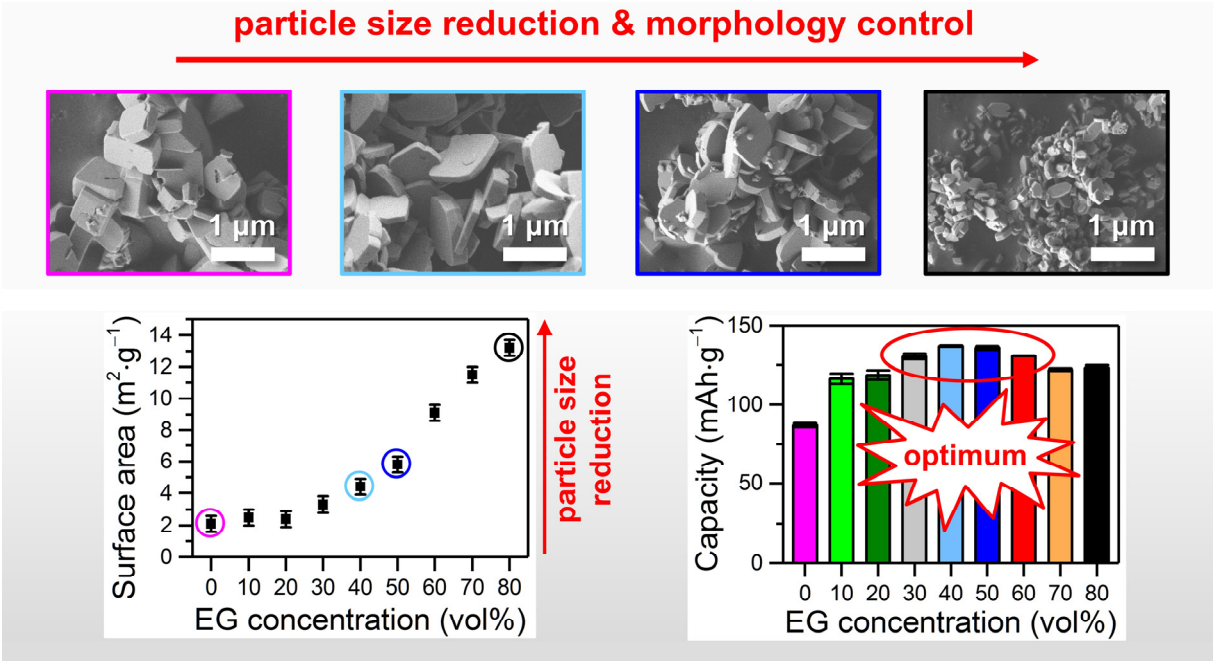

Figure 4.2 Particle size-tuned platelets of *Pnma*-$LiCoPO_4$ have been synthesized by a simple one-step microwave-assisted solvothermal (MWST) process by altering the concentration of the ethylene glycol (EG) co-solvent in the binary H_2O/EG solvent mixture between 0 and 80 vol% (increment step: 10 vol%). The particle size and specific surface area of the materials correlates with the EG concentration of the solvent (bottom left). Materials prepared from medium EG concentrations exhibit the best electrochemical performance, with discharge capacities of up to 137 mAh·g^{-1} being reached at 0.1 C (bottom right). The graphic was adapted from reference [36].

Using the facile microwave-assisted solvothermal (MWST) process with a 1:1 (*v*:*v*, *i.e.* 50 vol%:50 vol%) water/ethylene glycol (EG) mixture (Chapter 4.1.1) as a basis, the effect of the composition of the binary solvent on the structure, particle size and morphology, as well as the electrochemical performance of *Pnma*-$LiCoPO_4$ was examined. For that purpose, the concentration of the EG co-solvent was varied between 0 vol% (*i.e.,* pure H_2O) and 100 vol% (*i.e.,* pure EG) with an increment step size of 10 vol% (for experimental details see Chapter 3.2.2).

According to PXRD experiments, highly crystalline, pure olivine-type *Pnma*-$LiCoPO_4$ was obtained for EG contents between 0 vol% and 80 vol%. At concentrations above 90 vol% EG, the formation of the metastable *Pna*2_1-$LiCoPO_4$ phase[28] was observed. Since the *Pna*2_1 polymorph reportedly shows poor electrochemical performance,[28, 37] the focus of the further investigations was set on the electrochemically active, olivine materials obtained from 0–80 vol% EG. A structure redetermination and a thorough investigation of the structure–property relationships of the *Pna*2_1-$LiCoPO_4$ material obtained from pure (100 vol%) EG are presented in another study (see Chapter 4.2.2).

SEM studies revealed that at low EG concentrations (0–40 vol%), crystals with square platelet or cubic shapes and inhomogeneous particle size distributions were formed. Solvent mixtures with 50–80 vol% EG delivered uniform hexagonal platelets. The particle dimensions were significantly reduced from about 1.2 µm × 1.2 µm × 500 nm (0 vol% EG) to 200 nm × 100 nm × 50 nm (80 vol% EG) with increasing EG concentration (Figure 4.2, top), which was consistent with the increase in surface areas from ~2 $m^2 \cdot g^{-1}$ to ~13 $m^2 \cdot g^{-1}$ (Figure 4.2, bottom left). The particle size reduction could mainly be attributed to the higher viscosities of solvent blends with higher EG contents. According to TEM/SAED investigations, the EG co-solvent shows size-regulating properties, and as a soft template,[33-34] also promotes the crystal growth by selective adsorption on (010) faces. As a result, all platelets showed reduced dimensions along the [010] direction of the Li diffusion paths, which is beneficial to enhance the Li transport properties and thus, to improve the electrochemical performance of *Pnma*-$LiCoPO_4$.

The electrochemical performance of the materials strongly depended on the solvent composition, the overall size and thickness of the platelets along [010]. As expected, larger particles prepared from mixtures with low EG contents exhibited low to average discharge capacities (0 vol% EG: 87 $mAh \cdot g^{-1}$ at 0.1 C; *cf.* Figure 4.2, bottom right) and rate capabilities. The best performance was not observed for the smallest particles synthesized in solvents with high EG concentrations (80 vol% EG: 122 $mAh \cdot g^{-1}$) but for medium-sized particles obtained from 40–60 vol% EG (up to 137 $mAh \cdot g^{-1}$). This surprising finding could mainly be explained by increased side reactions of nano-sized powders with high surface areas with the electrolyte at high voltage (for a thorough discussion refer to Chapter 4.1.4). Overall, the findings suggest that in contrast to cathode materials with lower operating potential (*e.g.* $LiFePO_4$: 3.45 V),[38] which benefit from particle size reduction, a medium particle size range represents the optimum for high-voltage cathode materials such as *Pnma*-$LiCoPO_4$.

Author contributions: J. Ludwig conceived and designed this work, and carried out the synthesis, material characterization, and data analysis. D. Haering performed the electrochemical and BET measurements. J. Ludwig wrote the publication. All authors read and approved the final version of the manuscript.

4.1.3 Summary: Morphology-Controlled Microwave-Assisted Solvothermal Synthesis of High-Performance $LiCoPO_4$ as a High-Voltage Cathode Material for Li-Ion Batteries

Jennifer Ludwig, Cyril Marino, Dominik Haering, Christoph Stinner, Hubert A. Gasteiger, and Tom Nilges

J. Power Sources **2017,** *342*, 214–223.
DOI: 10.1016/j.jpowsour.2016.12.059

see Chapter 6.4

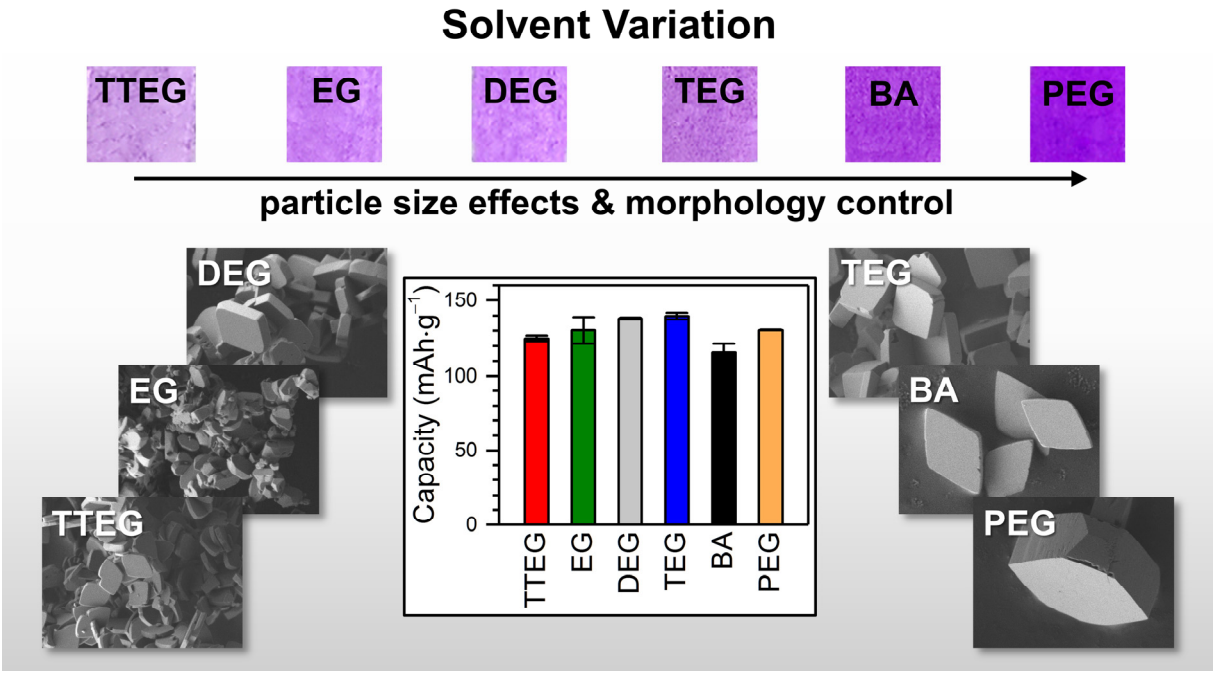

Figure 4.3 Morphology-tuned *Pnma*-$LiCoPO_4$ platelets with square, rhombic, and hexagonal shapes and dimensions between several hundred nanometers and several micrometers were obtained by a microwave-assisted solvothermal (MWST) process using an array of binary solvent blends of water and different co-solvents: ethylene glycol (EG), diethylene glycol (DEG), triethylene glycol (TEG), tetraethylene glycol (TTEG), polyethylene glycol 400 (PEG), and benzyl alcohol (BA). The colors of the powders, ranging from light pink (TTEG) to dark violet (PEG; see top), can be related to particle size effects with the color becoming darker and more intense for bigger crystallites. The materials demonstrate excellent electrochemical performances, with the highest initial discharge capacity of 141 $mAh \cdot g^{-1}$ at 0.1 C being reached for the sample produced from the TEG co-solvent (bottom center). The graphic was adapted from reference [39], Copyright (2016), with permission from Elsevier B.V.

Taking the rapid one-step microwave-assisted solvothermal (MWST) process at 250 °C presented in Chapter 4.1.1 as a starting point, the influence of the co-solvent in the binary water/polyol 1:1 (*v*:*v*) solvent blends on the morphology, size, orientation, and electro-

chemical performance of the *Pnma*-$LiCoPO_4$ crystals was investigated. The effect of six different polyol-type co-solvents was evaluated (for experimental details see Chapter 3.2.3): ethylene glycol (EG), diethylene glycol (DEG), triethylene glycol (TEG), tetraethylene glycol (TTEG), polyethylene glycol 400 (PEG), and benzyl alcohol (BA).

Powder X-ray diffraction and elemental analyses showed that the composition of the highly crystalline materials remains unchanged upon variation of the secondary solvent. In contrast, SEM and TEM/SAED studies revealed that the co-solvent plays a significant role in controlling the shape, size, and orientation of the *Pnma*-$LiCoPO_4$ crystals, resulting in the formation of variations between square (in the case of the co-solvents DEG and TEG), rhombic (TTEG, BA) and hexagonal (EG, PEG) shapes (Figure 4.3). The particles exhibited lengths in a range of 400–900 nm and thicknesses of 100–200 nm in the case of EG, DEG, TEG, and TTEG. Significantly bigger dimensions of about 2.5 µm × 2 µm × 0.5–1 µm and 9 µm × 7 µm × 3 µm were found for the samples produced from the BA and PEG co-solvents, respectively. This was consistent with the specific BET surface areas in the range of ~2–7 $m^2 \cdot g^{-1}$. Interestingly, the colors of the powders ranging from light pink to dark violet (see Figure 4.3, top) could be correlated with the particle size, with the shade becoming darker with increasing particle size and *vice versa* decreasing surface area. SAED experiments revealed that the smallest crystal dimension is along the [010] direction for all materials, which is the direction of the Li diffusion pathways in the olivine crystal structure. It could thus be inferred that, similarly to EG (*cf.* Chapters 4.1.1 and 4.1.2), the crystal growth towards anisotropic shapes is governed by the stabilization of the (010) crystal faces by selective adsorption of all polyol-type solvent molecules on the crystal surface.

The favorable crystal orientations, which facilitate Li diffusion, resulted in overall high initial discharge capacities for all materials. The rate performance at high C rates was found to correlate with the particle thickness along [010]. Therefore, the samples obtained from the DEG and TEG co-solvents with the smallest dimensions along the [010] direction (~100 nm) exhibited the best electrochemical performances (*cf.* Figure 4.3, center), delivering high initial discharge capacities of 138 $mAh \cdot g^{-1}$ and 141 $mAh \cdot g^{-1}$ at 0.1 C, and gravimetric energy densities of 662 $Wh \cdot kg^{-1}$ and 677 $Wh \cdot kg^{-1}$, respectively. The rate capability and cycle life of the morphology-tuned materials constitutes a significant improvement over materials prepared by other hydrothermal, solvothermal, and microwave-assisted procedures described in the literature and is the best performance reported for an uncoated *Pnma*-$LiCoPO_4$ material to date.

Author contributions: J. Ludwig conceived and designed this work, and carried out the synthesis, material characterization, and data analysis. C. Marino and D. Haering performed electrochemical measurements. J. Ludwig wrote the manuscript. All authors read and approved the final version of the manuscript.

4.1.4 Discussion

A simple and fast one-step microwave-assisted solvothermal (MWST) process for producing high-performance *Pnma*-type $LiCoPO_4$ was presented. The influence of the synthesis conditions on the material properties, especially the electrochemical performance, was investigated, which has barely been covered in previous reports but is necessary for developments in the field.

The MWST process delivers highly crystalline, high-performance (discharge capacities of up to 141 $mAh \cdot g^{-1}$ at 0.1 C) *Pnma*-$LiCoPO_4$ in a single step with a very short reaction time (30 min) and at low temperature (250 °C). This represents a considerable improvement over most conventional kinetically controlled, wet-chemical procedures, such as hydro- (HT) and solvothermal (ST) synthesis, which require relatively long reaction times (of several hours up to weeks)[17-19, 40] and post-processing of the material (*e.g.* by high-temperature annealing or carbon coating) to obtain a crystalline material with reasonable electrochemical performance.[17, 20-21] Thus, the MWST procedure offers the potential to lower the manufacturing costs with significant energy savings. Furthermore, the dielectric microwave heating and the possibility of stirring the reaction mixture ensure for more uniform reaction conditions with respect to temperature and concentration gradients compared to convective heating. As a result, materials with homogeneous particle size distributions and morphologies and superior electrochemical properties are obtained. Because of the additional option to monitor the temperature inside the reaction vessel *in situ*, the MWST process also guarantees a higher degree of reaction control and is more reproducible than the common 'black box' HT or ST approach, which is of particular significance for large-scale industry applications.

Being extremely flexible with respect to the synthesis design, the MWST process can be modified to tune the particle size and morphology of the material. Particle size control can be achieved by adjusting the solvent composition (EG content in the binary H_2O/EG mixture) whereas the crystal shape can be tailored by the choice of co-solvent (by replacing EG with higher polyols, such as DEG, TEG, TTEG, and PEG or the aromatic alcohol BA). In fact, this is the first time that these common material optimization strategies have been explored in detail and successfully accomplished for the MWST synthesis of *Pnma*-$LiCoPO_4$. The particle size was found to be reduced with increasing viscosity of the H_2O/EG solvent mixture, *i.e.* increasing concentration of the EG co-solvent, and the exact correlation between EG concentration, solvent viscosity and specific surface area of the product was revealed (for details please refer to the publication in Chapter 6.3). This finding can be explained by the fact that the ion diffusion rate is reduced in highly viscous (*i.e.*, EG-richer) solvents, which hinders the crystallization of larger particles.[33, 41] In addition, the solubility of the precursors is significantly reduced

compared to water,[41] which leads to a higher degree of supersaturation in solvents that contain more EG. As a result, the nucleation of crystals is favored over growth processes and smaller particles are formed.[36] An additional effect is that EG acts as complexing and capping agent, which hinders the growth of large crystals and prevents agglomeration without requiring the use of an additional dispersant.[42] Since the solvent viscosity–surface area correlation found allows to predict the particle size *a priori*, it is also highly relevant for the production of other active materials for which particles with tailored sizes are desirable. For the synthesis of size-controlled particles with shapes other than hexagonal platelets, similar rheological studies on alternative water/co-solvent systems will be required.

The use of different polyol-type co-solvents (EG, DEG, TEG, TTEG, PEG, and BA), which exhibit properties of both a dispersant and a soft template,[21, 43-44] proved to be a crucial factor for the production of crystals with anisotropic shapes and orientations. In agreement with reports on $LiFePO_4$,[33-34, 45-46] the TEM/SAED studies showed that all co-solvents appear to be selectively adsorbing on (010) crystal faces by forming hydrogen bonds between the hydroxyl groups and the oxygen atoms on the surface of the crystals. As a result, the (010) surface energy is dramatically increased and the crystal growth along the [010] direction is inhibited. All particles obtained in this work thus exhibited reduced dimensions along the preferred [010] direction of the Li diffusion pathways in the olivine crystal structure, which is beneficial to improve Li-ion transport along this path. The fact that different shapes (square, rhombic, and hexagonal platelets) were obtained depending on the solvent system is likely related to different solvent properties and the amount of hydroxyl groups, which may affect the adsorption on additional crystal faces other than the (010) one. However, the crystal growth mechanism under solvothermal conditions is complex and not completely understood to date, even less for binary solvent systems. In order to fully elucidate the relationship between crystal face stabilities and co-solvents, advanced quantum chemical simulation techniques would be required (as for example demonstrated by Fisher and Islam for the hydrothermal synthesis of $LiFePO_4$),[47] which is beyond the scope of this work. Nevertheless, the possibility to synthesize *Pnma*-$LiCoPO_4$ particles with favorable [010] crystal orientations, different shapes and sizes in a simple approach represents a major advancement in the field. Based on the findings, it is likely that the material properties can be further modified upon simple modification of the process design, which is of potential interest for industrial manufacturing.

Owing to the high crystallinity, homogeneous particle size distributions, and the tuned crystal properties with reduced [010] dimensions and improved Li-ion transport properties, all materials produced from the MWST process exhibited above-average to cutting-edge electrochemical performances with maximum discharge capacities in the range of 137–141 $mAh \cdot g^{-1}$ being reached for the best materials of the three studies (Chapters 4.1.1–4.1.3) at a rate of 0.1 C, corresponding to gravimetric energy densities of 658–677 $Wh \cdot kg^{-1}$ (based on capacity

and voltage). Interestingly, in all studies, the discharge capacities and rate capabilities were mainly correlated with the thickness along the [010] direction and to a minor extent, the overall particle dimensions. The particle shape, on the other hand, did not seem to play a major role. Whereas the square platelets produced from DEG and TEG co-solvents (138 $mAh \cdot g^{-1}$ and 141 $mAh \cdot g^{-1}$, *cf.* Chapter 4.1.3) showed a performance improvement over the hexagonal platelets produced from 50 vol% EG (137 $mAh \cdot g^{-1}$, *cf.* Chapter 4.1.1), this effect seems to be mainly attributed to the smaller dimensions along [010] (~100 nm *vs.* ~100–220 nm) since the overall dimensions (600–900 nm × 600–900 nm × 100 nm *vs.* 700–800 nm × 400–600 nm × 100–220 nm) and surface areas (~4 $m^2 \cdot g^{-1}$ *vs.* ~6 $m^2 \cdot g^{-1}$) of the materials were comparable. This is consistent with the fact that the large hexagonal platelets produced from BA and PEG co-solvents with large [010] dimensions (2.5 µm × 2 µm × 0.5–1 µm and 9 µm × 7 µm × 3 µm, *cf.* Chapter 4.1.3) showed the lowest performance of the series, especially in terms of rate capability at higher C rates and cycle life, which are mainly determined by the length of the Li diffusion pathways.

Although one would expect a further increase in capacities and C rate capabilities when the [010] dimensions are further reduced (< 100 nm) due to shortened Li migration pathways, the studies on the influence of the particle size (Chapter 4.1.2), however, revealed that this trend appears to be valid for particles in a (sub)micron size range only. Whereas the biggest particles of the series (produced from water and 10 vol% EG, dimensions of up to ~1 µm × 1 µm × 1 µm) showed below-average performances (87 $mAh \cdot g^{-1}$ and 116 $mAh \cdot g^{-1}$ at 0.1 C), the sample with the smallest and most homogeneous particles as well as the smallest dimensions along [010] (80 vol% EG, dimensions: ~200 nm × 100 nm × 50 nm) was surprisingly not the best performing of the series (122 $mAh \cdot g^{-1}$ at 0.1 C). Instead, the maximum performance (136–137 $mAh \cdot g^{-1}$ at 0.1 C) was reached for particles with a medium size range (40–50 vol% EG; ~800 nm × 800 nm × 100 nm and ~800–900 nm × 500–550 nm × 130–180 nm). This can be explained by taking into account that at high voltage, side reactions involving the oxidation of the electrolyte occur.[3, 7] These reactions compete with the (de)intercalation reaction of $LiCoPO_4$ since the decomposition products of the electrolyte form resistive films on the particle surface that impede Li diffusion.[48] Since electrolyte oxidation at high voltage and the resulting parasitic currents are estimated to be increasing proportionally to the specific surface area (and *vice versa* smaller particles),[25] the high specific surface areas of materials with small particles worsen these effects, which in turn results in poorer electrochemical performance. This is consistent with the fact that the performances observed for the samples with medium-sized particles and BET surface areas (40–50 vol% EG, ~4–6 $m^2 \cdot g^{-1}$) were better than those for small particles and larger surface areas (80 vol% EG, ~13 $m^2 \cdot g^{-1}$) because side reactions are less pronounced in this case. It is noteworthy that electrolyte oxidation and surface area only seem to be crucial factors influencing the electrochemical performance when the particle

dimensions are in the submicron range, *i.e.* when the thickness along [010] and thus the Li migration pathways are reasonably small (< 200 nm). For larger particles (0–10 vol% EG, [010] dimension: ~1 µm) with small surface areas (~2 $m^2 \cdot g^{-1}$) and hence less side reactions, the length of the Li diffusion pathways remains the main factor dominating the electrochemical performance. In conclusion, the findings stand in stark contrast to the general assumption that particle size reduction helps to improve the electrochemical performance of *Pnma*-$LiCoPO_4$.[49-50] Due to increased side reactions and electrolyte oxidation of materials with larger surface areas at high voltage, particle size reduction is not feasible to optimize its performance. Unlike cathode materials with lower operating voltage such as $LiFePO_4$ (3.45 V *vs.* Li/Li^+[38]), which generally benefit from particle size reduction,[51-52] a medium particle size range thus represents the optimum for high-voltage cathode materials such as *Pnma*-$LiCoPO_4$. Although this observation was also made for other types of high-voltage cathode materials (*e.g.* layered oxides and spinels)[53-55] this effect had not been discussed for olivine-type $LiCoPO_4$ prior to this work.

Another finding with potential implications on the electrochemical performance is the identification of amorphous $Li_2SO_4 \cdot H_2O$ as a side product of the process, which was revealed by elemental analysis and thermal studies using TGA/DSC and temperature-dependent *in situ* PXRD. Although other procedures based on the same or similar precursor systems ($LiOH \cdot H_2O$ – $CoSO_4 \cdot 7\ H_2O$ – H_3PO_4 or Li_3PO_4 – $CoSO_4 \cdot 7\ H_2O$) have been described in the literature for about a decade,[17, 20, 26, 30] this is the first report on this side product in a *Pnma*-$LiCoPO_4$ material. Interestingly, the lithium sulfate forms inclusions inside the *Pnma*-$LiCoPO_4$ particles that cannot be removed despite intensive washing (for details see Chapter 6.2). Although further studies showed that the phase is supposedly electrochemically inactive because *Pnma*-$LiCoPO_4$ with various amounts of Li_2SO_4 showed comparable performance (*cf.* supporting materials of Chapter 6.2), it has to be taken into account that it reduces the amount of active material in the sample and thus, the capacity (note that specific capacities in this work were calculated on the basis of the weight of the as-prepared *Pnma*-$LiCoPO_4$ powders in the electrodes, neglecting the weight of the Li_2SO_4 impurity). Furthermore, as a result of the Li_2SO_4 inclusions, the particles were found to exhibit a system of interconnected pores (d = 10–20 nm). In brief, both *Pnma*-$LiCoPO_4$ and Li_2SO_4 are formed in parallel during the reaction, producing composite particles. The highly water-soluble Li_2SO_4 is then dissolved in the aqueous phase of the solvent and pores appear on the surface of the particles where the Li_2SO_4 phase was formerly located.[25] The pore system potentially reduces the mechanical stability of the particles, which might have an impact on the cycle life of the material because particle cracking is more likely. The presence of this phase or possibly other amorphous impurities, which are not detectible by standard techniques such as PXRD, might also be a factor contributing to the inferior electrochemical performance of materials reported in the literature. For that matter, the investigations on the lithium sulfate secondary phase highlight the importance of

comprehensively characterizing active materials prior to electrochemical testing.

In Figure 4.4, the capacities at 0.1 C of the best-performing *Pnma*-$LiCoPO_4$ materials of the three studies of this work (2 × 137 $mAh \cdot g^{-1}$ and 141 $mAh \cdot g^{-1}$, corresponding to 82% and 84% of the theoretical capacity; Chapters 4.1.1–4.1.3) are compared to the state of the art of uncoated *Pnma*-$LiCoPO_4$ as well as carbon-coated *Pnma*-$LiCoPO_4$/C in conventional (HT, ST) and microwave-assisted hydro- and solvothermal (MWHT, MWST) synthesis (as discussed in Chapter 1.2.2). To provide a broader comparison, materials produced from supercritical fluid (SCF) processes are also included. (For the comparison, it is important to note that the capacities of pure $LiCoPO_4$ and coated $LiCoPO_4$/C are comparable to only a limited degree and that differences in the cell design, electrode formulation and charging protocol influence the electrochemical performance.) In the case of pure and non-processed (*i.e.*, no annealing or C-coating) *Pnma*-$LiCoPO_4$, reflecting the intrinsic material properties, the as-prepared MWST materials deliver the best electrochemical performances to date with regard to capacity, rate capability, and cycle life. This may be related to the fact that our materials are highly crystalline and exhibit tuned crystal orientations with reduced dimensions along the [010] direction of the Li transport pathways. Conventional HT or ST materials, on the other hand, generally suffer from antisite defects and disordered structures that are detrimental to the performance as demonstrated in a number of studies.[56-62] Remarkably, our MWST samples still deliver a state-of-the-art performance (*i.e.* > 75% of the theoretical capacity of 167 $mAh \cdot g^{-1}$) in comparison with materials that underwent further treatments such as post-annealing at high temperature (800–900 °C) or conductive carbon coatings.

In fact, the only performance better than that of the MWST samples reported to date is for carbon-coated $LiCoPO_4$/C nanosheets, which reached a capacity of 153 $mAh \cdot g^{-1}$ and were produced by a high-pressure high-temperature (HPHT) supercritical fluid (SCF) process introduced by Rui and co-workers in 2013.[22] This complex procedure, however, which involves a liquid-phase exfoliation followed by a supercritical solvothermal lithiation process, is not feasible from an economical point of view since it requires a long synthesis time (> 1 week), specialized equipment (autoclaves suitable for high pressures and temperature, *e.g.* using graphite gaskets), toxic chemicals (formamide) and only produces material on a milligram scale (yield: < 10 mg). In that respect, our simple and fast (30 min) one-step MWST approach can be considered competitive, also because it allows modification of the material by simple variation of the process parameters. Furthermore, while carbon coatings provide an improvement in rate capability,[63] they can cause a significant decrease in practical energy density if amounts greater than a few weight percent are used. Hence, only by avoiding carbon coatings (as in our case) or keeping the C contents at low levels (*e.g.* < 2 wt%), high energy densities are achievable, which are of significance for applications such as electric mobility. Another important aspect is that our materials were tested in a regular setup using standard electrolytes

(EC/DMC) and reasonably high active material loadings (4–5 $mg \cdot cm^{-2}$) whereas the mass loading used by Rui *et al.*[22] was rather low (2 $mg \cdot cm^{-2}$). Additional tests on our material with high loadings up to 12 $mg \cdot cm^{-2}$ demonstrated promising results (see supporting materials of Chapter 6.2 for details). However, before *Pnma*-$LiCoPO_4$ can reach practical applicability as a suitable candidate for next-generation lithium-ion batteries, further developments will be required. While synthetic modification strategies of the active material itself are an important factor as our MWST studies have demonstrated, further improvements on the performance, especially to tackle the capacity fade, will also heavily rely on the development of electrolyte systems suitable for high voltage (*e.g.*, using ionic liquids or additives such as trimethylboroxine (TMB), fluoroethylene carbonate (FEC) or lithium bis(oxalato)borate (LiBOB))[35, 64-68] and the electrode composition.[69]

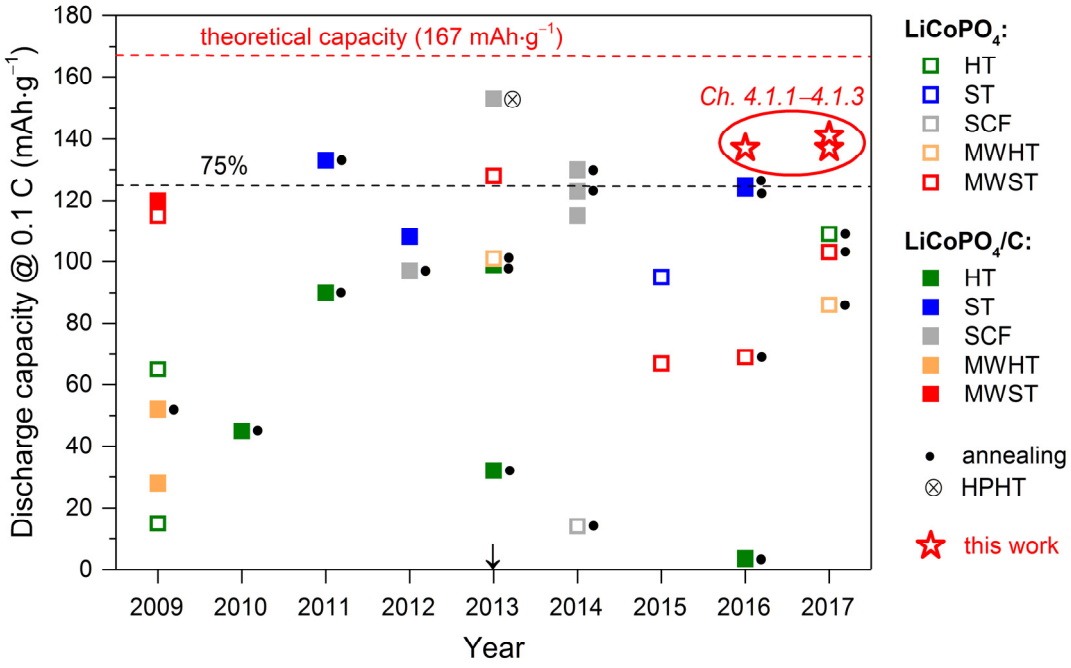

Figure 4.4 Comparison of the initial discharge capacities obtained for the *Pnma*-$LiCoPO_4$ materials of this work (☆)[25, 36, 39] prepared by microwave-assisted solvothermal synthesis (*cf.* Chapters 4.1.1–4.1.3) at 0.1 C with the state of the art for uncoated *Pnma*-$LiCoPO_4$ (□) and carbon-coated *Pnma*-$LiCoPO_4$/C (■) materials synthesized *via* hydrothermal (HT),[18, 20-21, 26-27, 70] solvothermal (ST),[19, 21, 27, 71-72] supercritical fluid (SCF)[22, 73-77] as well as microwave-assisted hydrothermal (MWHT)[78-80] and solvothermal (MWST)[23-24, 37, 81-82] procedures as reported between 2009 and 2017 (the year 2013, marking the start of this work, is indicated by an arrow ↓). Dots (●) right to the symbols mark materials that underwent additional post heat treatments at high temperatures. The dashed black line corresponds to 75% (125 $mAh \cdot g^{-1}$) of the theoretical capacity (167 $mAh \cdot g^{-1}$, red dashed line), which represents a reasonably high performance for the material. It is evident that apart from a capacity of 153 $mAh \cdot g^{-1}$, which was reached in 2013 for *Pnma*-$LiCoPO_4$/C nanosheets prepared by a complex high-pressure high-temperature (HPHT) supercritical fluid process (⊗),[22] the materials prepared in this work reached the highest capacities reported for any untreated and treated (C-coating, annealing) *Pnma*-$LiCoPO_4$ material. The figure was modified and updated on basis of the references [25] and [39] with permission from The Royal Society of Chemistry and Elsevier B.V.

4.2 Metastable Lithium Cobalt Phosphates: $Co_{11}Li[(OH)_5O][(PO_3OH)(PO_4)_5]$, *Pna*2$_1$-$LiCoPO_4$, *Cmcm*-$LiCoPO_4$, and *Cmcm*-$Li_{0.5-\delta}CoPO_4$

Following the investigations on the olivine-type high-voltage cathode material *Pnma*-$LiCoPO_4$, this part focuses on metastable lithium cobalt phosphates, in specific the *Pna*2$_1$- and *Cmcm*-$LiCoPO_4$ polymorphs as well as two new phases, $Li_{0.5-\delta}CoPO_4$, the first Li-deficient derivative of *Cmcm*-$LiCoPO_4$, and the framework compound $Co_{11}Li[(OH)_5O][(PO_3OH)(PO_4)_5]$.

Compared to the thermodynamically stable *Pnma*-$LiCoPO_4$, the *Pna*2$_1$ and *Cmcm* analogs have been less studied. Despite the recent advance,[28, 37, 83-84] there are fundamental aspects that have to be further addressed. In both cases, the crystal structure solutions showed issues such as non-standard space groups, apocryphal site occupancies, and unsatisfactory reliability factors. Moreover, the thermal studies left some questions open. In the case of *Pna*2$_1$-$LiCoPO_4$, previous reports[28, 37] presented contradictory results, while the thermal analysis of *Cmcm*-$LiCoPO_4$ lacked high-temperature data and analysis of the post-TGA material.[37] Furthermore, the electrochemical performances of both phases were found to be poor.[28, 37] However, to date, no attempt was made to optimize (*e.g.* using particle size and morphology control similar to *Pnma*-$LiCoPO_4$) or to fully understand the reasons for this unsatisfactory performance. In addition, the magnetic properties of *Cmcm*-$LiCoPO_4$ were not yet reported.

Therefore, new microwave-assisted solvothermal (MWST) or polyol (PO) synthesis pathways towards size- and shape-tuned *Pna*2$_1$- and *Cmcm*-$LiCoPO_4$ materials have been developed. Based on X-ray and neutron powder diffraction data (PXRD, PND), revised crystal structures are presented. The materials were further characterized using a plethora of techniques, including elemental analysis, scanning electron microscopy (SEM), infrared (IR) and X-ray absorption (XAS) spectroscopy, electrochemical and magnetic measurements, which allows a careful analysis of their structure–property relationships. The thermal properties were examined using a combination of TGA/DSC (thermogravimetric analysis/differential scanning calorimetry) as well as *ex* and *in situ* PXRD experiments.

Using kinetically controlled hydrothermal (HT) and polyol (PO) approaches, the mixed-valent Co(II,III) phases $Co_{11}Li[(OH)_5O][(PO_3OH)(PO_4)_5]$ and *Cmcm*-$Li_{0.5-\delta}CoPO_4$ are reported for the first time. While $Co_{11}Li[(OH)_5O][(PO_3OH)(PO_4)_5]$ plays a significant role as a competing phase in the hydrothermal synthesis of *Pnma*-$LiCoPO_4$, *Cmcm*-$Li_{0.5-\delta}CoPO_4$ represents the first Li-deficient derivative of *Cmcm*-$LiCoPO_4$, which is accessible by a direct polyol synthesis approach. The phases were completely characterized using PXRD (and PND), elemental and thermal analysis, SEM, IR and XAS as well as magnetic measurements.

4.2.1 Summary: $Co_{11}Li[(OH)_5O][(PO_3OH)(PO_4)_5]$, a Lithium-Stabilized, Mixed-Valent Cobalt(II,III) Hydroxide Phosphate Framework

Jennifer Ludwig, Stephan Geprägs, Dennis Nordlund, Marca M. Doeff, and Tom Nilges

Manuscript submitted for publication, **2017.** see Chapter 6.5

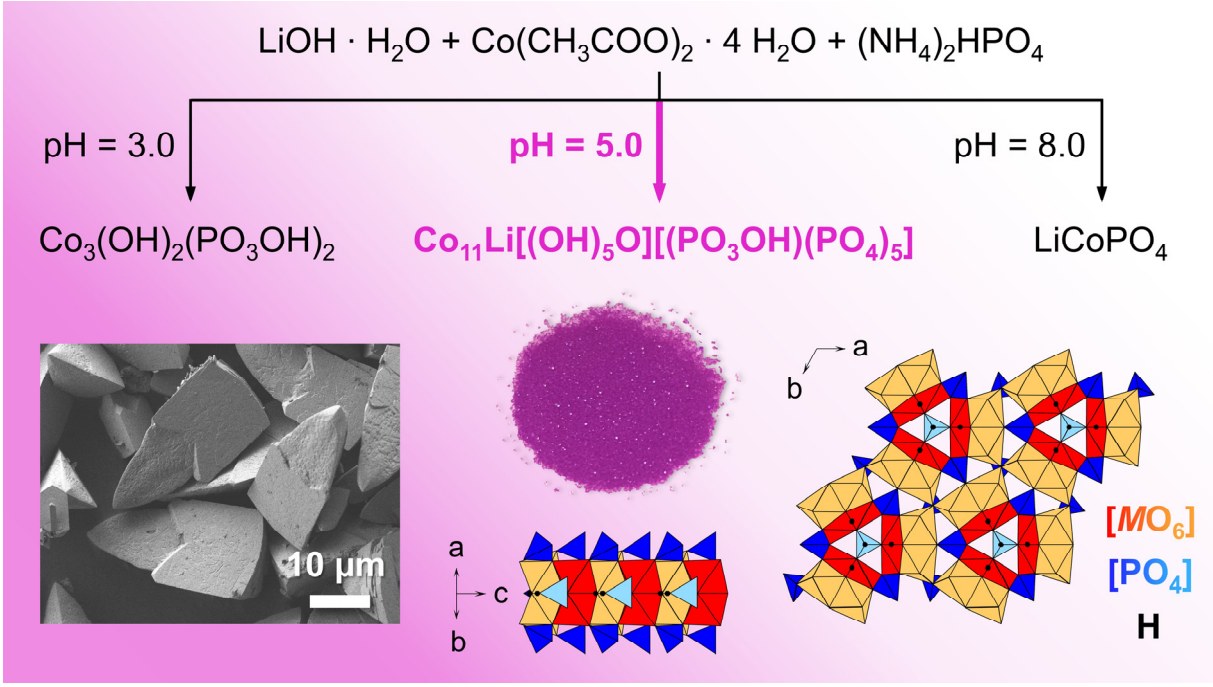

Figure 4.5 A new metastable, lithium-stabilized cobalt(II,III) hydroxide phosphate framework compound with the crystal-chemical composition $Co_{11.0(1)}Li_{1.0(2)}[(OH)_5O][(PO_3OH)(PO_4)_5]$ (space group: *P*31*m*, *Z* = 1, simplified bulk composition: $Co_{1.84(2)}Li_{0.16(3)}(OH)PO_4$) was prepared by hydrothermal synthesis. Because the synthesis is highly pH-sensitive, the formation of $Co_3(OH)_2(PO_3OH)_2$ and olivine-type *Pnma*-$LiCoPO_4$ competes in the process, and a pH value of 5.0 is crucial for obtaining the pure, single-phase title compound (top). The violet powder (center) consists of crystals with dimensions of about 15 µm × 30 µm that exhibit a unique elongated triangular pyramid morphology (bottom left). The main structural feature are alternating double chains of $[M_2O_8(OH)]$ (*M* = Co, Li) dimer units, which run along the [001] direction and are connected *via* $[PO_4]$ and $[PO_3(OH)]$ tetrahedra (bottom center and right). The graphic was adapted from reference [85]/the manuscript in Chapter 6.5.

While optimizing a hydrothermal process for producing olivine-type *Pnma*-$LiCoPO_4$ in the precursor system $LiOH \cdot H_2O$ – $Co(CH_3COO)_2 \cdot 4\ H_2O$ – $(NH_4)_2HPO_4$ (for experimental details see Chapter 3.2.4), the pH value of the reaction medium was identified as a key parameter that controls the phase formation. Whereas pure *Pnma*-$LiCoPO_4$ was only obtained under alkaline conditions at pH = 8.0, $Co_3(OH)_2(PO_3OH)_2$[86] was formed in acidic media with $3.0 \leq pH \leq 4.5$. (At $pH \leq 2.5$, no precipitates were obtained, suggesting that all components

were dissolved under highly acidic conditions.) In the intermediate pH region, a novel lithium-stabilized cobalt(II,III) hydroxide phosphate compound with the crystal-chemical composition $Co_{11.0(1)}Li_{1.0(2)}[(OH)_5O][(PO_3OH)(PO_4)_5]$ was found, which competes with *Pnma*-$LiCoPO_4$ as reaction product at $5.5 \leq pH \leq 7.5$ and can be obtained in phase pure form in a very narrow region at pH = 5.0 (*cf.* Figure 4.5, top). The synthesis conditions, the crystal structure, and material properties were discussed.

The violet crystals exhibit a unique triangular pyramid morphology (dimensions: 15 µm × 30 µm) with a nanosheet-like primary structure (Figure 4.5, bottom left). PXRD experiments reveal that the phase with the simplified empirical formula $Co_{1.84(2)}Li_{0.16(3)}(OH)PO_4$ is isostructural with the Fe- and Mg-bearing phosphate minerals satterlyite[87] and holtedahlite.[88] It crystallizes trigonally, in the space group *P*31*m* (*a* = 11.2533(4) Å, *c* = 4.9945(2) Å, *V* = 547.75(3) Å^3, *Z* = 1) and features a partial Li substitution on both Co sites, which was further substantiated by elemental analysis. First experiments suggested that the Li substitution is crucial for the stabilization of the framework since the synthesis of a Li-free *P*31*m*-type $Co_2(OH)PO_4$ phase proved unsuccessful. The dominant structural motif are alternating double chains running along the [001] direction, which are built from octahedral [$M_2O_8(OH)$] (*M* = Co, Li) dimer units and interconnected by tetrahedral [PO_4] and [$PO_3(OH)$] groups (Figure 4.5, bottom center and right). The occurrence of three independent OH groups was confirmed by infrared spectroscopy. Co *L*-edge X-ray absorption spectroscopy revealed that the framework hosts Co ions that have a mixed valence state (+II/+III). Based on charge-balance arguments, the occurrence of (6 ± 2)% Co^{3+} (*cf.* theoretically expected value: ~9%) is the result of the incorporation of Li^+ ions in the structure. Magnetic measurements demonstrated a paramagnetic to antiferromagnetic transition at *T* = 25 K and a spin-glass-like behavior with a blocking temperature of *T* ~9 K. Thermal analysis revealed that the phase is metastable and shows a complex two-step decomposition mechanism. Driven by a redox reaction and the intrinsic instability of Co^{3+}, the framework decomposes into CoO,[89] $Co_3(PO_4)_2$,[90] and olivine-type *Pnma*-$LiCoPO_4$ with release of H_2O and O_2. Surprisingly, the oxidation of oxide ions to oxygen was found to be the first (558 °C, exothermic) and the dehydration the second (633 °C, endothermic) step of the decomposition.

Author contributions: J. Ludwig conceived and designed this work, and carried out the synthesis, material characterization (PXRD, IR, SEM/EDS), and data analysis. S. Geprägs and D. Nordlund performed and analyzed magnetic and XAS measurements, respectively. J. Ludwig wrote the manuscript. All authors read and approved the final version of the manuscript.

4.2.2 Summary: Synthesis and Characterization of Metastable, 20 nm-Sized *Pna*2_1-$LiCoPO_4$ Nanospheres

Jennifer Ludwig, Dennis Nordlund, Marca M. Doeff, and Tom Nilges

J. Solid State Chem. **2017,** *248*, 9–17. see Chapter 6.6

DOI: 10.1016/j.jssc.2017.01.015

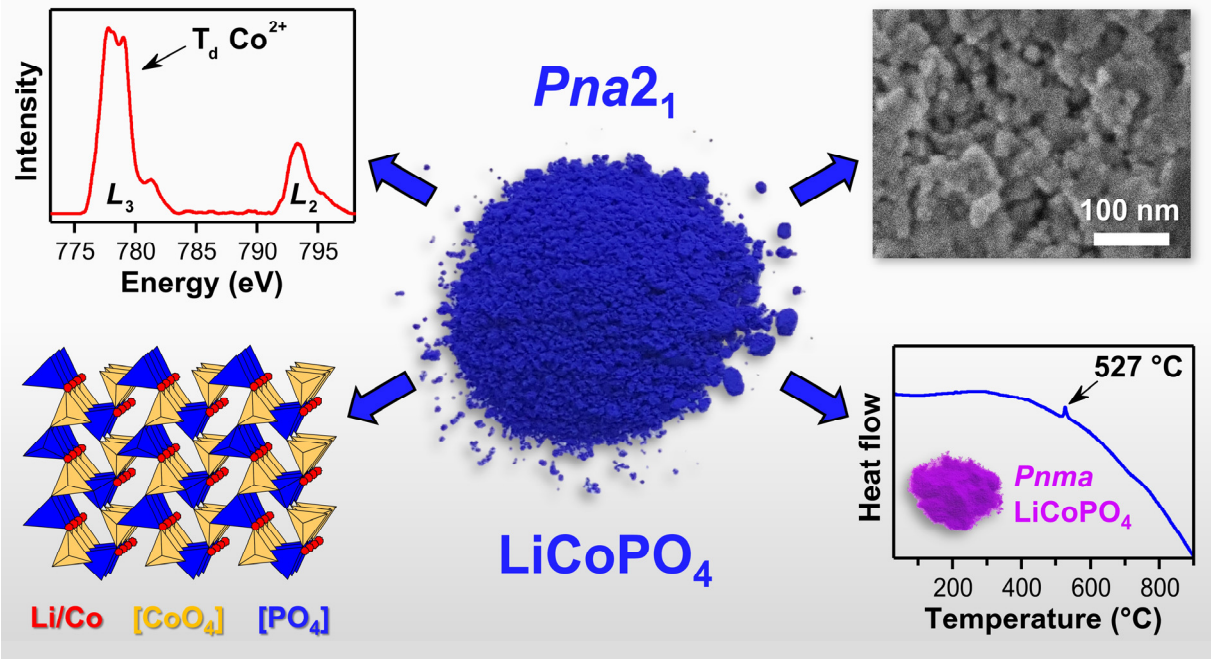

Figure 4.6 Overview on the structure–property relationships of 15–20 nm-sized *Pna*2_1-$LiCoPO_4$ nanospheres (SEM image: top right) made by a microwave-assisted solvothermal (MWST) process. The crystal structure (bottom left) features tetrahedral [CoO_4] (yellow) and [PO_4] (blue) units with Co–Li antisite defects on the tetrahedrally coordinated Li sites (red). The local tetrahedral symmetry of the Co^{2+} ions in the structure was confirmed by Co $L_{2,3}$-edge X-ray absorption spectroscopy (top left). As demonstrated by DSC data (bottom right), the blue powder (center) transforms to violet, olivine-type *Pnma*-$LiCoPO_4$ at 527 °C (exothermic). The graphic was adapted from reference [29], Copyright (2017), with permission from Elsevier Inc.

Based on the study on the particle size-controlled microwave-assisted solvothermal synthesis of olivine-type *Pnma*-$LiCoPO_4$ upon variation of the ethylene glycol (EG) concentration of the binary H_2O/EG solvent (Chapter 4.1.2), a novel synthesis route towards the metastable, exclusively tetrahedrally coordinated (crystal structure see Figure 4.6, bottom left) *Pna*2_1-$LiCoPO_4$ polymorph was found by using pure (100 vol%) EG as a solvent (for experimental details refer to Chapter 3.2.5). Since the particle size was found to be reduced with increasing viscosity of the solvent (see also Chapters 4.1.2 and 4.1.4), the synthesis in pure

EG yielded uniform, spherical *Pna*2_1-$LiCoPO_4$ nanoparticles with diameters of about 15–20 nm (Figure 4.6, top right). The structure–property relationships of the dark blue nanomaterial (Figure 4.6, center) were studied comprehensively with the help of PXRD, elemental and thermal analysis, SEM, BET surface area analysis, IR and XAS spectroscopy, as well as electrochemical measurements. Furthermore, the kinetically controlled formation and crystal growth mechanisms were discussed.

In contrast to previous reports[28, 37] on *Pna*2_1-type $LiCoPO_4$, the results indicated that the compound with the empirical formula $Li_{0.95(1)}Co_{1.03(1)}PO_4$ is non-stoichiometric and exhibits an excess of cobalt. A redetermination of the crystal structure showed that the material features a disordered cation substructure with 4.8(8)% Co mixing on the Li sites. Since Li migration is hindered due to the defects, the occurrence of Co–Li antisite mixing provided an explanation for the poor electrochemical performance of *Pna*2_1-$LiCoPO_4$, which demonstrated a discharge capacity of only 6 $mAh \cdot g^{-1}$.[28] Another explanation is the high surface area of the material (~61 $m^2 \cdot g^{-1}$), which promotes parasitic side reactions at high voltage (as discussed in detail in Chapter 4.1.4). Co $L_{2,3}$-edge soft X-ray absorption spectroscopy confirmed the tetrahedral coordination of the divalent Co^{2+} ions in the structure in the form of $[CoO_4]$ units (Figure 4.6, top left).

A thorough investigation of the thermal stability using TGA/DSC and temperature-dependent *in situ* PXRD experiments revealed that the compound undergoes several phase transitions upon heating. The thermal behavior of *Pna*2_1-$LiCoPO_4$ is hence more complex than previously assumed.[28, 37] At 527 °C, the material converts to olivine-type *Pnma*-$LiCoPO_4$ (Figure 4.6, bottom right). Interestingly, it was found that the *Pna*2_1 phase re-emerges as a stable high-temperature modification at temperatures above 800 °C since a partial and reversible transformation of *Pnma*-$LiCoPO_4$ back to *Pna*2_1-$LiCoPO_4$ was observed. After cooling to ambient temperature, single-phase *Pnma*-$LiCoPO_4$ was obtained. It was further shown that the temperature of the *Pna*2_1–*Pnma* phase transition strongly depends on the atmosphere used upon heating (air *vs.* Ar) as well as the particle size of the material (nano- *vs.* micron-sized particles), with the transition temperature decreasing with increasing crystal dimensions.

Author contributions: J. Ludwig conceived and designed this work, and performed the material synthesis and characterization using *ex* and *in situ* PXRD, EDS, IR, and galvanostatic cycling (under the supervision of T. Nilges and M. M. Doeff). D. Nordlund collected XAS spectra. J. Ludwig interpreted the data and wrote the manuscript. All authors read and approved the final version of the manuscript.

4.2.3 Summary: *In Situ* Studies and Magnetic Properties of the *Cmcm* Polymorph of $LiCoPO_4$ with a Hierarchical Dumbbell-Like Morphology Synthesized by Easy Single-Step Polyol Synthesis

Carlos Alarcón-Suesca,† **Jennifer Ludwig,†** Viktor Hlukhyy, Christoph Stinner, and Tom Nilges († equally contributing co-authors)

Inorganics **2016,** *4*, 35. see Chapter 6.7
DOI: 10.3390/inorganics4040035

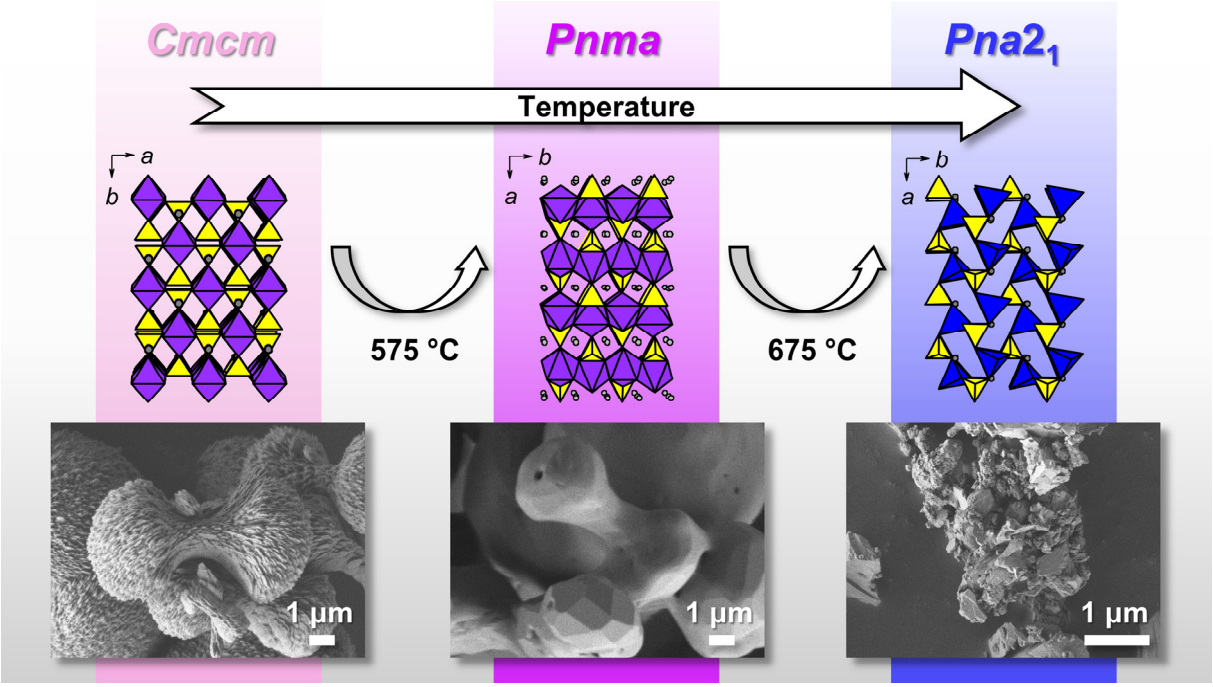

Figure 4.7 Hierarchically structured particles of *Cmcm*-$LiCoPO_4$ with a dumbbell-like morphology have been synthesized by a one-step polyol process. *In situ* PXRD and TGA/DSC studies reveal that the compound transforms to *Pnma*-$LiCoPO_4$ at 575 °C, which is then converted to *Pna*2_1-$LiCoPO_4$ above 675 °C (top). The crystal structures of the three modifications are displayed in the center. [CoO_6] octahedra are drawn in purple, [CoO_4] tetrahedra in blue, [PO_4] tetrahedra in yellow, and Li ions in grey, respectively. SEM images (bottom) indicate that the morphology is not maintained during the phase transitions upon heating. The graphic was created using reference [91] as a template.

The synthesis of the *Cmcm* polymorph of $LiCoPO_4$ has been reported by high-pressure high-temperature solid-state (T = 900 °C, p > 6 GPa)[83] or microwave-assisted techniques.[37] In this work, two alternative, kinetically controlled synthesis pathways towards *Cmcm*-$LiCoPO_4$ using solvothermal (ST) and polyol (PO) synthesis (see Chapters 3.2.6 and 3.2.7) were presented. Both approaches require only low temperatures (T ~200 °C), do not need the use of

dried solvents or expensive equipment and are hence more feasible than previous methods. The thermal and the magnetic properties of *Cmcm*-$LiCoPO_4$ were investigated for the first time.

Whereas the product of the solvothermal process showed impurities of Li_3PO_4[92] and olivine-type *Pnma*-$LiCoPO_4$, the polyol technique delivered single-phase *Cmcm*-$LiCoPO_4$. SEM studies suggested that the synthesis method has a strong influence on the morphology. Both processes resulted in the formation of complex, hierarchically organized structures in a single step without requiring any additives or templates. Whereas the material prepared by ST synthesis featured irregular agglomerates of ~5–10 µm in size and leaf-shaped primary particles (5–6 µm × 0.5–1 µm × 80 nm), dumbbell-like shapes (~1–4 µm) built from nanosheet-type primary particles with dimensions of 20–40 nm × 3–4 nm were obtained from PO synthesis. It was further shown that the size and shape of the primary particles can be influenced by altering the mixing sequence of the starting materials in the polyol process.

The pure material obtained from the polyol process was further characterized. The thermal stability was assessed by TGA/DSC and temperature-dependent *in situ* PXRD analysis. Several structural changes between all reported $LiCoPO_4$ polymorphs (*Pnma*, *Cmcm*, and *Pna*2_1) were observed upon heating, reflecting the different thermodynamic stabilities of the phases (Figure 4.7, center and top). At 575 °C, the *Cmcm*-$LiCoPO_4$ material is converted to the *Pnma* structure. Interestingly, the *Pnma*-$LiCoPO_4$ intermediate then completely transforms to the *Pna*2_1 modification at temperatures above 675 °C, indicating that *Pna*2_1-$LiCoPO_4$ represents a stable high-temperature modification. This is also consistent with the findings for the thermal stabilities of the *Pnma*- and *Pna*2_1-$LiCoPO_4$ phases as discussed in Chapters 4.1.1 and 4.2.2. After cooling to room temperature, the thermodynamically most stable olivine-type *Pnma*-$LiCoPO_4$ phase was obtained. The studies were completed by *ex situ* PXRD and SEM experiments of samples annealed at different temperatures, revealing that the nanosheet-like primary structure of the dumbbells continuously changed upon heating (Figure 4.7, bottom). Above 400 °C, the sample started sintering and formed a more compact material while preserving the dumbbell-like shape. Around 700 °C, corresponding to the temperature of the *Pnma*–*Pna*2_1 phase transition, the dumbbells conglomerated. The particle shape was destroyed upon further heating and finally, irregular particles were formed. Magnetic measurements demonstrated that *Cmcm*-$LiCoPO_4$ shows a long-range antiferromagnetic order below the Néel temperature T_N = 11 K at 10 kOe and T_N = 9 K at 25 kOe, respectively. The magnetization curves suggested the presence of a metamagnetic transition.

Author contributions: C. Alarcón-Suesca and J. Ludwig conceived and designed this work, and carried out the synthesis and data interpretation. J. Ludwig performed XRD and IR, and V. Hlukhyy magnetic measurements. J. Ludwig and C. Alarcón-Suesca wrote the manuscript. All authors read and approved the final version of the manuscript.

4.2.4 Summary: Direct Synthesis and Characterization of Mixed-Valent $Li_{0.5-\delta}CoPO_4$, a Li-Deficient Derivative of the *Cmcm* Polymorph of $LiCoPO_4$

Jennifer Ludwig, Carlos Alarcón-Suesca, Stephan Geprägs, Dennis Nordlund, Marca M. Doeff, Inés Puente Orench, and Tom Nilges

RSC Adv., **2017,** *7*, 28069–28081. see Chapter 6.8
DOI: 10.1039/c7ra04043a

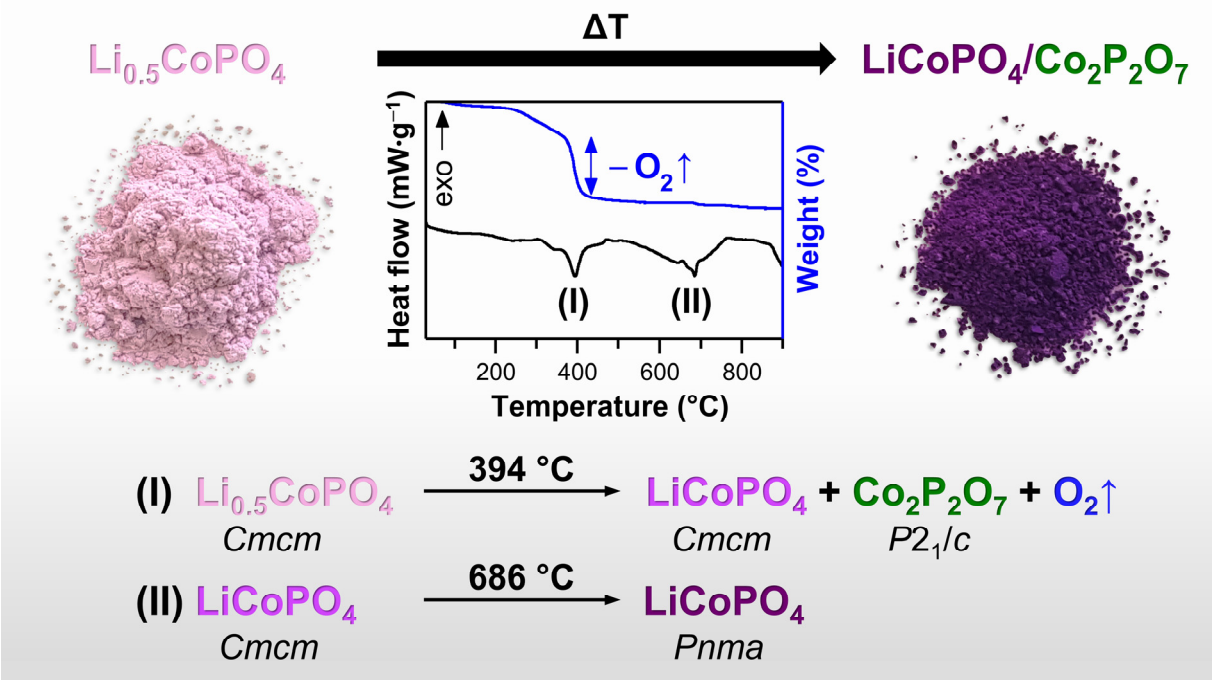

Figure 4.8 A Li-deficient, mixed-valent Co(II,III) derivative of the *Cmcm*-$LiCoPO_4$ polymorph with the nominal composition $Li_{0.5-\delta}CoPO_4$ has been prepared by polyol synthesis. Upon heating, the pale pink *Cmcm*-$Li_{0.5-\delta}CoPO_4$ (here: simplified with $\delta = 0$) material (top left) decomposes to *Pnma*-$LiCoPO_4$ and α-$Co_2P_2O_7$ in a two-step mechanism (bottom). *Cmcm*-$Li_{1-\gamma}CoPO_4$ (here: $\gamma = 0$) is formed as an intermediate under release of oxygen, which was revealed by TGA/DSC analysis (top center). Adapted from reference [93]. – Published by The Royal Society of Chemistry.

Based on the study on *Cmcm*-$LiCoPO_4$ presented in Chapter 4.2.3, a direct polyol synthesis route towards the first Li-deficient structural derivative with the nominal composition $Li_{0.5-\delta}CoPO_4$ was developed. In contrast to the sub-stoichiometric phases Li_xCoPO_4 (x = 0; ⅔) derived from olivine-type *Pnma*-$LiCoPO_4$, which are only accessible by chemical or electrochemical delithiation in a top-down approach,[94-98] the *Cmcm* derivative was obtained by a direct bottom-up approach by altering the molar n(Li):n(Co):n(P) ratio of the starting materials

in the process (for experimental details see Chapter 3.2.7). The light pink *Cmcm*-type $Li_{0.5-\delta}CoPO_4$ material (Figure 4.8, top left) was fully characterized using powder X-ray (PXRD) and neutron diffraction (PND), elemental analysis, SEM, IR and XAS spectroscopy, as well as electrochemical and magnetic measurements. The thermal stability was evaluated with the help of TGA/DSC and *in situ* PXRD experiments. The results were discussed in context of the 'fully' lithiated *Cmcm*-$LiCoPO_4$ phase, for which an improved structure solution (revealing a sub-stoichiometry reflected by the revised sum formula $Li_{1-\gamma}CoPO_4$) as well as Co *L*-edge XAS data were presented for the first time.

PXRD experiments and elemental analysis of the novel *Cmcm*-$Li_{0.5-\delta}CoPO_4$ (with δ = 0.11(2) (PXRD) and 0.05(5) (AAS), respectively) and its 'fully' lithiated counterpart $Li_{1-\gamma}CoPO_4$ (γ = 0.06(2); 0.07(5)) indicated that both structures are non-stoichiometric and feature vacancies on both cation sites. The sub-stoichiometry was further confirmed by neutron powder diffraction experiments. Co *L*-edge X-ray absorption spectroscopy indicated that, unlike *Cmcm*-$Li_{1-\gamma}CoPO_4$, which features only octahedrally coordinated Co^{2+} ions as expected, the Li-deficient structure *Cmcm*-$Li_{0.5-\delta}CoPO_4$ bears about (71 ± 3)% Co^{2+} and (29 ± 3)% Co^{3+} ions, which is in agreement with charge-balance arguments. According to SEM studies, both materials showed a similar hierarchical, dumbbell-like morphology. Despite the nanostructure of the primary particles, both compounds demonstrated poor electrochemical performances, with initial discharge capacities of only ~3 $mAh \cdot g^{-1}$ being reached. This was mainly related to the intrinsically low Li conductivity caused by the lack of suitable Li migration pathways in the crystal structure. No evidence was found that *Cmcm*-$Li_{0.5-\delta}CoPO_4$ represents an intermediate phase upon delithiation of *Cmcm*-$Li_{1-\gamma}CoPO_4$.

A comprehensive investigation of the thermal stability revealed that *Cmcm*-$Li_{0.5-\delta}CoPO_4$ shows a complex, two-step decomposition mechanism upon heating (Figure 4.8, center and bottom). In the first step (I, exothermic) at 394 °C, it decomposes to α-$Co_2P_2O_7$ ($P2_1/c$)[99] and $Li_{1-\gamma}CoPO_4$ (*Cmcm*)[83, 93] under release of oxygen. This redox reaction is driven by the reduction of Co^{3+} in the $Li_{0.5-\delta}CoPO_4$ structure by O^{2-} ions during the pyrophosphate formation (*i.e.*, the coupling of isolated [PO_4] units to [P_2O_7]). The resulting Co^{2+}-only phase *Cmcm*-$Li_{1-\gamma}CoPO_4$ then irreversibly converts to the thermodynamically more stable olivine *Pnma*-$LiCoPO_4$ structure at 686 °C (II) in an endothermic process.

Author contributions: J. Ludwig performed the material characterization using *in situ* and *ex situ* PXRD, SEM/EDS, IR spectroscopy, and electrochemical measurements, and analyzed the data. C. Alarcón-Suesca performed the material synthesis. S. Geprägs and D. Nordlund performed and analyzed magnetic and XAS measurements, respectively. I. Puente Orench and C. Alarcón-Suesca conducted neutron diffraction experiments. J. Ludwig wrote the manuscript. All authors read and approved the final version of the manuscript.

4.2.5 Discussion

Several metastable lithium cobalt phosphate phases, the novel framework structure $Co_{11}Li[(OH)_5O][(PO_3OH)(PO_4)_5]$ as well as the *Pna*2_1- and *Cmcm*-$LiCoPO_4$ polymorphs have been explored, which have been considerably less studied than the olivine-type *Pnma*-$LiCoPO_4$ phase. Moreover, the first Li-deficient derivative of the *Cmcm*-$LiCoPO_4$ structure, $Li_{0.5-\delta}CoPO_4$, was obtained from a direct polyol synthesis approach. The studies provided insights into the structure–property relationships of this class of materials from a fundamental point of view, which might help to understand and modify the material properties with regard to potential future applications.

The trigonal $Co_{11}Li[(OH)_5O][(PO_3OH)(PO_4)_5]$ framework was found to compete as a product of a hydrothermal process towards *Pnma*-$LiCoPO_4$ over a wide pH range (pH = 5.5–7.5), and hence plays a significant role as a side phase in the synthesis of the high-voltage cathode material. In fact, the phase was also obtained in the MWST syntheses discussed in Chapters 4.1.1–4.1.3 when the synthesis conditions, especially the pH value, were not optimized (studies not included in this work). Reflections of the phase were also evident in the PXRD patterns of other *Pnma*-$LiCoPO_4$ materials in the literature,[27] however, they have not been assigned correctly but ascribed to a mixture of LiP_5, $Li_{0.62}CoO_2$, and CoO. For that matter, the discovery and investigation of this phase makes a significant contribution towards a deeper understanding and optimization of the wet-chemical production of *Pnma*-$LiCoPO_4$ and possibly other Co-based cathode materials as well. Whether or not the isostructural Fe, Mn, and Ni homologues of the phase exist (note that the iron phase would be a synthetic analog to the mineral satterlyite;[87, 100] see below) and also represent side products of the hydrothermal synthesis of the other members of the olivine family, Li*M*PO_4 (*M* = Fe, Mn, Ni), will have to be explored in further experiments.

Although the simplified empirical formula $Co_{1.84(2)}Li_{0.16(3)}(OH)PO_4$ suggests that the trigonal (space group: *P*31*m*) phase represents a new polymorph of $Co_2(OH)PO_4$, for which orthorhombic (*Pnnm*)[101] and tetragonal ($I4_1/amd$)[102] structures are known, it does not represent a $Co_2(OH)PO_4$ polymorph in the strict sense due to structural reasons, in particular the proton distribution (for details, please refer to the manuscript in Chapter 6.5). Instead, the phase is isostructural with the natural phosphate minerals satterlyite[87, 100] $Fe_{9.24}Mg_{2.76}(OH,O)_6(PO_3OH)(PO_4)_5$ (found at the Big Fish River area, Yukon Territory, Canada), and holtedahlite[88] $Mg_{12}(OH,O)_6(CO_3)_{0.24}(PO_3OH)_{0.76}(PO_4)_5$ (from Modum, Norway), which are found only in very limited geographical regions. The unit cell volume of 547.70(3) Å^3 ranks between the Fe (V = 562.71(9) Å^3)[87] and Mg (V = 539.3(3) Å^3)[103] counterparts, which is consistent with the ionic radii (CN = 6) of Fe^{2+} (high spin (HS): 0.78 Å),

Co^{2+}/Li^{+} (HS: 0.745 Å), and Mg^{2+} (0.72 Å).[104] Apart from synthetic holtedahlite $Mg_{12}(OH,O)_6(PO_3OH)(PO_4)_5$[103], the novel Co analog represents the only synthetic phase of that structure family, which underlines that the hydrothermal technique, mimicking nature, is a powerful tool to obtain compounds isostructural with hydrothermal minerals as well as original structures[105] and hence, allows to further explore the class of transition-metal phosphates.

In agreement with investigations on satterlyite, which appears to be stabilized by a certain Mg content,[87] the Co framework is likely stabilized by Li substitution on both Co sites, which was substantiated by elemental analysis and PXRD studies. The assumption that Li has a stabilizing effect is further supported by the diagonal relationship between lithium and magnesium,[106] which suggests that both elements exhibit similar chemical properties, as well as the fact that both ions exhibit similar ionic radii (Mg^{2+}: 0.72 Å, Li^{+}: 0.76 Å; CN = 6)[104] and charge densities. In fact, within the scope this work, all attempts to prepare a Li-free *P*31*m*-framework proved unsuccessful and resulted in the formation of single-phase $Co_3(OH)_2(PO_3OH)_2$.[86] However, it was possible to prepare solid solutions of the composition $Co_{2-x}Li_x(OH)PO_4$ (x = 0.15(1)–0.35(3); based on PXRD data), which indicated that there is a certain phase width. As a result of the Li substitution (charge-balance) and supported by XAS studies, the octahedrally coordinated Co ions adopt a mixed valence state (+II, +III; both high spin), which significantly affects the magnetic and thermal behavior of the phase.

Magnetic measurements on the mixed-valent *P*31*m*-$Co_{1.84(2)}Li_{0.16(3)}(OH)PO_4$ phase revealed that the finite Li^{+} and Co^{3+} contents in the $Co_2(OH)PO_4$ framework result in a reduction of the paramagnetic to antiferromagnetic transition as well as the blocking temperature of the spin-glass-like behavior compared to the Li-free *Pnnm*- and *I*4$_1$/*amd*-$Co_2(OH)PO_4$ phases.[102, 107] At high temperature (T > 100 K), the new framework exhibits a Curie–Weiss behavior with a Weiss temperature of (-68 ± 2) K, which is similar to the reported $Co_2(OH)PO_4$ polymorphs[102, 107] and indicates that the interaction between the neighboring magnetic ions is predominantly antiferromagnetic. The low-temperature behavior suggests a paramagnetic to antiferromagnetic transition at T ~25 K. Whereas this temperature is close to the transition temperature found for the *I*4$_1$/*amd* modification (20 K),[102] it is much lower than that of *Pnnm*-$Co_2(OH)PO_4$ (71 K).[107] A second maximum of the magnetic susceptibility was found at T ~9 K, below which the phase exhibited a magnetic hysteresis with a finite remanent magnetization. However, no saturation of the magnetization was observed up to 7 T. Similar to the *Pnnm* phase below 15 K,[107] this indicates a spin-glass-like behavior with a blocking temperature of around 9 K. However, in order to elucidate the structure-related magnetic details of the framework in detail, further experiments will be required.

The investigations on the thermal stability showed that the phase undergoes a complex, two-step decomposition to CoO,[89] $Co_3(PO_4)_2$,[90] and *Pnma*-$LiCoPO_4$ with release of oxygen and water. The formation of CoO and $Co_3(PO_4)_2$ as decomposition products is consistent with

a report[101] on *Pnnm*-$Co_2(OH)PO_4$. In the case of the *I*4$_1$/*amd* polymorph, no decomposition products have been reported.[102] The formation of *Pnma*-$LiCoPO_4$ as an additional Li-containing decomposition product provides further evidence for the partial Li substitution of the *P*31*m*-type $Co_2(OH)PO_4$ framework in $Co_{11}Li[(OH)_5O][(PO_3OH)(PO_4)_5]$. Surprisingly, the oxidation, which is driven by the intrinsic instability of the Co^{3+} ions in the framework, occurs at lower temperature (558 °C, mass loss: 0.6 wt%) than the dehydration step (633 °C, mass loss: 4.6 wt%). This finding possibly provides further insights into the thermal stability of *Pnnm*-$Co_2(OH)PO_4$ as well, since the TGA data of this material showed two very similar weight loss steps (initial: 0.4 wt%, ~600 °C: 3.8 wt%). Whereas the second step was attributed to the dehydration of *Pnnm*-$Co_2(OH)PO_4$, the first step was explained by so-called 'surface effects'.[101] Because the *Pnnm* material was prepared by hydrothermal synthesis and Co^{2+} is prone to oxidation in aqueous media, however, it is possible that the initial step is also related to O_2 release due to the presence of a small amount of Co^{3+}. Therefore, the oxidation state of the Co ions in *Pnnm*-type $Co_2(OH)PO_4$ should be reassessed. Because of the presence of mixed-valent Co ions in a complex hydroxide–hydrogen phosphate–phosphate matrix and its interesting thermal properties, $Co_{11}Li[(OH)_5O][(PO_3OH)(PO_4)_5]$ may act as a good oxygen-evolving catalyst (OEC) for example for water splitting, similar to the well-established Co–Pi (cobalt–phosphate) catalyst system.[108-111] Consecutive studies on the new phase should therefore focus onto exploring its catalytic properties.

The investigations on the *Pna*2$_1$- and *Cmcm*-$LiCoPO_4$ polymorphs addressed important aspects that remained unclear or untouched in other reports.[28, 37, 83] While previous synthesis methods, especially for producing *Cmcm*-$LiCoPO_4$, required special equipment and complex procedures (*cf.* high-pressure high-temperature solid-state and microwave-assisted solvothermal syntheses under water-free conditions),[37, 83] two alternative, one-step soft-chemical approaches at low temperature, using solvothermal (ST) and polyol (PO) methods, have been developed. The use of a variety of polyol solvents in these new pathways (DEG, TEG, TTEG, and PEG) further allows for morphological tuning of the material, even towards hierarchically organized structures, which has hitherto not been explored. In the case of *Pna*2$_1$-$LiCoPO_4$, the use of pure ethylene glycol (MWST process) instead of pure water as described for the MWHT process by Jähne *et al.*[28] resulted in a significant particle size reduction towards a nanostructured (d = 15–20 nm) material. With the help of rheological measurements, the size reduction could clearly be related to the increased viscosity of EG compared to water (EG: 15.7(2) mPa·s *vs.* H_2O: 0.89(5) mPa·s; measured at 25 °C and a shear rate of 100 s^{-1};[29, 36] for a thorough discussion please refer to Chapter 4.1.4). Further studies (for details see Chapter 6.6) demonstrated that by using lower process temperatures, morphological and size tuning of *Pna*2$_1$-$LiCoPO_4$ is not restricted to water-free solvents.

Since both the *Pna*2$_1$- and *Cmcm*-$LiCoPO_4$ phases undergo a transition to the thermodynamically stable *Pnma* structure upon heating, the materials might be used as intermediates to produce particle size- and morphology-controlled *Pnma*-$LiCoPO_4$ by post-annealing, a synthesis pathway that has only been explored for *Pna*2$_1$-$LiCoPO_4$ to date.[79] Since the phase transition temperatures towards *Pnma*-$LiCoPO_4$ (T ~500–600 °C) are significantly lower than the temperatures required for the direct solid-state synthesis of the olivine (T = 800–900 °C), [112] and because nanoparticles with diameters < 50 nm have only been accessible using high energy-consuming ball-milling procedures,[113] this approach could pave the way for an easy and scalable production of the high-voltage cathode material *Pnma*-$LiCoPO_4$ with significant energy savings. In that respect, the comprehensive investigations on the thermal behavior of the metastable $LiCoPO_4$ polymorphs by using a combined approach of TGA/TSC as well as *ex situ* and temperature-dependent *in situ* PXRD investigations make a significant contribution.

In the case of *Cmcm*-$LiCoPO_4$, it was demonstrated that the transformation to *Pnma*-$LiCoPO_4$ is exothermic and occurs at 575 °C, which is considerably higher than previously assumed.[37] Interestingly, studies in the high-temperature region, which has not been investigated prior to this work, revealed that *Pnma*-$LiCoPO_4$ is only stable up to 625 °C. At 650 °C, no reflections were visible, indicating that the material undergoes amorphization, while at 675 °C *Pna*2$_1$-$LiCoPO_4$ is formed. After cooling to room temperature, the stable *Pnma*-$LiCoPO_4$ was obtained. A similar behavior was observed for the nanostructured *Pna*2$_1$-$LiCoPO_4$. An exothermic phase transition to the *Pnma* phase was found to occur at 527 °C, which is comparable to the transition temperature of *Cmcm*-$LiCoPO_4$ (575 °C) but significantly higher than stated for *Pna*2$_1$-$LiCoPO_4$ by other groups (*cf.* Jähne *et al*.:[28] 221 °C, exothermic; Kreder *et al*.:[37] 340 °C, endothermic). Furthermore, it could be clarified that the transition is in fact exothermic. The discrepancy in transition temperature could be explained by further studies on a micron-sized *Pna*2$_1$ material (also produced by the MWST process, for details see Chapter 6.6), which revealed that the temperature of the *Pna*2$_1$–*Pnma* phase transition increases with the particle size. This is also in line with the findings in the literature (*cf.* Jähne[28]: ~5 µm, Kreder[37]: ~200 nm × 1 µm, this work: ~15–20 nm). An explanation for this observation are probably crystal strains, which are more likely to occur in bigger particles than in small ones. Similar to the thermal behavior of *Cmcm*-$LiCoPO_4$, the *Pna*2$_1$-$LiCoPO_4$ phase re-emerges when the *Pnma*-$LiCoPO_4$ intermediate is heated to higher temperatures (T > 800 °C), but is then transformed back to *Pnma*-$LiCoPO_4$ upon cooling. The investigations on the high-temperature behavior of the *Cmcm* and *Pna*2$_1$ as well as the *Pnma* phase (*cf.* Chapter 4.1.1) give thus new impulses to critically review the thermodynamic relation of all three $LiCoPO_4$ polymorphs. Since all polymorphs demonstrated a high-temperature transformation to the *Pna*2$_1$ structure, it can be concluded that *Pna*2$_1$-$LiCoPO_4$ represents a stable high-temperature modification whereas *Pnma*-$LiCoPO_4$ becomes metastable in this temperature range. The

findings are in contrast to all previous reports[28, 37] which suggested – on the basis of low-temperature and *ex situ* data – that the *Pna*2$_1$-$LiCoPO_4$ polymorph is a metastable low-temperature modification only since *Pnma*-$LiCoPO_4$, which represents the thermodynamically stable phase at room temperature, was found as an end-product of the transition. Our studies impressively demonstrate the drawbacks of relying solely on post-TGA/DSC analyses and at the same time the significance to study the thermal behavior *in situ* in order to get a thorough understanding of the underlying processes.

In addition to the studies on morphological tuning and the thermal stability, the redetermination of the crystal structures of the two polymorphs provided further insights. Whereas previous studies[28, 37] suggested that the phases are stoichiometric, *i.e.* exhibit an ideal molar ratio of *n*(Li):*n*(Co):*n*(P) = 1:1:1, we found that both compounds are in fact non-stoichiometric. The significant deviations of the empirical formulas derived from elemental analysis (*Pna*2$_1$: $Li_{0.95(2)}Co_{1.05(1)}P_{1.00(2)}O_4$, *Cmcm*: $Li_{0.93(5)}Co_{0.91(3)}P_{1.00(2)}O_4$) from the ideal composition $Li_1Co_1PO_4$ prompted us to further investigate the crystal structures. In the case of the *Cmcm* polymorph, the deficit both in Li and Co suggested a defective structure that features vacancies in the cation substructure. This was confirmed by a refinement of the occupancy factors of the Li and Co sites on the basis of X-ray and neutron powder diffraction data (X-ray: 94(2)% Li and 95.5(5)% Co; neutron: 90(3)% Li and 95(6)% Co). Note that there was no indication for antisite defects in *Cmcm*-$Li_{1-\gamma}CoPO_4$. Since the compositions found by the three techniques (elemental analysis, PXRD, PND) differed to a certain extent, the revised sum formula of the *Cmcm* polymorph was denoted as *Cmcm*-$Li_{1-\gamma}CoPO_4$ to best reflect the off-stoichiometries within three standard deviations. The refinement of the occupancy on the Li site of *Pna*2$_1$-$LiCoPO_4$ resulted in a statistically significant over-occupation of 124(8)% whereas the Co site was found to be fully occupied within standard deviations. The high electron density strongly indicated that there is a partial substitution of the Li site with Co. An over-occupation of 122% Li was also reported by Jähne and co-workers,[28] but no Co occupancy on this site was assumed. Similar to the isostructural phase δ_1-$LiZnPO_4$ (space group: *Pna*2$_1$), for which a disordered Li–Zn distribution was described for both the Li and Zn sites (8% Zn on the Li position, and *vice versa*),[114] it could be concluded that Co–Li antisite mixing appears on the Li site (95.2(8)% Li and 4.8(8)% Co) of the *Pna*2$_1$-$LiCoPO_4$ structure.

Despite the off-stoichiometry of both the *Pna*2$_1$ and *Cmcm* phases, it is noteworthy that the compositions are charge-balanced within standard deviations and that the structures contain only Co^{2+} ions. In addition to the local symmetries (T_d coordination in *Pna*2$_1$-$LiCoPO_4$ and O_h in *Cmcm*-$Li_{1-\gamma}CoPO_4$) of the Co ions, the occurrence of Co^{2+} was confirmed by Co *L*-edge X-ray absorption spectra, which were reported for the first time. In the case of *Cmcm*-$Li_{1-\gamma}CoPO_4$, the broadening of the spectrum compared to a CoO reference[115] provided further proof for the occurrence of vacancies and the resulting disorder in the cation substructure.

Both materials demonstrated poor electrochemical performances, with capacities of only 3–6 mAh·g^{-1} being reached. This could be related to the intrinsically low electrical and ionic conductivities as both structures lack suitable Li migration pathways. The Li–Li distances being rather large in both cases (~5 Å; *i.e.* twice as large as in the olivine structure), the Li sites are practically isolated and the activation energy for Li migration will be very high. In the case of *Pna*2$_1$-$LiCoPO_4$, the conductivity is additionally reduced due to the Co–Li antisite defects with Co ions blocking Li diffusion paths. This is likely also reason for the generally poor performance observed in other electrochemical studies about *Pna*2$_1$-$LiCoPO_4$[28, 37] and is in line with reports[17, 45, 57-58, 60-61] on olivine-$LiFePO_4$ showing that cation-mixing significantly reduces the performance. The blocking of Li channels also explains why the particle size reduction approach, a common strategy to overcome diffusional limitations and to improve the electrochemical performance (as outlined in Chapter 1.2.1), did not succeed in this case. Hence, to achieve further progress in the field, it will be crucial to find a synthesis pathway towards a stoichiometric *Pna*2$_1$-$LiCoPO_4$ material without antisite defects (*e.g.* by increasing the synthesis temperature). However, similar to the findings on the effect of the particle size on the performance of *Pnma*-$LiCoPO_4$ (discussion see Chapter 4.1.4), the decomposition of the electrolyte at the high operating voltage (5.0 V *vs.* Li/Li$^+$)[28] has to be considered, because side reactions will be exacerbated by the high surface area of the material (~61 m^2/g). For that matter, the practical application of the phase will in this case also depend on the development of novel electrolytes which are suitable for the potential window (*e.g.* using ionic liquids or additives[35, 65]).

Upon simple variation of the molar *n*(Li):*n*(Co):*n*(P) ratio of the starting materials in the polyol process towards *Cmcm*-$Li_{1-\gamma}CoPO_4$, the novel Li-deficient phase *Cmcm*-$Li_{0.5-\delta}CoPO_4$ was obtained, with δ similarly to γ in *Cmcm*-$Li_{1-\gamma}CoPO_4$ reflecting the variation in off-stoichiometry found by elemental analysis and Rietveld refinements of X-ray and neutron powder diffraction data. As opposed to chemical or electrochemical Li extraction (top-down) routes starting from fully lithiated $LiCoPO_4$ which are described for the *Pnma* phase in the literature,[96-97] this is the first time that a sub-stoichiometric Li_xCoPO_4-type phase has been synthesized by a direct (bottom-up) soft-chemical approach. Interestingly, *Cmcm*-$Li_{0.5-\delta}CoPO_4$ is significantly more stable under air than its delithiated *Pnma* counterparts $Li_{2/3}CoPO_4$ and in particular $CoPO_4$, which are reportedly extremely sensitive to air and moisture and undergo rapid amorphization.[2-3, 94, 97] Another significant difference is the fact that the cell volume of *Cmcm*-$Li_{0.5-\delta}CoPO_4$ shows a slight increase of 0.7% compared to *Cmcm*-$Li_{1-\gamma}CoPO_4$ whereas for the delithiated phases $Li_{2/3}CoPO_4$ and $CoPO_4$ derived from *Pnma*-$LiCoPO_4$, a decrease of up to ~7% (for *Pnma*-$CoPO_4$) in cell volume was observed, which is consistent with the smaller ionic radius of Co^{3+} compared to Co^{2+}.[3, 74, 97] This observation might be explained by the fact that the *Cmcm*-$Li_{0.5-\delta}CoPO_4$ material was produced by a kinetically controlled synthesis pathway

while the *Pnma*-type Li_xCoPO_4 (x = 0, ⅔) phases were obtained by electrochemical delithiation. As a result, the Li ions and voids are most likely statistically distributed within the *Cmcm* structure.[93] This would also be consistent with investigations on olivine-$LiFePO_4$, which revealed that materials synthesized at low temperature are prone to disorder, resulting in larger cell volumes than expected.[57] However, the PXRD and PND studies could not provide any information about the ordering of the Li^+, Co^{2+}, and Co^{3+} ions or the vacancies in *Cmcm*-$Li_{0.5-\delta}CoPO_4$. Based on charge distribution considerations, it is possible that the vacancies in the *Cmcm*-$Li_{0.5-\delta}CoPO_4$ are located next to the Co^{3+} centers, which would be consistent with DFT (density functional theory) studies[116] on the Li^+–vacancy distribution in olivine-$Li_{2/3}CoPO_4$.

The fact that disorder occurs in the cation substructure was further substantiated by Co *L*-edge XAS spectroscopy, which showed broadening of the *Cmcm*-$Li_{0.5-\delta}CoPO_4$ spectrum compared to Co^{2+} and Co^{3+} reference materials.[115, 117] Fitting of the spectrum indicated a lower Co^{3+} contribution ((71 ± 3)% Co^{2+} and (29 ± 3)% Co^{3+}, both high spin) than expected on the basis of the nominal composition $Li_{0.5-\delta}CoPO_4$ (*i.e.*, ~50% Co^{2+} and ~50% Co^{3+}). This is possibly related to surface reduction effects because Co^{3+} is significantly less stable than Co^{2+}. In fact, the tetraethylene glycol (TTEG) solvent used in the polyol process also acts as a weak reducing agent[118-119] and XAS spectra obtained at different probing depths indicated that the bulk of the particles contains a higher portion of Co^{3+} than the surface.

The difference of the Co oxidation states both in *Cmcm*-$Li_{0.5-\delta}CoPO_4$ (Co^{2+}, Co^{3+}) and *Cmcm*-$Li_{1-\gamma}CoPO_4$ (Co^{2+} only) suggests that the phases should exhibit different magnetic properties, which were first reported for both compounds in this work. The measurements indicate a long-range antiferromagnetic to paramagnetic transition at T_N = 10.5 K for $Li_{0.5-\delta}CoPO_4$, and T_N = 12 K for $Li_{1-\gamma}CoPO_4$, respectively. The latter, which was confirmed by the study focusing on *Cmcm*-$LiCoPO_4$ only (Chapter 4.2.3), is comparable to reported values for *Pna*2$_1$-$LiCoPO_4$ (T_N = 11 K),[28] but much lower than that of *Pnma*-$LiCoPO_4$ (T_N = 21.6 K).[120-121] This demonstrates the close relation between structural and magnetic properties. The reduction of the transition temperature in *Cmcm*-$Li_{0.5-\delta}CoPO_4$ compared to *Cmcm*-$Li_{1-\gamma}CoPO_4$ is possibly related to the vacancies on the Co site, which lead to a weakening of the Co–O–Co super exchange interaction.[122-123] Above T_N, the magnetic susceptibility of both *Cmcm*-$Li_{0.5-\delta}CoPO_4$ and *Cmcm*-$Li_{1-\gamma}CoPO_4$ follow a Curie–Weiss behavior. Furthermore, the phases exhibit similar effective magnetic moments μ_{eff} = (5.20 ± 0.02) μ_B for $Li_{0.5-\delta}CoPO_4$ and (5.08 ± 0.02) μ_B for $Li_{1-\gamma}CoPO_4$, respectively. Both values exceed the spin-only values of high-spin Co^{2+} (3.9 μ_B) and Co^{3+} (4.8 μ_B), which indicates a non-negligible orbital contribution.[84] The slightly larger effective magnetic moment μ_{eff} of *Cmcm*-$Li_{0.5-\delta}CoPO_4$ further supports the occurrence of mixed-valent Co(II,III) ions in the structure. Whereas *Cmcm*-$Li_{1-\gamma}CoPO_4$ exhibits a magnetic double-hysteresis loop that indicates a spin-flip transition at a critical field of around ± 3 T, which is much lower than for *Pnma*-$LiCoPO_4$,[124] an almost linear dependence of the

magnetization on the applied field was observed in the case of *Cmcm*-$Li_{0.5-\delta}CoPO_4$. No hysteresis with a finite remanence caused by a weak ferromagnetic phase due to the mixed valence state of the Co ions was found.[121] However, the difference of the magnetic susceptibility recorded under field-cooled (FC) and zero field-cooled (ZFC) conditions suggests the formation of magnetic domains below T ~5 K. Below this temperature, the presence of Co^{3+} ions and the defects on the Co sites might cause competing magnetic interactions that result in a complex antiferromagnetic state. A similar phenomenon was described by Jensen and co-workers[125] for *Pna*2_1-$LiCoPO_4$. Therefore, the magnetic properties of the two *Cmcm* phases $Li_{0.5-\delta}CoPO_4$ and $Li_{1-\gamma}CoPO_4$ should be investigated more thoroughly in the future, for example by refining the magnetic structures on the basis of neutron diffraction data.

Studies on the thermal stability of *Cmcm*-$Li_{0.5-\delta}CoPO_4$ showed that the phase exhibits a complex two-step thermal decomposition mechanism, which is driven by the mixed valence state of the Co ions in the structure. The decompositions leads to the crystallization of the same decomposition products (*i.e.*, *Pnma*-$LiCoPO_4$ and α-$Co_2P_2O_7$) under oxygen evolution as reported for the Li-poor phase *Pnma*-Li_xCoPO_4.[96] However, there are some mechanistic differences between *Cmcm*-$Li_{0.5-\delta}CoPO_4$ and *Pnma*-Li_xCoPO_4, which are possibly related to the fact that our studies were performed on the pure material whereas the studies on Li_xCoPO_4 were based on charged *Pnma*-$LiCoPO_4$ electrodes. First of all, the decomposition of *Cmcm*-$Li_{0.5-\delta}CoPO_4$ phase occurs at higher temperatures (T = 394 °C) than that of charged *Pnma*-Li_xCoPO_4 cathodes (T < 200 °C),[96] suggesting that the *Cmcm* structure is significantly more thermally stable. Furthermore, different intermediates seem to be involved (*Cmcm*-$Li_{1-\gamma}CoPO_4$ *vs.* a possibly amorphous compound). The decomposition process of *Pnma*-Li_xCoPO_4 cathodes appears to be triggered by the presence of carbon.[96, 98] Considering that the C content of the *Cmcm*-$Li_{0.5-\delta}CoPO_4$ sample was negligible (0.4(3) wt%; for details see Chapter 6.8), there is hence no indication that this is also the case for the Li-deficient *Cmcm* phase. Therefore, the intrinsic thermal stability of pure, carbon-free *Pnma*-Li_xCoPO_4 (x = 0, ⅔) instead of electrodes should be assessed in the future. In that context, by compositional tuning (*e.g.* by variation of the molar ratio of the starting materials), the novel polyol synthesis approach might provide an alternative bottom-up pathway towards these delithiated *Pnma*-Li_xCoPO_4 (x = 0, ⅔) phases as opposed to chemical or electrochemical delithiation. Furthermore, it potentially also paves the way to the discovery and investigation of new Li-deficient structures derived from other lithium transition-metal phosphates, such as the Fe-, Mn-, and Ni-based members of the olivine *Pnma*-Li*M*PO_4[38] and the non-olivine *Cmcm*-Li*M*PO_4[126] groups. Due to the presence of mixed-valent Co ions similar to the $Co_{11}Li[(OH)_5O][(PO_3OH)(PO_4)_5]$ framework, *Cmcm*-$Li_{0.5-\delta}CoPO_4$ could probably also be of potential interest for catalytic applications (*e.g.* for oxygen evolution reactions), which will have to be investigated in further studies.

To conclude, the studies on metastable cobalt phosphates revealed that this class of materials exhibits a rich structural chemistry, which is characterized by disorder phenomena, defect formation, and heterovalent cation substructures. The structural diversity results in interesting and complex physical features, particularly with regard to magnetic and thermal properties. As shown for other transition-metal phosphates, this opens up a diverse portfolio of potential applications, for example in adsorption,[127] semiconductive glasses,[128] nonlinear optics,[129] catalysis,[108-110, 130] and batteries.[5, 38, 131-132] The synthetic (crystal engineering by kinetically controlled wet-chemical approaches) and analytic (complementary *ex* and *in situ* techniques) methodology used in this work, which helped to gain a deeper understanding of the structure–property relationships of these materials and their modification, will be crucial for further developments on the path towards practical applicability.

4.3 References

[1] Okada, S.; Sawa, S.; Egashira, M.; Yamaki, J.; Tabuchi, M.; Kageyama, H.; Konishi, T.; Yoshino, A., Cathode properties of phospho-olivine Li*M*PO_4 for lithium secondary batteries. *J. Power Sources* **2001,** *97–98*, 430–432.

[2] Bramnik, N. N.; Bramnik, K. G.; Buhrmester, T.; Baehtz, C.; Ehrenberg, H.; Fuess, H., Electrochemical and structural study of $LiCoPO_4$-based electrodes. *J. Solid State Electrochem.* **2004,** *8*, 558–564.

[3] Bramnik, N. N.; Nikolowski, K.; Baehtz, C.; Bramnik, K. G.; Ehrenberg, H., Phase Transitions Occurring upon Lithium Insertion–Extraction of $LiCoPO_4$. *Chem. Mater.* **2007,** *19*, 908–915.

[4] Markevich, E.; Sharabi, R.; Gottlieb, H.; Borgel, V.; Fridman, K.; Salitra, G.; Aurbach, D.; Semrau, G.; Schmidt, M. A.; Schall, N.; Bruenig, C., Reasons for capacity fading of $LiCoPO_4$ cathodes in $LiPF_6$ containing electrolyte solutions. *Electrochem. Commun.* **2012,** *15*, 22–25.

[5] Zaghib, K.; Guerfi, A.; Hovington, P.; Vijh, A.; Trudeau, M.; Mauger, A.; Goodenough, J. B.; Julien, C. M., Review and analysis of nanostructured olivine-based lithium recheargeable batteries: Status and trends. *J. Power Sources* **2013,** *232*, 357–369.

[6] Hayashi, K.; Nemoto, Y.; Tobishima, S.-I.; Yamaki, J.-I., Mixed solvent electrolyte for high voltage lithium metal secondary cells. *Electrochim. Acta* **1999,** *44*, 2337–2344.

[7] Egashira, M.; Takahashi, H.; Okada, S.; Yamaki, J.-I., Measurement of the electrochemical oxidation of organic electrolytes used in lithium batteries by microelectrode. *J. Power Sources* **2001,** *92*, 267–271.

[8] Delacourt, C.; Laffont, L.; Bouchet, R.; Wurm, C.; Leriche, J. B.; Morcrette, M.; Tarascon, J. M.; Masquelier, C., Toward understanding of electrical limitations (electronic, ionic) in Li*M*PO_4 (*M* = Fe, Mn) electrode materials. *J. Electrochem. Soc.* **2005,** *152*, A913–A921.

[9] Wolfenstine, J., Electrical conductivity of doped $LiCoPO_4$. *J. Power Sources* **2006,** *158*, 1431–1435.

[10] Prabu, M.; Selvasekarapandian, S.; Kulkarni, A. R.; Karthikeyan, S.; Hirankumar, G.; Sanjeeviraja, C., Ionic transport properties of $LiCoPO_4$ cathode material. *Solid State Sci.* **2011,** *13*, 1714–1718.

[11] Prabu, M.; Selvasekarapandian, S.; Reddy, M. V.; Chowdari, B. V. R., Impedance studies on the 5-V cathode material, $LiCoPO_4$. *J. Solid State Electrochem.* **2012,** *16*, 1833–1839.

[12] Allen, J. L.; Thompson, T.; Sakamoto, J.; Becker, C. R.; Jow, T. R.; Wolfenstine, J., Transport properties of $LiCoPO_4$ and Fe-substituted $LiCoPO_4$. *J. Power Sources* **2014,** *254*, 204–208.

[13] Morgan, D.; Van der Ven, A.; Ceder, G., Li Conductivity in Li_xMPO_4 (*M* = Mn, Fe, Co, Ni) Olivine Materials. *Electrochem. Solid-State Lett.* **2003,** *7*, A30–A32.

[14] Fisher, C. A. J.; Hart, P. V. M.; Islam, M. S., Lithium Battery Materials $LiMPO_4$ (*M* = Mn, Fe, Co, and Ni): Insights into Defect Association, Transport Mechanisms, and Doping Behavior. *Chem. Mater.* **2008,** *20*, 5907–5915.

[15] Brutti, S.; Panero, S., Recent advances in the development of $LiCoPO_4$ as high voltage cathode material for Li-ion batteries. *ACS Symp. Ser.* **2013,** *1140*, 67–99.

[16] Huang, X.; Ma, J.; Wu, P.; Hu, Y.; Dai, J.; Zhu, Z.; Chen, H.; Wang, H., Hydrothermal synthesis of $LiCoPO_4$ cathode materials for rechargeable lithium-ion batteries. *Mater. Lett.* **2005,** *59*, 578–582.

[17] Chen, J.; Wang, S.; Whittingham, M. S., Hydrothermal synthesis of cathode materials. *J. Power Sources* **2007,** *174*, 442–448.

[18] Zhao, Y.; Wang, S.; Zhao, C.; Xia, D., Synthesis and electrochemical performance of $LiCoPO_4$ micron-rods by dispersant-aided hydrothermal method for lithium ion batteries. *Rare Met.* **2009,** *28*, 117–121.

[19] Brutti, S.; Manzi, J.; De Bonis, A.; Di Lecce, D.; Vitucci, F.; Paolone, A.; Trequattrini, F.; Panero, S., Controlled synthesis of $LiCoPO_4$ by a solvo-thermal method at 220 °C. *Mater. Lett.* **2015,** *145*, 324–327.

[20] Kotobuki, M.; Mizuno, Y.; Munakata, H.; Kanamura, K., Electrochemical properties of hydrothermally synthesized $LiCoPO_4$ as a high voltage cathode material for lithium secondary battery. *Phosphorus Res. Bull.* **2010,** *24*, 12–15.

[21] Wang, F.; Yang, J.; Nuli, Y.; Wang, J., Novel hedgehog-like 5 V $LiCoPO_4$ positive electrode material for rechargeable lithium battery. *J. Power Sources* **2011,** *196*, 4806–4810.

[22] Rui, X.; Zhao, X.; Lu, Z.; Tan, H.; Sim, D.; Hng, H. H.; Yazami, R.; Lim, T. M.; Yan, Q., Olivine-Type Nanosheets for Lithium Ion Battery Cathodes. *ACS Nano* **2013,** *7*, 5637–5646.

[23] Murugan, A. V.; Muraliganth, T.; Ferreira, P. J.; Manthiram, A., Dimensionally Modulated, Single-Crystalline Li*M*PO_4 (*M* = Mn, Fe, Co, and Ni) with Nano-Thumblike Shapes for High-Power Energy Storage. *Inorg. Chem.* **2009,** *48*, 946–952.

[24] Rogers, R. E.; Clarke, G. M.; Matthew, O. N.; Ganter, M. J.; DiLeo, R. A.; Staub, J. W.; Forney, M. W.; Landi, B. J., Impact of microwave synthesis conditions on the rechargeable capacity of $LiCoPO_4$ for lithium ion batteries. *J. Appl. Electrochem.* **2013,** *43*, 271–278.

[25] Ludwig, J.; Marino, C.; Haering, D.; Stinner, C.; Nordlund, D.; Doeff, M. M.; Gasteiger, H. A.; Nilges, T., Facile, ethylene glycol-promoted microwave-assisted solvothermal synthesis of high-performance $LiCoPO_4$ as a high-voltage cathode material for lithium-ion batteries. *RSC Adv.* **2016,** *6*, 82984–82994.

[26] Kotobuki, M., Hydrothermal synthesis of carbon-coated $LiCoPO_4$ cathode material from various Co sources. *Int. J. Energy Environ. Eng.* **2013,** *4*, 25–32.

[27] Wu, B.; Xu, H.; Mu, D.; Shi, L.; Jiang, B.; Gai, L.; Wang, L.; Liu, Q.; Ben, L.; Wu, F., Controlled solvothermal synthesis and electrochemical performance of $LiCoPO_4$ submicron single crystals as a cathode material for lithium ion batteries. *J. Power Sources* **2016,** *304*, 181–188.

[28] Jähne, C.; Neef, C.; Koo, C.; Meyer, H.-P.; Klingeler, R., A new $LiCoPO_4$ polymorph *via* low temperature synthesis. *J. Mater. Chem. A* **2013,** *1*, 2856–2862.

[29] Ludwig, J.; Nordlund, D.; Doeff, M. M.; Nilges, T., Synthesis and characterization of metastable, 20 nm-sized *Pna*2_1-$LiCoPO_4$ nanospheres. *J. Solid State Chem.* **2017,** *248*, 9–17.

[30] Chen, J.; Vacchio, M. J.; Wang, S.; Chernova, N.; Zavalij, P. Y.; Whittingham, M. S., The hydrothermal synthesis and characterization of olivines and related compounds for electrochemical applications. *Solid State Ion.* **2008,** *178*, 1676–1693.

[31] Friend, J. A. N., The hydrates of lithium sulfate and their solubility in water between −16° and +103°. *J. Chem. Soc.* **1929**, 2330–2333.

[32] Linke, W. F.; Seidell, A., *Solubilities of Inorganic and Metal Organic Compounds Vol. II. 4th ed*. Am. Chem. Soc.: **1966;** p 1941 pp.

[33] Kuppan, S.; Balaya, P.; Reddy, M. V.; Chowdari, B. V. R.; Vittal, J. J., Morphology controlled synthesis of $LiFePO_4$/C nanoplates for Li-ion batteries. *Energy Environ. Sci.* **2010,** *3*, 457–464.

[34] Song, J.; Wang, L.; Shao, G.; Shi, M.; Ma, Z.; Wang, G.; Song, W.; Liu, S.; Wang, C., Controllable synthesis, morphology evolution and electrochemical properties of $LiFePO_4$ cathode materials for Li-ion batteries. *Phys. Chem. Chem. Phys.* **2014,** *16*, 7728–7733.

[35] Freiberg, A.; Metzger, M.; Haering, D.; Bretzke, S.; Puravankara, S.; Nilges, T.; Stinner, C.; Marino, C.; Gasteiger, H. A., Anodic Decomposition of Trimethylboroxine as Additive for High Voltage Li-Ion Batteries. *J. Electrochem. Soc.* **2014,** *161*, A2255–A2261.

[36] Ludwig, J.; Haering, D.; Doeff, M. M.; Nilges, T., Particle size-controllable microwave-assisted solvothermal synthesis of the high-voltage cathode material $LiCoPO_4$ using water/ethylene glycol solvent blends. *Solid State Sci.* **2017,** *65*, 100–109.

[37] Kreder, K. J.; Assat, G.; Manthiram, A., Microwave-Assisted Solvothermal Synthesis of Three Polymorphs of $LiCoPO_4$ and Their Electrochemical Properties. *Chem. Mater.* **2015,** *27*, 5543–5549.

[38] Padhi, A. K.; Nanjundaswamy, K. S.; Goodenough, J. B., Phospho-olivines as Positive-Electrode Materials for Rechargeable Lithium Batteries. *J. Electrochem. Soc.* **1997,** *144*, 1188–1194.

[39] Ludwig, J.; Marino, C.; Haering, D.; Stinner, C.; Gasteiger, H. A.; Nilges, T., Morphology-controlled microwave-assisted solvothermal synthesis of high-performance $LiCoPO_4$ as a high-voltage cathode material for Li-ion batteries. *J. Power Sources* **2017,** *342*, 214–223.

[40] Recham, N.; Oro-Sole, J.; Djellab, K.; Palacin, M. R.; Masquelier, C.; Tarascon, J. M., Hydrothermal synthesis, silver decoration and electrochemistry of Li*M*PO_4 (*M* = Fe, Mn, and Co) single crystals. *Solid State Ionics* **2012,** *220*, 47–52.

[41] Teng, F.; Santhanagopalan, S.; Asthana, A.; Geng, X.-B.; Mho, S.-I.; Shahbazian-Yassar, R.; Meng, D. D.-S., Self-assembly of $LiFePO_4$ nanodendrites in a novel system of ethylene glycol-water. *J. Cryst. Growth* **2010,** *312*, 3493–3502.

[42] Feldmann, C., Polyol-mediated synthesis of nanoscale functional materials. *Solid State Sci.* **2005,** *7*, 868–873.

[43] Zhang, X.; Ai, Z.; Jia, F.; Zhang, L., Generalized One-Pot Synthesis, Characterization, and Photocatalytic Activity of Hierarchical BiO*X* (*X* = Cl, Br, I) Nanoplate Microspheres. *J. Phys. Chem. C* **2008,** *112*, 747–753.

[44] Wu, M.; Wang, Z. H.; Yuan, L. X.; Zhang, W. X.; Hu, X. L.; Huang, Y. H., Morphology-controllable solvothermal synthesis of nanoscale $LiFePO_4$ in a binary solvent. *Chin. Sci. Bull.* **2012,** *57*, 4170–4175.

[45] Qin, X.; Wang, J.; Xie, J.; Li, F.; Wen, L.; Wang, X., Hydrothermally synthesized $LiFePO_4$ crystals with enhanced electrochemical properties: simultaneous suppression of crystal growth along [010] and antisite defect formation. *Phys. Chem. Chem. Phys.* **2012,** *14*, 2669–2677.

[46] Mathew, V.; Alfaruqi, M. H.; Gim, J.; Song, J.; Kim, S.; Ahn, D.; Kim, J., Morphology-controlled $LiFePO_4$ cathodes by a simple polyol reaction for Li-ion batteries. *Mater. Charact.* **2014,** *89*, 93–101.

[47] Fisher, C. A. J.; Islam, M. S., Surface structures and crystal morphologies of $LiFePO_4$. Relevance to electrochemical behaviour. *J. Mater. Chem.* **2008,** *18*, 1209–1215.

[48] Aurbach, D.; Markovsky, B.; Salitra, G.; Markevich, E.; Talyossef, Y.; Koltypin, M.; Nazar, L.; Ellis, B.; Kovacheva, D., Review on electrode-electrolyte solution interactions, related to cathode materials for Li-ion batteries. *J. Power Sources* **2007,** *165*, 491–499.

[49] Doan, T. N. L.; Taniguchi, I., Preparation of $LiCoPO_4$/C nanocomposite cathode of lithium batteries with high rate performance. *J. Power Sources* **2011,** *196*, 5679–5684.

[50] Liu, J.; Conry, T. E.; Song, X.; Yang, L.; Doeff, M. M.; Richardson, T. J., Spherical nanoporous $LiCoPO_4$/C composites as high performance cathode materials for rechargeable lithium-ion batteries. *J. Mater. Chem.* **2011,** *21*, 9984–9987.

[51] Delacourt, C.; Poizot, P.; Levasseur, S.; Masquelier, C., Size Effects on Carbon-Free $LiFePO_4$ Powders. *Electrochem. Solid-State Lett.* **2006,** *9*, A352–A355.

[52] Gaberscek, M.; Dominko, R.; Jamnik, J., Is small particle size more important than carbon coating? An example study on $LiFePO_4$ cathodes. *Electrochem. Commun.* **2007,** *9*, 2778–2783.

[53] Martha, S. K.; Sclar, H.; Szmuk Framowitz, Z.; Kovacheva, D.; Saliyski, N.; Gofer, Y.; Sharon, P.; Golik, E.; Markovsky, B.; Aurbach, D., A comparative study of electrodes comprising nanometric and submicron particles of $LiNi_{0.50}Mn_{0.50}O_2$, $LiNi_{0.33}Mn_{0.33}Co_{0.33}O_2$, and $LiNi_{0.40}Mn_{0.40}Co_{0.20}O_2$ layered compounds. *J. Power Sources* **2009,** *189*, 248–255.

[54] Karn, K. C.; Doeff, M. M., Electrode materials for lithium ion batteries. In *Mater. Matters* Aldrich Chemical Co., Inc.: Milwaukee, WI, USA, **2012;** Vol. 7, pp 56–60.

[55] Xiao, L.; Guo, Y.; Qu, D.; Deng, B.; Liu, H.; Tang, D., Influence of particle sizes and morphologies on the electrochemical performances of spinel $LiMn_2O_4$ cathode materials. *J. Power Sources* **2013,** *225*, 286–292.

[56] Islam, M. S.; Driscoll, D. J.; Fisher, C. A. J.; Slater, P. R., Atomic-Scale Investigation of Defects, Dopants, and Lithium Transport in the $LiFePO_4$ Olivine-Type Battery Material. *Chem. Mater.* **2005,** *17*, 5085–5092.

[57] Chen, J.; Whittingham, M. S., Hydrothermal synthesis of lithium iron phosphate. *Electrochem. Commun.* **2006,** *8*, 855–858.

[58] Chen, J.; Graetz, J., Study of Antisite Defects in Hydrothermally Prepared $LiFePO_4$ by in Situ X-ray Diffraction. *ACS Appl. Mater. Interfaces* **2011,** *3*, 1380–1384.

[59] Truong, Q. D.; Devaraju, M. K.; Tomai, T.; Honma, I., Direct observation of antisite defects in $LiCoPO_4$ cathode materials by annular dark- and bright-field electron microscopy. *ACS Appl. Mater. Interfaces* **2013,** *5*, 9926–9932.

[60] Jensen, K. M. O.; Christensen, M.; Gunnlaugsson, H. P.; Lock, N.; Boejesen, E. D.; Proffen, T.; Iversen, B. B., Defects in Hydrothermally Synthesized $LiFePO_4$ and $LiFe_{1-x}Mn_xPO_4$ Cathode Materials. *Chem. Mater.* **2013,** *25*, 2282–2290.

[61] Jensen, K. M. Ø.; Gunnlaugsson, H. P.; Christensen, M.; Iversen, B. B., Moessbauer spectroscopy study of defects in hydrothermally synthesized $LiFePO_4$ cathode material. *Hyperfine Interact.* **2014,** *226*, 73–78.

[62] Devaraju, M. K.; Truong, Q. D.; Tomai, T.; Hyodo, H.; Sasaki, Y.; Honma, I., Antisite defects in $LiCoPO_4$ nanocrystals synthesized *via* a supercritical fluid process. *RSC Adv.* **2014,** *4*, 52410–52414.

[63] Hong, Y.; Tang, Z.; Wang, S.; Quan, W.; Zhang, Z., High-performance $LiMnPO_4$ nanorods synthesized *via* a facile EG-assisted solvothermal approach. *J. Mater. Chem. A* **2015,** *3*, 10267–10274.

[64] Aravindan, V.; Cheah, Y. L.; Ling, W. C.; Madhavi, S., Effect of LiBOB additive on the electrochemical performance of $LiCoPO_4$. *J. Electrochem. Soc.* **2012,** *159*, A1435–A1439.

[65] Sharabi, R.; Markevich, E.; Fridman, K.; Gershinsky, G.; Salitra, G.; Aurbach, D.; Semrau, G.; Schmidt, M. A.; Schall, N.; Bruenig, C., Electrolyte solution for the improved cycling performance of $LiCoPO_4$/C composite cathodes. *Electrochem. Commun.* **2013,** *28*, 20–23.

[66] Markevich, E.; Salitra, G.; Fridman, K.; Sharabi, R.; Gershinsky, G.; Garsuch, A.; Semrau, G.; Schmidt, M. A.; Aurbach, D., Fluoroethylene Carbonate as an Important Component in Electrolyte Solutions for High-Voltage Lithium Batteries: Role of Surface Chemistry on the Cathode. *Langmuir* **2014,** *30*, 7414–7424.

[67] Hofmann, A.; Schulz, M.; Indris, S.; Heinzmann, R.; Hanemann, T., Mixtures of Ionic Liquid and Sulfolane as Electrolytes for Li-Ion Batteries. *Electrochim. Acta* **2014,** *147*, 704–711.

[68] Markevich, E.; Salitra, G.; Aurbach, D., Fluoroethylene Carbonate as an Important Component for the Formation of an Effective Solid Electrolyte Interphase on Anodes and Cathodes for Advanced Li-Ion Batteries. *ACS Energy Lett.* **2017,** *2*, 1337–1345.

[69] Hu, M.; Pang, X.; Zhou, Z., Recent progress in high-voltage lithium ion batteries. *J. Power Sources* **2013,** *237*, 229–242.

[70] Maeyoshi, Y.; Miyamoto, S.; Noda, Y.; Munakata, H.; Kanamura, K., Effect of organic additives on characteristics of carbon-coated $LiCoPO_4$ synthesized by hydrothermal method. *J. Power Sources* **2017,** *337*, 92–99.

[71] Li, M., Solvothermal synthesis of $LiCo_{1-x}Mn_xPO_4$/C cathode materials for lithium-ion batteries. *Ionics* **2012,** *18*, 507–512.

[72] Palmer, M. G.; Frith, J. T.; Hector, A. L.; Lodge, A. W.; Owen, J. R.; Nicklin, C.; Rawle, J., *In situ* phase behaviour of a high capacity $LiCoPO_4$ electrode during constant or pulsed charge of a lithium cell. *Chem. Commun.* **2016,** *52*, 14169–14172.

[73] Devaraju, M. K.; Rangappa, D.; Honma, I., Controlled synthesis of plate-like $LiCoPO_4$ nanoparticles via supercritical method and their electrode property. *Electrochim. Acta* **2012,** *85*, 548–553.

[74] Kaus, M.; Issac, I.; Heinzmann, R.; Doyle, S.; Mangold, S.; Hahn, H.; Chakravadhanula, V. S. K.; Kuebel, C.; Ehrenberg, H.; Indris, S., Electrochemical Delithiation/Relithiation of $LiCoPO_4$: A Two-Step Reaction Mechanism Investigated by *in Situ* X-ray Diffraction, *in Situ* X-ray Absorption Spectroscopy, and *ex Situ* $^7Li/^{31}P$ NMR Spectroscopy. *J. Phys. Chem. C* **2014,** *118*, 17279–17290.

[75] Truong, Q. D.; Devaraju, M. K.; Ganbe, Y.; Tomai, T.; Honma, I., Controlling the shape of $LiCoPO_4$ nanocrystals by supercritical fluid process for enhanced energy storage properties. *Sci. Rep.* **2014,** *4*, 3975.

[76] Truong, Q. D.; Devaraju, M. K.; Honma, I., Benzylamine-directed growth of olivine-type Li*M*PO_4 nanoplates by a supercritical ethanol process for lithium-ion batteries. *J. Mater. Chem. A* **2014,** *2*, 17400–17407.

[77] Devaraju, M. K.; Truong, Q. D.; Hyodo, H.; Tomai, T.; Honma, I., Supercritical fluid synthesis of $LiCoPO_4$ nanoparticles and their application to lithium ion battery. *Inorganics* **2014,** *2*, 233–247.

[78] Murugan, A. V.; Muraliganth, T.; Manthiram, A., One-Pot Microwave-Hydrothermal Synthesis and Characterization of Carbon-Coated Li*M*PO_4 (*M* = Mn, Fe, and Co) Cathodes. *J. Electrochem. Soc.* **2009,** *156*, A79–A83.

[79] Neef, C.; Meyer, H.-P.; Klingeler, R., Morphology-controlled two-step synthesis and electrochemical studies on hierarchically structured $LiCoPO_4$. *Solid State Sci.* **2015,** *48*, 270–277.

[80] Örnek, A., An impressive approach to solving the ongoing stability problems of $LiCoPO_4$ cathode: Nickel oxide surface modification with excellent core-shell principle. *J. Power Sources* **2017,** *356*, 1–11.

[81] Kreder, K. J.; Assat, G.; Manthiram, A., Aliovalent Substitution of V^{3+} for Co^{2+} in $LiCoPO_4$ by a Low-Temperature Microwave-Assisted Solvothermal Process. *Chem. Mater.* **2016,** *28*, 1847–1853.

[82] Kreder, K. J.; Manthiram, A., Vanadium-Substituted $LiCoPO_4$ Core with a Monolithic $LiFePO_4$ Shell for High-Voltage Lithium-Ion Batteries. *ACS Energy Lett.* **2017,** *2*, 64–69.

[83] Amador, U.; Gallardo-Amores, J. M.; Heymann, G.; Huppertz, H.; Moran, E.; Arroyo-de Dompablo, M. E., High pressure polymorphs of $LiCoPO_4$ and $LiCoAsO_4$. *Solid State Sci.* **2009,** *11*, 343–348.

[84] Baek, S. H.; Klingeler, R.; Neef, C.; Koo, C.; Buechner, B.; Grafe, H. J., Unusual spin fluctuations and magnetic frustration in olivine and non-olivine $LiCoPO_4$ detected by ^{31}P and ^{7}Li nuclear magnetic resonance. *Phys. Rev. B: Condens. Matter Mater. Phys.* **2014,** *89*, 134424/1–134424/6.

[85] Ludwig, J.; Geprägs, S.; Nordlund, D.; Doeff, M. M.; Nilges, T., $Co_{11}Li[(OH)_5O][(PO_3OH)(PO_4)_5]$, a Lithium-Stabilized, Mixed-Valent Cobalt(II,III) Hydroxide Phosphate Framework. **2017,** *submitted*.

[86] Effenberger, H., Structure refinement of tricobalt dihydroxide bis(hydrogen phosphate) and cobalt bis(dihydrogen phosphate) dihydrate. *Acta Crystallogr., Sect. C: Cryst. Struct. Commun.* **1992,** *C48*, 2104–2107.

[87] Kolitsch, U.; Andrut, M.; Giester, G., Satterlyite, $(Fe,Mg)_{12}(PO_3OH)(PO_4)_5(OH,O)_6$: crystal structure and infrared absorption spectra. *Eur. J. Mineral.* **2002,** *14*, 127–133.

[88] Raade, G.; Mladeck, M. H., Holtedahlite, a new magnesium phosphate from Modum, Norway. *Lithos* **1979,** *12*, 283–287.

[89] Sasaki, S.; Fujino, K.; Takeuchi, Y., X-ray determination of electron-density distributions in oxides, magnesium oxide, manganese(II) oxide, cobalt oxide, and nickel(II) oxide, and atomic scattering factors of their constituent atoms. *Proc. Jpn. Acad., Ser. B* **1979,** *55*, 43–48.

[90] Anderson, J. B.; Kostiner, E.; Miller, M. C.; Rea, J. R., Crystal structure of cobalt orthophosphate $Co_3(PO_4)_2$. *J. Solid State Chem.* **1975,** *14*, 372–377.

[91] Alarcón-Suesca, C.; Ludwig, J.; Hlukhyy, V.; Stinner, C.; Nilges, T., In Situ Studies and Magnetic Properties of the *Cmcm* Polymorph of $LiCoPO_4$ with a Hierarchical Dumbbell-Like Morphology Synthesized by Easy Single-Step Polyol Synthesis. *Inorganics* **2016,** *4*, 35.

[92] Keffer, C.; Mighell, A. D.; Mauer, F.; Swanson, H. E.; Block, S., Crystal structure of twinned low-temperature lithium phosphate. *Inorg. Chem.* **1967,** *6*, 119–125.

[93] Ludwig, J.; Alarcón-Suesca, C.; Geprägs, S.; Nordlund, D.; Doeff, M. M.; Puente Orench, I.; Nilges, T., Direct synthesis and characterization of mixed-valent $Li_{0.5-\delta}CoPO_4$, a Li-deficient derivative of the *Cmcm* polymorph of $LiCoPO_4$. *RSC Adv.* **2017,** *7*, 28069–28081.

[94] Wolfenstine, J.; Poese, B.; Allen, J. L., Chemical oxidation of $LiCoPO_4$. *J. Power Sources* **2004,** *138*, 281–282.

[95] Bramnik, N. N.; Bramnik, K. G.; Baehtz, C.; Ehrenberg, H., Study of the effect of different synthesis routes on Li extraction–insertion from $LiCoPO_4$. *J. Power Sources* **2005,** *145*, 74–81.

[96] Bramnik, N. N.; Nikolowski, K.; Trots, D. M.; Ehrenberg, H., Thermal stability of $LiCoPO_4$ cathodes. *Electrochem. Solid-State Lett.* **2008,** *11*, A89–A93.

[97] Ehrenberg, H.; Bramnik, N. N.; Senyshyn, A.; Fuess, H., Crystal and magnetic structures of electrochemically delithiated $Li_{1-x}CoPO_4$ phases. *Solid State Sci.* **2009,** *11*, 18–23.

[98] Theil, S.; Fleischhammer, M.; Axmann, P.; Wohlfahrt-Mehrens, M., Experimental investigations on the electrochemical and thermal behaviour of $LiCoPO_4$-based cathode. *J. Power Sources* **2013,** *222*, 72–78.

[99] El Bali, B.; Bolte, M., Rerefinement of cobalt diphosphate against new intensity data. *Acta Crystallogr., Sect. E: Struct. Rep. Online* **2002,** *58*, i32–i33.

[100] Mandarino, J. A.; Sturman, B. D.; Corlett, M. I., Satterlyite, a new hydroxyl-bearing ferrous phosphate from the Big Fish River area, Yukon Territory [Canada]. *Can. Mineral.* **1978,** *16*, 411–413.

[101] Harrison, W. T. A.; Vaughey, J. T.; Dussack, L. L.; Jacobson, A. J.; Martin, T. E.; Stucky, G. D., Two new adamite-type phases, $Co_2(OH)PO_4$ and $Zn_2(OH)PO_4$: structure-directing effect of organic additives. *J. Solid State Chem.* **1995,** *114*, 151–158.

[102] Wang, G.; Valldor, M.; Spielberg, E. T.; Mudring, A.-V., Ionothermal Synthesis, Crystal Structure, and Magnetic Study of Co_2PO_4OH Isostructural with Caminite. *Inorg. Chem.* **2014,** *53*, 3072–3077.

[103] Roemming, C.; Raade, G., The crystal structure of natural and synthetic holtedahlite. *Mineral. Petrol.* **1989,** *40*, 91–100.

[104] Shannon, R. D., Revised effective ionic radii and systematic studies of interatomic distances in halides and chalcogenides. *Acta Crystallogr., Sect. A* **1976,** *A32*, 751–767.

[105] Rabenau, A., The role of hydrothermal synthesis in preparative chemistry. *Angew. Chem.* **1985,** *97*, 1017–1032.

[106] A. F. Holleman; E. Wiberg; Wiberg, N., Die Gruppe der Alkalimetalle. In *Lehrbuch der Anorganischen Chemie*, 102nd ed.; Walter de Gruyter: Berlin, Germany, **2007;** p 1261.

[107] Rojo, J. M.; Mesa, J. L.; Lezama, L.; Pizarro, J. L.; Arriortua, M. I.; Fernandez, J. R.; Barberis, G. E.; Rojo, T., Spin-glass behavior in a three-dimensional antiferromagnet ordered phase: Magnetic structure of $Co_2(OH)(PO_4)$. *Phys. Rev. B: Condens. Matter Mater. Phys.* **2002,** *66*, 094406/1–094406/13.

[108] Kanan, M. W.; Nocera, D. G., In Situ Formation of an Oxygen-Evolving Catalyst in Neutral Water Containing Phosphate and Co^{2+}. *Science* **2008,** *321*, 1072–1075.

[109] Kanan, M. W.; Surendranath, Y.; Nocera, D. G., Cobalt-phosphate oxygen-evolving compound. *Chem. Soc. Rev.* **2009,** *38*, 109–114.

[110] Zhong, D. K.; Gamelin, D. R., Photoelectrochemical Water Oxidation by Cobalt Catalyst ("Co-Pi")/α-Fe_2O_3 Composite Photoanodes: Oxygen Evolution and Resolution of a Kinetic Bottleneck. *J. Am. Chem. Soc.* **2010,** *132*, 4202–4207.

[111] Li, Y.; Zhao, Y.; Zhang, Z., A porous graphene/cobalt phosphate composite as an efficient oxygen evolving catalyst. *Electrochem. Commun.* **2014,** *48*, 35–39.

[112] Jang, I. C.; Lim, H. H.; Lee, S. B.; Karthikeyan, K.; Aravindan, V.; Kang, K. S.; Yoon, W. S.; Cho, W. I.; Lee, Y. S., Preparation of $LiCoPO_4$ and $LiFePO_4$ coated $LiCoPO_4$ with improved battery performance. *J. Alloys Compd.* **2010,** *497*, 321–324.

[113] Rabanal, M. E.; Gutierrez, M. C.; Garcia-Alvarado, F.; Gonzalo, E. C.; Arroyo-de Dompablo, M. E., Improved electrode characteristics of olivine-$LiCoPO_4$ processed by high energy milling. *J. Power Sources* **2006,** *160*, 523–528.

[114] Jensen, T. R.; Norby, P.; Stein, P. C.; Bell, A. M. T., Preparation, structure determination and thermal transformation of a new lithium zinc phosphate, δ_1-$LiZnPO_4$. *J. Solid State Chem.* **1995,** *117*, 39–47.

[115] Hibberd, A. M.; Doan, H. Q.; Glass, E. N.; de Groot, F. M. F.; Hill, C. L.; Cuk, T., Co Polyoxometalates and a Co_3O_4 Thin Film Investigated by L-Edge X-ray Absorption Spectroscopy. *J. Phys. Chem. C* **2015,** *119*, 4173–4179.

[116] Strobridge, F. C.; Clement, R. J.; Leskes, M.; Middlemiss, D. S.; Borkiewicz, O. J.; Wiaderek, K. M.; Chapman, K. W.; Chupas, P. J.; Grey, C. P., Identifying the Structure of the Intermediate, $Li_{2/3}CoPO_4$, Formed during Electrochemical Cycling of $LiCoPO_4$. *Chem. Mater.* **2014,** *26*, 6193–6205.

[117] Hu, Z.; Wu, H.; Haverkort, M. W.; Hsieh, H. H.; Lin, H. J.; Lorenz, T.; Baier, J.; Reichl, A.; Bonn, I.; Felser, C.; Tanaka, A.; Chen, C. T.; Tjeng, L. H., Different Look at the Spin State of Co^{3+} Ions in a CoO_5 Pyramidal Coordination. *Phys. Rev. Lett.* **2004,** *92*, 207402/1–207402/4.

[118] Kim, D.-H.; Kim, J., Synthesis of $LiFePO_4$ Nanoparticles in Polyol Medium and Their Electrochemical Properties. *Electrochem. Solid-State Lett.* **2006,** *9*, A439–A442.

[119] Devaraju, M. K.; Honma, I., Hydrothermal and solvothermal process towards development of Li*M*PO_4 (*M* = Fe, Mn) nanomaterials for lithium-ion batteries. *Adv. Energy Mater.* **2012,** *2*, 284–297.

[120] Rivera, J. P., The linear magnetoelectric effect in $LiCoPO_4$ revisited. *Ferroelectrics* **1994,** *161*, 147–164.

[121] Kharchenko, N. F.; Kharchenko, Y. N.; Szymczak, R.; Baran, M.; Schmid, H., Weak ferromagnetism in the antiferromagnetic magnetoelectric crystal $LiCoPO_4$. *Low Temp. Phys.* **2001,** *27*, 895–898.

[122] Szewczyk, A.; Gutowska, M. U.; Wieckowski, J.; Wisniewski, A.; Puzniak, R.; Diduszko, R.; Kharchenko, Y.; Kharchenko, M. F.; Schmid, H., Phase transitions in single-crystalline magnetoelectric $LiCoPO_4$. *Phys. Rev. B: Condens. Matter Mater. Phys.* **2011,** *84*, 104419/1–104419/8.

[123] Tian, W.; Li, J.; Lynn, J. W.; Zarestky, J. L.; Vaknin, D., Spin dynamics in the magnetoelectric effect compound $LiCoPO_4$. *Phys. Rev. B: Condens. Matter Mater. Phys.* **2008,** *78*, 184429/1–184429/6.

[124] Kharchenko, N. F.; Khrustalev, V. M.; Savitskii, V. N., Magnetic field induced spin reorientation in the strongly anisotropic antiferromagnetic crystal $LiCoPO_4$. *Low Temp. Phys.* **2010,** *36*, 558–564.

[125] Jensen, M. H.; Bak, P., Mean-field theory of the three-dimensional anisotropic Ising model as a four-dimensional mapping. *Phys. Rev. B: Condens. Matter Mater. Phys.* **1983,** *27*, 6853–6868.

[126] Assat, G.; Manthiram, A., Rapid Microwave-Assisted Solvothermal Synthesis of Non-Olivine *Cmcm* Polymorphs of Li*M*PO_4 (*M* = Mn, Fe, Co, and Ni) at Low Temperature and Pressure. *Inorg. Chem.* **2015,** *54*, 10015–10022.

[127] Maspoch, D.; Ruiz-Molina, D.; Veciana, J., Old materials with new tricks: multifunctional open-framework materials. *Chem. Soc. Rev.* **2007,** *36*, 770–818.

[128] Hogarth, C. A.; Jamel Basha, M., Electrical conduction in cobalt-phosphate glasses. *J. Phys. D* **1983,** *16*, 869–878.

[129] Anderson, M. T.; Phillips, M. L. F.; Sinclair, M. B.; Stucky, G. D., Synthesis of Transition-Metal-Doped $KTiOPO_4$ and Lanthanide-Doped $RbTiOAsO_4$ Isomorphs That Absorb Visible Light. *Chem. Mater.* **1996,** *8*, 248–256.

[130] Millet, J.-M. M., FePO catalysts for the selective oxidative dehydrogenation of isobutyric acid into methacrylic acid. *Catal. Rev. - Sci. Eng.* **1998,** *40*, 1–38.

[131] Amine, K.; Yasuda, H.; Yamachi, M., Olivine $LiCoPO_4$ as 4.8 V electrode material for lithium batteries. *Electrochem. Solid-State Lett.* **2000,** *3*, 178–179.

[132] Masquelier, C.; Croguennec, L., Polyanionic (phosphates, silicates, sulfates) frameworks as electrode materials for rechargeable Li (or Na) batteries. *Chem. Rev.* **2013,** *113*, 6552–6591.

Chapter 5
Conclusions and Outlook

In light of global warming and the depletion of fossil fuel resources, the transition to electric mobility will significantly contribute to a more sustainable future. In order to meet the requirements for electric vehicles, the energy density of lithium-ion batteries (LIB) needs to be increased. Since cathodes remain the main determinant of the energy density of LIBs, novel cathode materials with higher voltage and capacity and thus, higher energy densities are needed. With a theoretical capacity of 167 $mAh \cdot g^{-1}$ and high energy density of 802 $Wh \cdot kg^{-1}$, a promising candidate is the high-voltage (4.8 V *vs.* Li/Li^+) cathode material *Pnma*-$LiCoPO_4$, which belongs to the phospho-olivine group $LiMPO_4$ (*M* = Fe, Mn, Co, Ni). Successful deployment of *Pnma*-$LiCoPO_4$, however, has proven challenging due to the limited stability of conventional electrolytes at high voltage, and its intrinsically low and one-dimensional ([010] direction) electrical and ionic conductivities. As a result, it generally exhibits poor electrochemical performance that is characterized by low capacities, rate capabilities, and cycle life.

(I) Microwave-Assisted Solvothermal (MWST) Synthesis and Optimization of Pnma-$LiCoPO_4$ as a High-Voltage Cathode Material for Lithium-Ion Batteries

A promising approach to improve the performance is controlling the size, shape, and orientation of the particles, which can be realized by kinetically controlled syntheses such as solvothermal methods. Among these, the microwave-assisted (MWST) approach is the most appealing since it is the only technique reported to deliver high-capacity *Pnma*-$LiCoPO_4$ in a simple one-step process. The technique being very new, the small number of previous studies lacked a thorough understanding of the influence of the synthesis parameters on the material properties, and the systematic exploration of particle size and morphology tuning options.

As a starting point of this work, a simple and fast (30 min), low-temperature (250 °C) microwave-assisted solvothermal (MWST) process using a binary water/ethylene glycol (EG) solvent mixture was developed. In a single step without any post-processing such as high-temperature annealing and carbon coating, the process delivered high-performance submicron *Pnma*-$LiCoPO_4$ particles with a hexagonal platelet morphology and reduced dimensions along the [010] direction of the Li diffusion paths. Due to these favorable crystal orientations that facilitate Li migration, the platelets demonstrated a discharge capacity of

137 mAh·g^{-1} (0.1 C; energy density: 658 Wh·kg^{-1}) and remarkable capacity retention of 68% after 100 cycles. This is a significant increase in performance over both a benchmark material prepared by conventional solid-state synthesis and previous results for the MWST technique.

Being very flexible with respect to the synthesis design, the novel MWST process could be modified to systematically implement particle size and morphology control. The size of the platelets could be reduced from the micron- to the nano-range by increasing the concentration of the EG co-solvent (0–80 vol%) and thus, the viscosity of the H_2O/EG solvent blend. The morphology, on the other hand, could be tuned to a variety of square, rhombic, and hexagonal platelet shapes by using polyols such as di-, tri-, tetra-, and polyethylene glycol (DEG, TEG, TTEG, PEG) as well as benzyl alcohol (BA) instead of EG as co-solvent. Regardless of the amount and type of co-solvent, the MWST process exclusively delivered platelet-shaped particles with reduced [010] dimensions. This suggests that all co-solvents act as soft templates, and promote the formation of anisotropic crystal shapes by selectively adsorbing on (010) faces and thus inhibiting the growth along [010]. As a result, all materials delivered above-average to cutting-edge electrochemical performances, with the performance being mainly correlated with particle thickness along [010], *i.e.* the length of the Li diffusion paths. In contrast to the common assumption that overall particle size reduction helps to improve the performance, it was revealed that due to increased side reactions of nano-sized materials with the electrolyte at high voltage, a medium submicron particle size range is the optimum for *Pnma*-$LiCoPO_4$. The best performance in this work was reached for micron-sized square platelets produced from a TEG co-solvent with a capacity of 141 mAh·g^{-1} at 0.1 C, corresponding to a gravimetric energy density of 677 Wh·kg^{-1}. This is the best performance achieved for an unprocessed, uncoated *Pnma*-$LiCoPO_4$ material to date, which is even comparable to the best values reported for C-coated, post-annealed *Pnma*-$LiCoPO_4$/C.

In brief, the studies demonstrated an efficient, simple, and fast MWST approach for the production of *Pnma*-$LiCoPO_4$ materials with tailored properties and cutting-edge electrochemical performances. Since no carbon coating is needed, high energy densities can be achieved, which are particularly desirable for electric mobility applications. By simple modification, the process further allows to precisely control the particle size and morphology of the product. The systematic investigations helped to understand the relationships between the synthesis parameters, material microstructure and electrochemical properties from a fundamental point of view, which had not been touched upon in previous studies but will be crucial for further developments. Since the one-step process does not involve any post-processing of the material (*e.g.* annealing, coating, ball milling), it comes along with significant energy and cost savings compared to other synthesis methods. It is potentially also applicable for the cost-effective, large-scale industrial production of commercial cathode materials such as $LiFePO_4$, spinels, and NMCs (lithium nickel manganese cobalt oxide, *e.g.* $LiNi_{1/3}Mn_{1/3}Co_{1/3}O_2$). Based on the

current findings, it is likely that the performance can be additionally improved by further modification of the synthesis design, for example by using alternative solvent systems (*e.g.* ethanol, ionic liquids), additives (*e.g.* glucose, cellulose), surfactants (*e.g.* cetyltrimethylammonium bromide (CTAB), sodium dodecylbenzenesulfonate (SDBS)), and templates (*e.g.* Pluronic P-123, *i.e.* PEG–PPG–PEG block-copolymer). Another promising approach will be cation doping, which has been reported to increase the conductivity of the material yet so far predominantly been realized for solid-state methods as opposed to wet-chemical syntheses. Nevertheless, future improvements on the path towards practical applicability of the high-voltage cathode material *Pnma*-$LiCoPO_4$ will not only depend on the synthetic optimization of the active material, but also on the development of novel electrolyte systems suitable for high voltage (*e.g.*, using ionic liquids or additives).

(II) Metastable Lithium Cobalt Phosphates: $Co_{11}Li[(OH)_5O][(PO_3OH)(PO_4)_5]$, $Pna2_1$-type $LiCoPO_4$, Cmcm-$LiCoPO_4$, and Cmcm-$Li_{0.5-\delta}CoPO_4$

The investigations on metastable lithium cobalt phosphates first focused on the *Pna*2_1- and *Cmcm*-$LiCoPO_4$ polymorphs, which have been less studied than the thermodynamically stable olivine-type *Pnma*-$LiCoPO_4$. In specific, this work addressed key aspects such as the synthetic accessibility, structural characterization, and thermal behavior of these phases that remained unclear or untouched in prior studies. While previous methods were rather complex, simple low-temperature synthesis routes (conventional/microwave-assisted solvothermal, polyol) were presented. In contrast to the literature, a fundamental revision of the crystal structures revealed that both phases are non-stoichiometric (revised formulas: *Cmcm*-$Li_{1-\gamma}CoPO_4$ and *Pna*2_1-$Li_{0.95(1)}Co_{1.03(1)}PO_4$) and feature disordered or defective cation substructures. In this context, the lack of suitable Li migration paths could be identified as an intrinsic cause of their poor electrochemical performances. Moreover, X-ray absorption spectra of both phases, confirming the local symmetries of the Co^{2+} ions (*Pna*2_1: T_d, *Cmcm*: O_h), and the magnetic properties of *Cmcm*-$LiCoPO_4$, indicating a long-range antiferromagnetic order below T_N = 11 K and a metamagnetic (spin-flip) transition, were reported for the first time. The comprehensive investigation of the thermal properties of both metastable $LiCoPO_4$ phases using *ex* and *in situ* methods finally gave clarity about their thermal stabilities and allowed to critically review the thermodynamic relation of all three $LiCoPO_4$ polymorphs. At elevated temperatures around 500–600 °C, both *Pna*2_1- and *Cmcm*-$LiCoPO_4$ transform to *Pnma*-$LiCoPO_4$, which in turn above 700–800 °C converts to *Pna*2_1-$LiCoPO_4$. This high-temperature *Pnma*–*Pna*2_1 transformation was also observed upon heating of *Pnma*-$LiCoPO_4$ produced by the MWST process. After cooling, *Pnma*-$LiCoPO_4$ was obtained in all cases. It could thus be derived that while *Pnma*-$LiCoPO_4$ is the most stable polymorph at room temperature, surprisingly, it is metastable

in the high-temperature regime. *Pna*2$_1$-$LiCoPO_4$, hitherto considered a low-temperature modification only, on the other hand represents the stable high-temperature $LiCoPO_4$ phase.

The employment of kinetically controlled synthesis routes further provided access to two new metastable, mixed-valent cobalt(II,III) phosphate phases. The trigonal framework $Co_{11}Li[(OH)_5O][(PO_3OH)(PO_4)_5]$, which is isostructural with the phosphate minerals satterlyite and holtedahlite, was identified as a key competing phase in the hydrothermal synthesis of *Pnma*-$LiCoPO_4$ that coexists with the olivine over a wide pH range (pH = 5.5–7.5). In fact, the discovery of this phase also enabled unambiguous assignment of impurities found in *Pnma*-$LiCoPO_4$ materials of other studies. Interestingly, it was not possible to produce a Li-free phase, suggesting that the framework is stabilized by Li substitution. On the other hand, the first Li-deficient derivative of *Cmcm*-$LiCoPO_4$ with the composition $Li_{0.5-\delta}CoPO_4$ could be prepared by a direct polyol route. Contrary common top-down (electro)chemical delithiation techniques described for Li-poor olivine phases, this is the first report of a simple bottom-up approach towards such a material. X-ray absorption spectra revealed that both phases feature heterovalent Co(II,III) ions. While the occurrence of Co^{3+} in $Co_{11}Li[(OH)_5O][(PO_3OH)(PO_4)_5]$ could be explained by Li substitution, it is the direct cause of the Li deficit in *Cmcm*-$Li_{0.5-\delta}CoPO_4$. As a result, both phases exhibit interesting magnetic and thermal properties. $Co_{11}Li[(OH)_5O][(PO_3OH)(PO_4)_5]$ demonstrated a paramagnetic to antiferromagnetic transition at T = 25 K and a spin-glass-like behavior with a blocking temperature of T ~9 K, and $Li_{0.5-\delta}CoPO_4$ exhibits long-range antiferromagnetic order below T_N = 10.5 K. Because of the intrinsic instability of Co^{3+}, both phases exhibit complex, multi-step thermal decomposition mechanisms with oxygen (and water) release that are driven by redox reactions.

In conclusion, the comprehensive investigations on the metastable *Pna*2$_1$- and *Cmcm*-$LiCoPO_4$ polymorphs impressively illustrate that despite the recent interest in these materials, important and interesting aspects had not been recognized. New insights lead to a reconsideration of prior work, and thus helped to gain a more fundamental understanding of the structure–property relationships of these phases. With regard to their use as high-voltage cathode materials or more likely, as precursors for *Pnma*-$LiCoPO_4$, further experiments will have to be directed at tackling the off-stoichiometry and defect formation. Kinetically controlled synthesis methods not only proved to be a powerful tool to modify known materials but also to stabilize novel, metastable phases. The interesting thermal and magnetic properties of the newly discovered, mixed-valent Co(II,III) phases $Co_{11}Li[(OH)_5O][(PO_3OH)(PO_4)_5]$ and *Cmcm*-$Li_{0.5-\delta}CoPO_4$ will certainly trigger subsequent studies. Important points will be to elucidate the charge ordering of the $Li^+/Co^{2+}/Co^{3+}$ ions in the structures, compositional tuning of the materials, and the exploration of their potential as oxygen-evolving catalysts.

Chapter 6
Publications and Manuscripts

6.1 Complete List of Publications

Publications and Manuscripts

[1] **Ludwig, J.;** Marino, C.; Haering, D.; Stinner, C.; Nordlund, D.; Doeff, M. M.; Gasteiger, H. A.; Nilges, T., Facile, ethylene glycol-promoted microwave-assisted solvothermal synthesis of high-performance $LiCoPO_4$ as a high-voltage cathode material for lithium-ion batteries. *RSC Adv.* **2016,** *6*, 82984–82994.
DOI: 10.1039/c6ra19767a

[2] **Ludwig, J.;** Haering, D.; Doeff, M. M.; Nilges, T., Particle size-controllable microwave-assisted solvothermal synthesis of the high-voltage cathode material $LiCoPO_4$ using water/ethylene glycol solvent blends. *Solid State Sci.* **2017,** *65,* 100–109.
DOI: 10.1016/j.solidstatesciences.2017.01.009

[3] **Ludwig, J.;** Marino, C.; Haering, D.; Stinner, C.; Gasteiger, H. A.; Nilges, T., Morphology-controlled microwave-assisted solvothermal synthesis of high-performance $LiCoPO_4$ as a high-voltage cathode material for Li-ion batteries. *J. Power Sources* **2017,** *342*, 214–223.
DOI: 10.1016/j.jpowsour.2016.12.059

[4] **Ludwig, J.;** Geprägs, S.; Nordlund, D.; Doeff, M. M.; Nilges, T., $Co_{11}Li[(OH)_5O][(PO_3OH)(PO_4)_5]$, a Lithium-Stabilized, Mixed-Valent Cobalt(II,III) Hydroxide Phosphate Framework. **2017,** *submitted.*

[5] **Ludwig, J.;** Nordlund, D.; Doeff, M. M.; Nilges, T., Synthesis and characterization of metastable, 20 nm-sized *Pna*2_1-$LiCoPO_4$ nanospheres. *J. Solid State Chem.* **2017,** *248,* 9–17.
DOI: 10.1016/j.jssc.2017.01.015

[6] Alarcón-Suesca, C.;† **Ludwig, J.;†** Hlukhyy, V.; Stinner, C.; Nilges, T., In Situ Studies and Magnetic Properties of the *Cmcm* Polymorph of $LiCoPO_4$ with a Hierarchical Dumbbell-Like Morphology Synthesized by Easy Single-Step Polyol Synthesis. *Inorganics* **2016,** *4*, 35. († equally contributing co-authors)
DOI: 10.3390/inorganics4040035

[7] **Ludwig, J.;** Alarcón-Suesca, C.; Geprägs, S.; Nordlund, D.; Doeff, M. M.; Puente Orench, I.; Nilges, T., Direct synthesis and characterization of mixed-valent $Li_{0.5-\delta}CoPO_4$, a Li-deficient derivative of the *Cmcm* polymorph of $LiCoPO_4$. *RSC Adv.* **2017,** *7,* 28069–28081.
DOI: 10.1039/c7ra04043a

Conference Contributions

[1] **Ludwig, J.;** Alarcón-Suesca, C.; Marino, C.; Haering, D.; Stinner, C. ; Gasteiger, H. A.; Nilges, T., Microwave-assisted solvothermal synthesis of high-performance $LiCoPO_4$ using various solvents. Poster, *MRS Fall Meeting & Exhibit*, Boston, USA **2015.** Symposium PP: Materials, Interfaces and Solid Electrolytes for High Energy Density Rechargeable Batteries.

[2] Alarcón-Suesca, C.; **Ludwig, J.;** Stinner, C.; Gasteiger, H. A.; Nilges, T., Synthesis of the high-pressure polymorph of $LiCoPO_4$ using a simple, single step polyol route. Poster, *MRS Fall Meeting & Exhibit*, Boston, USA **2015.** Symposium PP: Materials, Interfaces and Solid Electrolytes for High Energy Density Rechargeable Batteries.

6.2 Facile, Ethylene Glycol-Promoted Microwave-Assisted Solvothermal Synthesis of High-Performance $LiCoPO_4$ as a High-Voltage Cathode Material for Lithium-Ion Batteries

Jennifer Ludwig,[a] Cyril Marino,[b‡] Dominik Haering,[b] Christoph Stinner,[c] Dennis Nordlund,[d] Marca M. Doeff,[e] Hubert A. Gasteiger,[b] and Tom Nilges[a*]

[a] Technical University of Munich, Department of Chemistry, Synthesis and Characterization of Innovative Materials, Lichtenbergstr. 4, 85747 Garching, Germany

[b] Technical University of Munich, Department of Chemistry, Technical Electrochemistry, Lichtenbergstr. 4, 85747 Garching, Germany

[c] BMW AG, Petuelring 130, 80788 München, Germany

[d] Stanford Synchrotron Radiation Lightsource, SLAC National Accelerator Laboratory, 2575 Sand Hill Rd, Menlo Park, CA, 94025, USA

[e] Lawrence Berkeley National Laboratory, Environmental Energy Technologies Division, 1 Cyclotron Rd, Berkeley, CA, 94720, USA

‡ Present address: Paul Scherrer Institute, Electrochemical Energy Storage, 5232 Villigen PSI, Switzerland

RSC Adv. **2016,** *6*, 82984–82994.
DOI: 10.1039/c6ra19767a

RSC Advances

PAPER

View Article Online
View Journal | View Issue

Cite this: *RSC Adv.*, 2016, **6**, 82984

Facile, ethylene glycol-promoted microwave-assisted solvothermal synthesis of high-performance $LiCoPO_4$ as a high-voltage cathode material for lithium-ion batteries†

Jennifer Ludwig,[a] Cyril Marino,‡[b] Dominik Haering,[b] Christoph Stinner,[c] Dennis Nordlund,[d] Marca M. Doeff,[e] Hubert A. Gasteiger[b] and Tom Nilges*[a]

Received 4th August 2016
Accepted 23rd August 2016

DOI: 10.1039/c6ra19767a

www.rsc.org/advances

Olivine-type $LiCoPO_4$ is considered a promising high-voltage cathode material for next-generation lithium-ion batteries. However, preparing high-performance $LiCoPO_4$ by a simple approach has been challenging. Herein, we present a facile and rapid (30 min) one-step microwave-assisted solvothermal synthesis route using a 1 : 1 (v/v) water/ethylene glycol (EG) binary solvent mixture and a temperature of 250 °C. The technique delivers high-performance $LiCoPO_4$ nanoparticles without additional post-annealing or carbon coating steps. The as-prepared powder consists of single crystalline $LiCoPO_4$ and features a hexagonal platelet-like morphology with dimensions of 700–800 nm × 400–600 nm × 100–220 nm. Selected area electron diffraction (SAED) experiments reveal that the platelets show the smallest dimension along [010], which is the direction of the lithium diffusion pathways in the olivine crystal structure. Furthermore, the results indicate that the EG co-solvent plays an important role in tailoring the particle size, morphology, and crystal orientation of the material. Co L-edge soft X-ray absorption spectroscopy (XAS) of $LiCoPO_4$ are presented for the first time and confirm that the material only consists of Co^{2+}. Benefiting from the unique morphology, which facilitates Li-ion conduction, electrochemical measurements deliver an initial discharge capacity of 137 mA h g^{-1} at 0.1 C, a remarkably stable capacity retention of 68% after 100 cycles at 0.5 C, and a specific energy density of 658 W h kg^{-1} based on its capacity and voltage, which is the best performance of $LiCoPO_4$ obtained from microwave-assisted solvothermal synthesis to date.

Introduction

The scientific community predicts that effects on climate change due to the burning of fossil fuels will be significant within the next twenty years. Global warming is an important challenge for mankind and solutions need to be found. The development of electric vehicles powered by fuel cells or lithium-ion batteries can play a key role in reducing CO_2 gas emissions, which is considered to be a main cause of the greenhouse effect. For the past 30 years, scientists have been looking for the perfect combination of electrolyte, an anode material, and a cathode material for building the best Li-ion battery with high energy density, good cycling and acceptable safety characteristics. Since their introduction by Padhi *et al.*,[1] olivine-structured lithium transition-metal orthophosphates with the formula $LiMPO_4$ (M = Fe, Mn, Co, Ni) have attracted considerable attention as cathode materials for lithium-ion batteries due to their high specific capacities and thermal stability.[2–7] Within the phospho-olivine family, $LiFePO_4$ (LFP) has widely been investigated and is a fully developed material that is nowadays available for commercial applications.[8] The

[a]*Technical University of Munich, Department of Chemistry, Synthesis and Characterization of Innovative Materials, Lichtenbergstr. 4, 85747 Garching, Germany. E-mail: tom.nilges@lrz.tu-muenchen.de*

[b]*Technical University of Munich, Department of Chemistry, Technical Electrochemistry, Lichtenbergstr. 4, 85747 Garching, Germany*

[c]*BMW AG, Petuelring 130, 80788 München, Germany*

[d]*Stanford Synchrotron Radiation Lightsource, SLAC National Accelerator Laboratory, 2575 Sand Hill Rd, Menlo Park, CA, 94025, USA*

[e]*Lawrence Berkeley National Laboratory, Environmental Energy Technologies Division, 1 Cyclotron Rd, Berkeley, CA, 94720, USA*

† Electronic supplementary information (ESI) available: State of the art of HT, ST, SCF, MWHT, and MWST synthesis of LCP; PXRD measurement of an empty capillary; PXRD of $Li_2SO_4 \cdot H_2O$ obtained from the reaction solution; Rietveld fit of LCP-MW-w; cell parameters, atomic coordinates, thermal displacement parameters, and selected interatomic distances obtained from all Rietveld refinements; TGA/DSC and temperature-dependent *in situ* PXRD data of LCP-MW; FTIR and Raman spectra; additional SEM images; additional electrochemical measurements of LCP-MW materials with varying amounts of Li_2SO_4 and of electrodes with high loading. CCDC 1500138–1500140. For ESI and crystallographic data in CIF or other electronic format see DOI: 10.1039/c6ra19767a

‡ Present address: Paul Scherrer Institute, Electrochemical Energy Storage, 5232 Villigen PSI, Switzerland.

use of iron-based cathodes for lithium-ion batteries has several advantages, including abundant and cheap raw materials, high thermal stability and relatively low toxicity.[5,9,10] Moreover, with a theoretical capacity of 170 mA h g^{-1}, LFP operates at a voltage of 3.45 V *versus* Li/Li^+,[1] which is compatible with commercially available electrolytes used in current lithium-ion battery technology. However, in recent years the scientific community has increasingly been focusing on the isostructural $LiMnPO_4$ (LMP), $LiCoPO_4$ (LCP) and $LiNiPO_4$ (LNP) type phospho-olivines due to the possibility of increasing the specific energy with these compounds.[7,11–13] The Mn^{2+}/Mn^{3+}, Co^{2+}/Co^{3+}, and Ni^{2+}/Ni^{3+} redox couples have been shown to operate at much higher voltages of 4.1 V,[1] 4.8 V,[14] and 5.1 V,[15] respectively, and are thus paving the way for next generation high-energy-density olivine-based Li-ion batteries.[3]

The redox potential of LNP is too high for use with common electrolytes and the electrochemical activation of the compound remains a challenge.[3,15,16] The high-voltage cathode material LCP with a lower operating voltage features the highest energy of 802 W h kg^{-1} within the olivine family and a theoretical capacity of 167 mA h g^{-1}.[14] However, the low electronic[17,18] and ionic[19] conductivities of LCP as well as the limited oxidative stability of standard electrolytes[20,21] remain major obstacles to successful utilization. All these disadvantages result in an unsatisfactory electrochemical performance of LCP, including low practical capacities, poor rate performance, and short cycle life.[3]

Tremendous efforts have been made in recent years to mitigate these limitations. In particular, chemical doping,[17,22,23] carbon coating,[24,25] and particle size reduction[26–29] have been extensively used to improve the electrochemical activity of LCP. The importance of nanostructural engineering to the electrochemical performance has also been examined for other types of cathode materials, such as spinel-type transition metal oxides.[30] Theoretical studies suggest that despite the fact that Li^+ ions are located in one-dimensional channels along [010] and [001] in the olivine crystal structure (Fig. 1b and c), lithium diffusion is only promoted along the [010] pathway (Fig. 1b).[22,31,32] Thus, reducing the particle dimensions along the *b* direction can result in faster Li-ion diffusion and improved electrochemical properties as shown recently by Rui and co-workers.[29] After 50 cycles at 0.2 C, a discharge capacity of 136 mA h g^{-1} for $LiCoPO_4$/C nanosheets was reported compared to only 54 mA h g^{-1} for bulk particles, which is the best performance reported for carbon-coated LCP to date. Nanosheets exhibit a large surface-to-volume ratio that allows a more effective electrode–electrolyte contact area. Nevertheless, the multi-step preparation, which requires solid-state synthesis of a $NH_4CoPO_4 \cdot H_2O$ precursor, followed by a liquid-phase exfoliation and a high-pressure high-temperature lithiation by a supercritical fluid (SFC) process in ethanol precludes easy scale-up and industrial applicability. A simpler and faster synthetic approach towards high-performance LCP with small dimensions along [010] and the option for large-scale production is yet to be fully developed, to the best of our knowledge.

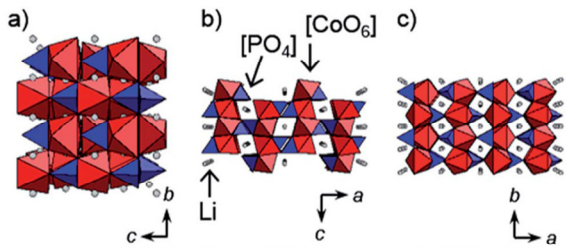

Fig. 1 Projections of the crystal structures of olivine-type $LiCoPO_4$ (space group *Pnma*) along the three crystallographic axes: (a) [100], (b) [010], and (c) [001]. $[CoO_6]$ octahedra are drawn in red, $[PO_4]$ tetrahedra in blue, and Li ions in grey.

With regard to the synthetic method, conventional solid-state reactions have been the dominant technique.[33–35] The process, however, generally requires high temperatures and an additional ball milling step, making this approach unfeasible for potential industrial applications. Hydrothermal (HT)[36–40] or solvothermal (ST)[29,41–44] approaches are of greater interest due to the facile and easily scalable process, mild reaction conditions, and the possibility of preparing nanomaterials with controllable and uniform particle sizes, shapes and crystal orientations.[45] From a practical point of view, however, the conventional HT or ST approach can be limited by slow reaction kinetics and non-uniform reaction conditions due to thermal gradients that are caused by the convective heating. This results in heterogeneous particle size distributions and morphologies and hence, inferior electrochemical performance.[46] Only a few reports of conventional hydro- or solvothermal products indicate a direct formation of crystalline LCP materials without high-temperature annealing in a single step.[36–38,44] Furthermore, the materials often show antisite defects and disordered structures and therefore require additional thermal treatments at very high temperatures (~800–900 °C), or additional carbon coating steps to obtain reasonable electrochemical performances.[37,39,42] The microwave-assisted (MW) approach, which is quite new in the research field of LCP,[47–51] is particularly appealing because of the direct dielectric heating by the use of microwave irradiation, which allows short reaction times of only several minutes and more uniform reaction conditions due to lower thermal gradients in the reaction vessel.[46,48,52] The method allows uniform nucleation and produces highly crystalline materials with homogeneous particle size distributions and morphologies.[48,52] The electrochemical performance of LCP obtained by MWST synthesis without post-calcination steps is comparable to ST materials that have been annealed at high temperature. A detailed overview of the state of the art in the hydrothermal and solvothermal synthesis of LCP, including supercritical fluid and microwave-assisted techniques is given in Table S1 (ESI).†

Very recently, combining an organic solvent and water in a mixed system has become popular in the solvothermal synthesis of $LiCoPO_4$ nanocrystals.[42,44,53] The solvent blend is supposed to be beneficial for effectively regulating the morphology and crystal orientation due to the soft template effect of the organic solvent,[42,54] and also promotes the complete dissolution of the reagents with the help of the water

View Article Online
RSC Advances Paper

component. However, the effect of crystallographic orientation and particle morphology on the electrochemical performance of LCP has barely been touched upon.[29,41,48,55]

Herein, a novel, simple and fast microwave-assisted solvothermal (MWST) approach towards high-performance LCP at moderate temperatures (250 °C) using ethylene glycol (EG) as a co-solvent is presented for the first time. Unlike other procedures, the innovative technique does not require any post-calcination steps or the use of carbon coatings to improve the electrochemical performance. The as-prepared LCP material is fully characterized by X-ray powder diffraction, elemental analysis, scanning and transmission electron microscopy, Brunauer–Emmett–Teller surface area measurements, infrared and Raman spectroscopy, thermogravimetric measurements as well as electrochemical measurements. Based on these measurements, the relationship between the synthesis, morphology, and electrochemical properties of the material is elucidated. Moreover, Co L-edge soft X-ray absorption spectroscopic data on LCP are presented for the first time.

Experimental

Microwave-assisted solvothermal synthesis

A microwave-assisted solvothermal (MWST) process based on a previous report for $LiMn_{0.7}Fe_{0.3}PO_4$ (ref. 56) was modified with regard to power of the microwave irradiation, synthesis temperature and pH in order to obtain pure olivine-type LCP. 22.5 mmol of $LiOH \cdot H_2O$ (Bernd Kraft, ≥99.0%), 7.5 mmol of $CoSO_4 \cdot 7H_2O$ (Chempur, 99%), and 7.5 mmol of H_3PO_4 (AppliChem, Ph. Eur., 85 wt% solution) were dissolved in 30 mL of a 1 : 1 (v/v) mixed solvent of deionized water (high-purity water type I, Millipore, 18.2 MΩ cm) and ethylene glycol (VWR AnalaR NORMAPUR, 99.9%). The molar ratio of Li : Co : P was 3 : 1 : 1. Note that the two additional moles of Li are necessary to bind the sulfate in the reaction (*cf.* Scheme 1a) and that a 1 : 1 : 1 ratio did not result in the formation of the olivine phase. 0.050 *g* ascorbic acid (Alfa Aesar, 99+%) was added as a reducing agent to prevent oxidation of Co^{2+} to Co^{3+} in the aqueous solution as well as a buffer to keep a suitable pH value to promote the crystallization of single-phase LCP. The resulting blue-violet mixture (pH 5.5, *cf.* graphical abstract) was stirred vigorously and then transferred into a 75 mL PTFE/TFM vessel (HTV-75, MLS GmbH). The solvothermal reaction was performed at 250 °C for 30 min under continuous stirring using an Ethos One microwave system (MLS GmbH, MR-8 HT high-temperature rotor). The internal temperature was maintained by adjusting the power of the microwave irradiation with the automatic T660 temperature control unit (maximum power: 600 W). After natural cooling, the pH of the solution was 5.0. The violet precipitate was collected by filtration, washed five times with 50 mL distilled water and 50 mL absolute ethanol (VWR AnalaR NORMAPUR, 99.95%) followed by drying in air at 150 °C for 12 h. The sample is denoted LCP-MW.

Structural, physical and chemical characterization

X-ray powder diffraction (XRD) patterns were collected on a Stoe STADI P diffractometer using Mo $K_{\alpha 1}$ radiation (Ge(111) monochromator, $\lambda = 0.70930$ Å) and a Dectris MYTHEN DCS 1K silicon solid-state detector. The samples were ground in a mortar and then sealed in 0.5 mm borosilicate glass capillaries (Hilgenberg, glass type no. 50, wall thickness: 0.01 mm). The data were measured in a 2θ range of 3–70° (PSD step: 0.015°; time/step: 25 s, 3 ranges, measurement time: 12 h). Silicon powder ($a = 5.43088$ Å) was used as an external standard. Rietveld fitting of the powder diffraction data was performed using the Jana2006 software package.[57] The background profile was fitted using a Chebyshev function with 35 coefficients. Peak asymmetry at small scattering angles was corrected by the axial divergence model described by Finger *et al.*[58] using empirically determined starting values for the parameters. Moreover, an absorption correction was applied (estimated packing fraction ~0.6).[59] General atomic positions as well as the isotropic thermal displacement parameters of Co, P, and O were refined. The thermal factors of Li, however, were kept fixed because they cannot be determined by X-ray powder diffraction (*cf.* low atomic scattering factor). Finally, the Berar's correction was applied to obtain more realistic values for the estimated standard uncertainties.[60]

Elemental analysis was performed using atomic absorption spectroscopy (Varian AA280FS sequential device) for the Li, and photometry (Shimadzu UV-160 device) for the Co and P contents, respectively. C, H, N, and S contents were analyzed by combustion analysis using a Hekatech Euro EA CHNSO instrument.

The morphologies of the particles were observed using a high-resolution scanning electron microscope (HR-SEM, JEOL JSM-7500F). The gentle beam (GB) mode (accelerating voltage: 1 kV) was used to reduce charging effects of the material. Energy-dispersive X-ray spectroscopy (EDS) was performed at an acceleration voltage of 15 kV and a probe current of 20 μA using a Noran system S1X (Thermo Electron Corporation, model 6714A01SUS-SN) probe attached to the scanning electron microscope.

Transmission electron microscopy (TEM, JEOL JEM-2010, 160 kV, LaB_6 cathode) and selected area electron diffraction (SAED) were performed using specimens dispersed in ethanol and then dropped onto 200 mesh carbon film. Magnetite was used as a reference material for the SAED studies, and the patterns were analyzed using the CrystalMaker software.[61]

The specific surface area of the powder was measured by N_2 adsorption using the Brunauer–Emmett–Teller (BET) method, where eleven points were measured. The measurement was performed on a Quantachrome Autosorb iQ instrument after degassing at 423 K for 12 h.

Soft X-ray absorption spectroscopy (XAS) measurements on the as-prepared $LiCoPO_4$ material were conducted at beamline 8-2 of Stanford Synchrotron Radiation Lightsource (SSRL) using a 1100 mm^{-1} spherical grating monochromator operated with 40 μm entrance and exit slits, providing ~2.0×10^{10} ph s^{-1} at 0.4 eV resolution in a 1 mm^2 beam spot. Two scans of the Co $L_{2,3}$-edge $\mu(E)$ spectra were acquired under ultrahigh vacuum (10^{-9} Torr) at room temperature in the Auger electron yield (AEY), total electron yield (TEY), and fluorescence yield (FY) modes, respectively.[62] After normalizing the spectra to the beam current, the background contribution was subtracted. The

energies scale was corrected using the values reported by Hibberd and co-workers.[63] Additionally, CoO and Co_3O_4 powders were used as reference samples for Co^{2+} and Co^{3+}. For better comparison and plotting, the intensity of all spectra was further normalized to a maximum intensity of 1.

Electrochemical measurements

The electrochemical performance was evaluated using Swagelok cells. The working electrodes were composed of 80 wt% of the as-prepared LCP powder, 10 wt% carbon (Super C65, Timcal), and 10 wt% polyvinylidene difluoride binder (PVDF, Kynar HSV 900, Arkema). LCP, Super C65 and PVDF were mixed with *N*-methyl-2-pyrrolidone (NMP, Sigma Aldrich) and then homogenized at 2000 rpm for 20 min using a planetary centrifugal vacuum mixer (Thinky). The electrode slurry was spread on aluminum foil (15 μm, MTI corporation) and dried at 55 °C for 3–4 h. Electrodes with diameters of 10 mm and typical loadings of 4–5 mg cm^{-2} were punched out, and pressed two times at 250 MPa for 1 min (KBr press, PerkinElmer). Afterwards, the electrodes were additionally dried for 2 h at 120 °C under vacuum in a Büchi B-585 glass oven. The test cells were assembled in an Ar-filled glove box (MBraun; <0.1 ppm H_2O, <0.1 ppm O_2). The cells were cycled between 3.5 V and 5.2 V in two different procedures: (a) three cycles each at 0.1 C, 0.2 C, 0.5 C, 1 C, and 2 C followed by 20 cycles at 0.5 C; (b) 2 initial cycles at 0.067 C followed by 100 cycles at 0.5 C rate. In both procedures, a constant voltage step at 5.2 V was added with a current limited to 0.05 C. Specific capacities were calculated on the basis of the weight of the as-prepared LCP powders in the electrodes (neglecting the weight of the lithium sulfate side phase, as it accounts for only <5 wt%; *cf.* Table 1); C-rates were calculated based on a theoretical specific capacity of 167 mA h g_{LCP}^{-1}.

Results and discussion

X-ray powder diffraction

Fig. 2 shows the Rietveld fit of the X-ray powder diffraction (XRD) data of the as-prepared sample LCP-MW obtained from the simple microwave-assisted solvothermal (MWST) process. All diffraction peaks can be fitted to the orthorhombic olivine structure model (space group *Pnma*, ICSD database no. 247497 (ref. 64)) with good reliability factors (Table S2, ESI†). The refined lattice parameters are $a = 10.1930(7)$ Å, $b = 5.9188(4)$ Å, and $c - 4.6959(3)$ Å. The refined atomic coordinates, thermal displacements parameters, and selected interatomic distances are given in Tables S3 and S4 (ESI†).

No crystalline impurity phases which are generally reported for products from solution-based routes (*e.g.* the poorly soluble Li_3PO_4)[65] are observed within the detection limit of the method. In contrast to conventional hydro- or solvothermal products, which are prone to antisite defects and disordered structures[37] and therefore often have to undergo thermal treatments at very high temperatures (~800–900 °C) to improve electrochemical activity,[39,42] the microwave technique delivers a highly crystalline $LiCoPO_4$ material within a short reaction time of only 30 min and without any post heat treatment. This is evidenced by the appearance of sharp and narrow diffraction peaks. Moreover, the refinement of the occupancies of the Li and Co sites neither suggested a Li-deficient nor a disordered structure. The Co and Li sites were kept fully occupied and an ordered structure was assumed for the refinement. The refined cell volume of 283.31(3) $Å^3$ is smaller than reported values for hydro-[37,66] and solvothermal[44,48] LCP, indicating fewer antisite defects. The observed background profile can mostly be attributed to the borosilicate capillary used (reference measurement of an empty capillary see Fig. S1, ESI†). However, the presence of amorphous impurity phases cannot be ruled out by the PXRD experiment.

Elemental analysis

The chemical composition of the XRD-pure sample LCP-MW was determined by CHNS, photometry, and AAS analyses. The results are given in Table 1. The measured absolute contents (in wt%) show a deficiency both in Co and P compared to the expected values. This can be attributed to the higher-than-expected amounts of Li and S, which result in a relative decrease of the former elements. The calculated Li : Co : P molar ratio is found to be 1.14(5) : 1.00(1) : 1.00(2). The deviation of the Li value from the theoretical value of 1 : 1 : 1 might be due to some amorphous or trace impurities. CHNS analysis shows that the sample does not contain detectable amounts of carbon that might add to the electrochemical performance, which is confirmed by the absence of any carbon D or G bands in the Raman spectrum (Fig. S7c and d, ESI†). This indicates that the washing step is efficient for the removal of the EG co-solvent or the ascorbic acid additive and their decomposition products. Also no H (*e.g.* from residual water) can be found, but significant amounts of sulfur are detected. Taking the slight excess of about 0.3 wt% Li into account, the S content of 1.5 ± 0.3 wt% can be related to a mixture of $Li_2SO_4 \cdot H_2O$ and Li_2SO_4 impurities. The Li_2SO_4 originates from $Li_2SO_4 \cdot H_2O$, a side product of the synthesis (Scheme 1a, see also Fig. S2, ESI†). The dehydrated form is obtained because of the drying step of the process at 150 °C (dehydration at 130 °C, Scheme 1b).[67,68]

Because Li_2SO_4 has hygroscopic properties,[69] we assume that a mixture of the anhydrous and monohydrate form is present, although the detected hydrogen amounts in the sample were negligible and the IR spectrum does neither show absorption

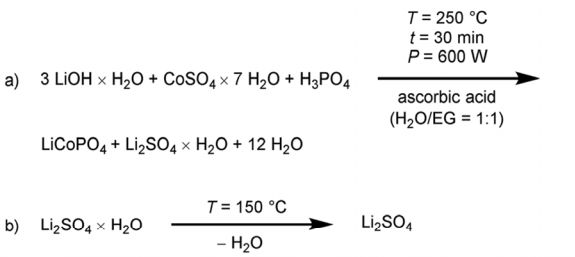

Scheme 1 (a) Reaction scheme of the microwave-assisted solvothermal synthesis, (b) dehydration of the lithium sulfate monohydrate side phase.

Table 1 Elemental analysis (CHNS, AAS, photometry) of the LCP samples LCP-MW and LCP-MW-w in comparison with the theoretical values[a,b,c]

Element	Theor.	(a) LCP-MW	(b) LCP-MW-w
S (wt%)	0	1.5(3)	1.6(3)
Li (wt%)	4.3	4.6(2)	4.5(2)
Co (wt%)	36.6	34.3(5)	34.1(5)
P (wt%)	19.3	18.0(5)	17.7(5)
n(Li) : n(P)	1	1.14(5)	1.13(5)
n(Co) : n(P)	1	1.00(1)	1.01(1)
Li_2SO_4 (wt%)	0	5(1)	6(1)
$LiCoPO_4$ (wt%)	100	94(2)	92(2)

[a] LCP-MW: as-synthesized, LCP-MW-w: after additional extensive washing with ice water to remove solution-accessible Li_2SO_4. [b] The molar ratios are calculated from the experimental results (in wt%) of the CHNS, AAS, and photometric analyses (standard deviations are given in parenthesis). [c] The values for C, H, and N were too low to be measured in all samples (= 0).

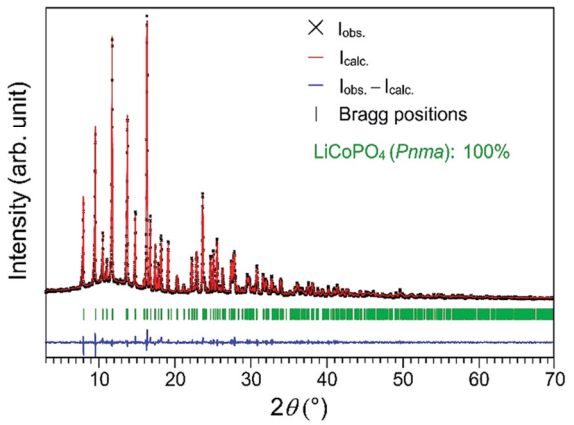

Fig. 2 Rietveld fit of the X-ray powder diffraction data of the as-prepared LCP-MW material obtained from the microwave-assisted solvothermal synthesis.

bands of water nor of lithium sulfate (*cf.* Fig. S7a and b, ESI†). In addition, the estimated 5 ± 1 wt% of lithium sulfate are amorphous and thus not detectable by PXRD in the LCP-MW powder. TGA/DSC and temperature-dependent *in situ* PXRD experiments indicate that the amorphous impurity can be crystallized upon heating (Fig. S4–S6, ESI†).

As equal molar amounts of $LiCoPO_4$ and $Li_2SO_4 \cdot H_2O$ are formed during the reaction according to Scheme 1a, we assume that the biggest portion of the water-soluble lithium sulfate is dissolved in the water component of the binary solvent and further removed by the washing step. In order to completely remove the impurity, we tried to wash the sample extensively with 1 L of ice water, as the solubility of lithium sulfate in water increases with decreasing temperature.[70,71] The S content of the corresponding sample LCP-MW-w remains similar (Table 1), indicating that the impurity cannot be removed by additional washing. We therefore infer that the remaining minor impurity might form inclusions inside the particles rather than being located on their surface, and that >94 ± 2 wt% of the sample are the pure LCP phase. Further experiments with alternative sulfate-free starting materials (*e.g.* chlorides, nitrates) indicate that the Li_2SO_4 impurity cannot be avoided because impure materials or inferior electrochemical performances were observed. Therefore, we consider the sulfate route as the most feasible one, as it also allows the removal of a major portion of the water-soluble side product by washing.

Scanning electron microscopy

Fig. 3 shows the SEM images of the as-prepared sample LCP-MW. The material consists of uniform, well-crystallized and dispersed hexagonal platelets with dimensions of about 400–600 nm × 700–800 nm and thicknesses ranging from about 100 nm to 250 nm. The observed particle size is consistent with the value of the specific surface area (BET) of 5.5 ± 0.5 $m^2 g^{-1}$. Furthermore, no agglomerates of particles are observed (Fig. 3a and c), indicating that the EG co-solvent helps to prevent agglomeration of the particles without requiring an additional dispersant. Moreover, small pores of 10–20 nm (*cf.* zoomed SEM image, Fig. S9,

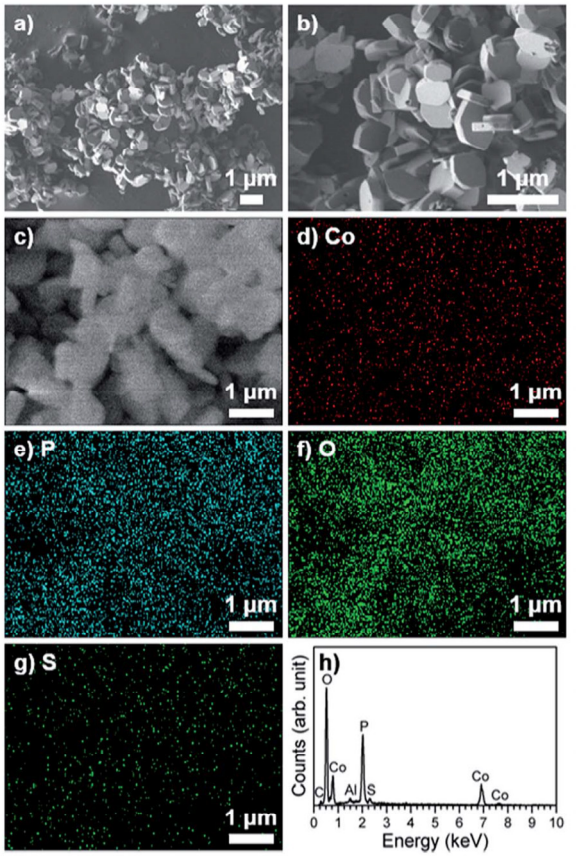

Fig. 3 (a and b) SEM images of LCP-MW recorded at 1 keV (GB mode), (c–g) SEM image and EDS maps for Co, P, O, and S obtained at 15 keV to optimize EDS signals, and (h) representative EDS spectrum. The C and Al signals derive from the carbon tape and the aluminum holder used for the measurement.

ESI,† and TEM images, Fig. 4) in diameter are found on the surface of the particles that can most probably be attributed to the formation mechanism. According to Scheme 1a, $LiCoPO_4$ and Li_2SO_4 are formed in parallel during the reaction and seem to initially form perfect hexagonal composite particles. The highly water soluble Li_2SO_4 is dissolved in solvent as well as in the washing water used after the synthesis. Hence, pores appear on the surface of the particles where the Li_2SO_4 impurity phase was formerly located. The pores, which might be interconnected, destabilize the particles, with some particles showing cracks probably due to mechanical stress during the synthesis produced by stirring and the washing step. As a result, the particle size distribution is slightly inhomogeneous. This explanation was confirmed by further experiments with different amounts of washing water, whereby the extent of fragmentation increased with increasing volumes of water. For instance, the SEM images of the extensively washed sample LCP-MW-w (Fig. S10†) show significantly more fragmented platelets. Therefore, the sample LCP-MW was chosen for further characterization.

Energy dispersive spectroscopic (EDS) analysis under SEM (15 kV; Fig. 3h) delivers a composition of 33 ± 2 wt% Co, 17.4 ± 0.5 wt% P, 48 ± 1 wt% O, and 1.4 ± 0.2 wt% S. These values are in good agreement with the results of the elemental analysis (Table 1). The corresponding Co : P molar ratio is 0.99(6). The elemental distribution was examined using EDS mapping (Fig. 3d–g; please note that the overview image of Fig. 3c suffers from charging effects due to the high accelerating voltage of 15 kV). As expected, all the elements are homogeneously distributed within the sample. It is affirmed that the sulfur shows a regular distribution within the particles, suggesting that the amorphous Li_2SO_4 phase is most likely forming inclusions in the hexagonal platelets and therefore cannot be removed by intensive washing as observed from elemental analysis for the sample LCP-MW-w (Table 1).

The results clearly indicate that the mixed solvent of H_2O and EG significantly influences the morphology of the obtained LCP powder. Whereas the water component promotes the complete dissolution of the reagents and therefore helps to form a more homogeneous reaction mixture, the EG component plays an important role in controlling the particle size and shape. The size-regulating effect can be attributed to the increased viscosity of the binary solvent in comparison to pure water. Hence, the ion diffusion rate is slowed down and therefore prevents the growth of large particles. As a result, comparably narrow particle size distributions are obtained. In addition, the EG components inhibits agglomeration of the primary particles. The polar EG molecules are reported to form long hydrogen-bonding chains, that can trap the cations present in the reaction mixture due to its chelating ability and therefore help the olivine to nucleate and grow into particles with specific morphologies.[54,72] Therefore, EG not only acts as a solvent, but also shows properties of a soft template.[54,73]

Transmission electron microscopy

In order to get a better understanding of the structure and morphology of the material and therefore the formation mechanism and crystal growth, transmission electron microscopy (TEM) in combination with selected area electron diffraction (SAED) experiments was performed. The low resolution image (Fig. 4a) is in agreement with the results of the SEM studies and shows well-defined hexagonal platelets with dimensions of 700–800 nm × 400–600 nm × 100–220 nm. In the SAED study, patterns of several individual crystals were taken to verify that all crystals exhibit identical orientations. In addition to that, diffraction patterns of perpendicular crystal faces were recorded. This approach allows reliable information about the crystal growth orientation as well as the thickness of the platelets. The frontal view of a regular hexagonal platelet (Fig. 4b and c) shows that the particles are highly ordered single crystals that are grown in the *ac* plane, the *c* axis being oriented diagonally along the longest dimension. The pore structure or inclusions within the particles, can be seen in the irregular transmission of the platelet that possesses an unflawed contour. The side view (Fig. 4d–f) reveals that the platelets show the smallest dimension along [010], which is the direction of the lithium diffusion pathways in the olivine crystal structure. Hence, the platelet-like morphology with shorter lithium diffusion pathways enhances the Li diffusion properties. The Fig. 4g–i show a highly fragmented platelet, the hexagonal shape of which is still indicated. Here, the pores have formed an interconnected system, which may be a result of the removal of the water soluble Li_2SO_4 impurity that is formed within the particles. Despite the defective morphology, the single-crystalline particle still shows high crystallinity.

In agreement with previous reports,[73,74] the TEM studies indicate that the EG co-solvent specifically adsorbs on the

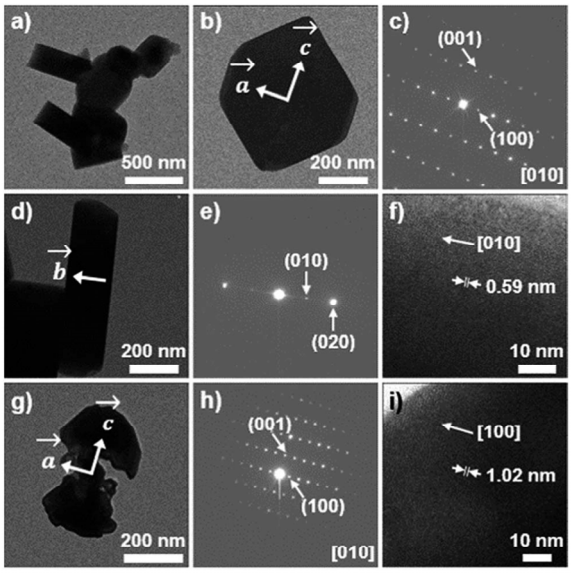

Fig. 4 TEM images, corresponding SAED (selected area electron diffraction) patterns, and HRTEM images of LCP-MW: (a) overview image, (b and c) frontal view of a hexagonal platelet, (d–f) side view of a platelet, and (g–i) particle with a porous structure as a result of the removal of the water soluble Li_2SO_4 impurity.

View Article Online
RSC Advances Paper

(010) crystal face, therefore dramatically decreasing its surface energy. As a result, the growth along [010] is inhibited. In addition, the nanoplatelets grow preferentially along the [001] direction of the (010) plane due to the higher surface energy of the (001) than that of the (100) plane,[72] promoting the formation of unique hexagonal platelets with reduced dimensions along *b*. A more thorough formation mechanism cannot be derived at this point and will have to be further examined. However, the observation of hexagonal shapes with exposed (010) faces is consistent with calculations of the surface energies of LFP by Fisher and Islam,[75] who suggested the favorable growth morphology under hydrothermal conditions to be an hexagonal prism terminated by (010), (100), and (101) faces.

Soft X-ray spectroscopy

The normalized soft XAS Co $L_{2,3}$-edge spectra for the sample LCP-MW are shown along with two reference compounds (CoO and Co_3O_4 powder) in Fig. 5. Whereas K-edge spectra have been obtained in various studies,[76–78] to the best of our knowledge, this is the first time the Co L-edge data of $LiCoPO_4$ are presented. The XAS was collected in the Auger electron yield (AEY), total electron yield (TEY), and fluorescence yield (FY) modes, corresponding to probing depths of 1–2 nm, 2–5 nm and 50 nm, respectively.[62] The absorption peaks of the $L_{2,3}$-edge XAS are sensitive to the oxidation state, spin state, and the chemical environment in the crystal.[79]

We note that the main peaks in the spectra line up with the CoO reference spectra. A comparison with Co $L_{2,3}$-edge spectra reported for other Co(II) and Co(III) compounds in various symmetries, as well as the lowest energy peak at 776.4 eV give strong evidence for octahedral Co^{2+} as expected, showing a similar crystal field strength as in CoO.[63,79–81] The well-defined multiplet structure indicates a highly ordered crystal structure and a low degree of covalence in the CoO_6 octahedra,[63] which is consistent with the sharp peaks observed in the PXRD (Fig. 2) and in general agreement with earlier findings for LFP through Fe $L_{2,3}$-edge spectra.[82,83] The oxidation state is consistently +II for all detection modes and hence, indicates that the sample is homogeneous from the top surfaces to volumes deep in the bulk. The absence of a shoulder at the characteristic peak energy for Co^{3+} (779.4 eV) shows that there are no significant amounts of Co^{3+} impurities, also not on the surface, which might reduce the electrochemical activity. The small amount of the ascorbic acid reductant used in the synthesis therefore seems to be sufficient to prevent oxidation of Co^{2+} in solution. The EG solvent can also act as a weak reducing agent.[73]

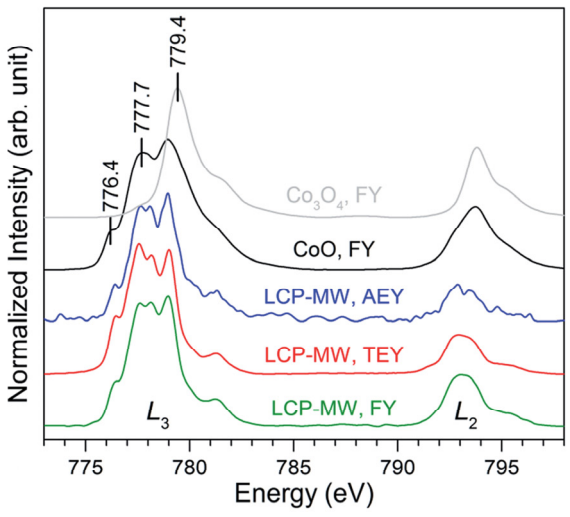

Fig. 5 Normalized soft XAS Co $L_{2,3}$-edge spectra of LCP-MW recorded in the AEY (blue), TEY (red), and FY (green) modes in comparison to the FY modes of the reference compounds CoO (black) and Co_3O_4 (grey). The energies corresponding to O_h Co^{2+} (776.4 eV), Co^{2+} (777.7 eV), and Co^{3+} (779.4 eV) are indicated.

Electrochemical characterization

The electrochemical performances of the LCP synthesized by MWST synthesis (LCP-MW) are presented in Fig. 6. In order to gauge the obtained data, a comparison with a LCP material with spherical nanoparticles (diameter ~50–60 nm, BET area ~25 $m^2\ g^{-1}$) obtained by solid-state synthesis (LCP-SS) as described in our previous work[84] was added. The rate capability of the LCP-MW electrode was investigated (Fig. 6a). The corresponding galvanostatic curves of the 3rd cycle at 0.1 C and 0.5 C are shown in Fig. 6b. During the 1st cycle at 0.1 C, LCP-MW reaches an initial discharge capacity of 137 mA h g^{-1} whereas only 125 mA h g^{-1} is obtained for LCP-SS. The charge curve (Fig. 6b) is characterized by two potential plateaus at 4.75 V and 4.86 V for LCP-MW. For LCP-SS, the plateaus are slightly at higher potential values with 4.8 V and 4.9 V. Both potential windows are in agreement with earlier reports for LCP.[85,86] The discharge curves also present two potential plateaus which are shifted to lower potential for LCP-SS. The corresponding gravimetric energy densities of the materials based on the mean values of the potential of ~4.8 V and ~4.75 V are 658 W h kg^{-1} for LCP-MW and 594 W h kg^{-1} for LCP-SS, respectively. For the first six cycles corresponding to rates of 0.1 C and 0.2 C, the difference in specific capacity between the samples was similar, with values of 120 mA h g^{-1} and 108 mA h g^{-1} found for LCP-MW and LCP-SS at the end of cycle 6, respectively. At these low C rates, the coulombic efficiency, which improved upon cycling, was higher for LCP-MW than for LCP-SS, at 96.7% and 94.5%, respectively, after six cycles. The low coulombic efficiency values in the first cycle are caused by the decomposition of the electrolyte during the charge at high potential.[87] The better efficiency obtained for LCP-MW can be explained by its lower surface area (~6 $m^2\ g^{-1}$ compared to ~25 $m^2\ g^{-1}$ (ref. 84) for LCP-SS), as parasitic currents from electrolyte oxidation at high potentials would be estimated to be proportional to the BET surface area. The about fourfold lower BET surface area of LCP-MW should thus lead to the observed substantially improved coulombic efficiency. From 0.5 C to 2 C, the difference in specific capacity between LCP-MW and LCP-SS increased. At the end of the cycling procedure at a 2 C rate, a specific capacity

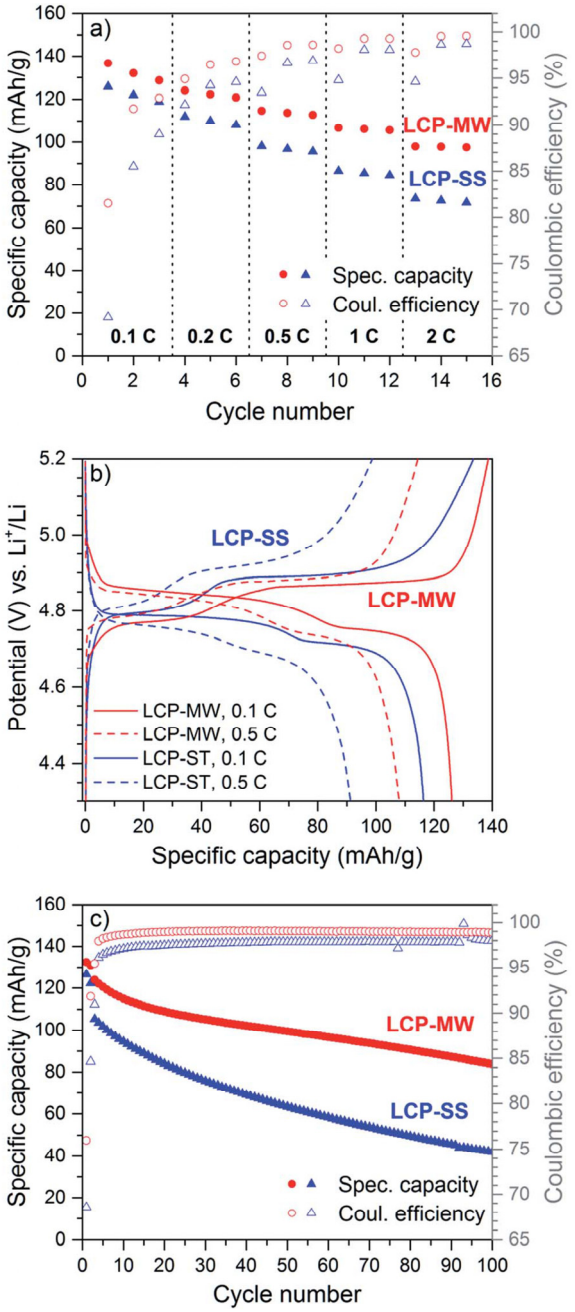

Fig. 6 (a) Specific capacity *vs.* C rate and coulombic efficiency obtained in each cycle for LCP-MW in comparison to LCP-SS, (b) galvanostatic curves for the 3rd cycle at 0.1 C and at 0.5 C, (c) comparison of the electrochemical stabilities of LCP-MW and LCP-SS at 0.5 C after the first two cycles at 0.067 C.

of 98 mA h g^{-1} was reached for LCP-MW, whereas 71 mA h g^{-1} was obtained for LCP-SS. LCP-MW is able to sustain higher currents than LCP-SS, probably due to its unique platelet-like shape with shorter lithium diffusion paths as discussed earlier. This hypothesis is also supported by the lower charge/discharge polarization of the LCP-MW compared to LCP-SS (Fig. 6b), despite of its fourfold lower BET area. Additionally, some tests at lower current (0.067 C) were done for LCP-SS but no improvement in the specific capacity was obtained.

The electrochemical stability of both LCP materials was investigated at 0.5 C rate after two formation cycles at 0.067 C (Fig. 6c). The very low coulombic efficiencies in the first two cycles are due to the very low C rates, at which parasitic currents from electrolyte oxidation more strongly affect the coulombic efficiency. For the first cycle at 0.5 C, the specific capacity reaches 123 mA h g^{-1} for LCP-MW and only 106 mA h g^{-1} for LCP-SS. After 100 cycles, a specific capacity of 84 mA h g^{-1} is obtained for LCP-MW whereas only half of this value is found for LCP-SS. A coulombic efficiency of 98.9% is quickly reached for LCP-MW, which is higher than the one of LCP-SS. The better electrochemical behavior in the 1st cycle combined with a higher coulombic efficiency are probably responsible of the higher stability observed for LCP-MW.

In order to elucidate whether the amorphous lithium sulfate impurity (~5 wt%) affects the electrochemical properties, samples with similar particle size and shape but varying amounts of Li_2SO_4 were synthesized by the MWST process. As all samples show comparable electrochemical performance within standard deviations (Fig. S11 and S12, ESI†), the results indicate that the impurity does not influence the electrochemical behavior, and that it is electrochemically inactive.

To sum up, we have demonstrated that the LCP produced by MWST synthesis outperforms a compound synthesized by a conventional solid-state reaction, which is the standard method for synthesizing $LiCoPO_4$ in the bulk scale.

Comparison with the literature

Research in the field of hydro- and solvothermal synthesis of LCP has been ongoing since 2005.[36] The electrochemical properties of materials synthesized by the hydrothermal technique were first reported in 2009 and a capacity of only 15 mA h g^{-1} reached.[38] An improvement of the performance has been exclusively realized by additional post-calcinations at temperatures as high as 900 °C and/or coating with conductive carbon to give $LiCoPO_4$/C, the only exception being the MWST synthesis (Fig. 7). Hence, it is important to note that the capacities of uncoated $LiCoPO_4$, which reflects the intrinsic capacity of the material, and $LiCoPO_4$/C are comparable to only a limited degree. In fact, by introducing carbon coatings, the energy density is decreased. Hence, the carbon content has to be kept a relatively low levels, even if there is an apparent improvement in rate capability.[88] In addition, also the cell design, charging protocol (C rate, potential window, CV step, *etc.*) as well as post-synthetic treatments influence the electrochemical performance.

In comparison to the state of the art in conventional as well as microwave-assisted hydro- and solvothermal synthesis of pure LCP-type materials, reflecting the intrinsic material properties, our material LCP-MW in fact delivers the best

View Article Online
RSC Advances Paper

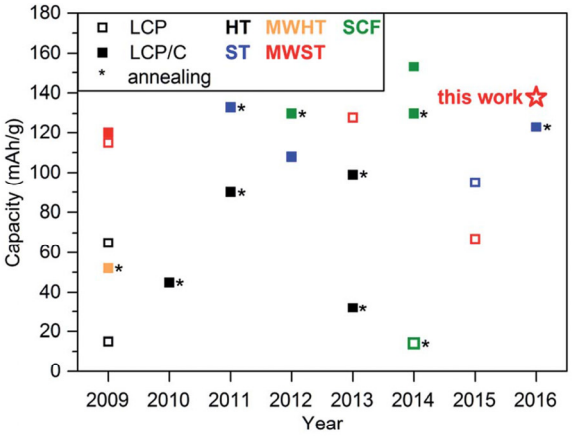

Fig. 7 Comparison of the initial discharge capacities obtained for $LiCoPO_4$ and carbon-coated $LiCoPO_4$/C materials synthesized *via* hydrothermal (HT),[38–40,42] solvothermal (ST),[42–44,53,90] microwave-assisted hydro- (MWHT)[47] and solvothermal (MWST),[48,50,51] and supercritical fluid (SCF)[28,29,55,78] procedures as reported between 2009 and 2016. Asterisks mark materials that underwent additional post-heat treatments at high temperatures. The star represents the capacity reached in this work using a MWST approach, which is the best reported for an untreated LCP-type material to date.

electrochemical performance to date. In comparison to materials that underwent further treatments such as post-annealing or conductive coatings, our as-prepared material also delivers a state-of-the-art performance, which is remarkable. Moreover, our material was tested in a regular setup using standard electrolytes (EC/DMC) and medium loadings (4–5 mg cm^{-2}). Additional tests with high loadings up to 12 mg cm^{-2} were done and present reasonable specific capacity (Fig. S13, ESI†). Further improvements can be expected upon optimization of the electrolyte (*e.g.*, using ionic liquids or additives such as trimethylboroxine[84,89]) and the electrode formulation.[13] In addition, the microwave method allows a considerable reduction of the production costs as it requires only moderate temperatures and produces highly crystalline materials in one step without further treatment. Once suitable electrolytes for high-voltage cathodes are available, materials like LCP might be sustainable candidates for future Li-ion battery applications.

Conclusions

High-performance $LiCoPO_4$ particles with uniform hexagonal platelet-like morphologies have been synthesized by a facile and rapid microwave-assisted solvothermal approach at moderate temperatures (250 °C) using a water/ethylene glycol (EG) (1 : 1) mixed solvent. Unlike conventional hydrothermal or solvothermal techniques, the process does not involve any additional post heat treatment or carbon coating. PXRD patterns indicate the direct formation of highly crystalline, olivine-type $LiCoPO_4$ from the microwave synthesis. SEM and TEM/SAED studies reveal that the hexagonal platelets feature dimensions of 800 nm × 300–400 nm in the (010) plane and a thickness of 200–300 nm along [010]. The results indicate that EG plays an important role in the formation of the $LiCoPO_4$ nanoplatelets by effectively regulating the particle size and morphology as well as tuning the crystal orientation.

The nanoplatelets exhibit excellent electrochemical properties, including a high initial discharge capacity of 137 mA h g^{-1} at 0.1 C, 114 mA h g^{-1} at 0.5 C, and 97 mA h g^{-1} at 2 C, high coulombic efficiency, and excellent rate capability. Moreover, the material displays a remarkable stable capacity retention of 68% after 100 cycles at 0.5 C. These attractive electrochemical features can be attributed to the unique submicron scale platelet-like morphology with shortened lithium-ion diffusion pathways along the *b* direction of the crystal structure. Never-theless, a possible effect of the amorphous, sulfur-containing Li_2SO_4/$Li_2SO_4 \cdot H_2O$ impurity (<5 wt%), which was identified by means of elemental analysis, EDS, and temperature-dependent X-ray powder diffraction experiments, on the electrochemical features will have to be addressed in further experiments.

To conclude, the present work provides an efficient and simple approach towards high-performance olivine-type cathode materials with designed morphology. Moreover, it clarifies the relationship between the synthesis method, material microstructure and electrochemical properties, which has hitherto barely been touched upon in the literature but is crucial for developments in the field. The short reaction time as well as the fact that the one-step microwave process does not involve any post-treatments (*e.g.* annealing, coating, ball milling) offer the potential to lower the manufacturing costs of cathode materials with significant energy savings in comparison to other synthesis techniques.

Abbreviations

AEY	Auger electron yield
AAS	Atomic absorption spectroscopy
DMC	Dimethyl carbonate
EC	Ethylene carbonate
EDS	Energy-dispersive X-ray spectroscopy
EG	Ethylene glycol
FY	Fluorescence yield
GB	Gentle beam
HT	Hydrothermal
LCP	Lithium cobalt phosphate
LFP	Lithium iron phosphate
LMP	Lithium manganese phosphate
LNP	Lithium nickel phosphate
MWST	Microwave-assisted solvothermal
NMP	*N*-Methyl-2-pyrrolidone
PTFE	Poly(tetrafluoroethylene)
PVDF	Polyvinylidene difluoride
PXRD	Powder X-ray diffraction
SAED	Selected area electron diffraction
SFC	Supercritical fluid
SEM	Scanning electron microscope
SS	Solid-state
ST	Solvothermal

TEM	Transmission electron microscopy
TEY	Total electron yield
XAS	X-ray absorption spectroscopy

Acknowledgements

The authors would like to thank the BMW AG, the state of Bavaria, and the TUM for financial support and funding. The soft XAS experiments were carried out at the Stanford Synchrotron Radiation Lightsource, a Directorate of SLAC National Accelerator Laboratory and an Office of Science User Facility operated for the US Department of Energy Office of Science by Stanford University (contract no. DE-AC02-76SF00515). Furthermore, we thank Prof. J. Mink for Raman, K. Rodewald for SEM, and M. Hanzlik for TEM measurements. We also thank U. Ammari of the microanalytical laboratory of the TUM for elemental analyses. The help of Y. Li with the temperature-dependent PXRD measurements is gratefully acknowledged. J. Ludwig is further grateful to the Fonds der Chemischen Industrie for her fellowship.

References

1 A. K. Padhi, K. S. Nanjundaswamy and J. B. Goodenough, *J. Electrochem. Soc.*, 1997, **144**, 1188–1194.
2 J. M. Tarascon and M. Armand, *Nature*, 2001, **414**, 359–367.
3 S. Okada, S. Sawa, M. Egashira, J. Yamaki, M. Tabuchi, H. Kageyama, T. Konishi and A. Yoshino, *J. Power Sources*, 2001, **97–98**, 430–432.
4 M. Piana, M. Arrabito, S. Bodoardo, A. D'Epifanio, D. Satolli, F. Croce and B. Scrosati, *Ionics*, 2002, **8**, 17–26.
5 S.-Y. Chung, J. T. Bloking and Y.-M. Chiang, *Nat. Mater.*, 2002, **1**, 123–128.
6 B. L. Ellis, K. T. Lee and L. F. Nazar, *Chem. Mater.*, 2010, **22**, 691–714.
7 K. Zaghib, A. Guerfi, P. Hovington, A. Vijh, M. Trudeau, A. Mauger, J. B. Goodenough and C. M. Julien, *J. Power Sources*, 2013, **232**, 357–369.
8 W.-J. Zhang, *J. Power Sources*, 2011, **196**, 2962–2970.
9 B. Kang and G. Ceder, *Nature*, 2009, **458**, 190–193.
10 Y. Wang, P. He and H. Zhou, *Energy Environ. Sci.*, 2011, **4**, 805–817.
11 A. Yamada, M. Hosoya, S.-C. Chung, Y. Kudo, K. Hinokuma, K.-Y. Liu and Y. Nishi, *J. Power Sources*, 2003, **119–121**, 232–238.
12 C. M. Julien and A. Mauger, *Ionics*, 2013, **19**, 951–988.
13 M. Hu, X. Pang and Z. Zhou, *J. Power Sources*, 2013, **237**, 229–242.
14 K. Amine, H. Yasuda and M. Yamachi, *Electrochem. Solid-State Lett.*, 2000, **3**, 178–179.
15 J. Wolfenstine and J. Allen, *J. Power Sources*, 2005, **142**, 389–390.
16 L. Dimesso, C. Spanheimer and W. Jaegermann, *Solid State Sci.*, 2012, **14**, 1372–1377.
17 J. Wolfenstine, *J. Power Sources*, 2006, **158**, 1431–1435.
18 J. L. Allen, T. Thompson, J. Sakamoto, C. R. Becker, T. R. Jow and J. Wolfenstine, *J. Power Sources*, 2014, **254**, 204–208.
19 M. Prabu, S. Selvasekarapandian, A. R. Kulkarni, S. Karthikeyan, G. Hirankumar and C. Sanjeeviraja, *Solid State Sci.*, 2011, **13**, 1714–1718.
20 K. Hayashi, Y. Nemoto, S.-I. Tobishima and J.-I. Yamaki, *Electrochim. Acta*, 1999, **44**, 2337–2344.
21 M. Egashira, H. Takahashi, S. Okada and J.-I. Yamaki, *J. Power Sources*, 2001, **92**, 267–271.
22 C. A. J. Fisher, P. V. M. Hart and M. S. Islam, *Chem. Mater.*, 2008, **20**, 5907–5915.
23 J. L. Allen, T. R. Jow and J. Wolfenstine, *J. Power Sources*, 2011, **196**, 8656–8661.
24 J. Wolfenstine, J. Read and J. L. Allen, *J. Power Sources*, 2007, **163**, 1070–1073.
25 P. R. Kumar, V. Madhusudhanrao, B. Nageswararao, M. Venkateswarlu and N. Satyanarayana, *J. Solid State Electrochem.*, 2016, **20**, 1855–1863.
26 J. Liu, T. E. Conry, X. Song, L. Yang, M. M. Doeff and T. J. Richardson, *J. Mater. Chem.*, 2011, **21**, 9984–9987.
27 S. Brutti, P. Reale, E. Piciollo, V. Gentili, P. G. Bruce, B. Scrosati and S. Panero, *Prepr. Symp. – Am. Chem. Soc., Div. Fuel Chem.*, 2012, **57**, 737–739.
28 M. K. Devaraju, D. Rangappa and I. Honma, *Electrochim. Acta*, 2012, **85**, 548–553.
29 X. Rui, X. Zhao, Z. Lu, H. Tan, D. Sim, H. H. Hng, R. Yazami, T. M. Lim and Q. Yan, *ACS Nano*, 2013, **7**, 5637–5646.
30 M.-S. Park, J. Kim, K. J. Kim, J.-W. Lee, J. H. Kim and Y. Yamauchi, *Phys. Chem. Chem. Phys.*, 2015, **17**, 30963–30977.
31 D. Morgan, A. Van der Ven and G. Ceder, *Electrochem. Solid-State Lett.*, 2003, **7**, A30–A32.
32 S.-I. Nishimura, G. Kobayashi, K. Ohoyama, R. Kanno, M. Yashima and A. Yamada, *Nat. Mater.*, 2008, **7**, 707–711.
33 N. N. Bramnik, K. G. Bramnik, T. Buhrmester, C. Baehtz, H. Ehrenberg and H. Fuess, *J. Solid State Electrochem.*, 2004, **8**, 558–564.
34 J. Wolfenstine, U. Lee, B. Poese and J. L. Allen, *J. Power Sources*, 2005, **144**, 226–230.
35 M. E. Rabanal, M. C. Gutierrez, F. Garcia-Alvarado, E. C. Gonzalo and M. E. Arroyo-de Dompablo, *J. Power Sources*, 2006, **160**, 523–528.
36 X. Huang, J. Ma, P. Wu, Y. Hu, J. Dai, Z. Zhu, H. Chen and H. Wang, *Mater. Lett.*, 2005, **59**, 578–582.
37 J. Chen, S. Wang and M. S. Whittingham, *J. Power Sources*, 2007, **174**, 442–448.
38 Y. Zhao, S. Wang, C. Zhao and D. Xia, *Rare Met.*, 2009, **28**, 117–121.
39 M. Kotobuki, Y. Mizuno, H. Munakata and K. Kanamura, *Phosphorus Res. Bull.*, 2010, **24**, 12–15.
40 M. Kotobuki, *Int. J. Energy Environ. Eng.*, 2013, **4**, 25–27.
41 J. Su, B.-Q. Wei, J.-P. Rong, W.-Y. Yin, Z.-X. Ye, X.-Q. Tian, L. Ren, M.-H. Cao and C.-W. Hu, *J. Solid State Chem.*, 2011, **184**, 2909–2919.
42 F. Wang, J. Yang, Y. Nuli and J. Wang, *J. Power Sources*, 2011, **196**, 4806–4810.
43 M. Li, *Ionics*, 2012, **18**, 507–512.

44 S. Brutti, J. Manzi, A. De Bonis, D. Di Lecce, F. Vitucci, A. Paolone, F. Trequattrini and S. Panero, *Mater. Lett.*, 2015, **145**, 324–327.
45 M. K. Devaraju and I. Honma, *Adv. Energy Mater.*, 2012, **2**, 284–297.
46 J. A. Gerbec, D. Magana, A. Washington and G. F. Strouse, *J. Am. Chem. Soc.*, 2005, **127**, 15791–15800.
47 A. V. Murugan, T. Muraliganth and A. Manthiram, *J. Electrochem. Soc.*, 2009, **156**, A79–A83.
48 A. V. Murugan, T. Muraliganth, P. J. Ferreira and A. Manthiram, *Inorg. Chem.*, 2009, **48**, 946–952.
49 C. Neef, C. Jaehne and R. Klingeler, *Lect. Notes Impedance Spectrosc.*, 2012, **3**, 91–93.
50 R. E. Rogers, G. M. Clarke, O. N. Matthew, M. J. Ganter, R. A. DiLeo, J. W. Staub, M. W. Forney and B. J. Landi, *J. Appl. Electrochem.*, 2013, **43**, 271–278.
51 K. J. Kreder, G. Assat and A. Manthiram, *Chem. Mater.*, 2015, **27**, 5543–5549.
52 I. Bilecka and M. Niederberger, *Nanoscale*, 2010, **2**, 1358–1374.
53 B. Wu, H. Xu, D. Mu, L. Shi, B. Jiang, L. Gai, L. Wang, Q. Liu, L. Ben and F. Wu, *J. Power Sources*, 2016, **304**, 181–188.
54 M. Wu, Z. H. Wang, L. X. Yuan, W. X. Zhang, X. L. Hu and Y. H. Huang, *Chin. Sci. Bull.*, 2012, **57**, 4170–4175.
55 Q. D. Truong, M. K. Devaraju, Y. Ganbe, T. Tomai and I. Honma, *Sci. Rep.*, 2014, **4**, 3975.
56 H. Liang and L. Zhang, *Russ. J. Electrochem.*, 2014, **50**, 297–300.
57 V. Petricek, M. Dusek and L. Palatinus, *Z. Kristallogr. - Cryst. Mater.*, 2014, **229**, 345–352.
58 L. W. Finger, D. E. Cox and A. P. Jephcoat, *J. Appl. Crystallogr.*, 1994, **27**, 892–900.
59 D. T. Cromer and D. A. Liberman, *Acta Crystallogr., Sect. A: Cryst. Phys., Diffr., Theor. Gen. Crystallogr.*, 1981, **A37**, 267–268.
60 J. F. Berar and P. Lelann, *J. Appl. Crystallogr.*, 1991, **24**, 1–5.
61 D. C. Palmer, *CrystalMaker 2.5.5*, CrystalMaker Software Ltd, Begbroke, Oxfordshire, England, 2012.
62 F. Lin, D. Nordlund, I. M. Markus, T.-C. Weng, H. L. Xin and M. M. Doeff, *Energy Environ. Sci.*, 2014, **7**, 3077–3085.
63 A. M. Hibberd, H. Q. Doan, E. N. Glass, F. M. F. de Groot, C. L. Hill and T. Cuk, *J. Phys. Chem. C*, 2015, **119**, 4173–4179.
64 V. Koleva, E. Zhecheva and R. Stoyanova, *Eur. J. Inorg. Chem.*, 2010, 4091–4099.
65 M. K. Devaraju, Q. D. Truong, H. Hyodo, T. Tomai and I. Honma, *Inorganics*, 2014, **2**, 233–247.
66 J. Chen, M. J. Vacchio, S. Wang, N. Chernova, P. Y. Zavalij and M. S. Whittingham, *Solid State Ionics*, 2008, **178**, 1676–1693.
67 H. Tanaka, *Thermochim. Acta*, 1982, **52**, 195–199.
68 F. Valdivieso, V. Bouineau, M. Pijolat and M. Soustelle, *Solid State Ionics*, 1997, **101–103**, 1299–1303.
69 R. Weintraub, A. Apelblat and A. Tamir, *Anal. Chim. Acta*, 1984, **166**, 325–327.
70 J. A. N. Friend, *J. Chem. Soc.*, 1929, 2330–2333.
71 W. F. Linke and A. Seidell, *Solubilities of In-organic and Metal Organic Compounds*, Am. Chem. Soc., 4th edn, 1966, vol. 2.
72 J. Song, L. Wang, G. Shao, M. Shi, Z. Ma, G. Wang, W. Song, S. Liu and C. Wang, *Phys. Chem. Chem. Phys.*, 2014, **16**, 7728–7733.
73 S. Kuppan, P. Balaya, M. V. Reddy, B. V. R. Chowdari and J. J. Vittal, *Energy Environ. Sci.*, 2010, **3**, 457–464.
74 X. Qin, J. Wang, J. Xie, F. Li, L. Wen and X. Wang, *Phys. Chem. Chem. Phys.*, 2012, **14**, 2669–2677.
75 C. A. J. Fisher and M. S. Islam, *J. Mater. Chem.*, 2008, **18**, 1209–1215.
76 M. Nakayama, S. Goto, Y. Uchimoto, M. Wakihara, Y. Kitajima, T. Miyanaga and I. Watanabe, *J. Phys. Chem. B*, 2005, **109**, 11197–11203.
77 J. L. Shui, Y. Yu, X. F. Yang and C. H. Chen, *Electrochem. Commun.*, 2006, **8**, 1087–1091.
78 M. Kaus, I. Issac, R. Heinzmann, S. Doyle, S. Mangold, H. Hahn, V. S. K. Chakravadhanula, C. Kuebel, H. Ehrenberg and S. Indris, *J. Phys. Chem. C*, 2014, **118**, 17279–17290.
79 F. M. F. de Groot, M. Abbate, J. van Elp, G. A. Sawatzky, Y. J. Ma, C. T. Chen and F. Sette, *J. Phys.: Condens. Matter*, 1993, **5**, 2277–2288.
80 M. M. van Schooneveld, R. Kurian, A. Juhin, K. Zhou, J. Schlappa, V. N. Strocov, T. Schmitt and F. M. F. de Groot, *J. Phys. Chem. C*, 2012, **116**, 15218–15230.
81 M. Ghiasi, M. U. Delgado-Jaime, A. Malekzadeh, R.-P. Wang, P. S. Miedema, M. Beye and F. M. F. de Groot, *J. Phys. Chem. C*, 2016, **120**, 8167–8174.
82 A. Augustsson, G. V. Zhuang, S. M. Butorin, J. M. Osorio-Guillen, C. L. Dong, R. Ahuja, C. L. Chang, P. N. Ross, J. Nordgren and J. H. Guo, *J. Chem. Phys.*, 2005, **123**, 184717.
83 X.-J. Wang, C. Jaye, K.-W. Nam, B. Zhang, H.-Y. Chen, J. Bai, H. Li, X. Huang, D. A. Fischer and X.-Q. Yang, *J. Mater. Chem.*, 2011, **21**, 11406–11411.
84 A. Freiberg, M. Metzger, D. Haering, S. Bretzke, S. Puravankara, T. Nilges, C. Stinner, C. Marino and H. A. Gasteiger, *J. Electrochem. Soc.*, 2014, **161**, A2255–A2261.
85 N. N. Bramnik, K. Nikolowski, C. Baehtz, K. G. Bramnik and H. Ehrenberg, *Chem. Mater.*, 2007, **19**, 908–915.
86 H. Ehrenberg, N. N. Bramnik, A. Senyshyn and H. Fuess, *Solid State Sci.*, 2009, **11**, 18–23.
87 N. N. Bramnik, K. Nikolowski, D. M. Trots and H. Ehrenberg, *Electrochem. Solid-State Lett.*, 2008, **11**, A89–A93.
88 Y. Hong, Z. Tang, S. Wang, W. Quan and Z. Zhang, *J. Mater. Chem. A*, 2015, **3**, 10267–10274.
89 R. Sharabi, E. Markevich, K. Fridman, G. Gershinsky, G. Salitra, D. Aurbach, G. Semrau, M. A. Schmidt, N. Schall and C. Bruenig, *Electrochem. Commun.*, 2013, **28**, 20–23.
90 J. Manzi, M. Curcio and S. Brutti, *Nanomaterials*, 2015, **5**, 2212–2230.

RSC Advances

Supplementary Information

Facile, ethylene glycol-promoted microwave-assisted solvothermal synthesis of high-performance $LiCoPO_4$ as a high-voltage cathode material for lithium-ion batteries

Jennifer Ludwig,[a] Cyril Marino,[b‡] Dominik Haering,[b] Christoph Stinner,[c] Dennis Nordlund,[d] Marca M. Doeff,[e] Hubert A. Gasteiger[b] and Tom Nilges[a*]

[a] *Technical University of Munich, Department of Chemistry, Synthesis and Characterization of Innovative Materials, Lichtenbergstr. 4, 85747 Garching, Germany*
[b] *Technical University of Munich, Department of Chemistry, Technical Electrochemistry, Lichtenbergstr. 4, 85747 Garching, Germany*
[c] *BMW AG, Petuelring 130, 80788 München, Germany*
[d] *Stanford Synchrotron Radiation Lightsource, SLAC National Accelerator Laboratory, 2575 Sand Hill Rd, Menlo Park, CA, 94025, USA*
[e] *Lawrence Berkeley National Laboratory, Environmental Energy Technologies Division, 1 Cyclotron Rd, Berkeley, CA, 94720, USA*
‡ Present address: *Paul Scherrer Institute, Electrochemical Energy Storage, 5232 Villigen PSI, Switzerland*
* E-Mail: tom.nilges@lrz.tu-muenchen.de

1 State of the art

Table S1 State of the art in the (a) hydrothermal (HT), (b) solvothermal (ST), (c) supercritical fluid (SCF), (d) microwave-assisted hydrothermal (MWHT), and (e) microwave-assisted solvothermal (MWST) synthesis of $LiCoPO_4$[a,b]

Ref.	Material	Reactants	Solvent *T* *t*	Morphology (particle size)	Remarks on synthesis	Cell type	Electrode composition	Electrolyte	C rate (remarks)	Discharge capacity, 1st cycle
a) Hydrothermal (HT) synthesis										
1	LCP	$LiOH \cdot H_2O$ $Co(CH_3COO)_2 \cdot 4\ H_2O$ $(NH_4)_2HPO_4$	H_2O 220 °C 5 h	agglomerates (10–45 μm) of prisms (1 μm × 1 μm × 2 μm)	–	–[c]	50:45:5 wt% (LCP:–[c]:–[c])	1 M $LiPF_6$ in EC/DMC = 1:1 (v/v)	0.1 C	15 mAh/g
1	LCP	$LiOH \cdot H_2O$ $Co(CH_3COO)_2 \cdot 4\ H_2O$ $(NH_4)_2HPO_4$	H_2O 300 °C 5 h	rods (300–700 nm × 5 μm)	PVP dispersant	–[c]	50:45:5 wt% (LCP:–[c]:–[c])	1 M $LiPF_6$ in EC/DMC = 1:1 (v/v)	0.1 C	65 mAh/g
2	LCP/C	Li_3PO_4 $CoSO_4 \cdot 7\ H_2O$	H_2O 200 °C 3 h	agglomerates (< 20 μm) of irregular particles (200–500 nm)	C-coating (CMC) post-annealing (700 °C, 1 h, 3% H_2/Ar)	CR2032 coin cell	75:15:10 wt% (LCP/C: Ketjan black: PVDF)	1 M $LiPF_6$ in EC/DEC = 1:1 (v/v)	0.1 C (CCCV)	45 mAh/g
3	LCP/C	$LiOH \cdot H_2O$ $CoSO_4 \cdot 7\ H_2O$ $(NH_4)_3PO_4 \cdot 3\ H_2O$	H_2O 200 °C 8 h	prismatic rods (0.5 × 3 μm)	C-coating (glucose) post-annealing (750 °C, 2 h, Ar)	CR2016 coin cell	70:20:10 wt% (LCP/C: carbon black: PVDF)	1 M $LiPF_6$ in EC/DMC = 1:1 (v/v)	0.1 C	90 mAh/g
4	LCP/C	Li_3PO_4 $CoSO_4 \cdot 7\ H_2O$	H_2O 200 °C 3 h	agglomerates (< 20 μm) of irregular particles (200–500 nm)	C-coating (CMC) post-annealing (700 °C, 1 h, 3% H_2/Ar)	CR2032 coin cell	75:15:10 wt% (LCP/C: Ketjan black: PVDF)	1 M $LiPF_6$ in EC/EMC = 3:7 (v/v)	0.1 C (CCCV)	99 mAh/g
4	LCP/C	Li_3PO_4 $CoCl_2$	H_2O 200 °C 3 h	agglomerates (< 20 μm) of square-like particles (0.5–2 μm)	C-coating (CMC) post-annealing (700 °C, 1 h, 3% H_2/Ar)	CR2032 coin cell	75:15:10 wt% (LCP/C: Ketjan black: PVDF)	1 M $LiPF_6$ in EC/EMC = 3:7 (v/v)	0.1 C (CCCV)	32 mAh/g
b) Solvothermal (ST) synthesis										
3	LCP/C	$LiOH \cdot H_2O$ $CoSO_4 \cdot 7\ H_2O$ $(NH_4)_3PO_4 \cdot 3\ H_2O$	BA/H_2O = 1:1 (v/v) 200 °C 8 h	microspheres (2–3 μm) of nanorods (35–50 nm × 1 μm)	C-coating (glucose) post-annealing (750 °C, 2 h, Ar)	CR2016 coin cell	70:20:10 wt% (LCP/C: carbon black: PVDF)	1 M $LiPF_6$ in EC/DMC = 1:1 (v/v)	0.1 C	133 mAh/g
5	LCP/C	LiCl $Co(NO_3)_2 \cdot 6\ H_2O$ H_3PO_4	EG 200 °C 10 h	agglomerates (2–3 μm) of irregular particles (200 nm)	C-coating (glucose)	CR2032 coin cell	80:10:10 wt% (LCP/C: acetylene black: PVDF)	1 M $LiPF_6$ in EC/DMC = 1:1 (v/v)	0.2 C	108 mAh/g
6, 7	LCP	$LiOH \cdot H_2O$ LiH_2PO_4 $CoSO_4 \cdot 7\ H_2O$	EG/H_2O = 2:1 (v/v) 220 °C 15 h	hexagonal/octagonal platelets (50–100 nm × 1 μm)	–	Swagelok cell	80:10:10 wt% (LCP: Super P: PVDF)	1 M $LiPF_6$ in EC/DMC = 1:1 (w/w)	0.1 C	95 mAh/g
8	LCP/C	Li_3PO_4 $CoSO_4 \cdot 7\ H_2O$	EG/H_2O = 4:1 (v/v) 180 °C 24 h	spindle-shaped particles (500 nm)	C-coating (sucrose) post-annealing (650 °C, 5 h, Ar)	CR2025 coin cell	75:15:10 wt% (LCP/C: Super P: PVDF)	1 M $LiPF_6$ in FEC/DMC = 1:4 (v/v)	0.1 C	123 mAh/g

Ref.	Material	Reactants	Solvent *T* *t*	Morphology (particle size)	Remarks on synthesis	Cell type	Electrode composition	Electrolyte	C rate (remarks)	Discharge capacity, 1st cycle
c) Supercritical fluid (SCF) synthesis										
9	LCP/C	lithium acetyl acetonate $CoCl_2 \cdot 6\ H_2O$ H_3PO_4	ethanol 400 °C 4 min	platelets (5–15 nm × 50–250 nm × 100–200 nm)	Oleylamine surfactant C-coating (PEDOT, MWCNT, wet ball milling) post-annealing (300 °C, 2 h, H_2/Ar)	beaker-type 3 electrode glass cell	83:10:7 wt% (LCP/C: acetylene black:PTFE)	1 M $LiPF_6$ in EC/DEC = 1:1 (v/v)	0.2 C	130 mAh/g
10	LCP/C	$LiCH_3COO \cdot H_2O$ $NH_4CoPO_4 \cdot H_2O$ (from $(NH_4)_3PO_4 \cdot 3\ H_2O$)	ethanol 400 °C 2 h	nanosheets (2 nm × 500 nm)	PVP additive liquid-phase exfoliation/ solvothermal HPHT lithiation	coin cell[c]	80:10:10 wt% (LCP/C: MWCNT: PVDF)	1 M $LiPF_6$ in EC/DEC = 1:1 (w/w)	0.2 C	153 mAh/g[d]
11	LCP/C	lithium acetyl acetonate $Co(CH_3COO)_2 \cdot 4\ H_2O$ H_3PO_4	ethanol 400 °C 6 min	nanorods (50 nm × 0.5–1 μm)	HMD additive C-coating (sucrose) post-annealing (650 °C, 1 h, Ar)	CR2032 coin cell	80:10:10 wt% (LCP/C: acetylene black: PTFE)	1 M $LiPF_6$ in EC/DMC = 1:1 (v/v)	0.1 C	130 mAh/g
12	LCP	$LiCH_3COO$ $Co(CH_3COO)_2 \cdot 4\ H_2O$ H_3PO_4	EG 400 °C 10 min	irregular particles (0.7 μm)	post-annealing (650 °C, 4 h, Ar)	Swagelok cell	80:20 wt% (LCP: Super P)	1 M $LiPF_6$ in EC/DMC = 1:1 (w/w)	0.05 C	14 mAh/g
d) Microwave-assisted hydrothermal (MWHT) synthesis										
13	LCP/C	$LiOH \cdot H_2O$ $CoSO_4 \cdot 7\ H_2O$ H_3PO_4	H_2O 230 °C 15 min 600 W	cubes (1–5 μm)	C-coating (glucose) post-annealing (700 °C, 4 h, Ar)	CR2032 coin cell	75:12.5:12.5 wt% (LCP/C:–[c]: TAB)	1 M $LiPF_6$ in EC/DEC = 1:1 (v/v)	0.1 C	52 mAh/g
e) Microwave-assisted solvothermal (MWST) synthesis										
14	LCP	$LiOH \cdot H_2O$ $Co(CH_3COO)_2 \cdot 4\ H_2O$ H_3PO_4	TEG 300 °C 15 min 0–600 W	nano-thumblike particles (80 nm × 200 nm)	–	CR2032 coin cell	75:12.5:12.5 wt% (LCP:–[c]: TAB)	1 M $LiPF_6$ in EC/DEC = 1:1 (v/v)	0.1 C	115 mAh/g
14	LCP/C	$LiOH \cdot H_2O$ $Co(CH_3COO)_2 \cdot 4\ H_2O$ H_3PO_4	TEG 300 °C 15 min 0–600 W	nano-thumblike particles (80 nm × 200 nm)	MWCNT nano-composite	CR2032 coin cell	75:12.5:12.5 wt% (LCP/C:–[c]: TAB)	1 M $LiPF_6$ in EC/DEC = 1:1 (v/v)	0.1 C	120 mAh/g
15	LCP	$LiOH \cdot H_2O$ $Co(CH_3COO)_2 \cdot 4\ H_2O$ H_3PO_4	TEG –[c] 15 min 2000 W	irregular particles (0.2–1 μm)	–	CR2032 coin cell	80:10:10 wt% (LCP: Super C65: PVDF)	1 M $LiPF_6$ in EC/EMC = 1:2 (v/v)	0.1 C (CCCV)	128 mAh/g
16	LCP	$LiOH \cdot H_2O$ $Co(CH_3COO)_2 \cdot 4\ H_2O$ H_3PO_4	TEG 260 °C 30 min 800 W	nanorods (200 nm × 1 μm)	–	CR2032 coin cell	70:20:10 wt% (LCP: graphite: PTFE)	1 M $LiPF_6$ in EC/DMC = 1:1 (v/v)	0.1 C	67 mAh/g

[a] All reports, including procedures using additional post heat treatments and conductive carbon coatings to improve the performance, are presented. In case several materials were covered in a report, the best performing sample is listed. Differences regarding the cell design (cell type, electrolyte) and charging protocol (C rate, potential window, CV step, etc.) are highlighted as they affect the electrochemical performance.

[b] abbreviations: BA, benzyl alcohol; CCCV, constant-current, constant-voltage charging; CMC, carboxy methyl cellulose; DEC, dimethyl carbonate; DMC, dimethyl carbonate, EC, ethylene carbonate; EG, ethylene glycol; EMC, ethyl methyl carbonate; FEC, fluoroethylene carbonate; HMD, hexamethylenediamine; HPHT, high-pressure high-temperature; HT, hydrothermal; LCP, lithium cobalt phosphate, $LiCoPO_4$; MWCNT, multi-walled carbon nanotubes; MWST, microwave-assisted solvothermal; PEDOT, poly(3,4-ethylenedioxythiophene); PTFE, poly(tetrafluoroethylene); PVDF, polyvinylidene difluoride; PVP, Poly(*N*-vinylpyrrolidone); SCF, supercritical fluid; ST, solvothermal; TAB, teflonized acetylene black; TEG, tetraethylene glycol.

[c] not specified

[d] The specific capacity values were on the basis of pure LCP rather than of LCP/C (carbon content 4.4 wt%).

2 X-ray powder diffraction data, Rietveld refinements

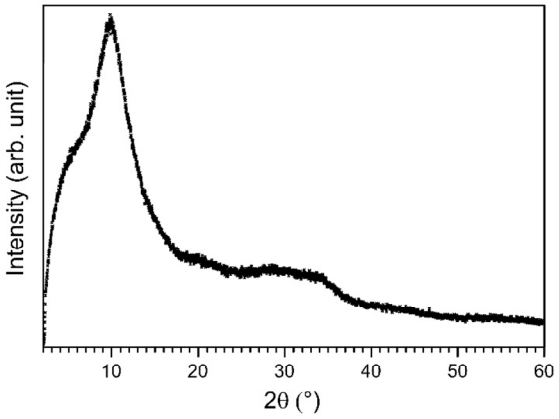

Fig. S1 X-ray diffraction pattern (transmission geometry, Mo $K_{\alpha 1}$ radiation, measurement time: 12 h) showing the background profile of an empty borosilicate glass capillary (Hilgenberg, glass type no. 50, length: 80 mm, diameter: 0.5 mm, wall thickness: 0.01 mm). As the maximum intensity of the empty capillary is about 1/10 of the intensity measured when filled with sample, it can be derived that the capillary significantly contributes to the background profile that is observed when the capillary is filled with sample.

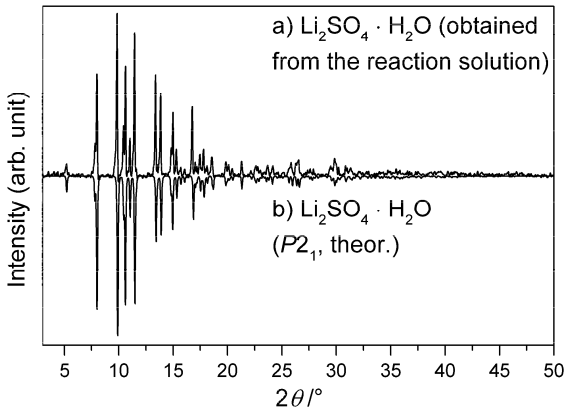

Fig. S2 X-ray powder diffraction pattern (transmission geometry, Mo $K_{\alpha 1}$ radiation, measurement time: 20 min) of the white powder obtained from evaporating the reaction solution after the microwave-assisted solvothermal synthesis. The theoretical pattern of $Li_2SO_4 \cdot H_2O$ (ICSD database entry no. 62124) is displayed mirrored in (b). The data confirm that $Li_2SO_4 \cdot H_2O$ was formed as a by-product of the reaction. The powder exhibits comparably low crystallinity, which is also in good agreement with reports that the crystallization of the compound is challenging due to its inverse solubility (i.e., its increasing solubility with decreasing temperature).[17]

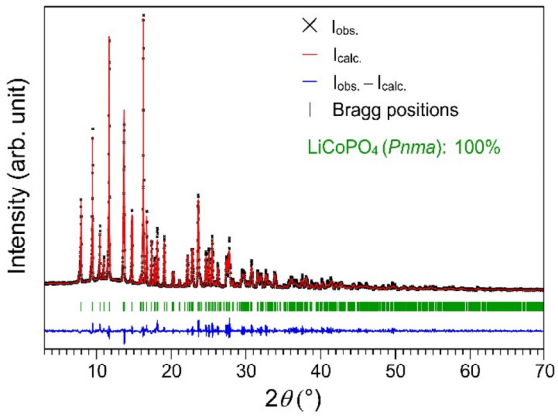

Fig. S3 Rietveld fit of the X-ray powder diffraction data (transmission geometry, Mo $K_{\alpha 1}$ radiation, measurement time: 12 h) of LCP-MW-w obtained from microwave-assisted solvothermal synthesis and after intensive, additional washing with ice water. The diffraction pattern is similar to LCP-MW (Fig. 2 in the main article) and comparable cell parameters can be derived (Table S2b).

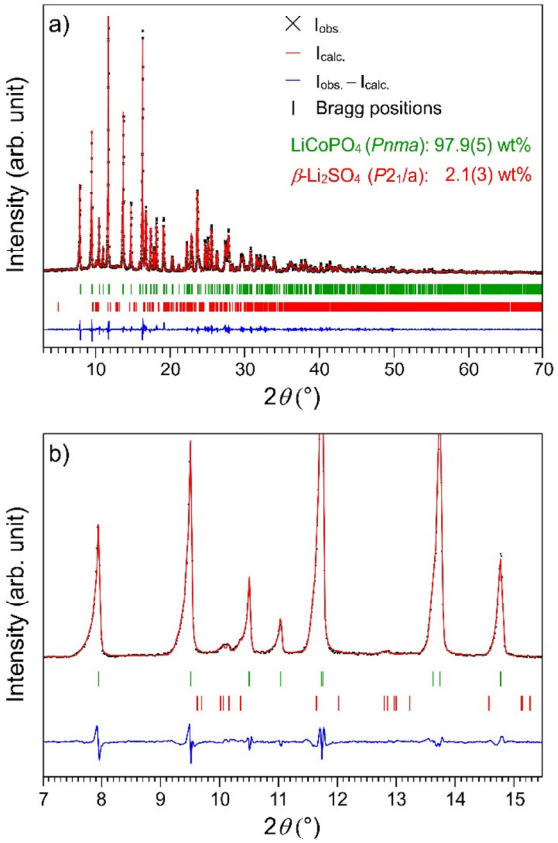

Fig. S4 Rietveld fit of the X-ray powder diffraction data (transmission geometry, Mo $K_{\alpha 1}$ radiation, measurement time: 12 h) of the sample LCP-MW-T obtained after the TGA/DSC measurement under Argon up to 750 °C (see Fig. S5): (a) full pattern, and (b) zoomed view at small 2θ where the peaks of the β-Li_2SO_4 (space group $P2_1/a$) impurity, which crystallizes upon heating, are observed.

Table S2 Refined crystallographic data of $LiCoPO_4$ samples obtained from microwave-assisted solvothermal synthesis: (a) as prepared (LCP-MW), (b) after intensive washing (LCP-MW-w), and (c) after TGA/DSC measurement (LCP-MW-T)[a]

Empirical formula	a) LCP-MW	b) LCP-MW-w	c) LCP-MW-T
M_r (g·mol^{-1})	160.8	160.8	160.8
Crystal system	orthorhombic	orthorhombic	orthorhombic
Space group	*Pnma* (no. 62)	*Pnma* (no. 62)	*Pnma* (no. 62)
Z	4	4	4
a (Å)	10.1930(7)	10.1931(8)	10.1852(9)
b (Å)	5.9188(4)	5.9195(5)	5.9114(5)
c (Å)	4.6959(3)	4.6961(4)	4.6913(4)
V (Å^3)	283.31(3)	283.35(4)	282.46(4)
F(000)	308	308	308
ρ (calcd.) (g·cm^{-3})	3.7710(6)	3.7704(7)	3.7823(8)
T (K)	298	298	298
λ (Å)	0.70930	0.70930	0.70930
R_p	0.0564	0.0633	0.0752
R_{wp}	0.0744	0.0856	0.0996
R_{exp}	0.0550	0.0557	0.0549
R_F	0.0409	0.0331	0.0344
R_B	0.0646	0.0572	0.0575
χ^2	1.35	1.54	1.81
Data/restraints/parameter	4469/0/61	4463/0/61	4469/0/62
Crystalline phase composition	100 wt% $LiCoPO_4$	100 wt% $LiCoPO_4$	97.9(5) wt% $LiCoPO_4$ 2.1(3) wt% Li_2SO_4

[a] The estimated standard deviations (e.s.d's) were calculated by the Berar's procedure und are indicated in parentheses.

Table S3 Fractional atomic coordinates and isotropic thermal displacement parameters refined from X-ray powder diffraction data of $LiCoPO_4$ (*Pnma*, *Z* = 4, *T* = 298 K) samples obtained from microwave-assisted solvothermal synthesis: (a) as prepared (LCP-MW), (b) after intensive washing (LCP-MW-w), and (c) after TGA/DSC measurement (LCP-MW-T)[a]

Sample	Atom	Wyckoff position	Occupancy	*x*/a	*y*/b	*z*/c	U_{iso} (Å^2)
a) LCP-MW	Li1	4*a*	1	0	0	0	0.0139[b]
	Co1	4*c*	1	0.2212(2)	¼	0.5210(7)	0.0120(10)
	P1	4*c*	1	0.4046(6)	¼	0.0823(12)	0.0073(16)
	O1	4*c*	1	0.4054(15)	¼	0.766(2)	0.004(2)
	O2	4*c*	1	0.0442(14)	¼	0.292(2)	0.002(2)
	O3	8*d*	1	0.3361(10)	0.0475(14)	0.2160(15)	0.003(2)
b) LCP-MW-w	Li1	4*a*	1	0	0	0	0.0139[b]
	Co1	4*c*	1	0.2214(3)	¼	0.5224(8)	0.0087(12)
	P1	4*c*	1	0.4044(6)	¼	0.0833(13)	0.0036(18)
	O1	4*c*	1	0.4048(17)	¼	0.770(3)	0.003(2)
	O2	4*c*	1	0.0444(16)	¼	0.294(3)	0.003(2)
	O3	8*d*	1	0.3365(11)	0.0485(16)	0.2160(17)	0.003(2)
c) LCP-MW-T	Li1	4*a*	1	0	0	0	0.0139[b]
	Co1	4*c*	1	0.2212(3)	¼	0.5202(9)	0.0085(12)
	P1	4*c*	1	0.4047(7)	¼	0.0827(14)	0.007(2)
	O1	4*c*	1	0.4052(18)	¼	0.758(3)	0.006(2)
	O2	4*c*	1	0.0436(16)	¼	0.295(3)	0.002(2)
	O3	8*d*	1	0.3341(12)	0.0465(17)	0.2147(18)	0.004(2)

[a] The estimated standard deviations (e.s.d's) were calculated by means of the Berar's procedure und are indicated in parentheses.
[b] The Li displacement factor has been fixed in all cases because it cannot be deduced properly by means of X-ray diffraction due to the low atomic scattering factor.

Table S4 Selected interatomic distances refined from X-ray powder diffraction data of $LiCoPO_4$ (*Pnma*, $Z = 4$, $T = 298$ K) samples obtained from microwave-assisted solvothermal synthesis: (a) as prepared (LCP-MW), (b) after intensive washing (LCP-MW-w), and (c) after TGA/DSC measurement (LCP-MW-T)[a]

Atom pair			*d* (Å)		
			a) LCP-MW	b) LCP-MW-w	c) LCP-MW-T
Li1	O1	×2	2.162(9)	2.178(11)	2.141(12)
	O2	×2	2.068(8)	2.073(9)	2.074(9)
	O3	×2	2.157(9)	2.154(10)	2.173(11)
Co1	O1	×1	2.201(14)	2.202(16)	2.181(18)
	O2	×1	2.100(13)	2.099(15)	2.093(16)
	O3	×2	2.069(9)	2.073(10)	2.055(10)
	O3	×2	2.205(9)	2.206(10)	2.196(11)
P1	O1	×1	1.488(13)	1.470(15)	1.523(16)
	O2	×1	1.540(15)	1.540(17)	1.527(18)
	O3	×2	1.523(9)	1.514(11)	1.532(11)

[a] The estimated standard deviations (e.s.d's) were calculated by applying the Berar's correction und are indicated in parentheses.

3 Thermal stability of LCP-MW

Experimental details

The thermal stability of the single-phase material LCP-MW up to 750 °C was assessed by thermal analysis on a simultaneous TGA/DSC 1 STAR system (Mettler Toledo). Experiments were run at a heating rate of 10 °C/min in an argon stream (10 mL/min, specimen weight: 5 mg). Monitoring of the cooling cycle was not possible due to the setup. The sample that was treated thermally is denoted LCP-MW-T in the following.

In addition to the TGA/DSC experiments, the thermal stability was further examined by temperature-controlled *in situ* PXRD studies using a PANalytical X'Pert Pro diffractometer with monochromatized Cu K_α radiation and an XCelerator detector. The instrument was equipped with an Anton Paar HTK-1200 hot stage, a TCU 1000N temperature controller, and a corundum flat plate sample holder. The scans were collected between 20° and 26° 2θ in Bragg-Brentano geometry (step size: 0.022°, time/step: 1000 s, total measurement time: 76 h). The samples were heated in air at a rate of 5 °C/min, and the patterns collected in a temperature range of 30–900 °C with an increment step of 100 °C, each temperature being held for 5 min before starting the data collection.

Results and discussion

The thermal behavior of the sample LCP-MW was assessed by TGA/DSC and complementary temperature-dependent *in situ* PXRD hot-stage measurements. The TGA/DSC data of the heating cycle are presented in Fig. S5a, the corresponding PXRD data of the sample after the TGA/DSC measurement are presented in Fig. S4. The material is found to be thermally stable up to 750 °C and shows an overall mass loss of only 0.7 wt%, which in agreement with literature.[16, 18] The zoomed view (Fig. S5b) shows an endothermic event at 590 °C that can only be attributed to the reconstructive phase transformation from monoclinic β-Li_2SO_4 (space group $P2_1/a$) to cubic α-Li_2SO_4 (space group $Fm\bar{3}m$)[19-23] and is accompanied by a mass loss of ~0.35 wt%. Moreover, a mass loss of ~0.1 wt% at a temperature of 70–250 °C, and of ~0.2 wt% from 390 °C to 460 °C is observed; both events are not correlated with DSC signals. The observed mass loss might be attributed to the removal of entrained residual water remaining from the synthesis, and the dehydration of traces of the $Li_2SO_4 \cdot H_2O$ impurity.[24, 25] Although these signals show only a low intensity, they are most likely originating from the $Li_2SO_4 \cdot H_2O/Li_2SO_4$ phase.

The PXRD data of the sample LCP-MW-T after TGA/DSC (Fig. S4a) support this observation. Here, traces of crystalline Li_2SO_4 are observed. The refinement of the diffraction pattern delivers a phase fraction of 2.1(3) wt% for the low-temperature phase β-Li_2SO_4 (space group $P2_1/a$).[23] The zoomed view (Fig. S4b) clearly shows the main diffraction peaks of the phase at 10.1° and 12.8° 2θ, respectively. The refined fraction of Li_2SO_4 (2.1(3) wt%, *cf.* Table S2c) is smaller than the one estimated by elemental analysis (5(1) wt%, *cf.* Table 1), which is due to the limitations of the Rietveld method (fractions are not accurately determined if phases show different particle sizes and crystallinities) and the fact that the intensity of the main peaks is comparably small. However, it can be inferred that >94(2) wt% of the sample are the pure LCP phase.

The results as well as the reduction of the amorphous peak at small angles in the PXRD pattern indicate that the lithium sulfate impurity is obtained in amorphous form from the MWST synthesis and can be crystallized upon heating. This is in good agreement with reports that the crystallization of the compound is challenging due to its inverse solubility.[17] Besides that, the LCP phase also seems to increase in crystallinity upon thermal treatment, as it can be derived by the significantly smaller cell volume of about 282.46(4) Å^3 (Table S2c). Further details on the refined data of the sample LCP-MW-T can be found in Tables S2, S3, and S4.

In addition to the TGA/DSC experiments, temperature-controlled PXRD studies were carried out to systematically investigate the behavior of LCP-MW upon heating *in situ*. The powder diffraction patterns in a temperature range of 30–900 °C (step size: 100 °C) are displayed in Fig. S6. The focus was set on the 2θ range of 20–26°, the region in which reflections of the $Li_2SO_4 \cdot H_2O/Li_2SO_4$ side phase are expected. In agreement with the TGA/DSC data, no phase changes are observed between 30 °C and 600 °C. Here, the main peaks of the olivine phase (101), (210), (011), and (111) as well as a small reflection that is deriving from the corundum flat plate sample holder at ~24.7° are observed. Signals originating from the lithium sulfate hydrate impurity and its dehydrated form are not detected. This is in agreement with a report[26] that upon dehydration of $Li_2SO_4 \cdot H_2O$, an amorphous unstable anhydride phase is formed. Due to thermal expansion, the $LiCoPO_4$ peaks are continually broadening and shifted to lower angles, indicating bigger lattice dimensions. At 700 °C, a peak around 21.8° is emerging, which can be attributed to the (111) reflection of high-temperature α-Li_2SO_4 (space group $Fm\bar{3}m$)[23] The fact that the phase transition occurs at slightly higher temperatures compared to the DSC might be due to the different atmospheres used for the measurements (air vs. argon), the different heating rates (10 °C/min vs. 5 °C/min), and thermal losses. At a nominal temperature of 900 °C, which is above the melting point of Li_2SO_4,[27] it is possible that the real temperature reached in this experiment was below the melting point due to thermal losses. Therefore, the (111) peak of α-Li_2SO_4 is still visible. Besides, an additional reflection at ~22.1° 2θ is observed. In agreement with current investigations in our group, the peak corresponds to the characteristic (210) reflection of the metastable $Pna2_1$-polymorph of $LiCoPO_4$,[28] which, in contrast to any previous reports about the thermal behavior of olivine-type LCP,[16, 18] is formed at high temperature.

The cooled sample (25 °C) has significantly broader peaks than the initial sample (30 °C) and the reflections are shifted to higher 2θ values due to thermal contraction. According to the reversible phase transformation from β-Li_2SO_4 to α-Li_2SO_4,[19] peaks of low-temperature β-Li_2SO_4 are indicated, which is also consistent with our ex situ PXRD study (Fig. S4). Moreover, reflections of $Li_2SO_4 \cdot H_2O$ arise at 21.6°, 23.0° (shoulder of (210) reflection of LCP), and 25.1° 2θ. The hydrate is formed from the reaction of the hygroscopic Li_2SO_4 with air moisture[29] during the cooling process. The results of the temperature-dependent PXRD study demonstrate and confirm our assumption that the $Li_2SO_4 \cdot H_2O/Li_2SO_4$ secondary phase in the as-obtained LCP-MW product is amorphous and can be crystallized upon heating.

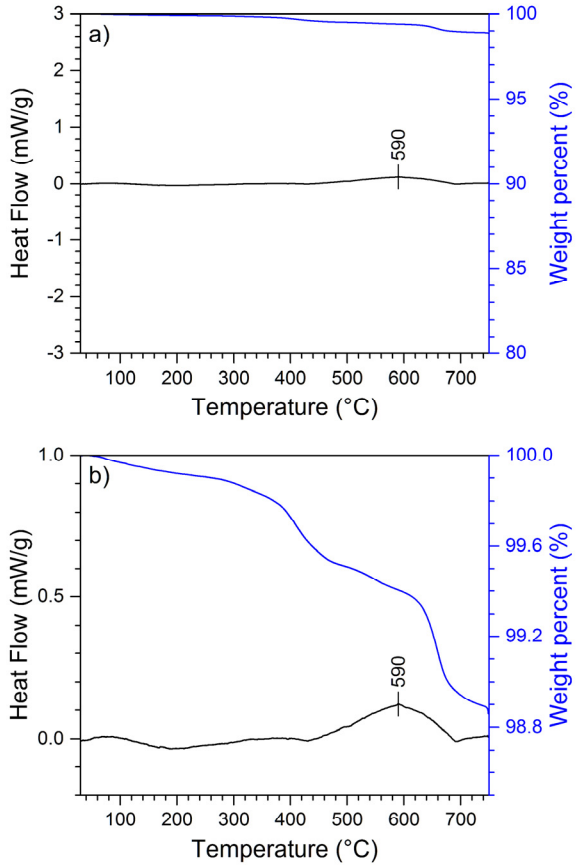

Fig. S5 (a) DSC and TGA plots for the as-prepared material LCP-MW, (b) zoomed view to clarify the weak signals. DSC data are drawn in black, and TGA data in blue.

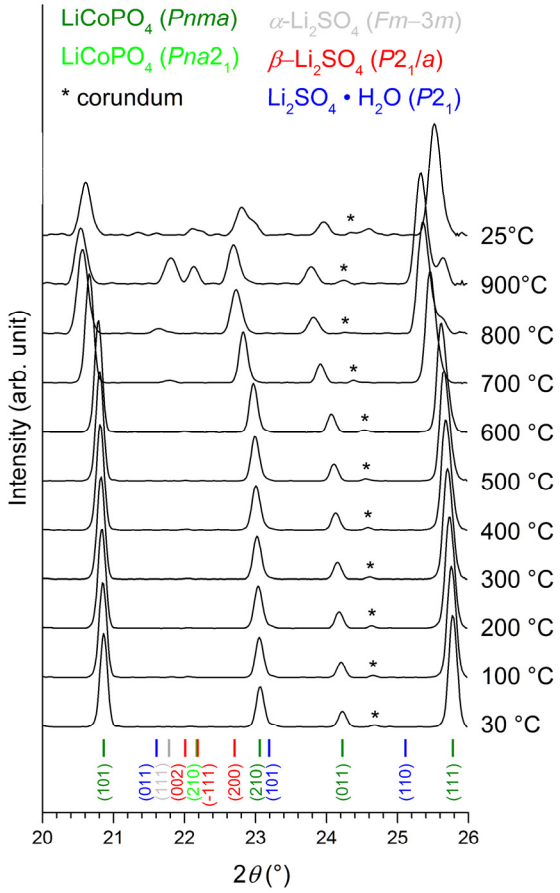

Fig. S6 Temperature-controlled *in situ* X-ray powder diffraction patterns (Bragg-Brentano geometry, Cu $K_{\alpha 1}$ radiation) of the sample LCP-MW in comparison to the main Bragg reflections of the phases $LiCoPO_4$ (*Pnma*, dark green), $LiCoPO_4$ (*Pna*2_1, light green), α-Li_2SO_4 ($Fm\bar{3}m$, red), β-Li_2SO_4 ($P2_1/a$, red), and $Li_2SO_4 \cdot H_2O$ ($P2_1$, blue) from 20° to 26° 2θ. Signals arising from the corundum flat plate sample holder are marked with *.

4 Infrared and Raman spectroscopy

Experimental details

ATR-FTIR spectra were recorded on a Perkin Elmer FTIR spectrometer (diamond ATR, Spectrum Two; located inside an argon-filled glovebox) in a range of 400–4000 cm^{-1}.
Raman spectra were measured by using a Labram HR 800 spectrometer. The instrument was equipped with a 800 mm focal length spectrograph and a cooled (–70 °C), back-thinned CCD detector (pixel size 26 × 26 μm). The samples were excited by an air-cooled doubled Nd:YAG laser (532 nm), and several input laser powers of 0.056, 0.56, and 5.6 mW were applied. No sample decomposition was observed at any excitation power.

Results and discussion

The FTIR and Raman spectra of LCP-MW are presented in Fig. S7 and the observed vibrations are summed up in Table S5. The IR spectrum is displayed in the full region from 400 cm^{-1} to 4000 cm^{-1} (Fig. S7a) and also in the region of 400–1600 cm^{-1} (Fig. S7b) for clarity. The spectrum does not show any absorption bands of water or other impurities and is in good agreement with reported values.[6, 30-33] In general, it is dominated by the four fundamental intramolecular vibrations of the $[PO_4]$ groups. The bands at 1145 cm^{-1}, 1098 cm^{-1}, and 1044 cm^{-1} are associated with the asymmetric stretching vibrations of P–O (ν_3), which is split up in a triplet due to interactions with the Co–O bonds. The strong singlet at 975 cm^{-1} corresponds to the symmetric stretching vibration of the P–O bond (ν_1). All the observed bonds are broadened, which is a result of the asymmetric bonding situation in the $[PO_4]$ units in the olivine crystal structure. The asymmetry is well confirmed by the refined bond lengths (Table S4a). The triplet observed at 549–640 cm^{-1} is related to antisymmetric bending vibrations of O–P–O (ν_4). The signal at 576 cm^{-1} is related to asymmetric vibrations of the octahedral $[CoO_6]$ units[31] and therefore confirms the olivine structure. The absorption at 471 cm^{-1} can be explained by the symmetric bending vibration of O–P–O (ν_2) or a contribution of Li ion "cage modes", which represent translational vibrations of the Li ions inside a potential caused by the neighbor oxygen atoms, as discussed in the literature.[34] Due to splitting effects, these bands are overlapping with the phosphate bending vibrations, and an unambiguous assignment cannot therefore be made.
In the IR spectrum, no bands are observed that could be assigned to the lithium sulfate impurity. As it can be derived from the IR spectrum of a mixture of Li_2SO_4 and $Li_2SO_4 \cdot H_2O$ (Fig. S8c,d), the main absorption of the impurity overlaps with one of the ν_3 modes of the P–O vibrations in $LiCoPO_4$. Moreover, it is notable that the IR spectrum remains unaltered for the intensively washed sample LCP-MW-w (Fig. S8a,b).
In the Raman spectrum (Fig. S7c,d), four stretching bands are observed at 1132 cm^{-1}, 1063 cm^{-1}, 977 cm^{-1}, and 938 cm^{-1}, which are in excellent agreement with data reported previously.[34-36] The latter very sharp band is attributed to the intramolecular symmetric stretching vibrations (ν_1) of the $[PO_4]^{3-}$ anion, whereas the two weaker ones are correlated with the asymmetric stretching modes (ν_3). The bending modes of the phosphate group are observed at lower energy. The bands observed at 655 cm^{-1}, 622 cm^{-1}, and 578 cm^{-1} arise from symmetric bending modes (ν_4) while the one at 437 cm^{-1} is from the asymmetric ν_2 mode.[35, 36] Other minor bands have been assigned by the use of density functional theory simulations.[37] The absence of any carbon D or G bands confirms the results of the CHNS analysis that did not detect any carbon in the sample. Moreover, signals that could be attributed to the lithium sulfate secondary phase (i.e. modes of the $[SO_4]^{2-}$ anion) are not detected as expected, because Raman spectroscopy generally provides a lower sensitivity compared to IR.

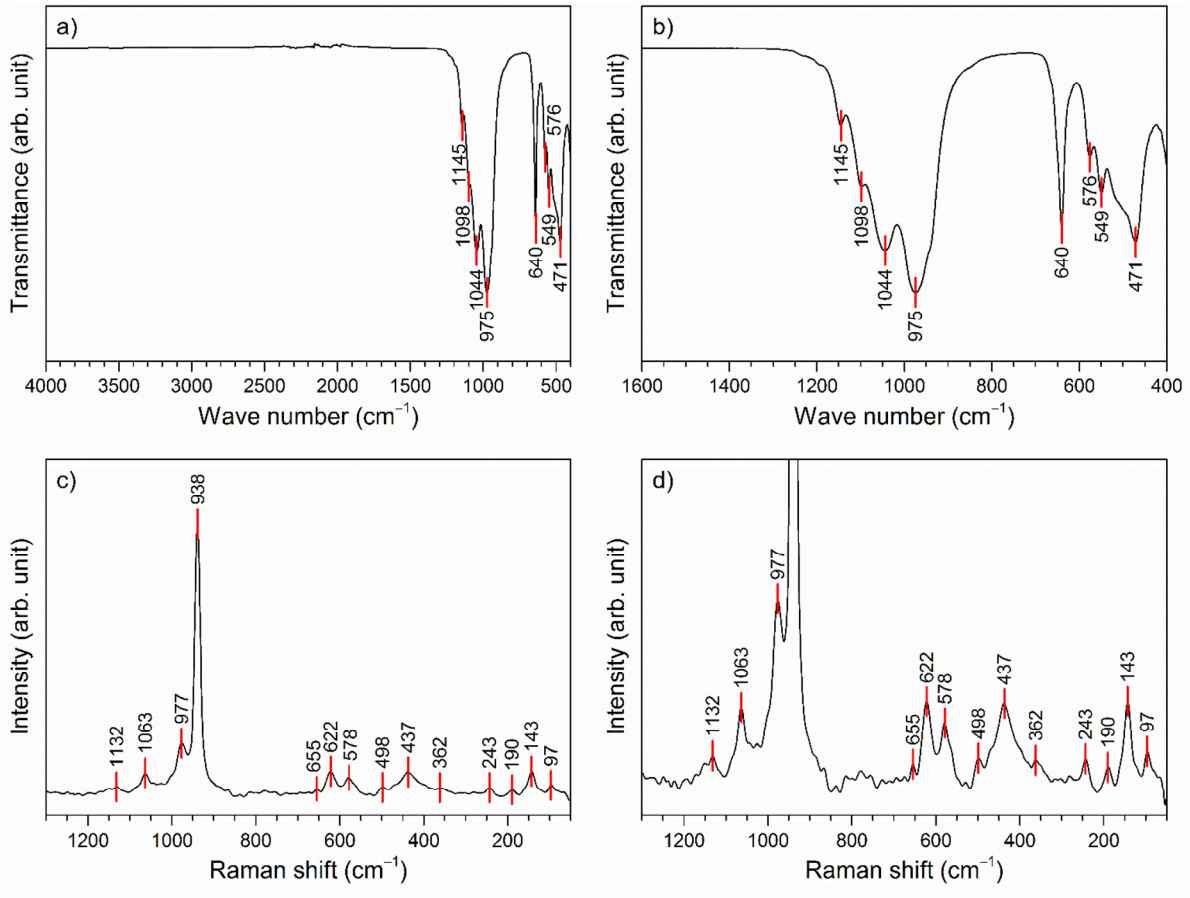

Fig. S7 (a) Full FTIR, (b) zoomed FTIR, (c) Raman, and (d) zoomed Raman spectra of LCP-MW. The sample does not contain any detectable amounts of water or carbon.

Table S5 Assignments of the most important (a) IR and (b) Raman bands of LCP-MW as observed in the IR and Raman spectra.[30-32, 34-37]

Vibrational mode		a) FTIR	b) Raman
Asymmetric stretching vibrations of P–O	v_3	1145 cm^{-1}	1132 cm^{-1}
		1098 cm^{-1}	1063 cm^{-1}
		1044 cm^{-1}	977 cm^{-1}
Symmetric stretching vibrations of P–O	v_1	975 cm^{-1}	938 cm^{-1}
Asymmetric bending vibrations of O–P–O	v_4	640 cm^{-1}	655 cm^{-1}
		576 cm^{-1}	622 cm^{-1}
		549 cm^{-1}	578 cm^{-1}
Symmetric bending vibration of O–P–O	v_2	471 cm^{-1}	437 cm^{-1}

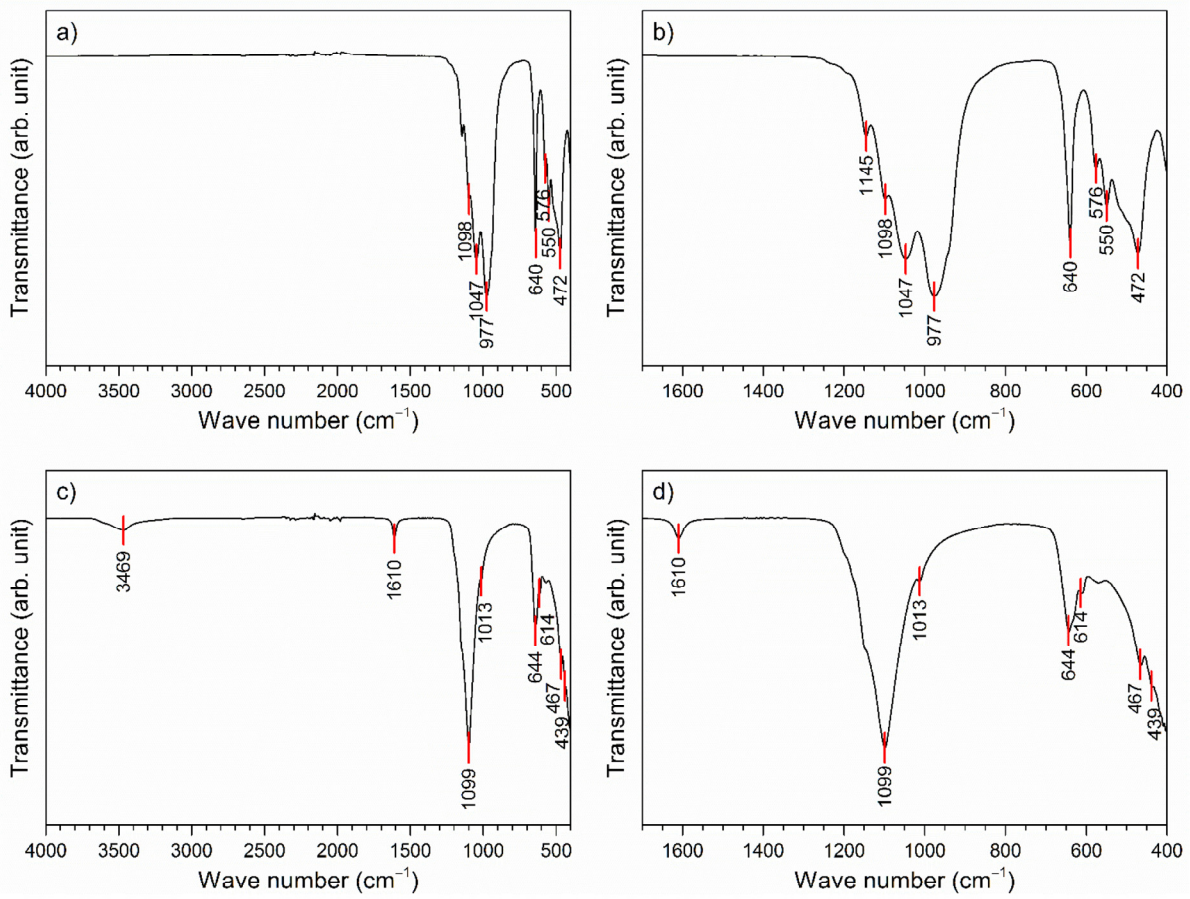

Fig. S8 Full and zoomed FTIR spectra of (a,b) LCP-MW-w (after intensive washing) and (c,d) a mixture of Li_2SO_4 and $Li_2SO_4 \cdot H_2O$.

5 Additional scanning electron microscopy images

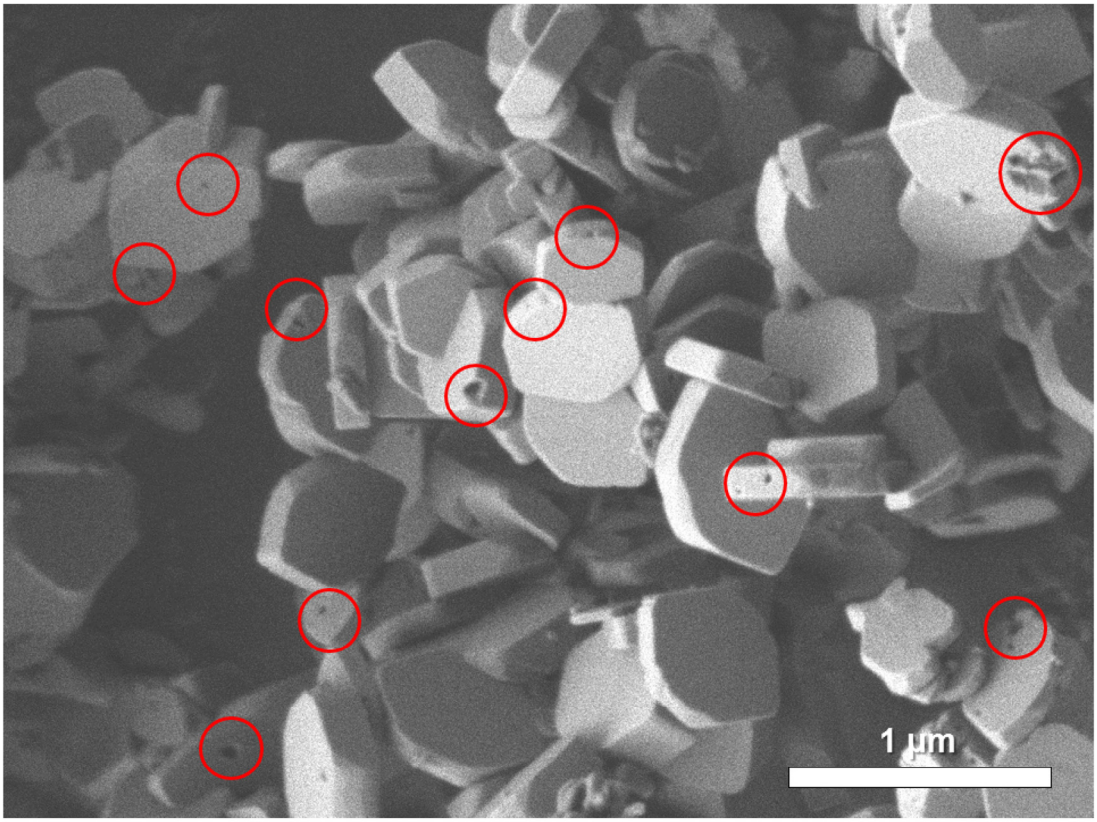

Fig. S9 SEM image of the sample LCP-MW (*cf.* Fig. 3b) showing small pores (diameter: 10–20 nm) on the surface of the particles (indicated by red circles). The pores, which might form an interconnected system, destabilize the particles, with some particles showing damage probably due to mechanical stress during the synthesis produced by stirring and the washing step.

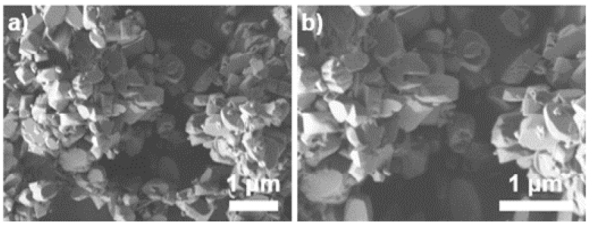

Fig. S10 SEM images of the sample LCP-MW-w (after intensive washing) at two different magnifications (a,b). It can be inferred that increased washing results in a higher portion of damaged particles.

6 Additional electrochemical measurements

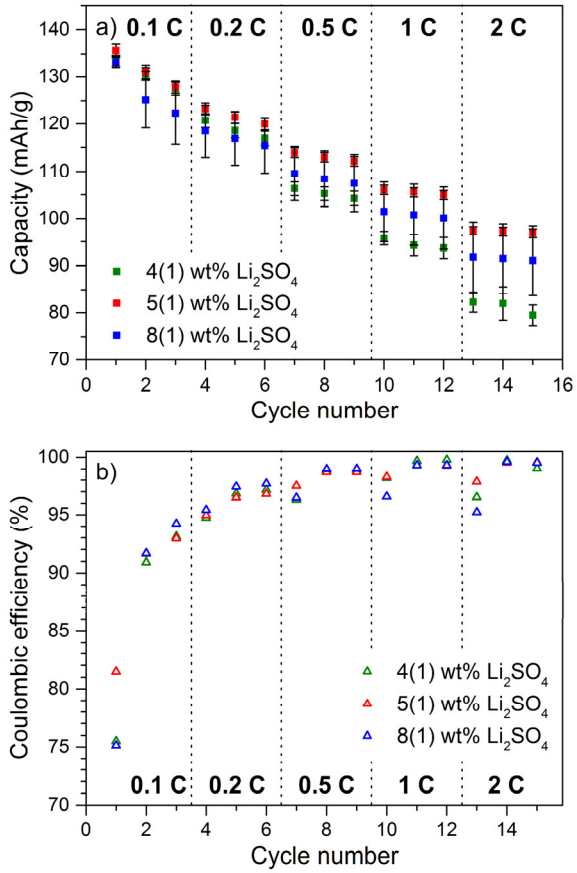

Fig. S11 (a) Specific capacities vs. C rate and (b) coulombic efficiencies (standard deviations omitted for clarity) obtained in each cycle for LCP-MW samples with different quantities of the lithium sulfate impurity. It can be inferred that the Li_2SO_4 content does not affect the electrochemical performance within standard deviations.

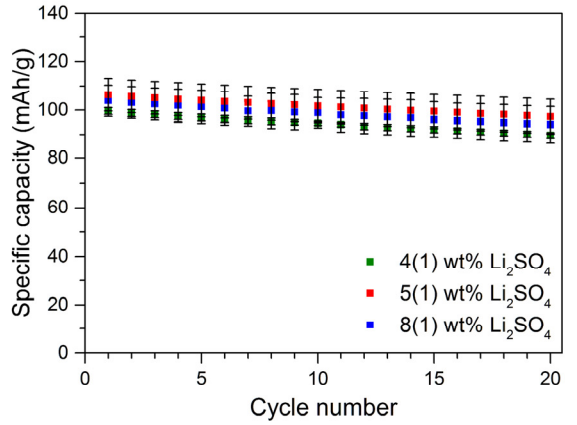

Fig. S12 Comparison of the electrochemical stabilities of LCP-MW MW samples with different quantities of the lithium sulfate impurity at 0.5 C after the first 15 cycles of C rate testing. It can be inferred that the Li_2SO_4 content does not affect the electrochemical stability within standard deviations.

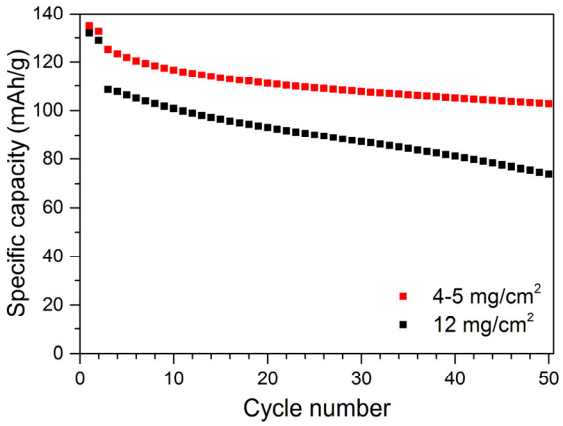

Fig. S13 Comparison of the electrochemical stabilities of LCP-MW electrodes with different loadings of 4–5 mg/cm² and 12 mg/cm². Testing was performed in Swagelok cells using electrodes with an 80:10:10 wt% composition ratio at 0.5 C after two initial cycles at C/15. It can be inferred that electrodes with high loadings still present reasonable capacities.

References

1 Y. Zhao, S. Wang, C. Zhao and D. Xia, *Rare Met. (Beijing, China)*, 2009, **28**, 117-121.
2 M. Kotobuki, Y. Mizuno, H. Munakata and K. Kanamura, *Phosphorus Res. Bull.*, 2010, **24**, 12-15.
3 F. Wang, J. Yang, Y. Nuli and J. Wang, *J. Power Sources*, 2011, **196**, 4806-4810.
4 M. Kotobuki, *Int. J. Energy Environ. Eng.*, 2013, **4**, 25, 27 pp.
5 M. Li, *Ionics*, 2012, **18**, 507-512.
6 S. Brutti, J. Manzi, A. De Bonis, D. Di Lecce, F. Vitucci, A. Paolone, F. Trequattrini and S. Panero, *Mater. Lett.*, 2015, **145**, 324-327.
7 J. Manzi, M. Curcio and S. Brutti, *Nanomaterials*, 2015, **5**, 2212-2230.
8 B. Wu, H. Xu, D. Mu, L. Shi, B. Jiang, L. Gai, L. Wang, Q. Liu, L. Ben and F. Wu, *J. Power Sources*, 2016, **304**, 181-188.
9 M. K. Devaraju, D. Rangappa and I. Honma, *Electrochim. Acta*, 2012, **85**, 548-553.
10 X. Rui, X. Zhao, Z. Lu, H. Tan, D. Sim, H. H. Hng, R. Yazami, T. M. Lim and Q. Yan, *ACS Nano*, 2013, **7**, 5637-5646.
11 Q. D. Truong, M. K. Devaraju, Y. Ganbe, T. Tomai and I. Honma, *Sci. Rep.*, 2014, **4**, 3975/1-3975/8.
12 M. Kaus, I. Issac, R. Heinzmann, S. Doyle, S. Mangold, H. Hahn, V. S. K. Chakravadhanula, C. Kuebel, H. Ehrenberg and S. Indris, *J. Phys. Chem. C*, 2014, **118**, 17279-17290.
13 A. V. Murugan, T. Muraliganth and A. Manthiram, *J. Electrochem. Soc.*, 2009, **156**, A79-A83.
14 A. V. Murugan, T. Muraliganth, P. J. Ferreira and A. Manthiram, *Inorg. Chem.*, 2009, **48**, 946-952.
15 R. E. Rogers, G. M. Clarke, O. N. Matthew, M. J. Ganter, R. A. DiLeo, J. W. Staub, M. W. Forney and B. J. Landi, *J. Appl. Electrochem.*, 2013, **43**, 271-278.
16 K. J. Kreder, G. Assat and A. Manthiram, *Chem. Mater.*, 2015, **27**, 5543-5549.
17 A. Silambarasan, E. N. Rao, S. V. Rao, P. Rajesh and P. Ramasamy, *CrystEngComm*, 2016, **18**, 2072-2080.
18 J. Chen, M. J. Vacchio, S. Wang, N. Chernova, P. Y. Zavalij and M. S. Whittingham, *Solid State Ionics*, 2008, **178**, 1676-1693.
19 F. D. Rossini, D. D. Wagman, W. H. Evans, S. Levine and I. Jaffe, *Natl. Bur. Stand. Circ. (U. S.)*, 1952, **No. 500**, 1266 pp.
20 T. Forland and J. Krogh-Moe, *Acta Chem. Scand.*, 1957, **11**, 565-567.
21 A. G. Nord, *Crystal structure of the low temperature modification of lithium sulfate (α-Li_2SO_4). Three dimensional refinement*, Univ. Stockholm, 1973.
22 N. W. Alcock, D. A. Evans and H. D. B. Jenkins, *Acta Crystallogr., Sect. B*, 1973, **29**, 360-361.
23 L. Nilsson, J. O. Thomas and B. C. Tofield, *J. Phys. C*, 1980, **13**, 6441-6451.
24 H. Tanaka, *Thermochim. Acta*, 1982, **52**, 195-199.
25 F. Valdivieso, V. Bouineau, M. Pijolat and M. Soustelle, *Solid State Ionics*, 1997, **101-103**, 1299-1303.
26 Y. Seto, H. Sato and Y. Masuda, *Thermochim. Acta*, 2002, **388**, 21-25.
27 G. Hatem and M. Gaune-Escard, *Calorim. Anal. Therm.*, 1983, **14**, 96-103.
28 C. Jaehne, C. Neef, C. Koo, H.-P. Meyer and R. Klingeler, *J. Mater. Chem. A*, 2013, **1**, 2856-2862.
29 R. Weintraub, A. Apelblat and A. Tamir, *Anal. Chim. Acta*, 1984, **166**, 325-327.
30 D. Shanmukaraj and R. Murugan, *Ionics*, 2004, **10**, 88-92.
31 Gangulibabu, D. Bhuvaneswari, N. Kalaiselvi, N. Jayaprakash and P. Periasamy, *J. Sol-Gel Sci. Technol.*, 2009, **49**, 137-144.
32 P. N. Poovizhi and S. Selladurai, *Ionics*, 2011, **17**, 13-19.
33 J. Su, B.-Q. Wei, J.-P. Rong, W.-Y. Yin, Z.-X. Ye, X.-Q. Tian, L. Ren, M.-H. Cao and C.-W. Hu, *J. Solid State Chem.*, 2011, **184**, 2909-2919.
34 C. M. Burba and R. Frech, *J. Electrochem. Soc.*, 2004, **151**, A1032-A1038.
35 W. Paraguassu, P. T. C. Freire, V. Lemos, S. M. Lala, L. A. Montoro and J. M. Rosolen, *J. Raman Spectrosc.*, 2005, **36**, 213-220.
36 E. Markevich, R. Sharabi, O. Haik, V. Borgel, G. Salitra, D. Aurbach, G. Semrau, M. A. Schmidt, N. Schall and C. Stinner, *J. Power Sources*, 2011, **196**, 6433-6439.
37 V. I. Fomin, V. P. Gnezdilov, V. S. Kumosov, A. V. Peschanskii, V. V. Eremenko, S. Gentil and J. P. Rivera, *Low Temp. Phys.*, 1999, **25**, 829-832.

6.3 Particle Size-Controllable Microwave-Assisted Solvothermal Synthesis of the High-Voltage Cathode Material $LiCoPO_4$ Using Water/Ethylene Glycol Solvent Blends

Jennifer Ludwig,[a] Dominik Haering,[b] Marca M. Doeff,[c] and Tom Nilges[a]*

[a] Technical University of Munich, Department of Chemistry, Synthesis and Characterization of Innovative Materials, Lichtenbergstr. 4, 85747 Garching, Germany

[b] Technical University of Munich, Department of Chemistry, Technical Electrochemistry, Lichtenbergstr. 4, 85747 Garching, Germany

[c] Lawrence Berkeley National Laboratory, Environmental Energy Technologies Division, 1 Cyclotron Rd, Berkeley, CA, 94720, USA

Solid State Sci. **2017,** *65*, 100–109.
DOI: 10.1016/j.solidstatesciences.2017.01.009

Solid State Sciences 65 (2017) 100–109

Contents lists available at ScienceDirect

Solid State Sciences

journal homepage: www.elsevier.com/locate/ssscie

Particle size-controllable microwave-assisted solvothermal synthesis of the high-voltage cathode material $LiCoPO_4$ using water/ethylene glycol solvent blends

Jennifer Ludwig [a], Dominik Haering [b], Marca M. Doeff [c], Tom Nilges [a, *]

[a] Technical University of Munich, Department of Chemistry, Synthesis and Characterization of Innovative Materials, Lichtenbergstr. 4, 85747 Garching, Germany
[b] Technical University of Munich, Department of Chemistry, Technical Electrochemistry, Lichtenbergstr. 4, 85747 Garching, Germany
[c] Lawrence Berkeley National Laboratory, Environmental Energy Technologies Division, 1 Cyclotron Rd, 94720 Berkeley, CA, USA

ARTICLE INFO

Article history:
Received 27 October 2016
Received in revised form
9 January 2017
Accepted 23 January 2017
Available online 25 January 2017

Keywords:
Lithium cobalt phosphate
Solvothermal synthesis
Microwave synthesis
Particle size control
High-voltage cathode
Lithium-ion batteries

ABSTRACT

Particle size-tuned platelets of the high-voltage cathode material $LiCoPO_4$ for Li-ion batteries have been synthesized by a simple one-step microwave-assisted solvothermal process using an array of water/ethylene glycol (EG) solvent mixtures. Particle size control was achieved by altering the concentration of the EG co-solvent in the mixture between 0 and 100 vol%, with amounts of 0–80 vol% EG producing single phase, olivine-type $LiCoPO_4$. The particle sizes of the olivine materials were significantly reduced from about 1.2 μm × 1.2 μm × 500 nm (0 vol% EG) to 200 nm × 100 nm × 50 nm (80 vol% EG) with increasing EG content, while specific surface areas increased from 2 to 13 $m^2\ g^{-1}$. The particle size reduction could mainly be attributed to the modified viscosities of the solvent blends. Owing to the soft template effect of EG, the crystals exhibited the smallest dimensions along the [010] direction of the Li diffusion pathways in the olivine crystal structure, resulting in enhanced lithium diffusion properties. The relationship between the synthesis, crystal properties and electrochemical performance was further elucidated, indicating that the electrochemical performances of the as-prepared materials mainly depend on the solvent composition and the respective particle size range. $LiCoPO_4$ products obtained from reaction media with low and high EG contents exhibited good electrochemical performances (initial discharge capacities of 87–124 mAh g^{-1} at 0.1 C), whereas materials made from medium EG concentrations (40–60 vol% EG) showed the highest capacities and gravimetric energy densities (up to 137 mAh g^{-1} and 658 Wh kg^{-1} at 0.1 C), excellent rate capabilities, and cycle life.

1. Introduction

A practical approach to increasing specific energies in Li-ion batteries would be to replace cathode materials that are currently used with those that operate at significantly higher redox potentials. The theoretical specific energy of the phospho-olivine $LiCoPO_4$ (LCP), which is redox active at ~4.8 V *vs.* Li/Li^+ [1], is about 800 Wh kg^{-1}, compared to about 580 Wh kg^{-1} for the isostructural compound $LiFePO_4$ (LFP), which operates at ~3.45 V *vs.* Li/Li^+ [2], and is used commercially in devices for applications such as plug-in hybrid electric vehicles [3]. Successful deployment of $LiCoPO_4$, however, has proven challenging due to its low and one-dimensional ([010] direction) electronic and ionic conductivities [4–6] and the limited oxidative stability of conventional electrolytic solutions [7]. Due to these issues, LCP materials frequently demonstrate poor electrochemical performance, including low capacities, low rate capabilities and capacity fading [8–11].

In addition to chemical doping [5,6] and coating with conductive carbon [12,13] to address the conductivity issues, synthetic methods that result in particle size reduction and good morphology control to improve the kinetics have been attempted [14]. The latter approach mainly involves kinetically controlled soft-chemical synthesis methods, including hydrothermal [15–17], solvothermal [18–21], sol-gel [22,23], and polyol [24,25] techniques. In solvothermal synthesis, for instance, the solvent composition has been shown to affect the particle size [26]. However, most of these processes are combined with high-temperature annealing and

* Corresponding author.
E-mail address: tom.nilges@lrz.tum.de (T. Nilges).

http://dx.doi.org/10.1016/j.solidstatesciences.2017.01.009
1293-2558/

carbon coating steps to ensure good crystallinity and sufficient electronic conductivity of the material [17,18,26].

We have recently reported [27] a facile, one-step microwave-assisted solvothermal (MWST) route to highly crystalline LCP, which requires no additional treatments such as high-temperature annealing or carbon coating. Under optimum conditions, hexagonal platelets with the smallest dimension along [010], the direction of Li diffusion in the olivine crystal structure [4,6], are formed using a binary 1:1 (v:v) water/ethylene glycol (EG) solvent. The tuned crystal properties result in very good electrochemical performance (137 mAh g^{-1} at 0.1 C rate, using realistic active material loadings of 4–5 mg cm^{-2} in the composite electrodes). These promising results and the advantages of the microwave synthesis technique, which include extremely short reaction times and more uniform reaction conditions with lower temperature gradients resulting in monodisperse particles with controlled particle size range [27–32], prompted us to investigate this approach further to determine if we could further improve the electrochemical properties of LCP. In this work, we report the effect of the composition of binary water/ethylene glycol solvent mixtures on the structure, particle size and morphology, and electrochemical performance of LCP materials made by microwave-assisted solvothermal synthesis.

2. Experimental

2.1. Microwave-assisted solvothermal synthesis

$LiCoPO_4$ powders were synthesized by a microwave-assisted solvothermal (MWST) process [27] using 0.944 g $LiOH \cdot H_2O$ (Bernd Kraft, ≥ 99.0%), 2.108 g $CoSO_4 \cdot 7\ H_2O$ (Chempur, 99%), and 0.865 g (0.506 mL) H_3PO_4 (AppliChem, *Ph. Eur.*, 85 wt% solution) in a molar ratio of Li:Co:P = 3:1:1, and 0.075 g ascorbic acid (Alfa Aesar, 99+%) as reducing agent to prevent oxidation of Co^{2+} to Co^{3+} in the aqueous solution. The two additional equivalents of Li are required to bind the SO_4^{2-} ions in the reaction. The reactants were dispersed in 30 mL of various water/ethylene glycol solvent mixtures (H_2O: Millipore water type I, 18.2 MΩ · cm; EG: VWR AnalaR NORMAPUR, 99.9%). The EG concentration was varied in the range of 0–100 vol% with an increment step of 10 vol% while keeping all other parameters constant in order to ensure reliable and comparable results. In the following, the samples are designated LCP-0, LCP-10, (…), LCP-100, corresponding to the amount of EG in vol% (v:v) used in the solvent.

The resulting violet reaction mixtures (pH ~ 5.0) were homogenized and then transferred into 75 mL PTFE/TFM vessels (HTV-75, MLS GmbH). The synthesis was performed at 250 °C for 30 min using an Ethos One microwave system (MLS) equipped with an MR-8 HT high-temperature rotor. The system was operated at a maximum power of 600 W, and the microwave irradiation was adjusted automatically by the T660 temperature control unit. After the microwave treatment, the vessels were naturally cooled down. The pH of the solutions was 5.0–5.5. The products, which exhibited colors ranging from light pink to dark blue (detailed image see supplementary material, Fig. S1), were collected by filtration. The powders were washed several times with deionized water and absolute ethanol (VWR BDH PROLABO AnalaR NORMAPUR, 99.95%) and dried in air at 150 °C for 12 h.

2.2. Materials characterization

2.2.1. X-ray powder diffraction (PXRD) and Rietveld refinements

A Stoe STADI P diffractometer (Mo $K_{\alpha 1}$ radiation, $\lambda = 0.70930$ Å; Ge (111) monochromator; Dectris MYTHEN DCS 1 K silicon solid-state detector) was used to collect PXRD data of the ground powders, which were sealed in 0.5 mm capillaries (Hilgenberg, borosilicate glass, wall thickness: 0.01 mm). The measurements were performed in a 2θ range of 3–60° (PSD step: 0.015°; time/step: 30 s, 3 ranges, measurement time: 12 h). The data were calibrated using an external Si standard ($a = 5.43088$ Å). Rietveld refinements of the diffraction patterns were performed with the Jana2006 software [33] using the olivine crystal structure model (space group *Pnma*, ICSD database entry no. 247497 [34]). In order to ensure that the data were comparable, the same set of parameters was applied for all refinements. The background was fitted using a Chebyshev polynomial (35 coefficients), and peak asymmetry was corrected using the axial divergence model [35]. In addition, an absorption correction was applied (packing fraction: ~0.6). General atomic positions as well as the isotropic thermal displacement parameters of Co, P, and O were refined without restraints, whereas the parameters of Li were kept fixed due to its low atomic scattering factor. More realistic standard deviations were obtained by applying the Berar's correction [36].

2.2.2. Elemental analysis

Atomic absorption spectroscopy (Varian AA280FS sequential device) and photometry (Shimadzu UV-160 device) were used to analyze the Li, Co, and P contents. A Hekatech Euro EA CHNSO combustion analyzer was used to determine the C, H, N, and S contents.

2.2.3. Scanning electron microscopy (SEM)

The morphology of the powders was examined by high-resolution scanning electron microscopy (HR-SEM) on a JEOL JSM-7500 F instrument using an accelerating voltage of 1 kV, a LEI (lower electron secondary image) detector, and a working distance of 8 mm. The samples were prepared on conductive carbon tape attached to an aluminum stub.

2.2.4. Transmission electron microscopy (TEM)

A JEOL JEM-2010 transmission electron microscope (LaB_6 cathode, max. resolution: 0.2 nm) was used at 160 kV to perform selected area electron diffraction (SAED) experiments. Ethanolic dispersions of the powders were dried on 200 mesh carbon film for sample preparation.

2.2.5. BET surface area analysis

The specific surface areas were measured by the Brunauer–Emmett–Teller (BET) method on a Quantachrome Autosorb iQ device using N_2 physisorption after a degassing period of 12 h at 423 K (11 measurement points).

2.2.6. Rheometry

The dynamic viscosities of the H_2O/EG solvent mixtures containing 0–100 vol% (v:v; increment step: 10 vol%) EG were measured at 25 °C using an MCR 302 Anton Paar Modular Compact Rheometer in parallel plate–plate geometry (PP-50 plate, diameter: 49.991 mm, gap: 0.250 mm). 10 mL of the solvent blends were prepared using a Brand Transferpette S (1–10 mL, error: ≤ ± 0.6%). A sample volume of ~0.5 mL was used for each measurement. Per solvent mixture, six measurements were performed in a shear rate range of 1–120 s^{-1} (40 measurement points, time/measurement: 10.2 s); the average viscosity was determined at a shear rate of 100 s^{-1}.

2.2.7. Electrochemical measurements

The electrochemical properties of electrodes made from the as-obtained LCP powders were tested using Swagelok cells with Li foil (Rockwood Lithium, 450 μm, battery grade, > 99.8%) as anode, two glass fiber separators (VWR, 691, 250 μm), and 80 μL electrolyte (1 M $LiPF_6$ in ethylene carbonate (EC)/dimethyl carbonate (DMC), 1:1

(w:w), Merck, LP30). The electrodes were prepared by mixing the LCP powders with conductive carbon (Super C65, Timcal), polyvinylidene difluoride (PVDF, Kynar HSV 900, Arkema) and *N*-methyl-2-pyrrolidone (NMP, Sigma Aldrich) in a 80:10:10 wt% ratio followed by homogenization with a Thinky planetary centrifugal vacuum mixer (2000 rpm, 20 min). The mixture was spread on Al foil (15 μm, MTI) with a doctor-blade coater. Electrodes with a diameter of 10 mm and loadings of 4–5 mg cm^{-2} were cut out, pressed (KBr press, PerkinElmer) and dried at 120 °C for 2 h in a vacuum oven (Büchi B-585). The cells were assembled in a glove box (MBraun; Ar atmosphere, < 0.1 ppm H_2O, < 0.1 ppm O_2). Galvanostatic cycling was performed in a potential window of 3.5–5.2 V for three cycles each at 0.1 C, 0.2 C, 0.5 C, 1 C, and 2 C to test the C-rate capability, followed by 15 cycles at 0.5 C to evaluate the cycle life. The C rates were calculated from the theoretical capacity (167 mAh g^{-1}), neglecting a minor Li_2SO_4 impurity, which does not does not affect the electrochemical performance as shown in our previous work [27]. The potentiostatic step during CCCV (constant-current, constant-voltage) charging was limited to a current of 0.05 C. To ensure reproducibility, two cells per material were tested.

3. Results and discussion

3.1. X-ray powder diffraction

Fig. 1 shows the X-ray powder diffraction patterns of the samples LCP-0–LCP-80 prepared from the MWST process using concentrations of 0–80 vol% ethylene glycol in the binary solvent. The diffraction patterns can be fitted to the olivine crystal structure model (space group *Pnma*) [34] with overall excellent reliability factors (Figs. S2a–i), and no crystalline impurities were observed. (Note that the background observed in the PXRD patterns in Fig. S2 can be both attributed to the capillary used for the measurement and an amorphous Li_2SO_4 impurity as shown in our previous work [27].) The refined lattice parameters and cell volumes (Table S1) are comparable and in good agreement with reported values [27,30,37]. Considering the three sigma rule, there is evidence for a slight increase of the cell volume for samples made with higher EG concentrations. Although the narrow diffraction peaks suggest that all materials are highly crystalline as obtained from the MW synthesis without post-calcination, the increase of *V* with increasing amounts of EG in the solvent indicates that these products may have defects. The refinement of the occupancies, however, did not suggest Li-deficiencies or disordered structures. Consequently, the occupancy factors of all atomic sites were set to 1 and no site-mixing was assumed. Detailed crystal data (atomic coordinates, isotropic thermal displacement parameters, interatomic distances) are displayed in Tables S3 and S4.

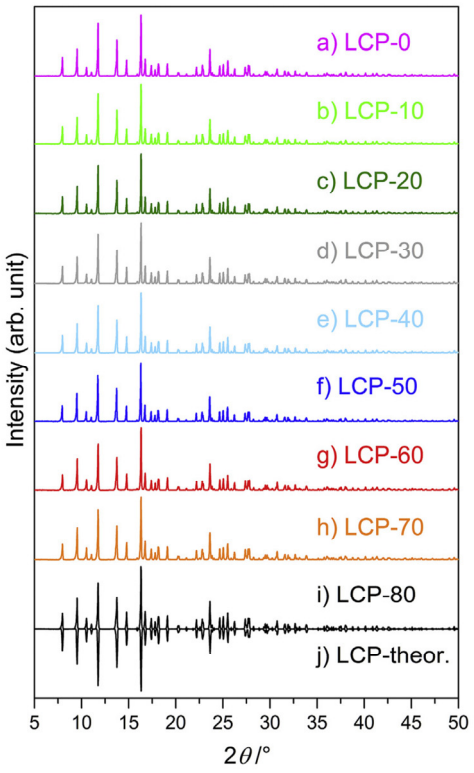

Fig. 1. X-ray powder diffraction patterns (Mo $K_{\alpha 1}$ radiation) of LCP powders obtained from MWST synthesis using increasing concentrations of EG (0–80 vol%) as co-solvent in a binary mixture with water: (a) LCP-0, (b) LCP-10, (c) LCP-20, (d) LCP-30, (e) LCP-40, (f) LCP-50, (g) LCP-60, (h) LCP-70, and (i) LCP-80. The theoretical pattern of LCP (*Pnma*) based on ICSD database entry no. 247497 [34] is displayed mirrored in (j).

Interestingly, the sample made with 90 vol% EG (LCP-90; *cf.* Fig. S2j, Table S2) contains a mixture of 87.4(4) wt% olivine LCP (*Pnma*) and 12.6(4) wt% of another, metastable LCP polymorph ($Pna2_1$ [38]), while LCP-100 is pure $Pna2_1$-LCP (not shown). The observation that at high EG contents, the metastable $Pna2_1$-modification is obtained, is consistent with another report [26] and indicates that the solvent significantly affects the phase formation during the solvothermal synthesis. A possible explanation is that diffusion plays a major role in the crystallization of the olivine phase during the process. In solvents with high EG contents, the viscosity and the boiling point of the mixture are increased (as discussed later in section 3.4), resulting in slower diffusion rates and reaction kinetics. Another possibility might be the decreased solubility of the precursors in solvent mixtures which contain less water [39]. Therefore, due to kinetic reaction control, the formation of the metastable product ($Pna2_1$-LCP) is favored over the thermodynamic product (*Pnma*-LCP). As the $Pna2_1$-LCP polymorph reportedly shows poor electrochemical performance [38,40], this work will mainly focus on the electrochemically active, pure olivine materials LCP-0–80. A structure redetermination and thorough investigation of the formation and material properties of the $Pna2_1$ polymorph of $LiCoPO_4$ based on the material LCP-100 is presented in another study [41].

3.2. Elemental analysis

The elemental compositions of the samples were analyzed by CHNS, AAS, and photometry. The results for LCP-0–80 are displayed in Table 1 (LCP-90: Table S5, LCP-100: reference [41]). While all the samples are slightly deficient both in Co and P compared to the theoretical values, with the deficit increasing as more EG was used in the synthesis, the Li content increases. The excess of Li is more evident when considering the molar ratios *n*(Li):*n*(P) and *n*(Co):*n*(P). Whilst the Co:P ratios are close to the expected ratio of 1:1 for all samples, the Li:P ratios range from 0.99(2):1 (LCP-0) to 1.22(2):1 (LCP-80). Taking the respective standard deviations into account, the observed rise in Li contents is significant.

The variation in Li contents can be explained by taking the CHNS analyses into consideration. Whilst no hydrogen and carbon are detected, which could be attributed to entrapped water or residues of the organic EG solvent and/or ascorbic acid reductive, substantial amounts of S are found, which increase linearly with higher vol% EG, similarly to the Li contents. As discussed in our previous work

Table 1
Elemental composition of the LCP samples synthesized by the MWST process using increasing concentrations of the co-solvent EG (0–80 vol%) in binary mixtures with water in comparison with the theoretical values.[a,b]

Element	Theor.	LCP-0	LCP-10	LCP-20	LCP-30	LCP-40	LCP-50	LCP-60	LCP-70	LCP-80
S (wt%)	0	0.3(3)	0.5(3)	0.8(3)	0.9(3)	1.1(3)	1.4(3)	1.8(3)	2.1(3)	2.3(3)
Li (wt%)	4.3	4.1(1)	4.3(1)	4.4(1)	4.3(1)	4.3(1)	4.2(1)	4.6(1)	4.6(1)	4.8(1)
Co (wt%)	36.6	35.9(5)	35.6(5)	34.7(5)	34.8(5)	34.6(5)	34.1(5)	33.8(5)	33.4(5)	33.5(5)
P (wt%)	19.3	18.6(3)	18.5(3)	18.5(1)	18.2(3)	18.2(3)	17.9(3)	17.7(3)	17.5(3)	17.5(3)
n(Li):*n*(P)	1	0.99(2)	1.04(2)	1.06(2)	1.05(2)	1.05(2)	1.05(2)	1.16(3)	1.18(2)	1.22(2)
n(Co):*n*(P)	1	1.02(1)	1.01(1)	0.99(1)	1.00(1)	1.00(1)	1.00(1)	1.00(1)	1.01(1)	1.01(1)
Li_2SO_4 (wt%)[c]	0	0.9(10)	1.9(10)	2.8(10)	2.9(10)	3.9(10)	4.6(10)	6.2(10)	7.1(10)	7.9(10)
$LiCoPO_4$ (wt%)[d]	100	96.3(16)	96.1(16)	95.9(16)	94.5(16)	94.6(16)	92.8(16)	92.0(16)	90.6(16)	90.9(16)

[a] The composition is determined from the experimental results in wt% (standard deviations are given in parentheses).
[b] The C, H, and N contents were too low to be measured in all samples (= 0).
[c] Calculation based on the moles of S and the surplus of Li found.
[d] Calculation based on the moles of P found.

[27], the excess of Li and all of the detected S result from a minor Li_2SO_4 impurity, which is formed as an amorphous side product in the MWST reaction. The estimated Li_2SO_4 contents are found to be very low (*i.e.* not significant) for products obtained from water-rich solvents (*e.g.* 0.9(10) wt% for LCP-0) and continuously increase (Fig. S3) to rather high fractions for products obtained from EG-rich media (*e.g.* 7.9(10) wt% for LCP-80). This is also consistent with the observed Li:P molar ratios. An explanation for this is that Li_2SO_4 is a water soluble compound [42]. Therefore, when equal moles of $LiCoPO_4$ and Li_2SO_4 are formed in the reaction, the major portion of lithium sulfate is dissolved in the aqueous phase of the solvent. Residues on the surface of the particles are further removed by the washing step with water, while a minor fraction is found to form inclusions that cannot be leached out [27]. With increasing EG concentrations and less water, the solubility of Li_2SO_4 in the solvent blend during the reaction is decreased. As a result, more Li_2SO_4 inclusions emerge in the particles upon crystallization. The fraction of the olivine active material is reduced to ~90 wt% for samples containing more Li_2SO_4 (*cf.* LCP-70, LCP-80).

3.3. Scanning electron microscopy

Fig. 2 shows the SEM images of the samples LCP-0–LCP-80 prepared using different amounts of EG in the solvent blend. The samples obtained from hydrothermal synthesis (0 vol% EG, LCP-0, Fig. 2a) and 10 vol% EG (LCP-10, Fig. 2b) exhibit irregular morphologies that vary from square platelets with a wide dimension range of about 0.5–1.2 μm × 0.5–1.2 μm and thicknesses of 150–500 nm to cubic shapes (~1 μm × 1 μm × 1 μm), some of the crystals being intergrown. Higher portions of EG (20–40 vol%), corresponding to the materials LCP-20, LCP-30, and LCP-40 (Fig. 2c–e), result in square platelets with edge lengths in the range of ~0.8–1.2 μm. With increasing EG concentration, the particle size distributions become more homogeneous and the base areas are marginally reduced. Moreover, the edges of the square base areas appear rounder (*cf.* LCP-40). The thickness of the platelets is reduced from about 150 to 500 nm (LCP-20) to a uniform 100 nm (LCP-40). Whereas a very small portion of 10 vol% EG has no significant impact on the particle size and morphology in comparison to the pure hydrothermal product LCP-0, moderate amounts up to 40 vol% EG help to prevent agglomeration and intergrowth of crystals, and reduce the thickness of the platelets. When the EG amount is raised to 50 vol% (LCP-50), corresponding to a 1:1 ratio (v:v), uniform hexagonal platelets of ~800–900 nm in length, 500–550 nm in width, and 130–180 nm in thickness (Fig. 2f) are produced as observed in our previous work [27]. At higher EG contents of 60–80 vol%, hexagonal platelets with overall smaller dimensions ranging from ~250 to 400 nm × 100–150 nm × 70 nm (LCP-60) to ~200–300 nm × 100–150 nm × 50–60 nm (LCP-80) and narrow particle size distributions were obtained (Fig. 2g–i). The overall size reduction with increasing EG concentration is in stark contrast to the fact that for LCP-20–40, primarily only the thickness is decreased. When comparing the hexagonal platelets to the ones obtained in 50 vol% EG, it is notable that the aspect ratio (length/width) of the base areas changes from approximately 1.6 (LCP-50) to about 2 (LCP-80). The particle size is further decreased for the non-olivine samples LCP-90 (Fig. S4) and LCP-100 [41].

Detailed images of broken crystals of LCP-60–80 at higher magnification (Fig. 2j–l) reveal that the hexagonal platelets exhibit a system of interconnected pores (diameter: ~10–20 nm), which are more prominent at higher EG concentrations and were also observed in our previous report [27]. The pores reduce the mechanical stability of the particles, which break upon stirring and during the washing step after the synthesis. In contrast, only very few pores and less fragmentation are observed for the bigger and mechanically more stable square platelets obtained from solvents containing more water (LCP-0–40). Here, the damage is more likely the result of the break-up of intergrown crystals. This finding is confirmed by TEM studies discussed later. The pores are the consequence of the formation mechanism, in which $LiCoPO_4$ and $Li_2SO_4 \cdot H_2O$ are obtained [27]. In mixtures with higher EG concentrations, the solubility of $Li_2SO_4 \cdot H_2O$ is decreased and a smaller amount dissolved. Hence, the composite crystals contain more Li_2SO_4 inclusions upon crystallization, which is in good agreement with the linearly increasing amounts of S found by CHNS analysis (*cf.* Table 1; Fig. S3). The pores observed on the breaking edges of fragmented particles (Fig. 2j–l) are due to the removal of the inclusions upon washing. As the major portion of inclusions remains within the particles, the results of the elemental analysis are representative for the bulk materials.

The SEM studies reveal that primarily, the particle size and to a minor extent, the morphology of the crystals are affected by the solvent composition. The particle size and/or thickness is reduced at higher EG concentrations in the H_2O/EG solvent. At the same time, the morphology evolves from cubes and square platelets to hexagonal platelets.

3.4. BET surface area analysis

As expected from the SEM images, BET measurements deliver comparatively small specific surface areas for the materials LCP-0–80, which increase with increasing amounts of EG in the mixed H_2O/EG solvent (Fig. 3a). The samples LCP-0–LCP-30 show very similar small values of ~2–3 $m^2\ g^{-1}$, indicating that the corresponding EG concentrations between 0 and 30 vol% have little

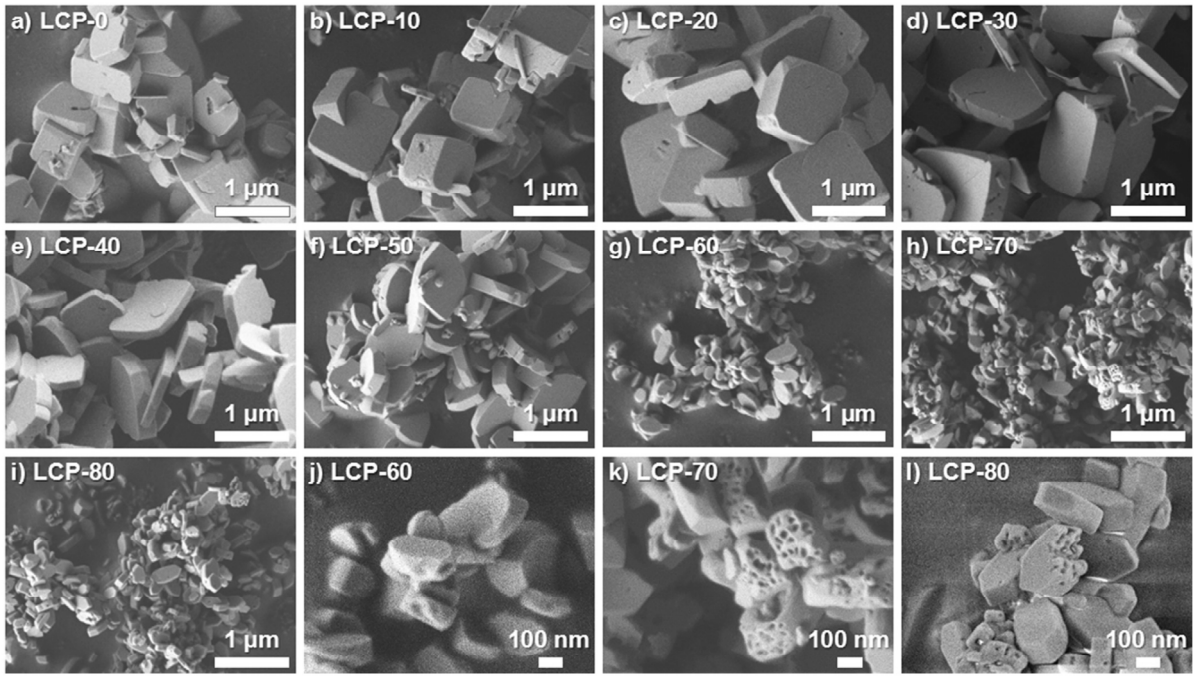

Fig. 2. SEM images of the LCP samples obtained from MWST synthesis using increasing concentrations of EG (0–80 vol%) in binary H_2O/EG solvent blends: (a) LCP-0, (b) LCP-10, (c) LCP-20, (d) LCP-30, (e) LCP-40, (f) LCP-50, (g, j) LCP-60, (h, k) LCP-70, and (i, l) LCP-80.

effect on the particle size and thus, the surface area. For EG amounts between 40 vol% and 80 vol%, the surface areas are increased by a factor of two (LCP-40: ~4 $m^2\ g^{-1}$) to six (LCP-80: ~13 $m^2\ g^{-1}$) compared to the sample obtained from a pure water solvent (LCP-0: ~2 $m^2\ g^{-1}$). Significantly higher surface areas up to ~61 $m^2\ g^{-1}$ are obtained for the non-olivine materials LCP-90 and LCP-100 (the latter are discussed in another study [41]). The correlation between BET surface areas and EG concentration is consistent with what has been observed previously for $LiMnPO_4$ [43].

Another interesting observation is that the colors of the powders (ranging from light pink for LCP-0 to dark blue for LCP-100; Fig. 3b), are related to the particle size and respective BET surface areas, as well as the structure. The color of the olivine samples LCP-0–80 is getting lighter for bigger surface areas, and hence, smaller particles, which is in line with a previous study of our group [44]. For the non-olivine samples LCP-90 and LCP-100, the blue color is caused by the presence of the metastable $Pna2_1$-polymorph of LCP, which exhibits a dark blue color [38,41] due to the occurrence of a tetrahedral [CoO_4] chromophore in the structure as opposed to the octahedral [CoO_6] unit in the *Pnma*-LCP olivine.

Plotting the measured dynamic viscosities of the solvent mixtures, which are in good agreement with reported values [45,46], versus the EG contents (Fig. 3c) reveals that the viscosities follow a similar exponential increase as the BET surface areas (Fig. 3a). Therefore, the increase in surface area and *vice versa* the decrease in particle size are highly correlated with the increasing viscosities of the solvents containing more of the EG co-solvent. An explanation for the key role of the EG concentration in tuning the particle size is that, because EG has a higher viscosity than water (EG: 15.7(2) mPa · s *vs.* H_2O: 0.89(5) mPa · s in our experiment at 25 °C), the ion diffusion rate in the solvent is reduced upon crystallization, which impedes the growth of large particles [39,47]. Furthermore, the solubility of the precursors in the solvent is reduced compared to pure water [39], resulting in a higher degree of supersaturation in EG-rich media. Hence, nucleation is favored over growth processes during crystal formation, which leads to the formation of smaller particles.

However, it has to be noted that the viscosities were measured at ambient temperature and not the reaction temperature (250 °C), which is above the boiling points of the mixtures [48] (*cf.* boiling point of pure EG: 198 °C [49]). Because the viscosity of the mixtures decreases with increasing temperature [46], and the particle size is more effectively regulated in mixtures that contain more EG, the size-regulating effect seems to play a major role in the precipitation step before the microwave-synthesis and the heat-up phase of the reaction, at which the solvents are still liquid. We therefore infer that the nucleation step is the most important with regard to controlling the crystal size by using binary aqueous solvents.

The solvent viscosity–BET surface area relation demonstrates that adjusting the viscosity of the solvent by varying the composition is a simple way to produce materials with tailored particle size using solvothermal synthesis, and also to predict the surface areas. The opportunity to modify this material property, which is crucial for the electrochemical performance of active materials in general, by a single synthesis parameter is of high interest for the commercial production of a variety of materials.

3.5. Transmission electron microscopy

The representative samples of the series LCP-0, LCP-30, LCP-50, and LCP-80 were further characterized by TEM (transmission electron microscopy) and SAED (selected area electron diffraction) to examine the crystal orientations and thicknesses as well as to gain further insights into the crystal formation and growth. To

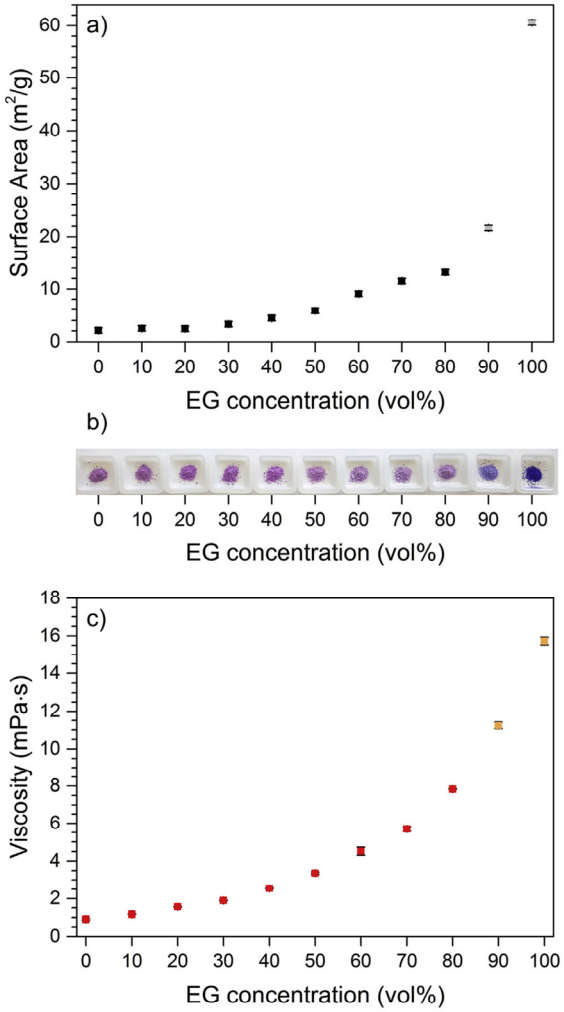

Fig. 3. (a) Specific surface areas of the LCP samples obtained from MWST synthesis versus the EG concentrations (0 100 vol%) used in the H_2O/EG solvent mixture, (b) color range of the as-obtained LCP powders, and (c) measured dynamic viscosities of the mixed solvents (average from six measurements, $T = 25$ °C, shear rate: 100 s^{-1}; error bars are smaller than data points where not visible). The data points of LCP-90 and LCP-100, which contain non-olivine LCP and are discussed in another report [41], are highlighted in different colors (grey, orange) in (a, c). (For interpretation of the references to colour in this figure legend, the reader is referred to the web version of this article.)

ensure that all crystals of a material are oriented identically, SAED patterns of five to six individual crystals were taken for each material. In addition, patterns of perpendicular crystal faces were collected. The respective TEM images and SAED patterns are presented in Fig. 4.

In general, the particle sizes and morphologies observed in the TEM images are in good agreement with the SEM studies. All the platelets are highly crystalline single crystals that are grown along the *ac* plane and show the smallest dimensions along the *b* axis, which is in the direction of the lithium diffusion pathways. Furthermore, the pore structures or Li_2SO_4 inclusions within the particles observed in the SEM (*cf.* Fig. 2i, k, l) are confirmed by the irregular transmission of the particles and are also more

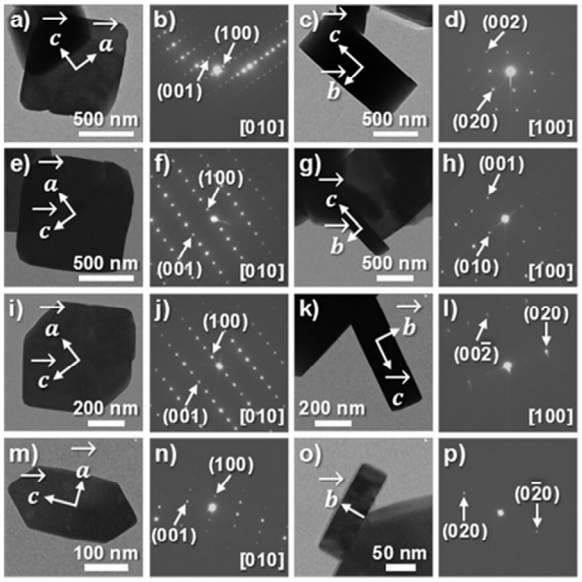

Fig. 4. TEM images and corresponding SAED patterns of the LCP samples synthesized by the MWST technique using various concentrations of EG (in vol%) as co-solvent in a mixture with water: (a–d) LCP-0, (e–h) LCP-30, (i–l) LCP-50, (m–p) LCP-80. Perpendicular crystal faces are displayed for each sample.

pronounced for higher EG contents (LCP-50 and LCP-80, Fig. 4i, m, o). The samples LCP-0 and LCP-30 consist of crystals with a square platelet morphology with the *a* and *c* axes being oriented along the diagonals of the base areas (Fig. 4a, e). The dimensions in the *ac* plane are similar (~1 μm × 1 μm), but the dimension along [010] is reduced from approximately 600 nm to about 250 nm with the use of 30 vol% EG (Fig. 4c, g). In contrast, the hexagonal platelets of LCP-50 and LCP-80 show different dimensions in the base areas as well as the thicknesses. The particles of LCP-50 exhibit dimensions of ~800 nm × 600 nm × 180 nm (Fig. 4i, k), while the platelets of LCP-80 are significantly smaller with a reduced size of ~300 nm × 150 nm × 50 nm (Fig. 4m, o). In both cases, the *c* axis is oriented along the longer side of the hexagonal base areas, the hexagonal shape of LCP-80 being elongated along [001].

The TEM studies reveal that the EG co-solvent not only plays a key role in controlling the particle size by its higher viscosity compared to water (*cf.* Fig. 3c). It also helps to promote the growth of crystals with defined morphology and orientation [43,50]. An explanation for the anisotropic crystal properties is the soft template effect of the solvent [47]. EG molecules adsorb on the surface of the LCP nanocrystals by forming hydrogen-bonds between the hydroxyl groups and the oxygen atoms on the surface on the crystals, altering the surface energies of crystal faces. For $LiMnPO_4$, it was reported [43] that the EG molecules preferentially adsorb on the (100) planes, then the (010) planes, and the least favorable, the (001) planes, resulting in limited particle growth rates along the [100] and [010] directions compared to [001]. This is consistent with our observation that the platelets show a higher aspect ratio (*i.e.* elongation along *c*) for solvents containing more EG, but also with the reduction of the particle thickness along [010] [43]. Because Li-ion conduction in the olivine crystal structure is anisotropic, the reduced particle dimensions of our materials in the [010] direction are expected to significantly enhance Li diffusion and thus, the electrochemical performance.

3.6. Electrochemical characterization

The olivine materials LCP-0–80 were tested in Swagelok half-cells without further processing (*e.g.* annealing, carbon coating). The specific discharge capacities and respective coulombic efficiencies at different C rates are displayed in Fig. 5. The corresponding galvanostatic curves can be found in Fig. S5. For better comparison of the trends in the test series, the first discharge capacity obtained at each C rate is displayed in Fig. 5a for the various cells. Generally, no obvious correlation of the performance with the particle size and thickness along [010] can be deduced. One would expect an increase in absolute capacities and C rate capabilities with decreasing [010] dimension due to shortened Li diffusion pathways, *i.e.*, the lowest value for LCP-0 (~600 nm, Fig. 4c) and the highest for LCP-80 (~50 nm, Fig. 4o). Instead, the following trends are observed at every C rate, with the capacity decreasing at higher rates (Fig. 5a): (1) LCP-0 and LCP-10 deliver low performances, (2) good to average performances are observed for LCP-20, LCP-30, LCP-60, LCP-70, and LCP-80, and (3) the best performance of the series is achieved for the samples LCP-40–60.

The relatively low capacities of LCP-0 and LCP-10 at both low (87 mAh g^{-1} and 116 mAh g^{-1} at 0.1 C) and high rates (Fig. 5b) can be explained by the large particle sizes (>1 μm) and large dimensions along the [010] Li diffusion pathway (150–500 nm) as well as the inhomogeneous shapes (platelets, cubes) and particle sizes in both materials. Nevertheless, the performance of the hydrothermal sample LCP-0 is still better than that of other hydrothermally synthesized $LiCoPO_4$ samples [17,29], probably due to the improved crystallinity, which is the result of the microwave irradiation used for the synthesis [30]. The effect of decreasing the [010] dimension from ~150 to 500 nm (LCP-20) to ~100 nm (LCP-40) is reflected in the increase in discharge capacity from 119 mAh g^{-1} to 137 mAh g^{-1} at 0.1 C. Moreover, these materials show more uniform particle sizes and morphologies compared to LCP-0 and LCP-10. The highest capacities at every rate and best coulombic efficiencies are achieved for the hexagonal platelets of LCP-50. The value of 136 mAh g^{-1} at 0.1 C corresponds to a gravimetric energy density of 653 Wh kg^{-1} (based on its capacity and discharge potential of 4.8 V). LCP-40 reaches a capacity of 137 mAh g^{-1} at 0.1 C (energy density of 658 Wh kg^{-1}), but exhibits a lower rate capability. Both results are among the best results for LCP so far [21,26,30,32], and comparable to our previous work [27]. This is surprising as the particles exhibit bigger dimensions (~130–180 nm) in the [010] Li diffusion direction compared to LCP-60–80 (~50–70 nm). Unexpectedly, these samples with the smallest and most homogeneous particles as well as the smallest dimension along [010] are not the best performing of the series, suggesting that there is no linear correlation with the particle size or [010] dimension, which is reflected by the somewhat lower initial discharge capacities (122–131 mAh g^{-1} at 0.1 C) and C rate capabilities. Because LCP is electrochemically active above 4.6 V, side reactions involving the oxidation of the electrolyte [7,9] upon charging have to be taken into account. These reactions compete with the (de)intercalation reaction of LCP since the decomposition products of the electrolyte are likely to form resistive films on the particle surface that impede Li diffusion [51]. As electrolyte oxidation at high voltage is estimated to be proportional to the BET surface area [27], the high specific surface areas of the materials LCP-60–80 (~9–13 m^2 g^{-1} *vs.* ~4–6 m^2 g^{-1} for LCP-40 and LCP-50) exacerbate these side reactions, resulting in poorer performance and lower coulombic efficiencies (Fig. 5b and c). This finding strongly contrasts the general assumption [13,52] that particle size reduction helps to improve the electrochemical performance. Consequently, due to increased side reactions, the particle size reduction is not necessarily beneficial to performance, particularly for high-voltage materials. Also note that the performances cannot be directly correlated with the contents of the Li_2SO_4 side phase, which rise linearly with increasing EG concentration used for the synthesis (*cf.* Table 1 and Fig. S3). This is in line with previous

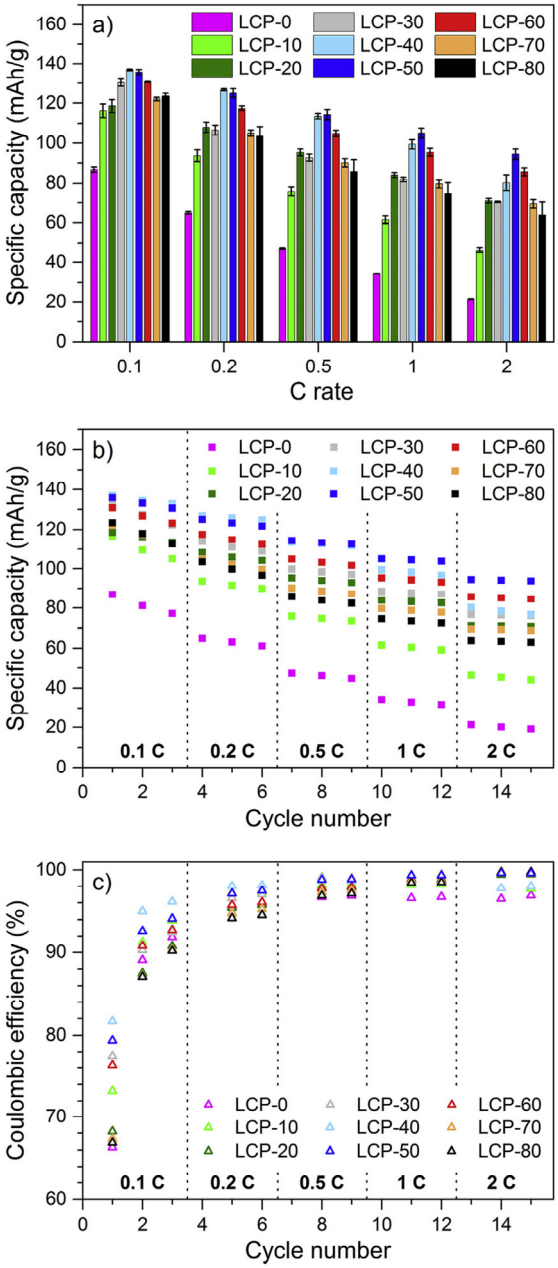

Fig. 5. (a) Specific discharge capacities *vs.* C rate for the 1st cycle of each C rate (error bars represent standard deviations from two cells), (b) specific discharge capacities *vs.* C rate for the first three cycles at each C rate, and (c) coulombic efficiencies for the LCP samples made by the MWST process using increasing amounts of EG (0–80 vol%). The efficiencies of the 1st cycle after each C rate increase are omitted in (c) as they cannot the determined in these cases. All data points present the average values from two cells. Data points which are not visible are overlapped by other symbols. The error bars in (b, c) are omitted for clarity. Conditions: 1 M $LiPF_6$ in EC:DMC (1:1, w:w) at 25 °C.

results [27], which suggested that the impurity does not affect the electrochemical performance and is electrochemically inactive.

Following the C rate test, the cycle life of the LCP electrodes was tested for 15 cycles at a 0.5 C discharge rate (Fig. 6). The total capacities (Fig. 6a), capacity retentions, and coulombic efficiencies (Fig. 6b) follow the same trends as observed in the rate capability tests at higher C rates (*cf.* Fig. 5a and b, cycles 10–15), with the minimum being reached for LCP-0, and the maximum for LCP-40 and LCP-50. Despite the variation in capacity, the samples LCP-20–80 show an excellent electrochemical stability, which is among the best performances reported as LCP materials have been shown to suffer from poor cycling stability [7,10]. The cycle life of the best-performing materials in terms of absolute capacity, LCP-40 and LCP-50, however, differs greatly. While LCP-50 with a specific capacity of 101 mAh g^{-1} maintains 94% of its original value in the 15th cycle, LCP-40 shows rapid fading and only reaches a capacity of 73 mAh g^{-1} (79%), which is only the fourth best value of the sample series. The deviant cycle life may be the consequence of different particle size ranges, thicknesses along [010], and crystal shapes. The influence of the shape is further supported by the fact that capacity fading is faster for samples with a square platelet morphology (LCP-0–40) than for materials that contain hexagonal shapes (LCP-50–80).

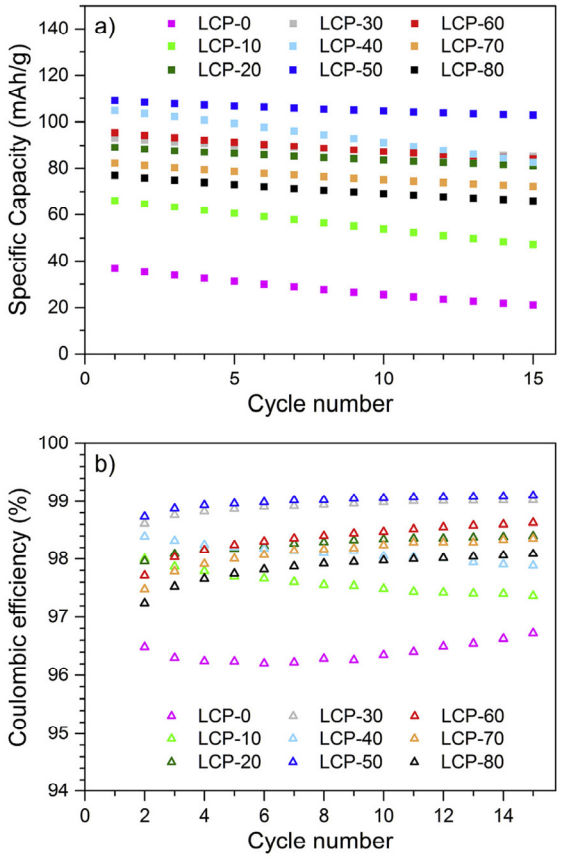

Fig. 6. Comparison of the (a) electrochemical stabilities and (b) coulombic efficiencies of the LCP samples prepared by MWST synthesis using increasing amounts of EG (0–80 vol%) at 0.5 C after the first 15 cycles of C rate testing. The data present the average values from two cells, the error bars are omitted for clarity. The coulombic efficiencies of the 1st cycle are not shown as they cannot be determined due to the C rate change before the cycle life test. Conditions: 1 M $LiPF_6$ in EC:DMC (1:1, w:w) at 25 °C.

In brief, the electrochemical performance is the result of superimposed effects such as crystallite size, particle shape, and thickness in the [010] direction of the Li diffusion pathways. Consequently, a straightforward explanation for the observed trends cannot be deduced from our current findings. The results, however, indicate that with the exception of LCP-0 and LCP-10, all the samples synthesized in solvents with medium EG contents and respective medium particle sizes show above-average to excellent discharge capacities, rate capabilities and cycle life because of fewer side reactions but sufficiently shortened Li diffusion pathways, the optimum being reached at 50 vol% EG. In comparison to previous reports of poor cycling stability for LCP [8–11], the cycle life was significantly improved. This suggests that in contrast to cathode materials with lower operating voltage like LFP (3.45 V *vs.* Li/Li^+ [2]) [53,54], a medium particle size range seems to be beneficial for high-voltage cathode materials such as LCP. This finding is overall consistent with reports about the influence of the particle size on the performance of other high-voltage cathode materials [55–57].

4. Conclusions

Particle size-controlled powders of the high-voltage cathode material $LiCoPO_4$ (LCP) with platelet-like morphologies have been synthesized *via* a rapid one-step microwave-assisted solvothermal route at moderate temperatures using a variety of water/ethylene glycol (EG) mixed solvents. Particle size control was demonstrated by varying the concentration of the EG co-solvent in the solvent mixtures between 0 and 100 vol% with an increment step of 10 vol %.

X-ray powder diffraction experiments reveal that highly crystalline, pure olivine-type LCP (space group *Pnma*) is obtained for EG contents between 0 and 80 vol%. At higher EG concentrations, the formation of a metastable LCP polymorph ($Pna2_1$) was observed. SEM studies indicate that, whereas at low EG amounts (0–40 vol%), the formation of square platelets or cubic crystals with inhomogeneous particle size distributions is preferred, uniform hexagonal platelets are formed in solvent mixtures with 50–80 vol% EG. Owing to the higher viscosity of the reaction medium with increasing EG concentrations, the particle dimensions are significantly reduced from approximately 1.2 μm × 1.2 μm × 500 nm to 200 nm × 100 nm × 50 nm in EG-rich mixtures, which is consistent with an increase in BET surface areas. According to TEM studies, EG not only exhibits a size-regulating effect, but is also a soft template which promotes the crystal growth by selective adsorption on crystal faces. As a result, all particles show the reduced dimensions along the [010] direction of the Li diffusion pathways in the crystal structure, which is beneficial to enhance the Li-ion diffusivity and thus improve the electrochemical performance.

The performance of the as-prepared LCP materials strongly depends on the solvent composition, and the respective size range and thickness of the platelets. LCP made from mixtures with low and high EG contents exhibit average specific capacities and rate capabilities, which is the result of big and inhomogeneous crystallite sizes, and increased side reactions of powders with high specific surface areas with the electrolyte at high voltage. The materials synthesized in medium EG concentrations of 40–60 vol%, on the other hand, show the highest initial discharge capacities of up to 137 mAh g^{-1} at 0.1 C, excellent rate performance, and cycle life although the materials did not undergo further treatment (annealing, coating). Our findings suggest that in contrast to cathode materials with lower operating voltage (*e.g.* LFP), a medium particle size range is the optimum for high-voltage materials such as LCP.

To conclude, the present work not only provides a simple and efficient, but also energy- and cost-saving approach towards particle size control of cathode materials by microwave-assisted synthesis. It was also shown that the electrochemical performance can be improved by simply adjusting one synthesis parameter such as the solvent composition and respective viscosity, which might be of interest for large-scale industrial manufacturing. Therefore, the influence of the solvent mixing ratio on the material properties should also be investigated for alternative co-solvents with morphology-tuning properties, such as polyols (*e.g.* diethylene glycol, triethylene glycol, tetraethylene glycol, polyethylene glycol).

Funding sources

This work was supported by BMW AG, the Fonds der Chemischen Industrie as well as the TUM Graduate School.

Author contributions

J. L. conceived and designed this work, and carried out the synthetic experiments and material characterization. D. H. performed the BET measurements and electrochemical tests. J. L. wrote the publication. All authors participated in discussion of the results and this manuscript.

Acknowledgements

The authors would like to thank BMW and the TUM Graduate School for financial support. We also thank C. Stinner and H. Gasteiger for their participation in the discussion of the results. The help of U. Ammari with elemental analyses, K. Rodewald with SEM, and M. Hanzlik with TEM measurements is gratefully acknowledged. Special thanks go to C. Marino for the help with the electrochemical measurements and for proofreading this manuscript. J. Ludwig is further grateful to the Fonds der Chemischen Industrie for her PhD fellowship.

Abbreviations

AAS	Atomic absorption spectroscopy
BET	Brunauer–Emmett–Teller
CCCV	Constant-current, constant-voltage
DMC	Dimethyl carbonate
EC	Ethylene carbonate
EG	Ethylene glycol
HR	High-resolution
LCP	Lithium cobalt phosphate, $LiCoPO_4$
LEI	Lower electron secondary image
LFP	Lithium iron phosphate, $LiFePO_4$
MWST	Microwave-assisted solvothermal
NMP	*N*-Methyl-2-pyrrolidone
PVDF	Polyvinylidene difluoride
PXRD	X-ray powder diffraction
SAED	Selected area electron diffraction
SEM	Scanning electron microscope
TEM	Transmission electron microscopy

Appendix A. Supplementary data

Colors of LCP-0–LCP-100, Rietveld fits and crystallographic data of LCP-0–LCP-90; elemental analysis of LCP-90; S and Li_2SO_4 contents *versus* EG concentration; SEM images of LCP-90; galvanostatic curves of LCP-0–LCP-80 in the first three cycles at various C rates. This material can be found at http://dx.doi.org/10.1016/j.solidstatesciences.2017.01.009. Further details of the crystal structure investigations may be obtained from FIZ Karlsruhe, 76344 Eggenstein-Leopoldshafen, Germany (Fax: +49 7247 808 666; E-mail: crysdata@fiz-karlsruhe.de), on quoting the deposition numbers CSD 432131–432140.

References

[1] K. Amine, H. Yasuda, M. Yamachi, Electrochem. Solid-State Lett. 3 (2000) 178–179.
[2] A.K. Padhi, K.S. Nanjundaswamy, J.B. Goodenough, J. Electrochem. Soc. 144 (1997) 1188–1194.
[3] W.-J. Zhang, J. Power Sources 196 (2011) 2962–2970.
[4] D. Morgan, A. Van der Ven, G. Ceder, Electrochem. Solid-State Lett. 7 (2003) A30–A32.
[5] J. Wolfenstine, J. Power Sources 158 (2006) 1431–1435.
[6] C.A.J. Fisher, P.V.M. Hart, M.S. Islam, Chem. Mat. 20 (2008) 5907–5915.
[7] M. Egashira, H. Takahashi, S. Okada, J.-I. Yamaki, J. Power Sources 92 (2001) 267–271.
[8] S. Okada, S. Sawa, M. Egashira, J. Yamaki, M. Tabuchi, H. Kageyama, T. Konishi, A. Yoshino, J. Power Sources 97–98 (2001) 430–432.
[9] N.N. Bramnik, K. Nikolowski, C. Baehtz, K.G. Bramnik, H. Ehrenberg, Chem. Mat. 19 (2007) 908–915.
[10] E. Markevich, R. Sharabi, H. Gottlieb, V. Borgel, K. Fridman, G. Salitra, D. Aurbach, G. Semrau, M.A. Schmidt, N. Schall, C. Bruenig, Electrochem. Commun. 15 (2012) 22–25.
[11] K. Zaghib, A. Guerfi, P. Hovington, A. Vijh, M. Trudeau, A. Mauger, J.B. Goodenough, C.M. Julien, J. Power Sources 232 (2013) 357–369.
[12] J. Wolfenstine, J. Read, J.L. Allen, J. Power Sources 163 (2007) 1070–1073.
[13] J. Liu, T.E. Conry, X. Song, L. Yang, M.M. Doeff, T.J. Richardson, J. Mat. Chem. 21 (2011) 9984–9987.
[14] S. Brutti, P. Reale, E. Piciollo, V. Gentili, P.G. Bruce, B. Scrosati, S. Panero, Prepr. Symp. - Am. Chem. Soc. Div. Fuel Chem. 57 (2012) 737–739.
[15] X. Huang, J. Ma, P. Wu, Y. Hu, J. Dai, Z. Zhu, H. Chen, H. Wang, Mat. Lett. 59 (2005) 578–582.
[16] J. Chen, M.J. Vacchio, S. Wang, N. Chernova, P.Y. Zavalij, M.S. Whittingham, Solid State Ionics 178 (2008) 1676–1693.
[17] M. Kotobuki, Y. Mizuno, H. Munakata, K. Kanamura, Phosphorus Res. Bull. 24 (2010) 12–15.
[18] F. Wang, J. Yang, Y. Nuli, J. Wang, J. Power Sources 196 (2011) 4806–4810.
[19] J. Su, B.-Q. Wei, J.-P. Rong, W.-Y. Yin, Z.-X. Ye, X.-Q. Tian, L. Ren, M.-H. Cao, C.-W. Hu, J. Solid State Chem. 184 (2011) 2909–2919.
[20] X. Rui, X. Zhao, Z. Lu, H. Tan, D. Sim, H.H. Hng, R. Yazami, T.M. Lim, Q. Yan, ACS Nano 7 (2013) 5637–5646.
[21] S. Brutti, J. Manzi, A. De Bonis, D. Di Lecce, F. Vitucci, A. Paolone, F. Trequattrini, S. Panero, Mat. Lett. 145 (2015) 324–327.
[22] D. Gangulibabu, N. Bhuvaneswari, N. Kalaiselvi, P. Jayaprakash, J. Periasamy, Sol-Gel Sci. Technol. 49 (2009) 137–144.
[23] M.S. Bhuwaneswari, L. Dimesso, W. Jaegermann, J. Sol-Gel Sci. Technol. 56 (2010) 320–326.
[24] P.R. Kumar, M. Venkateswarlu, M. Misra, A.K. Mohanty, N. Satyanayana, J. Nanosci, Nanotechnol. 11 (2011) 3314–3322.
[25] N. Padmanathan, S. Selladurai, Asian J. Chem. 25 (2013) 9605–9609.
[26] B. Wu, H. Xu, D. Mu, L. Shi, B. Jiang, L. Gai, L. Wang, Q. Liu, L. Ben, F. Wu, J. Power Sources 304 (2016) 181–188.
[27] J. Ludwig, C. Marino, D. Haering, C. Stinner, D. Nordlund, M.M. Doeff, H.A. Gasteiger, T. Nilges, RSC Adv. 6 (2016) 82984–82994.
[28] J.A. Gerbec, D. Magana, A. Washington, G.F. Strouse, J. Am. Chem. Soc. 127 (2005) 15791–15800.
[29] A.V. Murugan, T. Muraliganth, A. Manthiram, J. Electrochem. Soc. 156 (2009) A79–A83.
[30] A.V. Murugan, T. Muraliganth, P.J. Ferreira, A. Manthiram, Inorg. Chem. 48 (2009) 946–952.
[31] I. Bilecka, M. Niederberger, Nanoscale 2 (2010) 1358–1374.
[32] R.E. Rogers, G.M. Clarke, O.N. Matthew, M.J. Ganter, R.A. DiLeo, J.W. Staub, M.W. Forney, B.J. Landi, J. Appl. electrochem. 43 (2013) 271–278.
[33] V. Petricek, M. Dusek, L. Palatinus, Z. Kristallogr, Cryst. Mat. 229 (2014) 345–352.
[34] V. Koleva, E. Zhecheva, R. Stoyanova, Eur. J. Inorg. Chem. (2010) 4091–4099.
[35] L.W. Finger, D.E. Cox, A.P. Jephcoat, J. Appl. Crystallogr. 27 (1994) 892–900.
[36] J.F. Berar, P. Lelann, J. Appl. Crystallogr. 24 (1991) 1–5.
[37] J. Chen, S. Wang, M.S. Whittingham, J. Power Sources 174 (2007) 442–448.
[38] C. Jaehne, C. Neef, C. Koo, H.-P. Meyer, R. Klingeler, J. Mat. Chem. A 1 (2013) 2856–2862.
[39] F. Teng, S. Santhanagopalan, A. Asthana, X.-B. Geng, S.-I. Mho, R. Shahbazian-Yassar, D.D.-S. Meng, J. Cryst. Growth 312 (2010) 3493–3502.
[40] K.J. Kreder, G. Assat, A. Manthiram, Chem. Mat. 27 (2015) 5543–5549.
[41] J. Ludwig, D. Nordlund, M.M. Doeff, T. Nilges, J. Solid State Chem. 248 (2017) 9–17.
[42] W.F. Linke, A. Seidell, Solubilities of in-organic and metal organic compounds, in: Am. Chem. Soc, fourth ed., vol. II, 1966.
[43] Y. Hong, Z. Tang, S. Wang, W. Quan, Z. Zhang, J. Mat. Chem. A 3 (2015) 10267–10274.
[44] J. Ludwig, C. Marino, D. Haering, C. Stinner, H.A. Gasteiger, T. Nilges, J. Power

Sources 342 (2017) 214–223.
[45] N.G. Tsierkezos, I.E. Molinou, J. Chem. Eng. Data 43 (1998) 989–993.
[46] T. Sun, A.S. Teja, J. Chem. Eng. Data 48 (2003) 198–202.
[47] S. Kuppan, P. Balaya, M.V. Reddy, B.V.R. Chowdari, J.J. Vittal, Energy Environ. Sci. 3 (2010) 457–464.
[48] H.M. Trimble, W. Potts, Ind. Eng. Chem. 27 (1935) 66–68.
[49] S. Rebsdat, D. Mayer, Ethylene glycol, in: Ullmann's Encyclopedia of Industrial Chemistry, Wiley-VCH, 2000, pp. 531–546.
[50] X. Qin, J. Wang, J. Xie, F. Li, L. Wen, X. Wang, Phys. Chem. Chem. Phys. 14 (2012) 2669–2677.
[51] D. Aurbach, B. Markovsky, G. Salitra, E. Markevich, Y. Talyossef, M. Koltypin, L. Nazar, B. Ellis, D. Kovacheva, J. Power Sources 165 (2007) 491–499.
[52] T.N.L. Doan, I. Taniguchi, J. Power Sources 196 (2011) 5679–5684.
[53] C. Delacourt, P. Poizot, S. Levasseur, C. Masquelier, Electrochem. Solid-State Lett. 9 (2006) A352–A355.
[54] M. Gaberscek, R. Dominko, J. Jamnik, Electrochem. Commun. 9 (2007) 2778–2783.
[55] S.K. Martha, H. Sclar, Z. Szmuk Framowitz, D. Kovacheva, N. Saliyski, Y. Gofer, P. Sharon, E. Golik, B. Markovsky, D. Aurbach, J. Power Sources 189 (2009) 248–255.
[56] K.C. Karn, M.M. Doeff, Mat. Matters (Milwaukee, WI, U. S.) 7 (2012) 56–60.
[57] L. Xiao, Y. Guo, D. Qu, B. Deng, H. Liu, D. Tang, J. Power Sources 225 (2013) 286–292.

Supplementary material

Particle size-controllable microwave-assisted solvothermal synthesis of the high-voltage cathode material $LiCoPO_4$ using water/ethylene glycol solvent blends

Jennifer Ludwig [a], Dominik Haering [b], Marca M. Doeff [c], and Tom Nilges [a]*

[a] Technical University of Munich, Department of Chemistry, Synthesis and Characterization of Innovative Materials, Lichtenbergstr. 4, 85747 Garching, Germany

[b] Technical University of Munich, Department of Chemistry, Technical Electrochemistry, Lichtenbergstr. 4, 85747 Garching, Germany

[c] Lawrence Berkeley National Laboratory, Environmental Energy Technologies Division, 1 Cyclotron Rd, Berkeley, CA, 94720, USA

* Corresponding author. E-mail: tom.nilges@lrz.tum.de, Tel.: +49 89 289 13110, Fax: +49 89 289 13762

Supplementary material

1 Colors of the as-obtained $LiCoPO_4$ powders LCP-0–LCP-100

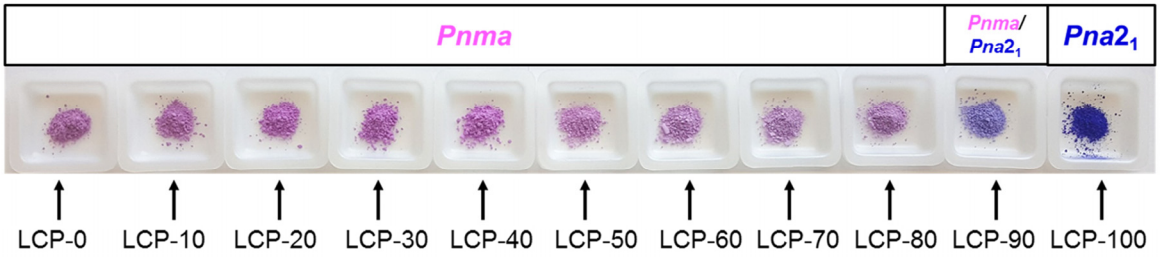

Fig. S1 Colors of the $LiCoPO_4$ samples synthesized by the microwave-assisted solvothermal technique using increasing concentrations of EG (0–100 vol%) as a co-solvent in a binary mixture with water. The color range of LCP-0–LCP-80, which contain olivine-type $LiCoPO_4$ (space group *Pnma*), can be explained by particle size effects, the violet color getting brighter and showing a more bluish cast with decreasing particle size. The color of LCP-90 and LCP-100 is due to the presence of the metastable (blue) $LiCoPO_4$ polymorph (space group $Pna2_1$).

Supplementary material

2 Rietveld refinements of the X-ray powder diffraction (PXRD) patterns of LCP-0–LCP-90

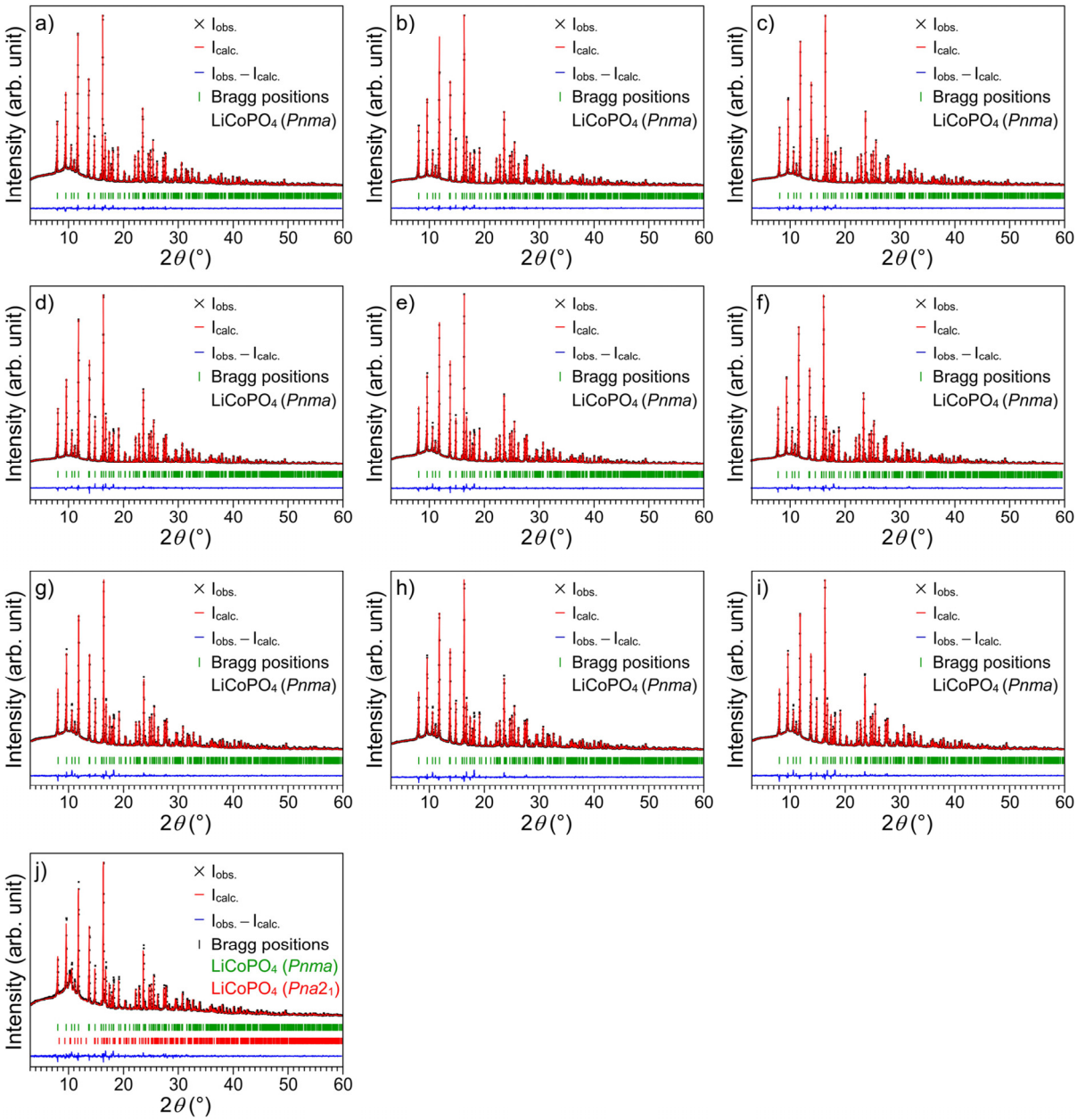

Fig. S2 Rietveld fits of the X-ray powder diffraction data of the $LiCoPO_4$ samples obtained from MWST synthesis using increasing concentrations of EG (0–100 vol%) as co-solvent in a binary mixture with water: (a) LCP-0, (b) LCP-10, (c) LCP-20, (d) LCP-30, (e) LCP-40, (f) LCP-50, (g) LCP-60, (h) LCP-70, (i) LCP-80, and (j) LCP-90. The samples LCP-0–LCP-80 contain pure olivine-type $LiCoPO_4$ (*Pnma*), whereas LCP-90 contains a mixture of the olivine (*Pnma*) and the metastable (*Pna*2_1) $LiCoPO_4$ polymorphs. Note that the background of the patterns observed in these figures can be both attributed to the capillary used for the measurement and an amorphous Li_2SO_4 impurity as shown in our previous work. [27]

Table S1 Refined crystallographic data (T = 298 K) of the $LiCoPO_4$ samples LCP-0–LCP-80 prepared by MWST synthesis using increasing concentrations of EG (0–80 vol%) in a H_2O/EG solvent mixture [a]

Sample	**LCP-0**	**LCP-10**	**LCP-20**	**LCP-30**	**LCP-40**	**LCP-50**	**LCP-60**	**LCP-70**	**LCP-80**
Empirical formula	$LiCoPO_4$	$LiCoPO_4$	$LiCoPO_4$	$LiCoPO_4$	$LiCoPO_4$	$LiCoPO_4$	$LiCoPO_4$	$LiCoPO_4$	$LiCoPO_4$
M_r ($g \cdot mol^{-1}$)	160.8	160.8	160.8	160.8	160.8	160.8	160.8	160.8	160.8
Crystal system	orthorhombic	orthorhombic	orthorhombic	orthorhombic	orthorhombic	orthorhombic	orthorhombic	orthorhombic	orthorhombic
Space group (no.)	*Pnma* (62)	*Pnma* (62)	*Pnma* (62)	*Pnma* (62)	*Pnma* (62)	*Pnma* (62)	*Pnma* (62)	*Pnma* (62)	*Pnma* (62)
Z	4	4	4	4	4	4	4	4	4
a (Å)	10.2135(2)	10.21345(18)	10.21295(14)	10.21486(18)	10.2125(2)	10.2097(2)	10.2119(3)	10.2142(3)	10.2168(3)
b (Å)	5.92610(12)	5.92745(11)	5.92858(9)	5.92810(11)	5.92961(14)	5.92785(13)	5.93285(16)	5.93254(17)	5.93183(18)
c (Å)	4.70622(10)	4.70578(9)	4.70513(7)	4.70718(9)	4.70545(12)	4.70315(10)	4.70313(13)	4.70414(14)	4.70546(14)
V ($Å^3$)	284.849(10)	284.887(9)	284.888(7)	285.042(9)	284.944(12)	284.641(11)	284.942(13)	285.053(15)	285.172(14)
F(000)	308	308	308	308	308	308	308	308	308
ρ(calcd) ($g \cdot cm^{-3}$)	3.7506(2)	3.7501(2)	3.7501(1)	3.7480(2)	3.7493(2)	3.7533(2)	3.7494(2)	3.7479(3)	3.7463(2)
R_p	0.0234	0.0246	0.0210	0.0258	0.0241	0.0236	0.0233	0.0257	0.0238
R_{wp}	0.0306	0.0326	0.0284	0.0342	0.0332	0.0325	0.0323	0.0354	0.0333
R_{exp}	0.0284	0.0266	0.0220	0.0256	0.0216	0.0260	0.0244	0.0264	0.0243
R_F	0.0253	0.0209	0.0213	0.0228	0.0255	0.0244	0.0302	0.0303	0.0291
R_B	0.0378	0.0323	0.0315	0.0362	0.0395	0.0394	0.0480	0.0474	0.0468
χ^2	1.08	1.23	1.29	1.34	1.54	1.25	1.32	1.34	1.37
Data/restraints/ parameter	3800/0/63	3800/0/63	3800/0/63	3800/0/63	3800/0/63	3802/0/63	3800/0/63	3800/0/63	3800/0/63

[a] The estimated standard deviations were calculated by applying the Berar's correction und are indicated in parentheses.

Supplementary material

Table S2 Refined cell parameters (T = 298 K) of the $LiCoPO_4$ sample LCP-90 prepared by MWST synthesis using 90 vol% of the co-solvent EG in a binary mixture with water [a]

Sample	**LCP-90**
Empirical formula	$LiCoPO_4$
M_r ($g \cdot mol^{-1}$)	160.8
Crystal system	orthorhombic
Space group (no.)	*Pnma* (62)
Z	4
a (Å)	10.2165(3)
b (Å)	5.9268(2)
c (Å)	4.70434(17)
V ($Å^3$)	284.855(18)
F(000)	308
ρ (calcd.) ($g \cdot cm^{-3}$)	3.7505(3)
R_p	0.0255
R_{wp}	0.0338
R_{exp}	0.0304
R_F	0.0348
R_D	0.0554
χ^2	1.11
Data/restraints/parameter	3802/0/64
Phase composition	87.4(4) wt% $LiCoPO_4$ (*Pnma*)
	12.6(4) wt% $LiCoPO_4$ ($Pna2_1$)

[a] The estimated standard deviations were calculated by applying the Berar's correction und are indicated in parentheses.

Supplementary material

Table S3 Refined fractional atomic coordinates and isotropic thermal displacement parameters of the $LiCoPO_4$ (*Pnma*, $Z = 4$, $T = 298$ K) samples LCP-0–LCP-90 prepared by MWST synthesis using increasing concentrations of EG (0–90 vol%) in a H_2O/EG solvent mixture [a]

Sample	Atom	Wyckoff position	Occupancy	*x*/a	*y*/b	*z*/c	U_{iso} (Å^2)
LCP-0	Li1	4*a*	1	0	0	0	0.0139 [b]
	Co1	4*c*	1	0.22136(12)	¼	0.5207(4)	0.0096(5)
	P1	4*c*	1	0.4049(3)	¼	0.0831(6)	0.0094(8)
	O1	4*c*	1	0.4044(7)	¼	0.7603(12)	0.007(2)
	O2	4*c*	1	0.0465(7)	¼	0.2939(12)	0.0056(19)
	O3	8*d*	1	0.3342(5)	0.0445(7)	0.2201(8)	0.0052(13)
LCP-10	Li1	4*a*	1	0	0	0	0.0139 [b]
	Co1	4*c*	1	0.22139(10)	¼	0.5207(3)	0.0105(4)
	P1	4*c*	1	0.4048(2)	¼	0.0823(5)	0.0084(7)
	O1	4*c*	1	0.4041(6)	¼	0.7613(10)	0.0061(16)
	O2	4*c*	1	0.0461(6)	¼	0.2935(10)	0.0050(16)
	O3	8*d*	1	0.3347(4)	0.0457(6)	0.2191(7)	0.0061(11)
LCP-20	Li1	4*a*	1	0	0	0	0.0139 [b]
	Co1	4*c*	1	0.22133(10)	¼	0.5210(3)	0.0112(4)
	P1	4*c*	1	0.4050(2)	¼	0.0822(4)	0.0081(6)
	O1	4*c*	1	0.4037(5)	¼	0.7631(9)	0.0060(15)
	O2	4*c*	1	0.0450(5)	¼	0.2955(9)	0.0049(14)
	O3	8*d*	1	0.3340(4)	0.0458(6)	0.2178(6)	0.0062(10)
LCP-30	Li1	4*a*	1	0	0	0	0.0139 [b]
	Co1	4*c*	1	0.22140(11)	¼	0.5207(3)	0.0119(5)
	P1	4*c*	1	0.4049(2)	¼	0.0829(5)	0.0095(7)
	O1	4*c*	1	0.4042(6)	¼	0.7625(11)	0.0066(17)
	O2	4*c*	1	0.0457(6)	¼	0.2931(10)	0.0056(17)
	O3	8*d*	1	0.3348(4)	0.0451(6)	0.2188(7)	0.0058(11)
LCP-40	Li1	4*a*	1	0	0	0	0.0139 [b]
	Co1	4*c*	1	0.22130(14)	¼	0.5208(4)	0.0110(6)
	P1	4*c*	1	0.4050(3)	¼	0.0821(6)	0.0060(9)
	O1	4*c*	1	0.4039(7)	¼	0.7643(13)	0.005(2)
	O2	4*c*	1	0.0448(8)	¼	0.2947(13)	0.006(2)
	O3	8*d*	1	0.3342(5)	0.0470(8)	0.2171(9)	0.0046(14)
LCP-50	Li1	4*a*	1	0	0	0	0.0139 [b]
	Co1	4*c*	1	0.22131(13)	¼	0.5210(4)	0.0118(6)
	P1	4*c*	1	0.4050(3)	¼	0.0821(6)	0.0074(8)
	O1	4*c*	1	0.4040(7)	¼	0.7661(13)	0.006(2)
	O2	4*c*	1	0.0450(7)	¼	0.2942(13)	0.005(2)
	O3	8*d*	1	0.3351(5)	0.0470(8)	0.2166(8)	0.0049(13)

Supplementary material

LCP-60	Li1	4*a*	1	0	0	0	0.0139 [b]
	Co1	4*c*	1	0.22130(16)	¼	0.5208(5)	0.0130(7)
	P1	4*c*	1	0.4049(3)	¼	0.0817(7)	0.0076(10)
	O1	4*c*	1	0.4054(8)	¼	0.7680(15)	0.006(2)
	O2	4*c*	1	0.0445(9)	¼	0.2948(15)	0.005(2)
	O3	8*d*	1	0.3355(6)	0.0485(9)	0.2160(10)	0.0041(16)
LCP-70	Li1	4*a*	1	0	0	0	0.0139 [b]
	Co1	4*c*	1	0.22134(16)	¼	0.5212(5)	0.0142(8)
	P1	4*c*	1	0.4046(3)	¼	0.0821(7)	0.0061(10)
	O1	4*c*	1	0.4056(9)	¼	0.7689(15)	0.006(2)
	O2	4*c*	1	0.0448(9)	¼	0.2946(15)	0.005(2)
	O3	8*d*	1	0.3358(6)	0.0490(9)	0.2157(10)	0.0044(16)
LCP-80	Li1	4*a*	1	0	0	0	0.0139 [b]
	Co1	4*c*	1	0.22124(17)	¼	0.5214(5)	0.0120(8)
	P1	4*c*	1	0.4049(4)	¼	0.0822(7)	0.0069(10)
	O1	4*c*	1	0.4052(9)	¼	0.7688(16)	0.005(3)
	O2	4*c*	1	0.0446(9)	¼	0.2931(15)	0.005(2)
	O3	8*d*	1	0.3354(6)	0.0483(10)	0.2169(10)	0.0046(16)
LCP-90	Li1	4*a*	1	0	0	0	0.0139 [b]
	Co1	4*c*	1	0.2215(2)	¼	0.5215(6)	0.0123(10)
	P1	4*c*	1	0.4045(5)	¼	0.0822(10)	0.0079(14)
	O1	4*c*	1	0.4048(12)	¼	0.771(2)	0.005(3)
	O2	4*c*	1	0.0444(12)	¼	0.294(2)	0.005(3)
	O3	8*d*	1	0.3360(8)	0.0483(13)	0.2170(13)	0.005(2)

[a] The estimated standard deviations were calculated using the Berar's procedure und are indicated in parentheses.
[b] Li positions and thermal displacement parameters have been fixed as they cannot be deduced by means of X-ray diffraction due to the low atomic scattering factor of Li.

Table S4 Selected interatomic distances as refined from X-ray powder diffraction data of the $LiCoPO_4$ (*Pnma*, $Z = 4$, $T = 298$ K) samples LCP-0–90 obtained from MWST synthesis using increasing concentrations of EG (0–90 vol%) in a H_2O/EG solvent mixture [a]

Atom pair			*d* (Å)									
			LCP-0	**LCP-10**	**LCP-20**	**LCP-30**	**LCP-40**	**LCP-50**	**LCP-60**	**LCP-70**	**LCP-80**	**LCP-90**
Li1	O1	×2	2.156(5)	2.160(4)	2.167(3)	2.163(4)	2.170(5)	2.173(5)	2.173(6)	2.175(6)	2.177(6)	2.184(8)
	O2	×2	2.082(4)	2.079(3)	2.083(3)	2.078(4)	2.081(5)	2.079(4)	2.081(5)	2.081(5)	2.076(5)	2.076(7)
	O3	×2	2.162(5)	2.161(4)	2.170(4)	2.161(4)	2.172(5)	2.166(5)	2.165(6)	2.165(6)	2.165(6)	2.159(8)
Co1	O1	×1	2.183(7)	2.183(6)	2.183(5)	2.187(6)	2.189(7)	2.192(7)	2.211(8)	2.213(9)	2.211(9)	2.211(12)
	O2	×1	2.081(7)	2.086(6)	2.091(5)	2.090(6)	2.093(8)	2.092(7)	2.095(8)	2.095(9)	2.100(9)	2.103(12)
	O3	×2	2.061(4)	2.067(4)	2.062(3)	2.064(4)	2.068(5)	2.068(5)	2.078(6)	2.080(5)	2.076(6)	2.078(8)
	O3	×2	2.194(5)	2.195(4)	2.196(3)	2.199(4)	2.195(5)	2.201(5)	2.201(6)	2.203(6)	2.201(6)	2.202(8)
P1	O1	×1	1.519(6)	1.511(5)	1.502(5)	1.508(6)	1.496(7)	1.486(7)	1.476(8)	1.473(8)	1.475(8)	1.462(11)
	O2	×1	1.558(7)	1.556(6)	1.540(6)	1.552(6)	1.541(8)	1.543(8)	1.540(9)	1.545(9)	1.543(10)	1.544(13)
	O3	×2	1.556(5)	1.547(4)	1.549(4)	1.549(4)	1.541(5)	1.536(5)	1.526(6)	1.520(6)	1.529(6)	1.524(8)

[a] The estimated standard deviations were calculated by applying the Berar's correction und are indicated in parentheses.

Supplementary material

3 Additional elemental analysis data

Table S5 Elemental composition of the $LiCoPO_4$ sample LCP-90 obtained from MWST synthesis using 90 vol% of the co-solvent EG in a binary mixture with water in comparison with the theoretical values [a]

Element	LCP-90	Theoretical
C (wt%)	0.4(3)	0
H (wt%)	– [b]	0
N (wt%)	– [b]	0
S (wt%)	1.7(3)	0
Li (wt%)	4.8(1)	4.3
Co (wt%)	32.8(5)	36.6
P (wt%)	17.5(3)	19.3
n(Li):*n*(P)	1.23(2)	1
n(Co):*n*(P)	0.99(1)	1
Li_2SO_4 (wt%) [c]	5.7(10)	0
$LiCoPO_4$ (wt%) [d]	90.7(16)	100

[a] The composition was determined from the experimental results in wt% of the CHNS, AAS, and photometric analyses (standard deviations are given in parentheses).
[b] The value was too low to be measured (= 0).
[c] Calculation based on the moles of S and the surplus of Li found.
[d] Calculation based on the moles of P found.

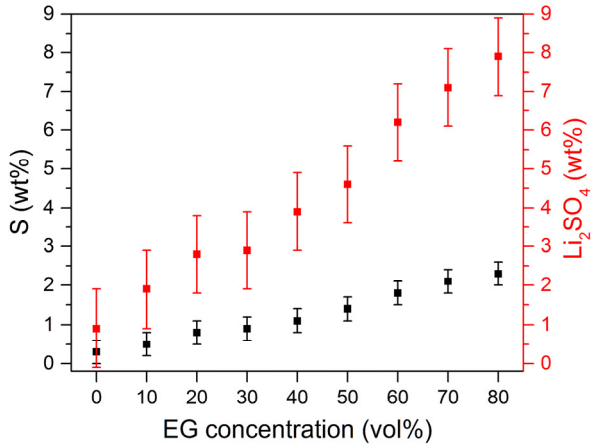

Fig. S3 Sulfur contents determined by CHNS analysis (black) and respective calculated amounts of Li_2SO_4 (red) in the $LiCoPO_4$ samples obtained from MWST synthesis versus the EG concentrations (0–80 vol%) used as co-solvent in a binary mixture with water.

Supplementary material

4 Scanning electron microscopy (SEM) images of LCP-90

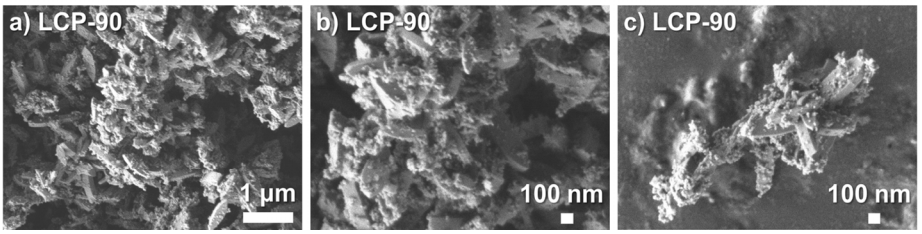

Fig. S4 (a–c) SEM images at various magnifications of the $LiCoPO_4$ sample LCP-90 obtained from MWST synthesis using 90 vol% of the co-solvent EG in a binary mixture with water. The sample exhibits two types of morphologies: nanospheres (diameter ~15 nm), which are located on the surface of hexagonal platelets (~300–600 nm × 80–150 nm × 30–60 nm). Combining the information from PXRD (Fig. S2j) and SEM, the hexagonal platelets can be assigned with a high degree of certainty to the olivine $LiCoPO_4$ (space group *Pnma*), and the spheres to the metastable $LiCoPO_4$ (*Pna*2_1) modification. The hexagonal base areas of the olivine particles are more elongated in comparison to LCP-50–80, which is reflected in the notably higher aspect ratio of ~4.

Supplementary material

5 Galvanostatic curves of LCP-0–LCP-80 in the first three cycles at various C rates

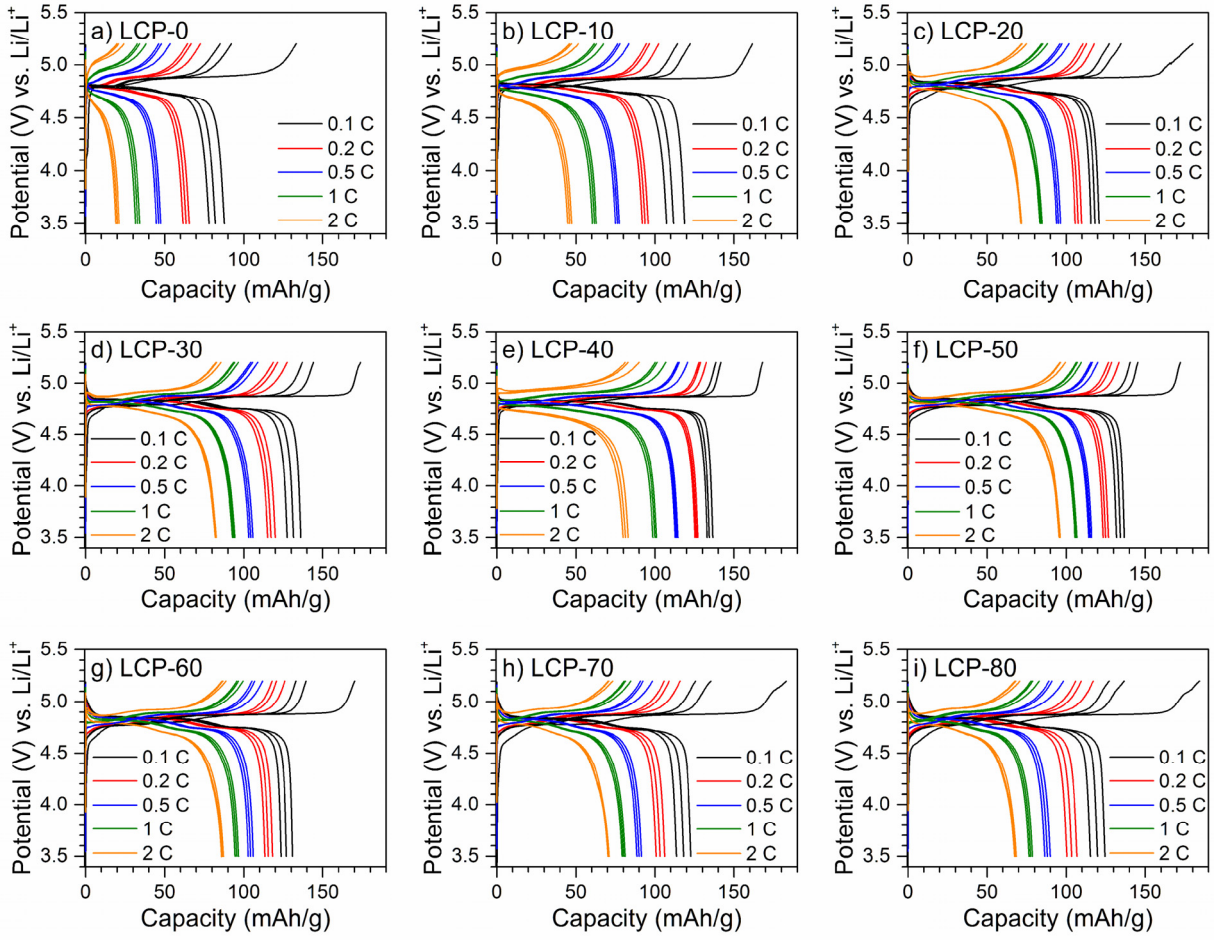

Fig. S5 Galvanostatic curves of electrodes based on the $LiCoPO_4$ samples LCP-0–80 synthesized by the MWST process using increasing concentrations of EG (0–80 vol%) as co-solvent in a binary mixture with water: (a) LCP-0, (b) LCP-10, (c) LCP-20, (d) LCP-30, (e) LCP-40, (f) LCP-50, (g) LCP-60, (h) LCP-70, and (i) LCP-80. Electrochemical testing was performed in Swagelok cells between 3.5 and 5.2 V using metallic Li as anode and 1 M $LiPF_6$ in ethylene carbonate/dimethyl carbonate (1:1, w:w) as electrolyte. The charge and discharge curves are displayed for the first three cycles of each C rate.

6.4 Morphology-Controlled Microwave-Assisted Solvothermal Synthesis of High-Performance $LiCoPO_4$ as a High-Voltage Cathode Material for Li-Ion Batteries

Jennifer Ludwig,[a] Cyril Marino,[b‡] Dominik Haering,[b] Christoph Stinner,[c] Hubert A. Gasteiger,[b] and Tom Nilges[a*]

[a] Technical University of Munich, Department of Chemistry, Synthesis and Characterization of Innovative Materials, Lichtenbergstr. 4, 85747 Garching, Germany

[b] Technical University of Munich, Department of Chemistry, Technical Electrochemistry, Lichtenbergstr. 4, 85747 Garching, Germany

[c] BMW AG, Petuelring 130, 80788 München, Germany

‡ Present address: Paul Scherrer Institute, Electrochemical Energy Storage, 5232 Villigen PSI, Switzerland

J. Power Sources **2017,** *342*, 214–223.
DOI: 10.1016/j.jpowsour.2016.12.059

Journal of Power Sources 342 (2017) 214–223

Contents lists available at ScienceDirect

Journal of Power Sources

journal homepage: www.elsevier.com/locate/jpowsour

Morphology-controlled microwave-assisted solvothermal synthesis of high-performance $LiCoPO_4$ as a high-voltage cathode material for Li-ion batteries

Jennifer Ludwig [a], Cyril Marino [b, 1], Dominik Haering [b], Christoph Stinner [c], Hubert A. Gasteiger [b], Tom Nilges [a, *]

[a] Technical University of Munich, Department of Chemistry, Synthesis and Characterization of Innovative Materials, Lichtenbergstr. 4, 85747, Garching, Germany
[b] Technical University of Munich, Department of Chemistry, Technical Electrochemistry, Lichtenbergstr. 4, 85747, Garching, Germany
[c] BMW AG, Petuelring 130, 80788, München, Germany

HIGHLIGHTS

- Preparation of $LiCoPO_4$ platelets by simple microwave-assisted solvothermal process.
- Influence of solvent on morphology and electrochemical performance is investigated.
- Co-solvent plays a key role in tuning the size, shape and orientation of crystals.
- $LiCoPO_4$ from triethylene glycol co-solvent shows best electrochemical performance.
- Discharge capacity of 141 mAh g^{-1} and energy density of 677 Wh kg^{-1} are reached.

GRAPHICAL ABSTRACT

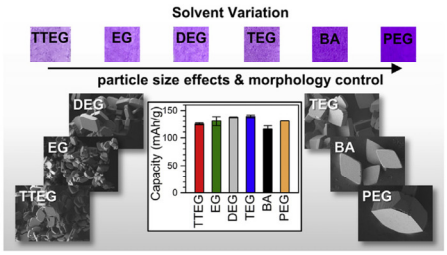

ARTICLE INFO

Article history:
Received 4 October 2016
Received in revised form
24 November 2016
Accepted 14 December 2016

Keywords:
Lithium cobalt phosphate
Solvothermal synthesis
Microwave synthesis
Morphology control
High-voltage cathode
Lithium-ion batteries

ABSTRACT

High-performance particles of the high-voltage cathode material $LiCoPO_4$ for Li-ion batteries are synthesized by a simple and rapid one-step microwave-assisted solvothermal route at moderate temperatures (250 °C). Using a variety of water/alcohol 1:1 (v:v) solvent mixtures, including ethylene glycol (EG), diethylene glycol (DEG), triethylene glycol (TEG), tetraethylene glycol (TTEG), polyethylene glycol 400 (PEG), and benzyl alcohol (BA), the focus of the study is set on optimizing the electrochemical performance of the material by controlling the particle size and morphology. Scanning electron microscopy studies reveal a strong influence of the co-solvent on the particle size and morphology, resulting in the formation of variations between square, rhombic and hexagonal platelets. According to selected area electron diffraction experiments, the smallest crystal dimension is in the [010] direction for all materials, which is along the lithium diffusion pathways of the olivine crystal structure. The anisotropic crystal orientations with enhanced Li-ion diffusion properties result in high initial discharge capacities and

* Corresponding author.
E-mail address: tom.nilges@lrz.tum.de (T. Nilges).
[1] Present address: Paul Scherrer Institute, Electrochemical Energy Storage, 5232 Villigen PSI, Switzerland.

http://dx.doi.org/10.1016/j.jpowsour.2016.12.059

J. Ludwig et al. / Journal of Power Sources 342 (2017) 214–223 215

gravimetric energy densities (up to 141 mAh g^{-1} at 0.1 C and 677 Wh kg^{-1} for $LiCoPO_4$ obtained from TEG), excellent rate capabilities, and cycle life for 20 cycles.

1. Introduction

Since the electrochemical activity of $LiFePO_4$ (LFP) was first reported [1], lithium transition-metal phosphates have been receiving increasing attention as alternative cathode materials for lithium-ion batteries (LIBs) [2–7]. Although $LiFePO_4$ has been intensively studied and is now commercially used [8], the scientific community has recently been focusing on the manganese (LMP), cobalt (LCP) or nickel (LNP) based phospho-olivines. Among these, the high-voltage cathode material $LiCoPO_4$ (LCP), which operates at 4.8 V and shows a theoretical capacity of 167 mAh g^{-1} [9], offers the potential to increase the gravimetric energy density to 802 Wh kg^{-1} (LFP: 580 Wh kg^{-1}), and thus, might bring a significant improvement for LIBs [10,11].

LCP crystallizes orthorhombically, in space group *Pnma* as a derivative of the olivine structure. In the structure, Li^+ and Co^{2+} occupy octahedral sites and P^{+5} is located in the tetrahedral sites of a distorted hexagonal close-packed (*hcp*) oxygen array [12]. The crystal structure contains two types of polyhedra: [CoO_6] octahedra and [PO_4] tetrahedra (Fig. 1). The [CoO_6] octahedra form zigzag chains that run in parallel to the crystallographic *c* axis. The chains are linked by the [PO_4] tetrahedra, resulting in a three-dimensional network structure. The Li^+ ions are located in one-dimensional channels along [010] and [001]. However, theoretical studies suggest that Li diffusion is only promoted along the [010] (*b*) direction because of a significantly lower activation energy [13–15].

Due to the highly anisotropic nature of the Li-ion transport in the olivine structure, one approach to improve the electrochemical performance of the cathode material is to control the particle size and morphology. Kinetically controlled solution-based approaches have been reported to be successfully tuning the particle size and morphology [16]. However, most of these methods require comparably long reaction times and further post heat treatments at temperatures as high as 900 °C (*cf.* sol-gel [17–19], polyol synthesis [20–22]). In this regard, the hydrothermal (HT) [23–29] and solvothermal (ST) [30–35] synthesis techniques are better alternatives as they generally i) require only moderate synthesis temperatures, ii) are cost-effective, iii) environmentally benign, and iv) easily scalable [36]. Besides, this low-temperature approach enables the formation of very small and homogeneous particles. Nevertheless, single-step solvothermal approaches towards crystalline LCP without additional annealing at high temperatures have only rarely been reported to date [23,24,28,34]. The conventional hydrothermal or solvothermal synthesis pathways are also characterized by slow reaction kinetics and irregular reaction conditions due to thermal gradients in the reaction vessel [37].

Among solution-based methods, the microwave-assisted approach is considered particularly appealing as it only requires very short reaction times of only a few minutes at moderate temperatures below 300 °C, giving crystalline materials with homogeneous particle size distributions [38–42]. This has been demonstrated in our previous report [43]. Here, a microwave-assisted solvothermal synthesis route using a 1:1 (v:v) water/ethylene glycol (EG) solvent mixture at 250 °C resulted in single crystalline, hexagonal platelets of $LiCoPO_4$ with dimensions of 700–800 nm × 400–600 nm × 100–220 nm, the smallest dimension being along the [010] direction of the Li diffusion pathways in the olivine structure. Electrochemical measurements showed that this material delivers an initial discharge capacity of 137 mAh g^{-1} at 0.1 C. Despite the excellent energy density, the C rate capability and cycling stability of the material need improvement before LCP can be considered a viable alternative to commercial LFP.

Our approach to tackle this challenge is to enhance the Li-ion diffusion properties of the material by particle size and morphology control, which is accomplished by modification of the synthesis parameters. To the best of our knowledge, the effect of the solvent used in the synthesis on the material properties has not been investigated either for the solvothermal or the microwave-assisted synthesis of $LiCoPO_4$. In this work, we evaluate the effect of the co-solvent of the microwave-assisted solvothermal synthesis on the particle size, morphology, and crystal orientation as well as on the electrochemical performance of LCP. We analyzed the influence of six different co-solvents in the material properties keeping important synthesis parameters like reaction conditions, including temperature, time, pH value, type of starting materials, and solvent ratio [29,44] constant. The LCP materials are characterized by X-ray powder diffraction, elemental analysis,

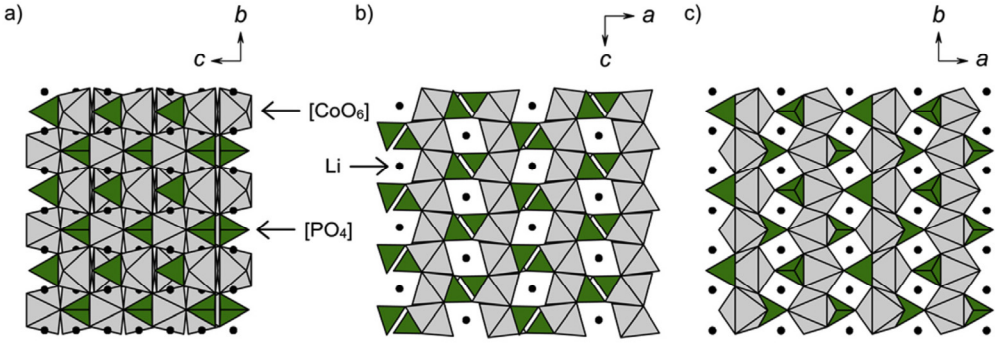

Fig. 1. Polyhedral representation of the olivine crystal structure (space group *Pnma*) of $LiCoPO_4$ viewed along the (a) [100], (b) [010], and (c) [001] axes. Li ions are drawn in black, [CoO_6] octahedra in grey, and [PO_4] tetrahedra in green. (For interpretation of the references to colour in this figure legend, the reader is referred to the web version of this article.)

Brunauer–Emmett–Teller surface area measurements, scanning and transmission electron microscopy as well as electrochemical tests.

2. Experimental

2.1. Microwave-assisted solvothermal synthesis

$LiCoPO_4$ powders were synthesized by a modified microwave-assisted solvothermal (MWST) process according to our previous report [43]. $LiOH \cdot H_2O$ (Bernd Kraft, ≥ 99%), $CoSO_4 \cdot 7H_2O$ (Chempur, 99%), and H_3PO_4 (AppliChem, Ph. Eur., 85 wt% solution) were used in a Li:Co:P molar ratio of 3:1:1, and 0.075 g ascorbic acid (Alfa Aesar, 99+%) was added as a reducing agent. (Note that the two additional equivalents of Li are required to bind the sulfate in the stoichiometric reaction: $3\ LiOH \cdot H_2O + CoSO_4 \cdot 7H_2O + H_3PO_4 \rightarrow LiCoPO_4 + Li_2SO_4 \cdot H_2O + 12H_2O$.) The raw materials were dissolved in a total volume of 30 mL of 1:1 (v:v) binary solvents composed of deionized water (water type I, Millipore, 18.2 MΩ cm) and the following organic co-solvents: ethylene glycol (EG; VWR BDH PROLABO AnalaR NORMAPUR, 99.9%), diethylene glycol (DEG; Merck, ≥ 99%), triethylene glycol (TEG; Merck, ≥ 99%), tetraethylene glycol (TTEG; Merck, ≥ 98%), polyethylene glycol 400 (PEG; M_w = 380–420, Merck, for synthesis), and benzyl alcohol (BA; AppliChem PanReac, ≥ 99.5%). The corresponding LCP samples are denoted by the co-solvent that was used as follows: LCP-EG, LCP-DEG, LCP-TEG, LCP-TTEG, LCP-PEG, and LCP-BA.

The resulting violet gels were stirred vigorously for 20 min before being transferred into 75 mL capacity PTFE/TFM vessels (HTV-75, MLS GmbH), which were equipped with a temperature probe placed inside a thermowell to monitor the internal temperature of the vessel. The pH of the homogeneous mixtures prior to the reaction was 5.0–5.5. The solvothermal reaction was performed with an Ethos One microwave synthesis system (MLS GmbH) equipped with an MR-8 HT high-pressure high-temperature rotor. The easyCONTROL-640 software (MLS GmbH) was used to program the reaction temperature and time. For the synthesis, the sample temperature was ramped to 250 °C within 15 min, kept at 250 °C for 30 min under stirring, followed by natural cooling to ambient temperature. The automatic temperature control unit (T660, MLS GmbH) allowed continuous monitoring of the temperature inside the vessel, and the programmed temperature profile was followed automatically by adjusting the microwave power (maximum power: 600 W). The pH of the solutions after the reaction was 4.5–5.0. The precipitates, which exhibited colors ranging from light pink to dark violet (*cf.* graphical abstract), were collected by suction filtration, washed five times with deionized water (high-purity water type I, Millipore, 18.2 MΩ cm; to remove a highly water-soluble lithium sulfate side phase [43]) and absolute ethanol (VWR AnalaR NORMAPUR, 99.95%), and then dried in air at 150 °C overnight.

2.2. Structural, physical and chemical characterization

X-ray powder diffraction (PXRD) data were collected on a Stoe STADI P diffractometer using Mo $K_{\alpha 1}$ radiation (λ = 0.70930 Å, Ge(111) monochromator, Dectris MYTHEN DCS 1K silicon solid-state detector). The ground powders were sealed in glass capillaries (Hilgenberg, borosilicate glass type no. 50, diameter: 0.5 mm, wall thickness: 0.01 mm), which were then measured for 12 h in a 2θ range of 3–60° (PSD step: 0.015°; time/step: 30 s, 3 ranges). An external calibration was performed using a Si standard (a = 5.43088 Å). Rietveld analysis of the powder diffraction patterns was performed with the Jana2006 software [45]. The background profile, which can mainly be attributed to the capillaries according to a reference measurement published in our previous work [43], was fitted with a Chebyshev polynomial function with 35 coefficients. The peak asymmetry especially at low scattering angles was corrected by the axial divergence model described by Finger et al. [46] using empirically determined starting values. The refinement of the general atomic positions as well as the isotropic displacement parameters of Co, P, and O was performed without restrictions after applying an absorption correction (estimated packing fraction ~0.6) [47]. On the contrary, the thermal displacement factors of Li were fixed as they cannot be deduced by means of X-ray powder diffraction. The Berar's factor was applied to the standard uncertainties of all refined parameters to obtain more realistic values [48].

The elemental composition was determined by atomic absorption spectroscopy (AAS) using a Varian AA280FS sequential device for Li, and by photometry using a Shimadzu UV-160 device for Co and P contents. The C, H, N, and S contents were measured by combustion analysis (Hekatech Euro EA CHNSO Analyzer).

High-resolution scanning electron microscopy (HR-SEM) was performed on a JEOL JSM-7500F instrument (accelerating voltage: 1 kV, working distance: 8 mm, LEI (lower secondary electron image) detector). The samples were fixed on graphite tape which was attached to an aluminum stub.

Transmission electron microscopy (TEM) and selected area electron diffraction (SAED) images were obtained using a JEOL JEM-2010 electron microscope at 160 kV (LaB_6 cathode, max. resolution: 0.2 nm). For the measurements, small portions of the powders were dispersed in 1.5 μL ethanol with the help of an ultrasonic bath. As some of the micron-sized particles were subject to sedimentation, the dispersions were then dropped quickly onto a 300 mesh carbon film. Magnetite was used as a reference material for the SAED patterns.

The Brunauer–Emmett–Teller (BET) method was used to determine the specific surface areas of the powders (Quantachrome Autosorb iQ device) using N_2 physisorption (number of measurement points: 11). A degassing period of 12 h at 423 K was applied prior to the measurements.

2.3. Electrochemical characterization

The electrodes were made by mixing 80 wt% of the as-prepared LCP powder, 10 wt% carbon Super C65 (Timcal) and 10 wt% polyvinylidene difluoride (PVdF, Kynar HSV 900, Arkema) in *N*-methyl-2-pyrrolidone (NMP, Sigma Aldrich) using a planetary centrifugal vacuum mixer (Thinky) at 2000 rpm for 20 min. The resulting ink was spread on aluminum foil (15 μm, MTI) and dried at 55 °C for 3–4 h. Circular electrodes of 10 mm in diameter and typical loadings of 4–5 mg/cm^2 were punched out, pressed two times at 250 MPa for 1 min (KBr press, PerkinElmer), and dried for 2 h at 120 °C under vacuum (Büchi B-585 glass oven).

The electrochemical properties of the $LiCoPO_4$ cathodes were evaluated using Swagelok cells with pure Li foil (Rockwood Lithium, 450 μm, battery grade, > 99.8%) as anode, two glass fiber separators (VWR, 691, 250 μm) and 80 μL electrolyte (1 M $LiPF_6$ in ethylene carbonate (EC)/dimethyl carbonate (DMC); 1:1 (w:w), Merck, LP30). The cells were assembled in an Ar-filled glove box (MBraun; < 0.1 ppm H_2O, < 0.1 ppm O_2). Galvanostatic cycling was performed between 3.5 V and 5.2 V for 3 cycles at C/10, 3 cycles at C/5, 3 cycles at C/2, 3 cycles at 1 C, 3 cycles at 2 C followed by 15 cycles at C/2 (C rates based on a theoretical capacity of 167 mAh g^{-1}_{LCP}). Charges were performed in CCCV (constant-current, constant-voltage) mode with the potentiostatic step limited by a current of C/20. On calculation of the specific capacities using the weight of LCP powder in the electrodes, the weight of a minor Li_2SO_4 impurity was neglected as it only accounts for <5 wt% and

experiments [43] have shown that it does not have an impact on the electrochemical properties. In order to gain more reliable data, two cells were cycled for each material.

3. Results and discussion

3.1. X-ray powder diffraction

Fig. 2 shows the background corrected PXRD patterns of the $LiCoPO_4$ samples obtained from the microwave-assisted solvothermal process using an array of co-solvents in 1:1 (v:v) binary solvent blends. All patterns can be fully fitted to the orthorhombic structure model of olivine-type $LiCoPO_4$ (space group *Pnma*, ICSD database no. 24749749 [49]) using the Rietveld method, indicating that, unlike other solution-based methods, no post calcination at elevated temperatures is required to get single phase crystalline active material. This suggests that the co-solvent does not affect the formation of the pure olivine phase.

In order to ensure the comparability of the results, all datasets were refined using identical data/parameter ratios. The refined cell volumes of the samples (Table 1) are identical within three times the standard deviation and in good agreement with reported values [25], as indicated by the excellent reliability factors. The only exception is LCP-BA, which exhibits a slightly bigger cell volume. A tentative refinement of the occupancies of the *Li* and *Co* sites suggests that the materials are neither Li-deficient nor have a disordered cation sub-structure. We therefore infer that all sites are fully occupied and that there are no antisite defects. The detailed Rietveld plots, the refined atomic coordinates, isotropic thermal displacement parameters, as well as selected interatomic distances are presented in Fig. A1 and Tables A1 and A2 (see Supplementary material). Note that the observed background can be attributed mainly to the capillaries with a small contribution from an amorphous lithium sulfate impurity [43].

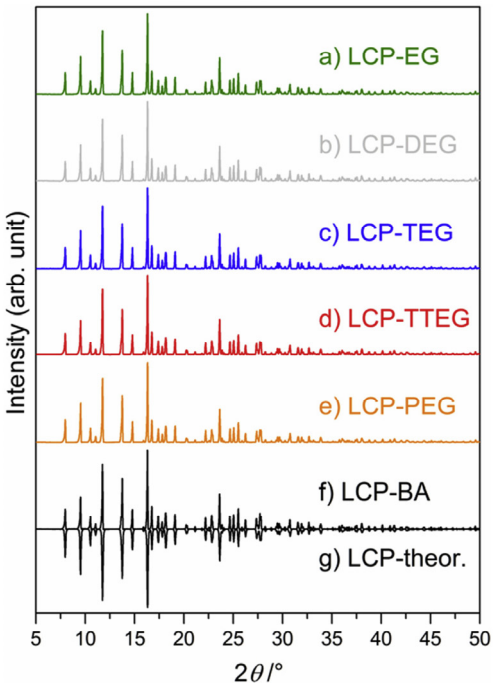

Fig. 2. X-ray powder diffraction patterns (Mo $K_{\alpha 1}$ radiation) of $LiCoPO_4$ powders obtained from MWST synthesis using various co-solvents in a 1:1 (v:v) mixture with water: (a) LCP-EG, (b) LCP-DEG, (c) LCP-TEG, (d) LCP-TTEG, (e) LCP-PEG, and (f) LCP-BA. The theoretical pattern based on ICSD database entry no. 247497 [49] is displayed mirrored in (g).

3.2. Elemental analysis

The chemical composition of the materials was determined by elemental analysis. The results are shown in Table 2. The molar ratio Li:Co:P is found to be equal within three standard deviations and close to the expected composition of *1:1:1 in all cases*. The amounts in wt%, however, show a deficiency both in Co and P in comparison to the theory. This can be attributed to a surplus of Li and S. Hydrogen could not be detected by CHNS analyses, indicating that the samples do not contain residual water from the aqueous phase of the solvent. Also no significant amounts of carbon were found, which might be caused by the decomposition of the organic co-solvent or the ascorbic acid additive. Thus, there is no carbon species or coating inherent that could increase the electronic conductivity of the material.

However, significant amounts of sulfur are found in all samples. Taking the slight excess of Li into account, the S contents can be related to a Li_2SO_4-type impurity. As discussed in our previous report [43], the Li_2SO_4 originates from $Li_2SO_4 \cdot H_2O$, which is obtained as a side product of the synthesis, which forms inclusions in the particles and therefore cannot be completely removed by the washing step. The fact that the estimated contents of $4–5 \pm 1$ wt% Li_2SO_4 (calculation based on the amount of S and surplus of Li found) are not detectable by PXRD is consistent with the background profile observed in the diffraction patterns, and our previous finding that the impurity is amorphous. The samples contain about $93–95 \pm 2$ wt% of the active material $LiCoPO_4$, the remainder being the secondary Li_2SO_4 phase. Note that capacities reported for the $LiCoPO_4$ samples were not corrected for the presence of the impurity.

3.3. Scanning electron microscopy

High-resolution SEM pictures (Fig. 3) of the as-prepared materials reveal that the co-solvent strongly affects the particle size as well as the morphology of the product. The images are displayed with similar magnifications for better comparison although, in some cases, the bigger particles sizes required a lower magnification. The sample obtained from a 50 vol% EG solvent (Fig. 3a), which is well reproduced using the process presented in our recent work [43], contains hexagonal platelets with dimensions of approximately 700–800 nm × 400–600 nm and thicknesses of about 200 nm. The particles suffer from cracking probably due to mechanical stress from stirring or cooling during the synthesis. Therefore, slightly inhomogeneous particles size distributions are observed. Moreover, small pores with a diameter of 10–20 nm are found that can be attributed to the formation mechanism [43]. In brief, the highly water-soluble Li_2SO_4 side phase, which is formed simultaneously with $LiCoPO_4$ in the synthesis, is partly leached out by the aqueous phase of the binary solvent as well as by the washing step. As a result, pores appear where the Li_2SO_4 inclusions have been located initially. A more detailed picture showing these defects can be found in Fig. A2b. When DEG and TEG are used as co-solvents, particles with similar and uniform square platelet-like morphologies are obtained. The platelets in LCP-DEG features edge lengths of 600–800 nm and thicknesses of 100–150 nm (Fig. 3b), whereas the platelets from LCP-TEG exhibit slightly larger dimensions of 900 nm × 900 nm × 100–150 nm (Fig. 3c). Due to the bigger crystallite size in both samples, we assume that the particles are mechanically more stable than the smaller ones and

Table 1
Lattice parameters of $LiCoPO_4$ (*Pnma*, $Z = 4$) prepared by MWST synthesis using different co-solvents as refined from X-ray powder diffraction data ($T = 298$ K) [a]

Sample	LCP-EG	LCP-DEG	LCP-TEG	LCP-TTEG	LCP-PEG	LCP-BA
a (Å)	10.2128(2)	10.2113(2)	10.21150(17)	10.2138(2)	10.2114(2)	10.2192(2)
b (Å)	5.92830(13)	5.92990(12)	5.92933(10)	5.92739(12)	5.92936(12)	5.92814(13)
c (Å)	4.70581(11)	4.70469(10)	4.70492(9)	4.70662(10)	4.70437(10)	4.70878(11)
V (Å^3)	284.911(11)	284.879(10)	284.870(9)	284.944(10)	284.837(10)	285.261(11)
$F(000)$	308	308	308	308	308	308
ρ (calcd) (g/cm^3)	3.7498(2)	3.7502(2)	3.7503(1)	3.7493(2)	3.7507(2)	3.7452(2)
R_p	0.0329	0.0251	0.0236	0.0298	0.0290	0.0292
R_{wp}	0.0433	0.0343	0.0320	0.0398	0.0404	0.0406
R_{exp}	0.0410	0.0275	0.0292	0.0256	0.0257	0.0280
R_F	0.0263	0.0265	0.0255	0.0237	0.0254	0.0322
R_B	0.0417	0.0444	0.0386	0.0379	0.0371	0.0605
χ^2	1.06	1.24	1.09	1.56	1.57	1.45
Data/restraints/parameter	3801/0/63	3800/0/63	3802/0/63	3801/0/63	3800/0/63	3800/0/63

[a] The estimated standard deviations were calculated by using the Berar's factor und are indicated in parentheses.

Table 2
Elemental analysis (CHNS, AAS, photometry) of the $LiCoPO_4$ samples obtained by MWST synthesis using various co-solvents in comparison with the theoretical composition of $LiCoPO_4$ [a,b]

Element	Theor.	LCP-EG	LCP-DEG	LCP-TEG	LCP-TTEG	LCP-PEG	LCP-BA
S (wt%)	0	1.4(3)	1.5(3)	1.4(3)	1.4(3)	1.3(3)	1.2(3)
Li (wt%)	4.3	4.2(2)	4.3(2)	4.3(2)	4.3(2)	4.3(2)	4.1(2)
Co (wt%)	36.6	34.1(1)	34.3(5)	34.4(5)	34.9(5)	34.3(5)	35.3(5)
P (wt%)	19.3	17.9(3)	18.2(3)	18.1(1)	18.2(3)	18.0(3)	18.0(3)
n(Li):n(P)	1	1.05(5)	1.06(5)	1.06(5)	1.05(5)	1.06(5)	1.02(5)
n(Co):n(P)	1	1.00(1)	0.99(1)	1.00(1)	1.01(1)	1.00(1)	1.03(1)
Li_2SO_4 (wt%)	0	5(1)	5(1)	5(1)	5(1)	4(1)	4(1)
$LiCoPO_4$ (wt%)	100	93(2)	94(2)	94(2)	95(2)	94(2)	93(2)

[a] The standard deviations are given in parentheses.
[b] The values of C, H, and N were too low to be measured in all samples (= 0).

hence, show merely minor defects caused by stirring. The sample LCP-TTEG bears crystallites with rhombohedral shapes. With dimensions of about 600–800 nm × 400–600 nm × 100–150 nm, these particles are the smallest of the series. The extent of fracture and inhomogeneity is similar to the one observed in LCP-EG. Some particles of LCP-TTEG exhibit notched corners at the obtuse angles of the rhombical base areas. This is probably the result of twinning of some of the crystals during crystal growth. When the twinned crystal break up (*e.g.* upon stirring), the notched corners supposedly appear at the former connecting point. Nevertheless, we could not find any twinned crystal species to confirm this hypothesis despite intensive efforts in the course of the HR-SEM characterization of this material. Applying PEG-400 as secondary solvent results in the formation of perfect hexagonal platelets with dimensions of about 9 μm × 7 μm × 3 μm (Fig. 3e). The sample LCP-BA consists of rhombic platelets that resemble the ones found in LCP-TTEG yet are bigger in size. Some of the crystals with dimensions of about 2.5 μm × 2 μm × 0.5–1 μm show notched edges as observed for LCP-TTEG that might also be caused by twinning (*cf.* Fig. A2i).

Brunauer–Emmett–Teller (BET) measurements of the as-prepared materials indicate that specific surface areas are as follows (error: ± 0.5 m^2 g^{-1}): LCP-EG 5.5 m^2 g^{-1}, LCP-DEG 3.7 m^2 g^{-1}, LCP-TEG 3.5 m^2 g^{-1}, LCP-TTEG 6.7 m^2 g^{-1}, LCP-PEG 0.8 m^2 g^{-1}, and LCP-BA 1.9 m^2 g^{-1}. These rather small surface areas are overall consistent with the various particle sizes observed in the SEM study (*i.e.* the bigger the particle size, the smaller the BET surface area and *vice versa*). The different colors of the powders, which range from light pink to dark violet (as displayed in the graphical abstract), can be related to particle size effects with the color getting darker and more intense for smaller surface areas and hence, bigger crystallites. Accordingly, the light pink color corresponds to small particle sizes (LCP-TEG), whereas the dark violet powder contains big crystallites (LCP-PEG). Further HR-SEM images of the samples at various magnifications are available in Fig. A2.

The results demonstrate that the polyol component of the reaction medium plays a significant role in regulating both the particle size and morphology of the product. Hence, a variety of shapes was obtained; hexagonal platelets for LCP-EG and LCP-PEG, square platelets for LCP-DEG and LCP-TEG, and rhombic platelets in the case of LCP-TTEG and LCP-BA. Additionally, the co-solvent helps to prevent agglomeration of the particles without requiring the use of an additional dispersant [22,50]. Moreover, big particles in the submicron range generally tend to agglomerate less than nanoparticles. The samples obtained from mixtures using an EG or TTEG co-solvent contain the smallest particles, yet a general tendency towards inhomogeneous particle size distributions and damaged crystals is found. The largest crystals are found in LCP-PEG and LCP-BA and show uniform sizes and shapes. Particles in a medium size range result from using DEG and TEG as co-solvents. The resulting nanoplatelets are homogeneous and show only small stirring-induced damage from the synthesis.

Regarding the formation mechanism, it has been reported that viscous solvents help to reduce particle sizes by inhibiting the crystal growth [50]. In contrast to this, the particle sizes and specific surface areas we found cannot be correlated to the viscosities of the co-solvents of the binary systems (Fig. 4). For instance, the syntheses using the co-solvents with the lowest (BA) as well as the highest viscosities (PEG) give products with the smallest surface areas (~1 m^2 g^{-1}). In contrast, the highest surface area was obtained from TTEG, which exhibits a medium viscosity. Hence, it can be concluded that in our process, the viscosity of the solvent does not play a crucial role in regulating the particle size of the product by limiting the crystal growth. Therefore, we assume the growth processes to be mainly governed by manipulating the surface stabilities of crystals facets by adsorption (*via* hydroxyl groups) rather

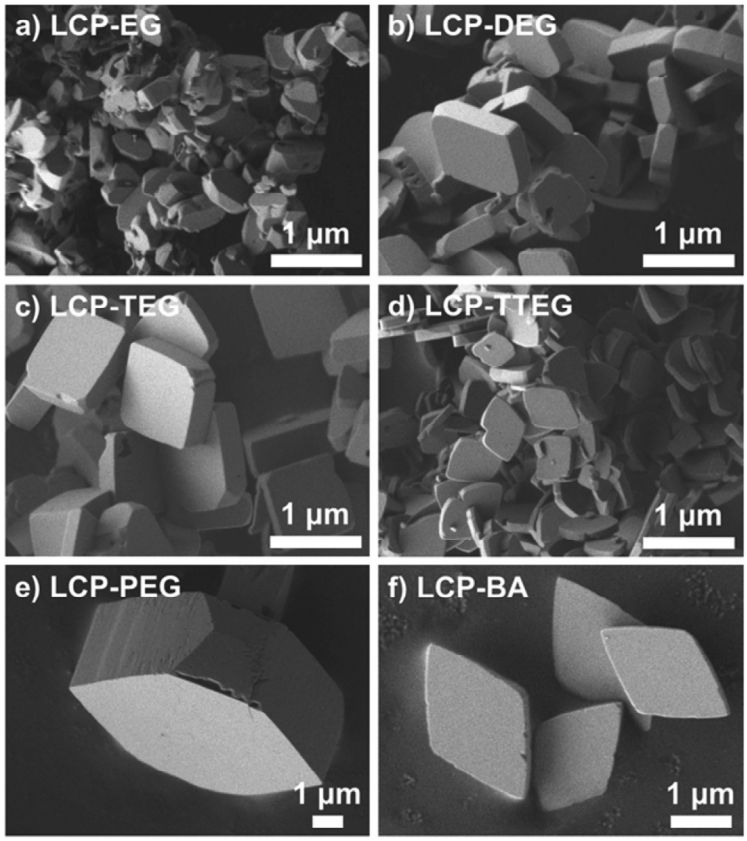

Fig. 3. SEM images of the $LiCoPO_4$ samples obtained from MWST synthesis using various co-solvents in a 1:1 (v:v) mixture with water: (a) LCP-EG, (b) LCP-DEG, (c) LCP-TEG, (d) LCP-TTEG, (e) LCP-PEG, and (f) LCP-BA. The samples (e) and (f) are displayed at lower magnification due to the particle size range.

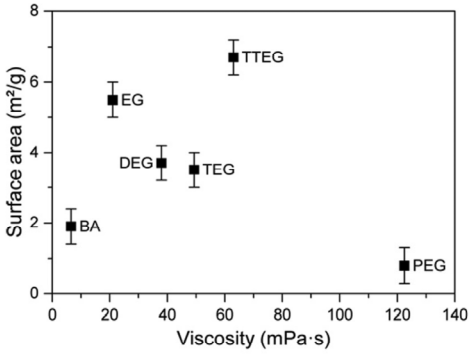

Fig. 4. Specific surface areas of the $LiCoPO_4$ samples obtained by the MWST process as a function of the dynamic viscosities of the co-solvents used.

than solvent viscosities. The reduction of the energies of specific facets due to solvent adsorption stabilizes the facets and hence, facilitates the anisotropic growth of particles depending on the solvent system [51,52]. The solvents therefore act as structure directing agents and show a soft template effect [30,50,53]. The crystal growth mechanism under solvothermal conditions is complex, however, and not completely understood to date; even less for binary solvent systems. Hence, a detailed formation mechanism of the observed crystals shapes in presence of various solvent mixtures cannot be determined at this point and will have to be examined in subsequent studies.

3.4. Transmission electron microscopy

Previous reports suggest that polyol-type solvents do not only act as mild reducing agents (hindering the oxidation of Co^{2+} to Co^{3+} in solution) but also as a soft templates that direct the growth by selective adsorption on certain crystal faces [30,51,54]. Consequently, we performed transmission electron microscopy (TEM) as well as selected area electron diffraction (SAED) studies on all the samples. In order to identify the crystal orientations, the measurements were performed using perpendicular directions. Hence, the images (Fig. 5) display front and side views of the crystals for all materials. In the SAED study, patterns of several individual crystals were taken for each sample to verify that all crystals are oriented identically. Additional low-resolution TEM images providing an overview over the particle shapes are presented in Fig. A3.

In general, the TEM images (Fig. 5 and Fig. A3) are in good agreement with the particle size ranges and morphologies observed via HR-SEM (*cf.* Fig. 3) and show front views of hexagonal platelets for LCP-EG (Fig. 5a) and LCP-PEG (Fig. 5q), square platelets for LCP-DEG (Fig. 5e) and LCP-TEG (Fig. 5i), and rhombic platelets in case of the materials LCP-TTEG (Fig. 5m) and LCP-BA (Fig. 5u). The

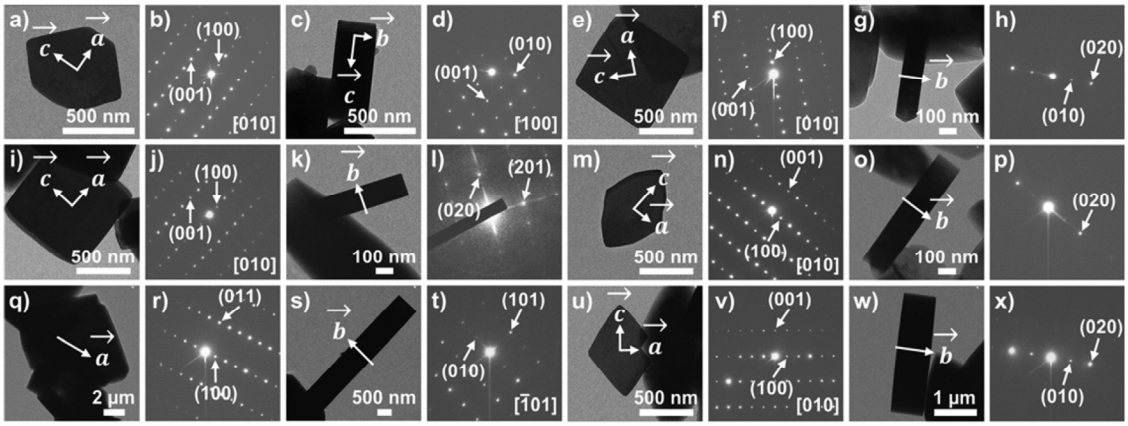

Fig. 5. TEM images and corresponding SAED (selected area electron diffraction) patterns of the $LiCoPO_4$ samples obtained by MWST synthesis using various co-solvents in a 1:1 (v:v) mixture with water: (a–d) LCP-EG, (e–h) LCP-DEG, (i–l) LCP-TEG, (m–p) LCP-TTEG, (q–t) LCP-PEG, and (u–x) LCP-BA. The front views and respective side views of crystals are displayed for each material. The respective zone axes are indicated in square brackets (where possible).

strong and distinct SAED peaks confirm that that the particles in all samples are highly-ordered single crystals. The thicknesses of the platelets with different base areas in size and shape was assessed using additional SAED patterns of the perpendicular side views. It can be inferred that all the examined platelet-like particles are single crystals grown with exposed (010) faces and show the smallest dimensions along the [010] axis of the Li-ion diffusion paths in the olivine crystal structure. The dimensions along [010] are ~200 nm for LCP-EG (Fig. 5c), ~100 nm for LCP-DEG and LCP-TEG (Fig. 5g,k), ~150 nm for LCP-TTEG (Fig. 5o), ~1–3 µm for LCP-PEG (Fig. 5s), and ~0.5–1 µm for LCP-BA (Fig. 5w). Although the square platelets obtained from DEG and TEG appear similar in SEM (*cf.* Fig. 3b and c) and LR-TEM images (Fig. 5e,i and Fig. A3b,c), the SAED experiments reveal that the base areas exhibit different orientations. Whereas the *a* and *c* axes are oriented along the diagonals of the square in LCP-DEG, they are along the median in LCP-TEG. Both in LCP-TTEG and LCP-BA, on the other hand, the axes are along the diagonals of the rhombical base areas with *c* being along the longer diagonal. These findings indicate that the co-solvents specifically adsorb on diverse crystal faces and therefore promote the crystal growth in different ways. The variety of anisotropic shapes (square, rhombic, hexagonal platelets) observed in our study indicates that the relative stabilities of the different crystal facets have been altered in various ways by solvent adsorption. Based on our TEM/SAED study, it can be inferred that the (010) face is stabilized by all polyol-type solvents, which is reflected by the fact that all crystals show reduced dimensions along the [010] direction. This finding is in line with previous reports [51,52,55,56]. A detailed mechanism elucidating the specific changes in surface energies of the individual crystal faces, however, cannot be derived at this point and will have to be examined in further studies with the help of theoretical calculations.

3.5. Electrochemical characterization

The tuned crystal orientations with shortened lithium-ion diffusion pathways along [010] and thus enhanced Li diffusion are expected to be particularly beneficial to achieve high-power capability in lithium-ion cells. Hence, the rate capability of the materials was tested at 0.1 C, 0.2 C, 0.5 C, 1 C, and 2 C for the first three cycles each in the beginning (Fig. 6). The corresponding galvanostatic curves at various C rates can be found in Fig. A4. The

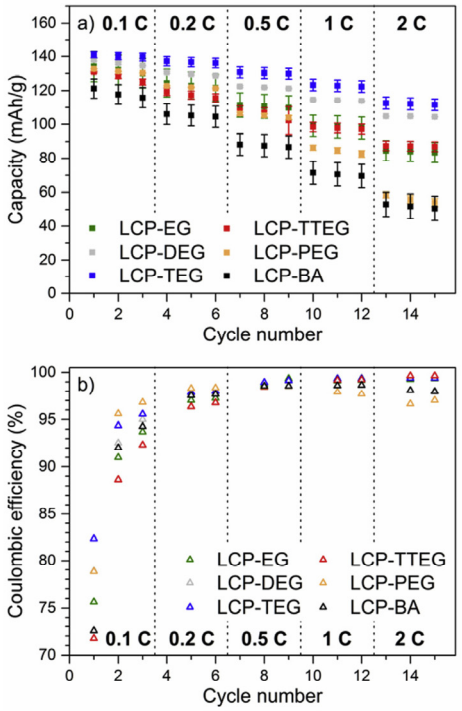

Fig. 6. (a) Specific capacities *vs.* C rate (error bars represent standard deviations from two cells) and (b) coulombic efficiencies (average from two cells; error bars are omitted for clarity) obtained in each cycle for the $LiCoPO_4$ samples synthesized by the MWST process using various co-solvents. The data point of the coulombic efficiency of LCP-DEG in the 1st cycle is not visible due to overlap with the symbol of LCP-PEG. The coulombic efficiencies of the 1st cycle after each C rate increase are omitted because they cannot the determined in these cases. Conditions: 1 M $LiPF_6$ in EC:DMC (1:1, w:w) at 25 °C.

initial capacities of cells containing the $LiCoPO_4$ samples, discharged at 0.1 C, were comparable and ranged from of a low of 121 mAh g^{-1} for LCP-BA to a high of 141 mAh g^{-1} for LCP-TEG in the

1st cycle (Fig. 6a). These capacities are among the best values reported [30,33,35,39,40] for any $LiCoPO_4$-type material to date. The initial capacities are only slightly reduced at 0.2 C. At C rates above 0.2 C, the capacities of the six LCP materials differ substantially and their rate capability can be clearly correlated with their dimensions along the [010] direction as derived from the TEM study (*cf.* Section 3.4 and Fig. 5): the highest capacities at 0.5 C, 1 C, and 2 C are obtained for LCP-DEG and LCP-TEG (both ~100 nm thickness along [010]; gray and blue symbols in Fig. 6a), followed by LCP-TTEG (~150 nm; red symbols) and LCP-EG (~200 nm; green symbols), while clearly the lowest rate capability is observed for both LCP-BA (~0.5–1 μm; black symbols) and LCP-PEG (~1–3 μm; orange symbols). As one would expect, the voltage hysteresis between charge and discharge also increases with increasing thickness in the [010] direction (most apparent by comparing the 1 C and 2 C charge/discharge curves shown in Fig. A4). The performance of the uniform, well-crystallized $LiCoPO_4$ hexagonal platelets obtained from the MWST process in 50 vol% EG, as shown in our previous work [43], can thus still be improved particularly at high C rates by using DEG or TEG as alternative co-solvents, which give a square platelet morphology. In the third cycle at 2 C, for instance, the capacities are increased by 25% and 34% compared to LCP-EG.

The coulombic efficiencies during this rate capability measurements are shown in Fig. 6b, whereby the first cycle after each C rate increase is omitted since the coulombic efficiency cannot really be determined in these cases. The low coulombic efficiency values in the first cycle at 0.1 C (72% for LCP-TTEG, 76% for LCP-EG, 79% for LCP-PEG and LCP-DEG, 82% for LCP-TEG) are probably caused by electrolyte decomposition upon charging at high potential [57,58]. A possible explanation for the variation in coulombic efficiency might be the substantially different BET surface areas of the materials (*cf.* Fig. 4), since parasitic currents from electrolyte oxidation at high potential should increase with the surface area. In this case, one would expect the highest coulombic efficiencies for LCP-PEG (~0.8 $m^2\ g^{-1}$) and the lowest for LCP-TTEG (~6.7 $m^2\ g^{-1}$), which indeed seems to be the case for the cycles at 0.1 C and 0.2 C (*cf.* orange *vs.* red triangles in Fig. 6b). This correlation, however, does not hold strictly for all six LCP materials and fails for all of the materials once the C rate increases above 0.2 C. As a matter of fact, at high C rates, the coulombic efficiency clearly increases with decreasing particle thickness in the [010] direction, analogous to the above discussed increased rate capability with decreasing [010] dimension. This is most likely related to the fact that the average cell voltage during charging at high C rates is substantially higher for materials with large thickness in the [010] direction (*cf.* LCP-PEG and LCP-BA, Fig. A4), which should lead to higher parasitic currents for electrolyte oxidation and thus to the observed lower coulombic efficiencies.

After the C rate testing, the cycle life of the LCP samples was evaluated for 15 cycles at a 0.5 C discharge rate (Fig. 7). The best performing sample LCP-TEG shows a capacity retention of the initial value of 96% in the 15th cycle and the worst performing sample LCP-BA a retention of 77%. The ranking of the different materials with respect to capacity and capacity retention follows the ranking in the rate capability tests at higher C rates, *i.e.*, the materials perform the better the lower the thickness in the [010] direction is (Fig. 7a). Despite the variation in absolute values, all of the samples show a reasonable electrochemical stability, which is among the best performances reported in the literature. This result is remarkable as $LiCoPO_4$ have been shown to suffer from poor cycling stability in general, most likely because of the instability of the electrolyte at high voltage [57,58]. A possible explanation for these high stabilities could be found in the comparatively small surface areas and thus reduced parasitic currents from electrolyte oxidation. This is consistent with the high coulombic efficiencies of

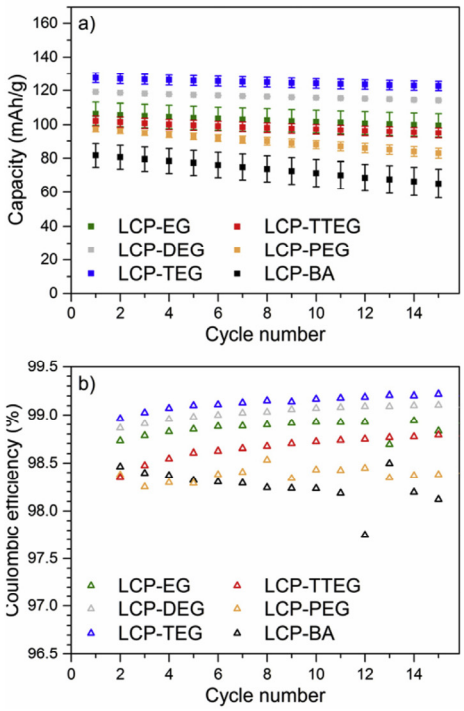

Fig. 7. Comparison of the (a) capacity retentions (error bars represent standard deviations from two cells), (b) coulombic efficiencies (average from two cells; error bars are omitted for clarity) of the $LiCoPO_4$ samples synthesized by the MWST process using various co-solvents at 0.5 C after the first 15 cycles of C rate testing. The coulombic efficiencies of the 1st cycle are omitted as they cannot be determined due to C rate change prior to the cycle life test. Conditions: 1 M $LiPF_6$ in EC:DMC (1:1, w:w) at 25 °C.

about 98–99% observed for all samples (Fig. 7b), which are following the same trend as the absolute capacities (TEG > DEG > EG > TTEG > PEG > BA). Note that the coulombic efficiencies in the 1st cycle (Fig. 7b) are omitted as they cannot be determined due to the testing protocol (C rate change prior to cycle life test).

The main factor identified to affect the rate capabilities of the materials is the thickness in the [010] direction of the Li diffusion pathways, which in turn is related to particle morphology and size. The relatively poorer electrochemical performance of the samples LCP-PEG and LCP-BA can be attributed to the big particle dimensions found in both materials, which leads to higher positive potentials during charge (*cf.* Fig. A4). The samples LCP-EG and LCP-TTEG show good performances because of their small particle sizes and beneficial crystal orientations. The rate capability, however, is worse than for the best samples LCP-DEG and LCP-TEG. Despite the fact that the base areas of the platelets from EG and TTEG are the smallest of the series, the dimensions along [010] are slightly bigger (~150–200 nm) than for LCP-DEG and LCP-TEG (~100 nm). Hence, Li diffusion may be slower. Furthermore, the higher surface areas in contact with the electrolyte (~6–7 $m^2\ g^{-1}$ *vs.* ~4 $m^2\ g^{-1}$) result in a more pronounced electrolyte decomposition at high potential [57,58], which is consistent with the lower coulombic efficiencies observed for LCP-EG and LCP-TTEG. Hence, our findings are in contrast to the assumption that particle size reduction helps to improve the electrochemical performance by shortening the diffusion pathways for lithium ions [33,39,59], However, the

observation that a medium particle size range is the most feasible for LCP as observed for LCP-DEG and LCP-TEG is in good agreement with our recent work [43], To sum up, the materials LCP-DEG and LCP-TEG deliver the highest discharge capacities and best rate capabilities of the series obtained from various co-solvents in the MWST synthesis. The superior electrochemical properties likely result from the extremely homogeneous particle size distributions, high crystallinities as well as the fact that the crystals show the smallest dimension along [010].

3.6. Comparison with the literature

In comparison to the state of the art in conventional as well as microwave-assisted hydrothermal and solvothermal synthesis (Fig. 8; thorough overview see Ref. [43]), our pure LCP material obtained from the TEG co-solvent with an initial discharge capacity of 141 mAh g^{-1} (0.1 C) and a gravimetric energy density of 677 Wh kg^{-1} based on its capacity and voltage, delivers the best electrochemical performance to date. It is important to note that the material presents a good performance at high C rate although it did not undergo further treatments such as annealing at high temperatures and carbon coating, which are common strategies to enhance the performance. In fact, only by avoiding C-coating, high energy densities can be achieved. Further optimization of the performance is likely with the development of electrolytes suitable for high voltage (*e.g.*, using ionic liquids or additives) [60–62].

4. Conclusions

In conclusion, high-performance platelets of the high-voltage cathode material $LiCoPO_4$ have been synthesized by a simple and fast microwave-assisted solvothermal synthesis approach at moderate temperatures using a variety of 1:1 (v:v) binary solvent blends of water and organic co-solvents. In order to understand the influence of the co-solvent on the morphology, particle size, and crystal orientation of the $LiCoPO_4$ particles, a systematic study has been conducted using the co-solvents ethylene glycol (EG), diethylene glycol (DEG), triethylene glycol (TEG), tetraethylene glycol (TTEG), polyethylene glycol 400 (PEG), and benzyl alcohol (BA).

X-ray powder diffraction studies and elemental analyses of the as-prepared materials indicate that the co-solvent does not affect the composition of highly crystalline materials. However, the secondary solvent plays a key role in tuning the shape, size, and orientation of the $LiCoPO_4$ crystals. SEM and TEM/SAED studies reveal that square, rhombic and hexagonal platelets are obtained depending on the solvent system. The particle dimensions vary between several hundred nanometers and several micrometers, and the crystal growth is in the (010) plane for all materials. Therefore, the smallest crystal dimension is in the favorable [010] direction of the Li-diffusion pathways of the olivine crystal structure. EG and TTEG, and to a minor extent, DEG and TEG, significantly reduce the particle size by hindering the fast growth of nanocrystals during the synthesis. The tuned crystal orientations result in overall high initial discharge capacities for the $LiCoPO_4$ materials obtained from all solvent mixtures. Among them, the samples obtained from the DEG and TEG co-solvents, which show the smallest dimension along [010], exhibit the best electrochemical performances, delivering high initial discharge capacities of 138 mAh g^{-1} and 141 mAh g^{-1}, and gravimetric energy densities of 662 Wh kg^{-1} and 677 Wh kg^{-1} at 0.1 C, respectively, as well as good rate capabilities and cycling stabilities when compared to materials prepared by other hydrothermal, solvothermal, and microwave-assisted procedures.

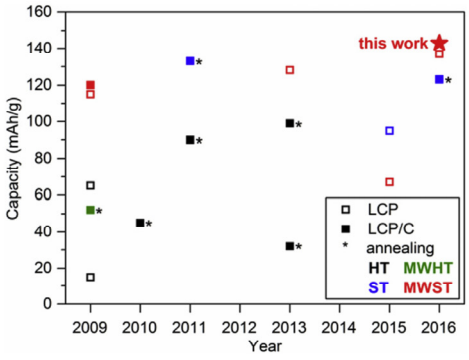

Fig. 8. Comparison of the initial capacities at a 0.1 C discharge rate obtained for $LiCoPO_4$ and carbon-coated $LiCoPO_4$/C materials synthesized via hydrothermal (HT), solvothermal (ST) and microwave-assisted (MW) procedures as reported [26,27,29,30,34,35,38–41,43,44] between 2009 and 2016. Asterisks mark materials that underwent additional post-heat treatments at high temperatures. The star represents the highest capacity reached in this work using a MWST approach (141 mAh g^{-1}, LCP-TEG).

The possibility of modifying the product morphology by simply changing one reaction parameter such as the co-solvent in a rapid and facile synthesis, as well as the fact that a medium particle size range seems to be beneficial for the electrochemical performance at high voltage, are relevant for industrial applications. However, subsequent studies should focus on a more thorough understanding of the influence of the solvents in tailoring the particle size, morphology, and crystal orientation. This synthesis pathway should be applicable for the preparation of other high-performance electrode materials with tuned crystal properties.

Author contributions

J. L. conceived and designed this work, and carried out the synthetic experiments and material characterization. C. M. and D. H. performed electrochemical measurements. J. L. wrote the publication. All authors participated in discussion of the results and this manuscript.

Funding sources

This work was supported by BMW AG, the Fonds der Chemischen Industrie as well as the TUM Graduate School.

Acknowledgements

The authors would like to thank BMW AG and the TUM Graduate School for financial support. We also thank K. Rodewald for SEM, and M. Hanzlik for TEM measurements. The help of U. Ammari with elemental analyses and D. Pritzl with a part of the syntheses are gratefully acknowledged. Special thanks go to M. M. Doeff for proofreading this manuscript. J. Ludwig is further grateful to the Fonds der Chemischen Industrie for her PhD fellowship.

Glossary

AAS	Atomic absorption spectroscopy
BA	Benzyl alcohol
BET	Brunauer–Emmett–Teller adsorption
CCCV	Constant-current, constant-voltage
DEG	Diethylene glycol
DMC	Dimethyl carbonate
EC	Ethylene carbonate
EG	Ethylene glycol

HR	High-resolution
HT	Hydrothermal
LCP	Lithium cobalt phosphate, $LiCoPO_4$
LEI	Lower secondary electron image
LFP	Lithium iron phosphate, $LiFePO_4$
LIB	Lithium-ion battery
LMP	Lithium manganese phosphate, $LiMnPO_4$
LNP	Lithium nickel phosphate, $LiNiPO_4$
LR	Low-resolution
MWST	Microwave-assisted solvothermal
NMP	*N*-Methyl-2-pyrrolidone
PEG	Polyethylene glycol
PVdF	Polyvinylidene difluoride
PXRD	Powder X-ray diffraction
SAED	Selected area electron diffraction
SEM	Scanning electron microscope
ST	Solvothermal
TEM	Transmission electron microscopy
TTEG	Tetraethylene glycol
TEG	Triethylene glycol

Appendix A. Supplementary data

Supplementary data related to this article can be found at http://dx.doi.org/10.1016/j.jpowsour.2016.12.059.

References

[1] A.K. Padhi, K.S. Nanjundaswamy, J.B. Goodenough, J. Electrochem. Soc. 144 (1997) 1188–1194.
[2] J.M. Tarascon, M. Armand, Nature 414 (2001) 359–367.
[3] S.-Y. Chung, J.T. Bloking, Y.-M. Chiang, Nat. Mater. 1 (2002) 123–128.
[4] A. Yamada, M. Hosoya, S.-C. Chung, Y. Kudo, K. Hinokuma, K.-Y. Liu, Y. Nishi, J. Power Sources 119–121 (2003) 232–238.
[5] B.L. Ellis, K.T. Lee, L.F. Nazar, Chem. Mater. 22 (2010) 691–714.
[6] Y. Wang, P. He, H. Zhou, Energy Environ. Sci. 4 (2011) 805–817.
[7] K. Zaghib, A. Guerfi, P. Hovington, A. Vijh, M. Trudeau, A. Mauger, J.B. Goodenough, C.M. Julien, J. Power Sources 232 (2013) 357–369.
[8] W.-J. Zhang, J. Power Sources 196 (2011) 2962–2970.
[9] K. Amine, H. Yasuda, M. Yamachi, Electrochem. Solid State Lett. 3 (2000) 178–179.
[10] S. Okada, S. Sawa, M. Egashira, J. Yamaki, M. Tabuchi, H. Kageyama, T. Konishi, A. Yoshino, J. Power Sources 97–98 (2001) 430–432.
[11] J.M. Lloris, V.C. Perez, J.L. Tirado, Electrochem. Solid State Lett. 5 (2002) A234–A237.
[12] F. Kubel, Z. Krist. 209 (1994) 755, 755.
[13] D. Morgan, A. Van der Ven, G. Ceder, Electrochem. Solid State Lett. 7 (2003) A30–A32.
[14] M.S. Islam, D.J. Driscoll, C.A.J. Fisher, P.R. Slater, Chem. Mater. 17 (2005) 5085–5092.
[15] S.-I. Nishimura, G. Kobayashi, K. Ohoyama, R. Kanno, M. Yashima, A. Yamada, Nat. Mater. 7 (2008) 707–711.
[16] S. Brutti, S. Panero, ACS Symp. Ser. 1140 (2013) 67–99.
[17] J. Yang, J.J. Xu, J. Electrochem. Soc. 153 (2006) A716–A723.
[18] M.S. Bhuwaneswari, L. Dimesso, W. Jaegermann, J. Sol Gel Sci. Technol. 56 (2010) 320–326.
[19] P.N. Poovizhi, S. Selladurai, Ionics 17 (2011) 13–19.
[20] P.R. Kumar, M. Venkateswarlu, M. Misra, A.K. Mohanty, N. Satyanayana, J. Nanosci. Nanotechnol. 11 (2011) 3314–3322.
[21] F. Wang, J. Yang, Dianhuaxue 19 (2013) 585–589.
[22] N. Padmanathan, S. Selladurai, Asian J. Chem. 25 (2013) 9605–9609.
[23] X. Huang, J. Ma, P. Wu, Y. Hu, J. Dai, Z. Zhu, H. Chen, H. Wang, Mater. Lett. 59 (2005) 578–582.
[24] J. Chen, S. Wang, M.S. Whittingham, J. Power Sources 174 (2007) 442–448.
[25] J. Chen, M.J. Vacchio, S. Wang, N. Chernova, P.Y. Zavalij, M.S. Whittingham, Solid State Ionics 178 (2008) 1676–1693.
[26] Y. Zhao, S. Wang, C. Zhao, D. Xia, Rare Met. Beijing China 28 (2009) 117–121.
[27] M. Kotobuki, Y. Mizuno, H. Munakata, K. Kanamura, Phosphorus Res. Bull. 24 (2010) 12–15.
[28] N. Recham, J. Oro-Sole, K. Djellab, M.R. Palacin, C. Masquelier, J.M. Tarascon, Solid State Ionics 220 (2012) 47–52.
[29] M. Kotobuki, Int. J. Energy Environ. Eng. 4 (2013) 25–32.
[30] F. Wang, J. Yang, Y. Nuli, J. Wang, J. Power Sources 196 (2011) 4806–4810.
[31] J. Su, B.-Q. Wei, J.-P. Rong, W.-Y. Yin, Z.-X. Ye, X.-Q. Tian, L. Ren, M.-H. Cao, C.-W. Hu, J. Solid State Chem. 184 (2011) 2909–2919.
[32] M. Li, Ionics 18 (2012) 507–512.
[33] X. Rui, X. Zhao, Z. Lu, H. Tan, D. Sim, H.H. Hng, R. Yazami, T.M. Lim, Q. Yan, ACS Nano 7 (2013) 5637–5646.
[34] S. Brutti, J. Manzi, A. De Bonis, D. Di Lecce, F. Vitucci, A. Paolone, F. Trequattrini, S. Panero, Mater. Lett. 145 (2015) 324–327.
[35] B. Wu, H. Xu, D. Mu, L. Shi, B. Jiang, L. Gai, L. Wang, Q. Liu, L. Ben, F. Wu, J. Power Sources 304 (2016) 181–188.
[36] M.K. Devaraju, I. Honma, Adv. Energy Mater. 2 (2012) 284–297.
[37] I. Bilecka, M. Niederberger, Nanoscale 2 (2010) 1358–1374.
[38] A.V. Murugan, T. Muraliganth, A. Manthiram, J. Electrochem. Soc. 156 (2009) A79–A83.
[39] A.V. Murugan, T. Muraliganth, P.J. Ferreira, A. Manthiram, Inorg. Chem. 48 (2009) 946–952.
[40] R.E. Rogers, G.M. Clarke, O.N. Matthew, M.J. Ganter, R.A. DiLeo, J.W. Staub, M.W. Forney, B.J. Landi, J. Appl. Electrochem. 43 (2013) 271–278.
[41] K.J. Kreder, G. Assat, A. Manthiram, Chem. Mater. 27 (2015) 5543–5549.
[42] K.J. Kreder, G. Assat, A. Manthiram, Chem. Mater. 28 (2016) 1847–1853.
[43] J. Ludwig, C. Marino, D. Haering, C. Stinner, D. Nordlund, M.M. Doeff, H.A. Gasteiger, T. Nilges, RSC Adv. 6 (2016) 82984–82994.
[44] J. Manzi, M. Curcio, S. Brutti, Nanomaterials 5 (2015) 2212–2230.
[45] V. Petricek, M. Dusek, L. Palatinus, Z. Krist. Cryst. Mater. 229 (2014) 345–352.
[46] L.W. Finger, D.E. Cox, A.P. Jephcoat, J. Appl. Crystallogr. 27 (1994) 892–900.
[47] D.T. Cromer, D.A. Liberman, Acta Crystallogr. Sect. A A37 (1981) 267 268.
[48] J.F. Berar, P. Lelann, J. Appl. Crystallogr. 24 (1991) 1–5.
[49] V. Koleva, E. Zhecheva, R. Stoyanova, Eur. J. Inorg. Chem. (2010) 4091–4099.
[50] M. Wu, Z.H. Wang, L.X. Yuan, W.X. Zhang, X.L. Hu, Y.H. Huang, Chin. Sci. Bull. 57 (2012) 4170–4175.
[51] V. Mathew, M.H. Alfaruqi, J. Gim, J. Song, S. Kim, D. Ahn, J. Kim, Mater. Charact. 89 (2014) 93–101.
[52] J. Song, L. Wang, G. Shao, M. Shi, Z. Ma, G. Wang, W. Song, S. Liu, C. Wang, Phys. Chem. Chem. Phys. 16 (2014) 7728–7733.
[53] X. Zhang, Z. Ai, F. Jia, L. Zhang, J. Phys. Chem. C 112 (2008) 747–753.
[54] S. Kuppan, P. Balaya, M.V. Reddy, B.V.R. Chowdari, J.J. Vittal, Energy Environ. Sci. 3 (2010) 457–464.
[55] C.A.J. Fisher, M.S. Islam, J. Mater. Chem. 18 (2008) 1209–1215.
[56] A. Whiteside, C.A.J. Fisher, S.C. Parker, M. Saiful Islam, Phys. Chem. Chem. Phys. 16 (2014) 21788–21794.
[57] M. Egashira, H. Takahashi, S. Okada, J.-I. Yamaki, J. Power Sources 92 (2001) 267–271.
[58] N.N. Bramnik, K. Nikolowski, D.M. Trots, H. Ehrenberg, Electrochem. Solid State Lett. 11 (2008) A89–A93.
[59] S. Brutti, P. Reale, E. Piciollo, V. Gentili, P.G. Bruce, B. Scrosati, S. Panero, Prepr. Symp. Am. Chem. Soc. Div. Fuel Chem. 57 (2012) 737–739.
[60] M. Hu, X. Pang, Z. Zhou, J. Power Sources 237 (2013) 229–242.
[61] R. Sharabi, E. Markevich, K. Fridman, G. Gershinsky, G. Salitra, D. Aurbach, G. Semrau, M.A. Schmidt, N. Schall, C. Bruenig, Electrochem. Commun. 28 (2013) 20–23.
[62] A. Freiberg, M. Metzger, D. Haering, S. Bretzke, S. Puravankara, T. Nilges, C. Stinner, C. Marino, H.A. Gasteiger, J. Electrochem. Soc. 161 (2014) A2255–A2261.

Appendix A: Supplementary material

Morphology-controlled microwave-assisted solvothermal synthesis of high-performance $LiCoPO_4$ as a high-voltage cathode material for Li-ion batteries

Jennifer Ludwig [a], Cyril Marino [b‡], Dominik Haering [b], Christoph Stinner [c], Hubert A. Gasteiger [b], and Tom Nilges [a*]

[a] Technical University of Munich, Department of Chemistry, Synthesis and Characterization of Innovative Materials, Lichtenbergstr. 4, 85747 Garching, Germany

[b] Technical University of Munich, Department of Chemistry, Technical Electrochemistry, Lichtenbergstr. 4, 85747 Garching, Germany

[c] BMW AG, Petuelring 130, 80788 München, Germany

[‡] Present address: Paul Scherrer Institute, Electrochemical Energy Storage, 5232 Villigen PSI, Switzerland

* Corresponding author. E-mail: tom.nilges@lrz.tum.de, Tel.: +49 89 289 13110, Fax: +49 89 289 13762

1. Rietveld refinements of X-ray powder diffraction (PXRD) data

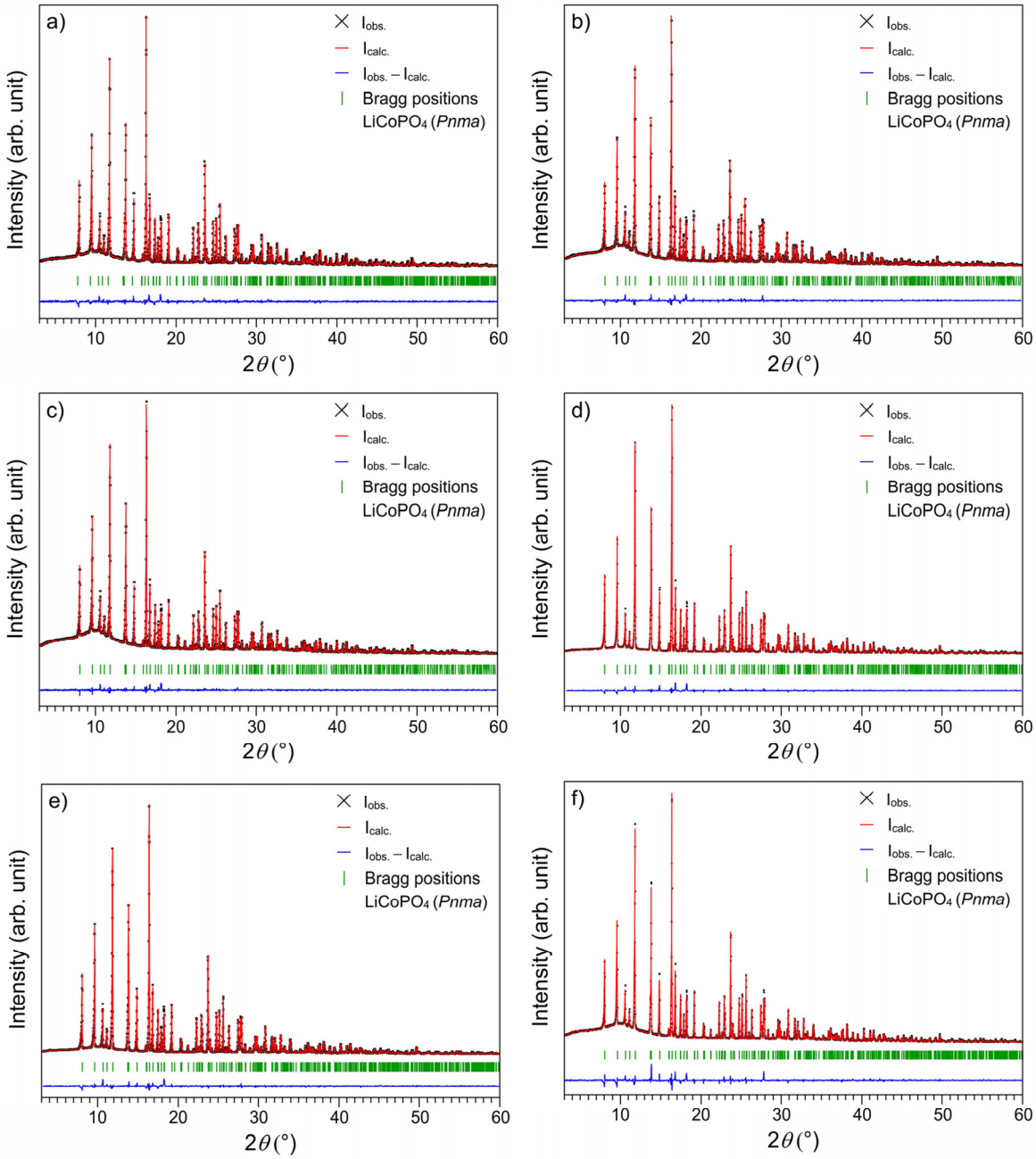

Fig. A.1 Rietveld fits of the X-ray powder diffraction patterns (transmission mode, Mo $K_{\alpha 1}$ radiation, measurement time: 12 h) of the $LiCoPO_4$ samples obtained from MWST synthesis using various co-solvents in a 1:1 (v:v) mixture with water: (a) LCP-EG, (b) LCP-DEG, (c) LCP-TEG, (d) LCP-TTEG, (e) LCP-PEG, and (f) LCP-BA.

Table A.1 Fractional atomic coordinates and isotropic thermal displacement parameters refined from X-ray powder diffraction data of the $LiCoPO_4$ (*Pnma*, $Z = 4$, $T = 298$ K) samples obtained from MWST synthesis using various co-solvents [a]

Sample	Atom	Wyckoff position	Occupancy	*x*/a	*y*/b	*z*/c	U_{iso} (Å^2)
LCP-EG	Li1	4*a*	1	0	0	0	0.0139 [b]
	Co1	4*c*	1	0.22124(14)	¼	0.5211(4)	0.0111(5)
	P1	4*c*	1	0.4049(3)	¼	0.0825(6)	0.0066(8)
	O1	4*c*	1	0.4051(8)	¼	0.7659(14)	0.005(2)
	O2	4*c*	1	0.0457(7)	¼	0.2931(13)	0.004(2)
	O3	8*d*	1	0.3351(5)	0.0473(8)	0.2183(9)	0.0039(13)
LCP-DEG	Li1	4*a*	1	0	0	0	0.0139 [b]
	Co1	4*c*	1	0.22126(14)	¼	0.5212(4)	0.0105(5)
	P1	4*c*	1	0.4052(3)	¼	0.0822(6)	0.0043(8)
	O1	4*c*	1	0.4041(7)	¼	0.7659(13)	0.004(2)
	O2	4*c*	1	0.0448(7)	¼	0.2950(13)	0.004(2)
	O3	8*d*	1	0.3347(5)	0.0479(8)	0.2175(9)	0.0038(13)
LCP-TEG	Li1	4*a*	1	0	0	0	0.0139 [b]
	Co1	4*c*	1	0.22126(12)	¼	0.5211(3)	0.0107(5)
	P1	4*c*	1	0.4049(3)	¼	0.0822(5)	0.0052(7)
	O1	4*c*	1	0.4040(6)	¼	0.7655(12)	0.0039(18)
	O2	4*c*	1	0.0453(7)	¼	0.2952(12)	0.0058(19)
	O3	8*d*	1	0.3351(5)	0.0473(7)	0.2164(8)	0.0049(12)
LCP-TTEG	Li1	4*a*	1	0	0	0	0.0139 [b]
	Co1	4*c*	1	0.22150(12)	¼	0.5210(3)	0.0119(4)
	P1	4*c*	1	0.4051(3)	¼	0.0829(5)	0.0094(7)
	O1	4*c*	1	0.4040(6)	¼	0.7622(12)	0.0072(18)
	O2	4*c*	1	0.0458(6)	¼	0.2930(11)	0.0048(17)
	O3	8*d*	1	0.3349(5)	0.0459(7)	0.2196(7)	0.0064(12)
LCP-PEG	Li1	4*a*	1	0	0	0	0.0139 [b]
	Co1	4*c*	1	0.22128(12)	¼	0.5211(3)	0.0155(5)
	P1	4*c*	1	0.4050(3)	¼	0.0820(5)	0.0089(7)
	O1	4*c*	1	0.4042(6)	¼	0.7654(12)	0.0063(17)
	O2	4*c*	1	0.0443(6)	¼	0.2953(11)	0.0055(17)
	O3	8*d*	1	0.3343(5)	0.0487(7)	0.2162(7)	0.0075(12)
LCP-BA	Li1	4*a*	1	0	0	0	0.0139 [b]
	Co1	4*c*	1	0.22150(16)	¼	0.5211(4)	0.0120(6)
	P1	4*c*	1	0.4051(3)	¼	0.0824(7)	0.0083(9)
	O1	4*c*	1	0.4044(8)	¼	0.7638(15)	0.005(2)
	O2	4*c*	1	0.0457(9)	¼	0.2922(15)	0.006(2)
	O3	8*d*	1	0.3346(6)	0.0473(9)	0.2199(10)	0.0071(15)

[a] The estimated standard deviations were calculated using the Berar's procedure und are indicated in parentheses. [b] The Li displacement parameters have been fixed as they cannot be deduced by means of X-ray diffraction due to the low atomic scattering factor.

Table A.2 Selected interatomic distances refined from X-ray powder diffraction data of the $LiCoPO_4$ (*Pnma*, $Z = 4$, $T = 298$ K) samples obtained from MWST synthesis using various co-solvents [a]

Atom pair			***d* (Å)**					
			LCP-EG	LCP-DEG	LCP-TEG	LCP-TTEG	LCP-PEG	LCP-BA
Li1	O1	×2	2.168(5)	2.173(5)	2.172(4)	2.163(4)	2.171(4)	2.167(6)
	O2	×2	2.078(4)	2.081(4)	2.083(4)	2.078(4)	2.081(4)	2.076(5)
	O3	×2	2.161(5)	2.167(5)	2.167(4)	2.158(4)	2.174(4)	2.162(6)
Co1	O1	×1	2.203(8)	2.194(7)	2.192(6)	2.183(6)	2.193(6)	2.190(8)
	O2	×1	2.089(7)	2.093(7)	2.088(7)	2.091(6)	2.096(6)	2.095(9)
	O3	×2	2.073(5)	2.074(5)	2.070(4)	2.069(4)	2.074(4)	2.076(5)
	O3	×2	2.197(5)	2.196(5)	2.203(4)	2.195(4)	2.194(4)	2.189(6)
P1	O1	×1	1.490(7)	1.488(7)	1.490(6)	1.510(6)	1.490(6)	1.500(8)
	O2	×1	1.553(8)	1.538(8)	1.545(7)	1.551(7)	1.535(7)	1.553(9)
	O3	×2	1.537(5)	1.536(5)	1.533(5)	1.546(4)	1.531(4)	1.544(6)

[a] The estimated standard deviations were calculated by applying the Berar's correction und are indicated in parentheses.

2. Additional scanning electron microscopy (SEM) images

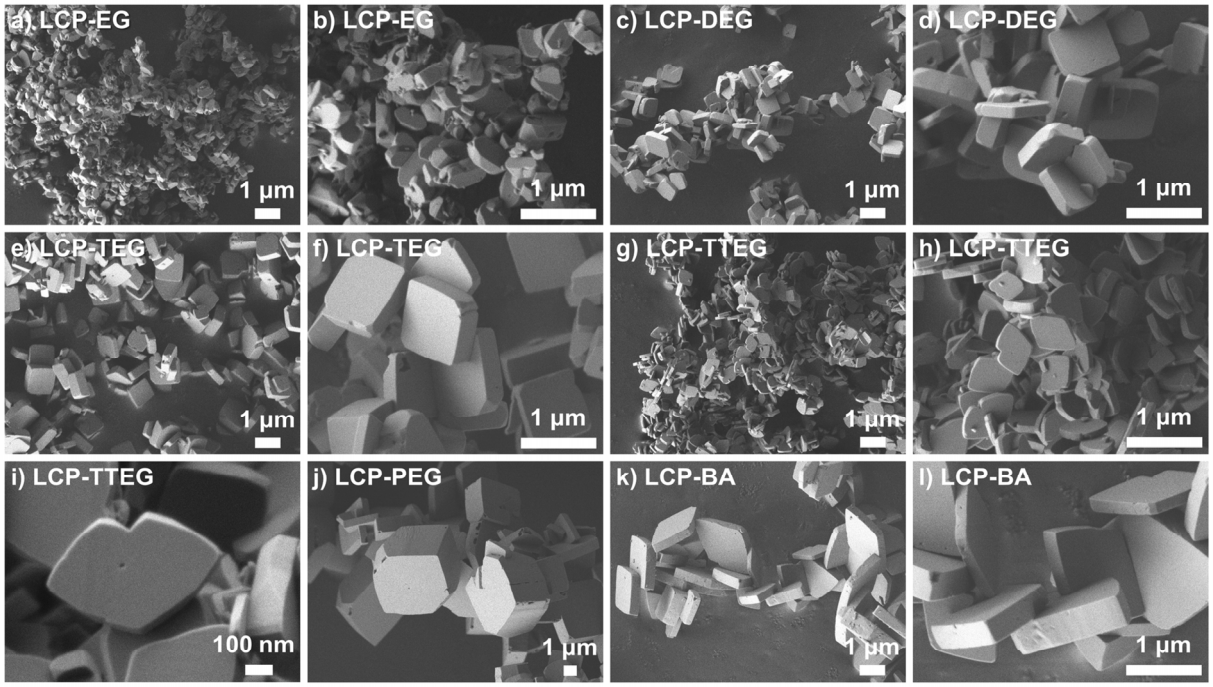

Fig. A.2 SEM images of the $LiCoPO_4$ samples obtained by the MWST process using various co-solvents in a 1:1 (v:v) mixture with water: (a,b) LCP-EG, (c,d) LCP-DEG, (e,f) LCP-TEG, (g,h,i) LCP-TTEG, (j) LCP-PEG, and (k,l) LCP-BA.

3. Additional transmission electron microscopy (TEM) images

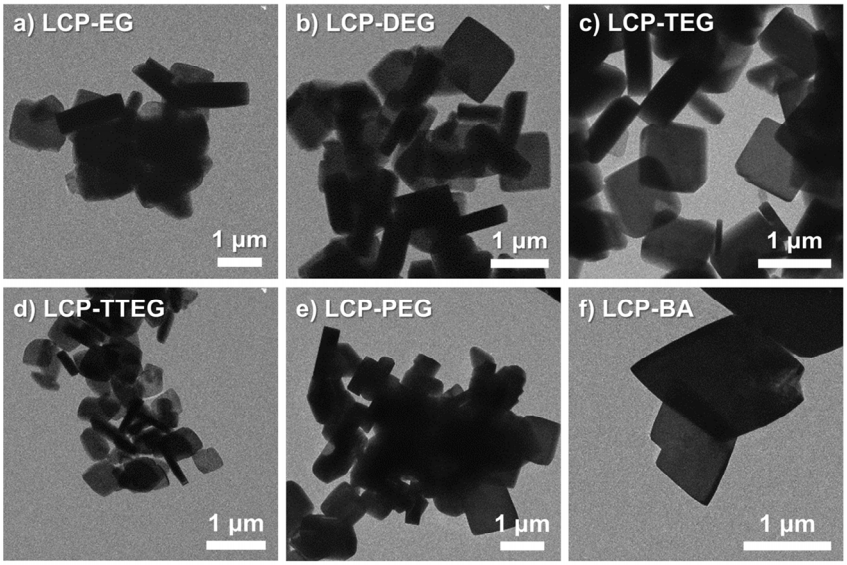

Fig. A.3 Low-resolution TEM images of the $LiCoPO_4$ samples obtained by MWST synthesis using various co-solvents in a 1:1 (v:v) mixture with water: (a) LCP-EG, (b) LCP-DEG, (c) LCP-TEG, (d) LCP-TTEG, (e) LCP-PEG, and (f) LCP-BA.

4. Additional electrochemical data – galvanostatic curves in the first and third cycle at various C rates

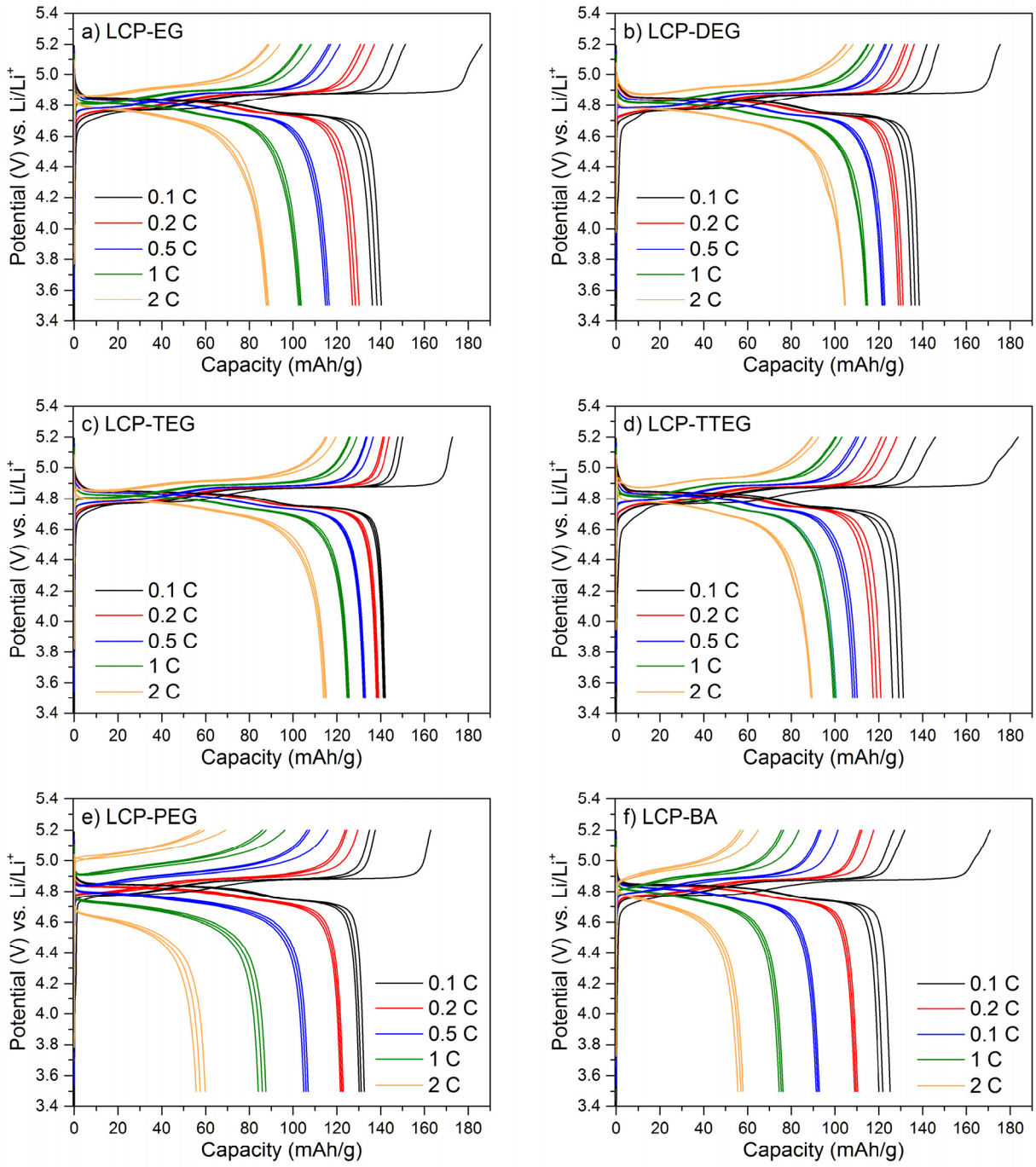

Fig. A.4 Galvanostatic curves of electrodes based on the $LiCoPO_4$ samples obtained from MWST synthesis using various co-solvents in a 1:1 (v:v) mixture with water: (a) LCP-EG, (b) LCP-DEG, (c) LCP-TEG, (d) LCP-TTEG, (e) LCP-PEG, and (f) LCP-BA. Electrochemical cycling was performed in Swagelok cells between 3.5 and 5.2 V using metallic Li as anode and 1 M $LiPF_6$ in ethylene carbonate/dimethyl carbonate (1:1, w:w) as electrolyte. The charge and discharge curves at 0.1 C, 0.2 C, 0.5 C, 1 C, and 2 C are displayed for the first three cycles each.

6.5 $Co_{11}Li[(OH)_5O][(PO_3OH)(PO_4)_5]$, a Lithium-Stabilized, Mixed-Valent Cobalt(II,III) Hydroxide Phosphate Framework

Jennifer Ludwig,[a] Stephan Geprägs,[b] Dennis Nordlund,[c] Marca M. Doeff,[d] and Tom Nilges[a]

[a] Technical University of Munich, Department of Chemistry, Synthesis and Characterization of Innovative Materials, Lichtenbergstr. 4, 85747 Garching, Germany

[b] Walther Meissner Institute, Bavarian Academy of Sciences and Humanities, Walther-Meissner-Str. 8, 85747 Garching, Germany

[c] Stanford Synchrotron Radiation Lightsource, SLAC National Accelerator Laboratory, 2575 Sand Hill Rd, Menlo Park, CA, 94025, USA

[d] Lawrence Berkeley National Laboratory, Energy Storage and Distributed Resources Division, 1 Cyclotron Rd, Berkeley, CA, 94720, USA

Manuscript submitted for publication, **2017.**

Reprinted with permission from Ludwig, J.; Geprägs, S.; Nordlund, D.; Doeff, M. M.; Nilges, T., $Co_{11}Li[(OH)_5O][(PO_3OH)(PO_4)_5]$, a Lithium-Stabilized, Mixed-Valent Cobalt(II,III) Hydroxide Phosphate Framework. *Inorg. Chem.* **2017,** *56,* 10950–10961 (**DOI:** 10.1021/acs.inorgchem.7b01152). Copyright 2017 American Chemical Society.

$Co_{11}Li[(OH)_5O][(PO_3OH)(PO_4)_5]$, a Lithium-Stabilized, Mixed-Valent Cobalt(II,III) Hydroxide Phosphate Framework

Jennifer Ludwig [a,], Stephan Geprägs [b], Dennis Nordlund [c], Marca M. Doeff [d], and Tom Nilges [a,*]*

[a] Technical University of Munich, Department of Chemistry, Synthesis and Characterization of Innovative Materials, Lichtenbergstr. 4, 85747 Garching, Germany

[b] Walther Meissner Institute, Bavarian Academy of Sciences and Humanities, Walther-Meissner-Str. 8, 85747 Garching, Germany

[c] Stanford Synchrotron Radiation Lightsource, SLAC National Accelerator Laboratory, 2575 Sand Hill Rd, Menlo Park, CA, 94025, USA

[d] Lawrence Berkeley National Laboratory, Energy Storage and Distributed Resources Division, 1 Cyclotron Rd, Berkeley, CA, 94720, USA

ABSTRACT. A new metastable phase, featuring a lithium-stabilized mixed-valence cobalt(II,III) hydroxide phosphate framework, $Co_{11.0(1)}Li_{1.0(2)}[(OH)_5O][(PO_3OH)(PO_4)_5]$, corresponding to the simplified composition $Co_{1.84(2)}Li_{0.16(3)}(OH)PO_4$, is prepared by hydrothermal synthesis. Because the pH-dependent formation of other phases such as $Co_3(OH)_2(PO_3OH)_2$ and olivine-type $LiCoPO_4$ competes in the process, a pH value of 5.0 is crucial for obtaining a single-phase material. The crystals with dimensions of 15 µm × 30 µm exhibit a unique elongated triangular pyramid morphology with a lamellar fine structure. Powder X-ray diffraction experiments reveal that the phase is isostructural with the natural phosphate minerals holtedahlite and satterlyite, and crystallizes in the trigonal space group *P*31*m* (*a* = 11.2533(4) Å, *c* = 4.9940(2) Å, *V* = 547.70(3) Å^3, *Z* = 1). The three-dimensional network structure is characterized by partially Li-substituted, octahedral $[M_2O_8(OH)]$ (*M* = Co, Li) dimer units which form double chains that run along the [001] direction and are connected by $[PO_4]$ and $[PO_3(OH)]$ tetrahedra. Because no Li-free *P*31*m*-type $Co_2(OH)PO_4$ phase could be prepared, it can be assumed that the Li ions are crucial for the stabilization of the framework. Co *L*-edge X-ray absorption spectroscopy demonstrates that the cobalt ions adopt the oxidation states +2 and +3 and hence, provides further evidence for the incorporation of Li in the charge-balanced framework. The presence of three independent hydroxyl groups is further confirmed by infrared spectroscopy. Magnetization measurements imply a paramagnetic to antiferromagnetic transition at *T* = 25 K and a spin-glass-like behavior with a blocking temperature of ~9 K. The metastable character of the phase is demonstrated by thermogravimetric analysis and differential scanning calorimetry, which above 558 °C reveal a two-step decomposition to CoO, $Co_3(PO_4)_2$, and olivine-type $LiCoPO_4$ with release of water and oxygen.

KEYWORDS. Cobalt lithium hydroxide phosphate, hydrothermal synthesis, metastable compounds, crystal structure, thermal stability

INTRODUCTION

Transition-metal phosphates offer great structural and chemical diversity, which allows for interesting physical properties and therefore opens up a great portfolio of possible applications, for example in adsorption,[1] semiconductive glasses,[2] nonlinear optics,[3] catalysis,[4-7] and batteries.[8-11] In particular iron phosphates have been the object of considerable study because of the relative abundance of iron in nature,[8, 12] whereas cobalt phosphates have been less investigated. An interesting catalyst for oxygen evolution reactions (OER) is, for example, the Co–Pi system, which contains mixed-valent Co ions in a complex hydroxide–hydrogen phosphate–phosphate environment.[5-7] Since many natural phosphates represent hydrothermal minerals, the hydrothermal synthesis technique, mimicking nature, is a powerful tool for preparing compounds isostructural with natural minerals as well as original structures[13] and hence, to further explore the class of cobalt phosphates.

The most prominent compound of this class is probably olivine-type $LiCoPO_4$ (space group: *Pnma*), which belongs to the group of lithium transition-metal orthophosphates $LiMPO_4$ (*M* = Fe, Mn, Co, Ni).[8] The three-dimensional network structure hosts zigzag chains of $[CoO_6]$ octahedra that run along the [001] direction and are connected by $[PO_4]$ tetrahedra, whereas the Li ions are located in channels running along the [010] and [001] directions.[8] $LiCoPO_4$ has been studied extensively in recent years because of its potential use as a high-voltage cathode material for lithium-ion batteries and high theoretical gravimetric energy density of 802 $Wh \cdot kg^{-1}$, which might bring a significant improvement to current Li-ion battery technology.[9-10, 14-16] In addition, also the magnetic properties have been investigated in a number of studies,[17-18] revealing a weak ferromagnetic moment in the antiferromagnetic state below the Néel temperature of T_N = 21.9 K.

Because of their interesting magnetic characteristics, the class of cobalt hydroxide phosphates has also been receiving increasing attention. The most important representative is $Co_2(OH)PO_4$, for which two polymorphs with orthorhombic (space group: *Pnnm*) and tetragonal ($I4_1/amd$) structures are known.[19-20] The orthorhombic $Co_2(OH)PO_4$ polymorph, which adopts the adamite structure type ($Zn_2(OH)AsO_4$, space group: *Pnnm*),[21-22] was first reported by Harrison and co-workers[19] in 1995. The three-dimensional network structure is built from chains of edge-sharing $[CoO_4(OH)_2]$ octahedra, which run along [001] and are cross-linked by dimers of edge-shared $[CoO_4(OH)]$ trigonal bipyramids and $[PO_4]$ tetrahedra. The compound was found to be the first ordered cobalt phosphate that exhibits a three-dimensional antiferromagnetic long-range order below *T* = 70 K and a spin-glass-like state with a blocking temperature of 13 K. This spin-glass-like behavior was related to a magnetic frustration of the Co^{2+} ions in the $[CoO_5]$ dimers due to the existence of antiferromagnetic interactions between

the neighboring $[CoO_6]_\infty$ chains as well as a ferromagnetic interaction between the chains and the dimers.[23] In a number of studies by de Pedro and co-workers,[24-26] it was further demonstrated that the magnetic properties of adamite-type *Pnnm*-$Co_2(OH)PO_4$ can be modified by substituting Co by other magnetic transition-metal ions such as Ni, Cu, and Mn. Furthermore, also the properties of solid solutions of phosphate and arsenate, $Co_2(OH)(PO_4)_{1-x}(AsO_4)_x$ (x = 0–1), have been explored.[27]

The tetragonal $Co_2(OH)PO_4$ polymorph (space group: $I4_1/amd$) was recently reported by Wang *et al.*[20] The phase is isostructural with the minerals caminite $Mg_{1.33}[SO_4(OH)_{0.66}(H_2O)_{0.33}]$ ($MgSO_4 \cdot ⅓\ Mg(OH)_2 \cdot ⅓\ H_2O$)[28] and lipscombite $Fe_{2-y}(OH)PO_4$ ($0 \le y \le 2/3$).[29] The three-dimensional framework features chains of face-sharing $[CoO_4(OH)_2]$ octahedra, which run along the [100] and [010] directions and are connected by tri-bridging OH groups and $[PO_4]$ tetrahedra. Magnetization experiments revealed a ferromagnetic moment below 20 K, which is most likely caused by a canted, antiferromagnetic spin structure. Furthermore, a two-step switching of the magnetization as a function of the magnetic field was found at 2 K. To explain this behavior, a spin-flip component perpendicular to the crystallographic [001] direction and a spin-flop component oriented along [001] were postulated.[20]

In this work, we report on the hydrothermal synthesis and characterization of a new trigonal, *P*31*m*-type cobalt hydroxide phosphate, which is stabilized by Li substitution and exhibits the crystal-chemical composition $Co_{11.0(1)}Li_{1.0(2)}[(OH)_5O][(PO_3OH)(PO_4)_5]$, simplified to $Co_{1.84(2)}Li_{0.16(3)}(OH)PO_4$ for better comparability with the sum formula $Co_2(OH)PO_4$ of the adamite- (*Pnnm*) and caminite-type ($I4_1/amd$) materials. The phase is isostructural with the natural phosphate minerals satterlyite[30-31] $Fe_{9.24}Mg_{2.76}(OH,O)_6(PO_3OH)(PO_4)_5$ (found at the Big Fish River area, Yukon Territory, Canada; simplified formula: $Fe_{1.54}Mg_{0.46}(OH)PO_4$), and holtedahlite[32] $Mg_{12}(OH,O)_6(CO_3)_{0.24}(PO_3OH)_{0.76}(PO_4)_5$ (from Modum, Norway; simplified: $Mg_2(OH)(CO_3)_{0.04}(PO_4)_{0.96}$) as well as its synthetic analogue $Mg_{12}(OH,O)_6(PO_3OH)(PO_4)_5$ (simplified: $Mg_2(OH)PO_4$).[33] The title compound is accessible at an intermediate pH value of 5.0 in the lithium–cobalt–(hydrogen) phosphate system, whereas the high-voltage cathode material $LiCoPO_4$ and the cobalt hydroxide hydrogen phosphate $Co_3(OH)_2(PO_3OH)_2$ are formed under alkaline (pH = 8.0) and acidic ($3.0 \le$ pH ≤ 4.5) conditions, respectively. We therefore started to discuss the structure of the title compound $Co_{11.0(1)}Li_{1.0(2)}[(OH)_5O][(PO_3OH)(PO_4)_5]$ first, before briefly investigating synthetic aspects and physical properties, including infrared and X-ray absorption spectroscopy, magnetic and thermal properties, in more detail.

EXPERIMENTAL SECTION

Hydrothermal Synthesis. $Co_{11.0(1)}Li_{1.0(2)}[(OH)_5O][(PO_3OH)(PO_4)_5]$ (or simplified: $Co_{1.84(2)}Li_{0.16(3)}(OH)PO_4$) crystals were prepared by hydrothermal synthesis using a Berghof digestec™ pressure digestion system equipped with 50 mL teflon-lined (TFM–PTFE) stainless steel pressure vessels (DAB-2), a heating block (DAH-412), and a programmable temperature control unit (BTC-3000; NiCr-Ni temperature probe). The starting materials $LiOH \cdot H_2O$ (Bernd Kraft, ≥ 99.0%), $Co(CH_3COO)_2 \cdot 4\ H_2O$ (Alfa Aesar, 98%), and $(NH_4)_2HPO_4$ (Merck EMSURE, ≥ 99.0%) were used in a Li:Co:P molar ratio of 2:1:1. First, 1.50 mmol $Co(CH_3COO)_2 \cdot H_2O$ and 1.50 mml $(NH_4)_2HPO_4$ were dissolved in 20 mL deionized water (high-purity water type I, Millipore, 18.2 MΩ·cm) to form a pink solution with pH = 5.5. A solution of 3.00 mmol $LiOH \cdot H_2O$ in 10 mL water was then added dropwise under continuous stirring. The pH of the resulting purple suspension (pH = 10) was adjusted to 5.0 using hydrochloric acid (Merck EMSURE, *Ph. Eur.*, 37 wt%) with the help of indicator test strips (Merck MColorpHast™, pH range: 2.0–9.0, pH graduation: 0.5) in order to obtain a phase pure material. To investigate the influence of the pH value on the phase formation, the pH of the reaction mixture was varied in a range of 3.0–8.0, with an increment step of 0.5, by adjusting the amount of HCl added. The mixture was stirred vigorously, transferred to the teflon-lined pressure vessel, and sealed quickly. The temperature was ramped to 220 °C within 2 h and kept at that temperature for 20 h, followed by natural cooling after the reaction. The violet precipitate (*cf.* TOC graphic) was recovered from the suspension (pH = 5.0) by filtration, washed five times with 25 mL deionized water and 25 mL absolute ethanol (VWR AnalaR NORMAPUR, 99.95%), and then dried in air at 150 °C for 12 h.

Powder X-ray Diffraction (PXRD) and Rietveld Refinements. PXRD data were collected using a Stoe STADI P diffractometer (Mo $K_{\alpha 1}$ radiation, Ge(111) monochromator, λ = 0.70930 Å) equipped with a Dectris MYTHEN DCS 1K silicon solid-state detector. The ground powders were sealed in borosilicate glass capillaries with a diameter of 0.5 mm (Hilgenberg), and then measured for 12 h in a 2θ range of 3–60° (PSD step: 0.015°; time/step: 30 s, three ranges). Silicon powder (a = 5.43088 Å) was used as external standard for the calibration of the patterns. Rietveld fitting was performed with the Jana2006 software[34] using the structure solution of the isostructural mineral satterlyite (simplified formula: $Fe_{1.54}Mg_{0.46}(OH)PO_4$; structure-chemical formula: $Fe_{9.24}Mg_{2.76}(OH,O)_6(PO_3OH)(PO_4)_5$, space group: $P31m$, ICSD no. 94842)[31] as a starting model. The background profile was fitted using a Chebyshev polynomial (35 coefficients), and peak asymmetry was corrected by the axial divergence model[35] embedded in Jana2006. An absorption correction[36] was applied using an estimated packing fraction of 0.6 for the capillary. The general atomic positions and isotropic

thermal displacement parameters of the Co, P, and O atoms were refined without restraints, whereas all parameters of the H atoms were kept fixed. Furthermore, a Li substitution on both Co sites was assumed, while keeping the sum of the Li and Co site occupancy factors at 1. The positional atomic parameters were then standardized using the Structure Tidy routine[37] implemented in the Platon software package.[38] Finally, the Berar's factor[39] was applied to all refined parameters to obtain more realistic standard uncertainties.

Elemental Analysis. The Li content was analyzed by atomic absorption spectroscopy (AAS) using a Varian AA280FS sequential device. The Co and P amounts were measured by photometry on a Shimadzu UV-160 instrument. A Hekatech Euro EA CHNSO analyzer was used to determine the C, H, N, and S contents.

Soft X-ray Absorption Spectroscopy (XAS). Soft X-ray absorption spectroscopy (XAS) measurements were performed at beamline 8-2 of Stanford Synchrotron Radiation Laboratory (SSRL) using a 1100 mm^{-1} spherical grating monochromator (TGM) operated with 30 µm slits, providing ~$2.0 \cdot 10^{10}$ $ph \cdot s^{-1}$ at 0.4 eV resolution in a 1 mm^2 beam spot as described in our previous work.[14] The powder sample was spread onto double-sided carbon tape and five scans of the Co $L_{2,3}$-edge μ(E) spectra were acquired under ultrahigh vacuum (10^{-9} Torr) at ambient temperature in the Auger electron yield (AEY; probing depth: ~2 nm), total electron yield (TEY; 2–5 nm), and fluorescence yield (FY; 50–100 nm) modes, respectively.[40] AEY was collected from a double-pass cylindrical mirror analyzer at a pass energy of 200 eV, TEY was observed through the drain current without bias, and FY was collected from a silicon diode (IRD AXUV-100) mounted at a higher glancing angle to reduce saturation effects. The spectra were normalized to the incoming flux and the energy scale aligned to meet the common energy scale of reference [41], followed by a linear background subtraction. The fitting, which was used to quantify the formal oxidation state of the Co ions, was limited to a small energy region across the L_3 edge (774–784 eV). In order to further experimentally evaluate the crystal field strength and symmetry, the experimental peak positions were extracted from the second derivatives.

Magnetic Measurements. DC magnetization measurements were performed using a Quantum Design MPMS XL7 SQUID (superconducting quantum interference device) magnetometer in the temperature range of T = 2–300 K under a magnetic field of up to 7 T. The powder sample was prepared using a calibrated gelatin capsule placed in a homogenous plastic straw. The temperature-dependence of the magnetic moment was measured in an applied magnetic field of 1 T after cooling the samples under a magnetic field of 7 T (field-cooled, FC) and 0 T (zero-field-cooled, ZFC). Magnetic hysteresis measurements were performed at magnetic field strengths between −7 T and 7 T at temperatures of 2 K, 10 K, 20 K, and 30 K, respectively.

Thermogravimetric Analysis (TGA) and Differential Scanning Calorimetry (DSC). The thermal stability was assessed by simultaneous TGA/DSC using a Mettler Toledo 1 STAR system. An alumina crucible was filled with a specimen weight of approximately 5 mg and then heated up to 900 °C under an argon stream (10 mL·min^{-1}) at a heating rate of 10 °C·min^{-1}. Note that only the heating cycle could be monitored due to the simultaneous instrument setup.

RESULTS AND DISCUSSION

Powder X-ray Diffraction and Rietveld Refinement

Fig. 1 shows the Rietveld fit of the as-prepared title compound $Co_{11.1(1)}Li_{0.9(1)}[(OH)_5O][(PO_3OH)(PO_4)_5]$ (simplified formula for better comparability with the adamite- (*Pnnm*)[19] and caminite-type ($I4_1/amd$)[20] $Co_2(OH)PO_4$ phases: $Co_{1.85(1)}Li_{0.15(1)}(OH)PO_4$), which was obtained from the hydrothermal process at pH = 5.0. According to scanning electron microscopy (SEM) (see inset of Fig. 1), the violet powder (*cf.* TOC graphic) consists of uniform crystals (~15 µm × 30 µm) with a unique elongated triangular pyramid morphology and a lamellar fine structure (for further details on the SEM analysis, please refer to the Supporting Information, section 2, and Fig. S2). The PXRD pattern (see Fig. 1 and Fig. S1) is in good agreement with the simulated patterns of the minerals satterlyite $Fe_{9.24}Mg_{2.76}(OH,O)_6(PO_3OH)(PO_4)_5$ (space group: *P*31*m*, *Z* = 1; ICSD no. 94842,[31] simplified: $Fe_{1.54}Mg_{0.46}(OH)PO_4$) and holtedahlite ($Mg_{12}(OH,O)_6(PO_3OH)(PO_4)_5$ (*P*31*m*, *Z* = 1; ICSD no. 64769,[33] simplified: $Mg_2(OH)PO_4$), suggesting that the phases are isostructural. In fact, all reflections can be fitted to the trigonal structure model of satterlyite[31] with good reliability factors (R_p = 4.04%, R_{wp} = 5.93%, χ^2 = 1.91; *cf.* Table 1; for atomic coordinates, thermal displacements parameters, and selected interatomic distances see Tables S7a and S8a). The unit cell volume of 547.70(3) Å^3 lies between the Fe (*V* = 562.71(9) Å^3)[31] and Mg (*V* = 539.3(3) Å^3)[33] counterparts (for a detailed comparison of the crystallographic data please refer to Table S1), which is in agreement with the trend of ionic radii (with coordination number CN = 6) of Fe^{2+} (high-spin (HS): 0.78 Å), Co^{2+} (HS: 0.745 Å), and Mg^{2+} (0.72 Å) [42] as well as the observed shifts in the PXRD patterns (Fig. S1).

Since the results of the elemental analysis suggested the presence of significant amounts of lithium in the material (see later in the discussion and Table 2), a partial substitution of the Co sites with Li was tentatively refined. The refinement resulted in statistically significant Li occupancies of 2.9(8)% on the Co1 site, and 12.2(8)% for the Co2 position. Mixed site occupation has also been reported for satterlyite, but with the divalent cation Mg^{2+}.[31] Although the Li population on the Co1 site is rather low and hard to determine with X-rays, we concluded that Li–Co mixing appears on both sites because further studies revealed that both sites show significant mixing for the solid solutions with the general composition $Co_{2-x}Li_x(OH)PO_4$ at overall higher Li contents *x* (see later in the text and Fig. S7). Moreover, the free refinement of the Co site occupancy factors (without Li substitution) indicated that both Co sites are not completely filled (occupancies: 97.3(7)% on Co1 and 88.1(7)% on Co2). These Co populations are comparable to the results of the Li/Co mixed model (occupancies: 97.1(8)% Co:2.9(8)% Li on Co1/Li1 (≡ *M*1) and 87.8(8)% Co:12.2(8)% Li on Co2/Li2 (≡ *M*2); see Table S7a). The crystal-

chemical formula $Co_{11.1(1)}Li_{0.9(1)}[(OH)_5O][(PO_3OH)(PO_4)_5]$ (Z = 1; corresponding to a simplified bulk composition of $Co_{1.85(1)}Li_{0.15(1)}(OH)PO_4$) is in good agreement with the composition derived from elemental analysis ($Co_{1.84(2)}Li_{0.16(3)}(OH)PO_4$, *cf.* Table 2) and the molar Co:P:O ratio of 1.87(6):1.00(2):5.0(1) derived from EDS (energy-dispersive X-ray spectroscopy) analysis (*cf.* Fig. S2). Note that this composition would not be charge-balanced assuming that the structure contains only divalent Co^{2+} ions. However, X-ray absorption experiments discussed later reveal that the deficit in positive electric charge due to the substitution by monovalent Li^+ ions is compensated by a corresponding amount of trivalent Co^{3+} in the framework.

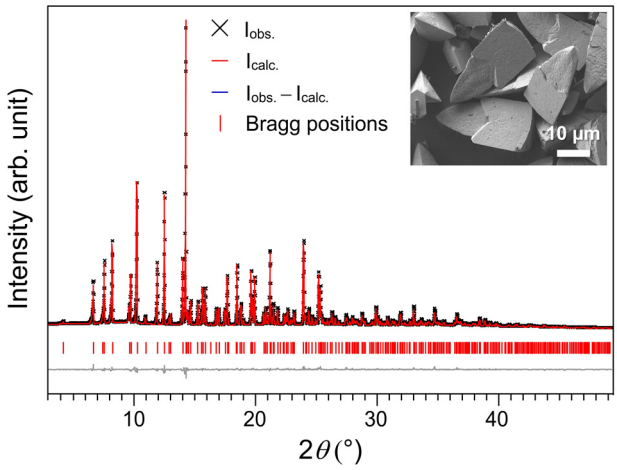

Figure 1. Rietveld fit of the powder X-ray diffraction data (Mo $K_{\alpha1}$ radiation, 0.5 mm capillary, measurement time: 12 h) of $Co_{1.85(1)}Li_{0.15(1)}(OH)PO_4$ (crystal-chemical formula: $Co_{11.1(1)}Li_{0.9(1)}[(OH)_5O][(PO_3OH)(PO_4)_5]$, space group: $P31m$, Z = 1) prepared by the hydrothermal process at pH = 5.0. Inset: Scanning electron microscopy image demonstrating that the sample consists of uniform, well-dispersed crystals with an elongated triangular pyramid morphology and dimensions of ~15 µm × 30 µm.

The proton positions could not be refined from the X-ray data due to the low atomic scattering factor of H, but the infrared (IR) spectrum (*cf.* Fig. S5) revealed the presence of three independent hydroxyl groups, which is consistent with the literature.[32, 43] The proton distribution in satterlyite and holtedahlite has been a subject of thorough discussions.[31, 33, 43] Whereas the H1 and H2 positions, which are bonded to O ligands of [MO_6] octahedra (see structure discussion) could be localized, the position of H3, which belongs to a hydrogen phosphate [PO_3(OH)] unit, is strongly disordered in both structures and was not detectable in synthetic holtedahlite.[33] Although there are seven possible proton positions in the structure (3 × H1, 3 × H2, and 1 × H1, *cf.* Table S7a), the CHNS analysis of our compound (*cf.* Table 2) indicated that the asymmetric unit contains only six protons. This is in agreement with the findings for the Mg and Fe counterparts,[31, 33, 43] which suggest that the H sites are only partially occupied and the protons are distributed among the three hydroxyl groups. Assuming that the

Co-containing phase also exhibits a disordered proton distribution, the correct crystal-chemical formula would therefore be $Co_{11.1(1)}Li_{0.9(1)}[(OH)_{6-x}O_x][(PO_4)_{1-x}(PO_3OH)_x](PO_4)_5$ (with Z = 1) because P3, which belongs to the hydrogen phosphate group, has the multiplicity × 1 (*cf.* Table S7a). Hence, the compound does not represent a polymorph of $Co_2(OH)PO_4$ in the strict sense, although the deviation from the ideal composition is small. A theoretical end-member without a hydrogen phosphate unit (*i.e.*, x = 0) would be $Co_{11.1(1)}Li_{0.9(1)}(OH)_6(PO_4)(PO_4)_5$, which is equivalent to 6 × $[Co_{1.85(1)}Li_{0.15(1)}(OH)PO_4]$. However, this configuration seems to be unlikely since we could distinguish three hydroxyl bands in the infrared spectrum, one of which is related to the $[PO_3(OH)]$ group (for a detailed discussion of the IR spectrum, please refer to the Supporting Information, section 3 and Fig. S5).

Table 1. Crystallographic parameters of $Co_{1.85(1)}Li_{0.15(1)}(OH)PO_4$ as refined from powder X-ray diffraction data (T = 298 K) [a]

Simplified formula	**$Co_{1.85(1)}Li_{0.15(1)}(OH)PO_4$**
Crystal-chemical formula	$Co_{11.1(1)}Li_{0.9(1)}[(OH)_5O][(PO_3OH)(PO_4)_5]$
M_r (g·mol^{-1})	1333.3
Space group (no.)	*P*31*m* (157)
Z	1
a (Å)	11.2533(4)
c (Å)	4.9940(2)
V (Å^3)	547.70(3)
F(000)	645
ρ (calcd.) (g·cm^{-3})	4.038(1)
R_p	0.0404
R_{wp}	0.0593
R_{exp}	0.0326
R_F	0.0474
R_B	0.0647
χ^2	1.91
Data/restraints/parameters	3803/0/91

[a] The standard deviations (in parentheses) were corrected using the Berar's factor.

Crystal Structure

The structure of $Co_{11.1(1)}Li_{0.9(1)}[(OH)_5O][(PO_3OH)(PO_4)_5]$ features octahedral [MO_6] (M = Co, Li) and tetrahedral [PO_4] building units that are connected to form a three-dimensional network. The M positions are characterized by two crystallographically independent Co sites that are partially substituted with Li. With 12.2(8)% Li, the $M2$ site is found to be richer in Li content than $M1$, which is substituted by 2.9(8)% Li (*cf.* Table S7a). The corresponding [($M1$)O_6] and [($M2$)O_6] octahedra are distorted and show $M1$–O distances in the range of 1.94(3)–2.25(3) Å (d_{av} = 2.11 Å), and $M2$–O distances of 2.10(2)–2.319(15) Å (d_{av} = 2.19 Å). The fact that the average M–O distances in the [($M2$)O_6] units, which are more highly substituted with Li, are slightly larger than in [($M1$)O_6] is consistent with the larger ionic radius of Li^+ compared to Co^{2+} (Li^+: 0.76 Å; Co^{2+} (HS): 0.745 Å).[42] However, taking into account the finite amount of Co^{3+} in the structure (see XAS discussion) and assuming that Li^+ and Co^{3+} are occupying the same M sites to form charge-balanced [MO_6] octahedra, a contraction of the $M2$–O bond distance would be expected because of the significantly smaller ionic radius of Co^{3+} (HS: 0.61 Å).[42] Therefore, although it is not possible to derive the $Li^+/Co^{2+}/Co^{3+}$ ordering in the structure without further experiments, it is likely that due to energetic reasons and similar to other compounds,[44] the Co^{3+} ions preferably reside on the $M1$ sites whereas the Li^+ ions reside on the $M2$ sites, which would be consistent with the $M1$–O and $M2$–O distances.

The three P positions are represented by three unique, distorted [PO_4] tetrahedra with average P–O distances of 1.52 Å (P1–O), 1.58 Å (P2–O), and 1.54 Å (P3–O). Each of these units is distorted, and one longer and three shorter bonds are observed (*cf.* Table S8a). The P3 tetrahedron is further characterized by a hydroxyl group (O9–H3), giving rise to [PO_3(OH)] hydrogen phosphate units, with the proton H3 being strongly disordered, as discussed earlier.

The [($M1$)O_6] and [($M2$)O_6] octahedra are condensed *via* shared faces ($M1$: O3, O4, O5; $M2$: O4, O5, O6; *cf.* Fig. 2a), forming $M1$–$M1$ respective $M2$–$M2$ pairs with d($M1$–$M1$) = 2.815(6) Å and d($M2$–$M2$) = 2.860(8) Å. Interestingly, the resulting dimer units [($M1$)$_2O_8$(OH)] and [($M2$)$_2O_8$(OH)] feature *cis*-configured μ_2-bridging hydroxyl groups (O4–H1 and O5–H2), which has been confirmed by infrared spectroscopy (*cf*. Fig. S5). Note that although the calculation of O–H distances is not reliable using powder X-ray diffraction, the IR spectrum qualitatively confirms the presence of different force constants and hence, bond lengths.

The [($M1$)$_2O_8$(OH)] and [($M2$)$_2O_8$(OH)] dimers of face-sharing [MO_6] octahedra are further linked by shared edges (O1–O4 and O2–O5) to form alternating double strands which run parallel to the [001] direction and represent the dominant feature of the structure (Fig. 2b–d). As indicated in Fig. 2e, each double chain shares corners with six further double chains, reflecting the trigonal symmetry of the structure. The three independent [PO_4] tetrahedra are

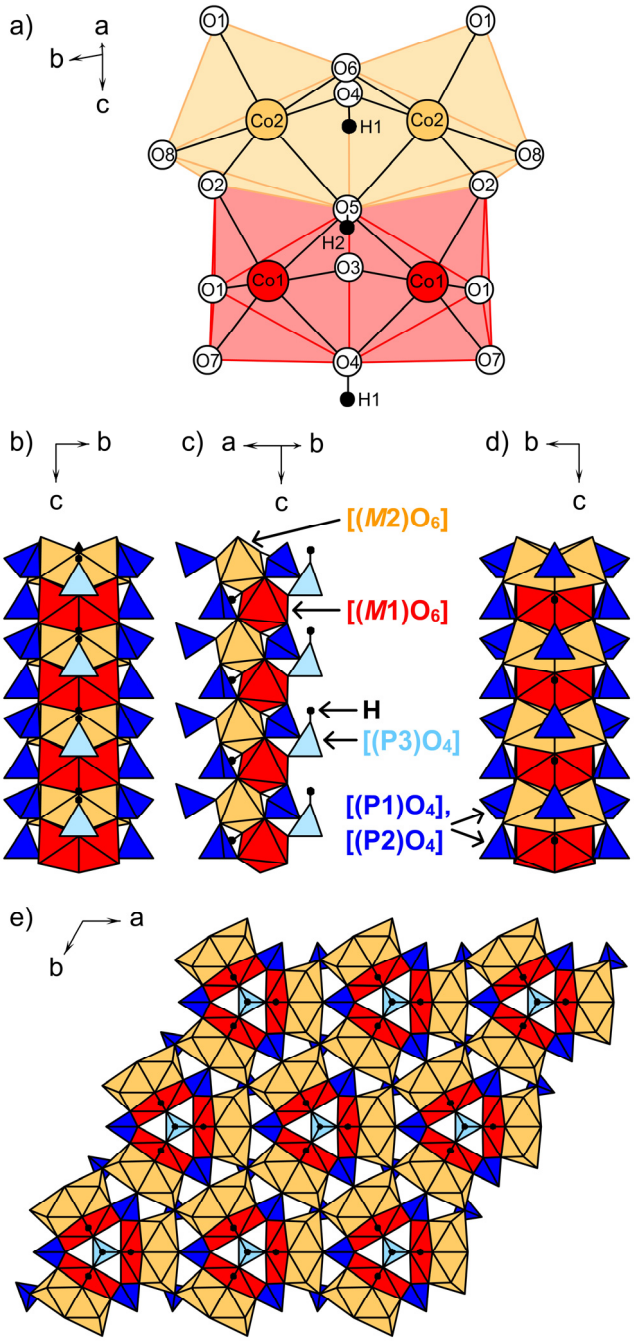

Figure 2. Polyhedral representation of the crystal structure of $Co_{11.1(1)}Li_{0.9(1)}[(OH)_5O][(PO_3OH)(PO_4)_5]$ (space group: *P*31*m*, *Z* = 1; simplified formula: $Co_{1.85(1)}Li_{0.15(1)}(OH)PO_4$). (a) The structure features two independent *M* (*M* = Co, Li) sites, *M*1 (red; populations: 97.1(8)% Co, 2.9(8)% Li) and *M*2 (orange; 87.8(8)% Co, 12.2(8)% Li), which are coordinated by O atoms (white) in an octahedral geometry. The $[(M1)O_6]$ (red) and $[(M2)O_6]$ (orange) units form face-sharing $[(M1)_2O_8(OH)]$ and $[(M2)_2O_8(OH)]$ dimers with μ_2-bridging OH groups (H: black; occupancy: 83.3%). (b–d) Through edge-sharing of the dimers along [001], alternating double chains are formed (viewed along different directions), which represent the dominant structural motif. (e) The double chains are further connected by three different, tetrahedral $[PO_4]$ units to form a three-dimensional network in which each double chain shares corners with six other double chains. Whereas the $[(P1)O_4]$ and $[(P2)O_4]$ tetrahedra (dark blue) share all apical O atoms with the network, the $[(P3)O_3(OH)]$ group (light blue) only contributes three O atoms.

located in the channels of the resulting three-dimensional framework that run along [001]. Whereas the [(P1)O_4] and [(P2)O_4] units are linked *via* all four corners, the [(P3)O_3(OH)] group shares only three apical O atoms with the network.

Elemental Analysis

Table 2 compares the results of the elemental analysis of the XRD-pure sample with the theoretically expected values of a Li-free $Co_2(OH)PO_4$ material as well as the expected values based on the refined composition $Co_{1.85(1)}Li_{0.15(1)}(OH)PO_4$ from the PXRD data. The CHNS analysis indicates that the sample does not contain any detectable amounts of nitrogen or carbon, which might be present due to residues or decomposition products of the $(NH_4)_2HPO_4$ and $Co(CH_3COO)_2 \cdot 4\ H_2O$ precursors. This demonstrates that the washing step is sufficient to remove any side products formed in the synthesis. In contrast, 0.5(3) wt% H are found, which can be correlated to the hydroxyl groups in the structure as demonstrated by IR spectroscopy (see later in the discussion). Entrapped water as a possible source for hydrogen can be clearly ruled out because no water absorption bands are observed in the IR spectrum (*cf*. Fig. S5).

In comparison to the ideal composition of a Li-free $Co_2(OH)PO_4$ phase (Table 2a), which was suggested for the *Pnnm* and *I*4_1/*amd* polymorphs,[19-20] a considerable amount of Li (0.5(1) wt%; *i.e.* significant within three standard deviations) is found in the as-prepared *P*31*m*-type compound whereas the Co content shows a deficit of approximately 2.2 wt% (Table 2c). The corresponding Li:Co:P molar ratio of 0.16(3):1.84(2):1.00(2) suggests that Co (starting from two equivalents Co in the idealized, Li-free composition $Co_2(OH)PO_4$) is partially substituted by Li, which agrees with the X-ray diffraction experiments (Table 2b). Taking into account the H and O contents, the empirical formula of the material on the basis of the elemental analysis is $Co_{1.84(2)}Li_{0.16(3)}(OH)PO_4$ (from this point on, this formula is used for the pure material synthesized at pH = 5.0 for simplicity).

Table 2. Elemental composition of (c) the as-synthesized material at pH = 5.0 in comparison with the theoretically expected values for (a) a Li-free $Co_2(OH)PO_4$-type phase and (b) the composition derived from X-ray diffraction [a,b]

Element	a) Theoretical (Li-free phase)	b) Theoretical (expected from XRD) [c]	c) Measured
H (wt%)	0.4	0.5	0.5(3)
Co (wt%)	51.3	49.1(2)	49.0(5)
Li (wt%)	0	0.50(3)	0.5(1)
P (wt%)	13.5	13.9	14.0(3)
O(estd.) (wt%)	34.8	36.0	36(2) [d]
n(H):*n*(P)	1:1	1:1	0.99(7):1.00(2)
n(Co):*n*(P)	1:1	1.85(1):1	1.84(2):1.00(2)
n(Li):*n*(P)	0	0.15(1):1	0.16(3):1.00(2)
n(O):*n*(P)	5:1	5:1	5.0(3):1.00(2)
Empirical formula	$Co_2(OH)PO_4$	$Co_{1.85(1)}Li_{0.15(1)}(OH)PO_4$	$Co_{1.84(2)}Li_{0.16(3)}(OH)_{0.99(7)}PO_4$

[a] The molar composition was determined from the experimental results (in wt%) of the CHNS, AAS, and photometric analyses, which were normalized to the P content (standard deviations are provided in parentheses). [b] The C, N, and S values were below the detection limit (= 0). [c] Note that standard deviations are only provided for the Co and Li contents since all other atomic sites were assumed to be fully occupied in the structure determination, and hence, do not exhibit standard deviations (see also Table S7a). [d] The O content was estimated from the H, Co, Li, and P contents (in wt%) based on the assumption that the sum of these elements accounts for 100 wt%.

Synthesis Parameters

In order to gain further insights into the phase formation of $Co_{1.84(2)}Li_{0.16(3)}(OH)PO_4$ (general formula with varying Li contents *x*: $Co_{2-x}Li_x(OH)PO_4$), the influence of reaction conditions on the hydrothermal process based on the precursor system $LiOH \cdot H_2O$ – $Co(CH_3COO)_2 \cdot 4\ H_2O$ – $(NH_4)_2HPO_4$ was systematically investigated. While the temperature and reaction time demonstrated only minor influences, with the formation of the metastable $Co_{2-x}Li_x(OH)PO_4$ being preferred at low temperatures and shorter reaction times due to kinetic reaction control (not shown), the synthesis proved to be extremely sensitive towards the pH value of the reaction mixture. Upon variation of the pH value in a range of 3.0–8.0 (increment step: 0.5), a variety of Co-phosphates other than $Co_{2-x}Li_x(OH)PO_4$, namely the phases $Co_3(OH)_2(PO_3OH)_2$ (space group: $P2_1/c$, ICSD no. 67489)[45] and olivine-type $LiCoPO_4$ (*Pnma*, ICSD no. 431999),[16] were obtained. For pH values ≤ 2.5, no precipitate was formed from the reaction, suggesting that all components remained dissolved under strongly acidic conditions. The refined phase fractions *versus* the pH value of the reaction mixture are shown in Fig. 3 (for the individual Rietveld fits and details on the refinements please refer to Fig. S6 and

Tables S4–S10 in the Supporting Information). Under acidic conditions at 3.0 ≤ pH ≤ 4.5, the formation of phase pure $Co_3(OH)_2(PO_3OH)_2$ is favored, while $Co_{2-x}Li_x(OH)PO_4$ and $LiCoPO_4$ compete as reaction products at 5.5 ≤ pH ≤ 7.5. The pH at which pure $Co_{2-x}Li_x(OH)PO_4$ (with x = 0.15(1)) is formed is restricted to a very narrow region around pH 5.0. At pH = 5.5, the synthesis already yields 6.8(7) wt% $LiCoPO_4$ as a side product. The $LiCoPO_4$ fraction rises strongly until a single-phase olivine material is obtained under alkaline conditions (pH = 8.0). At pH > 8.0, a mixture of $LiCoPO_4$ and $Co_{11}(OH)_6(HPO_3)_8$ (space group: $P6_3mc$, ICSD no. 72431)[46] was obtained (not shown).

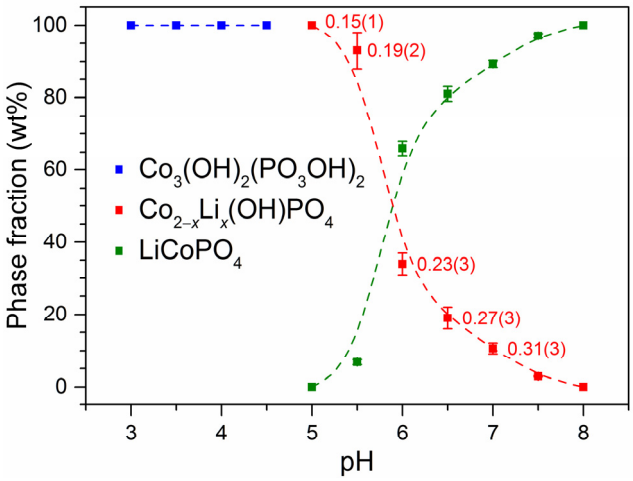

Figure 3. Phase fractions (in wt%; obtained from multi-component Rietveld refinements) *versus* pH value of the reaction mixture demonstrating that the formation of the phases $Co_3(OH)_2(PO_3OH)_2$ (space group: $P2_1/c$), $Co_{2-x}Li_x(OH)PO_4$ ($P31m$; the refined Li contents x are displayed in red along the data points for pH = 5.0–7.0 with standard deviations in parentheses), and $LiCoPO_4$ (*Pnma*) from the hydrothermal process is extremely pH-sensitive. It is evident that a pure $Co_{2-x}Li_x(OH)PO_4$-type material is only realized at pH = 5.0. Non-visible error bars are smaller than the data points. Data points not displayed correspond to a phase fraction of 0 wt%, meaning that no reflections of the respective phases were detected in the PXRD pattern.

The observed variation in reaction products strongly reflects the pH sensitivity of the hydrothermal process. One interesting aspect is that the phases $Co_3(OH)_2(PO_3OH)_2$, $Co_{2-x}Li_x(OH)PO_4$, and $LiCoPO_4$ involve phosphate groups with different degrees of protonation (HPO_4^{2-} → HPO_4^{2-}/PO_4^{3-} (*cf.* crystal structure) → PO_4^{3-}). This can be related to the dissociation equilibria of phosphoric acid:[47]

(1) $H_3PO_4 \rightleftharpoons H_2PO_4^- + H^+$, $pK_{a1} = 2.16$

(2) $H_2PO_4^- \rightleftharpoons HPO_4^{2-} + H^+$, $pK_{a2} = 7.21$

(3) $HPO_4^{2-} \rightleftharpoons PO_4^{3-} + H^+$, $pK_{a3} = 12.32$

According to the pK_a values, the predominant orthophosphate species in the pH range used for the hydrothermal synthesis (3.0–8.0) would be $H_2PO_4^-$ (dihydrogen phosphate) and

HPO_4^{2-} (hydrogen phosphate). However, under hydrothermal synthesis conditions, which involve high temperature and pressure and the presence of various reactants, the equilibria seem to be shifted towards HPO_4^{2-} and PO_4^{3-}. In this context, it is also worth noting that the phase fractions of $Co_{2-x}Li_x(OH)PO_4$ and $LiCoPO_4$ *versus* pH in Fig. 3 follow a trend that resembles the phosphate equilibrium curves. This is consistent with the fact that similar trends with respect to the phase formation were observed when alternative phosphate sources (such as *e.g.* H_3PO_4 and $NH_4H_2PO_4$) were used as starting materials (not shown). Furthermore, the cobalt and hydroxide contents per formula unit decrease with increasing pH value (Co^{2+}: $3 \rightarrow (2-x) \rightarrow 1$, OH^-: $2 \rightarrow 1 \rightarrow 0$), while the Li contents increase ($0 \rightarrow x \rightarrow 1$). This agrees with a report by Huang and co-workers,[48] who suggested that the formation of phases such as $Co_3(OH)_2(PO_3OH)_2$ and $LiCoPO_4$ is the result of a dissolution–recrystallization process involving $Co(OH)_2$ as intermediate. The formation of Li-deficient phases in acidic media was related to the corrosion of the crystals and the solubility of LiOH under these conditions.

In agreement with this finding, the structure refinements reveal that the metal content and distribution in the individual phases are also affected by the pH value. In the case of $Co_{2-x}Li_x(OH)PO_4$, the Li content x (and hence, the Co^{3+} content) almost linearly increases in a range of $0.15(1) \leq x \leq 0.31(3)$ with increasing pH value (Fig. 3 and Fig. S7a). There appears to be a preference for Li substitution on the *M*2 site for all compositions $Co_{2-x}Li_x(OH)PO_4$, although the Li occupancies on the *M*1 site increase more rapidly with higher pH (see Table S7, Fig. S7a). The cell volumes of $Co_{2-x}Li_x(OH)PO_4$ linearly decrease with increasing Li content x (Fig. S7b). According to the ionic radii (CN = 6) of Li^+ (0.76 Å) and Co^{3+} (HS: 0.61 Å) *versus* Co^{2+} (HS: 0.745 Å)[42] this decrease is mainly related to the concomitant increase of the Co^{3+} content, and hence, is in good agreement with what is expected for solid solutions according to Vegard's law.[49] Despite the fact that the refinement of Li contents is not very reliable by means of X-ray methods (*cf.* low atomic scattering factor of Li), this suggests that the phase displays a certain phase width. Therefore, future experiments should focus onto compositional tuning of $Co_{2-x}Li_x(OH)PO_4$ in order to identify the phase width and probably modify the material properties (*e.g.* by varying the stoichiometry of the precursors). It has to be pointed out that within the scope of our investigations, all attempts to prepare a Li-free *P*31*m*-$Co_2(OH)PO_4$ phase by using only $Co(CH_3COO)_2 \cdot 4\ H_2O$ and $(NH_4)_2HPO_4$ as precursors proved unsuccessful, resulting in single-phase $Co_3(OH)_2(PO_3OH)_2$ as the product (not shown). This suggests that the *P*31*m*-framework is probably stabilized by partial Li substitution (up to ~16 at%) as opposed to the lithium-free *Pnnm* and *I*4$_1$/*amd* $Co_2(OH)PO_4$ polymorphs. This would be in line with a report by Kolitsch *et al.*,[31] who suggested that a certain Mg content is necessary to stabilize the Fe homologue satterlyite. Whether a potential *P*31*m*-type $Co_2(OH)PO_4$ is experimentally accessible should be further investigated by optimizing the synthesis parameters. On the other hand, the maximum Li content we found was $x = 0.31(3)$, which suggests

that there is also an upper substitution limit above which the olivine structure $LiCoPO_4$ (*Pnma*) is apparently more stable. This might be explained the presence of more Co^{3+} in the structure, which could intrinsically destabilize the metastable framework.

For $LiCoPO_4$, it was revealed that the phase is more prone to antisite defects when prepared with increasing pH values, with the Co amount on the Li positions increasing (*cf.* Table S9). Since olivine-type $LiCoPO_4$ (*Pnma*) is a potential high-voltage cathode material for lithium-ion batteries,[8-10, 14-16] the investigation of the precursor system also provides valuable insights into this class of materials. The occurrence of antisite defects results in a blocking of the Li diffusion pathways, which reduces the electrochemical performance,[50] and hence suggests that the precursor system and the alkaline medium are not suitable for the production for high-performance cathode materials. The fact that $LiCoPO_4$ and $Co_{2-x}Li_x(OH)PO_4$ coexist over a wide pH range ($5.5 \leq pH \leq 7.5$) is furthermore highly relevant for the production of the material. In fact, we obtained $Co_{2-x}Li_x(OH)PO_4$ as a side phase with $LiCoPO_4$ using different solvothermal synthesis conditions especially when the pH value was not optimized. This is also in line with a report[51] on another polymorph of $LiCoPO_4$ (space group: $Pna2_1$), for which the orthorhombic *Pnnm*-type $Co_2(OH)PO_4$ polymorph was observed as a competing phase under non-ideal conditions. Interestingly, reflections originating from *P*31*m*-type $Co_{2-x}Li_x(OH)PO_4$ were also evident in PXRD patterns reported by other groups.[52] However, the peaks were correlated with other phases such as LiP_5, $Li_{0.62}CoO_2$, and CoO. For that matter, the investigations on $Co_{2-x}Li_x(OH)PO_4$ are highly significant for the wet-chemical synthesis of Co-containing cathode materials. Whether the homologue phases $M_{2-x}Li_x(OH)PO_4$ (*M* = Fe, Mn, Ni) exist and possibly also compete in the synthesis of the olivine-type cathode materials Li*M*PO_4 (*M* = Fe, Mn, Ni) is an interesting topic and should be investigated in consecutive studies.

X-ray Absorption Spectroscopy

In order to investigate the oxidation state of the Co ions in the structure, soft X-ray absorption spectroscopy on the $L_{2,3}$-edge was carried out, which is a powerful probe of the local electronic structure with sensitivity to symmetry, spin, valence, and covalency.[53-54] Fig. 4 shows the normalized Co L_3-edge spectra of $Co_{1.84(2)}Li_{0.16(3)}(OH)PO_4$ compared to reference spectra of octahedrally coordinated (O_h, CN = 6) high-spin (HS) Co^{2+} (from CoO)[41] and HS Co^{3+} (from Sr_2CoO_3Cl)[55]. The $Co_{1.84(2)}Li_{0.16(3)}(OH)PO_4$ spectra are shown for both the TEY mode (Fig. 4b), probing about 2–5 nm deep, and the AEY mode (Fig. 4a), probing at the very top of the surface (~2 nm). Unfortunately, the more bulk-sensitive FY spectrum (~50–100 nm) was not of sufficient quality to be analyzed or discussed further and is therefore not shown.

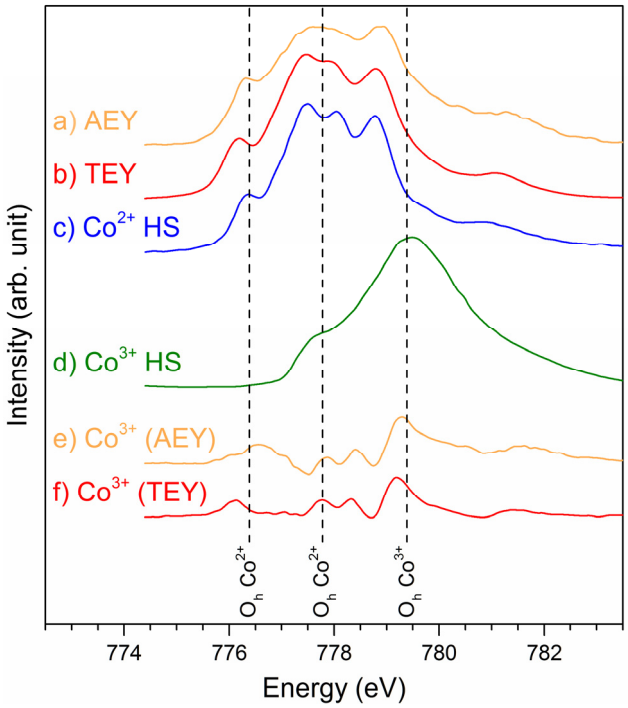

Figure 4. Normalized Co L_3-edge XAS spectra of $Co_{1.84(2)}Li_{0.16(3)}(OH)PO_4$ (prepared by hydrothermal synthesis at pH = 5.0) in the (a) AEY (orange) and (b) TEY (red) modes compared to reference spectra for octahedrally (O_h) coordinated (c) high-spin (HS) Co^{2+} (blue; CoO, adapted from ref. [41]), and (d) high-spin (HS) Co^{3+} (green; Sr_2CoO_3Cl, adapted from ref. [55]). (e) and (f) show the difference spectra resulting from the subtraction of 15% and 6% Co^{2+} from the AEY and TEY spectra of $Co_{1.84(2)}Li_{0.16(3)}(OH)PO_4$, respectively, which represents the Co^{3+} contributions. The increased Co^{3+} contribution at the top surface (AEY, *cf.* a,e) compared to the bulk (TEY; *cf.* b,f) of $Co_{1.84(2)}Li_{0.16(3)}(OH)PO_4$ is evident. All datasets have been aligned to match the common energy scale of reference [41]. The vertical dashed lines indicate the energies corresponding to O_h Co^{2+} (characteristic shoulder: 776.4 eV; doublet: 777.7 eV) as well O_h Co^{3+} (779.4 eV).

It is clearly observed that the AEY (Fig. 4a) and TEY (Fig. 4b) spectra of $Co_{1.84(2)}Li_{0.16(3)}(OH)PO_4$ both show strong commonalities with the reference spectrum of O_h HS Co^{2+} (Fig. 4c) in shape and energy positions of the main features (in particular, the lowest energy peak or shoulder at 776.4 eV is characteristic of octahedrally coordinated Co^{2+}).[41] It can thus be discerned that high-spin divalent Co ions in an octahedral crystal field dominate the spectrum, which is in agreement with the crystal structure that features octahedral [MO_6] (M = Co, Li) units and the pink color of the powder (*cf.* TOC graphic). The minima of the second derivatives (*cf.* Fig. S8), which correspond to the experimental peak positions, reveal a small but significant shift in the peak positions of $Co_{1.84(2)}Li_{0.16(3)}(OH)PO_4$ (*i.e.* peak splitting) compared to the HS Co^{2+} reference which indicates an increased crystal field strength.[41] Moreover, the increase of spectral weight for both the AEY and TEY modes at higher energies, which is associated with Co^{3+} (*cf.* Fig. 4d), indicates the presence of Co^{3+}. This is in line with charge-balance arguments, which suggest that the $Co_{1.84(2)}Li_{0.16(3)}(OH)PO_4$ framework bears mixed-

valent (+2/+3) Co ions due to the substitution of the Co sites by Li^+ ions. Provided that the lack of positive charge caused by the Li^+ substitution (0.16 eq per formula unit) is compensated by the same amount of Co^{3+} ions (0.16 eq), the expected Co^{3+} content of would be ~8.7% (0.16/1.84; based on a total of 1.84 eq Co).

In order to extract the formal oxidation state, the AEY and TEY spectra were fitted with both high-spin Co^{2+} and Co^{3+} octahedral standards. The fitting of the TEY spectrum (*cf*. Fig. S9b) reveals an average Co^{3+} contribution of around (6.2 ± 2.0)%, which is close to the expected Co^{3+} content (~8.7 %), whereas a higher Co^{3+} content of about (14.6 ± 5.0)% was found for the most surface-sensitive AEY mode (*cf*. Fig. S9a). It can therefore be concluded that the top surface exhibits a higher Co^{3+} concentration than the bulk, which is also apparent from Fig. 4e,f, representing the individual Co^{3+} contributions that were obtained from subtraction of the fitted Co^{2+} contributions from the AEY and TEY spectra, respectively. This gradient in the Co^{3+} concentration might be explained by the formation mechanism. In order to obtain an electronically balanced, Li-bearing framework, part of the Co^{2+} ions are probably oxidized to Co^{3+} *in situ*, compensating for the lack of positive charge due to the Li^+ substitution. It is likely that the oxidation preferably occurs on the particle surface since Co^{2+} is generally prone to oxidation in aqueous media. Therefore, it will be worth examining whether the Co oxidation (and Li substitution) can be hindered by using reducing agents such as glucose, ascorbic acid or hydrazine[14, 50] in the reaction mixture in order to produce a Li-free, Co^{2+}-only *P*31*m*-$Co_2(OH)PO_4$ framework.

Magnetic Properties

The magnetic properties of $Co_{1.84(2)}Li_{0.16(3)}(OH)PO_4$ are presented in Fig. 5. In the high temperature regime (T > 100 K), the magnetic susceptibility measured using a magnetic field of 1 T in field-cooled (FC) and zero-field-cooled (ZFC) conditions follow a Curie–Weiss law with a Weiss temperature of (−68 ± 2) K and an effective magnetic moment of (7.08 ± 0.05) μ_B (see Fig. S10). The negative Weiss temperature indicates that the dominant interaction between neighboring magnetic ions is antiferromagnetic. This is in agreement with reports on the Li-free *Pnnm*- and $I4_1/amd$-type $Co_2(OH)PO_4$ polymorphs.[20, 23] The low-temperature behavior of the magnetic susceptibility, however, is different from that of the reported $Co_2(OH)PO_4$ phases. The first maximum of the magnetic susceptibility at around T = 25 K together with an almost linear magnetic field dependence of the magnetization at 10 K suggest the onset of a long-range antiferromagnetic order of $Co_{1.84(2)}Li_{0.16(3)}(OH)PO_4$ below 25 K. This temperature is close to the transition temperature of 20 K found in the tetragonal ($I4_1/amd$) modification of $Co_2(OH)PO_4$,[20] while it is much lower than the transition temperature of 71 K of the

orthorhombic (*Pnnm*) $Co_2(OH)PO_4$ polymorph.[23] Furthermore, a second maximum of the ZFC magnetic susceptibility was found at around 9 K. Below this temperature, $Co_{1.84(2)}Li_{0.16(3)}(OH)PO_4$ exhibits a magnetic hysteresis with a finite remanent magnetization (see inset of Fig. 5 and Fig. S11), demonstrating the existence of a ferromagnetic component. However, no saturation of the magnetization is observed up to 7 T. This behavior is similar to that of *Pnnm*-$Co_2(OH)PO_4$ below 15 K,[23] indicating a spin-glass-like behavior with a blocking temperature of around 9 K. However, to further investigate this spin-glass-like behavior, AC-susceptibility measurements at different frequencies would be required. In total, the finite Li^+ and Co^{3+} concentrations in the $Co_2(OH)PO_4$ framework result in a reduction of the paramagnetic to antiferromagnetic transition as well as the blocking temperature of the spin-glass-like behavior. In order to unveil the structure-related magnetic details unambiguously, neutron diffraction measurements will be required.

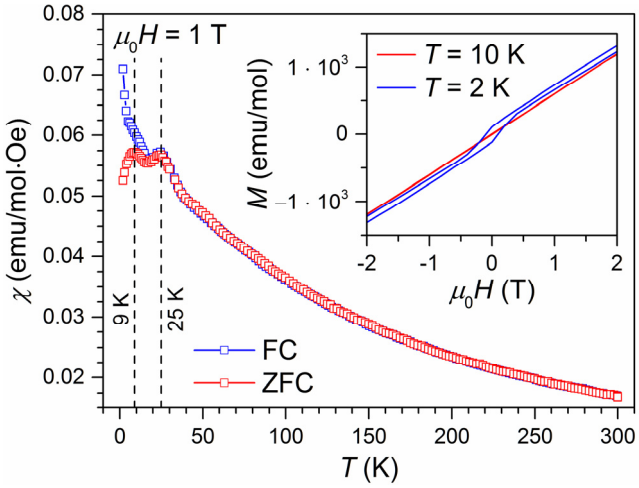

Figure 5. Magnetic susceptibility of $Co_{1.84(2)}Li_{0.16(3)}(OH)PO_4$ (prepared by hydrothermal synthesis at pH = 5.0) as a function of temperature measured at a magnetic field of 1 T under field-cooled (FC) and zero-field-cooled (ZFC) conditions. The vertical dashed lines indicate the temperature of the paramagnetic to antiferromagnetic transition (25 K) as well as the blocking temperature of the spin-glass-like behavior (9 K) at low temperature. Inset: Magnetic hysteresis curves measured at temperatures of T = 10 K and 2 K, respectively.

Thermal Stability

The thermal stability of $Co_{1.84(2)}Li_{0.16(3)}(OH)PO_4$ was investigated by TGA/DSC measurements, which demonstrate a metastable behavior of the material (Fig. 6a). Two signals are observed in the DSC curve, a small exothermic peak at 558 °C, and an endothermic peak at 663 °C. According to the TGA data, both transitions are accompanied by a weight loss that accounts for 4.6 wt% in total. The initial mass loss of about ~0.6 wt% starts around 440 °C,

and is then followed by a distinct step of ~4.0 wt%. The fact that the weight loss onset occurs at rather high temperature implies that no residues of water or the cobalt acetate precursor are present (in agreement with the CHNS analysis, *cf.* Table 2), hence confirming the purity of the material.

According to the X-ray powder diffractogram of the dark violet post-TGA/DSC powder (Fig. 6b, for details on the Rietveld refinement refer to Tables S11–S17), a mixture containing 72.3(10) wt% CoO (space group: $Fm\bar{3}m$; ICSD no. 9865),[56] 15.1(5) wt% $Co_3(PO_4)_2$ ($P2_1/c$, ICSD no. 4268),[57] and 12.6(10) wt% olivine-type $LiCoPO_4$ (*Pnma*, ICSD no. 431999)[16] was formed upon heating. The formation of CoO and $Co_3(PO_4)_2$ upon decomposition is consistent with a report[19] on the *Pnnm* polymorph of $Co_2(OH)PO_4$, for which the same phases were observed (note that for the $I4_1/amd$ polymorph, no decomposition products were reported[20]). The occurrence of the additional Li-containing phase $LiCoPO_4$ provides further evidence for the partial Li-substitution of the $P31m$-type $Co_2(OH)PO_4$ framework.

Based on the TGA/DSC, *ex situ* PXRD as well as the XAS experiments, which demonstrated the presence of Co^{3+} in the structure, the decomposition process of $Co_{1.84(2)}Li_{0.16(3)}(OH)PO_4$ may be described according to Fig. 6c. Whereas the second mass loss step of 4.1 wt%, which is correlated with the endothermic signal around 663 °C, can most likely be attributed to the loss of water from the hydroxyl groups of the framework (*cf.* $[PO_3(OH)]$ and $[M_2O_8(OH)]$ units), the small initial weight loss of 0.6 wt% accompanying the exothermic peak around 558 °C may be the result of oxygen release. This step is driven by a redox reaction, in which the O^{2-} ions are oxidized to elemental O_2 (Eq. II) by the definite amount of Co^{3+} ions, which are in turn reduced to Co^{2+} (Eq. I). The sum of the expected weight losses from H_2O and O_2 is consistent with the experimental TGA mass loss of 4.6 wt% (*cf.* Fig. 6a). In total, the exothermic oxidation takes place first followed by the endothermic dehydration step. Furthermore, the estimated mass fractions of the crystalline decomposition products $Co_3(PO_4)_2$, CoO, and $LiCoPO_4$ in the solid residue after H_2O/O_2 release are equivalent to the refined values obtained from our multi-component Rietveld analysis (Fig. 6b) within one standard deviation, which further supports the suggested mechanism.

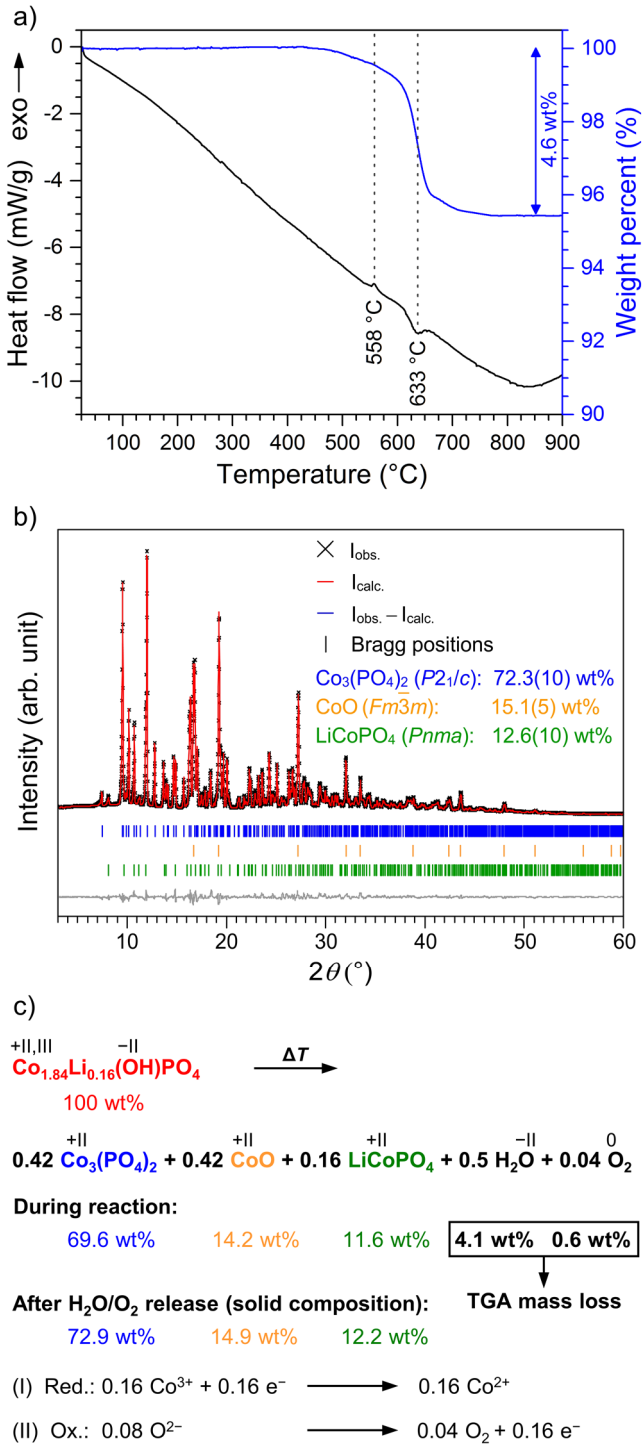

Figure 6. (a) DSC (black) and TGA (blue) curves of $Co_{1.84(2)}Li_{0.16(3)}(OH)PO_4$ measured under Ar in a temperature range of 30–900 °C (heating rate: 10 °C·min^{-1}). Two DSC signals are observed at 558 °C (exothermic) and 633 °C (endothermic), which are accompanied by a total weight loss of 4.6 wt%. (b) Rietveld fit of the powder X-ray diffraction data (Mo $K_{\alpha1}$ radiation, 0.5 mm capillary, measurement time: 12 h) of the post TGA/DSC-material demonstrating that a mixture of crystalline CoO (space group: $Fm\bar{3}m$; ICSD no. 9865),[56] $Co_3(PO_4)_2$ ($P2_1/c$, ICSD no. 4268),[57] and olivine-type $LiCoPO_4$ (*Pnma*, ICSD no. 431999)[16] was formed upon heating. (c) Proposed thermal decomposition process and theoretically expected weight fractions (in wt%) of the involved phases. It can be inferred that the DSC signals and the weight loss observed in the TGA (a) are correlated with the release of water (dehydration) and oxygen (oxidation of oxide ions) as a result of a redox reaction.

CONCLUSION

A novel metastable, lithium-stabilized heterovalent cobalt(II,III) hydroxyl phosphate framework with the empirical formula $Co_{1.84(2)}Li_{0.16(3)}(OH)PO_4$ and the structure-chemical formula $Co_{11.0(1)}Li_{1.0(2)}[(OH)_5O][(PO_3OH)(PO_4)_5]$ was prepared by hydrothermal synthesis. The synthesis conditions, the crystal structure, and material properties were discussed.

The pH value was identified as a key parameter of the hydrothermal process, and the phase pure $Co_{2-x}Li_x(OH)PO_4$-type material is exclusively produced at an intermediate pH value of 5.0 (with x = 0.16(3)). In contrast, $Co_3(OH)_2(PO_3OH)_2$ was formed in a more acidic medium ($3.0 \leq pH \leq 4.5$), whereas olivine-type $LiCoPO_4$ was obtained under alkaline conditions (pH = 8.0). The uniform crystals of the material exhibit a unique triangular pyramid morphology (dimensions: 15 µm × 30 µm) with a nanosheet-like primary structure. The trigonal phase (space group: $P31m$, a = 11.2533(4) Å, c = 4.9945(2) Å, V = 547.75(3) Å^3, Z = 1) is isostructural with natural phosphate minerals (satterlyite, holtedahlite) and features a partial Li substitution on the Co sites. First experiments suggested that the Li substitution is crucial for the stabilization of the structure since the synthesis of a Li-free $P31m$-type $Co_2(OH)PO_4$ framework proved unsuccessful. The prevailing structural motif are double chains along the [001] direction, which are built from $[M_2O_8(OH)]$ (M = Co, Li) dimers and interconnected by tetrahedral $[PO_4]$ and $[PO_3OH]$ groups. Whereas the occurrence of the OH groups was confirmed by infrared spectroscopy, X-ray absorption spectroscopy studies revealed that the framework features mixed-valent Co ions (+2/+3), the occurrence of Co^{3+} likely being the result of the Li^+ substitution in order to obtain a charge-balanced framework. Magnetic measurements demonstrated a paramagnetic to antiferromagnetic transition at T = 25 K and a spin-glass-like behavior with a blocking temperature of around 9 K. The metastable character of the mixed-valent framework was confirmed by thermogravimetric analysis and differential scanning calorimetry. Driven by a redox reaction and the intrinsic instability of Co^{3+}, the structure decomposes into CoO, $Co_3(PO_4)_2$, and $LiCoPO_4$ in a two-step process, with the oxidation of oxide ions to oxygen being the first (558 °C, exothermic) and the dehydration the second (633 °C, endothermic) step.

To conclude, this work provides fundamental insights into the synthesis and structure–property relationships of cobalt hydroxide framework structures, and hence paves the way into modifying the material properties for potential applications. Due to the occurrence of mixed-valent Co(II,III) ions in the hydroxide–hydrogen phosphate–phosphate framework, it may act as a good oxygen-evolving catalyst (OEC; *e.g.* for water splitting), similarly to the cobalt–phosphate (Co–Pi) catalyst.[5-7] As first experiments revealed that the solid solutions $Co_{2-x}Li_x(OH)PO_4$ (x = 0.15(1)–0.35(3); refined from X-ray data) can be prepared, with the Li content increasing with the pH value of the reaction mixture, future studies should focus onto

compositional tuning of the material (*e.g.* by varying the stoichiometry of the starting materials), which might be of significance for its possible application in catalytic processes. In that context, the destabilizing effect of Co^{3+} as well as the charge ordering of the $Li^{+}/Co^{2+}/Co^{3+}$ ions in the structure should be examined. Furthermore, the synthesis of a non-Li-containing, $Co_2(OH)PO_4$ *P*31*m*-type cobalt(II) framework should be pursued. In order to completely resolve the structure, the proton distribution has to be determined with respect to the H positions, degree of saturation, and a possible delocalization. Since the formation of $Co_{2-x}Li_x(OH)PO_4$ as a side product of the hydrothermal synthesis of the olivine-type cathode material $LiCoPO_4$ (*Pnma*) was revealed, it will be interesting to explore whether the isostructural homologues $M_{2-x}Li_x(OH)PO_4$ (*M* = Fe, Mn, Ni) exist and hence, also represent side products of the respective hydrothermal synthesis processes towards the cathode materials $LiMPO_4$ (*M* = Fe, Mn, Ni).

ASSOCIATED CONTENT. Supporting Information. The following material is available free of charge on the ACS Publications website at DOI: 10.1021/acs.inorg-chem.xxxxxxx: 1. Comparison of the PXRD pattern and lattice parameters with satterlyite and holtedahlite; 2. SEM and EDS; 3. IR spectrum; 4. Rietveld refinements of the PXRD patterns of the samples obtained from hydrothermal syntheses in a pH range of 3.0–8.0; 5. Additional XAS data; 6. Additional magnetic data; 7. Rietveld refinement of the PXRD pattern of the post-TGA/DSC material (PDF).

CCDC 1544992, 1544996–1545001, and 1545128–1545137 contain the supplementary crystallographic data for this paper. The data can be obtained free of charge from The Cambridge Crystallographic Data Centre *via* www.ccdc.cam.ac.uk/structures. Alternatively, the cif files may also be obtained from FIZ Karlsruhe, 76344 Eggenstein-Leopoldshafen, Germany (e-mail: crysdata@fiz-karlsruhe.de), on quoting the CSD numbers 432907–432923.

AUTHOR INFORMATION

Corresponding Authors

* E-mail: jennifer.ludwig@tum.de and tom.nilges@lrz.tum.de, Tel.: +49 89 289 13110, Fax: +49 89 289 13762

Author Contributions

J. L. conceived and designed this work, and carried out the synthesis, material characterization (PXRD, IR, SEM/EDS), and data analysis (under the supervision of M. M. D. and T. N.). S. G. and D. N. performed and analyzed magnetic and XAS measurements, respectively. J. L. wrote the manuscript. All the authors approved the final version of this manuscript.

Funding Sources

This work has been funded by the Fonds der Chemischen Industrie and the TUM Graduate School. The soft XAS experiments were performed at SSRL (Stanford Synchrotron Radiation Lightsource), a Directorate of SLAC National Accelerator Laboratory supported by the US Department of Energy, Office of Science, and Office of Basic Energy Sciences under contract number DE-AC02-76SF00515.

ACKNOWLEDGMENT

The authors would like to thank P. Madhikar for TGA/DSC measurements, and U. Ammari for elemental analysis. The help of C. Denk with a part of the syntheses is gratefully acknowledged. J. Ludwig thanks the Fonds der Chemischen Industrie and the TUM Graduate School for financial support of her Ph.D. project.

ABBREVIATIONS

AAS, atomic absorption spectroscopy; AC, alternating current; AEY, Auger electron yield; CN, coordination number; DC, direct current; DSC, differential scanning calorimetry; EDS, energy-dispersive X-ray spectroscopy; FC, field-cooled; IR, infrared; FY, fluorescence yield; HS, high-spin; HT, hydrothermal; ICSD, Inorganic Crystal Structure Database; OEC, oxygen-evolving catalyst; OER, oxygen evolution reaction; PSD, position-sensitive detector; PTFE, poly(tetrafluoroethylene); PXRD, powder X-ray diffraction; SEM, scanning electron microscope; SQUID, superconducting quantum interference device; TEY, total electron yield; TFM, perfluoro(propylvinylether)-modified PTFE; TGA, thermogravimetric analysis; XAS, X-ray absorption spectroscopy; ZFC, zero-field-cooled.

REFERENCES

[1] Maspoch, D.; Ruiz-Molina, D.; Veciana, J., Old materials with new tricks: multifunctional open-framework materials. *Chem. Soc. Rev.* **2007,** *36*, 770–818.

[2] Hogarth, C. A.; Jamel Basha, M., Electrical conduction in cobalt-phosphate glasses. *J. Phys. D* **1983,** *16*, 869–878.

[3] Anderson, M. T.; Phillips, M. L. F.; Sinclair, M. B.; Stucky, G. D., Synthesis of Transition-Metal-Doped $KTiOPO_4$ and Lanthanide-Doped $RbTiOAsO_4$ Isomorphs That Absorb Visible Light. *Chem. Mater.* **1996,** *8*, 248–256.

[4] Millet, J.-M. M., FePO catalysts for the selective oxidative dehydrogenation of isobutyric acid into methacrylic acid. *Catal. Rev. - Sci. Eng.* **1998,** *40*, 1–38.

[5] Kanan, M. W.; Nocera, D. G., In Situ Formation of an Oxygen-Evolving Catalyst in Neutral Water Containing Phosphate and Co^{2+}. *Science* **2008,** *321*, 1072–1075.

[6] Kanan, M. W.; Surendranath, Y.; Nocera, D. G., Cobalt-phosphate oxygen-evolving compound. *Chem. Soc. Rev.* **2009,** *38*, 109–114.

[7] Zhong, D. K.; Gamelin, D. R., Photoelectrochemical Water Oxidation by Cobalt Catalyst ("Co-Pi")/α-Fe_2O_3 Composite Photoanodes: Oxygen Evolution and Resolution of a Kinetic Bottleneck. *J. Am. Chem. Soc.* **2010,** *132*, 4202–4207.

[8] Padhi, A. K.; Nanjundaswamy, K. S.; Goodenough, J. B., Phospho-olivines as Positive-Electrode Materials for Rechargeable Lithium Batteries. *J. Electrochem. Soc.* **1997,** *144*, 1188–1194.

[9] Amine, K.; Yasuda, H.; Yamachi, M., Olivine $LiCoPO_4$ as 4.8 V electrode material for lithium batteries. *Electrochem. Solid-State Lett.* **2000,** *3*, 178–179.

[10] Zaghib, K.; Guerfi, A.; Hovington, P.; Vijh, A.; Trudeau, M.; Mauger, A.; Goodenough, J. B.; Julien, C. M., Review and analysis of nanostructured olivine-based lithium recheargeable batteries: Status and trends. *J. Power Sources* **2013,** *232*, 357–369.

[11] Masquelier, C.; Croguennec, L., Polyanionic (phosphates, silicates, sulfates) frameworks as electrode materials for rechargeable Li (or Na) batteries. *Chem. Rev.* **2013,** *113*, 6552–6591.

[12] Abrahams, S. C.; Bernstein, J. L., Crystal structure of paramagnetic ludlamite, $Fe_3(PO_4)_2.4H_2O$, at 298 K. *J. Chem. Phys.* **1966,** *44*, 2223–2229.

[13] Rabenau, A., The role of hydrothermal synthesis in preparative chemistry. *Angew. Chem.* **1985,** *97*, 1017–1032.

[14] Ludwig, J.; Marino, C.; Haering, D.; Stinner, C.; Nordlund, D.; Doeff, M. M.; Gasteiger, H. A.; Nilges, T., Facile, ethylene glycol-promoted microwave-assisted solvothermal synthesis of high-performance $LiCoPO_4$ as a high-voltage cathode material for lithium-ion batteries. *RSC Adv.* **2016,** *6*, 82984–82994.

[15] Ludwig, J.; Haering, D.; Doeff, M. M.; Nilges, T., Particle size-controllable microwave-assisted solvothermal synthesis of the high-voltage cathode material $LiCoPO_4$ using water/ethylene glycol solvent blends. *Solid State Sci.* **2017,** *65*, 100–109.

[16] Ludwig, J.; Marino, C.; Haering, D.; Stinner, C.; Gasteiger, H. A.; Nilges, T., Morphology-controlled microwave-assisted solvothermal synthesis of high-performance $LiCoPO_4$ as a high-voltage cathode material for Li-ion batteries. *J. Power Sources* **2017,** *342*, 214–223.

[17] Rivera, J. P., The linear magnetoelectric effect in $LiCoPO_4$ revisited. *Ferroelectrics* **1994,** *161*, 147–164.

[18] Kharchenko, N. F.; Kharchenko, Y. N.; Szymczak, R.; Baran, M.; Schmid, H., Weak ferromagnetism in the antiferromagnetic magnetoelectric crystal $LiCoPO_4$. *Low Temp. Phys.* **2001,** *27*, 895–898.

[19] Harrison, W. T. A.; Vaughey, J. T.; Dussack, L. L.; Jacobson, A. J.; Martin, T. E.; Stucky, G. D., Two new adamite-type phases, $Co_2(OH)PO_4$ and $Zn_2(OH)PO_4$: structure-directing effect of organic additives. *J. Solid State Chem.* **1995,** *114*, 151–158.

[20] Wang, G.; Valldor, M.; Spielberg, E. T.; Mudring, A.-V., Ionothermal Synthesis, Crystal Structure, and Magnetic Study of Co_2PO_4OH Isostructural with Caminite. *Inorg. Chem.* **2014,** *53*, 3072–3077.

[21] Kokkoros, P., The structure of adamite. *Z. Kristallogr., Kristallgeom., Kristallphys., Kristallchem.* **1937,** *96*, 417–434.

[22] Hill, R. J., The crystal structure and infrared properties of adamite. *Am. Mineral.* **1976,** *61*, 979–986.

[23] Rojo, J. M.; Mesa, J. L.; Lezama, L.; Pizarro, J. L.; Arriortua, M. I.; Fernandez, J. R.; Barberis, G. E.; Rojo, T., Spin-glass behavior in a three-dimensional antiferromagnet ordered phase: Magnetic structure of $Co_2(OH)(PO_4)$. *Phys. Rev. B: Condens. Matter Mater. Phys.* **2002,** *66*, 094406/1–094406/13.

[24] de Pedro, I.; Rojo, J. M.; Jubera, V.; Fernandez, J. R.; Marcos, J. S.; Lezama, L.; Rojo, T., Effect of Ni^{2+} (S = 1) and Cu^{2+} (S = 1/2) substitution on the antiferromagnetic ordered phase $Co_2(OH)PO_4$ with spin glass behavior. *J. Mater. Chem.* **2004,** *14*, 1157–1163.

[25] de Pedro, I.; Jubera, V.; Rojo, J. M.; Lezama, L.; Sanchez Marcos, J.; Rodriguez Fernandez, J.; Mesa, J. L.; Rojo, T.; Arriortua, M. I., Magnetic properties of $Co_{2-x}Cu_x(OH)PO_4$ (x = 0, 1 and 2). *J. Magn. Magn. Mater.* **2004,** *272-276*, E665–E666.

[26] de Pedro, I.; Rojo, J. M.; Lezama, L.; Rojo, T., Spectroscopic and magnetic properties of $Co_{1.7}Mn_{0.3}(OH)PO_4$. *Z. Anorg. Allg. Chem.* **2007,** *633*, 1847–1852.

[27] de Pedro, I.; Rojo, J. M.; Rodriguez Fernandez, J.; Lezama, L.; Rojo, T., Synthesis, Spectroscopic and Magnetic Properties of the $Co_2(OH)(PO_4)_{1-x}(AsO_4)_x$ [$0 \le x \le 1$] Solid Solution. *Eur. J. Inorg. Chem.* **2010**, 2514–2522.

[28] Keefer, K. D.; Hochella, M. F., Jr.; De Jong, B. H. W. S., The structure of the magnesium hydroxide sulfate hydrate $MgSO_4 \cdot 1/3Mg(OH)_2 \cdot 1/3H_2O$. *Acta Crystallogr., Sect. B* **1981,** *B37*, 1003–1006.

[29] Gheith, M. A., Lipscombite: a new synthetic "iron lazulite.". *Am. Mineral.* **1953,** *38*, 612–628.

[30] Mandarino, J. A.; Sturman, B. D.; Corlett, M. I., Satterlyite, a new hydroxyl-bearing ferrous phosphate from the Big Fish River area, Yukon Territory [Canada]. *Can. Mineral.* **1978,** *16*, 411–413.

[31] Kolitsch, U.; Andrut, M.; Giester, G., Satterlyite, $(Fe,Mg)_{12}(PO_3OH)(PO_4)_5(OH,O)_6$: crystal structure and infrared absorption spectra. *Eur. J. Mineral.* **2002,** *14*, 127–133.

[32] Raade, G.; Mladeck, M. H., Holtedahlite, a new magnesium phosphate from Modum, Norway. *Lithos* **1979,** *12*, 283–287.

[33] Roemming, C.; Raade, G., The crystal structure of natural and synthetic holtedahlite. *Mineral. Petrol.* **1989,** *40*, 91–100.

[34] Petricek, V.; Dusek, M.; Palatinus, L., Crystallographic Computing System JANA2006: General features. *Z. Kristallogr. - Cryst. Mater.* **2014,** *229*, 345–352.

[35] Finger, L. W.; Cox, D. E.; Jephcoat, A. P., A correction for powder diffraction peak asymmetry due to axial divergence. *J. Appl. Crystallogr.* **1994,** *27*, 892–900.

[36] Cromer, D. T.; Liberman, D. A., Anomalous dispersion calculations near to and on the long-wavelength side of an absorption edge. *Acta Crystallogr., Sect. A* **1981,** *A37*, 267–268.

[37] Gelato, L. M.; Parthe, E., STRUCTURE TIDY - a computer program to standardize crystal structure data. *J. Appl. Cryst.* **1987,** *20*, 139–143.

[38] Spek, A. L., Structure validation in chemical crystallography. *Acta Crystallogr., Sect. D: Biol. Crystallogr.* **2009,** *65*, 148–155.

[39] Berar, J. F.; Lelann, P., E.S.D.'s and estimated probable error obtained in Rietveld refinements with local correlations. *J. Appl. Crystallogr.* **1991,** *24*, 1–5.

[40] Lin, F.; Nordlund, D.; Markus, I. M.; Weng, T.-C.; Xin, H. L.; Doeff, M. M., Profiling the nanoscale gradient in stoichiometric layered cathode particles for lithium-ion batteries. *Energ. Environ. Sci.* **2014,** *7*, 3077–3085.

[41] Hibberd, A. M.; Doan, H. Q.; Glass, E. N.; de Groot, F. M. F.; Hill, C. L.; Cuk, T., Co Polyoxometalates and a Co_3O_4 Thin Film Investigated by L-Edge X-ray Absorption Spectroscopy. *J. Phys. Chem. C* **2015,** *119*, 4173–4179.

[42] Shannon, R. D., Revised effective ionic radii and systematic studies of interatomic distances in halides and chalcogenides. *Acta Crystallogr., Sect. A* **1976,** *A32*, 751–767.

[43] Brunet, F.; Schaller, T., Protons in the magnesium phosphates phosphoellenbergerite and holtedahlite: an IR and NMR study. *Am. Mineral.* **1996,** *81*, 385–394.

[44] Strobridge, F. C.; Clement, R. J.; Leskes, M.; Middlemiss, D. S.; Borkiewicz, O. J.; Wiaderek, K. M.; Chapman, K. W.; Chupas, P. J.; Grey, C. P., Identifying the Structure of the Intermediate, $Li_{2/3}CoPO_4$, Formed during Electrochemical Cycling of $LiCoPO_4$. *Chem. Mater.* **2014,** *26*, 6193–6205.

[45] Effenberger, H., Structure refinement of tricobalt dihydroxide bis(hydrogen phosphate) and cobalt bis(dihydrogen phosphate) dihydrate. *Acta Crystallogr., Sect. C: Cryst. Struct. Commun.* **1992,** *C48*, 2104–2107.

[46] Marcos, M. D.; Amoros, P.; Beltran-Porter, A.; Martinez-Manez, R.; Attfield, J. P., Novel crystalline microporous transition-metal phosphites $M_{11}(HPO_3)_8(OH)_6$ (*M* = Zn, Co, Ni). X-ray powder diffraction structure determination of the cobalt and nickel derivatives. *Chem. Mater.* **1993,** *5*, 121–128.

[47] Haynes, W. M., Dissociation Contants of Inorganic Acids and Bases In *CRC Handbook of Chemistry and Physics*, 94th ed.; CRC Press: Boca Raton, FL, USA, **2013;** pp 5–92.

[48] Huang, X.; Ma, J.; Wu, P.; Hu, Y.; Dai, J.; Zhu, Z.; Chen, H.; Wang, H., Hydrothermal synthesis of $LiCoPO_4$ cathode materials for rechargeable lithium-ion batteries. *Mater. Lett.* **2005,** *59*, 578–582.

[49] Vegard, L., Die Konstitution der Mischkristalle und die Raumfüllung der Atome. *Z. Physik* **1921,** *5*, 17–26.

[50] Chen, J.; Vacchio, M. J.; Wang, S.; Chernova, N.; Zavalij, P. Y.; Whittingham, M. S., The hydrothermal synthesis and characterization of olivines and related compounds for electrochemical applications. *Solid State Ion.* **2008,** *178*, 1676–1693.

[51] Jähne, C.; Neef, C.; Koo, C.; Meyer, H.-P.; Klingeler, R., A new $LiCoPO_4$ polymorph *via* low temperature synthesis. *J. Mater. Chem. A* **2013,** *1*, 2856–2862.

[52] Wu, B.; Xu, H.; Mu, D.; Shi, L.; Jiang, B.; Gai, L.; Wang, L.; Liu, Q.; Ben, L.; Wu, F., Controlled solvothermal synthesis and electrochemical performance of $LiCoPO_4$ submicron single crystals as a cathode material for lithium ion batteries. *J. Power Sources* **2016,** *304*, 181–188.

[53] de Groot, F. M. F.; Abbate, M.; van Elp, J.; Sawatzky, G. A.; Ma, Y. J.; Chen, C. T.; Sette, F., Oxygen 1s and cobalt 2p x-ray absorption of cobalt oxides. *J. Phys.: Condens. Matter* **1993,** *5*, 2277–2288.

[54] de Groot, F. M. F.; Fuggle, J. C.; Thole, B. T.; Sawatzky, G. A., The 2p x-ray absorption of 3d transition-metal compounds: an atomic multiplet description including the crystal field. *Phys. Rev. B: Condens. Matter* **1990,** *42*, 5459–5468.

[55] Hu, Z.; Wu, H.; Haverkort, M. W.; Hsieh, H. H.; Lin, H. J.; Lorenz, T.; Baier, J.; Reichl, A.; Bonn, I.; Felser, C.; Tanaka, A.; Chen, C. T.; Tjeng, L. H., Different Look at the Spin State of Co^{3+} Ions in a CoO_5 Pyramidal Coordination. *Phys. Rev. Lett.* **2004,** *92*, 207402/1–207402/4.

[56] Sasaki, S.; Fujino, K.; Takeuchi, Y., X-ray determination of electron-density distributions in oxides, magnesium oxide, manganese(II) oxide, cobalt oxide, and nickel(II) oxide, and atomic scattering factors of their constituent atoms. *Proc. Jpn. Acad., Ser. B* **1979,** *55*, 43–48.

[57] Anderson, J. B.; Kostiner, E.; Miller, M. C.; Rea, J. R., Crystal structure of cobalt orthophosphate $Co_3(PO_4)_2$. *J. Solid State Chem.* **1975,** *14*, 372–377.

For Table of Contents Only

SYNOPSIS. A new metastable compound, featuring a lithium-stabilized mixed-valent cobalt(II,III) hydroxide phosphate framework, $Co_{11.0(1)}Li_{1.0(2)}[(OH)_5O][(PO_3OH)(PO_4)_5]$ (space group: *P*31*m*, *Z* = 1, simplified composition: $Co_{1.84(2)}Li_{0.16(3)}(OH)PO_4$), was prepared by hydrothermal synthesis. The dominant structural feature are alternating double chains of $[M_2O_8(OH)]$ (*M* = Co, Li) dimer units, which run along the [001] direction and are connected *via* $[PO_4]$ and $[PO_3(OH)]$ tetrahedra. The synthesis conditions, crystal structure, and physical properties of the material are discussed.

TOC GRAPHIC

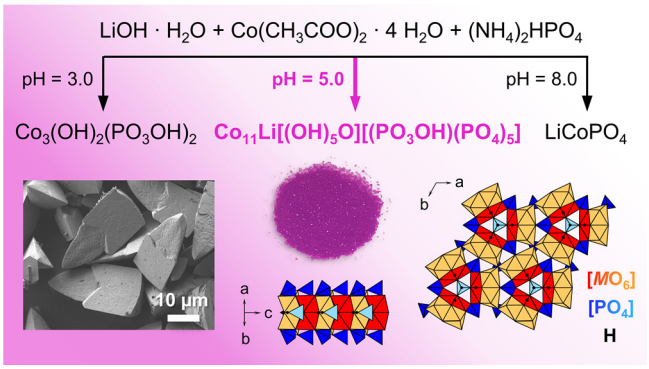

Supporting Information

$Co_{11}Li[(OH)_5O][(PO_3OH)(PO_4)_5]$, a Lithium-Stabilized, Mixed-Valent Cobalt(II,III) Hydroxide Phosphate Framework

Jennifer Ludwig [a,*], Stephan Geprägs [b], Dennis Nordlund [c], Marca M. Doeff [d], and Tom Nilges [a,*]

[a] Technical University of Munich, Department of Chemistry, Synthesis and Characterization of Innovative Materials, Lichtenbergstr. 4, 85747 Garching, Germany

[b] Walther Meissner Institute, Bavarian Academy of Sciences and Humanities, Walther-Meissner-Str. 8, 85747 Garching, Germany

[c] Stanford Synchrotron Radiation Lightsource, SLAC National Accelerator Laboratory, 2575 Sand Hill Rd, Menlo Park, CA, 94025, USA

[d] Lawrence Berkeley National Laboratory, Energy Storage and Distributed Resources Division, 1 Cyclotron Rd, Berkeley, CA, 94720, USA

* Corresponding authors. E-mail: jennifer.ludwig@tum.de and tom.nilges@lrz.tum.de, Tel.: +49 89 289 13110, Fax: +49 89 289 13762

Supporting Information

Table of Contents

Note

The supplementary crystallographic data for this paper can be obtained free of charge from The Cambridge Crystallographic Data Centre (CCDC) via www.ccdc.cam.ac.uk/structures on quoting the following CCDC numbers:

Section 4. Influence of the pH value of the reaction mixture on the phase formation: $Co_3(OH)_2(PO_3OH)_2$ (pH 3.0–4.5, CCDC 1544992 and 1544996–1544998); $Co_{2-x}Li_x(OH)PO_4$ ($0.15(1) \le x \le 0.31(3)$, pH 5.0–7.0, CCDC 1544999–1545001 and 1545128–1545129); $LiCoPO_4$ (pH 6.0–8.0, CCDC 1545130–1545134).

Section 7. Rietveld refinement of the PXRD data of the post-TGA/DSC material: $Co_3(PO_4)_2$ (CCDC 1545135), CoO (CCDC 1545136), and $LiCoPO_4$ (CCDC 1545137).

Alternatively, the cif files may also be obtained from FIZ Karlsruhe, 76344 Eggenstein-Leopoldshafen, Germany (e-mail: crysdata@fiz-karlsruhe.de), on quoting the following CSD deposition numbers:

$Co_3(OH)_2(PO_3OH)_2$ (pH 3.0–4.5, CSD 432907–432910); $Co_{2-x}Li_x(OH)PO_4$ ($0.15(1) \le x \le 0.31(3)$, pH 5.0–7.0, CSD 432911–432915); $LiCoPO_4$ (pH 6.0–8.0, CSD 432916–432920); $Co_3(PO_4)_2$ (post-TGA/DSC, CSD 432921), CoO (post-TGA/DSC, CSD 432922), and $LiCoPO_4$ (post-TGA/DSC, CSD 432923).

Supporting Information

1 Comparison of the Powder X-ray Diffraction Pattern and Lattice Parameters of $Li_{0.15(1)}Co_{1.85(1)}(OH)PO_4$ with the Isostructural Compounds Satterlyite and Holtedahlite

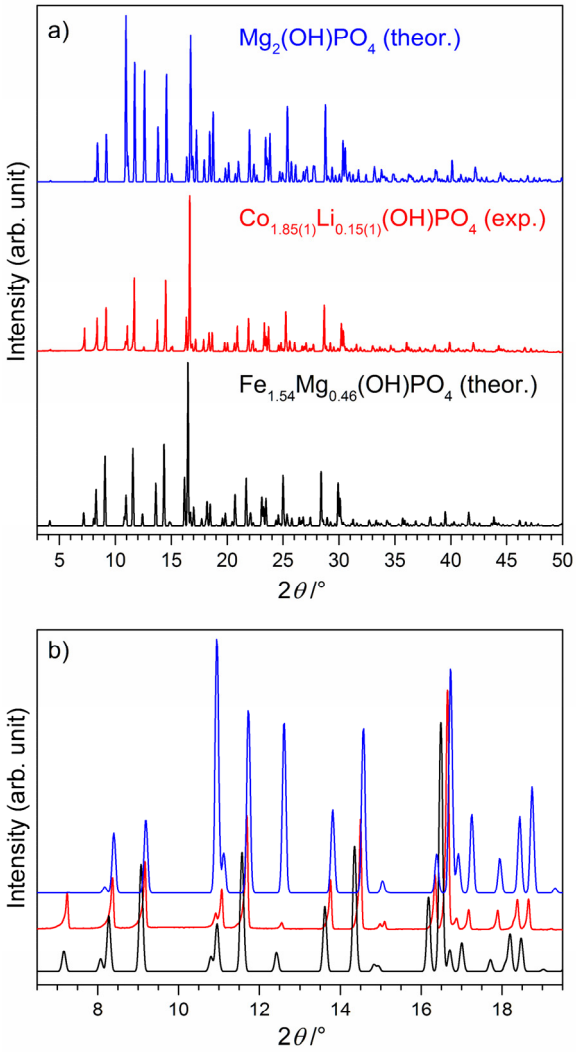

Figure S1. (a) Comparison of the powder X-ray diffraction pattern (Mo $K_{\alpha1}$ radiation, 0.5 mm capillary, measurement time: 12 h) of the $Co_{1.85(1)}Li_{0.15(1)}(OH)PO_4$ powder (crystal-chemical formula: $Co_{11.1(1)}Li_{0.9(1)}[(OH)_5O][(PO_3OH)(PO_4)_5]$, space group: *P*31*m*, *Z* = 1) prepared hydrothermal synthesis at pH = 5.0 (red) to the theoretical patterns calculated from single crystal data of the minerals $Mg_2(OH)PO_4$ (blue, synthetic holtedahlite, crystal-chemical formula: $Fe_{9.24}Mg_{2.76}(OH,O)_6(PO_3OH)(PO_4)_5$, space group: *P*31*m*, *Z* = 1; ICSD no. 64769)[1] and $Fe_{1.54}Mg_{0.46}(OH)PO_4$ (black, satterlyite, crystal-chemical formula: $Mg_{12}(OH,O)_6(PO_3OH)(PO_4)_5$, space group: *P*31*m*, *Z* = 1; ICSD no. 92842)[2]. The pattern of the as-prepared material is similar to the Mg and Fe counterparts, which indicates that the compounds are isostructural. (b) Zoomed view of the 2θ region of 6.5–19.5° highlighting the shift of the diffraction peaks of the as-prepared material compared to the Mg and Fe homologues. The shift to bigger angles compared to the Mg counterpart holtedahlite, and to smaller angles compared to the Fe homologue satterlyite is related to the respective cell volumes (*cf.* Table S1), which is in agreement with Vegard's rule[3] and the ionic radii for CN = 6 (Fe^{2+} > Co^{2+} > Mg^{2+}). The significant differences in peak intensities observed for the pattern of holtedahlite can be explained by the different atomic scattering factor of Mg compared to Co and Fe.

Supporting Information

Table S1. Lattice parameters of (a) $Co_{1.85(1)}Li_{0.15(1)}(OH)PO_4$ (prepared by hydrothermal synthesis at pH = 5.0) as refined from powder X-ray diffraction data (T = 298 K) in comparison with single crystal data of the isostructural phases (b) $Mg_2(OH)(CO_3)_{0.04}(PO_4)_{0.96}$ (natural holtedahlite), (c) $Mg_2(OH)PO_4$ (synthetic holtedahlite), and (d) $Fe_{1.54}Mg_{0.46}(OH)PO_4$ (satterlyite) taken from the literature[1, 2]

Mineral name	**a) This work** [a]	**b) Natural holtedahlite** [b]	**c) Synthetic holtedahlite** [b]	**d) Satterlyite** [c]
Simplified formula	$Co_{1.85(1)}Li_{0.15(1)}(OH)PO_4$	$Mg_2(OH)(CO_3)_{0.04}(PO_4)_{0.96}$	$Mg_2(OH)PO_4$	$Fe_{1.54}Mg_{0.46}(OH)PO_4$
Data type	powder	single crystal	single crystal	single crystal
ICSD no.	–	67048	64769	94842
Crystal-chemical formula	$Co_{11.1(1)}Li_{0.9(1)}[(OH)_5O][(PO_3OH)(PO_4)_5]$	$Mg_{12}(OH,O)_6(CO_3)_{0.24}(PO_3OH)_{0.76}(PO_4)_5$	$Mg_{12}(OH,O)_6(PO_3OH)(PO_4)_5$	$Fe_{9.24}Mg_{2.76}(OH,O)_6(PO_3OH)(PO_4)_5$
M_r (g·mol^{-1})	1333.3	949.0	963.5	1255.7
Space group (no.)	$P31m$ (157)	$P31m$ (157)	$P31m$ (157)	$P31m$ (157)
Z	1	1	1	1
a (Å)	11.2533(4)	11.203(3)	11.186(3)	11.355(1)
c (Å)	4.9940(2)	4.977(1)	4.977(1)	5.0394(5)
V (Å^3)	547.70(3)	541.0(3)	539.3(3)	562.71(9)
F(000)	645	– [d]	480	613
ρ (calcd.) (g·cm^{-3})	4.038(1)	2.913	2.966	3.728
R_p	0.0404	0.031	0.033	0.0215
R_{wp}	0.0593	0.035	0.032	0.0488
χ^2	1.91	2.26	1.81	1.146
Data/restraints/ parameters	3803/0/91	1202/0/87	718/0/84	2320/0/95

[a] The estimated standard deviations (in parentheses) were calculated using the Berar's correction. [b] Data taken from reference [1]. [c] Data taken from reference [2]. [c] Data have not been provided in the cif file and publication.

Supporting Information

2 Scanning Electron Microscopy (SEM) and Energy-Dispersive X-ray Spectroscopy (EDS) of $Co_{1.84(2)}Li_{0.16(3)}(OH)PO_4$

Experimental Details

Scanning Electron Microscopy (SEM) was performed using a JEOL JSM-7500F SEM in the LEI (lower secondary electron image) detection mode at an accelerating voltage of 1 kV and a working distance of 8 mm. A Noran system S1X system (Thermo Electron Corporation, model 6714A01SUS-SN) was used to perform semi-quantitative EDS (energy-dispersive X-ray spectroscopy) analysis (acceleration voltage: 15 kV, probe current: 20 µA). The sample was mounted on an aluminum stub using double-sided conductive carbon tape.

Results and Discussion

The SEM images (Fig. S2a) reveal that the $Co_{1.84(2)}Li_{0.16(3)}(OH)PO_4$ powder consists of uniform, well-dispersed crystals of about 15 µm × 30 µm in size, which exhibit a unique elongated triangular pyramid morphology that resembles a spearhead. The base consists of a triangular prism with an edge length of ~15 µm for the equilateral triangular base and a height of ~15 µm. The prism is further condensed with a triangular pyramid (height: ~15 µm), which forms the tip of the crystal as indicated in Fig. S2c. The junction between these two elements is characterized by a garland-shaped bow form, indicating that the crystals are twinned. The crystals further show a lamellar fine structure of condensed layers with thicknesses of ~100–200 nm (Fig. S2b) which suggests a layer-wise crystal growth. Because two-dimensional, nanosheet-structured materials have been reported to exhibit interesting properties,[4] it may be worth examining whether the lamellar layers of the crystals can be separated in further experiments, for example by using ultrasonic exfoliation techniques.

EDS analysis (Fig. S2d) gives an elemental composition of 50(2) wt% Co, 14.0(3) wt% P, and 36.1(7) wt% O, which corresponds to a Co:P:O molar ratio of 1.87(6):1.00(2):5.0(1). The observed deficit in Co is consistent with the results of the elemental analysis (*cf.* Table 2c in the main article). Additional EDS element mapping (see Fig. S3 and Table S2) and point analyses (Fig. S4, Table S3) further demonstrate that all elements are evenly distributed within the crystals.

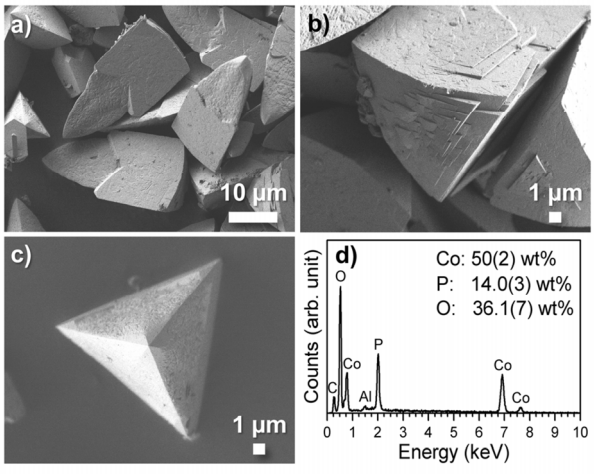

Figure S2. (a–c) SEM images and (d) corresponding EDS spectrum of $Co_{1.84(2)}Li_{0.16(3)}(OH)PO_4$ (prepared by hydrothermal synthesis at pH = 5.0). (a) The sample consists of uniform, well-dispersed crystals with a unique elongated triangular pyramid morphology and dimensions of ~15 µm × 30 µm. (b) highlights the lamellar fine structure, and (c) the pyramidal tip of the crystals. The C and Al signals observed in (d) are due to the carbon tape and the aluminum sample holder used for the measurement.

Supporting Information

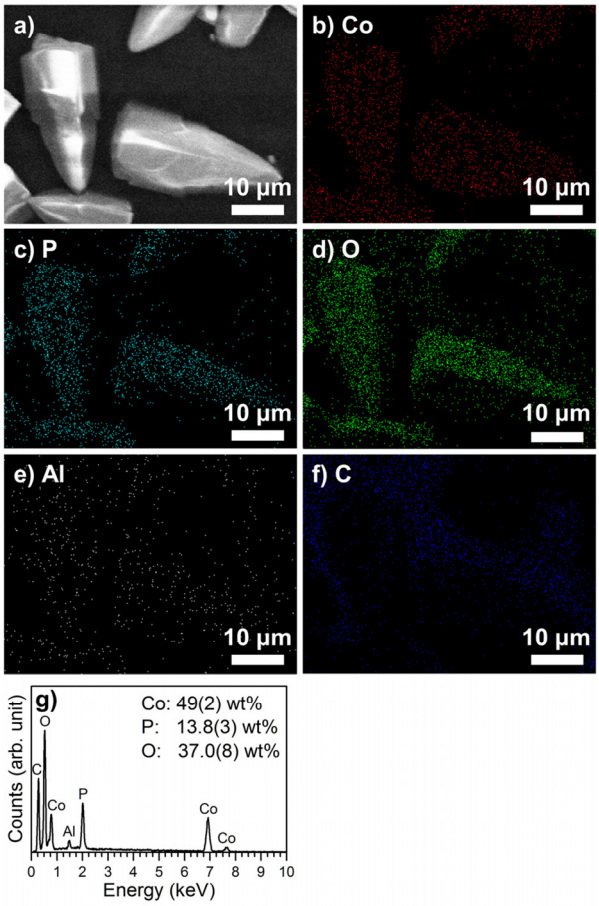

Figure S3. (a) SEM image, (b–f) EDS element maps, and (g) corresponding EDS spectrum (accelerating voltage: 15 kV) of the as-prepared $Co_{1.84(2)}Li_{0.16(3)}(OH)PO_4$ crystals (prepared by hydrothermal synthesis at pH = 5.0). It can be derived that the elements Co, P, and O are evenly distributed within the particles. The signals in the Al and C maps arise from the carbon tape and aluminum sample holder used for the measurement. Please note that (a) exhibits pronounced charging effects due to the high accelerating voltage and the low conductivity of the sample. Li could not be detected because the energy of the characteristic radiation is too low.

Table S2. Elemental composition of the as-synthesized $Co_{1.84(2)}Li_{0.16(3)}(OH)PO_4$ powder (prepared by hydrothermal synthesis at pH = 5.0) as derived from EDS element mapping analysis (*cf.* Fig. S3) [a]

Element	**Found**
Co (wt%)	49(2)
P (wt%)	13.8(3)
O (wt%)	37.0(8)
n(Co):*n*(P) [b]	1.87(6):1.00(2)
n(O):*n*(P) [b]	5.2(1):1.00(2)

[a] The estimated standard deviations are indicated in parentheses. [b] The molar ratios were derived from the Co, P, and O contents and normalized to the P content.

Supporting Information

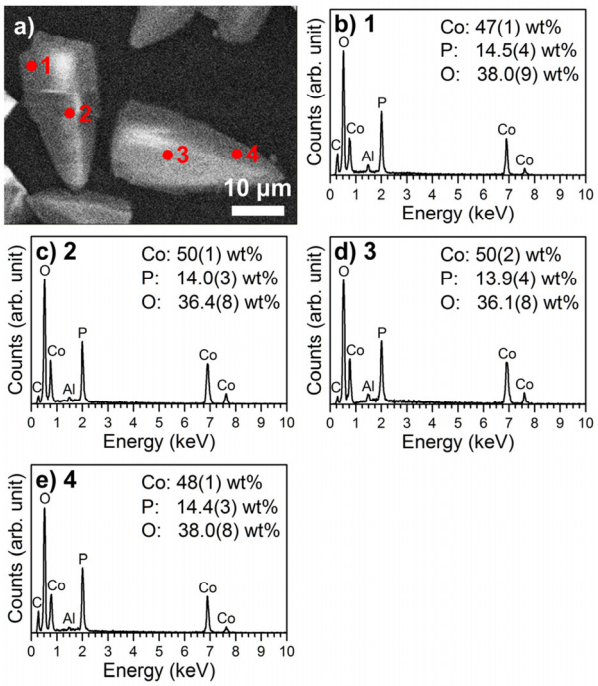

Figure S4. (a) SEM image, (b–e) corresponding EDS spectra (accelerating voltage: 15 kV) of the points 1–4 (as indicated in a) of the as-prepared $Co_{1.84(2)}Li_{0.16(3)}(OH)PO_4$ crystals (prepared by hydrothermal synthesis at pH = 5.0). The Al and C signals are due to the carbon tape and aluminum sample holder used for the measurement.

Table S3. Elemental composition of the as-synthesized $Co_{1.84(2)}Li_{0.16(3)}(OH)PO_4$ powder (prepared by hydrothermal synthesis at pH = 5.0) at the points 1–4 in the EDS point analysis (*cf.* Fig. S4) [a]

Point no.	**1**	**2**	**3**	**4**
Co (wt%)	47(1)	50(1)	50(2)	48(1)
P (wt%)	14.5(4)	14.0(3)	13.9(4)	14.4(3)
O (wt%)	38.0(9)	36.4(8)	36.1(8)	38.0(8)
n(Co):*n*(P) [b]	1.72(5):1.00(2)	1.87(5):1.00(2)	1.89(6):1.00(4)	1.73(5):1.00(2)
n(O):*n*(P) [b]	5.1(1):1.00(2)	5.0(1):1.00(2)	5.0(1):1.00(4)	5.1(1):1.00(2)

[a] The estimated standard deviations are indicated in parentheses. [b] The molar ratios were derived from the Co, P, and O contents and normalized to the P content.

Supporting Information

3 Infrared (IR) Spectrum of $Co_{1.84(2)}Li_{0.16(3)}(OH)PO_4$

Experimental Details

The Fourier-Transform Infrared (FTIR) spectrum of the powder (400–4000 cm^{-1}, 132 scans) was collected on a Varian 670 IR FTIR spectrometer equipped with a PIKE GladiATR diamond ATR (attenuated total reflection) stage.

Results and Discussion

Fig. S5b shows the FTIR spectrum of $Co_{1.84(2)}Li_{0.16(3)}(OH)PO_4$ in the range of 400–1800 cm^{-1}. The region of 3350–3700 cm^{-1} is presented in the inset. The omitted region of 1800–3350 cm^{-1}, which is displayed in the full spectrum in Fig. S5a, does not show any additional absorption bands. As expected, the spectrum is dominated by the fundamental vibrations of the tetrahedral $[PO_4]^{3-}$ groups. The number and frequency of the observed modes is in good agreement with reported spectra[2, 5, 6] of the isostructural Mg- and Fe-based hydroxide phosphates holtedahlite and satterlyite, and hence confirms the structure model. Compared to the free phosphate molecule, the spectrum becomes more complicated because the framework hosts three unique $[PO_4]^{3-}$ units whose respective fundamental and combination modes as well as overtones will overlap.[2] In addition to that, the fundamental vibrations exhibit further energy-splitting and broadening effects, which are to related to the distortion of the phosphate groups from the ideal T_d symmetry in the crystal structure (*cf.* Table S8a) as well as the coupling with *M*–O bonds (*M* = Co, Li).[7] The fact that the bands are slightly more broadened in comparison with its isostructural Fe and Mg counterparts is the result of the heterovalent Co ions (+2/+3) in $Co_{1.84(2)}Li_{0.16(3)}(OH)PO_4$ because the factor group splitting increases with the second ionization potential of the transition metal (Co^{3+} >> Co^{2+} > Fe^{2+} > Mg^{2+}).[8, 9] Taking into account the various modes, overlapping and splitting effects, a concise band assignment is therefore complicated and would require the use of density functional theory simulations, which is beyond the scope of this work.

Hence, the three main band systems observed in the spectrum can be assigned in simplified form as follows: The first region between 400 cm^{-1} and 700 cm^{-1} mainly corresponds to the symmetric and asymmetric intramolecular $[PO_4]^{3-}$ bending modes (ν_2, ν_4). The absorption band at 575 cm^{-1} is probably related to asymmetric vibration modes of the $[CoO_6]$ octahedra, whereas the ones at 418 cm^{-1} and 524 cm^{-1} might be due to O–Co–O bending modes.[10] Interestingly, the bands below 500 cm^{-1} were not observed in the spectra of holtedahlite or satterlyite.[2, 5] In agreement with other reports, [7, 8] the bands might be attributed to Li^+ ion "cage modes" that represent translational vibrations of the Li ions inside a potential determined by the neighboring oxygen atoms. Hence, these additional modes provide further evidence for the incorporation of Li in the structure. The second, broad band system with seven modes around 700–1400 cm^{-1} is associated with intramolecular stretching vibrations of the phosphate anions (ν_1, ν_3). In the high-energy range around 3500–3600 cm^{-1} (see inset of Fig. S5b), three sharp but weak bands are observed, which can be explained by stretching modes of the bridging hydroxyl groups of the $[M_2O_8(OH)]$ (*M* = Co, Li) dimer units (O4–H1 and O5–H2) as well as the disordered, apical OH group (O9–H3) of the hydrogen phosphate ($[PO_3(OH)]$ unit. This feature is consistent with the fact that three OH groups with different O–H distances can be distinguished in the crystal structure (*cf.* Table S8a and structure discussion in the main article), for which different force constants and hence energies are expected. The energy range further suggests that no or only weak hydrogen bonds are formed in the framework[6] while the observation of sharp bands rules out entrapped water. Because the refinement of O–H distances based on X-ray powder diffraction data is not reliable due to the low scattering factor of H, and the H positions were hence kept fixed in the refinement, a precise assignment of the IR bands to

individual OH groups on basis of bond lengths is not possible. Similarly to reports in the literature,[1, 2, 5, 6] however, it is likely that the higher frequency bands at 3581 cm^{-1} and 3548 cm^{-1} correspond to the stretching vibrations of the μ_2-bridging O4–H1 and O5–H2 groups because these groups show similar atomic environments (*i.e.*, both are attached to the double chains of face-sharing [MO_6] octahedra). The asymmetric band at 3506 cm^{-1}, on the other hand, can possibly be assigned to the hydrogen phosphate [(P3)O_3(OH)] group.[2]

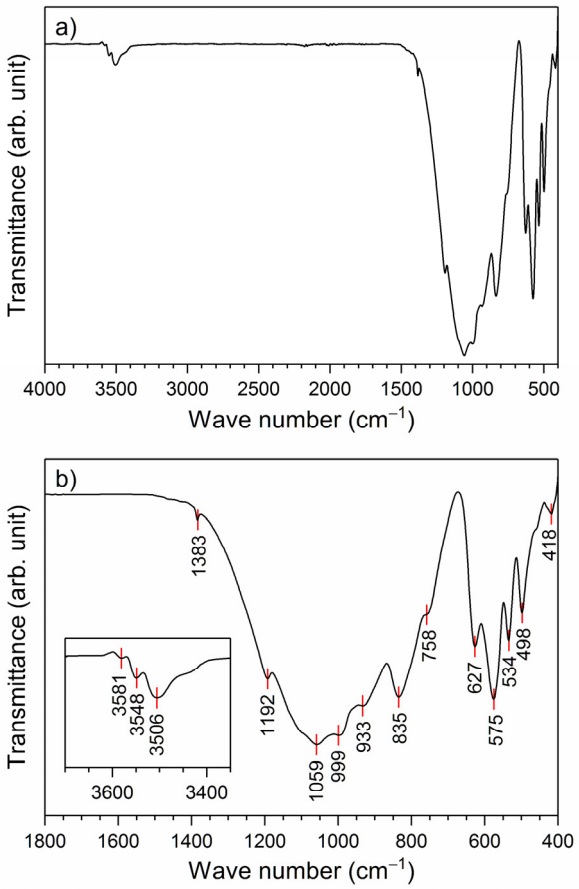

Figure S5. (a) Full FTIR spectrum in the wavenumber range of 400–4000 cm^{-1}, and (b) zoomed view of the FTIR spectrum in the region of 400–1800 cm^{-1} of the as-prepared $Co_{1.84(2)}Li_{0.16(3)}(OH)PO_4$ powder (prepared by hydrothermal synthesis at pH = 5.0). The absorption bands in the region of 400–1800 cm^{-1} are related to the vibrations of the phosphate groups, whereas the bands around 3500 cm^{-1} (inset of b) are associated with O–H stretching vibrations of the three independent hydroxyl groups. No additional absorption bands are observed, indicating that the sample does not contain any detectable amounts of water or other impurities. .

Supporting Information

4 Rietveld Refinements of the Powder X-ray Diffraction Patterns of the Samples Obtained from Hydrothermal Syntheses in a pH Range of 3.0–8.0 (Increment Step: 0.5)

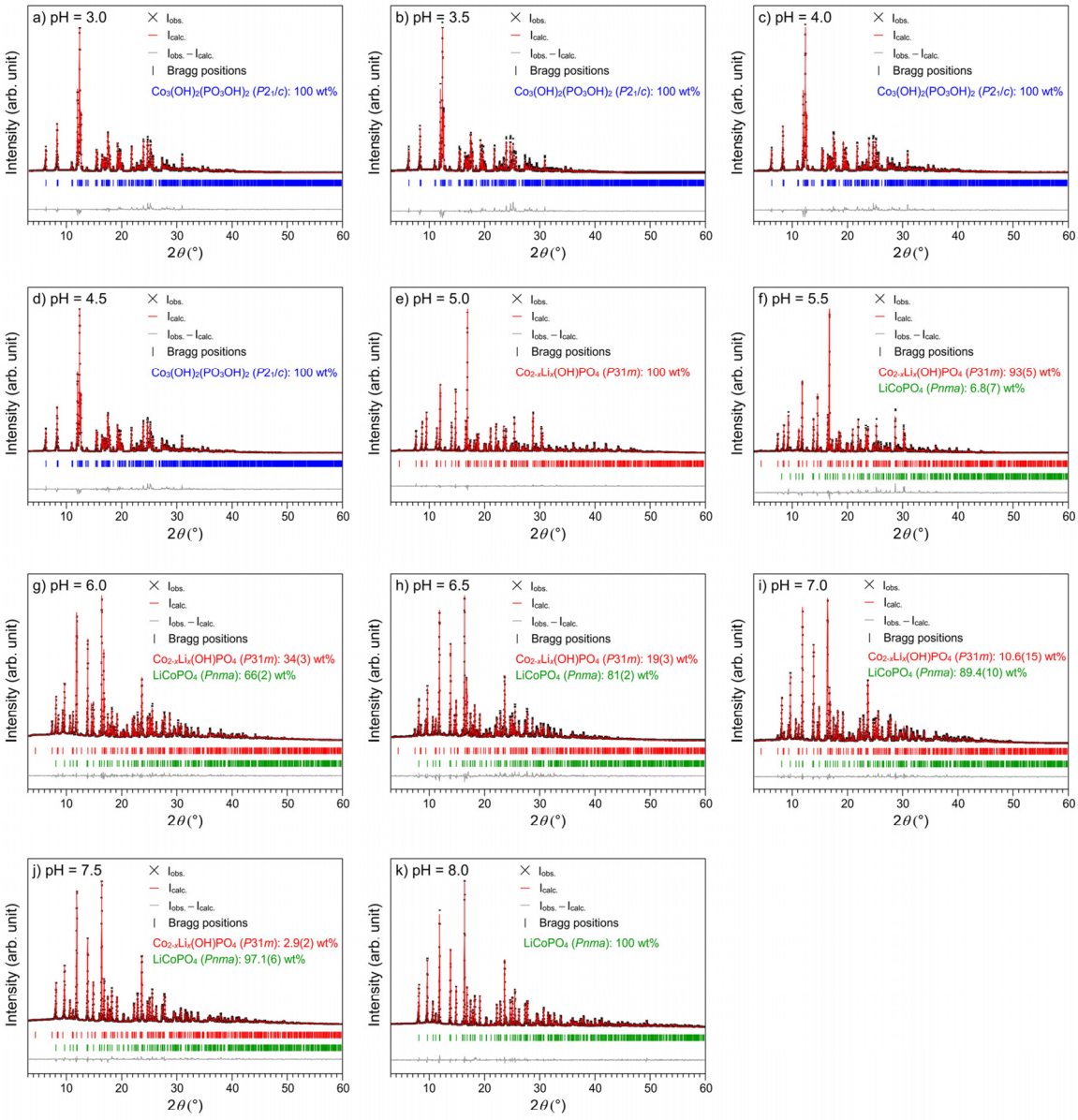

Figure S6. Rietveld fits of the PXRD patterns (Mo $K_{\alpha1}$ radiation, 0.5 mm capillary, measurement time: 12 h) of the samples prepared by hydrothermal syntheses in a pH range of 3.0–8.0 (increment step: 0.5). It can be derived that the pH value of the reaction mixture significantly influences the phase formation. At pH ≤ 4.5, phase pure $Co_3(OH)_2(PO_3OH)_2$ (space group: $P2_1/c$, Z = 2, ICSD no. 67489)[11] is obtained whereas phase pure $Co_{2-x}Li_x(OH)PO_4$ (crystal-chemical formula: $Co_{12-x}Li_x[(OH)_5O][(PO_3OH)(PO_4)_5]$, space group: $P31m$, Z = 1, this work) and olivine-type $LiCoPO_4$ (space group: $Pnma$, Z = 4, ICSD no. 431999)[12] are formed at pH values of 5.0 and 8.0, respectively. A mixture of $Co_{2-x}Li_x(OH)PO_4$ and $LiCoPO_4$ is obtained at pH = 5.5–7.5. The refined x values of $Co_{2-x}Li_x(OH)PO_4$ are as follows: pH 5.0: 0.15(1); pH 5.5: 0.19(2); pH 6.0: 0.23(3); pH 6.5: 0.27(3); pH 7.0: 0.31(3).

Table S4. Crystallographic details and refined phase fractions of the phases observed in the powder X-ray diffraction patterns (*cf.* Fig. S6, $T = 298$ K) of the materials prepared by hydrothermal syntheses in a pH range of 3.0–8.0 (increment step: 0.5) [a,b]

	a) pH = 3.0	b) pH = 3.5	c) pH = 4.0	d) pH = 4.5	e) pH = 5.0	f) pH = 5.5	
Phase	$Co_3(OH)_2(PO_3OH)_2$	$Co_3(OH)_2(PO_3OH)_2$	$Co_3(OH)_2(PO_3OH)_2$	$Co_3(OH)_2(PO_3OH)_2$	$Co_{1.85(1)}Li_{0.15(1)}(OH)PO_4$	$Co_{1.81(2)}Li_{0.19(2)}(OH)PO_4$	$LiCoPO_4$ [c]
Space group	$P2_1/c$	$P2_1/c$	$P2_1/c$	$P2_1/c$	$P31m$	$P31m$	$Pnma$
Content (wt%)	100	100	100	100	100	93(5)	6.8(7)
Z	2	2	2	2	1	1	4
a (Å)	7.5320(9)	7.5305(2)	7.5328(8)	7.5345(9)	11.2533(4)	11.2532(8)	10.219(6)
b (Å)	7.5148(9)	7.5128(2)	7.5155(8)	7.5172(9)	11.2533(4)	11.2532(8)	5.923(4)
c (Å)	7.3964(9)	7.3957(2)	7.3961(8)	7.3988(9)	4.9940(2)	4.9916(4)	4.706(3)
α (°)	90	90	90	90	90	90	90
β (°)	117.900(7)	117.8913(17)	117.896(6)	117.901(7)	90	90	90
γ (°)	90	90	90	90	120	120	90
V (Å^3)	369.98(8)	369.81(2)	370.06(7)	370.35(8)	547.70(3)	547.42(7)	284.8(3)
F(000)	390	390	390	390	645	621	
ρ (calcd.) (g·cm^{-3})	3.615(1)	3.617(1)	3.615(1)	3.612(1)	4.038(1)	4.008(1)	3.751(1)
R_c	0.0732	0.0947	0.0860	0.0727	0.0404	0.0635	
R_{wp}	0.1015	0.1305	0.1167	0.1000	0.0593	0.0982	
R_{exp}	0.0365	0.0375	0.0377	0.0359	0.0326	0.0362	
R_F	0.0713	0.1021	0.0872	0.0707	0.0474	0.0698	0.0842
R_B	0.1166	0.1573	0.1429	0.1142	0.0647	0.1054	0.1221
χ^2	2.83	3.48	3.10	2.79	1.91	2.64	
Data/restraints/ parameter	3803/0/75	3806/0/75	3810/0/75	3805/0/75	3803/0/91	3807/0/97	

[*Continuing Table S4*]

	g) pH = 6.0		h) pH = 6.5		i) pH = 7.0		j) pH = 7.5		k) pH = 8.0
Phase	$Co_{1.77(3)}Li_{0.23(2)}(OH)PO_4$	$LiCoPO_4$	$Co_{1.73(3)}Li_{0.27(3)}(OH)PO_4$	$LiCoPO_4$	$Co_{1.69(3)}Li_{0.31(3)}(OH)PO_4$	$LiCoPO_4$	$Co_{2-x}Li_x(OH)PO_4$ [c]	$LiCoPO_4$	$LiCoPO_4$
Space group	*P*31*m*	*Pnma*	*P*31*m*	*Pnma*	*P*31*m*	*Pnma*	*P*31*m*	*Pnma*	*Pnma*
Content (wt%)	34(3)	66(2)	19(3)	81(2)	10.6(15)	89.4(10)	2.9(2)	97.1(6)	100
Z	1	4	1	4	1	4	1	4	4
a (Å)	11.2531(7)	10.2164(7)	11.2529(11)	10.2213(10)	11.2524(8)	10.2213(8)	11.251(3)	10.2213(5)	10.2239(4)
b (Å)	11.2531(7)	5.9261(4)	11.2529(11)	5.9274(6)	11.2524(8)	5.9276(5)	11.251(3)	5.9270(3)	5.9266(3)
c (Å)	4.9898(4)	4.7073(3)	4.9873(7)	4.7101(5)	4.9858(5)	4.7105(4)	4.984(3)	4.7108(3)	4.7123(2)
α (°)	90	90	90	90	90	90	90	90	90
β (°)	90	90	90	90	90	90	90	90	90
γ (°)	120	90	120	90	120	90	120	90	90
V (Å^3)	547.22(7)	285.00(3)	546.92(11)	285.37(5)	546.71(8)	285.40(4)	546.5(4)	285.39(3)	285.53(2)
F(000)	626		637		649		639		310
ρ (calcd.) (g·cm^{-3})	3.965(1)	3.770(1)	3.933(1)	3.806(1)	3.897(1)	3.787(1)	4.051(1)	3.822(1)	3.822(1)
R_p	0.0581		0.0665		0.0572		0.0420		0.0440
R_{wp}	0.0794		0.0937		0.0817		0.0587		0.0635
R_{exp}	0.0339		0.0342		0.0343		0.0331		0.0302
R_F	0.0594	0.0544	0.0684	0.0659	0.0440	0.0382	0.0662	0.0462	0.0429
R_B	0.0897	0.0848	0.0990	0.0983	0.0747	0.0650	0.1148	0.0683	0.0581
χ^2	2.34		2.74		2.38		1.77		2.10
Data/restraints /parameter	3805/0/112		3806/0/112		3803/0/112		3805/0/69		3810/0/65

[a] The estimated standard deviations (in parentheses) were calculated using the Berar's correction. [b] For the phases $Co_{2-x}Li_x(OH)PO_4$, the simplified formula is provided for clarity. However, due to the fact that the H positions are not fully occupied in the structure, the correct X-ray formula with $Z = 1$ would correspond to the composition $Co_{12-x}Li_x[(OH)_5O][(PO_3OH)(PO_4)_5]$. [c] Note that at pH values of 5.5 and 7.5, only the lattice parameters of $LiCoPO_4$ and $Co_{2-x}Li_x(OH)PO_4$ could be refined. A structure refinement was not possible due to the small phase fractions of 6.8(7) wt% and 2.9(2) wt%, respectively. Hence, only the general composition $Co_{2-x}Li_x(OH)PO_4$ is provided for pH = 7.5.

Supporting Information

Table S5. Atomic positions and isotropic thermal displacement parameters of $Co_3(OH)_2(PO_3OH)_2$ (space group: $P2_1/c$, $Z = 2$) prepared by hydrothermal syntheses at pH = 3.0–4.5 as refined from powder X-ray diffraction data ($T = 298$ K) [a]

	Atom	Wyckoff position	Occupancy	*x*/a	*y*/b	*z*/c	U_{iso} (Å^2)
a) pH = 3.0	Co1	2*a*	1	0	0	0	0.026(3)
	Co2	4*e*	1	0.2553(12)	0.2253(11)	0.4816(12)	0.029(3)
	P1	4*e*	1	0.237(2)	0.620(2)	0.237(3)	0.027(4)
	O1	4*e*	1	0.182(4)	0.492(4)	0.358(4)	0.029(4)
	O2	4*e*	1	0.334(5)	0.533(5)	0.117(5)	0.028(3)
	O3	4*e*	1	0.052(4)	0.732(4)	0.109(4)	0.026(4)
	O4	4*e*	1	0.580(4)	0.252(4)	0.100(4)	0.021(3)
	O5	4*e*	1	0.265(4)	0.125(4)	0.227(5)	0.023(2)
	H1	4*e*	1	0.336 [b]	0.073 [b]	0.247 [b]	0.051 [b]
	H2	4*e*	1	0.618 [b]	0.307 [b]	0.041 [b]	0.010 [b]
b) pH = 3.5	Co1	2*a*	1	0	0	0	0.0327(9)
	Co2	4*e*	1	0.2558(4)	0.2245(3)	0.4820(4)	0.0349(8)
	P1	4*e*	1	0.2379(8)	0.6204(6)	0.2384(8)	0.0337(8)
	O1	4*e*	1	0.1820(13)	0.4939(14)	0.3572(14)	0.035(3)
	O2	4*e*	1	0.3326(13)	0.5348(13)	0.1171(14)	0.031(3)
	O3	4*e*	1	0.0553(14)	0.7312(13)	0.1073(14)	0.032(3)
	O4	4*e*	1	0.5785(12)	0.2513(13)	0.0994(13)	0.027(3)
	O5	4*e*	1	0.2669(13)	0.1260(10)	0.2299(13)	0.025(3)
	H1	4*e*	1	0.336 [b]	0.073 [b]	0.247 [b]	0.051 [b]
	H2	4*e*	1	0.618 [b]	0.307 [b]	0.041 [b]	0.010 [b]
c) pH = 4.0	Co1	2*a*	1	0	0	0	0.033(3)
	Co2	4*e*	1	0.2551(9)	0.2250(9)	0.4816(10)	0.035(3)
	P1	4*e*	1	0.236(3)	0.623(2)	0.237(3)	0.033(4)
	O1	4*e*	1	0.190(5)	0.494(5)	0.361(5)	0.030(9)
	O2	4*e*	1	0.330(5)	0.530(5)	0.114(5)	0.027(8)
	O3	4*e*	1	0.050(5)	0.729(4)	0.105(5)	0.020(7)
	O4	4*e*	1	0.580(4)	0.249(4)	0.100(4)	0.014(6)
	O5	4*e*	1	0.264(5)	0.125(4)	0.227(5)	0.022(7)
	H1	4*e*	1	0.336 [b]	0.073 [b]	0.247 [b]	0.051 [b]
	H2	4*e*	1	0.618 [b]	0.307 [b]	0.041 [b]	0.010 [b]

Supporting Information

[*Continuing Table S5*]

	Atom	Wyckoff position	Occupancy	*x*/a	*y*/b	*z*/c	U_{iso} (Å^2)
d) pH = 4.5	Co1	2*a*	1	0	0	0	0.033(3)
	Co2	4*e*	1	0.2552(9)	0.2255(9)	0.4816(10)	0.030(3)
	P1	4*e*	1	0.238(2)	0.620(2)	0.237(3)	0.025(4)
	O1	4*e*	1	0.183(4)	0.493(4)	0.359(4)	0.027(9)
	O2	4*e*	1	0.332(5)	0.534(5)	0.117(5)	0.028(9)
	O3	4*e*	1	0.053(4)	0.734(4)	0.109(4)	0.026(9)
	O4	4*e*	1	0.580(4)	0.252(4)	0.100(4)	0.021(8)
	O5	4*e*	1	0.265(4)	0.126(4)	0.227(5)	0.021(7)
	H1	4*e*	1	0.336 [b]	0.073 [b]	0.247 [b]	0.051 [b]
	H2	4*e*	1	0.618 [b]	0.307 [b]	0.041 [b]	0.010 [b]

[a] The estimated standard deviations (in parentheses) were calculated using the Berar's correction. [b] H positions and thermal displacement parameters have been kept fixed as they cannot be deduced by means of X-ray powder diffraction due to the low atomic scattering factor of H.

Supporting Information

Table S6. Selected interatomic distances of $Co_3(OH)_2(PO_3OH)_2$ (space group: $P2_1/c$, $Z = 2$) prepared by hydrothermal syntheses at pH = 3.0–4.5 as refined from powder X-ray diffraction data ($T = 298$ K) [a]

	Atom pair		*d* (Å)			
			a) pH = 3.0	**b) pH = 3.5**	**c) pH = 4.0**	**d) pH = 4.5**
Co1	O1	×2	2.08(4)	2.086(12)	2.12(4)	2.08(4)
	O3	×2	2.13(3)	2.138(10)	2.15(3)	2.12(3)
	O5	×2	2.14(2)	2.152(7)	2.13(3)	2.14(2)
	Co1–O average		2.12	2.13	2.13	2.11
Co2	O1	×1	2.16(3)	2.186(10)	2.17(4)	2.16(3)
	O2	×1	2.14(3)	2.142(10)	2.10(4)	2.14(4)
	O3	×1	2.09(3)	2.116(10)	2.08(4)	2.09(3)
	O4	×1	2.18(3)	2.172(9)	2.19(3)	2.18(3)
	O5	×1	2.06(4)	2.044(11)	2.06(4)	2.06(4)
	O5	×1	2.11(4)	2.118(10)	2.11(4)	2.11(4)
	Co2–O average		2.12	2.13	2.13	2.12
P1	O1	×1	1.50(4)	1.482(13)	1.49(5)	1.50(4)
	O2	×1	1.53(5)	1.525(14)	1.56(5)	1.52(5)
	O3	×1	1.52(3)	1.509(10)	1.51(3)	1.53(3)
	O4	×1	1.67(3)	1.663(9)	1.65(3)	1.67(3)
	P1–O average		1.56	1.54	1.55	1.56
H1	O4	×1	0.74(4) [b]	0.755(11) [b]	0.74(4) [b]	0.74(4) [b]
H2	O5	×1	0.62(3) [b]	0.620(9) [b]	0.63(3) [b]	0.62(3) [b]

[a] The estimated standard deviations (in parentheses) were calculated using the Berar's correction. [b] Note that the refinement of O–H distances is not reliable since the H positions and thermal displacement parameters have been kept fixed during the refinement (*cf.* low atomic scattering factor of H).

Supporting Information

Table S7. Atomic positions and isotropic thermal displacement parameters of $Co_{2-x}Li_x(OH)PO_4$ (crystal-chemical formula: $Co_{12-x}Li_x[(OH)_5O][(PO_3OH)(PO_4)_5]$, space group: *P*31*m*, *Z* = 1; refined *x* values are provided in parentheses) prepared by hydrothermal syntheses at pH = 5.0–7.0 as refined from powder X-ray diffraction data (*T* = 298 K) [a,b]

	Atom	Wyckoff position	Occupancy	*x*/a	*y*/b	*z*/c	U_{iso} (Å^2)
a) pH = 5.0	Co1/Li1	6*d*	0.971(8)/0.029(8)	0.1444(5)	0.3217(5)	0.6693(16)	0.0109(19)
(*x* = 0.15(1))	Co2/Li2	6*d*	0.878(8)/0.122(8)	0.1467(6)	0.4764(7)	0.206(2)	0.017(2)
	P1	3*c*	1	0.6530(15)	0	0.158(4)	0.012(3)
	P2	2*b*	1	⅓	⅔	0.720(5)	0.015(2)
	P3	1*a*	1	0	0	0.454(5)	0.012(3)
	O1	6*d*	1	0.255(3)	0.517(3)	0.830(5)	0.011(4)
	O2	6*d*	1	0.238(3)	0.355(4)	0.327(6)	0.013(4)
	O3	3*c*	1	0.128(2)	0	0.542(6)	0.010(3)
	O4	3*c*	1	0.272(3)	0	0.016(6)	0.009(3)
	O5	3*c*	1	0.372(4)	0	0.517(7)	0.014(4)
	O6	3*c*	1	0.526(3)	0	0.074(5)	0.013(3)
	O7	3*c*	1	0.741(3)	0	0.932(7)	0.010(3)
	O8	2*b*	1	⅓	⅔	0.393(7)	0.010(4)
	O9	1*a*	1	0	0	0.126(8)	0.012(3)
	H1	3*c*	0.833 [c]	0.195 [c]	0	0.104 [c]	0.021 [c]
	H2	3*c*	0.833 [c]	0.437 [c]	0	0.616 [c]	0.022 [c]
	H3	1*a*	1 [c]	0	0	0.000 [c]	0.022 [c]
b) pH = 5.5	Co1/Li1	6*d*	0.952(18)/0.048(18)	0.1440(11)	0.3269(11)	0.692(4)	0.024(4)
(*x* = 0.19(2))	Co2/Li2	6*d*	0.863(18)/0.137(18)	0.1488(12)	0.4784(15)	0.213(5)	0.029(4)
	P1	3*c*	1	0.654(3)	0	0.168(8)	0.018(2)
	P2	2*b*	1	⅓	⅔	0.727(15)	0.018(3)
	P3	1*a*	1	0	0	0.459(11)	0.019(3)
	O1	6*d*	1	0.260(5)	0.525(6)	0.843(9)	0.015(3)
	O2	6*d*	1	0.236(5)	0.356(7)	0.325(11)	0.015(3)
	O3	3*c*	1	0.131(5)	0	0.545(16)	0.011(2)
	O4	3*c*	1	0.279(8)	0	0.005(17)	0.013(3)
	O5	3*c*	1	0.383(6)	0	0.532(15)	0.012(2)
	O6	3*c*	1	0.529(6)	0	0.106(11)	0.012(2)
	O7	3*c*	1	0.740(8)	0	0.909(15)	0.014(3)
	O8	2*b*	1	⅓	⅔	0.40(2)	0.015(3)
	O9	1*a*	1	0	0	0.14(2)	0.013(4)
	H1	3*c*	0.833 [c]	0.195 [c]	0	0.104 [c]	0.021 [c]
	H2	3*c*	0.833 [c]	0.437 [c]	0	0.616 [c]	0.022 [c]
	H3	1*a*	1 [c]	0	0	0.000 [c]	0.022 [c]

Supporting Information

[*Continuing Table S7*]

	Atom	Wyckoff position	Occupancy	*x*/a	*y*/b	*z*/c	U_{iso} (Å^2)
c) pH = 6.0	Co1/Li1	6*d*	0.92(2)/0.08(2)	0.1452(14)	0.3206(17)	0.711(5)	0.019(4)
(*x* = 0.23(3))	Co2/Li2	6*d*	0.85(3)/0.15(3)	0.1459(16)	0.476(2)	0.212(6)	0.024(5)
	P1	3*c*	1	0.654(4)	0	0.169(17)	0.022(5)
	P2	2*b*	1	⅓	⅔	0.704(13)	0.013(3)
	P3	1*a*	1	0	0	0.460(14)	0.011(3)
	O1	6*d*	1	0.257(8)	0.520(11)	0.848(15)	0.008(2)
	O2	6*d*	1	0.239(7)	0.366(8)	0.345(13)	0.010(2)
	O3	3*c*	1	0.125(6)	0	0.548(16)	0.009(3)
	O4	3*c*	1	0.279(7)	0	0.009(17)	0.008(3)
	O5	3*c*	1	0.374(9)	0	0.553(19)	0.007(2)
	O6	3*c*	1	0.519(11)	0	0.101(19)	0.010(2)
	O7	3*c*	1	0.739(11)	0	0.912(18)	0.010(3)
	O8	2*b*	1	⅓	⅔	0.37(2)	0.013(3)
	O9	1*a*	1	0	0	0.15(2)	0.008(3)
	H1	3*c*	0.833 [c]	0.195 [c]	0	0.104 [c]	0.021 [c]
	H2	3*c*	0.833 [c]	0.437 [c]	0	0.616 [c]	0.022 [c]
	H3	1*a*	1 [c]	0	0	0.000 [c]	0.022 [c]
d) pH = 6.5	Co1/Li1	6*d*	0.90(3)/0.10(3)	0.146(3)	0.323(3)	0.704(7)	0.027(5)
(*x* = 0.27(3))	Co2/Li2	6*d*	0.83(3)/0.17(3)	0.147(3)	0.477(4)	0.211(8)	0.027(3)
	P1	3*c*	1	0.659(8)	0	0.17(2)	0.016(3)
	P2	2*b*	1	⅓	⅔	0.73(2)	0.014(2)
	P3	1*a*	1	0	0	0.47(3)	0.012(3)
	O1	6*d*	1	0.240(14)	0.521(14)	0.84(2)	0.012(3)
	O2	6*d*	1	0.247(9)	0.372(10)	0.343(16)	0.010(2)
	O3	3*c*	1	0.126(9)	0	0.56(3)	0.012(3)
	O4	3*c*	1	0.289(13)	0	0.01(3)	0.010(3)
	O5	3*c*	1	0.366(12)	0	0.52(3)	0.010(4)
	O6	3*c*	1	0.527(18)	0	0.09(4)	0.009(3)
	O7	3*c*	1	0.741(14)	0	0.90(3)	0.011(3)
	O8	2*b*	1	⅓	⅔	0.39(4)	0.015(3)
	O9	1*a*	1	0	0	0.13(4)	0.013(3)
	H1	3*c*	0.833 [c]	0.195 [c]	0	0.104 [c]	0.021 [c]
	H2	3*c*	0.833 [c]	0.437 [c]	0	0.616 [c]	0.022 [c]
	H3	1*a*	1 [c]	0	0	0.000 [c]	0.022 [c]

Supporting Information

[*Continuing Table S7*]

	Atom	Wyckoff position	Occupancy	*x*/a	*y*/b	*z*/c	U_{iso} (Å^2)
e) pH = 7.0	Co1/Li1	6*d*	0.87(3)/0.13(3)	0.145(2)	0.325(3)	0.701(5)	0.022(8)
(*x* = 0.31(3))	Co2/Li2	6*d*	0.82(3)/0.18(3)	0.145(2)	0.477(3)	0.233(7)	0.031(9)
	P1	3*c*	1	0.653(6)	0	0.180(19)	0.017(4)
	P2	2*b*	1	⅓	⅔	0.715(13)	0.015(4)
	P3	1*a*	1	0	0	0.46(2)	0.019(3)
	O1	6*d*	1	0.240(11)	0.523(14)	0.853(17)	0.014(3)
	O2	6*d*	1	0.239(7)	0.359(8)	0.359(14)	0.011(2)
	O3	3*c*	1	0.133(5)	0	0.545(13)	0.013(2)
	O4	3*c*	1	0.292(10)	0	0.016(17)	0.012(2)
	O5	3*c*	1	0.373(7)	0	0.525(15)	0.009(3)
	O6	3*c*	1	0.509(5)	0	0.103(14)	0.013(3)
	O7	3*c*	1	0.742(14)	0	0.90(3)	0.012(2)
	O8	2*b*	1	⅓	⅔	0.367(14)	0.010(4)
	O9	1*a*	1	0	0	0.135(15)	0.009(3)
	H1	3*c*	0.833 [c]	0.195 [c]	0	0.104 [c]	0.021 [c]
	H2	3*c*	0.833 [c]	0.437 [c]	0	0.616 [c]	0.022 [c]
	H3	1*a*	1 [c]	0	0	0.000 [c]	0.022 [c]

[a] The estimated standard deviations (in parentheses) were calculated using the Berar's correction. [b] Note that the structure of the $Co_{2-x}Li_x(OH)PO_4$ phase of the sample prepared at pH = 7.5 could not be refined due to the small phase fraction of only 2.9(2) wt%. [c] H positions, occupancy factors, and thermal displacement parameters have been kept fixed as they cannot be deduced by means of X-ray powder diffraction due to the low atomic scattering factor of H.

Supporting Information

Table S8. Selected interatomic distances of $Co_{2-x}Li_x(OH)PO_4$ (crystal-chemical formula: $Co_{12-x}Li_x[(OH)_5O][(PO_3OH)(PO_4)_5]$, space group: $P31m$, $Z = 1$; refined x values are provided in parentheses) prepared by hydrothermal syntheses at pH = 5.0–7.0 as refined from powder X-ray diffraction data (T = 298 K) [a,b]

	Atom pair		***d* (Å)**				
			a) pH = 5.0 (*x* = 0.15(1))	**b) pH = 5.5 (*x* = 0.19(2))**	**c) pH = 6.0 (*x* = 0.23(3))**	**d) pH = 6.5 (*x* = 0.27(3))**	**e) pH = 7.0 (*x* = 0.31(3))**
Co1/Li1	O1	×1	2.07(2)	2.08(5)	2.06(10)	2.04(14)	2.07(13)
	O2	×1	1.94(3)	2.05(6)	2.04(7)	2.05(9)	1.94(7)
	O3	×1	2.07(2)	2.11(5)	2.14(5)	2.11(9)	2.10(5)
	O4	×1	2.25(3)	2.12(7)	2.08(6)	2.13(11)	2.16(7)
	O5	×1	2.11(3)	2.16(6)	2.15(8)	2.14(11)	2.14(7)
	O7	×1	2.19(4)	2.10(10)	2.01(14)	2.00(18)	2.03(19)
	Co1/Li1–O average		2.11	2.10	2.08	2.08	2.07
	Co1/Li1	×1	2.815(6)	2.807(15)	2.83(2)	2.84(4)	2.82(3)
	Co1/Li1	×1	3.455(9)	3.56(2)	3.42(3)	3.46(6)	3.51(4)
	Co2/Li2	×1	2.888(12)	2.92(3)	3.04(4)	3.00(6)	2.89(4)
	Co2/Li2	×1	3.189(12)	3.10(3)	3.05(5)	3.066)	3.15(4)
	Co2/Li2	×1	4.048(11)	4.08(3)	4.16(3)	4.14(6)	4.05(4)
	Co2/Li2	×1	4.268(11)	4.21(3)	4.17(3)	4.18(6)	4.24(4)
Co2/Li2	O1	×1	2.16(3)	2.15(5)	2.12(8)	2.07(12)	2.11(9)
	O2	×1	2.16(5)	2.13(8)	2.10(10)	2.09(14)	2.16(11)
	O4	×1	2.26(37	2.27(7)	2.24(6)	2.17(11)	2.19(8)
	O5	×1	2.14(3)	2.16(6)	2.24(8)	2.14(12)	2.06(6)
	O6	×1	2.10(2)	2.09(5)	2.00(9)	2.09(15)	1.96(6)
	O8	×1	2.319(15)	2.29(4)	2.26(4)	2.30(9)	2.23(3)
	Co2/Li2–O average		2.19	2.18	2.16	2.14	2.12
	Co2/Li2	×1	2.860(8)	2.901(17)	2.84(2)	2.86(5)	2.84(3)
	Co2/Li2	×1	3.674(9)	3.633(18)	3.68(3)	3.67(6)	3.68(4)
	Co1/Li1	×1	2.888(12)	2.92(3)	3.04(4)	3.00(6)	2.89(4)
	Co1/Li1	×1	3.189(12)	3.10(3)	3.05(5)	3.06(6)	3.15(4)
	Co1/Li1	×1	4.048(11)	4.08(3)	4.16(3)	4.14(6)	4.05(4)
	Co1/Li1	×1	4.268(11)	4.21(3)	4.17(3)	4.18(6)	4.24(4)

Supporting Information

[*Continuing Table S8*]

	Atom pair		*d* (Å)				
			a) pH = 5.0 (*x* = 0.15(1))	**b) pH = 5.5 (*x* = 0.19(2))**	**c) pH = 6.0 (*x* = 0.23(3))**	**d) pH = 6.5 (*x* = 0.27(3))**	**e) pH = 7.0 (*x* = 0.31(3))**
P1	O2	×1	1.53(5)	1.51(9)	1.59(12)	1.55(15)	1.57(12)
	O2	×1	1.53(3)	1.51(6)	1.59(9)	1.55(12)	1.57(9)
	O6	×1	1.49(4)	1.44(7)	1.55(14)	1.5(2)	1.67(9)
	O7	×1	1.51(4)	1.62(9)	1.60(13)	1.64(17)	1.73(17)
	P1–O average		1.52	1.52	1.58	1.56	1.64
P2	O1	×1	1.56(3)	1.50(6)	1.60(10)	1.54(13)	1.58(12)
	O1	×1	1.56(3)	1.50(6)	1.60(11)	1.54(15)	1.58(14)
	O1	×1	1.56(4)	1.50(9)	1.60(14)	1.5(2)	1.58(18)
	O8	×1	1.63(4)	1.64(13)	1.68(13)	1.7(2)	1.74(10)
	P2–O average		1.58	1.54	1.62	1.57	1.62
P3	O3	×2	1.50(3)	1.53(6)	1.48(7)	1.50(12)	1.56(6)
	O3	×1	1.50(2)	1.53(5)	1.48(5)	1.50(9)	1.56(5)
	O9	×1	1.64(7)	1.59(13)	1.57(13)	1.7(2)	1.61(13)
	P3–O average		1.54	1.55	1.50	1.55	1.57
H1	O4	×1	0.98(3) [c]	1.07(9) [c]	1.06(8) [c]	1.16(14) [c]	1.17(11) [c]
H2	O5	×1	0.88(4) [c]	0.74(7) [c]	0.78(10) [c]	0.93(14) [c]	0.85(8) [c]
H3	O9	×1	0.63(7) [c]	0.70(12) [c]	0.75(10) [c]	0.66(19) [c]	0.67(8) [c]

[a] The estimated standard deviations (in parentheses) were calculated using the Berar's correction. [b] Note that the structure of the $Co_{2-x}Li_x(OH)PO_4$ phase of the sample prepared at pH = 7.5 could not be refined due to the low phase fraction of only 2.9(2) wt%. [c] Note that the refinement of O–H distances is not reliable since the H positions and thermal displacement parameters have been kept fixed during the refinement (*cf.* low atomic scattering factor of H).

Supporting Information

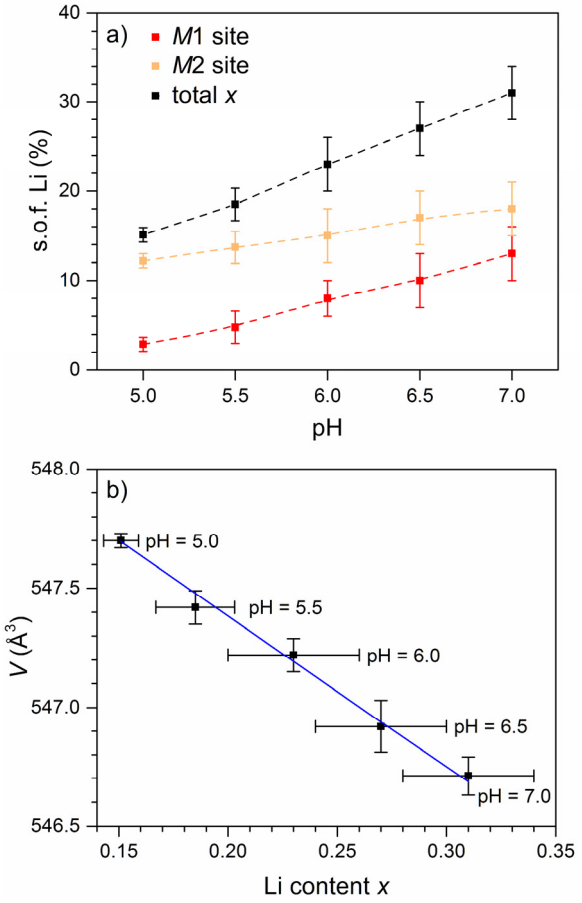

Figure S7. (a) Refined Li site occupancy factors in $Co_{2-x}Li_x(OH)PO_4$ (crystal-chemical formula: $Co_{12-x}Li_x[(OH)_5O][(PO_3OH)(PO_4)_5]$, space group: *P*31*m*, *Z* = 1) *versus* pH value of the reaction mixture for the *M*1 (red) and *M*2 (orange) sites (*M* = Co, Li) and total refined *x* values (black). It is evident that the total Li content *x* as well as the Li occupancies on both *M* sites exhibit a linear increase with increasing pH value, with the *M*2 site generally being richer in Li. Interestingly, the Li occupancies on the *M*1 site increase more rapidly with increasing overall Li content respective pH value. (b) Dependency of the cell volume *V* on the *x* value in $Co_{2-x}Li_x(OH)PO_4$. The cell volume almost linearly decreases as a function of *x*, which is in good agreement for a solid solution according to Vegard's law.[3] The decrease is mainly related to the smaller ionic radius of Co^{3+} compared to Co^{2+}.

Supporting Information

Table S9. Atomic positions and isotropic thermal displacement parameters of $LiCoPO_4$ (space group: *Pnma*, $Z = 4$) prepared by hydrothermal syntheses at pH = 6.0–8.0 as refined from powder X-ray diffraction data ($T = 298$ K) [a,b]

	Atom	Wyckoff position	Occupancy	*x*/a	*y*/b	*z*/c	U_{iso} (Å^2)
a) pH = 6.0	Li1/Co1	4*a*	0.982(4)/0.018(4)	0	0	0	0.0139 [c]
	Co2	4*c*	1	0.2216(3)	¼	0.5214(10)	0.0181(13)
	P1	4*c*	1	0.4056(9)	¼	0.0828(18)	0.021(2)
	O1	4*c*	1	0.4039(19)	¼	0.758(3)	0.034(4)
	O2	4*c*	1	0.049(2)	¼	0.287(4)	0.014(4)
	O3	8*d*	1	0.3340(15)	0.045(2)	0.221(2)	0.014(4)
b) pH = 6.5	Li1/Co1	4*a*	0.950(6)/0.050(6)	0	0	0	0.0139 [c]
	Co1	4*c*	1	0.2216(5)	¼	0.5213(14)	0.0189(19)
	P1	4*c*	1	0.4048(12)	¼	0.082(2)	0.022(3)
	O1	4*c*	1	0.406(3)	¼	0.755(3)	0.017(4)
	O2	4*c*	1	0.051(3)	¼	0.284(4)	0.014(4)
	O3	8*d*	1	0.335(2)	0.043(3)	0.223(3)	0.015(3)
c) pH = 7.0	Li1/Co1	4*a*	0.964(6)/0.036(6)	0	0	0	0.0139 [c]
	Co1	4*c*	1	0.2216(3)	¼	0.5217(9)	0.0180(16)
	P1	4*c*	1	0.4052(8)	¼	0.0846(16)	0.019(2)
	O1	4*c*	1	0.4043(19)	¼	0.756(3)	0.015(4)
	O2	4*c*	1	0.0487(17)	¼	0.298(3)	0.009(3)
	O3	8*d*	1	0.3361(13)	0.044(2)	0.221(2)	0.012(3)
d) pH = 7.5	Li1/Co1	4*a*	0.935(4)/0.065(4)	0	0	0	0.0139 [c]
	Co2	4*c*	1	0.2218(2)	¼	0.5210(6)	0.0131(10)
	P1	4*c*	1	0.4049(6)	¼	0.0838(11)	0.0135(16)
	O1	4*c*	1	0.4056(14)	¼	0.757(2)	0.011(3)
	O2	4*c*	1	0.0482(13)	¼	0.293(2)	0.007(3)
	O3	8*d*	1	0.3342(10)	0.0436(13)	0.2210(14)	0.007(2)
e) pH = 8.0	Li1/Co1	4*a*	0.928(4)/0.072(4)	0	0	0	0.0139 [c]
	Co2	4*c*	1	0.2213(2)	¼	0.5214(6)	0.0083(10)
	P1	4*c*	1	0.4046(5)	¼	0.0826(10)	0.0067(14)
	O1	4*c*	1	0.4043(13)	¼	0.765(2)	0.006(3)
	O2	4*c*	1	0.0450(12)	¼	0.295(2)	0.005(2)
	O3	8*d*	1	0.3342(9)	0.0464(14)	0.2177(15)	0.006(2)

[a] The estimated standard deviations (in parentheses) were calculated using the Berar's correction. [b] Note that the structure of the $LiCoPO_4$ phase of the sample prepared at pH = 5.5 could not be refined due to the low phase fraction of only 6.8(7) wt%. [c] The thermal displacement parameters of Li have been fixed as they cannot be deduced by means of X-ray powder diffraction due to the low atomic scattering factor of Li.

Supporting Information

Table S10. Selected interatomic distances of $LiCoPO_4$ (space group: *Pnma*, $Z = 4$) prepared by hydrothermal syntheses at pH = 6.0–8.0 as refined from powder X-ray diffraction data ($T = 298$ K) [a,b]

	Atom pair		*d* (Å)				
			a) pH = 6.0	**b) pH = 6.5**	**c) pH = 7.0**	**d) pH = 7.5**	**e) pH = 8.0**
Li1/Co1	O1	×2	2.153(13)	2.136(17)	2.147(12)	2.144(9)	2.170(9)
	O2	×2	2.067(12)	2.063(15)	2.101(11)	2.083(8)	2.080(7)
	O3	×2	2.161(13)	2.145(18)	2.146(12)	2.160(9)	2.168(9)
	Li1/Co1–O average		2.127	2.115	2.131	2.129	2.139
Co2	O1	×1	2.170(19)	2.18(3)	2.169(19)	2.185(14)	2.192(13)
	O2	×1	2.08(2)	2.07(3)	2.057(17)	2.075(13)	2.092(12)
	O3	×2	2.064(13)	2.062(17)	2.065(12)	2.060(8)	2.063(8)
	O3	×2	2.190(13)	2.198(17)	2.206(12)	2.194(8)	2.196(8)
	Co2–O average		2.126	2.128	2.128	2.128	2.134
P1	O1	×1	1.529(18)	1.54(2)	1.547(17)	1.537(12)	1.491(12)
	O2	×1	1.59(2)	1.62(3)	1.567(19)	1.576(14)	1.545(13)
	O3	×2	1.561(14)	1.567(19)	1.550(13)	1.561(9)	1.541(9)
	P1–O average		1.560	1.574	1.554	1.559	1.530

[a] The estimated standard deviations (in parentheses) were calculated using the Berar's correction. [b] Note that the structure of the $LiCoPO_4$ phase of the sample prepared at pH = 5.5 could not be refined due to the small phase fraction of only 6.8(7) wt%.

Supporting Information

5 Additional Co $L_{2,3}$-edge Soft X-ray Absorption Spectra of $Co_{1.84(2)}Li_{0.16(3)}(OH)PO_4$

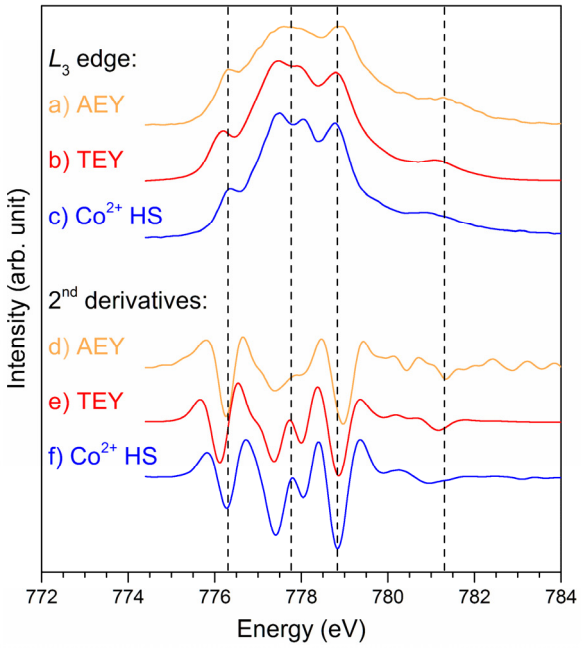

Figure S8. Normalized Co L_3-edge XAS spectra of $Co_{1.84(2)}Li_{0.16(3)}(OH)PO_4$ (prepared by hydrothermal synthesis at pH = 5.0) in the (a) AEY (orange) and (b) TEY (red) modes compared to a reference spectrum of octahedrally (O_h) coordinated, high-spin (HS) Co^{2+} (blue; CoO, adapted from ref. [13]) along with the respective second derivatives (d–f) corresponding to the experimental peak positions. The minima of the second derivatives reveal a small but significant shift in the peak positions of $Co_{1.84(2)}Li_{0.16(3)}(OH)PO_4$ compared to the HS Co^{2+} reference, indicating an increased crystal field strength. All datasets have been aligned to match the common energy scale of reference [13]. The vertical dashed lines indicate characteristic peak positions corresponding to O_h Co^{2+} (characteristic shoulder: 776.4 eV; doublet: 777.7 eV, local maximum: 778.8 eV, shoulder: 781.3 eV).

Supporting Information

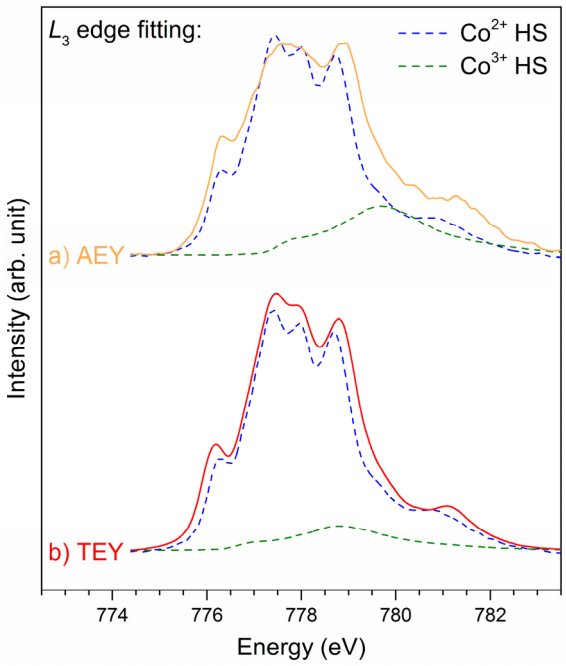

Figure S9. Fitting of the XAS spectra of $Co_{1.84(2)}Li_{0.16(3)}(OH)PO_4$ (prepared by hydrothermal synthesis at pH = 5.0) in the (a) AEY (orange) and (b) TEY (red) modes over the L_3 edge using Co^{2+} (HS (high-spin), dashed blue line, CoO, adapted from ref. [13]) and Co^{3+} (HS, dashed green line; Sr_2CoO_3Cl, from ref. [14]) octahedral standards. The fitting delivers relative contributions of approximately (15 ± 5)% Co^{3+} for the AEY mode, and (6 ± 2)% Co^{3+} for the TEY mode, respectively. All datasets have been aligned to match the common energy scale of ref. [13].

Supporting Information

6 Additional Magnetic Measurements of $Co_{1.84(2)}Li_{0.16(3)}(OH)PO_4$

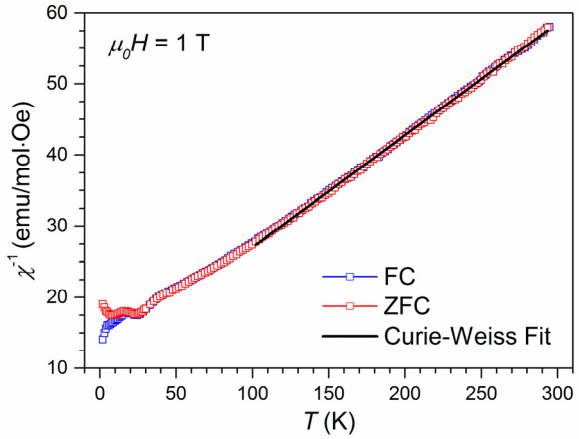

Figure S10. Inverse magnetic susceptibility of $Co_{1.84(2)}Li_{0.16(3)}(OH)PO_4$ (prepared by hydrothermal synthesis at pH = 5.0) recorded at a constant magnetic field of 1 T under ZFC (zero-field-cooled) and FC (field-cooled) conditions and the Curie–Weiss fit from T = 100K to 300 K.

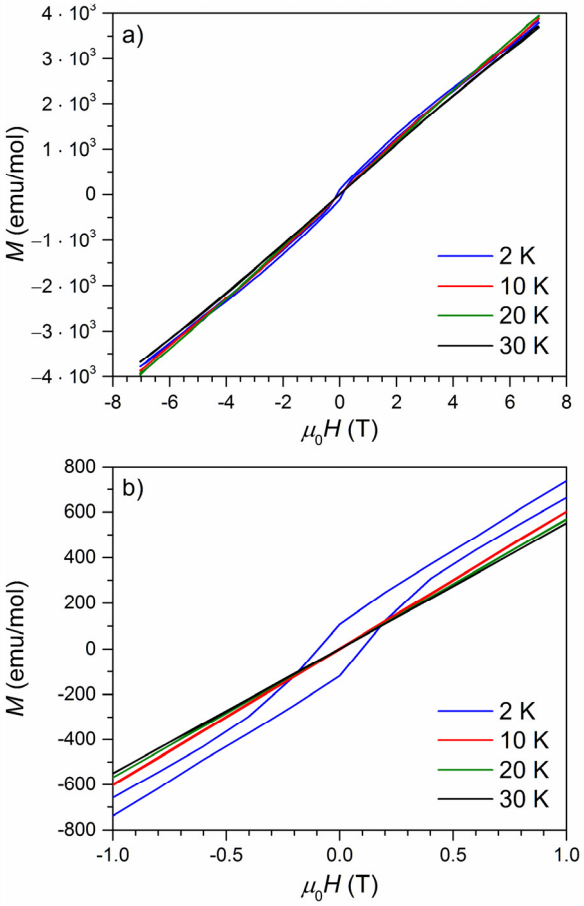

Figure S11. (a) Magnetization of $Co_{1.84(2)}Li_{0.16(3)}(OH)PO_4$ (prepared by hydrothermal synthesis at pH = 5.0) as a function of the applied field between −7 T and 7 T recorded at temperatures of 2 K, 10 K, 20 K, and, 30 K, respectively. (b) Zoomed view of the hysteresis curves between −1 T and 1 T.

Supporting Information

7 Rietveld Refinement of the Powder X-ray Diffraction Data of the Sample Obtained After the TGA/DSC Measurement of $Co_{1.84(2)}Li_{0.16(3)}(OH)PO_4$

Table S11. Crystallographic details and refined phase fractions of the crystalline phases observed in the powder X-ray diffraction pattern (T = 298 K) of the post-TGA/DSC (temperature range: 30–900 °C, atmosphere: Ar; *cf.* Fig. 6 in the main article) sample of $Co_{1.84(2)}Li_{0.16(3)}(OH)PO_4$ (prepared by hydrothermal synthesis at pH = 5.0) [a]

Phase	$Co_3(PO_4)_2$	CoO	$LiCoPO_4$
Space group	$P2_1/c$	$Fm\bar{3}m$	*Pnma*
Content (wt%)	**72.3(10)**	**15.1(5)**	**12.6(10)**
Z	2	4	4
a (Å)	5.0609(6)	4.2621(3)	10.242(6)
b (Å)	8.3683(9)	4.2621(3)	5.917(2)
c (Å)	8.7900(10)	4.2621(3)	4.728(2)
α (°)	90	90	90
β (°)	121.001(6)	90	90
γ (°)	90	90	90
V (Å^3)	319.09(6)	77.423(10)	286.5(2)
F(000)		140	
ρ (calcd.) (g·cm^{-3})	3.817(1)	6.428(1)	3.729(1)
R_p		0.0584	
R_{wp}		0.0810	
R_{exp}		0.0335	
R_F	0.0371	0.0269	0.0404
R_B	0.0627	0.0528	0.0770
χ^2		2.42	
Data/restraints/parameter		3813/0/100	

[a] The estimated standard deviations (in parentheses) were calculated using the Berar's correction.

Supporting Information

Table S12. Atomic positions and isotropic thermal displacement parameters of $Co_3(PO_4)_2$ (space group: $P2_1/c$, $Z = 2$) as refined from powder X-ray diffraction data ($T = 298$ K) of the post-TGA/DSC (temperature range: 30–900 °C, atmosphere: Ar) sample of $Co_{1.84(2)}Li_{0.16(3)}(OH)PO_4$ (prepared by hydrothermal synthesis at pH = 5.0) [a]

Atom	Wyckoff position	Occupancy	*x*/a	*y*/b	*z*/c	U_{iso} (Å^2)
Co1	2*a*	1	0	0	0	0.020(3)
Co2	4*e*	1	0.0217(14)	0.3590(7)	0.1140(10)	0.019(2)
P1	4*e*	1	0.338(3)	0.6949(17)	0.300(2)	0.018(3)
O1	4*e*	1	0.287(4)	0.645(3)	0.449(4)	0.012(3)
O2	4*e*	1	0.686(5)	0.692(4)	0.375(4)	0.015(5)
O3	4*e*	1	0.194(4)	0.583(3)	0.149(4)	0.014(3)
O4	4*e*	1	0.196(5)	0.861(4)	0.243(3)	0.010(2)

[a] The estimated standard deviations (in parentheses) were calculated using the Berar's correction.

Table S13. Selected interatomic distances of $Co_3(PO_4)_2$ (space group: $P2_1/c$, $Z = 2$) as refined from powder X-ray diffraction data ($T = 298$ K) of the post-TGA/DSC (temperature range: 30–900 °C, atmosphere: Ar) sample of $Co_{1.84(2)}Li_{0.16(3)}(OH)PO_4$ (prepared by hydrothermal synthesis at pH = 5.0) [a]

Atom pair			*d* (Å)
Co1	O1	×2	2.11(3)
	O2	×2	2.13(3)
	O4	×2	2.17(3)
	Co1–O average		2.14
Co2	O1	×1	2.25(3)
	O2	×1	2.00(4)
	O3	×1	2.02(3)
	O3	×1	2.04(3)
	O4	×1	2.06(3)
	Co2–O average		2.07
P1	O1	×1	1.52(4)
	O2	×1	1.53(4)
	O3	×1	1.47(3)
	O4	×1	1.52(3)
	P1–O average		1.51

[a] The estimated standard deviations (in parentheses) were calculated using the Berar's correction.

Supporting Information

Table S14. Atomic positions and isotropic thermal displacement parameters of CoO (space group: $Fm\bar{3}m$, $Z = 4$) as refined from powder X-ray diffraction data ($T = 298$ K) of the post-TGA/DSC (temperature range: 30–900 °C, atmosphere: Ar) sample of $Co_{1.84(2)}Li_{0.16(3)}(OH)PO_4$ (prepared by hydrothermal synthesis at pH = 5.0) [a]

Atom	Wyckoff position	Occupancy	*x*/a	*y*/b	*z*/c	U_{iso} (Å^2)
Co1	4*a*	1	0	0	0	0.0157(5)
O1	4*b*	1	½	½	½	0.014(3)

[a] The estimated standard deviations (in parentheses) were calculated using the Berar's correction.

Table S15. Selected interatomic distances of CoO (space group: $Fm\bar{3}m$, $Z = 4$) as refined from powder X-ray diffraction data ($T = 298$ K) of the post-TGA/DSC (temperature range: 30–900 °C, atmosphere: Ar) sample of $Co_{1.84(2)}Li_{0.16(3)}(OH)PO_4$ (prepared by hydrothermal synthesis at pH = 5.0) [a]

Atom pair			*d* (Å)
Co1	O1	×6	2.1311(3)

[a] The estimated standard deviations (in parentheses) were calculated using the Berar's correction.

Supporting Information

Table S16. Atomic positions and isotropic thermal displacement parameters of $LiCoPO_4$ (space group: *Pnma*, $Z = 4$) as refined from powder X-ray diffraction data ($T = 298$ K) of the post-TGA/DSC (temperature range: 30–900 °C, atmosphere: Ar) sample of $Co_{1.84(2)}Li_{0.16(3)}(OH)PO_4$ (prepared by hydrothermal synthesis at pH = 5.0) [a]

Atom	Wyckoff position	Occupancy	*x*/a	*y*/b	*z*/c	U_{iso} (Å^2)
Li1	4*a*	1	0	0	0	0.0139 [b]
Co1	4*c*	1	0.2181(19)	¼	0.515(5)	0.010(5)
P1	4*c*	1	0.395(5)	¼	0.122(4)	0.014(4)
O1	4*c*	1	0.423(4)	¼	0.771(3)	0.012(3)
O2	4*c*	1	0.063(4)	¼	0.283(4)	0.012(3)
O3	8*d*	1	0.351(5)	0.031(4)	0.216(5)	0.010(2)

[a] The estimated standard deviations (in parentheses) were calculated using the Berar's correction. [b] The thermal displacement parameter of Li has been kept fixed as it cannot be deduced by means of powder X-ray diffraction due to the low atomic scattering factor of Li.

Table S17. Selected interatomic distances of $LiCoPO_4$ (space group: *Pnma*, $Z = 4$) as refined from powder X-ray diffraction data ($T = 298$ K) of the post-TGA/DSC (temperature range: 30–900 °C, atmosphere: Ar) sample of $Co_{1.84(2)}Li_{0.16(3)}(OH)PO_4$ (prepared by hydrothermal synthesis at pH = 5.0) [a]

Atom pair			*d* (Å)
Li1	O1	×2	2.11(8)
	O2	×2	2.10(2)
	O3	×2	2.04(6)
	Li1–O average		2.08
Co1	O1	×1	2.41(3)
	O2	×1	1.93(2)
	O3	×2	2.04(5)
	O3	×2	2.36(5)
	Co1–O average		2.19
P1	O1	×1	1.69(2)
	O2	×1	1.78(5)
	O3	×2	1.44(6)
	P1–O average		1.59

[a] The estimated standard deviations (in parentheses) were calculated using the Berar's correction.

Supporting Information

8 References

[1] Roemming, C.; Raade, G., The crystal structure of natural and synthetic holtedahlite. *Mineral. Petrol.* **1989,** *40*, 91–100.

[2] Kolitsch, U.; Andrut, M.; Giester, G., Satterlyite, $(Fe,Mg)_{12}(PO_3OH)(PO_4)_5(OH,O)_6$: crystal structure and infrared absorption spectra. *Eur. J. Mineral.* **2002,** *14*, 127–133.

[3] Vegard, L., Die Konstitution der Mischkristalle und die Raumfüllung der Atome. *Z. Physik* **1921,** *5*, 17–26.

[4] Rui, X.; Zhao, X.; Lu, Z.; Tan, H.; Sim, D.; Hng, H. H.; Yazami, R.; Lim, T. M.; Yan, Q., Olivine-Type Nanosheets for Lithium Ion Battery Cathodes. *ACS Nano* **2013,** *7*, 5637–5646.

[5] Raade, G.; Mladeck, M. H., Holtedahlite, a new magnesium phosphate from Modum, Norway. *Lithos* **1979,** *12*, 283–287.

[6] Brunet, F.; Schaller, T., Protons in the magnesium phosphates phosphoellenbergerite and holtedahlite: an IR and NMR study. *Am. Mineral.* **1996,** *81*, 385–394.

[7] Burba, C. M.; Frech, R., Vibrational spectroscopic investigation of structurally-related $LiFePO_4$, $NaFePO_4$, and $FePO_4$ compounds. *Spectrochim. Acta, Part A* **2006,** *65A*, 44–50.

[8] Paques-Ledent, M. T.; Tarte, P., Vibrational studies of olivine-type compounds. II. Orthophosphates, -arsenates and -vanadates $A^IB^{II}X^VO_4$. *Spectrochim. Acta, Part A* **1974,** *30A*, 673–689.

[9] Ait Salah, A.; Jozwiak, P.; Garbarczyk, J.; Benkhouja, K.; Zaghib, K.; Gendron, F.; Julien, C. M., Local structure and redox energies of lithium phosphates with olivine- and Nasicon-like structures. *J. Power Sources* **2005,** *140*, 370–375.

[10] Julien, C.; Camacho-Lopez, M. A.; Mohan, T.; Chitra, S.; Kalyani, P.; Gopukumar, S., Combustion synthesis and characterization of substituted lithium cobalt oxides in lithium batteries. *Solid State Ionics* **2000,** *135*, 241–248.

[11] Effenberger, H., Structure refinement of tricobalt dihydroxide bis(hydrogen phosphate) and cobalt bis(dihydrogen phosphate) dihydrate. *Acta Crystallogr., Sect. C: Cryst. Struct. Commun.* **1992,** *C48*, 2104–2107.

[12] Ludwig, J.; Marino, C.; Haering, D.; Stinner, C.; Gasteiger, H. A.; Nilges, T., Morphology-controlled microwave-assisted solvothermal synthesis of high-performance $LiCoPO_4$ as a high-voltage cathode material for Li-ion batteries. *J. Power Sources* **2017,** *342*, 214–223.

[13] Hibberd, A. M.; Doan, H. Q.; Glass, E. N.; de Groot, F. M. F.; Hill, C. L.; Cuk, T., Co Polyoxometalates and a Co_3O_4 Thin Film Investigated by L-Edge X-ray Absorption Spectroscopy. *J. Phys. Chem. C* **2015,** *119*, 4173–4179.

[14] Hu, Z.; Wu, H.; Haverkort, M. W.; Hsieh, H. H.; Lin, H. J.; Lorenz, T.; Baier, J.; Reichl, A.; Bonn, I.; Felser, C.; Tanaka, A.; Chen, C. T.; Tjeng, L. H., Different Look at the Spin State of Co^{3+} Ions in a CoO_5 Pyramidal Coordination. *Phys. Rev. Lett.* **2004,** *92*, 207402/1–207402/4.

6.6 Synthesis and Characterization of Metastable, 20 nm-Sized *Pna*2_1-$LiCoPO_4$ Nanospheres

Jennifer Ludwig,[a] Dennis Nordlund,[b] Marca M. Doeff,[c] and Tom Nilges[a]

[a] Technical University of Munich, Department of Chemistry, Synthesis and Characterization of Innovative Materials, Lichtenbergstr. 4, 85747 Garching, Germany

[b] Stanford Synchrotron Radiation Lightsource, SLAC National Accelerator Laboratory, 2575 Sand Hill Rd, Menlo Park, CA, 94025, USA

[c] Lawrence Berkeley National Laboratory, Environmental Energy Technologies Division, 1 Cyclotron Rd, Berkeley, CA, 94720, USA

J. Solid State Chem. **2017,** *248,* 9–17.
DOI: 10.1016/j.jssc.2017.01.015

Journal of Solid State Chemistry 248 (2017) 9–17

Contents lists available at ScienceDirect

Journal of Solid State Chemistry

journal homepage: www.elsevier.com/locate/jssc

Synthesis and characterization of metastable, 20 nm-sized $Pna2_1$-$LiCoPO_4$ nanospheres

Jennifer Ludwig[a], Dennis Nordlund[b], Marca M. Doeff[c], Tom Nilges[a,*]

[a] Technical University of Munich, Department of Chemistry, Synthesis and Characterization of Innovative Materials, Lichtenbergstr. 4, 85747 Garching, Germany
[b] Stanford Synchrotron Radiation Lightsource, SLAC National Accelerator Laboratory, 2575 Sand Hill Rd, Menlo Park, CA 94025, USA
[c] Lawrence Berkeley National Laboratory, Environmental Energy Technologies Division, 1 Cyclotron Rd, Berkeley, CA 94720, USA

ARTICLE INFO

Keywords:
Lithium cobalt phosphate
Nanoparticles
Microwave-assisted solvothermal synthesis
Phase transitions
In situ powder X-ray diffraction
X-ray absorption spectroscopy

ABSTRACT

The majority of research activities on $LiCoPO_4$ are focused on the phospho-olivine (space group *Pnma*), which is a promising high-voltage cathode material for Li-ion batteries. In contrast, comparably little is known about its metastable $Pna2_1$ modification. Herein, we present a comprehensive study on the structure–property relationships of 15–20 nm $Pna2_1$-$LiCoPO_4$ nanospheres prepared by a simple microwave-assisted solvothermal process. Unlike previous reports, the results indicate that the compound is non-stoichiometric and shows cation-mixing with Co ions on the Li sites, which provides an explanation for the poor electrochemical performance. Co $L_{2,3}$-edge X-ray absorption spectroscopic data confirm the local tetrahedral symmetry of Co^{2+}. Comprehensive studies on the thermal stability using thermogravimetric analysis, differential scanning calorimetry, and *in situ* powder X-ray diffraction show an exothermic phase transition to olivine *Pnma*-$LiCoPO_4$ at 527 °C. The influence of the atmosphere and the particle size on the thermal stability is also investigated.

1. Introduction

Since their commercialization in 1991 by Sony [1], Li-ion batteries have become a key technology in portable electronics and electric vehicles. To increase specific energies in order to meet future demands, current research activities focus on cathode materials. Particular attention has been given to cathode materials that operate at significantly higher voltage than commercial materials (*e.g.* spinels and lithium-rich layered oxides), as well as new compounds. A promising candidate is the high-voltage cathode material $LiCoPO_4$. Three $LiCoPO_4$ polymorphs with orthorhombic crystal structures have been reported.

The most common and widely investigated olivine-type $LiCoPO_4$ crystallizes orthorhombically in the space group *Pnma* [2]. The structure consists of two types of polyhedra, $[CoO_6]$ octahedra and $[PO_4]$ tetrahedra, which form a three-dimensional network. The Li^+ ions are located in channels along the [010] and [001] directions. Since the first report by Padhi et al. [3] in 1997, intensive efforts [4–6] have been undertaken to optimize the electrochemical performance of the material, which is redox active at ~4.8 V *vs.* Li/Li^+ [7]. Recently, we have reported [8] a facile, one-step microwave-assisted solvothermal (MWST) route towards high-performance *Pnma*-$LiCoPO_4$ hexagonal platelets using a mixed 1:1 (v:v) water/ethylene glycol (EG) solvent. The optimized material delivers a specific capacity of 137 mAh/g and an energy density of 658 Wh/kg, which is one of the best performances reported to date. Furthermore, it was shown that – in contrast to previous reports on the thermal stability of *Pnma*-$LiCoPO_4$ [9,10] – the compound partially transforms to the $Pna2_1$ structure at 900 °C.

A high-pressure modification (6 GPa, 1173 K), which is isostructural to Na_2CrO_4 (space group *Cmcm*), was reported by Amador et al. [11] in 2009. Like the *Pnma* structure, the compound features a framework of $[CoO_6]$ and $[PO_4]$ units, in which Li ions occupy tetrahedral sites. Kreder et al. [10] demonstrated the low-temperature MWST synthesis and studied the electrochemical properties of the compound, which has an irreversible redox potential of ~4.3 V *vs.* Li/Li^+ and shows poor electrochemical performance (discharge capacity of 6 mAh/g). The

Abbreviations: AAS, Atomic absorption spectroscopy; DEC, Diethyl carbonate; DSC, Differential scanning calorimetry; EC, Ethylene carbonate; EDS, Energy-dispersive X-ray spectroscopy; EG, Ethylene glycol; FTIR, Fourier transform infrared spectroscopy; FWHM, Full width at half maximum; LEI, Lower secondary electron image; NMP, *N*-Methyl-2-pyrrolidone; PP, (Poly)propene, polypropylene; PVdF, Polyvinylidene difluoride; PXRD, Powder X-ray diffraction; SEM, Scanning electron microscope; TEY, Total electron yield; TGA, Thermogravimetric analysis; XAS, X-ray absorption spectroscopy

* Corresponding author.
E-mail address: tom.nilges@lrz.tum.de (T. Nilges).

http://dx.doi.org/10.1016/j.jssc.2017.01.015
Received 24 November 2016; Received in revised form 22 December 2016; Accepted 14 January 2017
Available online 15 January 2017

magnetic properties and an alternative polyol synthesis pathway at ambient pressure were recently reported [12]. A temperature-dependent *in situ* powder X-ray diffraction study revealed that a transition to the *Pnma* structure occurs at 575 °C, which is then fully converted to the *Pna*2$_1$ polymorph at 675 °C. After cooling to ambient temperature, the thermodynamically stable *Pnma*-LiCoPO$_4$ was obtained.

A third metastable polymorph, which adopts a δ_1-LiZnPO$_4$-like structure (space group *Pna*2$_1$), was experimentally reported and characterized by Jaehne *et al.* [13] in 2013 and later by Kreder and co-workers [10] (note that these structures were reported in *Pn*2$_1$*a*, a non-standard setting of *Pna*2$_1$). Unlike the other two polymorphs, the 3D framework exhibits only tetrahedral [PO$_4$] and [CoO$_4$] building units with no direct Li channels. The redox potential of 4.95 V *vs.* Li/Li$^+$ for *Pna*2$_1$-LiCoPO$_4$ is the highest of the three LiCoPO$_4$ modifications, which makes it a potential candidate for high-energy density applications. However, the electrochemical performance has been reported to be poor, with capacities of 27 mAh/g [13] and 33 mAh/g [10] being reached, which is only 16% and 20% of the theoretical capacity of 167 mAh/g$_{LiCoPO4}$. It was suggested that the applicability might be improved by particle size control in order to overcome kinetic limitations. Furthermore, the groups reported different thermal stabilities for their *Pna*2$_1$ materials upon heating under an argon atmosphere. Whereas Jaehne et al. [13] reported that the compound irreversibly transforms to the thermodynamically stable, olivine-type *Pnma*-LiCoPO$_4$ in an exothermic process at 221 °C, Kreder et al. [10] stated that the transition is endothermic and occurs at 340 °C. The reasons for these contradictory observations remained unclear.

Based on our work on the two other LiCoPO$_4$ polymorphs [8,12], we herein present a simple microwave-assisted solvothermal approach towards nanostructured *Pna*2$_1$-LiCoPO$_4$. The structure–property relationships of the material are investigated using powder X-ray diffraction, elemental analysis, scanning electron microscopy, BET surface area analysis, infrared spectroscopy, as well as electrochemical measurements. Furthermore, the formation and crystal growth mechanisms are discussed. A redetermination of the crystal structure allows further insights into the material properties, and elucidates a possible reason for the poor electrochemical behavior reported. Co $L_{2,3}$-edge soft X-ray spectroscopic data are presented for the first time and confirm the local symmetry of Co^{2+} in the structure. The thermal stability is thoroughly investigated using thermogravimetric analysis, differential scanning calorimetry, and temperature-dependent *in situ* powder X-ray diffraction studies.

2. Experimental

2.1. Microwave-assisted solvothermal synthesis

*Pna*2$_1$-LiCoPO$_4$ nanoparticles were obtained from a modified microwave-assisted solvothermal (MWST) process as reported previously [8]. 22.5 mmol LiOH·H$_2$O (Bernd Kraft, ≥99.0%), 7.5 mmol CoSO$_4$·7H$_2$O (Chempur, 99%), 7.5 mmol H$_3$PO$_4$ (AppliChem, Ph. Eur., 85 wt% solution), and 0.075 g ascorbic acid reductive (Alfa Aesar, 99+ %) were dissolved in 30 mL ethylene glycol (EG, VWR AnalaR NORMAPUR, 99.9%). The red violet suspension (pH =5.5) was stirred vigorously for 20 min and then transferred into a 75 mL reaction vessel (PTFE/TFM; HTV-75, MLS GmbH). An Ethos One microwave system (MLS GmbH) equipped with an MR-8 HT high-temperature rotor was used for the synthesis, which was performed at 250 °C for 30 min under continuous stirring and a maximum power of 600 W. The microwave irradiation was adjusted automatically by the T660 temperature control unit. The mixture (pH =5.0) was naturally cooled down after the reaction. The dark blue precipitate (picture see graphical abstract) was recovered by filtration, followed by washing several times with deionized water (high-purity water type I, Millipore, 18.2 MΩ cm; used to remove a highly water-soluble lithium sulfate side phase [8]) and absolute ethanol (VWR AnalaR NORMAPUR, 99.95%). The powder was then dried in air at 150 °C overnight.

2.2. Structural, chemical, and physical characterization

2.2.1. Powder X-ray diffraction (PXRD) and Rietveld refinement details

A STADI P diffractometer (Mo $K_{\alpha1}$ radiation, λ=0.70930 Å) equipped with a Ge(111) monochromator and a Dectris MYTHEN DCS 1 K silicon solid-state detector was used to collect PXRD data of the ground powder, which was sealed in a 0.5 mm borosilicate glass capillary (Hilgenberg). The measurement was performed in a 2θ range of 3–60° (PSD step: 0.015°; time/step: 30 s, three ranges, total measurement time: 12 h). Data were calibrated using an external silicon standard. The Jana 2006 software [14] was used to perform a Rietveld refinement of the diffraction pattern, using the structure solution of the homologue δ_1-LiZnPO$_4$ (space group *Pna*2$_1$; ICSD no. 79537 [15]) as a starting model. A Chebyshev polynomial was used for correcting the background, and the axial divergence model [16] for the peak asymmetry. An estimated packing fraction of ~0.6 was applied for absorption correction [17]. General atomic positions as well as the isotropic thermal displacement parameters of Co, P, and O were refined without restraints, whereas the displacement parameter and position of Li were kept fixed. Furthermore, a slightly disordered Li/Co distribution on the Li position was assumed. The Berar's correction [18] was applied to all refined parameters in order to obtain more realistic standard deviations.

2.2.2. Elemental analysis

The Li and Co contents of the material were determined by atomic absorption spectroscopy (AAS, Varian AA280FS device), and the P content by photometry (Shimadzu UV-160 device). The C, H, N, and S contents were measured by combustion analysis (Hekatech Euro EA CIINSO instrument).

2.2.3. Scanning electron microscopy (SEM) and energy-dispersive X-ray spectroscopy (EDS)

The morphology of the powder was determined using a JEOL JSM-7500F SEM (accelerating voltage: 1 kV, working distance: 8 mm, detector: LEI (lower secondary electron image). EDS analysis was performed with a Noran S1X system (Thermo Electron Corporation, model 6714A01SUS-SN, accelerating voltage: 15 kV, probe current: 20 μA). The powder was prepared on double-sided conductive carbon tape attached to an aluminum stub for the measurements.

2.2.4. BET surface area analysis

The specific surface area of the material was determined by the Brunauer–Emmett–Teller (BET) method (Quantachrome Autosorb iQ instrument) using nitrogen physisorption after a degassing period of 12 h at 150 °C (11 measurement points).

2.2.5. Rheometry

The dynamic viscosity of the ethylene glycol solvent (VWR AnalaR NORMAPUR, 99.9%) was determined at ambient temperature using an MCR 302 Anton Paar Modular Compact Rheometer in parallel plate–plate geometry (PP-50 plate, diameter: 49.991 mm, gap: 0.250 mm). A sample volume of ~0.5 mL was used for each measurement, and six measurements were performed in a shear rate range of 1–120 s^{-1} (40 measurement points). The average dynamic viscosity was determined at a shear rate of 100 s^{-1}. The values of high-purity water type I (Millipore, 18.2 MΩ cm) and a 1:1 (v: v) mixture of ethylene glycol and water were taken from another report [19]. In [19], we describe the particle-size controlled synthesis and characterization of olivine-type *Pnma*-LiCoPO$_4$.

2.2.6. Fourier-transform infrared (FTIR) spectroscopy

The FTIR spectrum was collected in a wavenumber range of 400–

4000 cm^{-1} (132 scans) using a Varian 670 IR FTIR spectrometer equipped with a PIKE GladiATR diamond ATR stage.

2.2.7. Soft X-ray absorption spectroscopy (soft XAS)

Co $L_{2,3}$-edge soft XAS measurements were performed at beamline 8-2 of Stanford Synchrotron Radiation Lightsource (SSRL). The sample was attached to an Al sample holder using double-sided conductive carbon tape. The incident beam was monochromatized using a spherical grating monochromator (SGM) with 1100 mm^{-1} ruling, where the exit and entrance slits were set to an intermediate resolution of 0.3 eV. The $L_{2,3}$-edge μ(E) spectra were collected at room temperature under ultrahigh vacuum (10^{-9} Torr) in the total electron yield (TEY) mode, obtained through the drain current, and corresponding to probing depths of 2–5 nm [20]. Co_3O_4 and CoO powders were used as references. All spectra are shown on a common energy scale as in reference [21]. The spectra were normalized to the incident photon flux and the background subtracted using a line. The intensity of the spectra was further normalized to a maximum of 1 for visual comparison.

2.2.8. Electrochemical measurements

The cathode slurries were prepared by mixing 80 wt% $LiCoPO_4$, 10 wt% carbon (Super C65, Timcal), and 10 wt% polyvinylidene difluoride (PVdF, Solvay) binder with *N*-methyl pyrrolidone (NMP) solvent in an agate mortar. The slurries were cast onto carbon-coated Al current collectors (Coveris Advanced Coatings) using a doctor-blade coater. The electrode sheets were dried at 120 °C for 5 h in a vacuum oven (Thermo Scientific) and then calendered (International Rolling Mills device) in order to increase the contact of the active material with the current collector. The electrode sheets were further vacuum dried for 12 h at 120 °C before being transferred into an Ar-filled glove-box (VAC, < 0.1 ppm H_2O, < 0.1 ppm O_2). Circular electrodes with a diameter of 14.3 mm and typical active material loadings of ~4 mg were punched out. CR2032 coin-type cells were assembled using the $LiCoPO_4$-containing cathode, Li foil (Alfa Aesar, 0.75 mm, 99.9%, metals basis) as anode, a microporous monolayer PP membrane as separator (Celgard 2400, 25 µm, polypropylene), and 1 M $LiPF_6$ dissolved in ethylene carbonate (EC)/diethyl carbonate (DEC) in a ratio of 1:1 (v: v) as electrolyte (Daikin). Charge–discharge cycling was carried out galvanostatically (BioLogic VMP3 potentiostat/galvanostat) between 3.0 V and 5.2 V at C rates of 0.1 C, 0.2 C, 0.5 C, and 1 C for three cycles each, followed by 20 cycles at 0.1 C. Current densities and specific capacities were calculated on basis of the weight of active material in the electrode. Two cells were measured to increase the reliability of the results.

2.2.9. Thermal analysis using temperature-dependent powder X-ray diffraction (PXRD), thermogravimetric analysis (TGA), and differential scanning calorimetry (DSC)

Thermal analysis was performed on a Mettler Toledo TGA/DSC 1 STAR system, which allows simultaneous thermogravimetric analysis (TGA) and differential scanning calorimetry (DSC). A specimen weight of ~5 mg was placed in an alumina crucible, and the experiment run in a temperature range of 30–900 °C (heating rate: 10 °C/min) under two different atmospheres: (1) an argon and (2) a synthetic air stream (both 10 mL/min). Note that only the heating cycle could be monitored due to the instrument setup.

The thermal stability was further assessed by temperature-controlled *in situ* PXRD studies on a PANalytical X'Pert Pro diffractometer in Bragg-Brentano geometry (Cu K_α radiation, XCelerator detector, Anton Parr HTK-1200 hot stage, TCU 1000N temperature controller). The sample, which was placed in a corundum flatplate sample holder, was heated up to 900 °C (heating rate: 5 °C/min, increment step: 100 °C) in air and alternatively under argon. Each temperature was held for 5 min before starting the data collection. The measurements were performed in a 2θ range of 15–70° (step: 0.022°), with the time/step and total measurement time being increased for the measurement under Ar due to lower the lower signal/noise ratio (air: 209.5 s/step, total measurement time: 145.5 h; Ar: 400 s/step, total measurement time: 277 h).

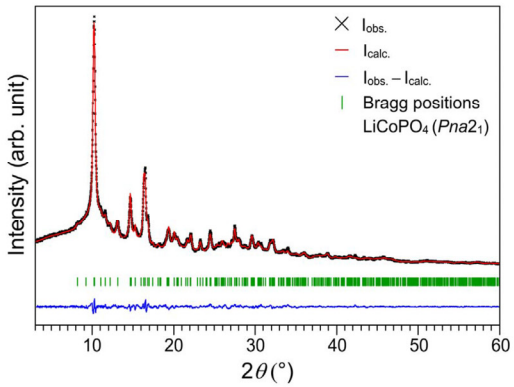

Fig. 1. Rietveld fit of the powder X-ray diffraction data (Debye-Scherrer geometry, Mo $K_{\alpha1}$ radiation) of nano-sized $Pna2_1$-$LiCoPO_4$.

3. Results and discussion

3.1. Powder X-ray diffraction and crystal structure

Fig. 1 shows the Rietveld fit of the powder X-ray diffraction pattern of the as-prepared powder. No crystalline impurities are detected and all reflections can be indexed using the orthorhombic space group $Pna2_1$ (note that the conventional cell setting is used rather than the non-standardized $Pn2_1a$). The broad reflections indicate that the sample is composed of nanoparticles. The particle size cannot be accurately determined by the Scherrer equation because the main signal consists of two reflections, (210) and (011), which are not well-resolved due to the peak width. Nevertheless, a tentative calculation delivers an estimated particle size of ~18 nm in diameter. The nanostructure of the particles is confirmed by SEM/BET analyses discussed in Section 3.3.

Using the structure solution of the homologue δ_1-$LiZnPO_4$ (ICSD no. 79537 [15]) as a starting model, the structure of $Pna2_1$-$LiCoPO_4$ can be solved with improved reliability factors (*e.g.* R_{wp} = 3.45%, χ^2 =1.27; Table 1) compared to previously published results (cf. reference

Table 1
Crystallographic parameters of nano-sized $Pna2_1$-$LiCoPO_4$ as refined from powder X-ray diffraction data (T=298 K) [a].

Empirical formula	$Li_{0.95(1)}Co_{1.03(1)}PO_4$
M_r (g/mol)	162.1
Crystal system	orthorhombic
Space group (no.)	$Pna2_1$ (33)
Z	4
a (Å)	10.035(4)
b (Å)	4.967(2)
c (Å)	6.716(2)
V (Å^3)	334.8(2)
F(000)	308
ρ (calcd.) (g/cm^3)	3.216(1)
R_p	0.0260
R_{wp}	0.0345
R_{exp}	0.0278
R_F	0.0213
R_B	0.0429
χ^2	1.27
Data/restraints/parameter	3802/0/71

[a] The estimated standard deviations were calculated by the Berar's procedure and are indicated in parentheses.

[10]: R_{wp} = 31.4%, χ^2 = 1.78; and [13]: R_{wp} = 3.49%, χ^2 = 1.83). The tentative refinement of the occupancy on the Li site resulted in a statistical significant value of 124(8)%, indicating that there is a partial substitution of the site with Co. An over-occupation of 122% Li was also reported by Jaehne and et al. [13], but no Co occupancy on this site was assumed. We concluded that Li/Co anti-site mixing appears on the Li site (occupancies: 95.2(8)% Li and 4.8(8)% Co, cf. Table S1). On the Co site, we found a Co population of 97.9(12)%, which corresponds to a full occupation within two standard deviations if only Co was used for refinement. If anti-site mixing is also applied for this site, the resulting overall composition would not be charge balanced. We therefore decided to refine this site as to be occupied by Co only and with a low defect concentration. The slightly disordered Li/Co distribution has certain similarities with the structure of δ_1-LiZnPO$_4$, for which Li/Zn mixing was described for both the Li and Zn sites (8% Zn on the Li position, and *vice versa*) [15]. To the best of our knowledge, this is the first time structural disorder has been reported for *Pna*2$_1$-LiCoPO$_4$. The increase in cell volume (334.8(2) Å^3) compared to olivine LiCoPO$_4$ (283.31(3) Å^3) [8] indicates that the compound is less dense. The empirical formula $Li_{0.95(1)}Co_{1.03(1)}PO_4$ is consistent with the composition determined by elemental analysis (see Section 3.2, Table 2). Note that for simplicity, the compound is referred to as *Pna*2$_1$-LiCoPO$_4$ in this work.

The structure of *Pna*2$_1$-LiCoPO$_4$ (Fig. 2) exhibits a three-dimensional framework, built from chains of corner-sharing, asymmetric [CoO$_4$] and [PO$_4$] tetrahedra (cf. interatomic distances, Table S2), and with four-coordinated Li/Co ions on interstitial positions [13,15]. Unlike the olivine *Pnma* polymorph, which shows Li channels along [010] and [001], no direct accessible Li channels are observed for *Pna*2$_1$-LiCoPO$_4$. For instance, along [001] (Fig. 2c) possible channels are blocked by [CoO$_4$] units, and only zig-zag-like voids occur along [100] with Li/Co–Li/Co distances of 5.053(4) Å ($\measuredangle$(Li/Co–Li/Co–Li/Co) = 166.5(1)°; Fig. 2a). Distorted six-ring tunnels of alternating [CoO$_4$] and [PO$_4$] units are observed along [010] (Fig. 2b), in which the Li/Co ions are located with d(Li/Co–Li/Co) = 4.967(4) Å. Despite these features, Li-ion transport is expected to be very limited due to the Li/Co mixing on the Li sites, with Co ions blocking the Li pathways and hence impeding diffusion. Moreover, the distances between Li sites are significantly larger than in the olivine (2.9594(4) Å [8]).

3.2. Elemental analysis

The results of the elemental analysis are displayed in Table 2. CHNS analysis indicates that the sample contains small amounts of carbon (0.4(3) wt%) and hydrogen (0.5(3) wt%), which is most likely caused by decomposition products of ethylene glycol or ascorbic acid. Water as a source for Hydrogen can be ruled out because the IR spectrum (see Fig. S3) does not show any absorption bands of water. (The estimated amount of water based on the determined H content is ~4.5 wt% and would be easily detected by IR). Compared to our previous work [8] on olivine-type *Pnma*-LiCoPO$_4$, which used a similar microwave-assisted solvothermal process, it is surprising that no significant amounts (0.1(3) wt%) of sulfur are detected in the material as LiCoPO$_4$ and Li$_2$SO$_4$ are formed during the reaction (3 LiOH·H$_2$O + CoSO$_4$·7H$_2$O + H$_3$PO$_4$ → LiCoPO$_4$ + Li$_2$SO$_4$·H$_2$O + 12 H$_2$O). Apparently, the small particle size and respective high surface area (~61 m^2/g) of the *Pna*2$_1$-LiCoPO$_4$ material are beneficial for the quantitative removal of the highly water-soluble Li$_2$SO$_4$ side phase during the washing step, compared to the olivine-type LiCoPO$_4$ (~6 m^2/g) [8].

Table 2
Composition of the as-synthesized *Pna*2$_1$-LiCoPO$_4$ nanoparticles in comparison with the theoretically expected values [a].

Element	Theoretical	Found
C (wt%)	0	0.4(3)
H (wt%)	0	0.5(3)
N (wt%)	0	–[b]
S (wt%)	0	0.1(3)[c]
Li (wt%)	4.3	3.7(1)
Co (wt%)	36.6	34.8(5)
P (wt%)	19.3	17.4(3)
n(Li):n(P)	1	0.95(2)
n(Co):n(P)	1	1.05(1)
Empirical formula	LiCoPO$_4$	$Li_{0.95(2)}Co_{1.05(1)}PO_4$

[a] The molar composition is calculated from the experimental values and normalized to the P content (standard deviations in parentheses).
[b] The N content was too low to be detected (=0).
[c] Note that the S content is not significant.

Furthermore, the compound shows a deficit in the Li, and an excess in the Co contents (in wt%) compared to the ideal $Li_1Co_1PO_4$ composition. The Li:Co:P molar ratio of 0.95(2):1.05(1):1.00(2) derived from elemental analysis indicates that *Pna*2$_1$-LiCoPO$_4$ is non-stoichiometric. This finding is in good agreement with the Rietveld refinement results (Table S1). Taking the respective standard deviations into account, these deviations are significant. This is different to other reports [10,13] where a stoichiometric 1:1:1 Li:Co:P composition for the compound was suggested. Our findings indicate that there is a certain phase width, which is probably affected by the synthesis process. Hence, future studies should focus on the non-stoichiometry in order to identify the composition range, which could pave the way to tailor the material properties and to obtain a stoichiometric material without anti-site defects (*e.g.* by varying the Li:Co:P molar ratios of the starting materials).

3.3. Scanning electron microscopy

High-resolution SEM (Fig. 3a) reveals that the as-prepared material consists of uniform, well-crystallized nanospheres with diameters of approximately 15–20 nm, which is in agreement with the broadened reflections observed in the PXRD pattern (Fig. 1). Moreover, some crystals are agglomerated to larger particles of ~30–60 nm. The observed particle size is in agreement with the high specific BET surface area of 60.6(5) m^2/g, which suggests an average diameter of about 31 nm using the equation $d = 6/(S{\cdot}\rho)$, with d being the particle diameter (m), S the specific surface area (m^2/kg), and ρ the density of the material (kg/m^3; here: 3.216 · 10^{-3} kg/m^3 as refined from PXRD data, cf. Table 1), and assuming that the particles are spherical and non-porous. The fact that the diameter derived from BET is slightly bigger than observed from SEM is due to the agglomeration. EDS analysis (Fig. 3b) delivers a composition of 35(1) wt% Co, 17.7(4) wt% P, and 48.2(7) wt% O, corresponding to a Co:P molar ratio of 1.04(3):1.00(2). The excess of Co is consistent with the results of the elemental analysis (Table 2).

3.4. Synthesis parameters

The formation of the metastable *Pna*2$_1$-LiCoPO$_4$ polymorph strongly depends on the synthesis conditions of the microwave-assisted solvothermal process. Jaehne et al. [13] identified the synthesis temperature, pH value, and precursor concentration as key parameters. In our procedure, however, the solvent type and composition seems to be a critical factor in obtaining the *Pna*2$_1$ modification. Whereas an aqueous system with 50 vol% ethylene glycol delivers hexagonal platelets of olivine *Pnma*-LiCoPO$_4$ at 250 °C (as shown in our previous work [8]), the metastable *Pna*2$_1$ modification is obtained when pure EG is used. A possible explanation is that diffusion plays an important role in the crystallization of the phases because the boiling points and viscosities of the reaction media differ significantly (EG: 15.7(2) mPa s (this work) *vs.* H$_2$O: 0.89(5) mPa s [19] *vs.* H$_2$O/EG 1:1 (v:v) mixture: 3.36(6) mPa s [19]; measured by rheometry at 25 °C and a shear rate of 100 s^{-1}). As a result, the ion diffusion rates and solubilities of the precursors are reduced in pure EG compared to aqueous solvents [22],

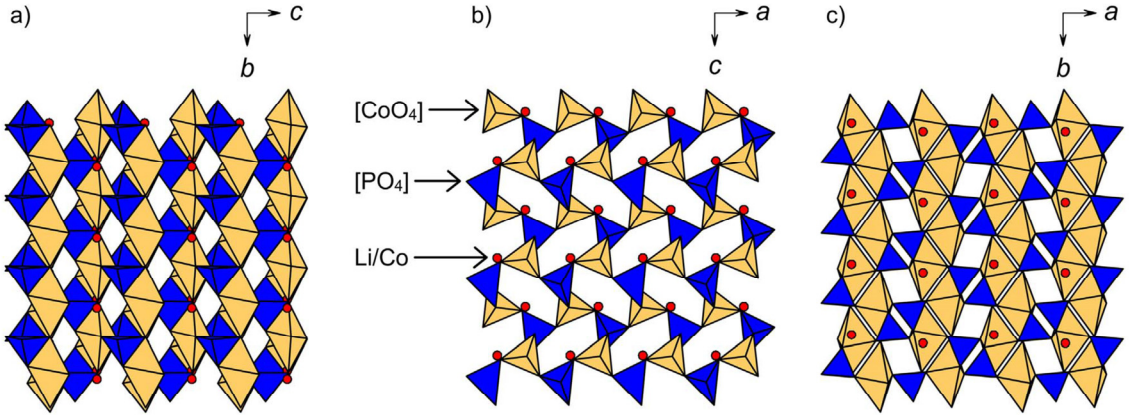

Fig. 2. Crystal structure of *Pna*2$_1$-LiCoPO$_4$ along the three crystallographic axes: (a) [100], (b) [010], and (c) [001]. [CoO$_4$] tetrahedra are drawn in light orange (occupancy of the Co ions: 97.9(12)%), [PO$_4$] tetrahedra in blue, and the mixed site containing 95.2(8)% Li and 4.8(8)% Co in red. (For interpretation of the references to color in this figure legend, the reader is referred to the web version of this article.)

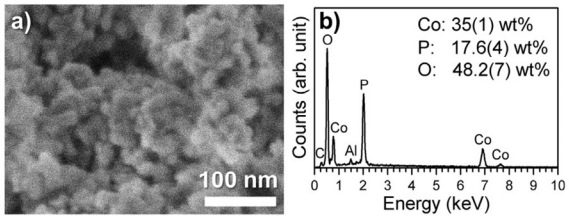

Fig. 3. (a) SEM image and (b) corresponding EDS spectrum of the *Pna*2$_1$-LiCoPO$_4$ powder prepared by microwave-assisted solvothermal synthesis. The sample contains spherical nanoparticles with a diameter of ~15–20 nm. The small C and Al signals observed in the EDS spectrum arise from the carbon tape and the aluminum holder used for the measurement.

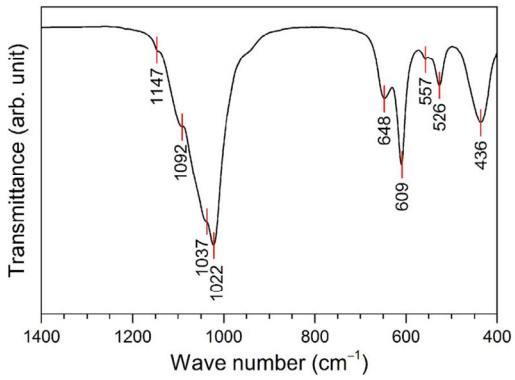

Fig. 4. FTIR spectrum of nano-sized *Pna*2$_1$-LiCoPO$_4$. The omitted region of 1400–4000 cm^{-1} (Fig. S3) does not show any absorption bands of water or other impurities.

favoring the formation of the metastable product (*Pna*2$_1$-LiCoPO$_4$) over the thermodynamic product (*Pnma*-LiCoPO$_4$) due to kinetic reaction control. Moreover, the particle size is affected, which is significantly reduced for *Pna*2$_1$-LiCoPO$_4$ compared to the size of olivine-type *Pnma*-LiCoPO$_4$ found in our previous work [8]. Due to the slower diffusion rates and the higher degree of supersaturation of the precursors in the viscous solvent, nucleation is favored over crystal growth, resulting in reduced particle dimensions. EG also acts as a complexing and capping agent, which effectively hinders the growth of large crystals and prevents agglomeration without the need of an additional surfactant [23].

The formation of *Pna*2$_1$-LiCoPO$_4$, however, is not limited to pure, water-free EG solvents if other parameters are varied. For instance, due to kinetic reaction control, the phase is also accessible by using shorter reaction times (≤10 min) in aqueous media (*e.g.* with 50 vol% EG) while keeping the reaction temperature at 250 °C (not shown). Another option is to decrease the temperature to 200 °C, while keeping the synthesis time at 30 min in order to obtain highly crystalline products. Here, the metastable phase is obtained for all solvent compositions. When pure water is used, for example, highly crystalline, micron-sized particles with cubic and square platelets morphologies are obtained (Figs. S1 and S2, Tables S3–S5). Employing lower process temperatures hence allows for the production of various particle sizes and morphologies by changing the solvent composition, which is of importance to modify the material properties.

3.5. Infrared spectroscopy

The FTIR spectrum of *Pna*2$_1$-LiCoPO$_4$ is shown in the region from 400 cm^{-1} to 1400 cm^{-1} (Fig. 4) and is in good agreement with a previous report [10]. In the omitted region of 1400–4000 cm^{-1} (Fig. S3), no absorption bands of water or other impurities appear, confirming the purity of the material. Generally, the spectrum is expected to be dominated by the four fundamental intramolecular vibrations of the [PO$_4$]$^{3-}$ tetrahedra, with the frequencies being closely related to the ones of the free molecule (1082 cm^{-1}, 980 cm^{-1}, 515 cm^{-1}, and 365 cm^{-1}) [24]. In the spectrum, two main regions can be distinguished: The first region between 400 cm^{-1} and 700 cm^{-1} is associated with the intramolecular [PO$_4$]$^{3-}$ bending modes (ν_2, ν_4); the region of 900–1200 cm^{-1} corresponds to the intramolecular stretching vibrations (ν_1, ν_3).

More specifically, the bands at 1147 cm^{-1}, 1092 cm^{-1}, and 1037 cm^{-1} are associated with the asymmetric stretching vibrations of P–O (ν_3), which is split up in a triplet due to interactions with the Co–O bonds ($\Delta\tilde{\nu}$ = 55 cm^{-1}), whereas the symmetric P–O stretching vibration (ν_1) can be observed at 1022 cm^{-1}. The peaks are significantly broadened as a result of the asymmetric bonding situation in the [PO$_4$] units in the crystal structure (cf. interatomic distances, Table S2). In comparison to the spectrum of olivine-type *Pnma*-LiCoPO$_4$ [8], the bands are shifted to lower wavenumbers. This is due to the less covalent character of the P–O bonds, *i.e.* longer P–O distances in the crystal structure (cf. Table S2 and ref [8].). The four bands observed in the region of at 526–648 cm^{-1} are related to antisymmetric O–P–O bending vibrations (ν_4). The absorption at 436 cm^{-1} might be explained by the symmetric bending vibration of O–P–O (ν_2) or a contribution of Li-ion cage modes [25]. A precise assignment of the

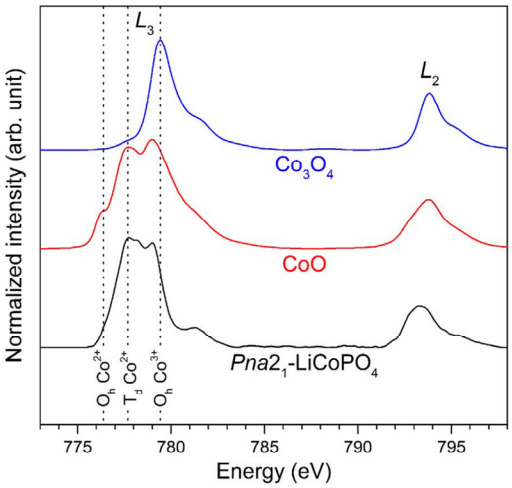

Fig. 5. Normalized soft-XAS Co $L_{2,3}$-edge spectra of *Pna*2$_1$-LiCoPO$_4$ (bottom) in the TEY detection mode in comparison with CoO (middle) and Co_3O_4 (top) as references. The energies corresponding to O_h Co^{2+}(776.4 eV), T_d Co^{2+}(777.7 eV) and O_h Co^{3+}(779.4 eV) are indicated by dotted lines. It is evident that the sample contains only tetrahedrally coordinated (T_d) Co^{2+}. (For interpretation of the references to color in this figure legend, the reader is referred to the web version of this article.)

absorption bands in the fingerprint region, however, would require the use of density functional theory calculations which is not in the focus of this work.

3.6. X-ray absorption spectroscopy

The normalized soft XAS Co $L_{2,3}$-edge spectrum of the material in the TEY mode is shown along with CoO and Co_3O_4 powders as reference materials in Fig. 5. Whereas the $L_{2,3}$-edge spectrum of olivine *Pnma*-LiCoPO$_4$ has been reported in our previous work [8], this is the first time the spectrum of the exclusively tetrahedrally coordinated *Pna*2$_1$-LiCoPO$_4$ polymorph is presented. In general, the absorption peaks of the $L_{2,3}$-edge XAS spectra are highly sensitive to the oxidation state, spin state, and the chemical environment of the transition metal in the crystal. Comparing the main peak at 777.7 eV with the energies of Co^{2+}(777.7 eV) and Co^{3+}(779.4 eV) $L_{2,3}$-edge spectra reported by Hibberd et al. [21] as well as the CoO (which contains O_h Co^{2+}) and Co_3O_4 reference spectra (T_d Co^{2+} and O_h Co^{3+}) shows that the material contains only Co^{2+}. The absence of a low-energy peak at 776.4 eV, which is characteristic for octahedral (O_h) Co^{2+}(cf. spectrum of CoO), provides evidence for a tetrahedral (T_d) coordination of Co^{2+} in the structure, as expected. The fact that the multiplet structure (caused by electron–electron interactions) is less well-defined than for olivine-type *Pnma*-LiCoPO$_4$, as shown in our previous work [8], is consistent with the fact that the structure is slightly disordered and shows a higher degree of covalence in the [CoO$_4$] tetrahedra. This is also indicated by the significantly shorter Co–O distances (cf. Table S2 and ref [8].). Because no shoulder or characteristic peak at 779.5 eV for T_d Co^{3+} [21] is present, it can be inferred that the sample does not contain significant amounts of Co^{3+}. Hence, the ascorbic acid reductant [26] used in the reaction mixture and the weak reducing effect of the ethylene glycol solvent [27] seem to be effectively preventing oxidation of Co^{2+} to Co^{3+} in solution.

3.7. Electrochemical characterization

The electrochemical performance of the 15–20 nm *Pna*2$_1$-LiCoPO$_4$ spheres was tested in coin cells. The rate capability and coulombic efficiency were investigated at 0.1 C, 0.2 C, 0.5 C, 1 C, and 2 C for three

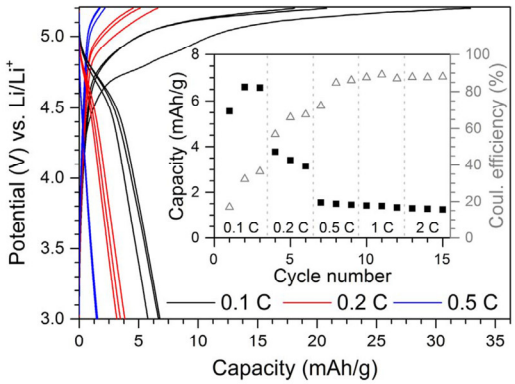

Fig. 6. Charge–discharge curves of nano-sized *Pna*2$_1$-LiCoPO$_4$ for the first three cycles at 0.1 C, 0.2 C, and 0.5 C each (the curves for 1 C and 2 C are not shown as the capacities were extremely low). Inset: Specific discharge capacities (■) and coulombic efficiencies (△) *vs.* cycle number for the first 15 cycles at various C rates (average from two cells; error bars are omitted for clarity). Conditions: 3.0–5.2 V, 1 M $LiPF_6$ in EC:DEC (1:1, v-v) at 25 °C.

cycles each (Fig. 6, inset), followed by 20 cycles at 0.1 C (Fig. S4). The galvanostatic curves of the first three cycles at 0.1 C, 0.2 C, and 0.5 C are displayed in Fig. 6. A distinct plateau region at ~4.9 V is only observed in the first charging half cycle. The higher potential compared to olivine LiCoPO$_4$ (~4.8 V *vs.* Li/Li$^+$ [7]) reflects the different coordination of Co in the crystal structures ([CoO$_4$] *vs.* [CoO$_6$] units). In the first three cycles at 0.1 C, a discharge capacity of only ~6 mAh/g is reached, corresponding to 4% of the theoretical capacity. Further capacity decrease is observed upon additional cycling. The high coulombic inefficiencies indicate that irreversible reactions occur. In addition, the nano-morphology of the material, which should favor rapid Li-diffusion, does not improve the performance in this case. It is possible that anti-site defects are effectively blocking possible Li pathways even at small crystal sizes.

There are a number of possible reasons for the extremely poor performance of the material, including the low electronic and ionic conductivities, mixed ion-occupation of sites, and the very high potential at which it is electroactive. The observed excess of cobalt in the material results in anti-site defects with Co blocking Li diffusion, which reduces the conductivity. This could also be the reason for the generally poor performance observed in other electrochemical studies about *Pna*2$_1$-LiCoPO$_4$ [10,13] and is in line with reports [28] on LiFePO$_4$ showing that cation-mixing significantly affects the performance. Furthermore, decomposition of the electrolyte at the extremely high operating potential seems to play a role [29], which is exacerbated by the high surface area of the material (~61 m^2/g), as parasitic currents from electrolyte oxidation at high potential are approximately proportional to the BET surface area [8]. Another possibility might be structural changes and/or amorphization upon cycling, which will have to be assessed in further experiments. As the performance could not be improved by particle size reduction, future studies should focus on a fundamental understanding of the cycling mechanism, and on finding electrolytes which are suitable for the potential window (*e.g.* using ionic liquids or additives [30,31]) in order to utilize the material which shows a high theoretical energy density of ~818 Wh/kg. Particular attention should be on optimizing the material in order to ensure cobalt-free channels. As shown for LiFePO$_4$ [28], this might be achieved by increasing the synthesis temperature.

3.8. Thermal stability

The thermal stability of the *Pna*2$_1$-LiCoPO$_4$ nanoparticles was assessed by simultaneous TGA/DSC and complementary temperature-dependent *in situ* PXRD measurements performed under air/

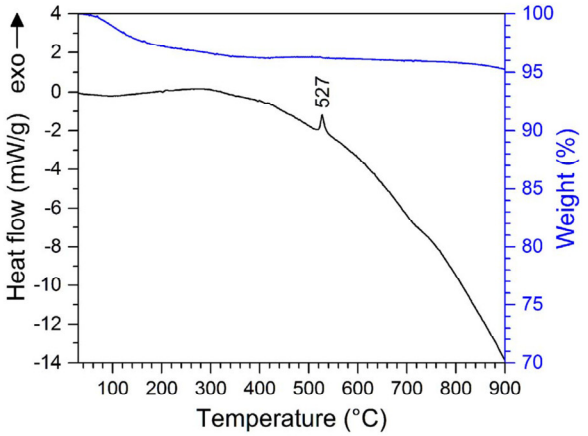

Fig. 7. DSC (black) and TGA (blue) curves of nano-sized *Pna*2$_1$-$LiCoPO_4$ in a temperature range of 30–900 °C (heating rate: 10 °C/min, atmosphere: synthetic air). An exothermic signal, which corresponds to the transformation to *Pnma*-$LiCoPO_4$, is observed at 527 °C. (For interpretation of the references to color in this figure legend, the reader is referred to the web version of this article.)

synthetic air (Figs. 7 and 8). In the TGA curve (Fig. 7), an overall mass loss of ~4.8 wt% is observed, which is probably due to the decomposition of organic residues of the EG solvent and ascorbic acid additive (cf. CHNS analysis, Table 2). The DSC curve shows a pronounced exothermic peak at 527 °C, which is not accompanied by a weight loss. The powder X-ray diffraction data (Fig. S5, Tables S6–S8) of the dark violet sample (see graphical abstract) obtained after the TGA/DSC measurement reveal that phase pure olivine-type *Pnma*-$LiCoPO_4$ was obtained, indicating that the signal corresponds to the phase transformation of the *Pna*2$_1$ to the *Pnma* polymorph.

In order to obtain further insights in the processes involved upon heating, the thermal stability was examined by temperature-dependent *in situ* powder X-ray diffractometry between 30 °C and 900 °C (Fig. 8; zoomed image in the range of 16–29° 2θ see Fig. S6). No phase transitions are observed from 30 °C to 400 °C, indicating that the material is thermally stable up to that temperature. The powder patterns show a very small shift of the reflections to smaller 2θ values due to thermal expansion, which is evident from the characteristic (210)/(011) reflections. Furthermore, the intensity of the (210)/(011) reflections increases and the peak width (FWHM) decreases, caused by ongoing crystallization and sintering (Fig. S6, Table S9). Between 400 °C and 500 °C, the *Pna*2$_1$-$LiCoPO_4$ starts to transform to the olivine *Pnma* polymorph. The signal observed in the DSC at 527 °C (Fig. 7) can hence be assigned to this phase transition. The lower transition temperature observed in the *in situ* X-ray experiment compared with DSC might be because of non-identical atmospheres (air *vs.* synthetic air stream), and different heating rates (10 °C/min *vs.* 5 °C/min) used for the measurements. The phase transformation is not fully complete until 600 °C because traces of the *Pna*2$_1$ phase are still present in the powder pattern at 500 °C as indicated by the small (210)/(011) main reflections at ~22.1° 2θ (Fig. S6f). As the wider temperature range of the phase transition in the *in situ* experiment is probably related to kinetic effects, the data can still be considered consistent with the TGA/DSC analysis. In the PXRD patterns at 600 °C and 700 °C, only reflections which can be assigned to *Pnma*-$LiCoPO_4$ are detected. At 800 °C, the characteristic (210)/(011) reflections of the metastable *Pna*2$_1$ phase become visible again (Fig. S6i). There are two possible explanations for the occurrence of the *Pna*2$_1$ phase above 800 °C, none of which can be ruled out. One possibility is that *Pna*2$_1$ slowly reemerges as a high-temperature modification of $LiCoPO_4$, which would be in line with our studies on the thermal stability of the *Cmcm* [12] (complete transformation to the *Pna*2$_1$ phase at 675 °C)

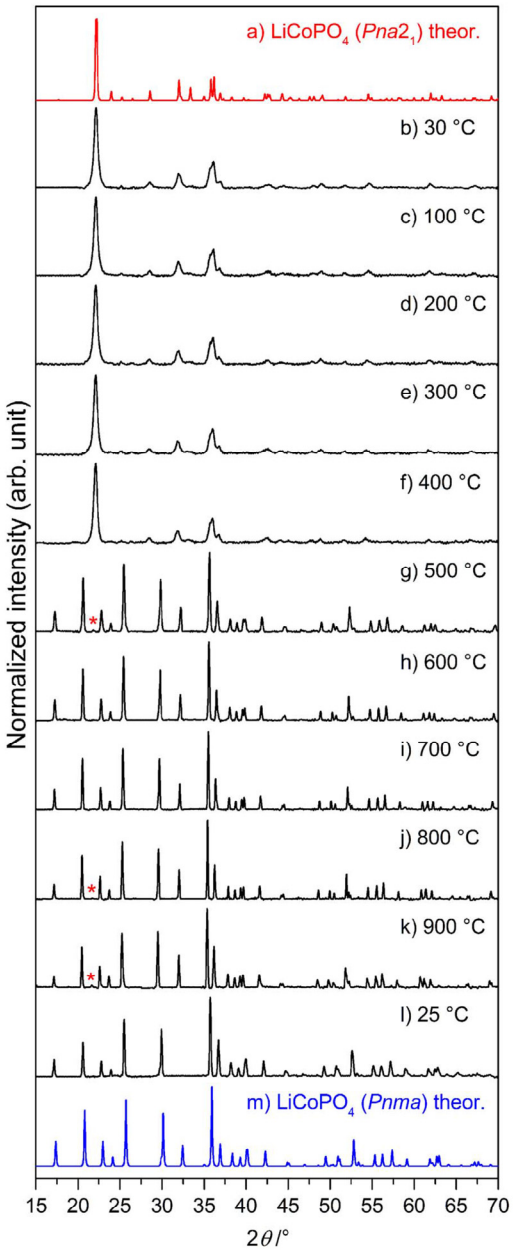

Fig. 8. *In situ* powder X-ray diffraction patterns (Bragg-Brentano geometry, Cu K_α radiation) of nano-sized *Pna*2$_1$-$LiCoPO_4$ measured in a range of 30–900 °C (b–k) in air, and after cooling down to 25 °C (l). Between 400 °C and 500 °C, the material starts to transform to olivine *Pnma*-$LiCoPO_4$. At 800 °C, reflections of the *Pna*2$_1$ phase reemerge. After cooling, pure *Pnma*-$LiCoPO_4$ is obtained. The theoretical patterns of *Pna*2$_1$- (a) and *Pnma*-$LiCoPO_4$ (m) are displayed in red and blue. The red asterisks (*) in (g, j, k) indicate the characteristic (210)/(011) main reflections of the *Pna*2$_1$ phase. (For interpretation of the references to color in this figure legend, the reader is referred to the web version of this article.)

and the *Pnma* [8] (partial transformation to *Pna*2$_1$ at 900 °C) $LiCoPO_4$ polymorphs. If this is the case, the phase transformation from the *Pnma* to the *Pna*2$_1$ phase is hindered or very slow up to 900 °C for this non-stoichiometric $LiCoPO_4$ material. Another option is that amorphous fractions directly crystallize to the *Pna*2$_1$ material at elevated

temperatures, whereas the majority of the *Pnma* phase is still stable. Further experiments at temperatures higher than 900 °C will be required to elucidate whether a quantitative transformation to *Pna*2$_1$-LiCoPO$_4$ or the crystallization of amorphous portions of the sample are the cause for this observation. Upon cooling from 900 °C to ambient temperature, the reflections of the *Pna*2$_1$ phase disappear, and pure *Pnma*-LiCoPO$_4$ is obtained. The observation that the phase pure olivine *Pnma* modification is obtained upon heating and cooling thereafter is consistent with our *ex situ* PXRD study (Fig. S5). The *in situ* PXRD studies combined with thermoanalytic data indicate that the *Pna*2$_1$ polymorph is metastable up to 527 °C where it transforms to the stable *Pnma*-LiCoPO$_4$. At approximately 800 °C, the *Pnma* phase becomes metastable and a slow transformation to the high-temperature *Pna*2$_1$ modification occurs. At room temperature, the *Pnma* phase represents the thermodynamically stable polymorph.

The findings of our combined X-ray and thermal analysis study differ from previous reports [10,13] as the phase transition temperature of 527 °C of the *Pna*2$_1$- to the *Pnma*-LiCoPO$_4$ modification found in this work is significantly higher. Jaehne et al. [13] reported an exothermic peak at 221 °C (Ar atmosphere, 1 °C/min) while Kreder et al. [10] on the other hand stated that the transition is endothermic and appears at 340 °C (Ar atmosphere, 10 °C/min). The difference is probably related to the heating rates as the transformation was also observed at lower temperature when a lower rate was applied. Furthermore, the different atmospheres might play a role. We therefore performed a similar study under an Ar stream. The data (DSC/TGA: Figs. S7 and S8, Tables S10–S12, *in situ* PXRD: Figs. S9 and S10, Table S13) indicate that the atmosphere slightly affects the thermal stability as the exothermic phase transition is shifted to higher temperature (580 °C). Another important aspect to explain these differences might be the particle size, with the temperature of the *Pna*2$_1$–*Pnma* phase transition supposedly increasing with decreasing particle size (cf. Jaehne [13]: ~5 µm, Kreder [10]: ~200 nm×1 µm, this work: ~15 nm). To verify this assumption, we performed a similar study on the micron-sized (~1 µm) material discussed in Section 3.4 (Figs. S11–S14, Tables S14–S17). Interestingly, the phase transition of *Pna*2$_1$- to *Pnma*-LiCoPO$_4$ occurs at significantly lower temperatures (between 200 °C and 300 °C) as demonstrated by the *in situ* PXRD study (Figs. S13 and S14). Our findings therefore indicate that the thermal stability and the phase transition kinetics are strongly related to the size of the particles. A possible reason for this is the occurrence of crystal strains, which are more likely to appear in bigger particles. This assumption has to be verified in an additional study and is beyond the scope of this article. However, also an influence of the off-stoichiometry and the resulting structural disorder cannot be ruled out.

As the *Pna*2$_1$–*Pnma* phase transformation can be used to produce electrochemically active olivine-type LiCoPO$_4$ by post-annealing [32], the present work provides a new synthesis pathway towards nano-scaled olivine *Pnma*-LiCoPO$_4$. Depending on the particle size, the temperatures can be tremendously lowered compared to the direct solid-state synthesis of the olivine, which requires temperatures above 800 °C [33]. Moreover, as particle size reduction is considered a major strategy to improve the electrochemical performance (rate capability, cycle life) of the olivine [6] but nanoparticles with diameters < 50 nm have only been accessible using high energy-consuming ball-milling steps [34], this approach could pave the way for an easy and scalable production of the high-voltage cathode material *Pnma*-LiCoPO$_4$ with significant energy savings. In that context, the present work provides fundamental insights which are required for that process.

4. Conclusions

A novel synthesis pathway towards nano-sized particles of the metastable, tetrahedrally coordinated *Pna*2$_1$-polymorph of LiCoPO$_4$ *via* a simple and rapid one-step microwave-assisted solvothermal route using ethylene glycol as a solvent was presented. The synthesis yielded nano-sized particles with diameters of only 15–20 nm. The reduced particle dimensions could be related to the high viscosity of the solvent or the capping of solvent molecules to intermediate phases or the final product, which inhibits crystal growth and also favors the formation of the metastable phase. In contrast to previous reports, powder X-ray diffraction experiments and elemental analysis indicated that the title compound with the empirical sum formula $Li_{0.95(1)}Co_{1.03(1)}PO_4$ is non-stoichiometric and exhibits an excess of cobalt. A redetermination of the crystal structure revealed that the material shows structural disorder with 4.8(8)% Co mixing on the Li sites. Co $L_{2,3}$-edge X-ray absorption spectroscopic data were reported for the first time, and confirmed the local tetrahedral symmetry of the Co^{2+} ions in the structure. Despite the reduced particle dimensions which should favor Li migration, the material delivered only low discharge capacities. The poor electrochemical performance could be related to the high surface area of the material, which promotes parasitic side reactions, as well as the fact that Li migration is probably hindered due to anti-site defects. Comprehensive studies on the thermal stability using combined thermogravimetric analysis, differential scanning calorimetry, and temperature-dependent *in situ* powder X-ray diffraction revealed that the material converts to the olivine-type *Pnma*-LiCoPO$_4$ modification at 527 °C, which is significantly higher than reported previously. Furthermore, the *Pna*2$_1$ phase was found to reemerge as a stable high-temperature polymorph at temperatures above 800 °C. After cooling to ambient temperature, a single-phase material of the thermodynamically stable *Pnma* modification was obtained. It was further shown that the temperature of the transformation is significantly affected by the atmosphere upon heating as well as the particle size of the material, with the temperature decreasing with increasing crystal dimensions.

The present work therefore provides new fundamental insights into the structure–property relations of the metastable *Pna*2$_1$-LiCoPO$_4$ polymorph. Before successful utilization as a high-voltage cathode material itself or as a precursor for olivine-type cathodes, further experiments should be directed towards tackling the off-stoichiometry and structural disorder by optimizing the synthesis parameters (*e.g.* reaction temperature and time, molar ratio of starting materials).

Author contributions

J. L. and T. N. conceived and designed this work, and J. L. performed material synthesis and characterization (under supervision of T. N. and M.M. D.). D. N. performed XAS measurements. J. L. and T. N. wrote the manuscript. All authors participated in the discussion of the results and have given approval to the final version of the manuscript.

Funding sources

This work was supported by the Fonds der Chemischen Industrie and the TUM Graduate School. The soft XAS experiments were carried out at Stanford Synchrotron Radiation Lightsource (SSRL), a Directorate of SLAC National Accelerator Laboratory, which is supported by the US Department of Energy, Office of Science, and Office of Basic Energy Sciences under contract no. DE-AC02-76SF00515.

Acknowledgements

The authors would like to thank U. Ammari for elemental analysis and K. Rodewald for SEM images. The help of D. Haering with BET, and P. Madkikar and M. Baumgartner with TGA/DSC measurements is gratefully acknowledged. J. Ludwig is grateful to the Fonds der Chemischen Industrie for her PhD fellowship.

Appendix A. Supporting information

Supplementary data associated with this article: 1. Rietveld refinement details of nano-sized *Pna*2_1-$LiCoPO_4$; 2. Structure and morphology of micron-sized *Pna*2_1-$LiCoPO_4$ (SEM/EDS, Rietveld refinement); 3. Full infrared spectrum of nano-sized *Pna*2_1-$LiCoPO_4$; 4. Electrochemical stability (cycle life) of nano-sized *Pna*2_1-$LiCoPO_4$ at 0.1 C; 5. Investigation of the thermal stability of nano-sized *Pna*2_1-$LiCoPO_4$ under air/synthetic air (Rietveld refinement, zoomed *in situ* PXRD); 6. Investigation of the thermal stability of nano-sized *Pna*2_1-$LiCoPO_4$ under argon (TGA/DSC, Rietveld refinement, *in situ* PXRD); 7. Investigation of the thermal stability of micron-sized *Pna*2_1-$LiCoPO_4$ under air/synthetic air (TGA/DSC, Rietveld refinement, *in situ* PXRD). The data can be found in the online version at doi:10.1016/j.jssc.2017.01.015. Further details of the crystal structure investigations may be obtained from FIZ Karlsruhe, 76344 Eggenstein-Leopoldshafen, Germany (fax: +49 7247 808 666; e-mail: crysdata@fiz-karlsruhe.de), on quoting the deposition numbers CSD 432281–432285.

References

[1] M. Thackeray, Lithium-ion batteries: an unexpected conductor, Nat. Mater. 1 (2) (2002) 81–82.

[2] A. Yamada, M. Hosoya, S.-C. Chung, Y. Kudo, K. Hinokuma, K.-Y. Liu, Y. Nishi, Olivine-type cathodes: achievements and problems, J. Power Sources 119–121 (0) (2003) 232–238.

[3] A.K. Padhi, K.S. Nanjundaswamy, J.B. Goodenough, Phospho-olivines as positive-electrode materials for rechargeable lithium batteries, J. Electrochem. Soc. 144 (4) (1997) 1188–1194.

[4] S. Okada, S. Sawa, M. Egashira, J. Yamaki, M. Tabuchi, H. Kageyama, T. Konishi, A. Yoshino, Cathode properties of phospho-olivine Li*M*PO_4 for lithium secondary batteries, J. Power Sources 97–98 (2001) 430–432.

[5] B. Kang, G. Ceder, Battery materials for ultrafast charging and discharging, Nature 458 (7235) (2009) 190–193.

[6] K. Zaghib, A. Guerfi, P. Hovington, A. Vijh, M. Trudeau, A. Mauger, J.B. Goodenough, C.M. Julien, Review and analysis of nanostructured olivine-based lithium recheargeable batteries: status and trends, J. Power Sources 232 (2013) 357–369.

[7] K. Amine, H. Yasuda, M. Yamachi, Olivine $LiCoPO_4$ as 4.8 V electrode material for lithium batteries, Electrochem. Solid-State Lett. 3 (4) (2000) 178–179.

[8] J. Ludwig, C. Marino, D. Haering, C. Stinner, D. Nordlund, M.M. Doeff, H.A. Gasteiger, T. Nilges, Facile, ethylene glycol-promoted microwave-assisted solvothermal synthesis of high-performance $LiCoPO_4$ as a high-voltage cathode material for lithium-ion batteries, RSC Adv. 6 (2016) 82984–82994.

[9] X. Huang, J. Ma, P. Wu, Y. Hu, J. Dai, Z. Zhu, H. Chen, H. Wang, Hydrothermal synthesis of $LiCoPO_4$ cathode materials for rechargeable lithium-ion batteries, Mater. Lett. 59 (5) (2005) 578–582.

[10] K.J. Kreder, G. Assat, A. Manthiram, Microwave-assisted solvothermal synthesis of three polymorphs of $LiCoPO_4$ and their electrochemical properties, Chem. Mater. 27 (16) (2015) 5543–5549.

[11] U. Amador, J.M. Gallardo-Amores, G. Heymann, H. Huppertz, E. Moran, M.E. Arroyo-de Dompablo, High pressure polymorphs of $LiCoPO_4$ and $LiCoAsO_4$, Solid State Sci. 11 (2) (2009) 343–348.

[12] C.E. Alarcón-Suesca, J. Ludwig, V. Hlukhyy, C. Stinner, T. Nilges, In situ studies and magnetic properties of the *Cmcm* polymorph of $LiCoPO_4$ with a hierarchical dumbbell-like morphology synthesized by easy single-step polyol synthesis, Inorganics 4 (2016) 35.

[13] C. Jaehne, C. Neef, C. Koo, H.-P. Meyer, R. Klingeler, A new $LiCoPO_4$ polymorph via low temperature synthesis, J. Mater. Chem. A 1 (8) (2013) 2856–2862.

[14] V. Petricek, M. Dusek, L. Palatinus, Crystallographic computing system JANA2006: general features, Z. Krist. - Cryst. Mater. 229 (5) (2014) 345–352.

[15] T.R. Jensen, P. Norby, P.C. Stein, A.M.T. Bell, Preparation, structure determination and thermal transformation of a new lithium zinc phosphate, δ_I-$LiZnPO_4$, J. Solid State Chem. 117 (1) (1995) 39–47.

[16] L.W. Finger, D.E. Cox, A.P. Jephcoat, A correction for powder diffraction peak asymmetry due to axial divergence, J. Appl. Crystallogr. 27 (6) (1994) 892–900.

[17] D.T. Cromer, D.A. Liberman, Anomalous dispersion calculations near to and on the long-wavelength side of an absorption edge, Acta Crystallogr., Sect. A A37 (2) (1981) 267–268.

[18] J.F. Berar, P. Lelann, E.S.D.'s and estimated probable error obtained in Rietveld refinements with local correlations, J. Appl. Crystallogr. 24 (1) (1991) 1–5.

[19] J. Ludwig, D. Haering, M.M. Doeff, T. Nilges, Particle size-controllable microwave-assisted solvothermal synthesis of the high-voltage cathode material $LiCoPO_4$ using water/ethylene glycol solvent blends, unpublished results, 2016.

[20] F. Lin, D. Nordlund, I.M. Markus, T.-C. Weng, H.L. Xin, M.M. Doeff, Profiling the nanoscale gradient in stoichiometric layered cathode particles for lithium-ion batteries, Energ. Environ. Sci. 7 (9) (2014) 3077–3085.

[21] A.M. Hibberd, H.Q. Doan, E.N. Glass, F.M.F. de Groot, C.L. Hill, T. Cuk, Co polyoxometalates and a Co_3O_4 thin film investigated by L-Edge X-ray absorption spectroscopy, J. Phys. Chem. C. 119 (8) (2015) 4173–4179.

[22] F. Teng, S. Santhanagopalan, A. Asthana, X.-B. Geng, S.-I. Mho, R. Shahbazian-Yassar, D.D.-S. Meng, Self-assembly of $LiFePO_4$ nanodendrites in a novel system of ethylene glycol-water, J. Cryst. Growth 312 (2010) 3493–3502.

[23] C. Feldmann, Polyol-mediated synthesis of nanoscale functional materials, Solid State Sci. 7 (7) (2005) 868–873.

[24] G. Herzberg, Infrared and Raman Spectra of Polyatomic Molecules, Van Nostrand, New York, 1975.

[25] C.M. Burba, R. Frech, Raman and FTIR spectroscopic study of Li_xFePO_4 ($0 \le x \le 1$), J. Electrochem. Soc. 151 (7) (2004) A1032–A1038.

[26] J. Chen, M.J. Vacchio, S. Wang, N. Chernova, P.Y. Zavalij, M.S. Whittingham, The hydrothermal synthesis and characterization of olivines and related compounds for electrochemical applications, Solid State Ion. 178 (31–32) (2008) 1676–1693.

[27] S. Kuppan, P. Balaya, M.V. Reddy, B.V.R. Chowdari, J.J. Vittal, Morphology controlled synthesis of $LiFePO_4$/C nanoplates for Li-ion batteries, Energy Environ. Sci. 3 (4) (2010) 457–464.

[28] J. Chen, S. Wang, M.S. Whittingham, Hydrothermal synthesis of cathode materials, J. Power Sources 174 (2) (2007) 442–448.

[29] N.N. Bramnik, K.G. Bramnik, T. Buhrmester, C. Baehtz, H. Ehrenberg, H. Fuess, Electrochemical and structural study of $LiCoPO_4$-based electrodes, J. Solid State Electrochem. 8 (8) (2004) 558–564.

[30] R. Sharabi, E. Markevich, K. Fridman, G. Gershinsky, G. Salitra, D. Aurbach, G. Semrau, M.A. Schmidt, N. Schall, C. Bruenig, Electrolyte solution for the improved cycling performance of $LiCoPO_4$/C composite cathodes, Electrochem. Commun. 28 (2013) 20–23.

[31] A. Freiberg, M. Metzger, D. Haering, S. Bretzke, S. Puravankara, T. Nilges, C. Stinner, C. Marino, H.A. Gasteiger, Anodic decomposition of trimethylboroxine as additive for high voltage Li-ion batteries, J. Electrochem. Soc. 161 (14) (2014) A2255–A2261.

[32] C. Neef, H.-P. Meyer, R. Klingeler, Morphology-controlled two-step synthesis and electrochemical studies on hierarchically structured $LiCoPO_4$, Solid State Sci. 48 (2015) 270–277.

[33] I.C. Jang, H.H. Lim, S.B. Lee, K. Karthikeyan, V. Aravindan, K.S. Kang, W.S. Yoon, W.I. Cho, Y.S. Lee, Preparation of $LiCoPO_4$ and $LiFePO_4$ coated $LiCoPO_4$ with improved battery performance, J. Alloy. Compd. 497 (1–2) (2010) 321–324.

[34] M.E. Rabanal, M.C. Gutierrez, F. Garcia-Alvarado, E.C. Gonzalo, M.E. Arroyo-deDompablo, Improved electrode characteristics of olivine-LiCoPO4 processed by high energy milling, J. Power Sources 160 (1) (2006) 523–528.

Supplementary material

Synthesis and characterization of metastable, 20 nm-sized *Pna*2$_1$-LiCoPO$_4$ nanospheres

Jennifer Ludwig [a], Dennis Nordlund [b], Marca M. Doeff [c], and Tom Nilges [a]*

[a] Technical University of Munich, Department of Chemistry, Synthesis and Characterization of Innovative Materials, Lichtenbergstr. 4, 85747 Garching, Germany

[b] Stanford Synchrotron Radiation Lightsource, SLAC National Accelerator Laboratory, 2575 Sand Hill Rd, Menlo Park, CA, 94025, USA

[c] Lawrence Berkeley National Laboratory, Environmental Energy Technologies Division, 1 Cyclotron Rd, Berkeley, CA, 94720, USA

* Corresponding author. E-mail: tom.nilges@lrz.tum.de, Tel.: +49 89 289 13110, Fax: +49 89 289 13762

1. Rietveld refinement details of nano-sized *Pna*2$_1$-LiCoPO$_4$

Table S1 Fractional atomic coordinates and isotropic thermal displacement parameters of nano-sized *Pna*2$_1$-LiCoPO$_4$ (Z = 4) as refined from powder X-ray diffraction data (T = 298 K) [a]

Atom	Wyckoff position	Occupancy	*x*/a	*y*/b	*z*/c	U_{iso} (Å^2)
Li1/Co1	4*a*	0.952(8)/0.048(8)	0.15412 [b]	0.18989 [b]	0.51848 [b]	0.0139 [b]
Co2	4*a*	0.979(12)	0.1544(12)	0.199(3)	0	0.019(6)
P1	4*a*	1	0.403(4)	0.233(9)	0.2404(17)	0.012(3)
O1	4*a*	1	0.080(6)	0.269(9)	0.259(9)	0.009(2)
O2	4*a*	1	0.084(4)	0.323(5)	0.791(5)	0.007(2)
O3	4*a*	1	0.365(3)	0.285(9)	0.528(9)	0.008(2)
O4	4*a*	1	0.311(2)	0.273(6)	0.051(6)	0.006(2)

[a] The estimated standard deviations (in parentheses) were calculated using the Berar's correction. [b] The atomic coordinates and thermal displacement parameter of Li have been fixed as they cannot be deduced by means of X-ray diffraction due to its low atomic scattering factor.

Table S2 Selected interatomic distances of nano-sized *Pna*2$_1$-LiCoPO$_4$ (Z = 4) as refined from powder X-ray diffraction data (T = 298 K) [a]

Atom pair			*d* (Å)
Li1/Co1	O1	×1	1.94(6)
	O2	×1	2.07(3)
	O3	×1	2.17(3)
	O4	×1	2.11(3)
Co2	O1	×1	1.92(6)
	O2	×1	1.69(3)
	O3	×1	2.07(5)
	O4	×1	1.65(3)
P1	O1	×1	1.77(7)
	O2	×1	2.07(5)
	O3	×1	1.99(7)
	O4	×1	1.59(4)

[a] The estimated standard deviations (in parentheses) were calculated using the Berar's correction.

2. Structure and morphology of micron-sized *Pna*2$_1$-LiCoPO$_4$

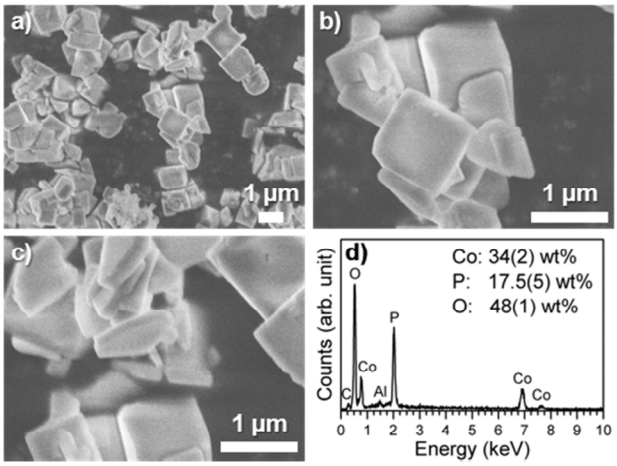

Figure S1 (a,b,c) SEM images and (d) corresponding EDS spectrum of micron-sized *Pna*2$_1$-LiCoPO$_4$ powder prepared by microwave-assisted solvothermal synthesis (T = 200 °C, t = 30 min) using water as a solvent. The sample exhibits irregular morphologies that vary from square platelets with dimensions of ~1 µm × 1 µm × 150 nm to cubic shapes with dimensions of ~1 µm × 1 µm × 1 µm. EDS analysis delivers a composition of 34(2) wt% Co, 17.5(5) wt% P, and 48(1) wt% O, corresponding to a Co:P molar ratio of 1.02(6):1.00(3), which is consistent with the empirical sum formula derived from Rietveld refinement (*cf.* Tables S3 and S4). The small C and Al signals observed in the EDS spectrum arise from the carbon tape and the aluminum holder used for the measurement.

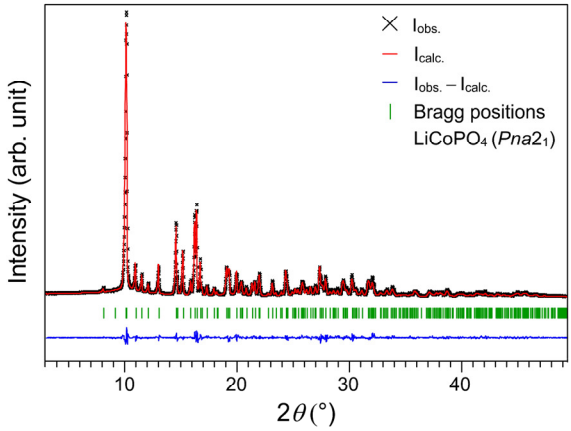

Figure S2 Rietveld fit of the powder X-ray diffraction data (transmission geometry, Mo $K_{\alpha 1}$ radiation) of micron-sized *Pna*2$_1$-LiCoPO$_4$ prepared by microwave-assisted solvothermal synthesis (T = 200 °C, t = 30 min) using water as a solvent. The observed pattern is drawn in black, the calculated pattern in red, the difference plot in blue, and the Bragg reflections of non-olivine *Pna*2$_1$-LiCoPO$_4$ in green, respectively. As all observed reflections can be indexed, it can be assumed that the sample is phase pure. Rietveld refinement details, atomic coordinates and thermal displacement parameters as well as selected interatomic distances can be found in Tables S3, S4, and S5.

Table S3 Cell parameters and Rietveld refinement details of micron-sized $Pna2_1$-$LiCoPO_4$ ($Z = 4$) as refined from powder X-ray diffraction data ($T = 298$ K) [a]

Empirical formula	**$Li_{1.01(1)}Co_{0.99(1)}PO_4$**
M_r (g/mol)	160.2
Crystal system	orthorhombic
Space group (no.)	$Pna2_1$
Z	4
a (Å)	10.0256(6)
b (Å)	4.9631(3)
c (Å)	6.7157(4)
V (Å^3)	334.16(3)
$F(000)$	307
ρ (calcd.) (g/cm^3)	3.184(1)
R_p	0.0524
R_{wp}	0.0692
R_{exp}	0.0428
R_F	0.0261
R_B	0.0475
χ^2	1.62
Data/restraints/parameter	3101/0/73

[a] The estimated standard deviations (in parentheses) were calculated using the Berar's correction.

Table S4 Fractional atomic coordinates and isotropic thermal displacement parameters of micron-sized $Pna2_1$-$LiCoPO_4$ ($Z = 4$) as refined from powder X-ray diffraction data ($T = 298$ K) [a]

Atom	**Wyckoff position**	**Occupancy**	***x*/a**	***y*/b**	***z*/c**	**U_{iso} (Å^2)**
Li1/Co1	4*a*	0.957(5)/0.043(5)	0.15412 [b]	0.18989 [b]	0.518475 [b]	0.0139 [b]
Li2/Co2	4*a*	0.056(11)/0.944(11)	0.1541(6)	0.1864(11)	0	0.0106(17)
P1	4*a*	1	0.4078(11)	0.189(2)	0.2457(13)	0.009(3)
O1	4*a*	1	0.0627(19)	0.255(4)	0.241(4)	0.006(2)
O2	4*a*	1	0.1141(19)	0.377(4)	0.780(3)	0.005(2)
O3	4*a*	1	0.343(2)	0.292(4)	0.510(5)	0.007(2)
O4	4*a*	1	0.331(2)	0.299(4)	0.081(3)	0.006(2)

[a] The estimated standard deviations (in parentheses) were calculated using the Berar's correction. [b] The atomic coordinates and thermal displacement parameter of Li have been fixed as they cannot be deduced by means of X-ray diffraction due to its low atomic scattering factor.

Table S5 Selected interatomic distances of micron-sized *Pna*2$_1$-$LiCoPO_4$ (*Pnma*, $Z = 4$) as refined from powder X-ray diffraction data ($T = 298$ K) [a]

Atom pair			***d* (Å)**
Li1/Co1	O1	×1	2.10(2)
	O2	×1	2.026(19)
	O3	×1	1.97(2)
	O4	×1	1.990(18)
Li2/Co2	O1	×1	1.89(2)
	O2	×1	1.801(19)
	O3	×1	1.96(2)
	O4	×1	1.94(2)
P1	O1	×1	1.58(2)
	O2	×1	1.58(2)
	O3	×1	1.95(3)
	O4	×1	1.45(2)

[a] The estimated standard deviations (in parentheses) were calculated using the Berar's correction.

3. Full infrared spectrum of nano-sized *Pna*2$_1$-LiCoPO$_4$

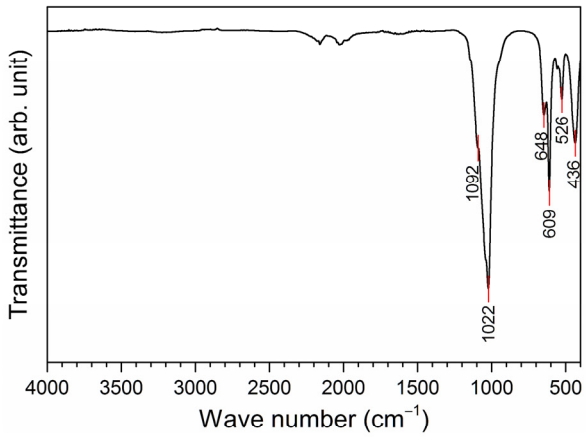

Figure S3 FTIR spectrum of nano-sized *Pna*2$_1$-LiCoPO$_4$. The sample does not contain any detectable amounts of water or carbon. The modes around 2000–2200 cm^{-1} are due to the diamond ATR setup.

4. Electrochemical stability (cycle life) of nano-sized *Pna*2$_1$-LiCoPO$_4$ at 0.1 C

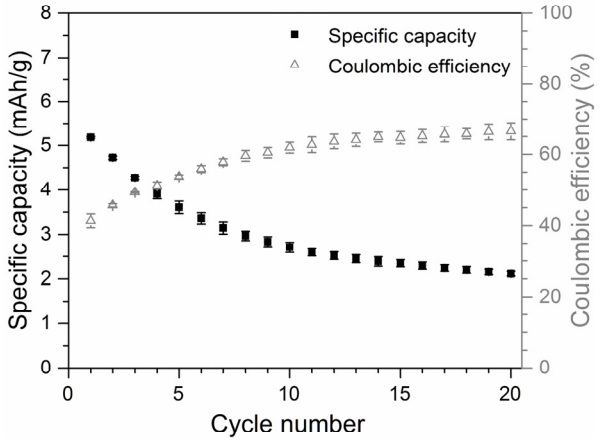

Figure S4 Specific discharge capacities (■) and respective coulombic efficiencies (Δ) *vs.* cycle number of nano-sized *Pna*2$_1$-LiCoPO$_4$ for 20 cycles at 0.1 C after the first 15 cycles of C rate testing (*cf.* Fig. 6). The error bars represent the standard deviation from two cells. Conditions: 3.0–5.2 V, 1 M $LiPF_6$ in EC:DEC (1:1, v:v) at 25 °C.

5. Investigation of the thermal stability of nano-sized *Pna*2$_1$-LiCoPO$_4$ under air/synthetic air

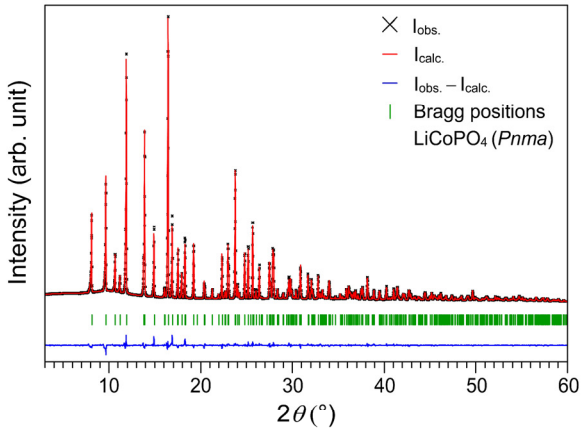

Figure S5 Rietveld fit of the powder X-ray diffraction data (transmission geometry, Mo $K_{\alpha1}$ radiation) of the dark violet powder obtained after the TGA/DSC measurement (temperature range: 30–900 °C, atmosphere: synthetic air, *cf.* Fig. 7) of nano-sized *Pna*2$_1$-LiCoPO$_4$. The observed pattern is drawn in black, the calculated pattern in red, the difference plot in blue, and the Bragg reflections of olivine *Pnma*-LiCoPO$_4$ in green. As all observed reflections can be indexed, it can be assumed that pure *Pnma*-LiCoPO$_4$ was formed upon heating. Rietveld refinement details, atomic coordinates and thermal displacement parameters as well as selected interatomic distances can be found in Tables S6, S7, and S8.

Table S6 Cell parameters and Rietveld refinement details of the *Pnma*-LiCoPO$_4$ (Z = 4, T = 298 K) sample obtained after the TGA/DSC measurement (temperature range: 30–900 °C, atmosphere: synthetic air) of nano-sized *Pna*2$_1$-LiCoPO$_4$ [a]

Sample	**LiCoPO$_4$ after TGA/DSC (air)**
M_r (g/mol)	160.8
Crystal system	orthorhombic
Space group (no.)	*Pnma* (62)
Z	4
a (Å)	10.2110(2)
b (Å)	5.92075(12)
c (Å)	4.70581(11)
V (Å^3)	284.498(10)
F(000)	308
ρ (calcd.) (g/cm^3)	3.755(1)
R_p	0.0305
R_{wp}	0.0408
R_{exp}	0.0275
R_F	0.0267
R_B	0.0430
χ^2	1.48
Data/restraints/parameter	3804/0/62

[a] The estimated standard deviations (in parentheses) were calculated using the Berar's correction.

Table S7 Fractional atomic coordinates and isotropic thermal displacement parameters refined from powder X-ray diffraction data of the *Pnma*-$LiCoPO_4$ (Z = 4, T = 298 K) sample obtained after the TGA/DSC measurement (temperature range: 30–900 °C, atmosphere: synthetic air) of nano-sized *Pna*2$_1$-$LiCoPO_4$ [a]

Atom	Wyckoff position	Occupancy	*x*/a	*y*/b	*z*/c	U_{iso} (Å^2)
Li1	4*a*	1	0	0	0	0.0139 [b]
Co1	4*c*	1	0.22168(12)	¼	0.5210(3)	0.0082(4)
P1	4*c*	1	0.4052(3)	¼	0.0835(6)	0.0075(7)
O1	4*c*	1	0.4032(7)	¼	0.7568(13)	0.0062(19)
O2	4*c*	1	0.0472(7)	¼	0.2895(12)	0.0049(19)
O3	8*d*	1	0.3336(5)	0.0431(7)	0.2220(8)	0.0035(12)

[a] The estimated standard deviations (in parentheses) were calculated using the Berar's correction. [b] The thermal displacement parameter of Li has been fixed as it cannot be deduced by means of X-ray diffraction due to its low atomic scattering factor.

Table S8 Selected interatomic distances as refined from powder X-ray diffraction data of the *Pnma*-$LiCoPO_4$ (Z = 4, T = 298 K) sample obtained after the TGA/DSC measurement (temperature range: 30–900 °C, atmosphere: synthetic air) of nano-sized *Pna*2$_1$-$LiCoPO_4$ [a]

Atom pair			*d* (Å)
Li1	O1	×2	2.151(5)
	O2	×2	2.069(4)
	O3	×2	2.159(5)
Co1	O1	×1	2.161(7)
	O2	×1	2.089(7)
	O3	×2	2.056(4)
	O3	×2	2.188(5)
P1	O1	×1	1.537(7)
	O2	×1	1.568(7)
	O3	×2	1.568(5)

[a] The estimated standard deviations (in parentheses) were calculated using the Berar's correction.

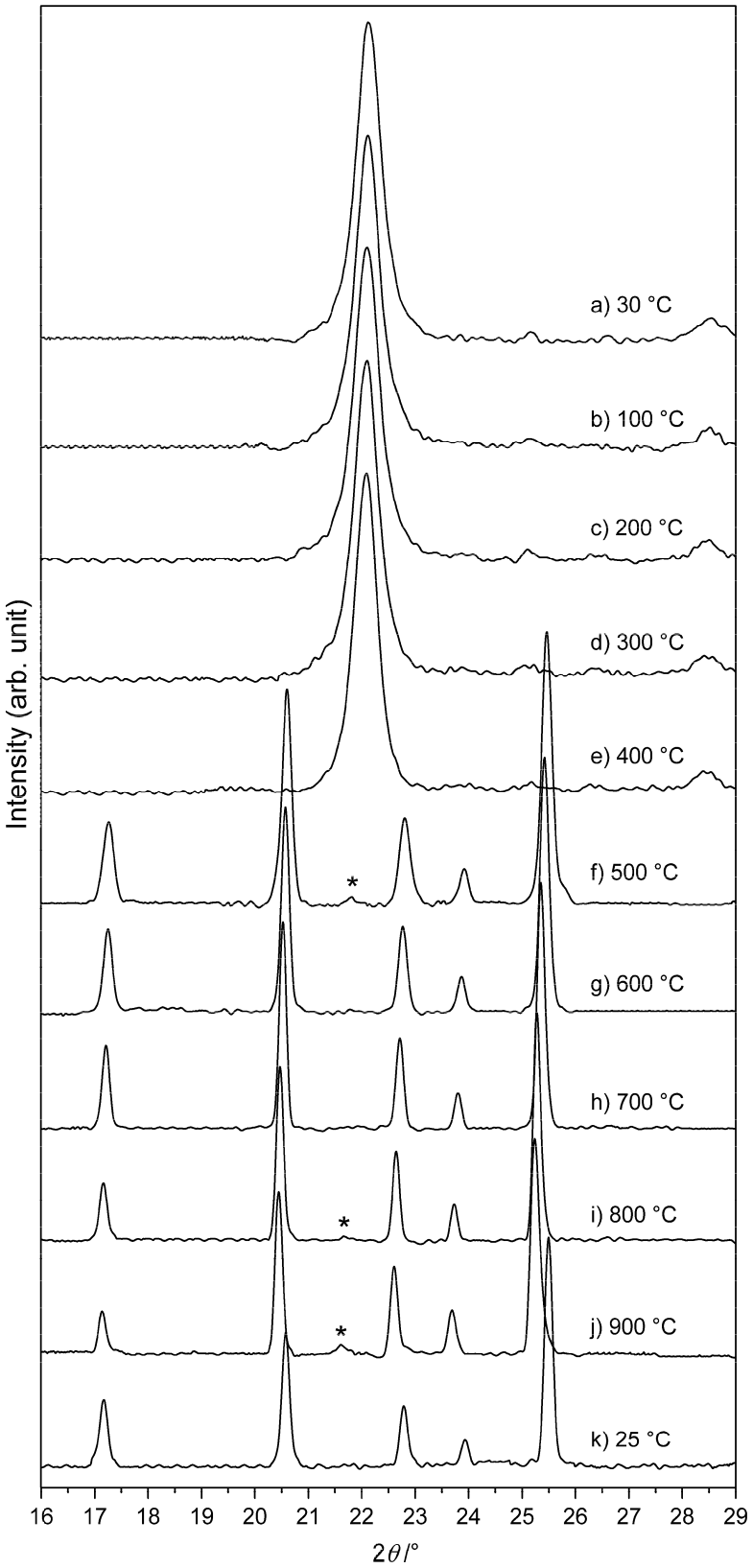

Figure S6 Zoomed view (2θ = 16–29°) of the normalized *in situ* powder X-ray diffraction patterns (Bragg-Brentano geometry, Cu K_α radiation, *cf.* Fig. 8) of nano-sized *Pna*2$_1$-$LiCoPO_4$ measured in air in a temperature range of 30–900 °C (a–j) and after cooling down to ambient temperature (25 °C, k). The characteristic (210)/(011) main reflections of the *Pna*2$_1$ phase at ~21.7° are clearly visible at 500 °C (f), 800 °C (i), and 900 °C (j) as indicated by the asterisks (*).

Table S9 Intensities, positions, and FWHM of the main reflections of *Pna*2$_1$-$LiCoPO_4$ and *Pnma*-$LiCoPO_4$ observed in the *in situ* powder X-ray diffraction patterns (Bragg-Brentano geometry, Cu K_α radiation, *cf.* Fig. S6) of nano-sized *Pna*2$_1$-$LiCoPO_4$ measured in air in a temperature range of 30–900 °C and after cooling down to ambient temperature (25 °C).

Temperature (°C)	$LiCoPO_4$ phase	Reflection (*hkl*)	Position (°/2θ)	Intensity (counts)	FWHM (°/2θ)
30	*Pna*2$_1$	(210)/(011)	22.11	1592	0.56
100	*Pna*2$_1$	(210)/(011)	22.11	1612	0.55
200	*Pna*2$_1$	(210)/(011)	22.10	1645	0.57
300	*Pna*2$_1$	(210)/(011)	22.10	1817	0.54
400	*Pna*2$_1$	(210)/(011)	22.08	1917	0.51
500	*Pna*2$_1$	(210)/(011)	21.81	55	–
	Pnma	(311)	35.63	2036	0.21
600	*Pnma*	(311)	35.58	2592	0.18
700	*Pnma*	(311)	35.49	2703	0.16
800	*Pnma*	(311)	35.41	2727	0.14
	*Pna*2$_1$	(210)/(011)	21.66	61	–
900	*Pnma*	(311)	35.36	1731	0.18
	*Pna*2$_1$	(210)/(011)	21.60	45	–
25	*Pnma*	(311)	35.73	1761	0.20

6. Investigation of the thermal stability of nano-sized *Pna*2$_1$-LiCoPO$_4$ under argon

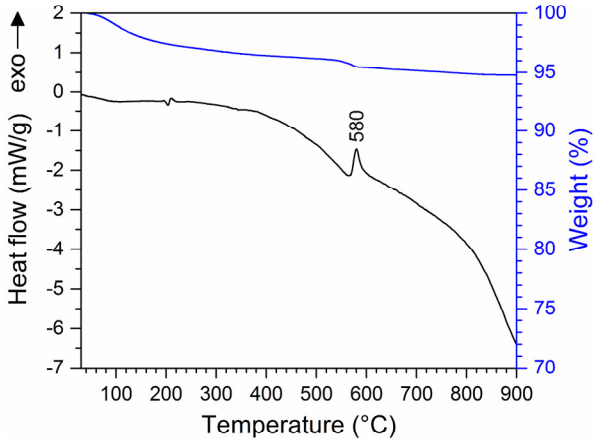

Figure S7 DSC (black) and TGA (blue) plots of nano-sized *Pna*2$_1$-LiCoPO$_4$ measured in a temperature range of 30–900 °C (heating rate: 10 °C/min, atmosphere: argon). The total weight loss observed in the TGA is ~5.2 wt%, which is due to the removal of adsorbed water and/or organic residues. The exothermic peak at 580 °C corresponds to the transformation of *Pna*2$_1$-LiCoPO$_4$ to olivine *Pnma*-LiCoPO$_4$.

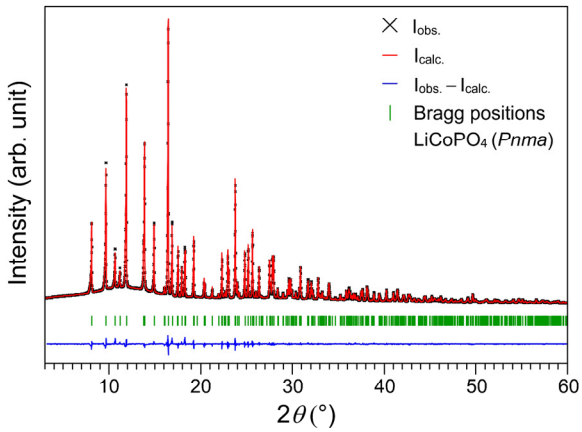

Figure S8 Rietveld fit of the powder X-ray diffraction data (transmission geometry, Mo $K_{\alpha1}$ radiation) of the dark violet powder obtained after the TGA/DSC measurement (temperature range: 30–900 °C, atmosphere: argon, *cf.* Fig. S7) of nano-sized *Pna*2$_1$-LiCoPO$_4$. The observed pattern is drawn in black, the calculated pattern in red, the difference plot in blue, and the Bragg reflections of olivine *Pnma*-LiCoPO$_4$ in green, respectively. As all observed reflections can be indexed, it can be derived that phase pure *Pnma*-LiCoPO$_4$ was formed upon heating. Rietveld refinement details, atomic coordinates and thermal displacement parameters as well as selected interatomic distances can be found in Tables S10, S11, and S12.

Table S10 Cell parameters and Rietveld refinement details of the *Pnma*-$LiCoPO_4$ ($Z = 4$, $T = 298$ K) sample obtained after the TGA/DSC measurement (temperature range: 30–900 °C, atmosphere: argon) of nano-sized *Pna*2$_1$-$LiCoPO_4$ [a]

Sample	**$LiCoPO_4$ after TGA/DSC (Ar)**
M_r (g/mol)	160.8
Crystal system	orthorhombic
Space group (no.)	*Pnma* (62)
Z	4
a (Å)	10.2114(3)
b (Å)	5.92985(16)
c (Å)	4.70439(13)
V (Å^3)	284.861(13)
F(000)	308
ρ (calcd.) (g/cm^3)	3.750(1)
R_p	0.0319
R_{wp}	0.0434
R_{exp}	0.0221
R_F	0.0257
R_B	0.0416
χ^2	1.96
Data/restraints/parameter	3804/0/62

[a] The estimated standard deviations (in parentheses) were calculated using the Berar's correction.

Table S11 Fractional atomic coordinates and isotropic thermal displacement parameters refined from powder X-ray diffraction data of the *Pnma*-$LiCoPO_4$ ($Z = 4$, $T = 298$ K) sample obtained after the TGA/DSC measurement (temperature range: 30–900 °C, atmosphere: argon) of nano-sized *Pna*2$_1$-$LiCoPO_4$ [a]

Atom	**Wyckoff position**	**Occupancy**	***x*/a**	***y*/b**	***z*/c**	**U_{iso} (Å^2)**
Li1	4*a*	1	0	0	0	0.0139 [b]
Co1	4*c*	1	0.22111(15)	¼	0.5210(4)	0.0077(5)
P1	4*c*	1	0.4050(3)	¼	0.0815(7)	0.0047(9)
O1	4*c*	1	0.4041(8)	¼	0.7654(15)	0.005(2)
O2	4*c*	1	0.0451(8)	¼	0.2934(14)	0.006(2)
O3	8*d*	1	0.3355(6)	0.0484(9)	0.2166(10)	0.004(2)

[a] The estimated standard deviations (in parentheses) were calculated using the Berar's correction. [b] The thermal displacement parameter of Li has been fixed as it cannot be deduced by means of X-ray diffraction due to its low atomic scattering factor.

Table S12 Selected interatomic distances as refined from powder X-ray diffraction data of the *Pnma*-$LiCoPO_4$ ($Z = 4$, $T = 298$ K) sample obtained after the TGA/DSC measurement (temperature range: 30–900 °C, atmosphere: argon) of nano-sized *Pna*2_1-$LiCoPO_4$ [a]

Atom pair			*d* (Å)
Li1	O1	×2	2.172(5)
	O2	×2	2.077(5)
	O3	×2	2.164(5)
Co1	O1	×1	2.194(8)
	O2	×1	2.092(8)
	O3	×2	2.077(5)
	O3	×2	2.201(5)
P1	O1	×1	1.487(8)
	O2	×1	1.547(9)
	O3	×2	1.529(6)

[a] The estimated standard deviations (in parentheses) were calculated using the Berar's correction.

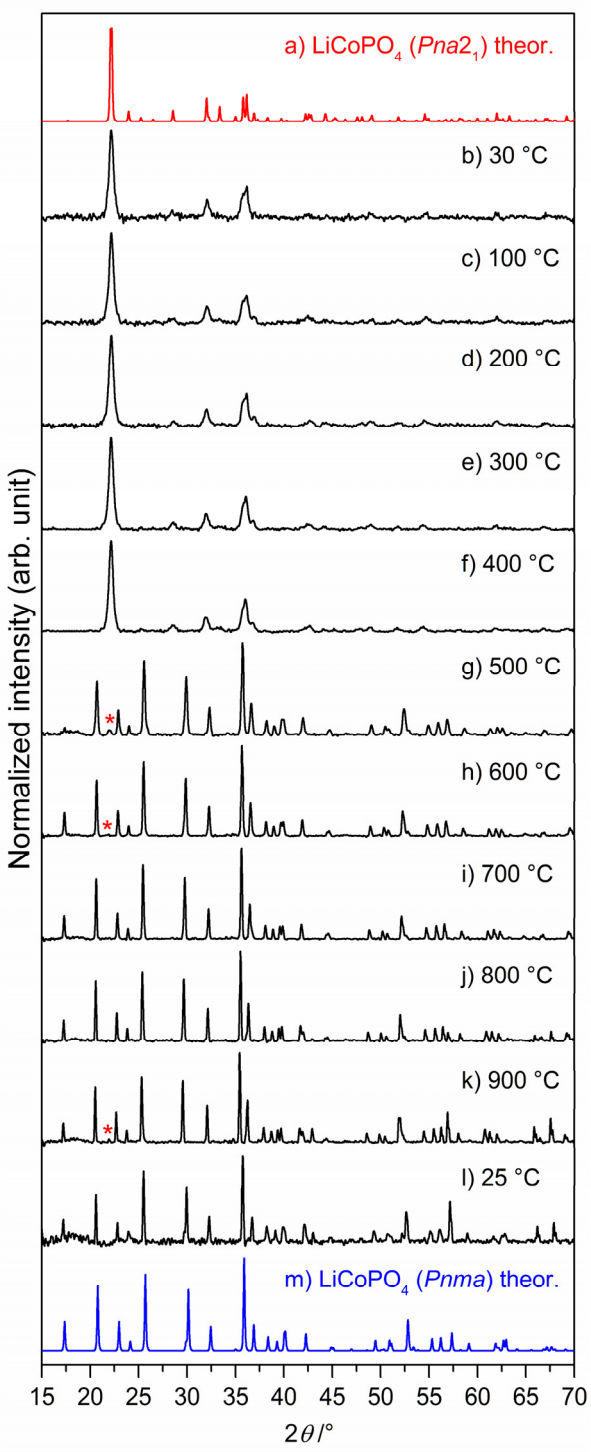

Figure S9 Normalized *in situ* powder X-ray diffraction patterns (Bragg-Brentano geometry, Cu K_α radiation) of nano-sized *Pna*2$_1$-$LiCoPO_4$ measured in a temperature range of 30–900 °C (b–k) under argon (heating rate: 5 °C/min), and after cooling down to 25 °C (l) in comparison to the theoretical patterns of *Pna*2$_1$-$LiCoPO_4$ (a, red) and *Pnma*-$LiCoPO_4$ (m, blue). Between 400 °C and 500 °C, the material starts to transform to the olivine *Pnma*-$LiCoPO_4$ polymorph with the phase transition being completed at 700 °C. At 900 °C, the characteristic (210)/(011) main reflections of the metastable *Pna*2$_1$ phase reemerges. After cooling, pure *Pnma*-$LiCoPO_4$ is obtained. The red asterisks (*) in (g, j, k) indicate the characteristic (210)/(011) main reflections of the *Pna*2$_1$ phase (detailed image see Fig. S10).

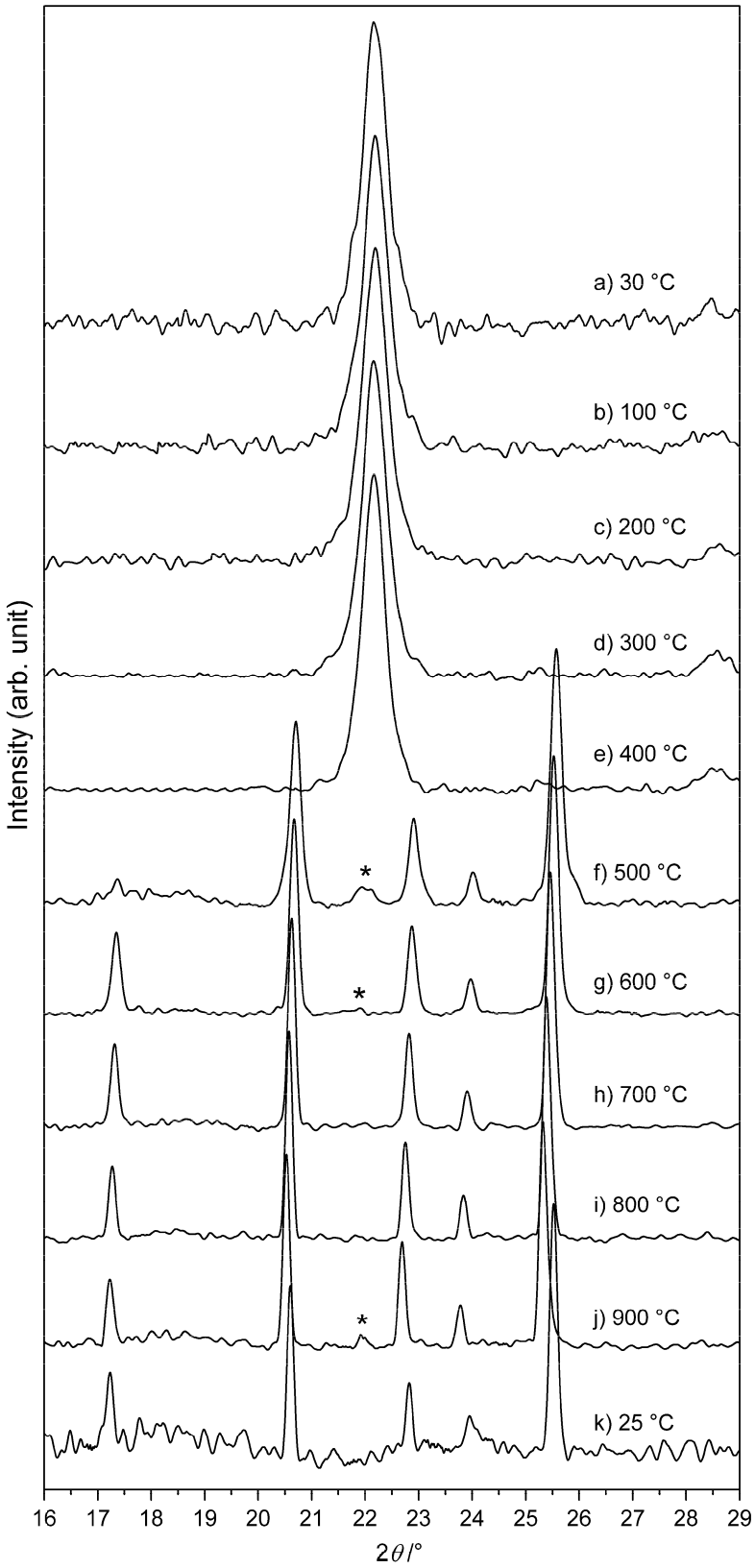

Figure S10 Zoomed view (2θ = 16–29°) of the normalized *in situ* powder X-ray diffraction patterns (Bragg-Brentano geometry, Cu K_α radiation) of nano-sized *Pna*2$_1$-$LiCoPO_4$ measured under argon in a temperature range of 30–900 °C and after cooling down to ambient temperature (25 °C). The characteristic (210)/(011) main reflections of the *Pna*2$_1$ phase are clearly visible as indicated by the asterisks (*).

Table S13 Intensities, positions, and FWHM of the main reflections of *Pna*2$_1$-$LiCoPO_4$ and *Pnma*-$LiCoPO_4$ observed in the *in situ* powder X-ray diffraction patterns (Bragg-Brentano geometry, Cu K_α radiation, *cf.* Fig. S10) of nano-sized *Pna*2$_1$-$LiCoPO_4$ measured under argon in a temperature range of 30–900 °C and after cooling down to ambient temperature (25 °C).

Temperature (°C)	$LiCoPO_4$ phase	Reflection (*hkl*)	Position (°/2θ)	Intensity (counts)	FWHM (°/2θ)
30	*Pna*2$_1$	(210)/(011)	22.15	359	0.55
100	*Pna*2$_1$	(210)/(011)	22.18	634	0.54
200	*Pna*2$_1$	(210)/(011)	22.20	876	0.57
300	*Pna*2$_1$	(210)/(011)	22.15	1140	0.54
400	*Pna*2$_1$	(210)/(011)	22.17	1343	0.51
500	*Pna*2$_1$	(210)/(011)	21.95	74/65	–
	Pnma	(311)	35.73	1477	0.25
600	*Pna*2$_1$	(210)/(011)	21.91	53	–
	Pnma	(311)	35.68	2116	0.21
700	*Pnma*	(311)	35.61	2273	0.19
800	*Pnma*	(311)	35.51	1779	0.17
900	*Pnma*	(311)	35.44	1365	0.18
	*Pna*2$_1$	(210)/(011)	21.91	56	–
25	*Pnma*	(311)	35.75	291	0.20

7. Investigation of the thermal stability of micron-sized *Pna*2$_1$-LiCoPO$_4$ under air/synthetic air

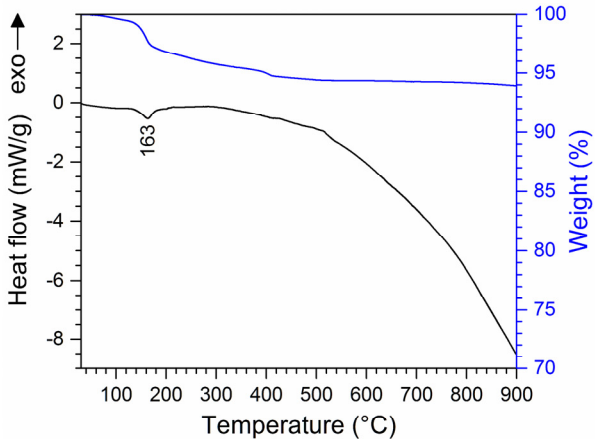

Figure S11 DSC (black) and TGA (blue) plots of micron-sized *Pna*2$_1$-LiCoPO$_4$ measured in a temperature range of 30–900 °C (heating rate: 10 °C/min, atmosphere: synthetic air). The total weight loss observed in the TGA is ~6.1 wt%, which is due to the removal of adsorbed water and/or organic residues. The endothermic signal observed in the DSC curve at 163 °C most likely corresponds to the removal of traces of the solvent or organic residues as it is accompanied by a weight loss. No signals are observed which can be correlated to the transformation of *Pna*2$_1$-LiCoPO$_4$ to olivine *Pnma*-LiCoPO$_4$.

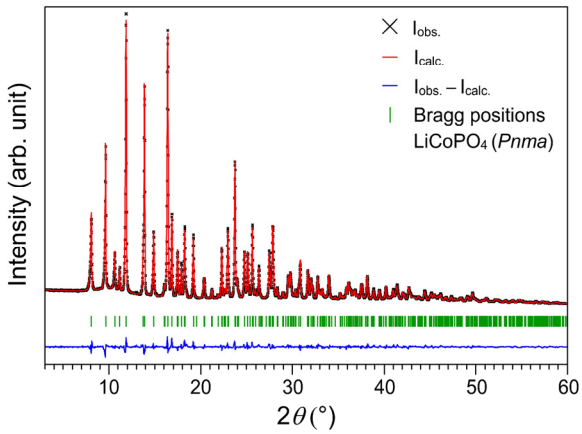

Figure S12 Rietveld fit of the powder X-ray diffraction data (transmission geometry, Mo $K_{\alpha 1}$ radiation) of the dark violet powder obtained after the TGA/DSC measurement (temperature range: 30–900 °C, atmosphere: synthetic air, *cf.* Fig. S11) of micron-sized *Pna*2$_1$-LiCoPO$_4$. The observed pattern is drawn in black, the calculated pattern in red, the difference plot in blue, and the Bragg reflections of olivine *Pnma*-LiCoPO$_4$ in green, respectively. As all observed reflections can be indexed, it can be derived that phase pure *Pnma*-LiCoPO$_4$ was formed upon heating. Rietveld refinement details, atomic coordinates and thermal displacement parameters as well as selected interatomic distances can be found in Tables S14, S15, and S16.

Table S14 Cell parameters and Rietveld refinement details of the *Pnma*-$LiCoPO_4$ ($Z = 4$, $T = 298$ K) sample obtained after the TGA/DSC measurement (temperature range: 30–900 °C, atmosphere: synthetic air) of micron-sized *Pna*2$_1$-$LiCoPO_4$ [a]

Sample	$LiCoPO_4$ after TGA/DSC (air)
M_r (g/mol)	160.8
Crystal system	orthorhombic
Space group (no.)	*Pnma* (62)
Z	4
a (Å)	10.2155(6)
b (Å)	5.9163(3)
c (Å)	4.7025(2)
V (Å^3)	284.21(3)
$F(000)$	308
ρ (calcd.) (g/cm^3)	3.759(1)
R_p	0.0363
R_{wp}	0.0471
R_{exp}	0.0261
R_F	0.0229
R_B	0.0391
χ^2	1.81
Data/restraints/parameter	3807/0/62

[a] The estimated standard deviations (in parentheses) were calculated using the Berar's correction.

Table S15 Fractional atomic coordinates and isotropic thermal displacement parameters as refined from powder X-ray diffraction data of the *Pnma*-$LiCoPO_4$ ($Z = 4$, $T = 298$ K) sample obtained after the TGA/DSC measurement (temperature range: 30–900 °C, atmosphere: synthetic air) of micron-sized *Pna*2$_1$-$LiCoPO_4$ [a]

Atom	Wyckoff position	Occupancy	*x*/a	*y*/b	*z*/c	U_{iso} (Å^2)
Li1	4*a*	1	0	0	0	0.0139 [b]
Co1	4*c*	1	0.22136(19)	¼	0.5214(5)	0.0089(7)
P1	4*c*	1	0.4044(5)	¼	0.0814(9)	0.0075(12)
O1	4*c*	1	0.4050(12)	¼	0.7663(19)	0.006(3)
O2	4*c*	1	0.0464(11)	¼	0.2888(18)	0.004(3)
O3	8*d*	1	0.3336(8)	0.0424(11)	0.2198(11)	0.003(2)

[a] The estimated standard deviations (in parentheses) were calculated using the Berar's correction. [b] The thermal displacement parameter of Li has been fixed as it cannot be deduced by means of X-ray diffraction due to its low atomic scattering factor.

Table S16 Selected interatomic distances refined from powder X-ray diffraction data of the *Pnma*-$LiCoPO_4$ ($Z = 4$, $T = 298$ K) sample obtained after the TGA/DSC measurement (temperature range: 30–900 °C, atmosphere: synthetic air) of micron-sized *Pna*2_1-$LiCoPO_4$ [a]

Atom pair			*d* (Å)
Li1	O1	×2	2.141(8)
	O2	×2	2.063(6)
	O3	×2	2.165(8)
Co1	O1	×1	2.177(12)
	O2	×1	2.096(11)
	O3	×2	2.044(7)
	O3	×2	2.199(7)
P1	O1	×1	1.529(10)
	O2	×1	1.573(12)
	O3	×2	1.567(7)

[a] The estimated standard deviations (in parentheses) were calculated using the Berar's correction.

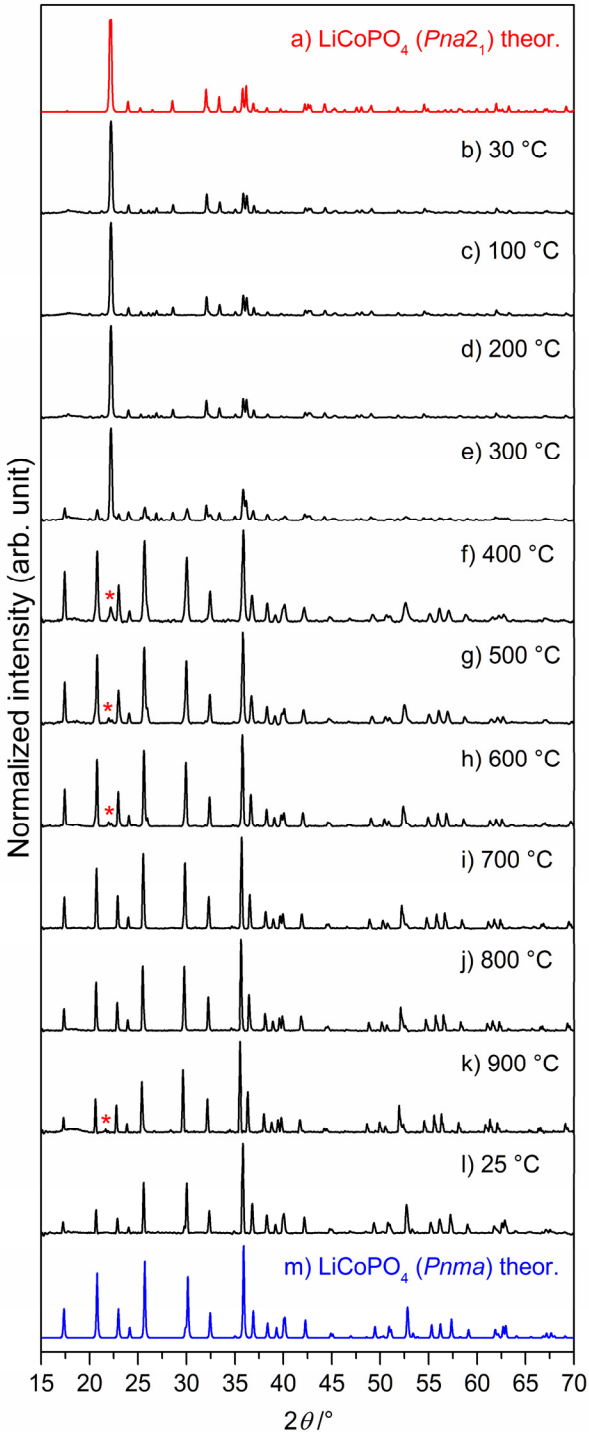

Figure S13 Normalized *in situ* powder X-ray diffraction patterns (Bragg-Brentano geometry, Cu K_α radiation) of micron-sized *Pna*2$_1$-$LiCoPO_4$ measured in a temperature range of 30–900 °C (b–k) in air (heating rate: 5 °C/min), and after cooling down to 25 °C (l) in comparison to the theoretical patterns of *Pna*2$_1$-$LiCoPO_4$ (a, red) and *Pnma*-$LiCoPO_4$ (m, blue). Between 200 °C and 300 °C, the material starts to transform to the olivine-type *Pnma*-$LiCoPO_4$ polymorph with the phase transition being completed at 700 °C. At 900 °C, the characteristic (210)/(011) main reflections of the metastable *Pna*2$_1$ phase reemerges. After cooling, pure *Pnma*-$LiCoPO_4$ is obtained. The red asterisks (*) in (f, g, h, k) indicate the characteristic (210)/(011) main reflections of the *Pna*2$_1$ phase (detailed image see Fig. S14).

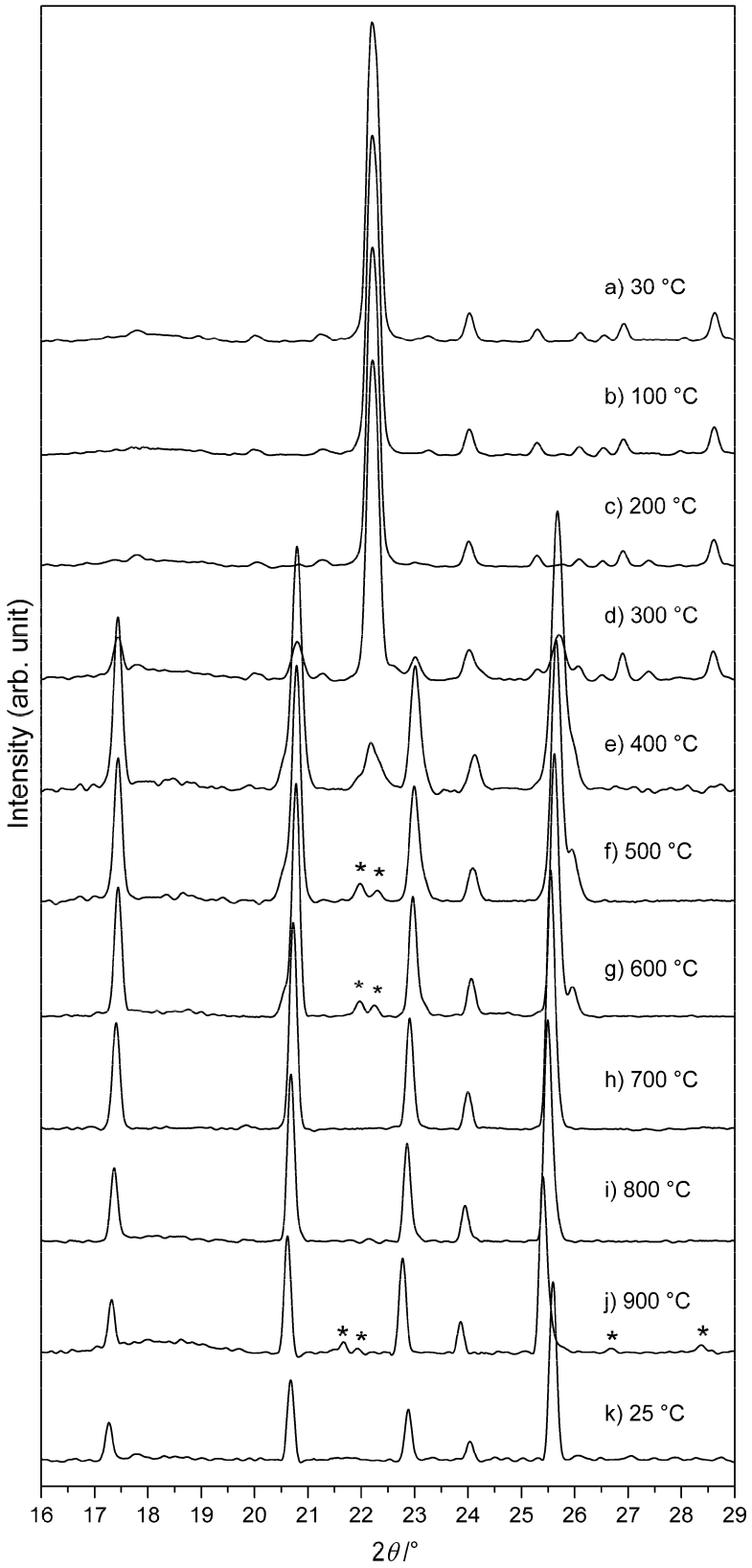

Figure S14 Zoomed view (2θ = 16–29°) of the normalized *in situ* powder X-ray diffraction patterns (Bragg-Brentano geometry, Cu K_α radiation) of micron-sized *Pna*2_1-$LiCoPO_4$ measured in air in a temperature range of 30–900 °C and after cooling (25 °C). It is evident that the transformation to *Pnma*-$LiCoPO_4$ starts between 200 and 300 °C (d) and is completed at 700 °C (h). Reflections of the *Pna*2_1 phase are clearly visible as indicated by the asterisks (*) in (f, g, j). The visible splitting of the (210)/(011) reflections at higher temperatures is the result of a change in the *a* and *c* cell parameters.

Table S17 Intensities, positions, and FWHM of the main reflections of *Pna*2$_1$-$LiCoPO_4$ and *Pnma*-$LiCoPO_4$ observed in the *in situ* powder X-ray diffraction patterns (Bragg-Brentano geometry, Cu K_α radiation, *cf.* Fig. S14) of micron-sized *Pna*2$_1$-$LiCoPO_4$ measured in air in a temperature range of 30–900 °C and after cooling down to ambient temperature (25 °C).

Temperature (°C)	$LiCoPO_4$ phase	Reflection (*hkl*)	Position (°/2θ)	Intensity (counts)	FWHM (°/2θ)
30	*Pna*2$_1$	(210)/(011)	22.20	7646	0.28
100	*Pna*2$_1$	(210)/(011)	22.20	7878	0.27
200	*Pna*2$_1$	(210)/(011)	22.22	8036	0.26
300	*Pna*2$_1$	(210)/(011)	22.22	4975	0.26
400	*Pna*2$_1$	(210)/(011)	22.18	371	–
	Pnma	(311)	35.87	2513	0.26
500	*Pna*2$_1$	(210)/(011)	21.98/22.30	178/104	–
	Pnma	(311)	35.82	3354	0.22
600	*Pna*2$_1$	(210)/(011)	21.97/22.25	189/137	–
	Pnma	(311)	35.78	4029	0.19
700	*Pnma*	(311)	35.68	4323	0.18
800	*Pnma*	(311)	35.63	4277	0.17
900	*Pnma*	(311)	35.51	2983	0.17
	*Pna*2$_1$	(210)/(011)	21.67/22.93	92/32	–
25	*Pnma*	(311)	35.82	3362	0.18

6.7 *In Situ* Studies and Magnetic Properties of the *Cmcm* Polymorph of $LiCoPO_4$ with a Hierarchical Dumbbell-Like Morphology Synthesized by Easy Single-Step Polyol Synthesis

Carlos Alarcón-Suesca,[a,†] **Jennifer Ludwig,**[**a,†**] Viktor Hlukhyy,[b] Christoph Stinner,[c] and Tom Nilges[a]

[a] Technical University of Munich, Department of Chemistry, Synthesis and Characterization of Innovative Materials, Lichtenbergstr. 4, 85747 Garching, Germany

[b] Technical University of Munich, Department of Chemistry, Chair of Inorganic Chemistry with Focus on Novel Materials, Lichtenbergstr. 4, 85747 Garching, Germany

[c] BMW AG, Petuelring 130, 80788 München, Germany

[†] These authors contributed equally to this work.

Inorganics **2016,** *4*, 35.
DOI: 10.3390/inorganics4040035

inorganics

MDPI

Article

In Situ Studies and Magnetic Properties of the *Cmcm* Polymorph of $LiCoPO_4$ with a Hierarchical Dumbbell-Like Morphology Synthesized by Easy Single-Step Polyol Synthesis

Carlos Alarcón-Suesca [1,†], Jennifer Ludwig [1,†], Viktor Hlukhyy [2], Christoph Stinner [3] and Tom Nilges [1,*]

[1] Synthesis and Characterization of Innovative Materials, Department of Chemistry, Technical University of Munich, Lichtenbergstraße 4, 85747 Garching, Germany; carlos.alarcon@tum.de (C.A-S.); jennifer.ludwig@tum.de (J.L.)

[2] Chair of Inorganic Chemistry with Focus on Novel Materials, Department of Chemistry, Technical University of Munich, Lichtenbergstraße 4, 85747 Garching, Germany; viktor.hlukhyy@tum.de

[3] BMW AG, Petuelring 130, 80788 München, Germany; christoph.stinner@bmw.de

* Correspondence: tom.nilges@lrz.tum.de; Tel.: +49-89-289-13111

† These authors contributed equally to this work.

Academic Editor: Richard Dronskowski

Received: 6 October 2016; Accepted: 10 November 2016; Published: 17 November 2016

Abstract: $LiCoPO_4$ (LCP) exists in three different structural modifications: LCP-*Pnma* (olivine structure), LCP-$Pn2_1a$ ($KNiPO_4$ structure type), and LCP-*Cmcm* (Na_2CrO_4 structure type). The synthesis of the LCP-C*mcm* polymorph has been reported via high pressure/temperature solid-state methods and by microwave-assisted solvothermal synthesis. Phase transitions from both LCP-$Pn2_1a$ and LCP-C*mcm* to LCP-*Pnma* upon heating indicates a metastable behavior. However, a precise study of the structural changes during the heating process and the magnetic properties of LCP-C*mcm* are hitherto unknown. Herein, we present the synthesis and characterization of LCP-*Cmcm* via a rapid and facile soft-chemistry approach using two different kinetically controlled pathways, solvothermal and polyol syntheses, both of which only require relatively low temperatures (~200 °C). Additionally, by polyol, method a dumbbell-like morphology is obtained without the use of any additional surfactant or template. A temperature-dependent in situ powder XRD shows a transition from LCP-C*mcm* at room temperature to LCP-*Pnma* and finally to LCP-$Pn2_1a$ at 575 and 725 °C, respectively. In addition to that, the determination of the magnetic susceptibility as a function of temperature indicates a long-range antiferromagnetic order below T_N = 11 K at 10 kOe and 9.1 K at 25 kOe. The magnetization curves suggests the presence of a metamagnetic transition.

Keywords: polymorph; $LiCoPO_4$-*Cmcm*; metamagnetic transition; in situ XRD; polyol; solvothermal; transition phase; hierarchical morphology

1. Introduction

Since their introduction by Whittingham [1] and commercialization in the early 1990s by Sony® [2], Li-ion batteries (LIB) have become a breakthrough technology in portable electronics. So far, LIB constituted the most appropriate method of energy storage in this sector because they show high energy density, low weight, design flexibility and long lifetime [3]. In current LIB technology, the electrochemical performance (e.g., cell voltage, capacity, Li^+ transportation rate) is mainly determined by the cathode material and, thus, intense research efforts are undertaken in this field [4]. Among several cathode materials, such as spinel types and lithium-rich layered oxides, lithium transition-metal

orthophosphates with the sum formula Li*M*PO_4 (*M* = Fe, Mn, Co, Ni) or simply L*M*P (LFP, LMP, LCP, LNP) have received particular attention due to their excellent electrochemical properties, good thermal stability, low cost and environmental friendliness [5]. While LFP and LMP have been widely investigated to date, LCP is still under investigation. In LCP, the Co^{2+}/Co^{3+} redox couple offers a high operating voltage of approximately 4.8 V versus Li/Li^+ [6]. Moreover, LCP shows a high theoretical energy density of 800 Wh/kg (superior compared to the 580 Wh/kg of LFP), exhibits the lowest hole polaron migration barrier of the phospho-olivine family and subsequently has the highest electronic conductivity compared to LFP, LMP and LNP [7]. Furthermore, LCP shows a reduced cobalt weight fraction per formula unit compared to commercial $LiCoO_2$, making it a lower-cost option [8,9]. LCP can exist in three polymorphs with orthorhombic crystal structures, and several electrochemical and physical properties have been reported so far [10–12]. The most widely investigated one is olivine-type LCP-*Pnma*. In the structure, Li^+ and Co^{2+} ions occupy octahedral sites and P^{+5} is located in a tetrahedral environment formed by a distorted hexagonal close-packed (*hcp*) array of oxygen atoms [13]. The [CoO_6] octahedra form zigzag chains that are running parallel to the crystallographic *c* axis (Figure 1a). The chains are linked by the [PO_4] tetrahedra, resulting in a 3D network structure [14]. The Li^+ ions are located in channels along [010] and [001]. However, studies for olivine structures show that Li^+ diffusion is only promoted along the *b* direction due to a lower activation energy [15–17]. The second polymorph (Figure 1b) is LCP-$Pn2_1a$. This modification was theoretically predicted by Hautier [6] based on ab initio DFT calculations and subsequently experimentally reported by Jaehne et al. [18]. Unlike the olivine structure, Co^{2+} cations are tetrahedrally coordinated in this structure. The framework features alternating corner-sharing [PO_4] and [CoO_4] tetrahedra along the *c* axis, the Li^+ diffusion paths are blocked by [CoO_4] tetrahedra and the compound shows a poor electrochemical performance. As a result, there are no direct Li^+ channels along any direction [6,18]. The third modification is LCP-*Cmcm*, which adapts the Na_2CrO_4-type structure (Figure 1c). This structure was first reported by Amador and co-workers[19] resulting from a high-pressure and high-temperature solid-state synthesis (6 GPa, 900 °C). In the structure, chains of edge-sharing [CoO_6] octahedra, which are running along the *c* direction, are cross-linked by [PO_4] tetrahedra along *a*. As a result, layers of the composition $[(CoO_6)(PO_4)]_\infty$ are generated. Moreover, the remaining tetrahedral sites are occupied by Li^+ ions and a high activation energy is required for Li^+-ion migration [19,20]. Recently, a microwave-assisted synthesis pathway was reported for LCP-C*mcm*. In this report, Manthiram et al. [21,22] claimed two conditions to be necessary for the formation of LCP-*Cmcm*: the use of fresh dried tetraethylene glycol (TTEG) as a solvent and the use of cobalt oxalate as a cobalt precursor. This synthesis was performed in a closed system using a temperature of 260 °C and a pressure below 30 bar. A transformation of LCP-*Cmcm* to LCP-*Pnma* revealed by thermal analysis was also reported in this study. Besides, an ex situ XRD analysis was conducted after a long annealing process (8 h) and posterior cooling of the material. However, there is no further information about the crystal structure at temperatures above 650 °C and/or further verification of any other possible transition during the cooling process. In addition, it is well known that morphology plays an important role in the electrochemical performance of cathode and anode materials for LIB [23–25]. Some reports explain the benefits of hierarchical dumbbell-shape morphologies such as larger surface area, high porosity and the formation of small-sized primary particles, leading to a reduction of the diffusion distance of lithium ions and an increase of reaction sites of Li^+-ions as well as preventing a decrease in volumetric energy density caused by low tap-density nanostructures [26,27]. Equally important, in order to achieve morphology control, the synthesis often requires the use of hydrothermal or solvothermal methods, sometimes microwave-assisted, as well as the use of expensive organic surfactants or additives, co-solvents and temperatures above 250 °C making the process expensive and complicated [28–30]. Herein, we report two alternative, kinetically controlled synthesis pathways towards the *Cmcm*-type LCP polymorph under mild conditions using a solvothermal as well as a polyol synthesis approach. Our synthesis is conducted at temperatures as low as 200 °C in a traditional round bottom flask. This simple synthesis does not require the use of water-free TTEG and is conducted using different cobalt ion precursors. The thermal behavior of LCP-*Cmcm* is examined comprehensively, revealing a

transformation of LCP-*Cmcm* to LCP-*Pnma* and finally to LCP-*Pn*2_1*a* at high temperature. Finally, the magnetic properties and metamagnetic transition of LCP-*Cmcm* are presented for the first time.

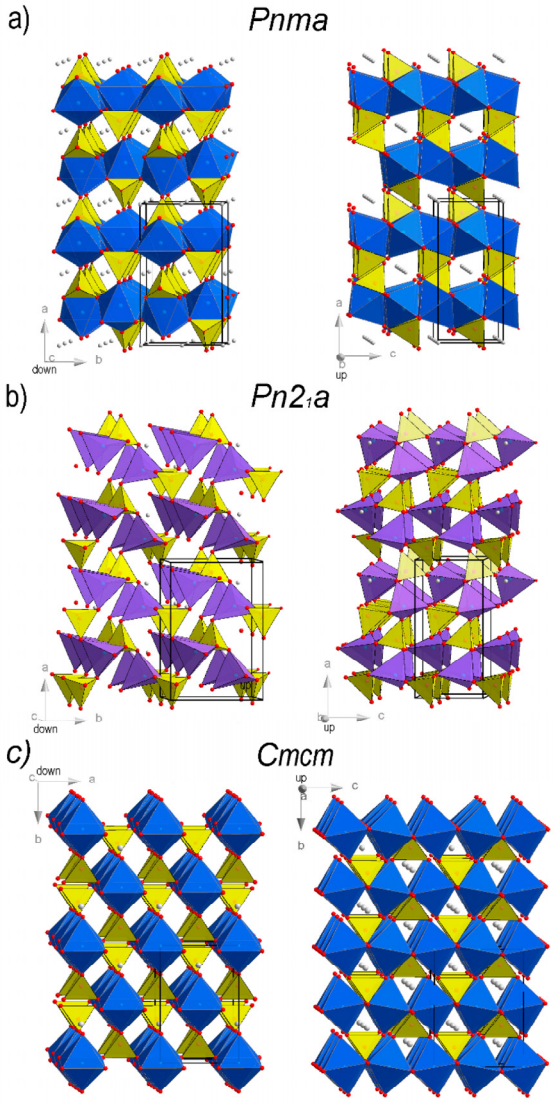

Figure 1. Projections of the crystal structures of the three orthorhombic polymorphs of $LiCoPO_4$ (LCP) along the crystallographic *c* and *b* axes with the space groups: (**a**) P*nma*; (**b**) P*n*2_1*a*; and (**c**) C*mcm*. [CoO_6] octahedra are drawn in blue, [PO_4] tetrahedra in yellow, [CoO_4] tetrahedra in purple, Li^+ ions in grey and O^{2-} ions in red.

2. Results and Discussion

2.1. X-ray Powder Diffraction

From solvothermal synthesis, the LCP polymorph with *Cmcm* symmetry was obtained from all solvents (see experimental section), yet varying amounts of Li_3PO_4 as well as traces of olivine-type LCP (space group *Pnma*) were observed as impurities (cf. Supplementary Materials, Figure S1, Tables S1–S3). The sample formed in diethylene glycol (DEG) solvent showed the smallest amount of impurities and was therefore selected for further characterization (designated as LCP-*Cmcm* (ST) in the following). Figure 2 shows the Rietveld refinement of the X-ray powder diffraction patterns

of the LCP-*Cmcm* samples obtained by solvothermal (ST) and polyol (PO) synthesis. The refined lattice parameters and refinement details are presented in Tables S2 and S3 of the Supplementary Materials. In the case of the solvothermal sample from the DEG solvent (Figure 2a), the refined lattice parameters are a = 5.4347(4) Å, b = 8.1638(5) Å, and c = 6.2135(4) Å. However, very small amounts of Li_3PO_4, which is often formed in solution-based synthesis [31,32] and olivine-type LCP (space group *Pnma*) are observed as side phases. For the polyol sample (Figure 2b), no impurities were detected. All of the identified reflections can be fully indexed using the space group *Cmcm*. The refined lattice parameters a = 5.4433(3) Å, b = 8.1694(4) Å, and c = 6.2129(3) Å are in good agreement with the values for LCP-*Cmcm* reported in the literature [19]. Atomic coordinates, thermal displacement parameters, and selected interatomic distances can be found in the Supplementary Materials (Tables S2–S4). Furthermore, the appearance of sharp diffraction peaks strongly reflects the high crystallinity of the samples produced at comparably low pressure, temperature and in a one-step synthesis without post-annealing. It has to be pointed out that, according to reference measurements presented in our previous work [33], the background can be fully attributed to the capillary and no amorphous components are present in the sample.

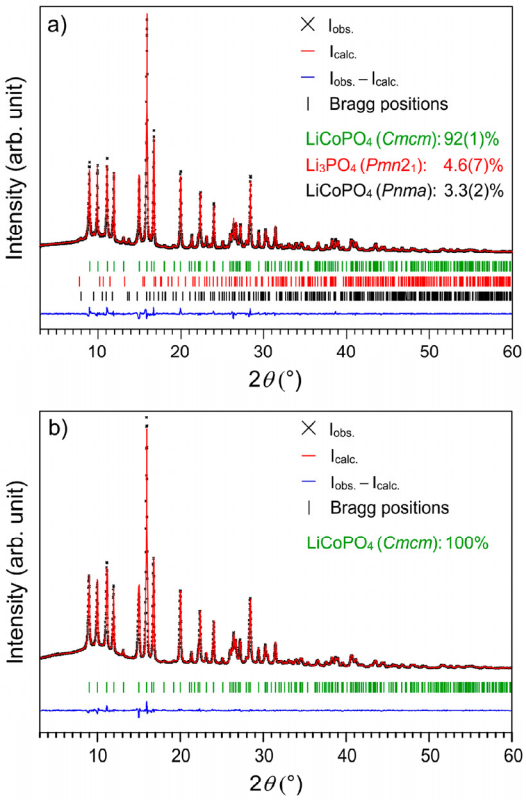

Figure 2. Rietveld fit of the X-ray powder diffraction data of LCP-*Cmcm* prepared by different synthesis pathways: (**a**) solvothermal; and (**b**) polyol synthesis.

2.2. Scanning Electron Microscopy (SEM)

High-resolution SEM images (Figure 3) of the two materials reveal that the synthesis conditions strongly affect the morphology of the particles. The solvothermal synthesis results in the formation of irregular macrostructures formed by agglomeration of primary platelets with overall dimensions of 5–10 µm (Figure 3a,b). The agglomerates consist of cross-linked, leaf-shaped platelets of about 0.5–1 µm × 5–6 µm in size, and about 80 nm in thickness. Complex morphologies like this are generally obtained by solvothermal or hydrothermal routes [34]. On the contrary, the polyol synthesis

results in the formation of agglomerates with dumbbell or bow-tie shapes in the size range of 1–4 µm, which are formed by nanosheet-like primary particles with average dimensions of 20–40 nm in length, and 3–4 nm in thickness (Figure 3c,d). Given the fact that to date the synthesis of cathode materials with dumbbell-like morphologies is only reported by the use of templates and/or under solvothermal/hydrothermal conditions, and sometimes assisted by microwave irradiation [26,27,29], it is remarkable that such a well-organized hierarchical morphology was obtained by a simple synthesis approach. Moreover, this morphology type allows for the obtainment of materials with high surface areas which offer a larger interface between the electrode and the electrolyte, a fast intercalation probability and an improved electron transport as reported for LFP [30]. In our case, the polyol synthesis is conducted without the use of special additives or under high temperature or high pressure conditions. We suggest in accordance with the literature that the tetraethylene glycol acts not only as a solvent and mild reducing agent but also as a soft template to direct the growth and self-assembly of structures with preferred orientations [35]. Furthermore, the mixing order of the precursors has an influence on the morphology of the final product. Figure 3e,f show LCP particles prepared after direct mixing of the cobalt acetate and lithium acetate solutions and the subsequent addition of phosphoric acid. In this case, no primary nanosheet-like particles were observed but even primary nano-dots with the same bow-like morphology. This implies that only by a simple variation of the mixing sequence, the morphology can be modified, thereby inducing a change from primary nano-needles to primary nano-dots without the use of any surfactant or organic template. The crystal structure remains unaltered (not shown). Results of Fourier transform infrared spectroscopy (FT-IR), including band assignment and literature comparison, are presented in Figure S2 and Table S4 in the Supplementary Materials section.

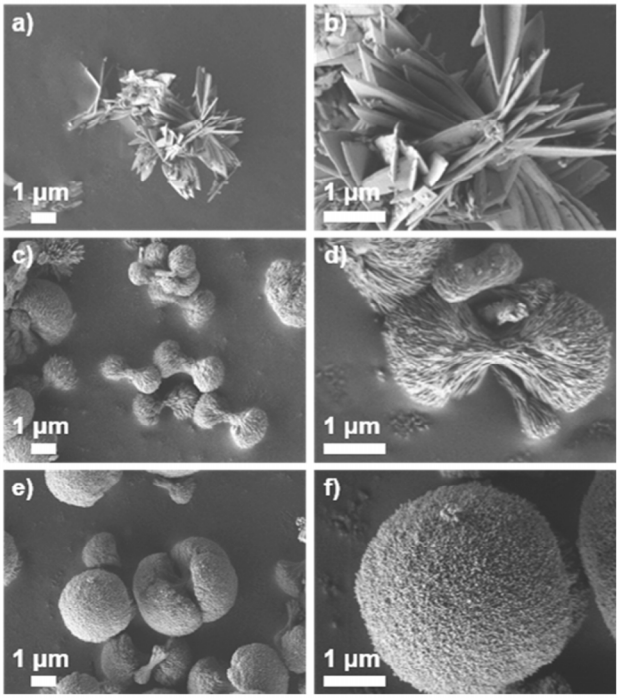

Figure 3. Scanning electron microscopy (SEM) images of LCP-*Cmcm* prepared by different procedures. (**a**,**b**) Solvothermal synthesis; (**c**,**d**) Polyol synthesis; Addition of H_3PO_4 to LiAc solution and posterior addition of $CoAc_2$ to H_3PO_4/LiAc mixture; (**e**,**f**) Polyol variation on the order of mixture: First mixture of $CoAc_2$ and LiAc with posterior addition of H_3PO_4 to the $CoAc_2$/LiAc mixture.

2.3. Elemental Analysis

The chemical composition of the samples was determined by means of CHNS (determination of the C, H, N, and S contents by combustion analysis) and AAS (atomic absorption spectroscopy) analyses. The results are given in Table 1. The Li:Co:P wt % ratio is found to be close to the theoretical composition 4.3:36.6:19.3 of $LiCoPO_4$ in both cases. The results correspond to Li:Co:P molar ratios of 0.99(5):0.97(3):1.00(2) and 0.93(5):0.91(5):1.00(2), implying that both materials are stoichiometric within three standard deviations. The CHNS analyses show that no significant amounts of hydrogen as well as carbon are present in the sample, which might be arising from residual water or the decomposition of residual organic polyol solvents and precursors. However, it has to be emphasized that, whereas the solvothermal sample tends to be stoichiometric, the phase pure polyol material seems to be deficient both in Li and Co. Hence, the results indicate that the synthesis method affects the stoichiometry of the phase. A more systematic investigation of the role of the synthesis route on the chemical composition will be the focus of oncoming research.

Table 1. Elemental analysis of LCP-*Cmcm* synthesized by (a) the solvothermal (ST) and (b) the polyol process (PO) [1,2].

Element	(a) LCP(ST)	(b) LCP(PO)	Theoretical
C (wt %)	0.7(3)	0.8(3)	0
H (wt %)	0.2(3)	0.4(3)	0
Li (wt %)	4.2(2)	4.1(2)	4.3
Co (wt %)	35(1)	34(1)	36.6
P (wt %)	18.9(3)	19.6(3)	19.3
n(Li):*n*(P)	0.99(5)	0.93(5)	1
n(Co):*n*(P)	0.97(3)	0.91(3)	1

[1] The composition is determined from the experimental values of the CHNS (combustion analysis to determine the C, H, N, and S contents) and AAS (atomic absorption spectroscopy) analyses (standard deviations in parentheses); [2] The N and S values were below the detection limit (= 0).

2.4. Thermal Stability and Phase Transformation

As reported previously, the polymorphs LCP-*Cmcm* and LCP-$Pn2_1a$ are metastable with transition temperatures to the thermodynamically stable LCP-*Pnma* of 220 and 550 °C, respectively [18,21,22]. However, all these conclusions were based on (a) TGA (thermogravimetric analysis)/DSC (differential scanning calorimetry) experiments which were only performed in a temperature range up to 700 and 500 °C, respectively, and (b) only supported by ex situ XRD analyses, which exclusively provide information about the particular phase at the end of the cooling process. Moreover, the reports were lacking additional SEM studies, which provide information about morphological changes upon heating. Taking the metastable behavior of LCP into consideration, it is important to examine the thermal behavior and respective phase transitions more thoroughly. The TGA/DSC data for the sample obtained by polyol synthesis are presented in Figure 4. In the TGA curve, a mass loss is observed between 200 and 300 °C, which can be attributed to the removal of residual water as well as to the decomposition of residues of the organic solvent. A strong signal occurs in the DSC experiment in the temperature range from 550 to 700 °C. At first glance, this effect can be attributed to the transition from LCP-*Cmcm* to LCP-*Pnma*, which represents a typical monotropic solid–solid phase transition of a metastable to a stable phase (irreversible process). Figure 5 shows the corresponding ex situ room temperature powder diffraction data of LCP-*Cmcm* produced by the polyol method, in the temperature range between 200 and 900 °C with an increment of 100 °C and posterior cooling. Herein, the transformation of LCP-*Cmcm* to LCP-*Pnma* takes place in the region between 500 and 700 °C. Moreover, the formation of an additional unidentified phase is evident. The corresponding peaks are marked with the symbol ♦.

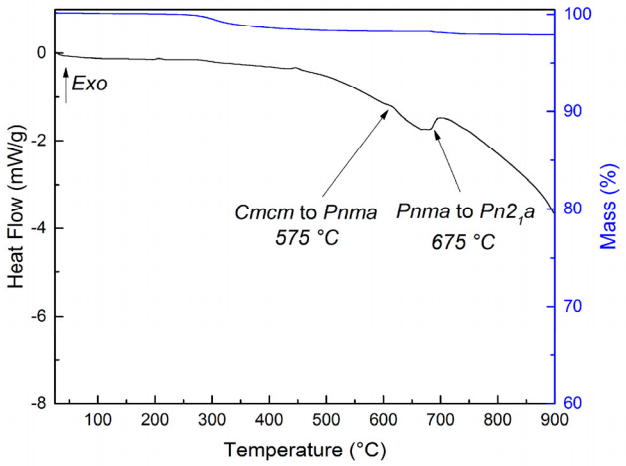

Figure 4. Thermal and gravimetric analyses for LCP-*Cmcm* (PO) obtained from the polyol route. TGA data are drawn in blue, and DSC data in black.

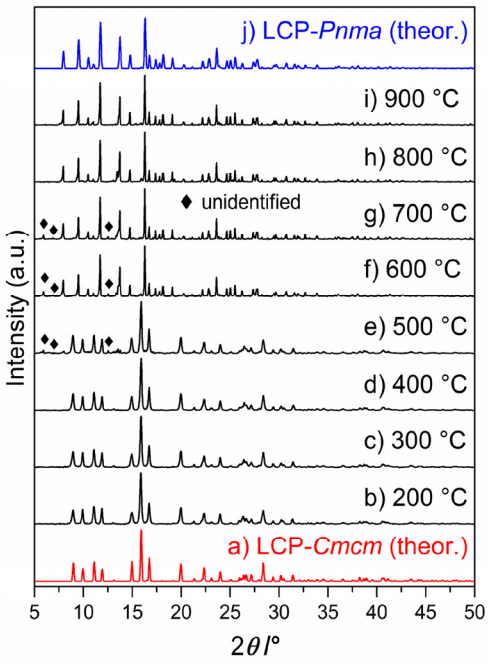

Figure 5. Ex situ X-ray powder diffraction patterns of LCP-*Cmcm* (PO) samples after heat treatment for 6 h in air in the temperature range from 200 to 900 °C (increment: 100 °C, **b**–**i**), in comparison with the theoretical patterns of LCP-*Cmcm* (**a**, **red**) and LCP-*Pnma* (**j**, **blue**). The quantitative transition from phase-pure LCP-*Cmcm* (**h**) to the olivine-type LCP-*Pnma* (**a**) can be observed upon heating. The reflections arising from an unidentified secondary phase are marked with the symbol ♦.

In order to elucidate the formation and stability of the phases at high temperatures without performing annealing and cooling steps in between, which is not suitable for the observation of metastable intermediates, we performed a temperature-dependent in situ powder XRD experiment between 21.8 and 600 °C. In Figure 6a, the section of the diffraction pattern is presented where the strongest reflections of LCP-*Cmcm*, (112) and (130), are observed. It can be clearly derived that the transformation to LCP-*Pnma* occurs at 575 °C. Hence, the data up to this temperature confirm the

metastable nature of LCP-*Cmcm*, which was reported previously [21]. To check the thermal stability, we further increased the temperature to 800 °C (Figure 6b). Surprisingly, the LCP-*Pnma* phase is only stable up to 625 °C, which is in strong contrast to any previous reports about the thermal behavior of olivine-type LCP [36,37]. The (101) and (210) peaks of LCP-*Pnma* are present from 575 to 625 °C. At 650 °C, no reflections are present in the measured range. Finally, starting from 675 °C, LCP-$Pn2_1a$ is formed, which is indicated by the characteristic (210) reflection. The two-phase transition temperatures found in the in situ XRD experiments are marked by two arrows in the DSC (differential scanning calorimetry) trace of Figure 4. After cooling from 800 °C to room temperature, the LCP-*Pnma* structure reemerges in the powder XRD (PXRD) pattern of the in situ study (see Figure S3). To the best of our knowledge, the complete thermal properties and phase stabilities touching all three LCP polymorphs are reported for the first time. Combining the information derived from in situ XRD and DSC experiments, it becomes obvious that the broad signal between 500 to 700 °C is caused by the phase transitions.

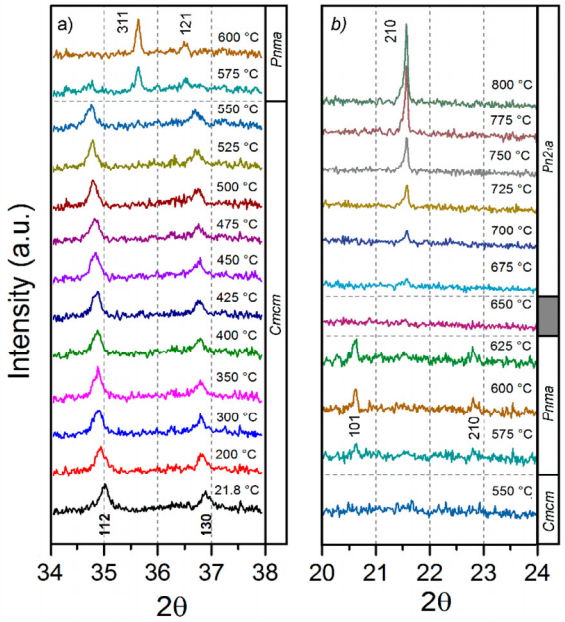

Figure 6. In situ X-ray powder diffraction patterns of LCP-*Cmcm* (PO): (**a**) Temperature range from 21.8 to 600 °C showing the transition from the *Cmcm* to the *Pnma* polymorph. The 2θ range is from 34° to 38° where the main reflection (112) of LCP-*Cmcm* is observed; (**b**) Temperature range from 550 to 800 °C in the 2θ range from 20° to 24°. The transition from the *Pnma* to the $Pn2_1a$ modification is evident from the disappearance of the *Pnma* (101) and (210) reflections and the emergence of the $Pn2_1a$ (210) reflection.

In addition, the morphology of the samples obtained from the ex situ annealing experiments on LCP-*Cmcm* (PO) was examined using SEM (Figure 7). The studies reveal that the nanosheet-like primary structure of the dumbbells continuously changes upon heating. After annealing at 400 °C (Figure 7c), the material starts to sinter and, finally, a denser and more compact material is formed. Simultaneously, the dumbbell-like shape is preserved (Figure 7d,e). At about 700 °C (Figure 7f), the phase transition of the material takes place and the dumbbells start to conglomerate. Further heating (Figure 7g,h) destroys the primary particle shape and results in irregular particles.

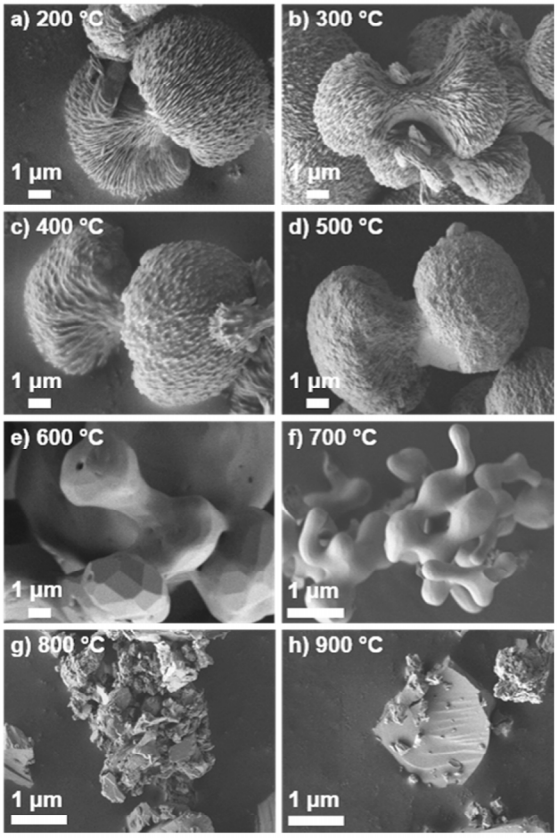

Figure 7. SEM images (**a**–**h**) of LCP-*Cmcm* (PO) after annealing in the temperature range from 200 to 900 °C (increment: 100 °C). The samples (**f**–**h**) are shown with higher resolution for clarity.

2.5. Magnetic Properties

The results of the static magnetic susceptibility as a function of the temperature measured on the LCP-*Cmcm* sample are shown in Figure 8. In the high temperature regime, the data obey the Curie-Weiss law $(\chi = \chi_0 + (N_A\mu_{eff}^2)/(3k_b(T-\theta_C)))$ with χ_0 being the temperature-independent contribution, μ_{eff} the effective magnetic moment, N_A the Avogadro number, θ_C the Weiss temperature (negative value), and k_b the Boltzmann constant. Table 2 shows the results of the Curie-Weiss fitting for the measurements at 1, 10 and 25 kOe.

Table 2. Results of the Curie-Weiss fitting in the high temperature regime for LCP-*Cmcm* sample produced by polyol method.

Variable	1 kOe	10 kOe	25 kOe
T_N (K)	12.7	12.7	9.1
θ_C (K)	−27.6	−27.7	−26.2
χ_0 (cm^3/mol)	1.35×10^{-1}	1.73×10^{-1}	1.48×10^{-1}
μ_{eff} (μ_B)	5.46	5.42	5.56

In Figure 8, the ZFC curves reveal a long range antiferromagnetic order below the Néel temperature T_N, as result of the antiparallel alignment of magnetic moments of cobalt atoms. As seen in Table 2, the values of the magnetic moments are slightly higher in comparison to the ones reported for high spin octahedral cobalt (II) complexes (4.7 to 5.2 μ_B) [38]. As reported for LCP-*Pnma*, the large value of the effective magnetic moment can be explained by the strongly coupled Co–O–Co superexchange

interactions with Co^{2+} magnetic moments or higher order interactions, such as, Co–O–P–O–Co [39,40]. On the other hand, the behavior of zero-field-cooled (ZFC) and field-cooled (FC) curves below the Néel temperature changes with the increasing magnetic field. At 1 kOe (Figure 8a) the ZFC–FC curves are overlapping, then at 10 kOe (Figure 8b), below the Néel temperature, the FC curve presents susceptibility values that are slightly higher in comparison with the ZFC data. Finally, at 25 kOe, the ZFC–FC curves present a branch point suggesting a magnetic transition depending of the temperature and magnitude of the external magnetic field. This behavior can be confirmed by the magnetization measurements. The isothermal measurements of the magnetization as a function of the applied field are shown in Figure 9. At room temperature (green line), the sample exhibits a paramagnetic behavior. However, when the temperature decreases to values near to T_N (11 K), the sample presents a slightly double hysteresis behavior (blue line) which is increased when the temperature reaches 2 K (black line). The magnetic field-induced phase transition occurs at about 10 kOe caused by the switching from an antiferromagnetic to ferro (or ferri) magnetic state upon increasing the magnetic field. In literature, a weak-ferromagnetic to an antiferromagnetic state transition in LCP-*Pnma* was reported [41], caused by a distortion of the octahedral, formed by cobalt and oxygen atoms at low temperatures (T = 23 K); however, in order to study the origin of these metamagnetic transitions as well as the magnetic structure in different magnetic states, neutron powder diffraction experiments are required for LCP-*Cmcm*.

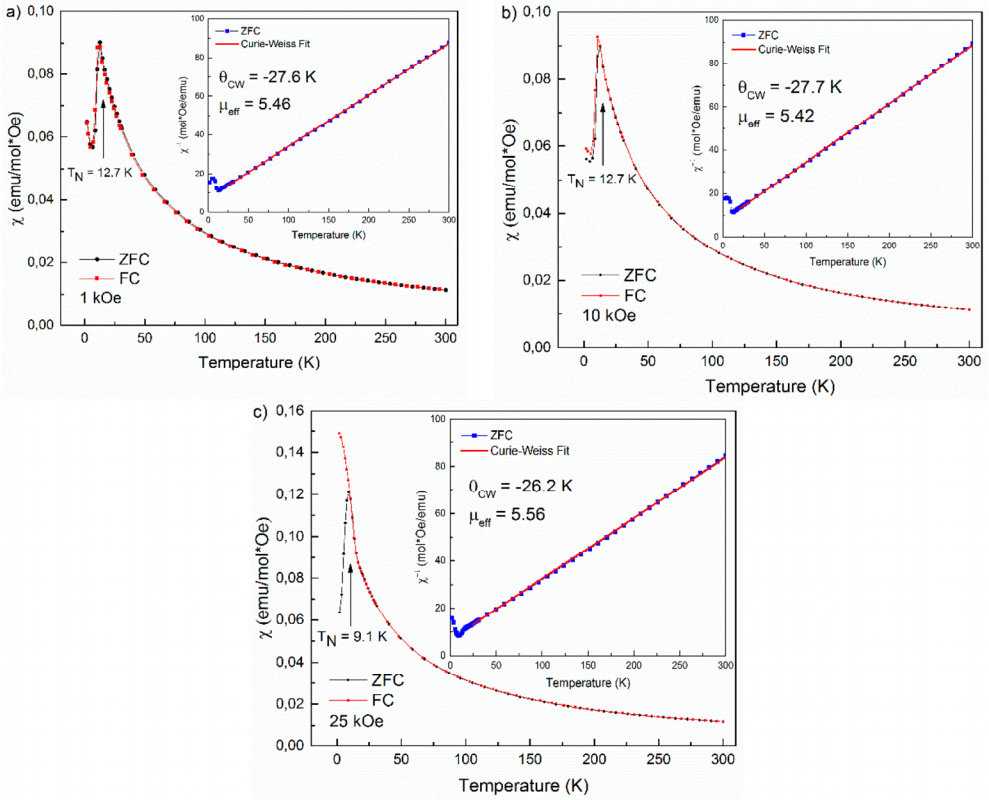

Figure 8. Magnetic susceptibility as a function of the temperature at zero-field-cooled/field-cooled (ZFC/FC) conditions under constant applied fields of: (**a**) 1 kOe; (**b**) 10 kOe; and (**c**) 25 kOe for LCP-*Cmcm* produced by polyol method. The inset shows the inverse magnetic susceptibility and the Curie-Weiss fitting of the high temperature data under ZFC conditions.

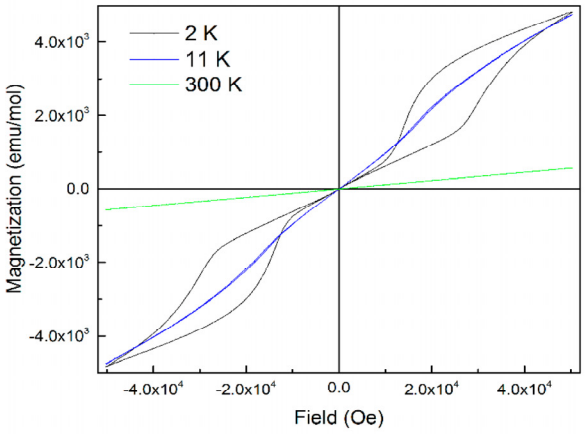

Figure 9. Magnetization as a function of the applied field between 5 and −5 T measured at 2, 11 and 300 K for the sample of LCP-*Cmcm* (PO).

3. Materials and Methods

3.1. Solvothermal Synthesis

For the solvothermal synthesis of LCP-*Cmcm*, stoichiometric amounts of $CoC_2O_4{\cdot}2H_2O$ (Alfa Aesar, Ward Hill, MA, USA, 98%) and LiH_2PO_4 (Sigma Aldrich, St. Louis, MO, USA, 99%) were introduced in 9 mL of solvent, whereas diethylene glycol (DEG; Merck, Darmstadt, Germany, ≥99.0%), triethylene glycol (TEG; Merck, ≥99%), and tetraethylene glycol (TTEG; Merck, ≥98%) were used. The resulting suspensions were homogenized for 20 min, transferred to Teflon-lined stainless steel pressure vessels (BERGHOF Products + Instruments GmbH, Eningen, Germany), and sealed. For the solvothermal treatment, the temperature was ramped to 220 °C within 2 h. After a reaction period of 7 days, the mixtures were cooled to ambient temperature. The resulting bright pink precipitates were separated by suction filtration, washed several times with distilled water (Millipore water type I, 18.2 MΩ·cm) and absolute ethanol (VWR BDH PROLABO AnalaR NORMAPUR, Radnor, PA, USA, 99.95%) followed by drying in air at 130 °C overnight.

3.2. Polyol Synthesis

Powder samples were prepared via a polyol process using cobalt acetate tetrahydrate ($Co(CH_3COO)_2{\cdot}4H_2O$, Merck, 99.99%), lithium acetate ($Li(CH_3COO)$, ChemPUR, Karlsruhe, Germany, 99+%) and H_3PO_4 (Merck, 85%) in a stoichiometric molar ratio of 1:3:10. Tetraethylene glycol (TTEG, Merck, ≥99.0%) was used as solvent. First, lithium acetate was solved in 125 mL of TTEG and, subsequently, phosphoric acid added dropwise. Cobalt acetate was dissolved in 75 mL of TTEG and then added to the prior solution. The mixture was refluxed at 200 °C for 14 h in a three-necked round bottom flask. After cooling down to room temperature, the precipitate was separated from the solvent by centrifugation (1500 rpm, 20 min) and washed several times with ethanol (VWR AnalaR NORMAPUR, 99.95%) in order to remove the solvent. The light pink powder was collected by suction filtration, washed with acetone (99% VWR, Semi grade), and dried in air at 120 °C overnight. The material obtained from the polyol process is denoted as LCP-*Cmcm* (PO).

3.3. Structural, Physical and Chemical Properties Determination

X-ray powder diffraction data were collected at room temperature on a STADI P diffractometer (STOE & Cie. GmbH, Darmstadt, Germany) using Mo Kα radiation (Ge(111) monochromator, λ = 0.70930 Å) equipped with a Mythen DCS 1K silicon solid-state detector (Dectris Ltd., Baden-Daettwil, Switzerland). The ground samples were sealed in glass capillaries (Hilgenberg,

Malsfeld, Germany, borosilicate glass type no. 50, length: 80 mm, diameter: 0.5 mm, wall thickness: 0.01 mm), which were then measured in a 2θ range of 3°–60° (PSD (position sensitive detector) step: 0.15°; time/step: 30 s, three ranges, total measurement time: 12 h). An external calibration was performed using Si (a = 5.43088 Å, NBS standard reference material). The JANA2006 software [42] was used for Rietveld analysis of the diffraction patterns. The structure data of the LNP polymorph (ICSD database no. 97767 [20]) were taken as a starting model and refined in the space group Cmcm.

The temperature-dependent XRD studies were done in situ with a Stoe STADI P diffractometer using Cu Kα radiation (Ge(111) monochromator, λ = 1.540598 Å) equipped with a Dectris Mythen 1K OEM (Dectris Ltd.) silicon solid-state detector. The data were collected between 19° and 37.93° 2θ. The detailed temperature program is provided in Table S5 in the Supplementary Materials.

High-resolution scanning electron microscopy (HR-SEM) was performed on a JSM-7500F instrument (JEOL, Tokyo, Japan) at an accelerating voltage of 1 kV. The powders were prepared on carbon tape, which was attached to an aluminum stub.

Elemental analysis of the sample was carried out by atomic absorption spectroscopy using a Varian AA280FS sequential device for the lithium and cobalt, and by photometry using a UV-160 device (Shimadzu, Kyoto, Japan) for the P contents. CHNS analysis was performed by combustion analysis using a Euro EA CHNSO Analyzer (HEKAtech, Wegberg, Germany).

Attenuated total reflectance (ATR)-FTIR data were collected on a 670 IR FTIR spectrometer (Varian, Palo Alto, CA, USA) equipped with a PIKE GladiATR ATR stage (400–4000 cm^{-1}, 132 scans) (see Supplementary Materials). The Resolution Pro software (Agilent, Santa Clara, CA, USA) was used for data handling.

The thermal analysis was carried out to assess the chemical stability of the powders up to 900 °C on a TGA/DSC 1 STAR system (Mettler Toledo, Columbus, OH, USA). Experiments were run at a heating rate of 10 °C·min^{-1} in an argon stream flowing at 10 mL·min^{-1} (specimen weight of 20 mg). The effect of the thermal treatment as a function of temperature was additionally examined using ex situ powder XRD studies (Mo Kα radiation (Ge(111) monochromator, λ = 0.70930 Å, 2θ range of 5°–50°, PSD step: 0.49°; time/step: 10 s, two ranges). For this purpose, approximately 50 mg of the sample were annealed for 6 h in air at temperatures ranging from 200 to 900 °C with an increment of 100 °C using a muffle furnace.

DC magnetization data were collected using a MPMS XL5 superconducting quantum interference device (SQUID, Quantum Design, San Diego, CA, USA). The temperature-dependent data were obtained by measurement of the magnetization from 1.8 to 300 K in an applied magnetic field of 1, 10 and 25 kOe, by using the powdered samples fixed in calibrated gelatin capsules held at the center of a drinking straw. The temperature-dependent measurements were performed in zero-field-cooled (ZFC) and field-cooled (FC) mode. Magnetization as a function of applied field measurements were done between 5 and −5 T at 2, 11 K, and room temperature.

4. Conclusions

$LiCoPO_4$-Cmcm was synthesized by two different kinetically controlled synthesis approaches. Whereas the product of the solvothermal process showed secondary phases of Li_3PO_4 and the olivine-type *Pnma* phase, the polyol process results in the formation of a single-phase LCP-Cmcm material in a one-step synthesis without post-annealing. Using the polyol method, a dumbbell-like morphology could be obtained by a simple one-step synthesis without the use of additional surfactants or templates. Moreover, by a simple methodology based on the variation of the mixing order of the educts, the morphology of the samples can be controlled. The temperature-dependent in situ powder X-ray diffraction (PXRD) analysis reveals the phase transitions between the three reported LCP polymorphs. Starting from the Cmcm phase, a transition to the *Pnma* structure is observed at 575 °C, which then converts to the $Pn2_1a$ polymorph at 675 °C. After cooling to ambient temperature, the thermodynamically stable *Pnma* modification is obtained. At temperatures above 675 °C, the $Pn2_1a$ polymorph is thermodynamically stable in contrast to that reported at room temperature. To the best

of our knowledge, this behavior is reported for the first time. Moreover, also the hitherto unknown magnetic properties of the *Cmcm* phase were investigated. The LCP-*Cmcm* polymorph shows an antiferromagnetic order below the Néel temperature at low fields (1 and 10 kOe) The measurements of the magnetic response confirm a transition from antiferromagnetic ordering to ferromagnetic (or ferrimagnetic) ordering at temperatures below T_N as a function of the applied field. This study paves the way for a novel methodology towards the synthesis and investigation of new polymorphs of transition-metal phosphates. Thus, our approach provides insights into studying potential cathode materials for lithium-ion batteries from a fundamental point of view.

Supplementary Materials: The following are available online at www.mdpi.com/2304-6740/4/4/35/s1. Rietveld refinement details, infrared spectra, PXRD pattern of the sample obtained after the temperature-dependent in situ PXRD measurement, temperature program for temperature-dependent PXRD measurements. Further details of the crystal structure investigation may be obtained from FIZ Karlsruhe, 76344 Eggenstein-Leopoldshafen, Germany (Fax: +49-7247-808-666; E-mail: crysdata@fiz-karlsruhe.de), on quoting the deposition numbers CSD 432183–432186.

Acknowledgments: The authors would like to thank the BMW AG, the DAAD, Colciencias, and the Fonds der Chemischen Industrie for financial support and the state of Bavaria and the TUM for X-Ray powder diffractometer funding. Furthermore, we thank Dr. Wilhelm Klein for the in situ XRD measurements, Katia Rodewald for SEM, Gergana Nenova for SQUID, and Pankaj Madkikar for thermogravimetric measurements. We further thank the microanalytical laboratory of the TUM for elemental analyses. Carlos Alarcón-Suesca and Jennifer Ludwig are further grateful to the DAAD, Fonds der Chemischen Industrie for their fellowships.

Author Contributions: The manuscript was written through contributions of Carlos Alarcón-Suesca, Jennifer Ludwig, Viktor Hlukhyy, Christoph Stinner and Tom Nilges. Carlos Alarcón-Suesca and Jennifer Ludwig contributed equally to this study.

Conflicts of Interest: The authors declare no conflict of interest.

References

1. Whittingham, M.S. Electrical energy storage and intercalation chemistry. *Science* **1976**, *192*, 1126–1127. [CrossRef] [PubMed]
2. Thackeray, M. Lithium-ion batteries: An unexpected conductor. *Nat. Mater.* **2002**, *1*, 81–82. [CrossRef] [PubMed]
3. Tarascon, J.M.; Armand, M. Issues and challenges facing rechargeable lithium batteries. *Nature* **2001**, *414*, 359–367. [CrossRef] [PubMed]
4. Xu, B.; Qian, D.; Wang, Z.; Meng, Y.S. Recent progress in cathode materials research for advanced lithium ion batteries. *Mater. Sci. Eng. R Rep.* **2012**, *73*, 51–65. [CrossRef]
5. Padhi, A.K.; Nanjundaswamy, K.S.; Goodenough, J.B. Phospho-olivines as positive-electrode materials for rechargeable lithium batteries. *J. Electrochem. Soc.* **1997**, *144*, 1188–1194. [CrossRef]
6. Hautier, G.; Jain, A.; Ong, S.P.; Kang, B.; Moore, C.; Doe, R.; Ceder, G. Phosphates as lithium-ion battery cathodes: An evaluation based on high-throughput ab initio calculations. *Chem. Mater.* **2011**, *23*, 3495–3508. [CrossRef]
7. Strobridge, F.C.; Clement, R.J.; Leskes, M.; Middlemiss, D.S.; Borkiewicz, O.J.; Wiaderek, K.M.; Chapman, K.W.; Chupas, P.J.; Grey, C.P. Identifying the structure of the intermediate, $Li_{2/3}CoPO_4$, formed during electrochemical cycling of $LiCoPO_4$. *Chem. Mater.* **2014**, *26*, 6193–6205. [CrossRef] [PubMed]
8. Sergio, B.; Stefania, P. Recent Advances in the Development of $LiCoPO_4$ as High Voltage Cathode Material for Li-Ion Batteries. In *Nanotechnology for Sustainable Energy*; American Chemical Society: Washington, DC, USA, 2013; Volume 1140, pp. 67–99.
9. Howard, W.F.; Spotnitz, R.M. Theoretical evaluation of high-energy lithium metal phosphate cathode materials in Li-ion batteries. *J. Power Sources* **2007**, *165*, 887–891. [CrossRef]
10. Wolfenstine, J.; Allen, J.L.; Jow, T.R.; Thompson, T.; Sakamoto, J.; Jo, H.; Choe, H. $LiCoPO_4$ mechanical properties evaluated by nanoindentation. *Ceram. Int.* **2014**, *40*, 13673–13677. [CrossRef]
11. Chen, H.; Chen, M.; Du, C.; Cui, Y.; Zuo, P.; Cheng, X.; Yin, G. Synthesis and electrochemical performance of hierarchical nanocomposite of carbon coated $LiCoPO_4$ crosslinked by graphene. *Mater. Chem. Phys.* **2016**, *171*, 6–10. [CrossRef]

12. Theil, S.; Fleischhammer, M.; Axmann, P.; Wohlfahrt-Mehrens, M. Experimental investigations on the electrochemical and thermal behaviour of $LiCoPO_4$-based cathode. *J. Power Sources* **2013**, *222*, 72–78. [CrossRef]
13. Yamada, A.; Hosoya, M.; Chung, S.-C.; Kudo, Y.; Hinokuma, K.; Liu, K.-Y.; Nishi, Y. Olivine-type cathodes: Achievements and problems. *J. Power Sources* **2003**, *119–121*, 232–238. [CrossRef]
14. Ellis, B.L.; Lee, K.T.; Nazar, L.F. Positive electrode materials for Li-ion and Li-batteries. *Chem. Mater.* **2010**, *22*, 691–714. [CrossRef]
15. Truong, Q.D.; Devaraju, M.K.; Ganbe, Y.; Tomai, T.; Honma, I. Controlling the shape of $LiCoPO_4$ nanocrystals by supercritical fluid process for enhanced energy storage properties. *Sci. Rep.* **2014**, *4*. [CrossRef] [PubMed]
16. Morgan, D.; van der Ven, A.; Ceder, G. Li conductivity in Li_xMPO_4 (M = Mn, Fe, Co, Ni) olivine materials. *Electrochem. Solid State Lett.* **2004**, *7*, A30–A32. [CrossRef]
17. Tealdi, C.; Spreafico, C.; Mustarelli, P. Lithium diffusion in $Li_{1-x}FePO_4$: The effect of cationic disorder. *J. Mater. Chem.* **2012**, *22*, 24870–24876. [CrossRef]
18. Jaehne, C.; Neef, C.; Koo, C.; Meyer, H.-P.; Klingeler, R. A new $LiCoPO_4$ polymorph via low temperature synthesis. *J. Mater. Chem. A* **2013**, *1*, 2856–2862. [CrossRef]
19. Amador, U.; Gallardo-Amores, J.M.; Heymann, G.; Huppertz, H.; Moran, E.; Arroyo, Y.D.D.M.E. High pressure polymorphs of $LiCoPO_4$ and $LiCoAsO_4$. *Solid State Sci.* **2009**, *11*, 343–348. [CrossRef]
20. Garcia-Moreno, O.; Alvarez-Vega, M.; Garcia-Alvarado, F.; Garcia-Jaca, J.; Gallardo-Amores, J.M.; Sanjuan, M.L.; Amador, U. Influence of the structure on the electrochemical performance of lithium transition metal phosphates as cathodic materials in rechargeable lithium batteries: A new high-pressure form of Li_xMPO_4 (M = Fe and Ni). *Chem. Mater.* **2001**, *13*, 2455. [CrossRef]
21. Kreder, K.J.; Assat, G.; Manthiram, A. Microwave-assisted solvothermal synthesis of three polymorphs of $LiCoPO_4$ and their electrochemical properties. *Chem. Mater.* **2015**, *27*, 5543–5549. [CrossRef]
22. Assat, G.; Manthiram, A. Rapid microwave-assisted solvothermal synthesis of non-olivine *Cmcm* polymorphs of $LiMPO_4$ (M = Mn, Fe, Co, and Ni) at low temperature and pressure. *Inorg. Chem.* **2015**, *54*, 10015–10022. [CrossRef] [PubMed]
23. Wang, F.; Zhao, M.; Song, X. Influence of the preparation conditions on the morphology and electrochemical performance of nano-sized Cu–Sn alloy anodes. *J. Alloy. Compd.* **2007**, *439*, 249–253. [CrossRef]
24. Pan, Q.; Jin, H.; Wang, H.; Yin, G. Flower-like cuo film-electrode for lithium ion batteries and the effect of surface morphology on electrochemical performance. *Electrochim. Acta* **2007**, *53*, 951–956. [CrossRef]
25. Tang, K.; Sun, J.; Yu, X.; Li, H.; Huang, X. Electrochemical performance of $LiFePO_4$ thin films with different morphology and crystallinity. *Electrochim. Acta* **2009**, *54*, 6565–6569. [CrossRef]
26. Dinh, H.-C.; Mho, S.-I.; Yeo, I.-H. Electrochemical analysis of conductive polymer-coated $LiFePO_4$ nanocrystalline cathodes with controlled morphology. *Electroanalysis* **2011**, *23*, 2079–2086. [CrossRef]
27. Ryu, W.-H.; Lim, S.-J.; Kim, W.-K.; Kwon, H. 3-D dumbbell-like $LiNi_{1/3}Mn_{1/3}Co_{1/3}O_2$ cathode materials assembled with nano-building blocks for lithium-ion batteries. *J. Power Sources* **2014**, *257*, 186–191. [CrossRef]
28. Zhou, N.; Uchaker, E.; Wang, H.-Y.; Zhang, M.; Liu, S.-Q.; Liu, Y.-N.; Wu, X.; Cao, G.; Li, H. Additive-free solvothermal synthesis of hierarchical flower-like $LiFePO_4$/C mesocrystal and its electrochemical performance. *RSC Adv.* **2013**, *3*, 19366–19374. [CrossRef]
29. Cao, J.; Zhu, Y.; Bao, K.; Shi, L.; Liu, S.; Qian, Y. Microscale Mn_2O_3 hollow structures: Sphere, cube, ellipsoid, dumbbell, and their phenol adsorption properties. *J. Phys. Chem. C* **2009**, *113*, 17755–17760. [CrossRef]
30. Zeng, G.; Caputo, R.; Carriazo, D.; Luo, L.; Niederberger, M. Tailoring two polymorphs of $LiFePO_4$ by efficient microwave-assisted synthesis: A combined experimental and theoretical study. *Chem. Mater.* **2013**, *25*, 3399–3407. [CrossRef]
31. Eftekhari, A. Surface modification of thin-film based $LiCoPO_4$ 5 V cathode with metal oxide. *J. Electrochem. Soc.* **2004**, *151*, A1456–A1460. [CrossRef]
32. Choi, D.; Li, X.; Henderson, W.A.; Huang, Q.; Nune, S.K.; Lemmon, J.P.; Sprenkle, V.L. $LiCoPO_4$ cathode from a $CoHPO_4 \cdot xH_2O$ nanoplate precursor for high voltage Li-ion batteries. *Heliyon* **2016**, *2*, e00081. [CrossRef] [PubMed]
33. Ludwig, J.; Marino, C.; Haering, D.; Stinner, C.; Nordlund, D.; Doeff, M.M.; Gasteiger, H.A.; Nilges, T. Facile, ethylene glycol-promoted microwave-assisted solvothermal synthesis of high-performance $LiCoPO_4$ as a high-voltage cathode material for lithium-ion batteries. *RSC Adv.* **2016**, *6*, 82984–82994. [CrossRef]

34. Yang, H.; Wu, X.-L.; Cao, M.-H.; Guo, Y.-G. Solvothermal synthesis of $LiFePO_4$ hierarchically dumbbell-like microstructures by nanoplate self-assembly and their application as a cathode material in lithium-ion batteries. *J. Phys. Chem. C* **2009**, *113*, 3345–3351. [CrossRef]
35. Mathew, V.; Alfaruqi, M.H.; Gim, J.; Song, J.; Kim, S.; Ahn, D.; Kim, J. Morphology-controlled $LiFePO_4$ cathodes by a simple polyol reaction for Li-ion batteries. *Mater. Charact.* **2014**, *89*, 93–101. [CrossRef]
36. Ni, J.; Wang, H.; Gao, L.; Lu, L. A high-performance $LiCoPO_4$/C core/shell composite for Li-ion batteries. *Electrochim. Acta* **2012**, *70*, 349–354. [CrossRef]
37. Huang, X.; Ma, J.; Wu, P.; Hu, Y.; Dai, J.; Zhu, Z.; Chen, H.; Wang, H. Hydrothermal synthesis of $LiCoPO_4$ cathode materials for rechargeable lithium ion batteries. *Mater. Lett.* **2005**, *59*, 578–582. [CrossRef]
38. Nicholls, D. 41-Cobalt. In *The Chemistry of Iron, Cobalt and Nickel*; Pergamon Press: Oxford, UK, 1973; pp. 1053–1107.
39. Szewczyk, A.; Gutowska, M.U.; Wieckowski, J.; Wisniewski, A.; Puzniak, R.; Diduszko, R.; Kharchenko, Y.; Kharchenko, M.F.; Schmid, H. Phase transitions in single-crystalline magnetoelectric $LiCoPO_4$. *Phys. Rev. B* **2011**, *84*, 104419. [CrossRef]
40. Tian, W.; Li, J.; Lynn, J.W.; Zarestky, J.L.; Vaknin, D. Spin dynamics in the magnetoelectric effect compound $LiCoPO_4$. *Phys. Rev. B* **2008**, *78*, 6. [CrossRef]
41. Rhee, C.H.; Kim, S.J.; Kim, C.S. Crystallographic and magnetic properties of $LiCoPO_4$ at low temperature. *J. Korean Phys. Soc.* **2010**, *56*, 611–614.
42. Petricek, V.; Dusek, M.; Palatinus, L. Crystallographic computing system Jana2006: General features. *Z. Kristallogr.* **2014**, *229*, 345–352.
43. Finger, L.W.; Cox, D.E.; Jephcoat, A.P. A correction for powder diffraction peak asymmetry due to axial divergence. *J. Appl. Crystallogr.* **1994**, *27*, 892–900. [CrossRef]
44. Cromer, D.T.; Liberman, D.A. Anomalous dispersion calculations near to and on the long-wavelength side of an absorption edge. *Acta Crystallogr. Sect. A* **1981**, *A37*, 267–268. [CrossRef]
45. Berar, J.F.; Lelann, P. E.S.D.'s and estimated probable error obtained in rietveld refinements with local correlations. *J. Appl. Crystallogr.* **1991**, *24*, 1–5. [CrossRef]
46. Steger, E.; Herzog, K. Zum schwingungsspektrum der phosphorsäure. I. Infrarot- und raman-spektren von phosphatlösungen. *Z. Anorg. Allg. Chem.* **1964**, *331*, 169–182. [CrossRef]
47. Jastrzębski, W.; Sitarz, M.; Rokita, M.; Bułat, K. Infrared spectroscopy of different phosphates structures. *Spectrochim. Acta A Mol. Biomol. Spectrosc.* **2011**, *79*, 722–727. [CrossRef] [PubMed]
48. Poovizhi, P.N.; Selladurai, S. Study of pristine and carbon-coated $LiCoPO_4$ olivine material synthesized by modified sol-gel method. *Ionics* **2011**, *17*, 13–19. [CrossRef]
49. Burba, C.M.; Frech, R. Vibrational spectroscopic investigation of structurally-related $LiFePO_4$, $NaFePO_4$, and $FePO_4$ compounds. *Spectrochim. Acta A Mol. Biomol. Spectrosc.* **2006**, *65*, 44–50. [CrossRef] [PubMed]

Inorganics **2016**, *4*, 35

Supplementary Materials: In Situ Studies and Magnetic Properties of the *Cmcm* Polymorph of $LiCoPO_4$ with a Hierarchical Dumbbell-Like Morphology Synthesized by Easy Single-Step Polyol Synthesis

Carlos Alarcón-Suesca, Jennifer Ludwig, Viktor Hlukhyy, Christoph Stinner and Tom Nilges

1. Structural, Physical and Chemical Properties

1.1. Rietveld Refinement Details

The background profile, which can rather be attributed to the capillaries used than to amorphous components of the material, was fitted with a Chebyshev polynomial function with 35 coefficients. Thereafter, the lattice parameters as well as the zero-point and scale factor were refined. A pseudo-Voigt profile function with three Gaussian and one Lorentzian coefficients was used for modeling the shape of the diffraction peaks; the profile was cut outside the 8 FWHM range. Because the FWHM of the peaks exhibited a marked anisotropy, anisotropic strain broadening implemented in JANA2006 [42] was tentatively refined. No correction for preferred orientation was applied. Peak asymmetry, which was especially observed at low scattering angles, was corrected by the axial divergence model described by Finger et al. [43]. The empirical starting values of the parameters S/L and H/L were set to −0.011 and 0.06, according to the characteristics of the instrument. The refinement of the general atomic positions of Co, P, and O was performed unrestrictedly, the atomic site occupancies as well as the thermal parameters were fixed. As Li positions and thermal displacement parameters cannot be deduced by means of X-ray diffraction because of the low atomic scattering factor, they have been fixed as well. After applying an absorption correction (estimated packing fraction ~0.6) [44], the temperature factors of the Co, P and O sites were refined freely. Finally, the Berar's factor was applied to obtain more realistic standard uncertainties [45].

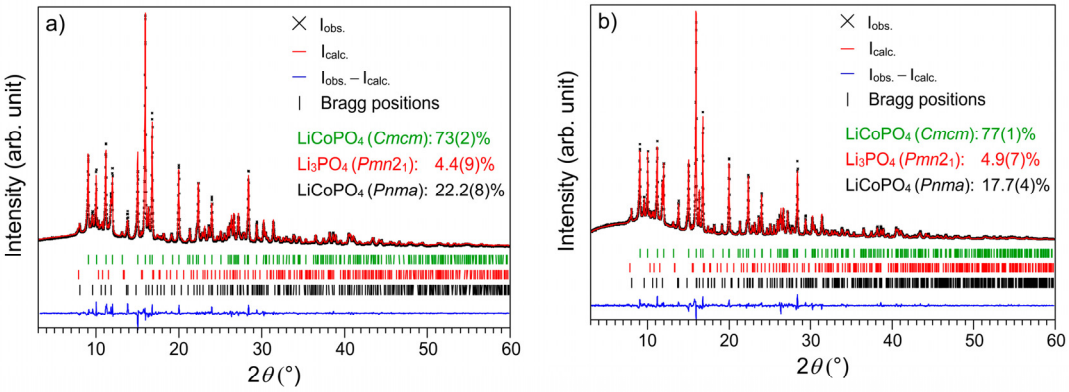

Figure S1. Rietveld fits of the X-ray powder diffraction patterns of LCP-*Cmcm* obtained from solvothermal synthesis using (**a**) TEG; and (**b**) TTEG as solvents.

Table S1. Crystallographic data, details of data collection, and structure refinement of LCP-*Cmcm* prepared by (a) solvothermal (ST) ((a) DEG, (b) TEG, and (c) TTEG solvent) and (d) polyol (PO) syntheses as refined from X-ray powder diffraction data at T = 298 K [a].

	(a) LCP (ST-DEG)	(b) LCP (ST-TEG)	(c) LCP (ST-TTEG)	(d) LCP (PO)
M_r (g·mol^{-1})	160.8			
Crystal system	orthorhombic			
Space group	*Cmcm* (no. 63)			
Z	4			
a (Å)	5.4347(4)	5.4354(5)	5.4341(4)	5.4433(3)
b (Å)	8.1638(5)	8.1680(7)	8.1676(5)	8.1694(4)
c (Å)	6.2135(4)	6.2159(5)	6.2176(4)	6.2129(3)
V (Å3)	275.68(3)	275.97(4)	275.96(3)	276.28(2)
F(000)	112	112	112	308
ρ (calcd) (g·cm^{-1})	3.8753(6)	3.8713(8)	3.8714(6)	3.8657(4)
R_p	0.032	0.041	0034	0.021
R_{wp}	0.041	0.057	047	0.027
R_{exp}	0.026	0.026	0.030	0.025
R_F	0.018	0.024	0.027	0.013
χ^2	1.57	2.16	1.57	1.08
Data/restraints/parameter	3802/0/75	3800/0/75	3800/0/75	3835/0/55
Phase composition	93(2) wt % $LiCoPO_4$ (*Cmcm*) 3.4(4) wt % $LiCoPO_4$ (*Pnma*) 4(2) wt % Li_3PO_4 ($Pmn2_1$)	73(2) wt % $LiCoPO_4$ (*Cmcm*) 22.2(8) wt % $LiCoPO_4$ (*Pnma*) 4.4(9) wt % Li_3PO_4 ($Pmn2_1$)	77(1) wt % $LiCoPO_4$ (*Cmcm*) 17.7(4) wt % $LiCoPO_4$ (*Pnma*) 4.9(7) wt % Li_3PO_4 ($Pmn2_1$)	100 wt % $LiCoPO_4$ (*Cmcm*)

[a] The estimated standard deviations (E.S.D's) were calculated by means of the Berar's procedure und are indicated in round brackets.

Table S2. Fractional atomic coordinates and isotropic thermal displacement parameters of (a) LCP-*Cmcm* (ST; from DEG), and (b) LCP-*Cmcm* (PO) as refined from X-ray powder diffraction data at T = 298 K [a].

Sample	Atom	Wyckoff Position	x/a	y/b	z/c	U_{iso} (Å^2)
LCP-*Cmcm* (ST)	Li1	4*c*	0	0.675 [b]	¼	0.019 [b]
	Co1	4*a*	0	0	0	0.0107(9)
	P1	4*c*	0	0.3527(6)	¼	0.0118(13)
	O1	8*f*	0	0.2469(6)	0.0505(11)	0.007(2)
	O2	8*g*	0.2289(9)	0.4653(8)	¼	0.006(2)
LCP-*Cmcm* (PO)	Li1	4*c*	0	0.675 [b]	¼	0.019 [2]
	Co1	4*a*	0	0	0	0.0107(5)
	P1	4*c*	0	0.3523(4)	¼	0.0064(8)
	O1	8*f*	0	0.2474(4)	0.0500(7)	0.0039(13)
	O2	8*g*	0.2255(6)	0.4653(5)	¼	0.0028(12)

[a] The estimated standard deviations (E.S.D's) were calculated by means of the Berar's procedure und are indicated in round brackets; [b] Li positions and thermal factors have been fixed as they cannot be deduced by means of X-ray diffraction due to the low atomic scattering factor.

Table S3. Selected interatomic distances in (a) LCP-*Cmcm* (ST; from DEG), and (b) LCP-*Cmcm* (PO) as refined from X-ray powder diffraction data at T = 298 K [a].

Sample	Atom Pair			d (Å)
(a) LCP-*Cmcm* (ST)	Li1	O1	×2	1.973(6)
		O2	×2	2.116(6)
	Co1	O1	×2	2.040(5)
		O2	×4	2.159(3)
	P1	O1	×2	1.511(7)
		O2	×2	1.547(6)
(b) LCP-*Cmcm* (PO)	Li1	O1	×2	1.968(4)
		O2	×2	2.107(4)
	Co1	O1	×2	2.045(3)
		O2	×4	2.174(2)
	P1	O1	×2	1.510(4)
		O2	×2	1.536(4)

[a] The estimated standard deviations (E.S.D's) were calculated by means of the Berar's procedure und are indicated in round brackets.

1.2. Infrared Spectroscopy

Attenuated total reflectance (ATR)-Fourier transform infrared spectroscopy (FTIR) data were collected on a Varian 670 IR FTIR spectrometer equipped with a PIKE GladiATR ATR stage (400–4000 cm^{-1}, 132 scans). The Agilent Resolution Pro software was used for data handling. Figure S2 shows the FT-IR spectrum of *Cmcm*-$LiCoPO_4$. Generally, the spectra of $LiCoPO_4$ polymorphs are dominated by the fundamental vibrations of the $[PO_4]^{3-}$ groups, which involve the displacement of oxygen atoms of the tetrahedral $[PO_4]^{3-}$ anions. Hence, the observed frequencies are closely related to those of the free phosphate molecule [46]. In the spectrum, four fundamental vibrations are present: symmetric bending vibrations (doublet) of O–P–O (ν_2 at 466–644 cm^{-1}), antisymmetric bending vibrations of the O–P–O fragment (ν_4 around 644 cm^{-1}), asymmetric stretching vibrations (triplet) of P–O (ν_3 around 1058 cm^{-1}), and symmetric stretching vibrations of P–O bond (ν_1 967–1146 cm^{-1}). Out of these, only the vibrations ν_2 and ν_3 are infrared active. However, theoretically non-active vibrations can be observed. Hence, a band due to symmetric stretching vibration around 937–970 cm^{-1} and a band due to deformation vibrations around 358–420 cm^{-1} are expected in some cases [47,48]. Table S4 resumes the assignments of the IR vibrations. Here, two main regions can be distinguished: The first between 400 and 700 cm^{-1} is associated with the intramolecular $[PO_4]^{3-}$ bending modes (ν_2 and ν_4); the region from 900 to 1200 cm^{-1} corresponds to the intramolecular stretching vibrations of the tetrahedral anion (ν_1 and ν_3). Furthermore, the spectrum shows a splitting in the relative intensities of the intramolecular $[PO_4]^{3-}$ bands due to the difference of the specific interactions between the diverse ions and the unit cell, specifically between the monovalent lithium ion and the phosphate anion [48]. In addition to that, the bands below 500 cm^{-1} could be attributed to Li-ion "cage modes," which represent translational vibrations of the Li-ions inside a potential energy environment determined by the neighbor oxygen atoms; however, due to splitting effect, this bands are overlapping with the phosphate bending vibrations [49].

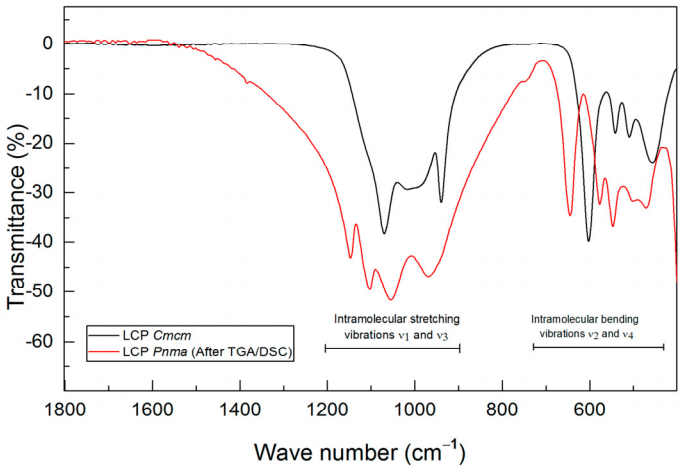

Figure S2. Comparison of the FTIR spectra of (**a**) the *Cmcm*-LCP (PO) obtained from the polyol route (**black**); and (**b**) *Pnma*-LCP obtained after the TGA/DSC measurement at 900 °C (**red**).

Table S4. Assignments of the internal and external IR vibrations for (a) LCP-*Cmcm* (PO) and (b) LCP-*Pnma* obtained after the TGA/DSC experiment.

	FT-IR Assignment	**Frequency (cm^{-1})**	
	Vibrational mode	**(a) LCP-*Cmcm***	**(b) LCP-*Pnma***
Intramolecular bending modes	Li^+ ion "cage modes"	457	470
	Symmetric bending vibration O–P–O	511	501
		541	547
	Asymmetric stretching modes [CoO_6] octahedra	603	577
	Asymmetric bending vibration O–P–O	-	646
Intramolecular stretching modes	Symmetric stretching vibrations P–O	941	970
	Asymmetric stretching vibrations P–O	1002	1050
	Asymmetric stretching vibration P=O	1071	1103
		–	1147

1.3. Temperature-Dependent In Situ X-Ray Powder Diffraction

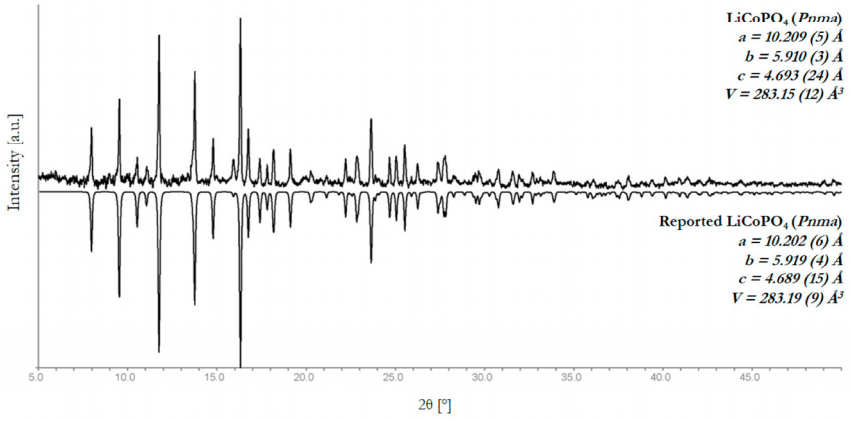

Figure S3. Room temperature PXRD of a LCP-*Cmcm* (PO) sample after the temperature-dependent in situ PXRD experiment. Heating to 800 °C and cooling to room temperature resulted in LCP-*Pnma* as the final product.

Table S5. Temperature program used for temperature-dependent PXRD measurements.

Temperature Range			Heating Rate
20 °C	to	200 °C	(50 °C/min)
200 °C	to	300 °C	(50 °C/min)
300 °C	to	350 °C	(10 °C/min)
350 °C	to	400 °C	(10 °C/min)
400 °C	to	425 °C	(2° C/min)
425 °C	to	450 °C	(2° C/min)
450 °C	to	475 °C	(2° C/min)
475 °C	to	500 °C	(2° C/min)
500 °C	to	525 °C	(10 °C/min)
525 °C	to	550 °C	(10 °C/min)
550 °C	to	575 °C	(10 °C/min)
575 °C	to	600 °C	(10 °C/min)
600 °C	to	625 °C	(10 °C/min)
625 °C	to	650 °C	(10 °C/min)
650 °C	to	675 °C	(10 °C/min)
675 °C	to	700 °C	(10 °C/min)
700 °C	to	725 °C	(10 °C/min)
725°C	to	750 °C	(10 °C/min)
750 °C	to	775 °C	(10 °C/min)
775 °C	to	800 °C	(10 °C/min)

6.8 Direct Synthesis and Characterization of Mixed-Valent $Li_{0.5-\delta}CoPO_4$, a Li-Deficient Derivative of the *Cmcm* Polymorph of $LiCoPO_4$

Jennifer Ludwig,[a] Carlos Alarcón-Suesca,[a] Stephan Geprägs,[b] Dennis Nordlund,[c] Marca M. Doeff,[d] Inés Puente Orench,[e,f,] and Tom Nilges[a]

[a] Technical University of Munich, Department of Chemistry, Synthesis and Characterization of Innovative Materials, Lichtenbergstr. 4, 85747 Garching, Germany

[b] Walther Meissner Institute, Bavarian Academy of Sciences and Humanities, Walther-Meissner-Str. 8, 85747 Garching, Germany

[c] Stanford Synchrotron Radiation Lightsource, SLAC National Accelerator Laboratory, 2575 Sand Hill Rd, Menlo Park, CA, 94025, USA

[d] Lawrence Berkeley National Laboratory, Energy Storage and Distributed Resources Division, 1 Cyclotron Rd, Berkeley, CA, 94720, USA

[e] Instituto de Ciencia de Materiales de Aragón, Pedro Cerbuna 12, 50009 Zaragoza, Spain

[f] Institut Laue-Langevin, 71 avenue des Martyrs, B.P. 156, 38042 Grenoble Cedex 9, France

RSC Adv. **2017,** *7*, 28069–28081.
DOI: 10.1039/c7ra04043a

Ludwig, J.; Alarcón-Suesca, C.; Geprägs, S.; Nordlund, D.; Doeff, M. M.; Puente Orench, I.; Nilges, T., Direct synthesis and characterization of mixed-valent $Li_{0.5-\delta}CoPO_4$, a Li-deficient derivative of the *Cmcm* polymorph of $LiCoPO_4$. *RSC Adv.* **2017,** *7,* 28069–28081. – Published by The Royal Society of Chemistry.

RSC Advances

PAPER

View Article Online
View Journal | View Issue

Cite this: *RSC Adv.*, 2017, **7**, 28069

Direct synthesis and characterization of mixed-valent $Li_{0.5-\delta}CoPO_4$, a Li-deficient derivative of the *Cmcm* polymorph of $LiCoPO_4$†

Jennifer Ludwig,[a] Carlos Alarcón-Suesca,[a] Stephan Geprägs,[b] Dennis Nordlund,[c] Marca M. Doeff,[d] Inés Puente Orench[ef] and Tom Nilges *[a]

While the majority of research activities on $LiCoPO_4$ is focussed on the thermodynamically stable olivine-type *Pnma* polymorph, the metastable $Pna2_1$ and *Cmcm* modifications have recently attracted considerable attention due to their interesting material properties. In this study, we present the first Li-deficient structural derivative of the *Cmcm* modification with the nominal composition $Li_{0.5-\delta}CoPO_4$. As opposed to the substoichiometric olivine (*Pnma*) phases Li_xCoPO_4 ($x = 0$; 2/3), which are exclusively accessible by electrochemical or chemical Li extraction techniques, this is also the first time that a direct soft-chemical synthesis route towards a Li_xCoPO_4-type material is accomplished. X-ray and neutron diffraction studies indicate that *Cmcm*-type $Li_{0.5-\delta}CoPO_4$ shows vacancies on both the Li and Co sites, whereas X-ray absorption spectra demonstrate that the structure features heterovalent Co ions (+2/+3) to compensate for the Li deficit. Magnetic measurements reveal a long-range antiferromagnetic order below 10.5 K. A thorough investigation of the thermal stability using thermogravimetric analysis, differential scanning calorimetry, and temperature-dependent *in situ* X-ray powder diffraction demonstrates that $Li_{0.5-\delta}CoPO_4$ is metastable and exhibits a complex, multi-step thermal decomposition mechanism. In the first step at 394 °C, it decomposes to α-$Co_2P_2O_7$ ($P2_1/c$) and $LiCoPO_4$ (*Cmcm*) upon O_2 release. The $LiCoPO_4$ (*Cmcm*) intermediate is then irreversibly transformed to olivine-type $LiCoPO_4$ (*Pnma*) at 686 °C. The material properties of $Li_{0.5-\delta}CoPO_4$ are further compared to the fully lithiated, isostructural $LiCoPO_4$ (*Cmcm*) phase, for which an improved structure solution as well as Co $L_{2,3}$-edge X-ray absorption spectra are reported for the first time.

Received 9th April 2017
Accepted 14th May 2017

DOI: 10.1039/c7ra04043a

rsc.li/rsc-advances

Introduction

In the last two decades, thermodynamically stable, olivine-type (space group: *Pnma*) $LiCoPO_4$ polymorphs have been extensively studied as a high-voltage cathode material for lithium-ion batteries (operating voltage: ~4.8 V *vs.* Li/Li^+; theoretical capacity: 167 mA h g^{-1}).[1–4] The three-dimensional network structure features $[CoO_6]$ octahedra, $[PO_4]$ tetrahedra, and Li^+ ions in octahedral voids.[5] The majority of research activities have been focused on optimizing the electrochemical performance of the material.[4,6,7] However, despite intensive efforts, the nature of the intermediate phase Li_xCoPO_4, which occurs upon the two-step Li insertion–extraction reaction of $LiCoPO_4$,[8] is still under investigation and debated in the literature. Earlier

[a]*Technical University of Munich, Department of Chemistry, Synthesis and Characterization of Innovative Materials, Lichtenbergstr. 4, 85747 Garching, Germany. E-mail: tom.nilges@lrz.tum.de*

[b]*Walther Meissner Institute, Bavarian Academy of Sciences and Humanities, Walther-Meissner-Str. 8, 85747 Garching, Germany*

[c]*Stanford Synchrotron Radiation Lightsource, SLAC National Accelerator Laboratory, 2575 Sand Hill Rd, Menlo Park, CA, 94025, USA*

[d]*Lawrence Berkeley National Laboratory, Energy Storage and Distributed Resources Division, 1 Cyclotron Rd, Berkeley, CA, 94720, USA*

[e]*Instituto de Ciencia de Materiales de Aragón, Pedro Cerbuna 12, 50009 Zaragoza, Spain*

[f]*Institut Laue-Langevin, 71 Avenue des Martyrs, B.P. 156, 38042 Grenoble Cedex 9, France*

† Electronic supplementary information (ESI) available: (1) Comparison of the PXRD patterns of $Li_{0.5-\delta}CoPO_4$ and $Li_{1-\gamma}CoPO_4$, (2) Rietveld refinement details from PXRD data, (3) Rietveld refinement details from neutron powder diffraction data, (4) additional illustrations of the crystal structure, (5) electrochemical characterization, (6) SEM and EDS analysis, (7) full IR spectra, (8) additional magnetic data, (9) Rietveld refinement details of the PXRD pattern of the sample obtained from the TGA/DSC measurement of $Li_{0.5-\delta}CoPO_4$ under air, (10) thermal stability under Ar (TGA/DSC, Rietveld refinement), (11) Rietveld fits and crystallographic data of the *in situ* PXRD patterns (30–700 °C; air), (12) additional *in situ* PXRD patterns (800 °C, 900 °C, and 25 °C; air). The cif files containing the crystallographic data of $Li_{0.5-\delta}CoPO_4$ and $Li_{1-\gamma}CoPO_4$ can be obtained from FIZ Karlsruhe, 76344 Eggenstein-Leopoldshafen, Germany (fax: +49 7247 808 666; e-mail: crysdata@fiz-karlsruhe.de), on quoting the CSD deposition numbers 432850 and 432851. For ESI and crystallographic data in CIF or other electronic format see DOI: 10.1039/c7ra04043a

investigations suggested compositions of $Li_{0.7}CoPO_4$ (ref. 8) and $Li_{0.6}CoPO_4$,[9] respectively, whereas a later report[10] stated a Li_x-$CoPO_4$ (x = 0.20–0.45) composition. Recently, the lithiation state of the intermediate was determined to be $Li_{2/3}CoPO_4$ by two independent studies.[11,12] Since the completely delithiated phase $CoPO_4$ is unstable and undergoes amorphization when exposed to air or moisture,[8,9] the application of inert gas atmospheres and/or *in situ* techniques is crucial. According to Bramnik *et al.*,[13] both lithium-poor, Co^{3+}-containing phases are intrinsically instable and exhibit a low thermal stability. Charged $LiCoPO_4$ electrodes were shown to decompose rapidly at temperatures below 200 °C, leading to gas evolution and the crystallization of $LiCoPO_4$ (only in the case of Li_xCoPO_4) and $Co_2P_2O_7$. In contrast, Theil *et al.*[14] claimed that Li_xCoPO_4 is thermally stable up to 550 °C and that the thermal instability of charged $LiCoPO_4$ electrodes can be solely ascribed to the instability of the $CoPO_4$ phase. To the best of our knowledge, these Li-deficient phases are exclusively accessible by electrochemical or chemical Li extraction from $LiCoPO_4$ (*Pnma*),[9,13] and a direct synthesis route has not been reported to date. Interestingly, in contrast to previous reports,[15,16] we recently demonstrated[17] that also the fully lithiated olivine-type $LiCoPO_4$ does not exhibit unlimited thermal stability since it transforms to the (at room temperature) metastable $Pna2_1$-$LiCoPO_4$ phase around 900 °C.

The less common, metastable $LiCoPO_4$ modifications, which crystallize in the space groups $Pna2_1$ (ref. 16, 18 and 19) and *Cmcm*, (ref. 16, 20 and 21) have recently attracted attention because of their interesting material properties and potential applicability as cathode materials for Li-ion batteries. The $Pna2_1$ modification exhibits a network of $[PO_4]$ and $[CoO_4]$ tetrahedra and Li^+ ions on tetrahedral sites.[18] To date, the polymorph has only been accessible by microwave-assisted synthesis techniques.[16,18,19] $Pna2_1$-type $LiCoPO_4$ shows the highest redox potential of ~5.0 V *vs.* Li/Li^+ compared to the other two $LiCoPO_4$ polymorphs.[16,18] A single redox peak was observed upon cycling, indicating that the compound is delithiated in one step. However, the electrochemical performance was found to be poor (maximum capacity: 33 mA h g^{-1}).[16,18,19] Magnetic measurements indicated a paramagnetic Curie–Weiss-like behavior at high temperatures, and a long-range antiferromagnetic order below T_N = 11 K.[18] Recently, a structure redetermination suggested that the material is non-stoichiometric and shows Li–Co anti-site defects, which provide an explanation for this poor performance.[19] A thorough investigation of the thermal stability revealed that $LiCoPO_4$ ($Pna2_1$) converts to the olivine $LiCoPO_4$ (*Pnma*) modification at 527 °C.[19] Interestingly, the $Pna2_1$ structure re-emerges as a stable high-temperature phase above 800 °C.[19]

The $LiCoPO_4$ (*Cmcm*) polymorph was first reported by Amador *et al.*[20] using a high-pressure, high-temperature synthesis route (6 GPa, 900 °C). Alternative pathways using low-temperature procedures such as microwave-assisted solvothermal[16] and polyol[21] synthesis have been demonstrated recently. The structure is built from $[CoO_6]$ and $[PO_4]$ units, with Li^+ ions occupying tetrahedral sites. $LiCoPO_4$ (*Cmcm*) shows a single redox peak at ~4.3 V *vs.* Li/Li^+ upon cycling,[16] which corresponds to the lowest redox potential of all the $LiCoPO_4$ polymorphs. A discharge capacity of only 6 mA h g^{-1} has been reported, which was associated with the poor conductivity of the material.[16] The magnetic characterization suggested a long-range antiferromagnetic order below T_N = 11 K at low fields (10 kOe) and the presence of a metamagnetic transition.[21] Investigations on the thermal stability showed that the structure is metastable and transforms to olivine-type $LiCoPO_4$ (*Pnma*) at 575 °C, which then transforms to the $Pna2_1$ modification at 675 °C. The thermodynamically stable *Pnma*-$LiCoPO_4$ phase was obtained after cooling.[21]

Based on our previous work on the three $LiCoPO_4$ polymorphs,[17,19,21] we herein present the first Li-deficient structural derivative of the *Cmcm* modification with the nominal composition $Li_{0.5-\delta}CoPO_4$. To the best of our knowledge, this is the first time that a sub-stoichiometric Li_xCoPO_4 phase has been synthesized directly (bottom-up) by a soft-chemical polyol approach as opposed to electrochemical or electrochemical Li extraction (top-down) techniques described in the literature.[9,13] The structure, morphology, oxidation state as well as electrochemical and magnetic properties of the novel *Cmcm*-type phase $Li_{0.5-\delta}CoPO_4$ are investigated. Moreover, the thermal properties are studied using thermogravimetry, differential scanning calorimetry, and temperature-dependent *in situ* X-ray powder diffraction. The results are discussed in context of the 'fully lithiated' $LiCoPO_4$ (*Cmcm*) phase, for which an improved structure solution (revealing a sub-stoichiometry reflected by the revised empirical formula $Li_{1-\gamma}CoPO_4$) as well as X-ray absorption spectra are presented for the first time.

Experimental

Synthesis of $Li_{0.5-\delta}CoPO_4$ (*Cmcm*) and $Li_{1-\gamma}CoPO_4$ (*Cmcm*)

Cmcm-type $LiCoPO_4$ samples with varied Li contents were obtained from a polyol process as described in our previous work[21] using $LiCH_3COO$ (ChemPur, 99+%), $(Co(CH_3COO)_2 \cdot 4H_2O$, Merck, 99.99%), and H_3PO_4 (Merck, 85 wt%) as precursors, and tetraethylene glycol (TTEG, Merck, ≥99.0%) as solvent. For the synthesis of $Li_{1-\gamma}CoPO_4$ (*Cmcm*), a Li : Co : P molar ratio of 3 : 1 : 10 was used, whereas $Li_{0.5-\delta}CoPO_4$ (*Cmcm*) was obtained from a modified process using a ratio of 1 : 1 : 10. First, H_3PO_4 was added dropwise to a solution of cobalt acetate in 125 mL TTEG. Then, a second solution containing lithium acetate in 75 mL TTEG was added. The resulting mixture was refluxed at 185 °C for 14 h in a round-bottom flask. After cooling, the precipitate was recovered by centrifugation (1500 rpm, 20 min, three times) and washed with ethanol (VWR AnalaR NORMAPUR, 99.95%). The light pink powder (*cf.* graphical abstract) was collected by filtration, washed with acetone (99%), and dried in air at 100 °C for 14 h. Note that in contrast to the delithiated *Pnma* structures Li_xCoPO_4 and in particular $CoPO_4$, which are sensitive to air and moisture,[8,9] the *Cmcm*-derivative $Li_{0.5-\delta}$-$CoPO_4$ is stable under air for at least several months.

X-ray powder diffraction (PXRD) and Rietveld refinement details

Room-temperature PXRD data of the ground powders sealed in borosilicate glass capillaries (0.5 mm, Hilgenberg) were

View Article Online
Paper RSC Advances

collected on a Stoe STADI P diffractometer (Mo $K_{\alpha 1}$ radiation, λ = 0.70930 Å; Ge(111) monochromator; Dectris MYTHEN DCS 1K silicon solid-state detector) in a 2θ range of 3–60° (PSD step: 0.015°; time per step: 30 s, three ranges, total measurement time: 12 h). The diffraction patterns were calibrated using an external silicon standard. The Jana2006 software[22] was used for the structure refinement by the Rietveld method, using the recently reported structure solution of $LiCoPO_4$ (*Cmcm*; ICSD no. 432186)[21] as a starting model. Details on the Rietveld refinement strategy and parameters used can be found in our previous work.[21]

Neutron powder diffraction (NPD) experiments

Neutron powder diffraction data were collected using the diffractometer D2B at the Institut Laue-Langevin (ILL, Grenoble, France), working at a calibrated wavelength of 1.5942 Å in a 2θ range of 5–160°. The data were recorded at 296 K with a collection time of 4 h per pattern. The data were analyzed by the Rietveld method with the FULLPROF program.[23] The line shape of the diffraction peaks was generated by a pseudo-Voigt function. The instrumental contribution to the peak broadening was determined using an instrument resolution function built from the refinement of a $Na_2Ca_3Al_2F_{14}$ standard, while the wavelength was refined using a Si standard.

Elemental analysis

Analysis of the Li, Co, and P contents was carried out by atomic absorption spectroscopy (AAS, Varian AA280FS sequential device) and photometry (Shimadzu UV-160 photometer). A Hekatech Euro EA CHNSO combustion analyzer was used to determine the C, H, N, and S amounts.

Soft X-ray absorption spectroscopy (soft XAS)

Co $L_{2,3}$-edge soft XAS spectra were collected at beamline 8–2 of Stanford Synchrotron Radiation Lightsource (SSRL), operating the spherical grating monochromator (SGM, ruling: 1100 mm^{-1}) with 40 × 40 μm slits (resolution: ~0.3 eV), as described in our previous work.[17] The XAS spectra presented in this report are derived from the total electron yield (TEY), measured *via* the drain current (probing depth: 2–5 nm). We also recorded Auger electron yield (AEY) and total fluorescence yield (FY) spectra *via* a cylindrical mirror analyzer and a silicon diode (AXUV100). These modes, which probe ~2 nm and 50–100 nm deep, respectively, ensured that the best quality TEY spectra was bulk representative and that the contribution from surface contamination was small. All spectra were normalized to the incoming flux and the energy scale was calibrated to match that of ref. 24, followed by a background subtraction to a line, and a final area normalization for comparison. In order to produce the most stable and reproducible fits, the fitting was limited to the region just around the L_3 edge (774–784 eV), in which the normalization was further restricted through another line subtraction and area normalization.

Fourier-transform infrared (FTIR) spectroscopy

IR spectra were collected on a Varian 670 FTIR spectrometer equipped with a PIKE GladiATR diamond ATR stage. The measurements were performed using 132 scans in a wavenumber range of 400–4000 cm^{-1}.

Magnetic measurements

DC magnetization measurements were performed using a Quantum Design MPMS XL7 SQUID magnetometer in the temperature range from 2 K to 300 K with a magnetic field of up to 7 T. The powder samples were placed inside gelatin capsules. The temperature-dependent magnetic moments were recorded under an applied magnetic field of 1 kOe after cooling the samples under a magnetic field of 7 T (field-cooled, FC) and 0 T (zero field-cooled, ZFC). Magnetic hysteresis measurements were carried out with magnetic field strengths between −7 T and 7 T at 2 K, 11 K, and 300 K, respectively.

Thermogravimetric analysis (TGA) and differential scanning calorimetry (DSC)

The stability of the material (specimen weight: ~10 mg) upon heating was assessed using a simultaneous Mettler Toledo TGA/DSC 1 STAR device, which did not allow to monitor the cooling cycle due to the setup. The measurement was run in a temperature range of 30–900 °C (heating rate: 10 °C min^{-1}) in an argon stream (10 mL min^{-1}), and additionally synthetic air (10 mL min^{-1}) in order to ensure comparability of the data with the *in situ* PXRD experiment.

Temperature-dependent *in situ* X-ray powder diffraction (PXRD)

Temperature-controlled PXRD was performed *in situ* under air using a PANalytical X'Pert Pro diffractometer (Bragg–Brentano geometry; Cu K_α radiation; XCelerator detector) equipped with an Anton Parr HTK-1200 hot stage and a TCU 1000N temperature controller. The material was placed inside a corundum flat plate sample holder and heated up to 900 °C in steps of 100 °C (heating rate: 5 °C min^{-1}), with each temperature being held for 5 min before collecting the data. The scans were recorded in a 2θ range of 15–70° (step: 0.022°; time per step: 209.5 s; total experiment time: 145.5 h).

Results and discussion

Rietveld refinement of X-ray and neutron powder diffraction data

Fig. 1a shows the Rietveld fit of the X-ray powder diffraction pattern of the as-prepared title compound $Li_{0.5-\delta}CoPO_4$. The pattern of a reproduced sample of *Cmcm*-type $LiCoPO_4$ (Fig. 1b) is in good agreement with our previous work.[21] In both cases, all the reflections can be indexed in the orthorhombic space group *Cmcm* and no additional reflections are observed, indicating that both materials are phase pure. While the pattern of $Li_{0.5-\delta}CoPO_4$ appears to be roughly similar to the one of $LiCoPO_4$, suggesting that the crystal structure of the Li-deficient

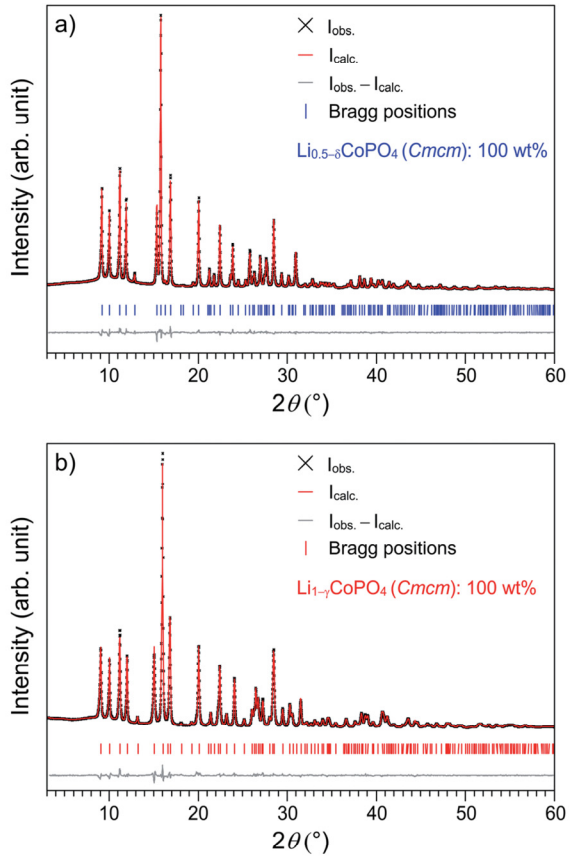

Fig. 1 Rietveld fits of the X-ray powder diffraction data (transmission geometry, Mo $K_{\alpha 1}$ radiation) of (a) $Li_{0.5-\delta}CoPO_4$ (*Cmcm*; refined composition: $Li_{0.39(2)}Co_{0.96(1)}PO_4$, $\delta = 0.11(2)$), and (b) $Li_{1-\gamma}CoPO_4$ (*Cmcm*, refined composition: $Li_{0.94(2)}Co_{0.96(1)}PO_4$, $\gamma = 0.06(2)$).

compound is strongly correlated with the one of the fully lithiated material, some shifts in the peak positions can be recognized. The most significant feature of the $Li_{0.5-\delta}CoPO_4$ pattern is the narrowing of the (200) and (112) reflections at 15.0° and 15.9° 2θ. Furthermore, a completely different peak pattern can be observed in the 2θ region of 25.5–27.5° (for a detailed view, please refer to Fig. S1, ESI†).

To gain further insights into the structural differences causing the peak shifts, a Rietveld refinement was performed, using the previously published structure solution of *Cmcm*-type $LiCoPO_4$ (ICSD no. 143186)[21] as a starting model. Since the elemental analysis indicated an approximate 50% deficit in Li for $Li_{0.5-\delta}CoPO_4$ compared to *Cmcm*-$LiCoPO_4$ (*cf.* Table 2) within standard deviations, the structures were at first refined with fixed Li site occupancy factors of 50% and 100%, respectively, resulting in good reliability factors (Table S1, ESI†). Taking into account that the empirical formulas derived from elemental analysis indicated a deficit in both Li and Co for the two materials (empirical formulas: $Li_{0.45(5)}Co_{0.93(3)}P_{1.00(2)}O_4$ and $Li_{0.93(5)}Co_{0.91(3)}P_{1.00(2)}O_4$; *cf.* Table 2), we tentatively refined the occupancy factors of the Li and Co sites after having applied an absorption correction.[25] In both cases, the free refinement resulted in statistically significant values for the occupancies (39(2)% Li and 96.4(5)% Co for $Li_{0.5-\delta}CoPO_4$; $\delta = 0.11(2)$ and 94(2)% Li and 95.5(5)% Co for $LiCoPO_4$, *cf.* Table S2, ESI†), indicating that both structures feature vacancies in the cationic substructures and are non-stoichiometric. In both cases, the reliability factors were significantly improved over the previous structure models with fixed occupancies (*cf.* Tables 1 and S1, ESI†). To simplify the sum formulas of both compounds while still reflecting the off-stoichiometry from the idealized formulas $Li_{0.5}CoPO_4$ and $LiCoPO_4$ (within three standard deviations), the compounds are referred to as $Li_{0.5-\delta}CoPO_4$ for the Li-deficient phase, and $Li_{1-\gamma}CoPO_4$ (with $\gamma = 0.06(2)$) for *Cmcm*-type $LiCoPO_4$ in this work. It is worth noting that on basis of these refinements, there was no indication for the occurrence of anti-site defects, which are profound for materials synthesized at low temperatures (as observed *e.g.* in *Pna*2_1-type $LiCoPO_4$).[19] Furthermore, in contrast to $Li_{0.94(2)}Co_{0.96(1)}PO_4$, the composition of the Li-deficient *Cmcm* derivative $Li_{0.39(2)}Co_{0.96(1)}PO_4$ would not be charge-balanced assuming that Co is only present in the oxidation state +2. We therefore assume that the deficit in positive electric charge caused by the lower Li^+ content is compensated by Co^{3+} in the framework, which was confirmed by X-ray absorption spectroscopic studies discussed later.

The refined cell parameters (Table 1) indicate a significant contraction along the *a* axis and an expansion along the *c* axis for $Li_{0.5-\delta}CoPO_4$ compared to $Li_{1-\gamma}CoPO_4$, while *b* is not significantly changed, hence providing an explanation for the peak shifts observed in the PXRD patterns. Furthermore, the respective cell volumes ($V = 278.116(19)$ Å^3 *vs.* 276.28(2) Å^3, corresponding to an increase of 0.7%) reveal that the $Li_{0.5-\delta}CoPO_4$ structure is less dense, which is consistent with the decrease in crystal densities. This is surprising since for the delithiated phases Li_xCoPO_4 and $CoPO_4$ derived from olivine-

Table 1 Crystallographic parameters of (a) $Li_{0.5-\delta}CoPO_4$ in comparison with (b) $Li_{1-\gamma}CoPO_4$ (both *Cmcm*, $Z = 4$) as refined from X-ray powder diffraction data ($T = 298$ K)[a]

Sample	(a) $Li_{0.5-\delta}CoPO_4$	(b) $Li_{1-\gamma}CoPO_4$
Empirical formula	$Li_{0.39(2)}Co_{0.96(1)}PO_4$	$Li_{0.94(2)}Co_{0.96(1)}PO_4$
M_r (g mol^{-1})	154.3	158.1
Crystal system	Orthorhombic	Orthorhombic
Space group (no.)	*Cmcm* (63)	*Cmcm* (63)
Z	4	4
a (Å)	5.3385(2)	5.4432(3)
b (Å)	8.1763(3)	8.1695(4)
c (Å)	6.3716(2)	6.2128(3)
V (Å^3)	278.116(19)	276.28(2)
F(000)	297	302
ρ (calcd) (g cm^{-3})	3.684(1)	3.800(1)
R_p	0.0257	0.0196
R_{wp}	0.0327	0.0255
R_{exp}	0.0267	0.0252
R_F	0.0143	0.0106
R_B	0.0254	0.0184
χ^2	1.23	1.01
Data/restraints/parameter	3800/0/59	3835/0/57

[a] The estimated standard deviations were calculated by the Berar's procedure and are indicated in parentheses.

View Article Online
Paper RSC Advances

type $LiCoPO_4$ (*Pnma*), a significant decrease in cell volume of up to ~7% ($CoPO_4$) was observed due to the smaller ionic radius of Co^{3+} compared to Co^{2+}.[8,9,11] The slight increase in cell volume might be explained by the fact that our Li-poor *Cmcm* material was produced from a kinetically controlled synthesis as opposed to *Pnma*-type $CoPO_4$, which was obtained by electrochemical Li extraction. As a result, the Li ions and voids are likely to be statistically distributed within the *Cmcm* structure. This would also be in line with investigations on olivine-type $LiFePO_4$, which revealed that materials synthesized at low temperature are prone to disorder, resulting in larger cell volumes than expected.[26] However, a thorough investigation of the Li^+/vacancy distributions in the structures is beyond this work.

In order to further verify the Li contents and the structure model, we performed additional neutron powder diffraction (NPD) studies of both samples. Rietveld refinements of the NPD data were carried out using the structure parameters obtained from the PXRD experiment as a starting model. Then, the atomic coordinates, thermal parameters as well as occupation factors of Li and Co were refined (see Fig. S2 (ESI†) for the Rietveld fits). The refined lattice parameters (Table S4, ESI†) are in good agreement with the X-ray data. The refinement of the site occupancy factors revealed 37(4)% Li and 98(2)% Co for $Li_{0.5-\delta}CoPO_4$ ($\delta = 0.13(4)$), and 90(3)% Li and 95(6)% Co for $Li_{1-\gamma}CoPO_4$ ($\gamma = 0.10(3)$) (Table S5, ESI†). The compositions and structural parameters of $Li_{0.37(4)}Co_{0.98(1)}PO_4$ and $Li_{0.90(2)}Co_{0.95(6)}PO_4$ are very close to the ones derived from the X-ray experiment and hence confirm the structure model.

Crystal structure

The structures of both *Cmcm*-type $LiCoPO_4$ materials feature rows of edge-sharing, distorted [CoO_6] octahedra which are running along the [001] direction as illustrated in Fig. 2a.[20,27] The $[CoO_6]_\infty$ rows are cross-linked along [100] by alternating pairs of edge-sharing, asymmetric [PO_4] and [LiO_4] units (note that the tetrahedrally coordinated Li ions are shown in Fig. 2 instead of [LiO_4] tetrahedra for clarity). As a result, layers of the composition $([CoO_6][LiO_4][PO_4])_\infty$ are formed in the *ac* plane (Fig. 2b). In these layers, every [CoO_6] octahedron shares two opposite O2–O2 edges with neighboring [CoO_6] units, and two apical O2 atoms with two different [PO_4] and [LiO_4] tetrahedra, which connect the $[CoO_6]_\infty$ strands (for details see Fig. S3, ESI†). The layers are in turn stacked in the sequence AB (indicated by black and grey boxes in Fig. 2a and c) along [010] with a displacement of $a/2$ *via* the apical O1 atoms of the [CoO_6] units so that a three-dimensional framework is formed. It has to be emphasized that despite the fact that Li channels seem to occur along [100] (Fig. 2a), the Li–Li distances are very large (d = 5.3385(4) Å and 5.4432(5) Å, *cf.* Table S3b and d, ESI†), so that these sites are considered isolated. Hence, Li migration will require a very high activation energy along this path and the Li mobility is extremely low in both structures.[20,27] The lack of suitable Li migration pathways is confirmed by electrochemical measurements (see Section 5 and Fig. S4, ESI†) that revealed a very poor performance for both *Cmcm* materials (discharge capacities of < 3 mA h g^{-1}), and is also in line with a previous report.[16] Hence, due to the intrinsically low Li-ion conductivity, the $Li_{0.5-\delta}CoPO_4$ and $Li_{1-\gamma}CoPO_4$ phases cannot be considered suitable for battery applications.

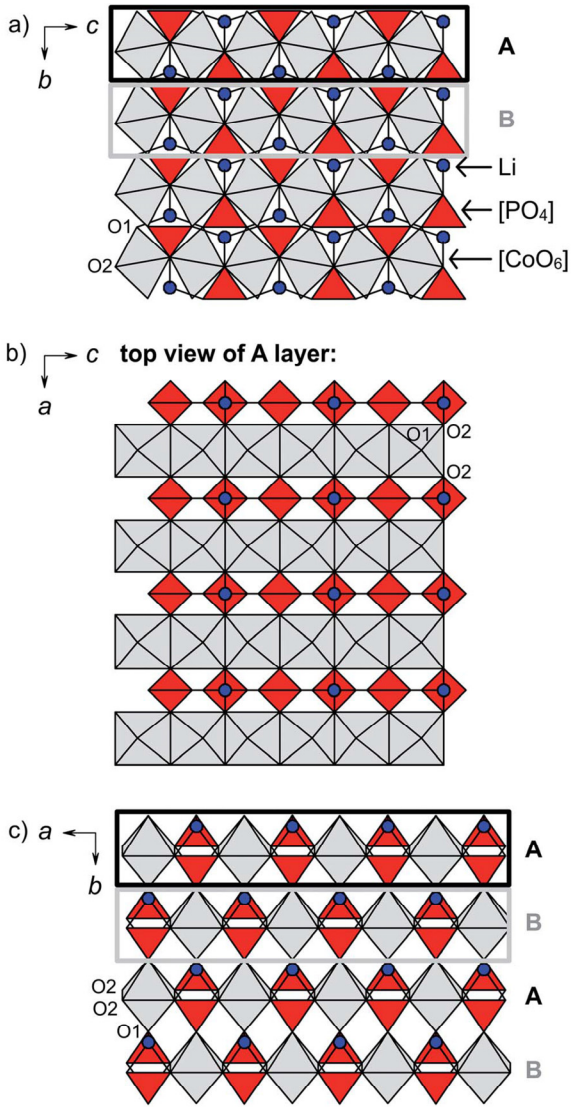

Fig. 2 Polyhedral illustration of the crystal structures of *Cmcm*-type $Li_{0.5-\delta}CoPO_4$ and $Li_{1-\gamma}CoPO_4$ viewed along (a) [100], (b) [010] (showing one A layer as indicated by the black boxes in a, c), and (c) [001]. [CoO_6] octahedra are displayed in grey, [PO_4] tetrahedra in red, and tetrahedrally coordinated Li ions in blue (for clarity, no T_d representation was used for the [LiO_4] units). The structure is built from $([CoO_6][LiO_4][PO_4])_\infty$ layers in the *ac* plane (b), which are stacked along *b* in the sequence AB (c). The layers consist of rows of edge-sharing [CoO_6] octahedra (a), which are connected by alternating pairs of [LiO_4] and [PO_4] units. The occupancies on the Li and Co sites are 39(2)% Li and 96.5(5)% Co for $Li_{0.5-\delta}CoPO_4$, and 94(2)% Li and 95.5(5)% Co for $Li_{1-\gamma}CoPO_4$.

The structural differences between $Li_{1-\gamma}CoPO_4$ and its Li-deficient analogue $Li_{0.5-\delta}CoPO_4$ can be derived from the cell parameters (Table 1) and the interatomic distances (Table S3b and d, ESI†). In general, the framework of $Li_{0.5-\delta}CoPO_4$ is contracted by ~0.10 Å in the *a* dimension and expanded by ~0.16 Å and ~0.01 Å along *c* and *b*, respectively, as also indicated by the distances between the Co centers in and between the layers. The average Co–O (2.122 Å in $Li_{0.5-\delta}CoPO_4$ *vs.* 2.123 Å in $LiCoPO_4$) and P–O (1.539 Å *vs.* 1.538 Å) distances in the $[CoO_6]$ and $[PO_4]$ units remain virtually unchanged, which is surprising since one would expect a decrease in the Co–O distances due to the occurrence of a definite amount of the smaller Co^{3+} ion compared to Co^{2+} in the structure. The individual bond lengths, however, reveal that both the $[CoO_6]$ and $[PO_4]$ units show a higher degree of distortion. This is reflected by the fact that the Co–O2 and P–O2 distances (in the $([CoO_6][LiO_4][PO_4])_\infty$ layers) are shortened, whereas the Co–O1 and P–O1 bonds (connecting the layers along *b*) are expanded, resulting in an increase of the distance between the A–B layers (*cf.* Co–P distances). On the other hand, the mean Li–O distances are increased by ~0.4 Å, leading to an expansion of the "channels" along [100]. This is consistent with the increase of the Li–Li distances by ~0.10 Å. However, it has to be noted that we cannot provide any information about the ordering of the Li^+, Co^{2+}, and Co^{3+} ions or the vacancies in the structure. Based on considerations on the charge distribution, it is likely that the vacancies in the $Li_{0.5-\delta}CoPO_4$ framework are located next to the Co^{3+} centers, which would be consistent with DFT (density functional theory) studies[12] on the Li^+/vacancy distribution in olivine-type $Li_{2/3}CoPO_4$.

Elemental analysis

The results of the elemental analysis of $Li_{0.5-\delta}CoPO_4$ (*Cmcm*) are compared to the values of *Cmcm*-type $LiCoPO_4$ from our recent report[21] in Table 2. The CHNS analyses are similar and show small amounts of hydrogen and carbon in both materials, which arise from residual tetraethylene glycol (TTEG) solvent or the decomposition products of TTEG and the acetate precursors. Whereas the Co and P contents (in wt%) are comparable within three standard deviations, it is evident that the novel compound contains about half the amount of Li (2.0(2) wt%) compared to the $LiCoPO_4$ (*Cmcm*) material (4.1(2) wt%). This is confirmed by the respective Li : Co : P molar ratios of 0.45(5):0.93(3):1.00(2) and 0.93(5):0.91(5):1.00(2). EDS measurements further substantiate the Co : P ratios found by elemental analyses. (Images of the obtained crystal morphologies and semi-quantitative EDS analyses are provided in Fig. S5, ESI†.) The empirical sum formulas derived from elemental analysis, $Li_{0.45(5)}Co_{0.93(3)}P_{1.00(2)}O_4$ and $Li_{0.93(5)}Co_{0.91(3)}P_{1.00(2)}O_4$, indicate a deficit both in Li and Co for both compounds and are also consistent with the results of the Rietveld refinements (*cf.* Table 1) within standard deviations. Based on the results of the elemental analysis, δ in this case is 0.05(5) in $Li_{0.5-\delta}CoPO_4$ (whereas γ is 0.07(5) in $Li_{1-\gamma}CoPO_4$), which is slightly smaller than derived from X-ray and neutron diffraction. Due to the kinetically controlled synthesis procedure, however, it is possible that the composition will slightly vary from batch to batch. Summarizing all efforts from diffraction experiments and elemental analysis to determine the Li and Co contents of the present phases, the notations $Li_{0.5-\delta}CoPO_4$ and $Li_{1-\gamma}CoPO_4$ seem therefore to best reflect the off-stoichiometries found by the different techniques within three standard deviations.

Table 2 Elemental analysis of (a) $Li_{0.5-\delta}CoPO_4$ (*Cmcm*) in comparison with (b) $Li_{1-\gamma}CoPO_4$ (*Cmcm*, data reproduced from ref. 21)[a,b]

Sample	(a) $Li_{0.5-\delta}CoPO_4$	(b) $Li_{1-\gamma}CoPO_4$
C (wt%)	0.4(3)	0.8(3)
H (wt%)	0.5(3)	0.4(3)
Li (wt%)	2.0(2)	4.1(2)
Co (wt%)	35(1)	34(1)
P (wt%)	20.0(3)	19.6(3)
n(Li) : *n*(P)	0.45(5)	0.93(5)
n(Co) : *n*(P)	0.93(3)	0.91(3)
Empirical formula	$Li_{0.45(5)}Co_{0.93(3)}P_{1.00(2)}O_4$	$Li_{0.93(5)}Co_{0.91(3)}P_{1.00(2)}O_4$

[a] The molar composition is calculated from the experimental values and normalized to the P content (standard deviations in parentheses). [b] The N and S contents were below the detection limit in both samples (= 0).

As shown in our previous work[21] on *Cmcm*-type $LiCoPO_4$, the synthesis method strongly affects the phase composition. Whereas it was observed that the composition (and also the morphology) can be slightly varied by changing the synthesis technique (solvothermal *vs.* polyol), the molar ratio of the Li, Co, and P precursors represents another, more effective approach towards compositional tuning. For the synthesis of $Li_{1-\gamma}CoPO_4$, the Li : Co : P molar ratio of the starting materials used was 3 : 1 : 10, whereas $Li_{0.5-\delta}CoPO_4$ was obtained from a Li : Co : P ratio of 1 : 1 : 10 (*cf.* experimental part). As a result, different amounts of Li are incorporated in the crystal structures of the products, although the molar amounts of the precursors and contents found in the obtained materials are not correlated linearly. Adjusting the molar ratio of the precursors might therefore provide a synthetic strategy towards other lithium cobalt or transition metal phosphate materials with modified Li contents. Given the fact that the delithiated *Pnma* phases $Li_{2/3}CoPO_4$ and $CoPO_4$ are only accessible by chemical or electrochemical Li extraction from the fully lithiated olivine-type $LiCoPO_4$ (*Pnma*) material[9,13] and also very instable, this bottom-up approach might also pave the way towards the direct and simple soft-chemical preparation of these Li-deficient intermediates. In that matter, the influence of the synthesis route on the chemical composition will have to be thoroughly examined in further experiments.

X-ray absorption spectroscopy

$L_{2,3}$-edge X-ray absorption spectroscopy is highly sensitive to the oxidation state as well as the spin state and chemical environment of transition metals.[28,29] We have therefore applied Co $L_{2,3}$-edge XAS to investigate the chemical state (valency and symmetry) of the cobalt ions in $Li_{0.5-\delta}CoPO_4$ (*Cmcm*) and $Li_{1-\gamma}CoPO_4$ (*Cmcm*). Fig. 3 displays the normalized TEY spectra over the L_3-edge region from this study along with reference

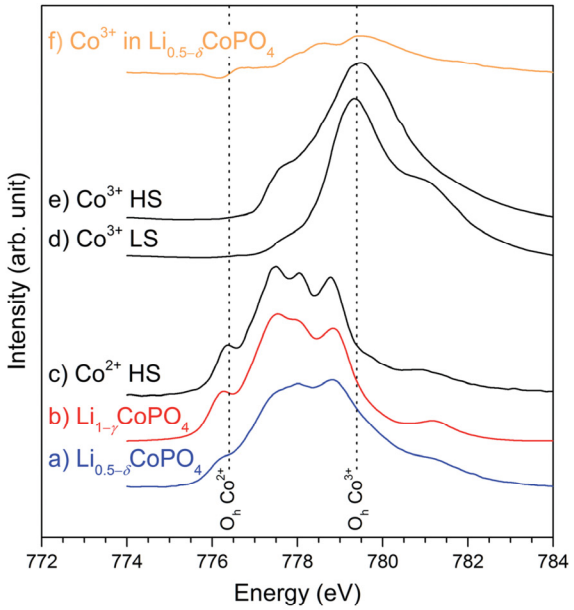

Fig. 3 Normalized Co L_3-edge XAS spectra in the TEY mode for (a) $Li_{0.5-\delta}CoPO_4$ (*Cmcm*, blue), (b) $Li_{1-\gamma}CoPO_4$ (*Cmcm*, red) along with reference spectra for (c) O_h high-spin Co^{2+} in CoO (adapted from ref. 24, black), and (d) low- and (e) high-spin Co^{3+} in $EuCoO_3$ and Sr_2CoO_3Cl (from ref. 30, both black). (f) shows the difference spectrum resulting from a subtraction of 71% Co^{2+} from $Li_{0.5-\delta}CoPO_4$ (orange, $Li_{1-\gamma}CoPO_4$ subtraction), representing the trivalent Co^{3+} ion in the compound. The Co^{3+} association and the lower energy shoulder spectral weight are apparent (see text). All datasets have been aligned to match the common energy scale of ref. 24. The vertical dashed lines indicate the energies corresponding to O_h Co^{2+} (776.4 eV) and O_h Co^{3+} (779.4 eV).

spectra (adapted from (ref. 24 and 30)) for octahedral (O_h) high-spin (HS) Co^{2+} as well as both low-spin (LS) and high-spin (HS) Co^{3+}. $Li_{1-\gamma}CoPO_4$ exhibits all characteristic features of octahedrally (O_h) coordinated Co^{2+}, including the low-energy peak at 776.4 eV that is uniquely ascribed to O_h Co^{2+}.[24,29] Furthermore, overall sharp features can be observed, which indicate a low degree of covalency and energetic alignment with an average octahedral crystal field strength in the order of 1 eV.[29] In fact, a broadening of the CoO spectrum results in a near identical spectrum to $Li_{1-\gamma}CoPO_4$, indicating high purity Co^{2+}, with local disorder being the main difference.

Charge balance arguments suggest that $Li_{0.5-\delta}CoPO_4$ (*Cmcm*) bears cobalt ions in nominal oxidation states of both +2 and +3. Fitting of the spectrum using principal Co^{2+} and Co^{3+} components results in relative contributions of approximately (71 ± 3)% Co^{2+} and (29 ± 3)% Co^{3+} (as opposed to (97 ± 3)% Co^{2+} and (3 ± 3)% Co^{3+} for $Li_{1-\gamma}CoPO_4$), where the symmetry and spin state of the trivalent Co has some, but not dominating effects on the distribution. These values are in line with the Co^{2+} and Co^{3+} contents expected on basis of the nominal composition $Li_{0.5-\delta}CoPO_4$ (~50% Co^{2+} and ~50% Co^{3+}), but where the Co^{3+} contribution derived from XAS is lower. The discrepancy can partly be explained by a small but noticeable reduction at the surface, in line with the fact that Co^{3+} is significantly less stable than Co^{2+}. Moreover, the material was produced using a TTEG solvent, which also acts as a weak reducing agent[31,32] and hence, might reduce the Co^{3+} concentration on the particle surface (*cf.* probing depth of TEY: 2–5 nm). We note that the more bulk sensitive spectra (FY, not shown) indicated higher spectral weight towards higher energies (and thus more Co^{3+} in the bulk), consistent with this hypothesis, but the spectra are not of high enough quality to be analyzed or discussed further.

In order to learn more about the symmetry and spin of the Co^{3+} sites, we have subtracted the fitted Co^{2+} contribution from the $Li_{0.5-\delta}CoPO_4$ spectrum (Fig. 3f). We note that while the main intensity difference is centered around the energy associated with the main peak of Co^{3+} (779.4 V), there is significant intensity on the low-energy side of this peak that is not accounted for by the LS Co^{3+}. Comparison with Co^{3+} ref. 30 of different spin indicates that the trivalent Co ions are primarily high-spin, which can be rationalized based on the tetragonal distortions in the [CoO_6] octahedra (*cf.* Table S3, ESI†) and the analogous HS Co^{3+} *L*-edge spectral assignment upon axial elongations and equatorial contractions in various perovskites[30,33,34]. The XAS thus indicates that the Li vacancies are indeed inducing distortions near the Co^{3+} sites that favor the HS Co^{3+} state. The HS Co^{3+} state is also consistent with a larger average Co–O distance (*i.e.*, larger ionic radius) than what would be expected from the (smaller) LS Co^{3+} that only occupies the t_{2g} orbitals and is associated with a stronger, more covalent Co–O interaction (*cf.* Table S3, ESI†). The presence of HS Co^{3+} is further consistent with the large magnetic moment (see later).

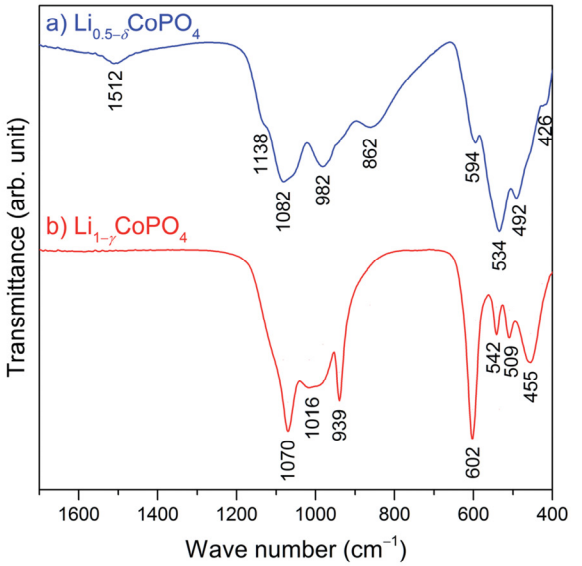

Fig. 4 Comparison of the FTIR spectra of (a) $Li_{0.5-\delta}CoPO_4$ (*Cmcm*, blue), and (b) $Li_{1-\gamma}CoPO_4$ (*Cmcm*, red, data reproduced from ref. 21). The omitted region of 1700–4000 cm^{-1} (*cf.* Fig. S6, ESI†) does not show any absorption bands of water or other impurities.

Infrared spectroscopy

Fig. 4 compares the infrared spectra of $Li_{0.5-\delta}CoPO_4$ (*Cmcm*) and $Li_{1-\gamma}CoPO_4$ (*Cmcm*; data reproduced from ref. 21) in the range of 400–1700 cm^{-1}. The omitted region from 1700 cm^{-1} to 4000 cm^{-1} is presented in Fig. S6 (ESI†) and does not show any absorption bands of water or other impurities. As expected, both spectra are dominated by the four fundamental vibrations of the pseudo-tetrahedral phosphate groups. Two regions can be distinguished, with the symmetric (ν_1) and asymmetric (ν_3) stretching vibrations of P–O being observed at higher frequencies, as well as the symmetric (ν_2) and asymmetric (ν_4) bending vibrations of the O–P–O group at lower frequencies. According to previous reports,[16,21] the absorption peaks of *Cmcm*-type $Li_{1-\gamma}CoPO_4$ (Fig. 4b) can be assigned as follows: the ν_1 and ν_3 stretching modes are observed at 1070 cm^{-1}, 1016 cm^{-1}, and 939 cm^{-1}, whereas the ν_2 and ν_4 deformation vibrations appear in the region of 455–602 cm^{-1}. Despite the structural similarity of the compounds, the IR spectrum of $Li_{0.5-\delta}CoPO_4$ (*Cmcm*, Fig. 4a) shows some distinct differences, in particular a shift of the band frequencies to slightly lower energies and band broadening, and the appearance of additional weak bands at 1512 cm^{-1} and 1138 cm^{-1}.

The changes observed for the Li-deficient phase $Li_{0.5-\delta}CoPO_4$ are in line with reports[35,36] on olivine-type Li_xFePO_4 ($0 \leq x \leq 1$) which demonstrated that the absorption modes of the $[PO_4]^{3-}$ groups are extremely sensitive to the delithiation of $LiFePO_4$ and the associated oxidation of Fe^{2+} to Fe^{3+}. As discussed, the average P–O distances in $Li_{1-\gamma}CoPO_4$ (*Cmcm*) remain virtually unchanged when less Li is incorporated in the structure (*cf.* Table S3, ESI†). Hence, the energies of the absorption modes are not changed drastically, indicating similar local structures of the $[PO_4]^{3-}$ units. This is in good agreement with a report by Popović and co-workers,[37] which suggested a linear correlation between the P–O bond lengths and stretching frequencies. The observed band splitting, on the other hand, is correlated with interactions between ions, in this case between the $[PO_4]^{3-}$ units and the adjacent Li^+ and $Co^{2+/3+}$ cations, *i.e.* the stronger the interaction, the larger the factor group splitting effects.[36] In fact, the P–Li and P–Co distances are reduced in $Li_{0.5-\delta}CoPO_4$ compared to $Li_{1-\gamma}CoPO_4$ (Table S3, ESI†), which leads to stronger interactions. Furthermore, it was shown[38,39] that the factor group splitting of the ν_3 modes increases with the second ionization potential of the transition metal due to the formation of strong bonds with the oxygen atoms of the $[PO_4]$ units, which causes a redistribution of electron density in the P–O bonds. This is reflected in the observation that the P–O1 bonds are expanded, and the P–O2 bonds shortened by ~0.02 Å each in $Li_{0.5-\delta}CoPO_4$ (*cf.* Table S3, ESI†). Due to the significantly higher ionization potential of Co^{3+} compared to Co^{2+}, the larger factor group splitting in the IR spectrum of $Li_{0.5-\delta}CoPO_4$ is therefore the result of the mixed valence state of the Co ions in the structure (Co^{2+}/Co^{3+}) as opposed to $Li_{1-\gamma}CoPO_4$ which contains Co^{2+} only. However, a thorough analysis of the spectra, including the assignment of the additional absorption band at 1512 cm^{-1}, would require a complete structural model, including the ordering of the Li^+, Co^{2+}, and Co^{3+} ions in the framework as well as DFT calculations, which is beyond the scope of this work. It is likely that the occurrence of additional modes is the result of a lower local symmetry in $Li_{0.5-\delta}CoPO_4$ due to a higher defect concentration.

Magnetic properties

Fig. 5 shows the magnetic susceptibility as function of temperature measured at a magnetic field of 0.1 T in field-cooled (FC) condition as well as the magnetic hysteresis recorded at a temperature of 2 K of $Li_{0.5-\delta}CoPO_4$ in comparison with $Li_{1-\gamma}CoPO_4$ (both *Cmcm*). The temperature dependence of the magnetic susceptibilities indicates a long-range antiferromagnetic to paramagnetic transition at T_N = 10.5 K for $Li_{0.5-\delta}CoPO_4$, and T_N = 12 K for $Li_{1-\gamma}CoPO_4$, respectively. The low transition temperature T_N of 12 K of the $Li_{1-\gamma}CoPO_4$ (*Cmcm*) phase is in agreement with our previous study[21] on *Cmcm*-type $LiCoPO_4$ and is comparable to the non-olivine, metastable $LiCoPO_4$ ($Pna2_1$) phase (T_N = 11 K),[18] but much lower than the well investigated olivine-type $LiCoPO_4$ (*Pnma*, T_N = 21.6 K).[40,41] This finding demonstrates the close relation between structural and magnetic properties. However, the further reduction of the observed transition temperature T_N of the Li-deficient $Li_{0.5-\delta}CoPO_4$ (*Cmcm*) compound might be related to the vacancies on the Co site, weakening the Co–O–Co super exchange interaction. Above the transition temperature, the magnetic susceptibility of both compounds follow the Curie–Weiss law (see Fig. S7, ESI†), $\chi = \chi_0 + (N_A\mu_{eff}^2)/(3k_b(T - \theta_C))$, where χ_0 is a temperature-independent contribution, μ_{eff} the effective magnetic moment, N_A the Avogadro number, θ_C the Weiss temperature, and k_b the Boltzmann constant. Fitting the high-temperature magnetic susceptibility with the Curie–Weiss law yields a higher Weiss temperature of −21.8 K of $Li_{0.5-\delta}CoPO_4$ compared to the stoichiometric $Li_{1-\gamma}CoPO_4$ (−28.2 K; *cf.* inset of Fig. S7, ESI†), which reflects the difference in transition

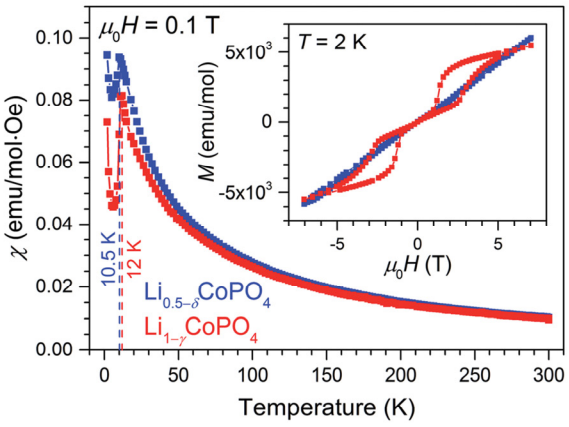

Fig. 5 Magnetic susceptibility as function of temperature of $Li_{0.5-\delta}CoPO_4$ (*Cmcm*, blue data points) and $Li_{1-\gamma}CoPO_4$ (*Cmcm*, red) measured at a magnetic field of 0.1 T in field-cooled condition. The vertical dashed lines mark the respective transition temperatures of both phases (10.5 K and 12 K). The inset shows the corresponding magnetic hysteresis curves recorded at T = 2 K.

View Article Online
Paper RSC Advances

temperatures T_N. Furthermore, similar effective magnetic moments of $\mu_{eff} = (5.20 \pm 0.02)\ \mu_B$ for $Li_{0.5-\delta}CoPO_4$ and $(5.08 \pm 0.02)\ \mu_B$ for $Li_{1-\gamma}CoPO_4$ were found. Both values exceed the spin-only value of high-spin Co^{2+} and Co^{3+} (3.9 μ_B and 4.8 μ_B, respectively), demonstrating a non-negligible orbital contribution.[42] Taking into account the finite angular momentum, effective magnetic moments of 5.2 μ_B and 5.5 μ_B for high-spin Co^{2+} and Co^{3+} in the O_h symmetry ($^5t_{2g}$ and $^4t_{1g}$ ground state) are expected in the weak spin–orbit coupling limit. Assuming the presence of only Co^{2+} in the $Li_{1-\gamma}CoPO_4$ compound, the observed values are slightly smaller than the expected ones. However, the larger effective magnetic moment μ_{eff} of $Li_{0.5-\delta}CoPO_4$ clearly supports the findings of a mixed valence state of Co in the Li-deficient compound as discussed in the previous sections.

The inset of Fig. 5 reveals a more distinct difference of the magnetic properties of $Li_{1-\gamma}CoPO_4$ and the Li-deficient $Li_{0.5-\delta}CoPO_4$ compounds. $LiCoPO_4$ exhibits a magnetic double-hysteresis loop at 2 K, demonstrating an antiferromagnetic ground state at 0 T (for the hysteresis curves at 11 K and 300 K see Fig. S8, ESI†). Furthermore, the double-hysteresis loop indicates a spin-flip transition at a critical field of around ±3 T, which is much lower than for *Pnma*-type $LiCoPO_4$.[43] Again, this can be attributed to the different structural properties. In contrast, an almost linear dependence of the magnetization as a function of the applied field is observed for $Li_{0.5-\delta}CoPO_4$ below T_N. No hysteresis with a finite remanence caused by a weak ferromagnetic phase due to the mixed-valence state of Co ions were found.[40] However, the difference of the magnetic susceptibility recorded under field-cooled (FC) and zero field-cooled (ZFC) conditions suggests the formation of magnetic domains below $T \approx 5$ K. Below this temperature, the finite amount of Co^{3+} ions as well as the observed defects on the Co sites might cause competing magnetic interactions resulting in a complex antiferromagnetic state as, for instance, described by Jensen and co-workers.[44]

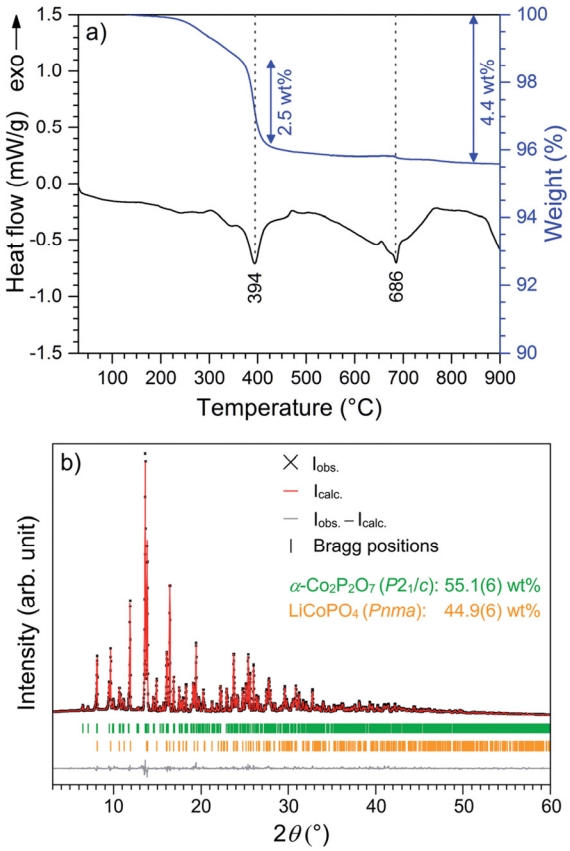

Fig. 6 (a) DSC (black) and TGA (blue) curves of $Li_{0.5-\delta}CoPO_4$ (*Cmcm*) measured in a temperature range of 30–900 °C (heating rate: 10 °C min^{-1}, atmosphere: synthetic air). Two endothermic DSC signals are observed at 394 °C (accompanied by a TGA weight loss step of ~2.5 wt%) and 686 °C, respectively. (b) Rietveld fit of the X-ray powder diffraction data (transmission geometry, Mo $K_{\alpha 1}$ radiation) of the dark violet post TGA/DSC-material demonstrating that mixture of olivine-type $LiCoPO_4$ (*Pnma*) and α-$Co_2P_2O_7$ ($P2_1/c$) was formed upon heating.

Thermal stability

The thermal stability of $Li_{0.5-\delta}CoPO_4$ (*Cmcm*) was investigated using TGA/DSC (Fig. 6) and temperature-dependent *in situ* X-ray powder diffraction, both performed under air (Fig. 7). The thermal behavior of $LiCoPO_4$ (*Cmcm*) has been discussed in detail in ref. 21. In the TGA curve (Fig. 6a), an overall mass loss of ~4.8 wt% is observed between 30 °C and 900 °C, which proceeds in several steps. The mass loss of ~1.3 wt% up to 360 °C is probably correlated with the decomposition of residues of the TTEG solvent and the acetate precursors (*cf.* CHNS analysis, Table 2). The DSC curve shows two pronounced, broad endothermic peaks at 394 °C and 686 °C, respectively, with the first signal being accompanied by a weight loss step of ~2.5 wt% and the second one of ~0.1 wt%. The corresponding X-ray powder diffraction pattern (Fig. 6b, refinement details see Tables S7–S11†) of the dark violet powder (*cf.* graphical abstract) obtained after the TGA/DSC measurement reveals that a mixture of 44.9(6) wt% olivine-type $LiCoPO_4$ (*Pnma*, ICSD no. 431999)[45] and 55.1(6) wt% of the low-temperature modification of cobalt pyrophosphate, α-$Co_2P_2O_7$ ($P2_1/c$, ICSD no. 280959)[46] was formed. Note that data obtained from a similar experiment using an argon atmosphere are in good agreement (Fig. S9 and S10, Tables S12–S16, ESI†).

In order to understand the signals observed in the TGA/DSC study and to identify possible intermediates of the heating process, we performed a temperature-controlled *in situ* PXRD experiment between room temperature (30 °C) and 900 °C with a step size of 100 °C (Fig. 7). The Rietveld fits of the individual PXRD patterns at each temperature up to 700 °C can be found in Fig. S11 (ESI†). The refined phase fractions and crystallographic details (atomic coordinates, thermal displacements parameters, bond lengths), reflecting the structural changes, are presented in Tables S17–S25.† (Note that the patterns at $T \geq 800$ °C, which are shown in Fig. S12 (ESI†), were of insufficient quality for a refinement because of the occurrence of strong reflections from the corundum sample holder.) Up to 300 °C, no change of

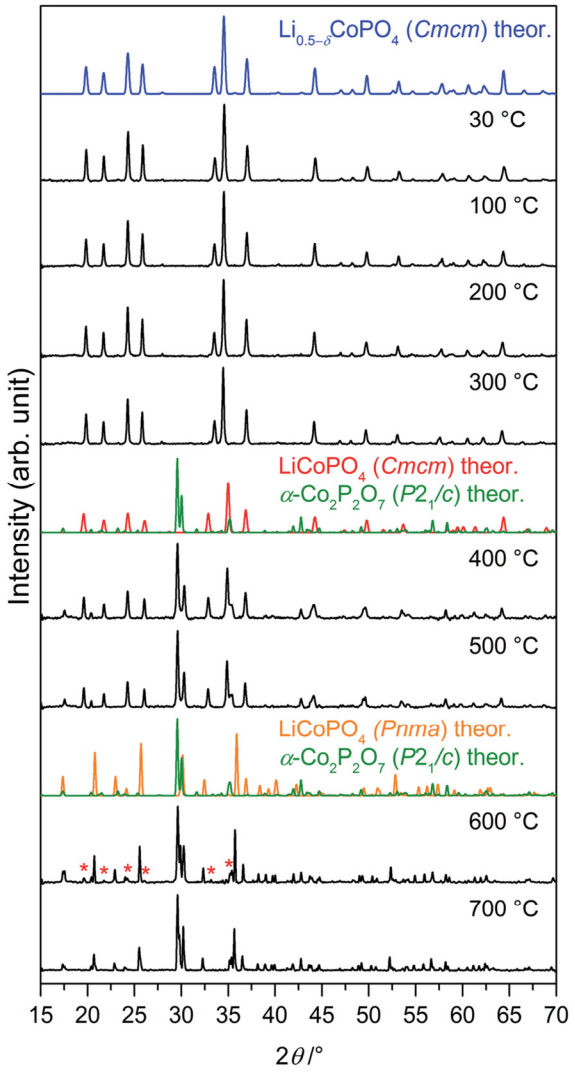

Fig. 7 *In situ* X-ray powder diffraction patterns (Bragg–Brentano geometry, Cu K_α radiation) of $Li_{0.5-\delta}CoPO_4$ (*Cmcm*) measured between 30 °C and 700 °C under air (heating rate: 5 °C min^{-1}; for patterns at 800 °C, 900 °C, and after cooling see Fig. S12, ESI†). The phase undergoes several transitions upon heating. The theoretical patterns of the involved phases, which were calculated from room temperature data, are displayed in color. Between 300 °C and 400 °C, $Li_{0.5-\delta}CoPO_4$ (*Cmcm*, this work, blue) decomposes to $LiCoPO_4$ (*Cmcm*, ICSD no. 432186,[21] red) and α-$Co_2P_2O_7$ ($P2_1/c$, ICSD no. 280959,[46] green). Above 500 °C, an irreversible transition of $LiCoPO_4$ (*Cmcm*, blue) to olivine-type $LiCoPO_4$ (*Pnma*, ICSD no. 431999,[45] orange) occurs. The reflections marked with red asterisks (*) in the pattern at 600 °C can be assigned to residues of $LiCoPO_4$ (*Cmcm*).

the diffraction patterns occurs, indicating that the $Li_{0.5-\delta}CoPO_4$ (*Cmcm*) phase is thermally stable up to that temperature. Between 300 °C and 400 °C, a mixture of the 'fully lithiated' $Li_{1-\gamma}CoPO_4$ (*Cmcm*) structure (referred to as $LiCoPO_4$ with $\gamma = 0$ in Fig. 7 since ICSD no. 432186 (ref. 21) was used for the theoretical pattern) and α-$Co_2P_2O_7$ ($P2_1/c$) is observed. Hence, the endothermic DSC signal at 395 °C can be explained by the decomposition of $Li_{0.5-\delta}CoPO_4$ (*Cmcm*) to these phases (the simultaneous mass loss will be explained later in the text). Between 500 °C and 600 °C, the *Cmcm*-type $Li_{1-\gamma}CoPO_4$ intermediate starts to convert to the thermodynamically more stable olivine *Pnma* structure, whereas the peaks of α-$Co_2P_2O_7$ remain unaltered. The fact that the low-temperature α-modification of $Co_2P_2O_7$ ($P2_1/c$) does not transform to the high-temperature β-$Co_2P_2O_7$ ($A2/m$)[47] phase, which would be expected at ~480 °C (ref. 48) for the pure material, suggests that the transformation is either kinetically hindered or very slow. Hence, the DSC signal at 688 °C corresponds to the transformation of the *Cmcm* to the *Pnma* $LiCoPO_4$ phase. The lower transition temperature found in the *in situ* PXRD study compared to the DSC data might be related to slightly different atmospheres (air *vs.* synthetic air) and heating rates (10 °C min^{-1} *vs.* 5 °C min^{-1}) being used. The phase transformation is not completed until 700 °C because traces of $Li_{1-\gamma}CoPO_4$ (*Cmcm*) can be identified in the diffraction pattern at 600 °C. Compared to the thermal stability of the pure, lithiated $LiCoPO_4$ (*Cmcm*) material (transformation to single-phase $LiCoPO_4$ (*Pnma*) at 575 °C),[21] the phase transition temperature is significantly increased. No further phase changes are observed in the PXRD patterns up to 700 °C, yet the diffraction peaks are shifted to lower angles, indicating bigger lattice dimensions due to thermal expansion. Unfortunately, it cannot be derived from the patterns at $T \geq 800$ °C (see Fig. S12, ESI†) whether the $Pna2_1$-type $LiCoPO_4$ structure reappears as a high-temperature phase as reported for all three, fully lithiated $LiCoPO_4$ polymorphs (*Pnma*,[17] $Pna2_1$,[19] and *Cmcm*[21]). The pattern of the cooled sample (25 °C; Fig. S12, ESI†) is consistent with the *ex situ* PXRD experiment (Fig. 6b) and shows reflections of α-$Co_2P_2O_7$ and *Pnma*-type $LiCoPO_4$, indicating that both phase transitions are irreversible.

The results of the thorough investigation of the thermal stability of the Li-deficient compound $Li_{0.5-\delta}CoPO_4$ demonstrate that the phase exhibits a complex behavior upon heating which involves several phase transitions. Based on the combined approach using TGA, DSC (Fig. 6), and *in situ* PXRD studies (Fig. 7), a decomposition mechanism can be proposed according to Scheme 1. Note that since it is not possible to determine the composition of the decomposition products and intermediates (which are likely to be deficient in Li and Co as well), the mechanism is presented on basis of the nominal composition $Li_{0.5-\delta}CoPO_4$ with $\delta = 0$. In the first step (eqn (I)), $LiCoPO_4$ (*Cmcm*) and $Co_2P_2O_7$ ($P2_1/c$; both with Co oxidation state +2) are formed from four equivalents of the Co^{2+}/Co^{3+} mixed-valent starting material $Li_{0.5-\delta}CoPO_4$ (*Cmcm*). This step is based on a redox reaction, in which the two Co^{3+} equivalents from the four $Li_{0.5-\delta}CoPO_4$ ($\delta = 0$) units are reduced by O^{2-} ions (eqn (Ia)), which are released upon the pyrophosphate formation (*i.e.*, coupling of isolated $[PO_4]$ tetrahedra to $[P_2O_7]$ units *via* shared corners). The O^{2-} ions are in turn oxidized to form elemental oxygen (eqn (Ib)) that is released. The O_2 release from the phosphate groups corresponds to an approximate mass loss of ~2.5 wt% which in full agreement with the TGA mass loss step observed at 394 °C (*cf.* Fig. 6a). The estimated mass fractions of $Li_{1-\gamma}CoPO_4$ (*Cmcm*, with $\gamma = 0$) and $Co_2P_2O_7$ after the

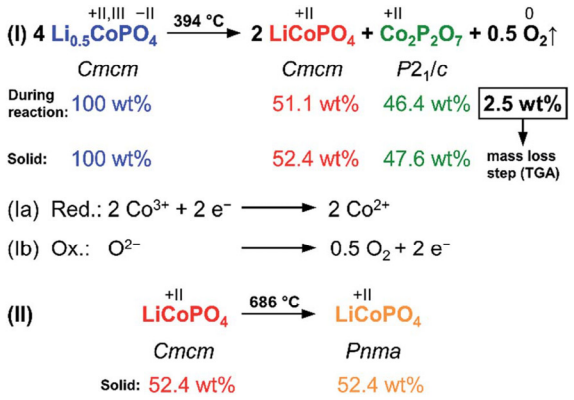

Scheme 1 Proposed two-step mechanism of the thermal decomposition of $Li_{0.5-\delta}CoPO_4$ (*Cmcm*, with $\delta = 0$) and theoretically expected weight fractions (in wt%) of the involved phases during the reaction as well as in the solid remainder after O_2 release. It can be inferred that the TGA weight loss (*cf.* Fig. 7) at 394 °C is due to the release of oxygen as a result of a redox process. The color code of the phases is related to Fig. 6 and 7.

oxygen release are ~52.4 wt% and ~47.6 wt%, respectively, and are very close to the refined values obtained from our Rietveld analysis (*cf.* Fig. 6, and Table S17, ESI†). The slight deviation of our refined values from the calculated ones can be explained by the fact that the nominal composition was used for this hypothesis and that the refinement of phase fractions on basis of the reflection intensities depends on the particle size and crystallinity. In the second step at 686 °C (eqn (II)), which was not accompanied by a significant mass loss in the TGA (Fig. 6a), $LiCoPO_4$ (*Cmcm*) is transformed to the thermodynamically more stable olivine-type $LiCoPO_4$ (*Pnma*) as observed in the PXRD study (Fig. 6b).

Interestingly, the decomposition leads to the crystallization of same phases (*Pnma*-type $LiCoPO_4$ and $Co_2P_2O_7$) under oxygen evolution as reported for the olivine-like Li-poor phase Li_xCoPO_4.[13] However, there are some significant mechanistic differences between $Li_{0.5-\delta}CoPO_4$ (*Cmcm*) and Li_xCoPO_4 (*Pnma*), which might be due to the fact that our studies are based on the pristine material whereas the studies on Li_xCoPO_4 were based on charged $LiCoPO_4$ electrodes. First of all, as reported by Bramnik *et al.*,[13] the decomposition of Li_xCoPO_4 cathodes occurs at much lower temperatures (<200 °C) suggesting that the Li-poor, *Cmcm*-type $Li_{0.5-\delta}CoPO_4$ phase (decomposition at 394 °C) is significantly more stable. (Note that compared to the results of Theil *et al.*,[14] on the other hand, *Cmcm*-type $Li_{0.5-\delta}CoPO_4$ seems to be less stable than Li_xCoPO_4, which was found to be thermally stable at least up to 550 °C. This discrepancy might be explained by different particle sizes and carbon contents.). Furthermore, in contrast to our material, the $Co_2P_2O_7$ crystallization was found to be not proceeding simultaneously, but at higher temperature than the Li_xCoPO_4 (*Pnma*) decomposition, which was related to a possibly amorphous intermediate.[13] In addition, the decomposition process was suggested to be promoted by carbon present in samples, which reacts with the released oxygen to form CO_2 gas.[13] The crucial influence/destabilizing effect of carbon on the thermal stability was also confirmed for charged $LiCoPO_4$ electrodes containing $CoPO_4$.[14] Based on this work, however, there is no indication that carbon affects the decomposition of the pristine $Li_{0.5-\delta}CoPO_4$ (*Cmcm*) material since the carbon content of our material is not significant (0.4(3) wt%, *cf.* Table 2). To clarify whether this is also the case for the pristine, carbon-free Li_xCoPO_4 ($x = 0$, 0.7; space group *Pnma*) olivine phases (as opposed to the studies[13,14] based on carbon-containing charged $LiCoPO_4$ electrodes), our direct synthetic approach might provide a pathway to get a deeper understanding of their intrinsic thermal stabilities as well.

Conclusions

In this study, a polyol synthesis pathway towards the first Li-deficient structural derivative of the *Cmcm* polymorph of $LiCoPO_4$ with the nominal composition $Li_{0.5-\delta}CoPO_4$ and its material properties were presented. To the best of our knowledge, this is also the first time that a sub-stoichiometric Li_xCoPO_4 phase was synthesized using a soft-chemical bottom-up approach as opposed to common chemical and electrochemical Li extraction techniques starting from $LiCoPO_4$-type materials.

Neutron and X-ray powder diffraction experiments as well as elemental analysis suggested that $Li_{0.5-\delta}CoPO_4$ (*Cmcm*) is non-stoichiometric and deficient both in Li and Co, which generates vacancies on both cation sub-lattices in the crystal structure. The occurrence of vacancies was also observed in the course of a structure redetermination of the 'fully lithiated' *Cmcm* phase, resulting in the revised formula $Li_{1-\gamma}CoPO_4$. Co $L_{2,3}$-edge X-ray absorption spectroscopy indicated that, unlike $Li_{1-\gamma}CoPO_4$ which exclusively contains octahedrally coordinated Co^{2+} ions, the Li-deficient structure bears both Co^{2+} and Co^{3+} ions to compensate for the Li deficit. Due to the reduced Li content and amount of electrochemically active Co^{2+} ions, the material exhibited a poor electrochemical performance. The thermal stability of $Li_{0.5-\delta}CoPO_4$ has been studied thoroughly using thermogravimetry, differential scanning calorimetry, and temperature-dependent *in situ* X-ray powder diffraction experiments. $Li_{0.5-\delta}CoPO_4$ (*Cmcm*) is metastable and shows a complex, two-step decomposition mechanism upon heating. At 394 °C, it decomposes to α-$Co_2P_2O_7$ ($P2_1/c$) and $Li_{1-\gamma}CoPO_4$ (*Cmcm*) in an endothermic reaction upon which oxygen is released as a result of a redox reaction. The $Li_{1-\gamma}CoPO_4$ (*Cmcm*) phase then irreversibly converts to the thermodynamically more stable $LiCoPO_4$ (*Pnma*) olivine structure at 686 °C.

To conclude, the present work paves the way towards the direct and simple soft-chemical preparation and investigation of Li-deficient structures derived from lithium transition-metal phosphates. Our methodology provides fundamental insights into the material properties, and hence to study Li-deficient intermediates that are probably involved in the charge/discharge steps of $LiCoPO_4$-type cathodes. It further helps to understand the complex structure chemistry of this class of cathode materials for Li-ion batteries. In that matter, future studies should focus on compositional tuning (*e.g.* by

modifying the amounts of the precursors in the synthesis) in order to identify other partially lithiated structural derivatives.

Author contributions

J. L. performed the material characterization using *in situ* and *ex situ* PXRD, SEM/EDS, IR spectroscopy, and electrochemical measurements, and analyzed the data (under supervision of T. N. and M. M. D.). C. A.-S. performed the synthesis. S. G. and D. N. performed and analyzed magnetic and XAS measurements, respectively. I. P. O. and C. A.-S. conducted neutron diffraction experiments. J. L. wrote the manuscript. All authors have given approval to the final version of the manuscript.

Funding sources

This work has been funded by the Fonds der Chemischen Industrie and the TUM Graduate School. The use of the Stanford Synchrotron Radiation Lightsource (SSRL), SLAC National Accelerator Laboratory, is supported by the US Department of Energy, Office of Science, and Office of Basic Energy Sciences (contract no. DE-AC02-76SF00515). We further thank the Institut Laue-Langevin (ILL) for beam time allocation, and the D2B team for technical support (proposal no. 5-31-2531).

Abbreviations

AAS	Atomic absorption spectroscopy
AEY	Auger electron yield
DFT	Density functional theory
DSC	Differential scanning calorimetry
EDS	Energy-dispersive X-ray spectroscopy
FC	Field-cooled
FTIR	Fourier-transform infrared
FY	Fluorescence yield
HS	High-spin
ICSD	Inorganic Crystal Structure Database
LS	Low-spin
NPD	Neutron powder diffraction
PXRD	Powder X-ray diffraction
SEM	Scanning electron microscope
SQUID	Superconducting quantum interference device
TEY	Total electron yield
TGA	Thermogravimetric analysis
TTEG	Tetraethylene glycol
XAS	X-ray absorption spectroscopy
ZFC	Zero field-cooled

Acknowledgements

The authors thank U. Ammari for elemental analysis, and D. Haering for TGA/DSC measurements. J. L. and C. A.-S. are grateful to the TUM Graduate School, the Fonds der Chemischen Industrie, DAAD and Colciencias for financial support of their Ph.D. work.

References

1 K. Amine, H. Yasuda and M. Yamachi, *Electrochem. Solid-State Lett.*, 2000, **3**, 178–179.
2 J. M. Tarascon and M. Armand, *Nature*, 2001, **414**, 359–367.
3 B. L. Ellis, K. T. Lee and L. F. Nazar, *Chem. Mater.*, 2010, **22**, 691–714.
4 K. Zaghib, A. Guerfi, P. Hovington, A. Vijh, M. Trudeau, A. Mauger, J. B. Goodenough and C. M. Julien, *J. Power Sources*, 2013, **232**, 357–369.
5 A. Yamada, M. Hosoya, S.-C. Chung, Y. Kudo, K. Hinokuma, K.-Y. Liu and Y. Nishi, *J. Power Sources*, 2003, **119–121**, 232–238.
6 S. Okada, S. Sawa, M. Egashira, J. Yamaki, M. Tabuchi, H. Kageyama, T. Konishi and A. Yoshino, *J. Power Sources*, 2001, **97–98**, 430–432.
7 B. Kang and G. Ceder, *Nature*, 2009, **458**, 190–193.
8 N. N. Bramnik, K. Nikolowski, C. Baehtz, K. G. Bramnik and H. Ehrenberg, *Chem. Mater.*, 2007, **19**, 908–915.
9 H. Ehrenberg, N. N. Bramnik, A. Senyshyn and H. Fuess, *Solid State Sci.*, 2009, **11**, 18–23.
10 H. Ju, J. Wu and Y. Xu, *Int. J. Energy Environ. Eng.*, 2013, **4**(22), 26.
11 M. Kaus, I. Issac, R. Heinzmann, S. Doyle, S. Mangold, H. Hahn, V. S. K. Chakravadhanula, C. Kuebel, H. Ehrenberg and S. Indris, *J. Phys. Chem. C*, 2014, **118**, 17279–17290.
12 F. C. Strobridge, R. J. Clement, M. Leskes, D. S. Middlemiss, O. J. Borkiewicz, K. M. Wiaderek, K. W. Chapman, P. J. Chupas and C. P. Grey, *Chem. Mater.*, 2014, **26**, 6193–6205.
13 N. N. Bramnik, K. Nikolowski, D. M. Trots and H. Ehrenberg, *Electrochem. Solid-State Lett.*, 2008, **11**, A89–A93.
14 S. Theil, M. Fleischhammer, P. Axmann and M. Wohlfahrt-Mehrens, *J. Power Sources*, 2013, **222**, 72–78.
15 X. Huang, J. Ma, P. Wu, Y. Hu, J. Dai, Z. Zhu, H. Chen and H. Wang, *Mater. Lett.*, 2005, **59**, 578–582.
16 K. J. Kreder, G. Assat and A. Manthiram, *Chem. Mater.*, 2015, **27**, 5543–5549.
17 J. Ludwig, C. Marino, D. Haering, C. Stinner, D. Nordlund, M. M. Doeff, H. A. Gasteiger and T. Nilges, *RSC Adv.*, 2016, **6**, 82984–82994.
18 C. Jaehne, C. Neef, C. Koo, H.-P. Meyer and R. Klingeler, *J. Mater. Chem. A*, 2013, **1**, 2856–2862.
19 J. Ludwig, D. Nordlund, M. M. Doeff and T. Nilges, *J. Solid State Chem.*, 2017, **248**, 9–17.
20 U. Amador, J. M. Gallardo-Amores, G. Heymann, H. Huppertz, E. Moran and M. E. Arroyo-de Dompablo, *Solid State Sci.*, 2009, **11**, 343–348.
21 C. Alarcón-Suesca, J. Ludwig, V. Hlukhyy, C. Stinner and T. Nilges, *Inorganics*, 2016, **4**, 35.
22 V. Petricek, M. Dusek and L. Palatinus, *Z. Kristallogr.–Cryst. Mater.*, 2014, **229**, 345–352.
23 J. Rodriguez-Carvajal, *Phys. B*, 1993, **192**, 55–69.
24 A. M. Hibberd, H. Q. Doan, E. N. Glass, F. M. F. de Groot, C. L. Hill and T. Cuk, *J. Phys. Chem. C*, 2015, **119**, 4173–4179.

25 D. T. Cromer and D. A. Liberman, *Acta Crystallogr., Sect. A: Cryst. Phys., Diffr., Theor. Gen. Crystallogr.*, 1981, **37**, 267–268.
26 J. Chen and M. S. Whittingham, *Electrochem. Commun.*, 2006, **8**, 855–858.
27 O. Garcia-Moreno, M. Alvarez-Vega, F. Garcia-Alvarado, J. Garcia-Jaca, J. M. Gallardo-Amores, M. L. Sanjuan and U. Amador, *Chem. Mater.*, 2001, **13**, 1570–1576.
28 F. M. F. de Groot, J. C. Fuggle, B. T. Thole and G. A. Sawatzky, *Phys. Rev. B: Condens. Matter*, 1990, **42**, 5459–5468.
29 F. M. F. de Groot, M. Abbate, J. van Elp, G. A. Sawatzky, Y. J. Ma, C. T. Chen and F. Sette, *J. Phys.: Condens. Matter*, 1993, **5**, 2277–2288.
30 Z. Hu, H. Wu, M. W. Haverkort, H. H. Hsieh, H. J. Lin, T. Lorenz, J. Baier, A. Reichl, I. Bonn, C. Felser, A. Tanaka, C. T. Chen and L. H. Tjeng, *Phys. Rev. Lett.*, 2004, **92**, 207402.
31 D.-H. Kim and J. Kim, *Electrochem. Solid-State Lett.*, 2006, **9**, A439–A442.
32 M. K. Devaraju and I. Honma, *Adv. Energy Mater.*, 2012, **2**, 284–297.
33 M. Abbate, J. C. Fuggle, A. Fujimori, L. H. Tjeng, C. T. Chen, R. Potze, G. A. Sawatzky, H. Eisaki and S. Uchida, *Phys. Rev. B: Condens. Matter Mater. Phys.*, 1993, **47**, 16124–16130.
34 S. Y. Istomin, O. A. Tyablikov, S. M. Kazakov, E. V. Antipov, A. I. Kurbakov, A. A. Tsirlin, N. Hollmann, Y. Y. Chin, H. J. Lin, C. T. Chen, A. Tanaka, L. H. Tjeng and Z. Hu, *Dalton Trans.*, 2015, **44**, 10708–10713.
35 C. M. Burba and R. Frech, *J. Electrochem. Soc.*, 2004, **151**, A1032–A1038.
36 C. M. Burba and R. Frech, *Spectrochim. Acta, Part A*, 2006, **65**, 44–50.
37 L. Popović, D. De Waal and J. C. A. Boeyens, *J. Raman Spectrosc.*, 2005, **36**, 2–11.
38 M. T. Paques-Ledent and P. Tarte, *Spectrochim. Acta, Part A*, 1974, **30**, 673–689.
39 A. Ait Salah, P. Jozwiak, J. Garbarczyk, K. Benkhouja, K. Zaghib, F. Gendron and C. M. Julien, *J. Power Sources*, 2005, **140**, 370–375.
40 N. F. Kharchenko, Y. N. Kharchenko, R. Szymczak, M. Baran and H. Schmid, *Low Temp. Phys.*, 2001, **27**, 895–898.
41 J. P. Rivera, *Ferroelectrics*, 1994, **161**, 147–164.
42 S. H. Baek, R. Klingeler, C. Neef, C. Koo, B. Buechner and H. J. Grafe, *Phys. Rev. B: Condens. Matter Mater. Phys.*, 2014, **89**, 134424.
43 N. F. Kharchenko, V. M. Khrustalev and V. N. Savitskii, *Low Temp. Phys.*, 2010, **36**, 558–564.
44 M. H. Jensen and P. Bak, *Phys. Rev. B: Condens. Matter Mater. Phys.*, 1983, **27**, 6853–6868.
45 J. Ludwig, C. Marino, D. Haering, C. Stinner, H. A. Gasteiger and T. Nilges, *J. Power Sources*, 2017, **342**, 214–223.
46 B. El Bali and M. Bolte, *Acta Crystallogr., Sect. E: Struct. Rep. Online*, 2002, **58**, i32–i33.
47 A. El Belghiti, A. Boukhari and E. M. Holt, *Acta Crystallogr., Sect. C: Cryst. Struct. Commun.*, 1994, **50**, 482–484.
48 M. Trojan and D. Brandova, *Sb. Ved. Pr. - Vys. Sk. Chemickotechnol. Pardubice*, 1985, **47**, 33–42.

Electronic Supplementary Material (ESI) for RSC Advances.

RSC Advances

Supplementary Information

Direct synthesis and characterization of mixed-valent $Li_{0.5-\delta}CoPO_4$, a Li-deficient derivative of the *Cmcm* polymorph of $LiCoPO_4$

Jennifer Ludwig,[a] Carlos Alarcón-Suesca,[a] Stephan Geprägs,[b] Dennis Nordlund,[c] Marca M. Doeff,[d] Inés Puente Orench,[e,f] and Tom Nilges[a]*

[a] *Technical University of Munich, Department of Chemistry, Synthesis and Characterization of Innovative Materials, Lichtenbergstr. 4, 85747 Garching, Germany*
[b] *Walther Meissner Institute, Bavarian Academy of Sciences and Humanities, Walther-Meissner-Str. 8, 85747 Garching, Germany*
[c] *Stanford Synchrotron Radiation Lightsource, SLAC National Accelerator Laboratory, 2575 Sand Hill Rd, Menlo Park, CA, 94025, USA*
[d] *Lawrence Berkeley National Laboratory, Energy Storage and Distributed Resources Division, 1 Cyclotron Rd, Berkeley, CA, 94720, USA*
[e] *Instituto de Ciencia de Materiales de Aragón, Pedro Cerbuna 12, 50009 Zaragoza, Spain*
[f] *Institut Laue-Langevin, 71 avenue des Martyrs, B.P. 156, 38042 Grenoble Cedex 9, France*
* Corresponding author. E-mail: tom.nilges@lrz.tum.de, Tel.: +49 89 289 13110, Fax: +49 89 289 13762

Note

The following crystal structure datasets were used as starting models for all Rietveld refinements presented in this material:
$LiCoPO_4$ (*Cmcm*, $Z = 4$, ICSD no. 432186, see ref. [1])
$LiCoPO_4$ (*Pnma*, $Z = 4$, ICSD no. 431999, see ref. [2])
α-$Co_2P_2O_7$ ($P2_1/c$, $Z = 4$, ICSD no. 280959, see ref. [3])

For details on the refinements, please refer to the experimental part in the main article.

1 Detailed comparison of the X-ray powder diffraction patterns of $Li_{0.5-\delta}CoPO_4$ (*Cmcm*) and $Li_{1-\gamma}CoPO_4$ (*Cmcm*)

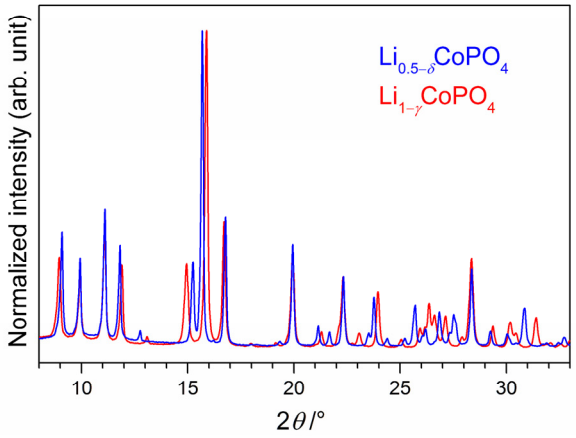

Figure S1 Comparison of the X-ray powder diffraction patterns (transmission geometry, Mo $K_{\alpha 1}$ radiation, measurement time: 12 h; displayed with normalized intensities for better comparison) of $Li_{0.5-\delta}CoPO_4$ (*Cmcm*, blue) and (b) $Li_{1-\gamma}CoPO_4$ (*Cmcm*, red) in the 2θ region of 25.5–27.5°. While the pattern of $Li_{0.5-\delta}CoPO_4$ appears to be roughly similar to the one of $LiCoPO_4$, indicating that the crystal structures are strongly correlated, some significant differences can be recognized. The (100) reflection at ~8.9° 2θ is shifted towards higher angles for $Li_{0.5-\delta}CoPO_4$, whereas the (021) and (002) reflections at ~11.9° and ~13.1° are shifted to larger values. A similar trend is observed for the (200) and (112) reflections at 15.0° and 15.9°, resulting in a narrowing of the two reflections. Furthermore, completely different peak patterns can be observed in the 2θ region of 25.5–27.5°. The described shifts are mainly related to changes in the cell dimensions.

2 Rietveld refinement details of $Li_{0.5-\delta}CoPO_4$ (*Cmcm*) and $Li_{1-\gamma}CoPO_4$ (*Cmcm*) based on X-ray powder diffraction data

Table S1 Crystallographic parameters of $Li_{0.5-\delta}CoPO_4$ and $Li_{1-\gamma}CoPO_4$ (both *Cmcm*, $Z = 4$) as refined from X-ray powder diffraction data ($T = 298$ K): (a,c) refinement with fixed Li and Co site occupancy factors (δ, $\gamma = 0$) compared to (b,d) the free refinement of the Li and Co occupancies ($\delta = 0.11(2)$, $\gamma = 0.06(2)$; *cf.* Table 1 in the main article) [a]

Empirical formula	**a) $Li_{0.5}CoPO_4$**	**b) $Li_{0.39(2)}Co_{0.96(1)}PO_4$**	**c) $LiCoPO_4$**	**d) $Li_{0.94(2)}Co_{0.96(1)}PO_4$**
M_r (g·mol^{-1})	157.4	154.3	160.8	158.1
Crystal system	orthorhombic	orthorhombic	orthorhombic	orthorhombic
Space group (No.)	*Cmcm* (63)	*Cmcm* (63)	*Cmcm* (63)	*Cmcm* (63)
Z	4	4	4	4
a (Å)	5.3386(2)	5.3385(2)	5.4433(3)	5.4432(3)
b (Å)	8.1763(4)	8.1763(3)	8.1694(4)	8.1695(4)
c (Å)	6.3714(3)	6.3716(2)	6.2128(3)	6.2128(3)
V (Å^3)	278.11(2)	278.116(19)	276.28(2)	276.28(2)
F(000)	302	297	308	302
ρ (calcd.) (g·cm^{-3})	3.759(1)	3.684(1)	3.867(1)	3.800(1)
R_p	0.0271	0.0257	0.0209	0.0196
R_{wp}	0.0347	0.0327	0.0272	0.0255
R_{exp}	0.0267	0.0267	0.0252	0.0252
R_F	0.0165	0.0143	0.0128	0.0106
R_B	0.0283	0.0254	0.0214	0.0184
χ^2	1.30	1.23	1.08	1.01
Data/restraints/ parameter	3800/0/57	3800/0/59	3835/0/55	3835/0/57

[a] The estimated standard deviations were calculated by the Berar's procedure and are indicated in parentheses.

Table S2 Fractional atomic coordinates and isotropic thermal displacement parameters of $Li_{0.5-\delta}CoPO_4$ and $Li_{1-\gamma}CoPO_4$ (both *Cmcm*, *Z* = 4) as refined from X-ray powder diffraction data (*T* = 298 K): (a,c) refinement with fixed Li and Co site occupancy factors (δ, γ = 0) compared to (b,d) the free refinement of the Li and Co occupancies (δ = 0.11(2), γ = 0.06(2)) [a]

Sample	Atom	Wyck. position	Occupancy	*x*/a	*y*/b	*z*/c	U_{iso} (Å^2)
a) $Li_{0.5}CoPO_4$	Li1	4*c*	0.5 [b]	0	0.675 [c]	¼	0.019 [c]
	Co1	4*a*	1	0	0	0	0.0150(7)
	P1	4*c*	1	0	0.3567(4)	¼	0.0131(9)
	O1	8*f*	1	0	0.2502(4)	0.0526(7)	0.0179(15)
	O2	8*g*	1	0.2347(6)	0.4621(5)	¼	0.0064(14)
b) $Li_{0.39(2)}Co_{0.96(1)}PO_4$	Li1	4*c*	0.39(2)	0	0.675 [c]	¼	0.019 [c]
	Co1	4*a*	0.964(5)	0	0	0	0.0133(6)
	P1	4*c*	1	0	0.3565(3)	¼	0.0152(9)
	O1	8*f*	1	0	0.2495(4)	0.0497(8)	0.0237(16)
	O2	8*g*	1	0.2355(6)	0.4633(4)	¼	0.0101(13)
c) $LiCoPO_4$	Li1	4*c*	1	0	0.675 [c]	¼	0.019 [c]
	Co1	4*a*	1	0	0	0	0.0107(5)
	P1	4*c*	1	0	0.3523(4)	¼	0.0064(8)
	O1	8*f*	1	0	0.2474(4)	0.0500(7)	0.0039(13)
	O2	8*g*	1	0.2255(6)	0.4653(5)	¼	0.0028(12)
d) $Li_{0.94(2)}Co_{0.96(1)}PO_4$	Li1	4*c*	0.94(2)	0	0.675 [c]	¼	0.019 [c]
	Co1	4*a*	0.955(5)	0	0	0	0.0091(5)
	P1	4*c*	1	0	0.3525(3)	¼	0.0097(8)
	O1	8*f*	1	0	0.2468(3)	0.0477(7)	0.0096(13)
	O2	8*g*	1	0.2273(5)	0.4667(5)	¼	0.0072(12)

[a] The estimated standard deviations were calculated by the Berar's procedure and are indicated in parentheses. [b] The occupancy of Li was kept fixed at 50% on basis of the Li contents determined by elemental analysis (see Table 2 in the main article), which indicated that $Li_{0.5-\delta}CoPO_4$ contains about half the amount of lithium compared to $Li_{1-\gamma}CoPO_4$. [c] Li positions and thermal displacement parameters have been fixed as they cannot be deduced by means of X-ray diffraction due to the low atomic scattering factor of Li.

Table S3 Selected interatomic distances of $Li_{0.5-\delta}CoPO_4$ and $Li_{1-\gamma}CoPO_4$ (both *Cmcm*, $Z = 4$) as refined from X-ray powder diffraction data ($T = 298$ K): (a,c) refinement with fixed Li and Co site occupancy factors (δ, $\gamma = 0$) compared to (b,d) the free refinement of the Li and Co occupancies ($\delta = 0.11(2)$, $\gamma = 0.06(2)$) [a]

Atom pair			Comment	*d* (Å)			
				a) $Li_{0.5}CoPO_4$	b) $Li_{0.39(2)}Co_{0.96(1)}PO_4$	c) $LiCoPO_4$	d) $Li_{0.94(2)}Co_{0.96(1)}PO_4$
Li1	O1	×2	$[LiO_4]$ unit	2.022(4)	2.007(5)	1.968(4)	1.957(4)
	O2	×2	$[LiO_4]$ unit	2.145(4)	2.140(3)	2.107(4)	2.104(3)
	Li–O average		$[LiO_4]$ unit	2.084	2.074	2.038	2.031
	Li1	×2	[100] direction	5.3386(5)	5.3385(4)	5.4433(6)	5.4432(5)
	Co1	×2	to next layer ([010])	3.0981(2)	3.09816(19)	3.0760(2)	3.0760(2)
	Co1	×4	within *ac* layer	3.4219(2)	3.42193(18)	3.4444(2)	3.4444(2)
	Li–Co average		–	3.3140	3.3140	3.3216	3.3216
	P1	×1	[010] direction	2.602(3)	2.604(3)	2.636(3)	2.635(3)
	P1	×2	[010] direction	3.0549(15)	3.0539(14)	3.0832(14)	3.0837(13)
	Li–P average		IR spectra	2.904	2.904	2.934	2.934
Co1	O1	×2	$[CoO_6]$ unit, to next layer ([010])	2.073(3)	2.065(3)	2.045(3)	2.038(3)
	O2	×4	$[CoO_6]$ unit (within *ac* layer)	2.154(2)	2.150(2)	2.174(2)	2.166(2)
	Co–O average		$[CoO_6]$ unit	2.127	2.122	2.131	2.123
	Li1	×2	to next layer ([010])	3.0981(2)	3.09816(19)	3.0760(2)	3.0760(2)
	Li1	×4	within *ac* layer	3.4219(2)	3.42193(18)	3.4444(2)	3.4444(2)
	Co–Li average		–	3.3140	3.3140	3.3216	3.3216
	Co1	×2	within *ac* layer ([001])	3.1857(3)	3.1858(2)	3.1064(3)	3.1064(3)
	Co1	×4	[010] to next layer	4.8824(3)	4.8824(3)	4.9084(4)	4.9084(3)
	Co1	×2	within *ac* layer ([100])	5.3386(5)	5.3385(4)	5.4433(6)	5.4432(5)
	Co–Co average		–	5.5723	4.5723	4.5916	4.5916
	P1	×2	to next layer ([010])	3.323(3)	3.321(3)	3.271(3)	3.272(2)
	P1	×4	within *ac* layer ([100])	3.3219(11)	3.3226(10)	3.3579(11)	3.3574(10)
	Co–P average		IR spectra	3.322	3.322	3.329	3.329
P1	O1	×2	$[PO_4]$ unit	1.530(5)	1.547(5)	1.510(4)	1.525(4)
	O2	×2	$[PO_4]$ unit	1.521(4)	1.531(4)	1.536(4)	1.550(4)
	P–O average		$[PO_4]$ unit	1.526	1.539	1.523	1.538
	Li1	×1	within *ac* layer ([010])	2.602(3)	2.604(3)	2.636(3)	2.635(3)
	Li1	×2	to next layer ([010])	3.0549(15)	3.0539(14)	3.0832(14)	3.0837(13)
	P–Li average		IR spectra	2.904	2.904	2.934	2.934
	P1	×2	[100] direction	5.3386(5)	5.3385(4)	5.4433(6)	5.4432(5)
	Co1	×2	to next layer ([010])	3.323(3)	3.321(3)	3.271(3)	3.272(2)
	Co1	×4	within *ac* layer ([100])	3.3219(11)	3.3226(10)	3.3579(11)	3.3574(10)
	P–Co average		IR spectra	3.322	3.322	3.329	3.329

[a] The estimated standard deviations were calculated by the Berar's procedure and are indicated in parentheses.

3 Rietveld refinement details of $Li_{0.5-\delta}CoPO_4$ (*Cmcm*) and $Li_{1-\gamma}CoPO_4$ (*Cmcm*) based on neutron powder diffraction data

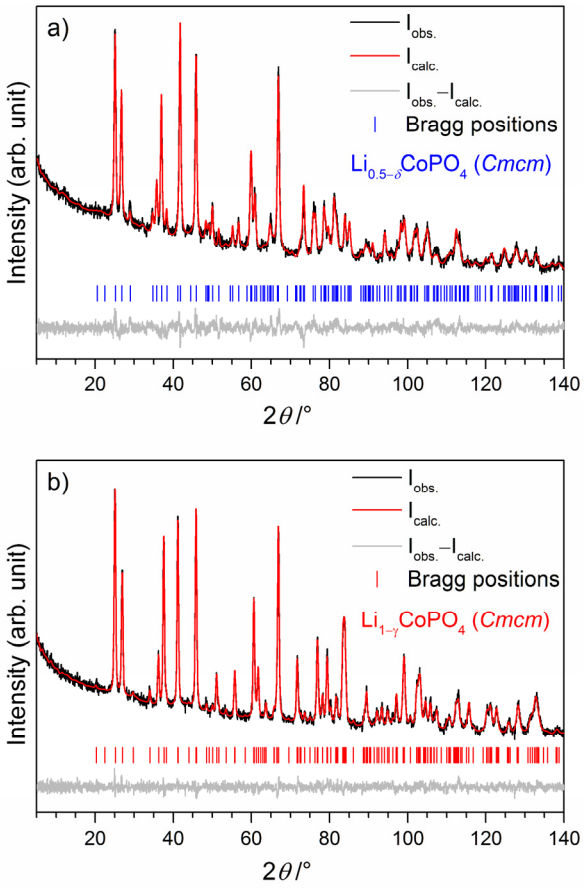

Figure S2 Rietveld fits of the neutron powder diffraction data (T = 296 K) of (a) $Li_{0.5-\delta}CoPO_4$ (*Cmcm*; refined composition: $Li_{0.37(4)}Co_{0.98(1)}PO_4$, δ = 0.13(4)), and (b) $Li_{1-\gamma}CoPO_4$ (*Cmcm*; refined composition: $Li_{0.90(2)}Co_{0.95(6)}PO_4$, γ = 0.10(2)).

Table S4 Crystallographic parameters of (a) $Li_{0.5-\delta}CoPO_4$ (δ = 0.13(4), *Cmcm*, Z = 4) and (b) $Li_{1-\gamma}CoPO_4$ (γ = 0.10(2), *Cmcm*, Z = 4) as refined from neutron powder diffraction data (T = 296 K) [a]

Empirical formula	**a) $Li_{0.37(4)}Co_{0.98(1)}PO_4$**	**b) $Li_{0.90(2)}Co_{0.95(6)}PO_4$**
M_r (g·mol^{-1})	154.3	157.8
Crystal system	orthorhombic	orthorhombic
Space group (No.)	*Cmcm* (63)	*Cmcm* (63)
Z	4	4
a (Å)	5.3385(2)	5.4432(0)
b (Å)	8.1763(3)	8.1695(0)
c (Å)	6.3716(2)	6.2128(0)
V (Å^3)	278.11(8)	276.27(2)
F(000)	12.99(7)	11.56(9)
ρ (calcd.) (g·cm^{-3})	3.711	3.788
R_p	0.0236	0.0237
R_{wp}	0.0299	0.0300
R_{exp}	0.0221	0.0256
R_F	0.0330	0.0207
R_B	0.052	0.0326
χ^2	1.88	1.38
Data/restraints/parameter	3200/0/14	3200/0/14

[a] The estimated standard deviations are indicated in parentheses.

Table S5 Fractional atomic coordinates and isotropic thermal displacement parameters of (a) $Li_{0.5-\delta}CoPO_4$ (δ = 0.13(4), *Cmcm*, *Z* = 4) and (b) $Li_{1-\gamma}CoPO_4$ (γ = 0.10(2), *Cmcm*, *Z* = 4) as refined from neutron powder diffraction data (*T* = 296 K) [a]

Sample	Atom	Wyck. position	Occupancy	*x*/a	*y*/b	*z*/c	U_{iso} (Å^2)
a) $Li_{0.37(4)}Co_{0.98(1)}PO_4$	Li1	4*c*	0.37(4)	0	0.543(4)	¼	0.023(10)
	Co1	4*a*	0.98(2)	0	0	0	0.006(3)
	P1	4*c*	1	0	0.3529(4)	¼	0.0094(7)
	O1	8*f*	1	0	0.2473(3)	0.0522(3)	0.0173(5)
	O2	8*g*	1	0.2365(5)	0.4629(3)	¼	0.0132(5)
b) $Li_{0.90(2)}Co_{0.95(6)}PO_4$	Li1	4*c*	0.90(3)	0	0.6760(11)	¼	0.017(3)
	Co1	4*a*	0.95(6)	0	0	0	0.0091(5)
	P1	4*c*	1	0	0.352700	¼	0.0098(9)
	O1	8*f*	1	0	0.2474(2)	0.0476(3)	0.0092(4)
	O2	8*g*	1	0.2280(4)	0.4668(2)	¼	0.0092(4)

[a] The estimated standard deviations are indicated in parentheses.

Table S6 Selected interatomic distances of (a) $Li_{0.5-\delta}CoPO_4$ (δ = 0.13(4), *Cmcm*, *Z* = 4) and (b) $Li_{1-\gamma}CoPO_4$ (γ = 0.10(2), *Cmcm*, *Z* = 4) as refined from neutron powder diffraction data (*T* = 296 K) [a]

Atom pair			*d* (Å)	
			a) $Li_{0.37(4)}Co_{0.98(1)}PO_4$	b) $Li_{0.90(2)}Co_{0.95(6)}PO_4$
Li1	O1	×2	2.58(2)	1.952(3)
	O2	×2	1.42(2)	2.112(8)
	Li1–O average		2.00	2.032
Co1	O1	×2	2.049(2)	2.043(2)
	O2	×4	2.1501(3)	2.163(2)
	Co1–O average		2.116	2.123
P1	O1	×2	1.528(3)	1.524(2)
	O2	×2	1.546(2)	1.552(2)
	P1–O average		1.537	1.538

[a] The estimated standard deviations are indicated in parentheses.

4 Additional illustrations of the crystal structures of $Li_{0.5-\delta}CoPO_4$ (*Cmcm*) and $Li_{1-\gamma}CoPO_4$ (*Cmcm*)

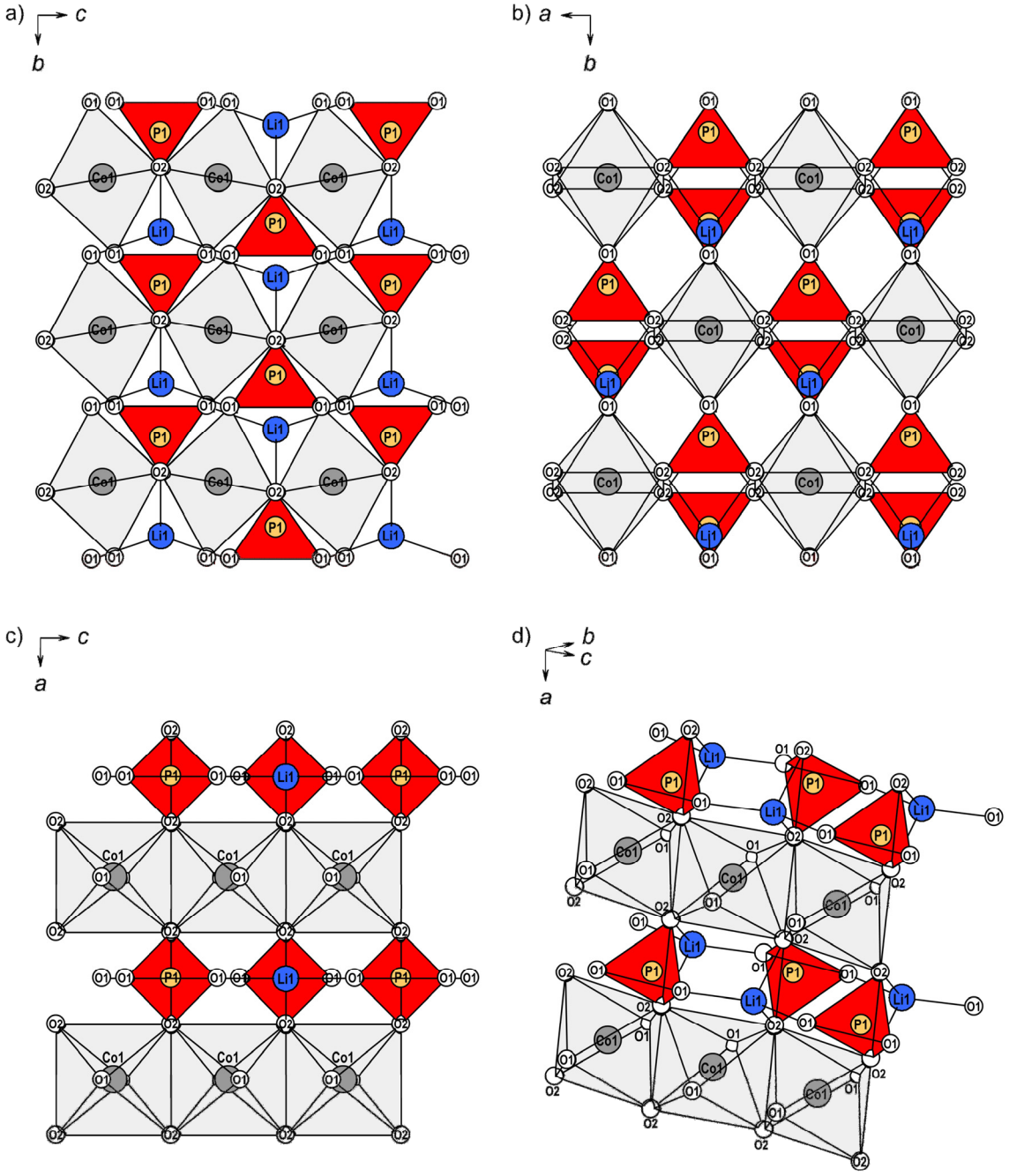

Figure S3 Detailed illustration of the crystal structures of *Cmcm*-type $Li_{0.5-\delta}CoPO_4$ and $Li_{1-\gamma}CoPO_4$ viewed along (a) [100], (b) [001], and (c) [010] (showing one layer of the composition $([CoO_6][LiO_4][PO_4])_\infty$). Li ions are drawn in blue, P atoms in orange, Co atoms in dark grey, and O atoms in white. $[CoO_6]$ octahedra are displayed in light grey, and $[PO_4]$ tetrahedra in red. The structure is built from $([CoO_6][LiO_4][PO_4])_\infty$ layers in the *ac* plane (c), which are stacked along *b* and connected *via* O1 atoms. In the layers, every $[CoO_6]$ octahedron shares two opposite O2–O2 edges with neighboring $[CoO_6]$ units, resulting in $[CoO_6]_\infty$ rows along [100], as well as two apical O2 atoms with two different $[PO_4]$ and $[LiO_4]$ tetrahedra (as demonstrated in d). The occupancies on the Li and Co sites are 39(2)% Li and 96.5(5)% Co for $Li_{0.5-\delta}CoPO_4$, and 94(2)% Li and 95.5(5)% Co for $Li_{1-\gamma}CoPO_4$.

5 Electrochemical stabilities (cycle life) of $Li_{0.5-\delta}CoPO_4$ (*Cmcm*) and $Li_{1-\gamma}CoPO_4$ (*Cmcm*)

Experimental details

The electrodes were prepared by mixing 80 wt% of the as-prepared lithium cobalt phosphate active material (*Cmcm*-type $Li_{0.5-\delta}CoPO_4$ or $Li_{1-\gamma}CoPO_4$), 10 wt% carbon (Super C65, Timcal), and 10 wt% polyvinylidene difluoride (PVDF, Solef, Solvay) binder in an agate mortar using *N*-methyl pyrrolidone (NMP) as solvent. The slurries were spread onto C-coated aluminum current collectors (Coveris Advanced Coatings) using a doctor-blade coater and then dried at 120 °C for 5 h in a vacuum oven (Thermo Scientific). The electrode sheets were calendered (International Rolling Mills device), and circular electrodes (diameter: 14.3 mm, average loading: ~4 mg) punched out. The electrochemical performance was tested using CR2032 coin cells with Li foil as anode (0.75 mm, Alfa Aesar, 99.9%, metals basis), a microporous monolayer PP membrane separator (Celgard 2400, 25 µm) and 1 M $LiPF_6$ in an ethylene carbonate (EC)/diethyl carbonate (DEC) mixture (1:1, *v*:*v*, Daikin) as electrolyte. The cells were assembled in an Ar-filled glove-box (VAC, < 0.1 ppm H_2O, < 0.1 ppm O_2). Charge–discharge cycling of two cells per material was carried out galvanostatically between 3.0 V and 5.2 V using a VMP3 multi-channel potentiostat/galvanostat (BioLogic) at 0.1 C, 0.2 C, 0.5 C, and 1 C for three cycles each in order to test the C rate capability, followed by 20 cycles at 0.1 C to evaluate the cycle life. Current densities and specific capacities were calculated using the weight of active material on the electrode. Note that the testing conditions, which were optimized for olivine-type $LiCoPO_4$ (*Pnma*), were not modified to improve the performance of the *Cmcm*-type materials.

Results and discussion

Since olivine-type $LiCoPO_4$ (*Pnma*) exhibits two two-phase redox reaction steps ($LiCoPO_4/Li_{2/3}CoPO_4$ and $Li_{2/3}CoPO_4/CoPO_4$)[4, 5] upon Li insertion–extraction, we assessed the electrochemical properties of both *Cmcm*-type materials, $Li_{0.5-\delta}CoPO_4$ and $Li_{1-\gamma}CoPO_4$, in order to elucidate whether the Li-deficient phase $Li_{0.5-\delta}CoPO_4$ represents an intermediate upon cycling of $Li_{1-\gamma}CoPO_4$ (*Cmcm*). The rate capabilities and coulombic efficiencies were investigated at 0.1 C, 0.2 C, 0.5 C, 1 C, and 2 C for three cycles each (Fig. S4a, inset), followed by 20 cycles at 0.1 C (Fig. S4b). The galvanostatic curves of the first cycle at 0.1 C (Fig. S4a) of both materials are similar despite the different Li contents and Co oxidation states and reveal that no plateau region is reached, which would be expected around ~4.3 V.[6] (Note that the corresponding curves at rates ≥ 0.2 C are not displayed as the capacities were extremely low). A discharge capacity of ~2.5 $mAh \cdot g^{-1}$ is obtained for both materials whereas the capacities upon first charge were 17 $mAh \cdot g^{-1}$ and 18 $mAh \cdot g^{-1}$, respectively. The large irreversible capacities are consistent with the high coulombic inefficiencies of about 85%, which indicate that irreversible reactions occur. The capacities are decreased upon further cycling. On basis of the comparably low capacities and the lack of a plateau region, it cannot be deduced whether $Li_{0.5-\delta}CoPO_4$ (*Cmcm*) represents an intermediate phase upon the delithiation of $Li_{1-\gamma}CoPO_4$ (*Cmcm*). The capacities and coulombic inefficiencies are most likely the result of the oxidation of cell components such as the conductive carbon and/or electrolyte decomposition at the high voltage used.[4, 7] Furthermore, the poor performance, which is in agreement with previous results on $LiCoPO_4$ (*Cmcm*)[6] is related to the intrinsically low Li-ion conductivities due to the lack of suitable Li migration pathways in the structure, as discussed in the main article. Therefore, future efforts should focus on optimizing the testing conditions (*e.g.* by the development of electrolyte suitable for the potential window) as well as the material (*e.g.* by carbon coating) in order to improve the performance and/or investigate the mechanisms which are responsible for the poor performance. The possibility of structural changes upon cycling might also be of special interest since the material is metastable (*cf.* thermal analysis section in the main article).

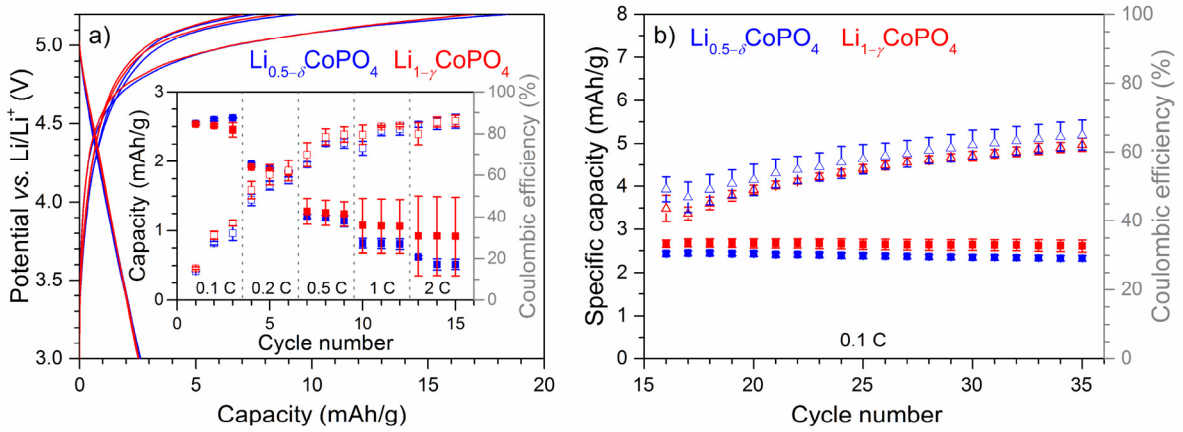

Figure S4 (a) Charge–discharge curves of $Li_{0.5-\delta}CoPO_4$ (*Cmcm*, blue), and $Li_{1-\gamma}CoPO_4$ (*Cmcm*, red) for the first three cycles at 0.1 C (the curves for rates ≥ 0.2 C are not shown as the capacities were very low). Inset: Specific discharge capacities (■) and coulombic efficiencies (□) vs. cycle number of both materials for the first 15 cycles at various C rates (capacities and error bars are derived from the values of two cells). (b) Specific discharge capacities (■) and respective coulombic efficiencies (Δ) (both average values from two cells) *vs.* cycle number of $Li_{0.5-\delta}CoPO_4$ (*Cmcm*, blue) and $Li_{1-\gamma}CoPO_4$ (*Cmcm*, red) for 20 cycles at 0.1 C after the first 15 cycles of C rate testing (a). The error bars represent the standard deviations from two cells. Conditions: 3.0–5.2 V, 1 M $LiPF_6$ in EC:DEC (1:1, v:v) at 25 °C.

6 Scanning electron microscopy (SEM) and energy-dispersive X-ray spectroscopy (EDS) of $Li_{0.5-\delta}CoPO_4$ (*Cmcm*) and $Li_{1-\gamma}CoPO_4$ (*Cmcm*)

Experimental details

A JEOL JSM-7500F high-resolution SEM using an accelerating voltage of 1 kV, a working distance of 8 mm, and a LEI (lower secondary electron image) detector was used to investigate the morphology of the material. Semi-quantitative EDS analysis was performed at an acceleration voltage of 15 kV and a probe current of 20 µA (Noran system S1X system, Thermo Electron Corporation, model 6714A01SUS-SN). The powder samples were prepared on conductive carbon tape which was attached to an aluminum stub.

Results and discussion

High-resolution SEM images (Fig. S5) reveal that both powders contain agglomerates with a dumbbell-like morphology. While the nanosheet-like primary particles of both materials are comparable in size and shape (length: ~50–100 nm, thickness: < 10 nm; Fig. S5b,e), the dumbbells of $Li_{0.5-\delta}CoPO_4$ are about 3–4 times larger than the ones observed in $LiCoPO_4$ (~4 µm × 6 µm *vs.* ~1 µm × 2 µm; Fig. S5a,d). The different dimensions of the agglomerates are most likely related to the different precursor concentrations in the TTEG solvent. As for the production of *Cmcm*-type $LiCoPO_4$, a higher portion of lithium acetate was used (while the amounts of cobalt acetate and phosphoric acid remained unaltered), a higher degree of supersaturation was reached in the viscous solvent. Consequently, nucleation was favored over crystal growth processes under these conditions, producing smaller particles. Because no additives or organic templates are required to obtain these complex morphologies, it can be inferred that TTEG exhibits a soft template effect, which allows to direct the growth and self-assembly of hierarchical structures with preferred orientations.[8] EDS analysis delivers a composition of 37(3) wt% Co, 20.5(8) wt% P, and 43(2) wt% O for $Li_{0.5-\delta}CoPO_4$ (Fig. S5c), and 36(1) wt% Co, 20.7(3) wt% P, and 43.4(6) wt% O for $Li_{1-\gamma}CoPO_4$ (Fig. S5f), corresponding to Co:P:O molar ratios of 0.94(8):1.00(4):4.0(2) and 0.91(3):1.00(1):4.06(6), respectively. The deficit in Co found for both samples is in line with the results of the elemental analysis (*cf.* Table 2 in the main article).

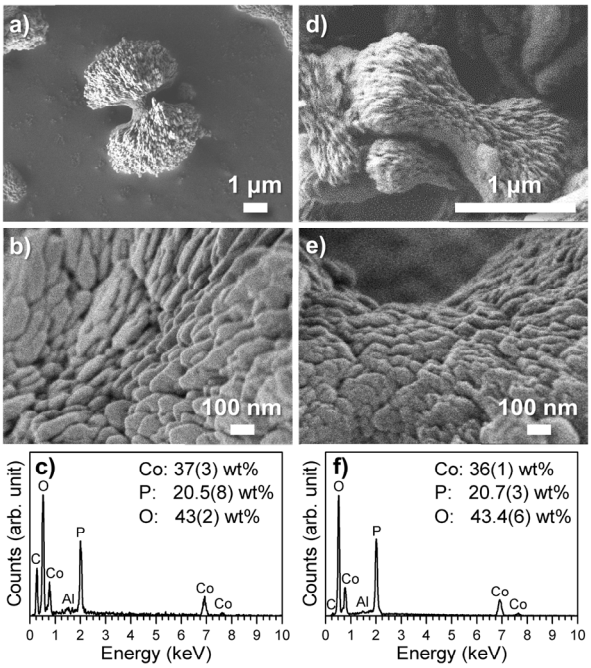

Figure S5 SEM images and corresponding EDS spectra of (a,b,c) $Li_{0.5-\delta}CoPO_4$ (*Cmcm*), and (d,e,f) $Li_{1-\gamma}CoPO_4$ (*Cmcm*). The C and Al signals observed in the EDS spectra (c,f) arise from the carbon tape and the aluminum sample holder used for the measurements.

7 Full infrared spectra of $Li_{0.5-\delta}CoPO_4$ (*Cmcm*) and $Li_{1-\gamma}CoPO_4$ (*Cmcm*)

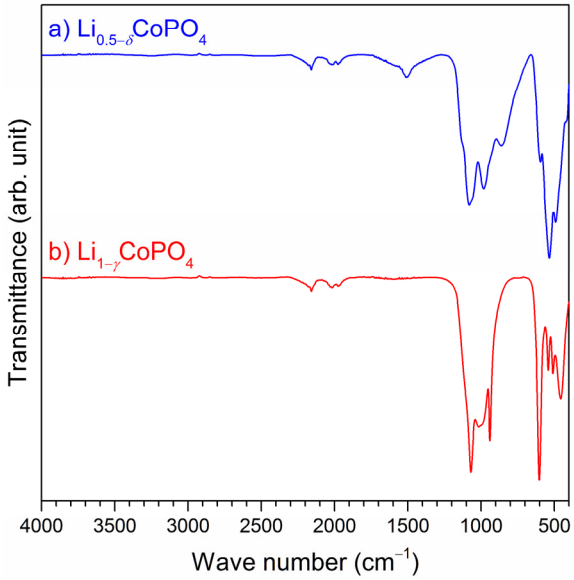

Figure S6 Comparison of the full FTIR spectra of (a) $Li_{0.5-\delta}CoPO_4$ (*Cmcm*, blue), and (b) $Li_{1-\gamma}CoPO_4$ (*Cmcm*, red, data reproduced from reference [1]). The samples do not contain any detectable amounts of water or other impurities. The absorption bands around 2000–2200 cm^{-1} are because of the diamond ATR setup.

8 Additional magnetic measurements of $Li_{0.5-\delta}CoPO_4$ (*Cmcm*) and $Li_{1-\gamma}CoPO_4$ (*Cmcm*)

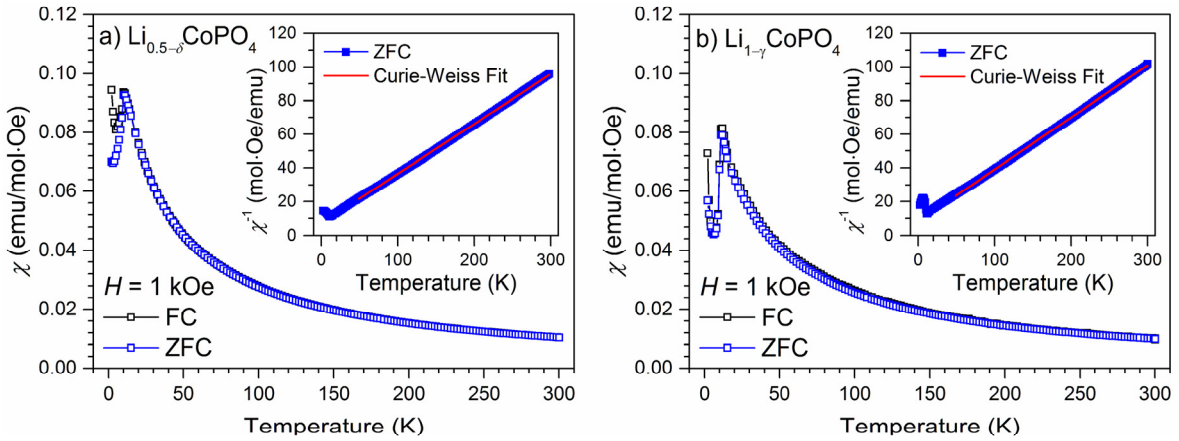

Figure S7 Magnetic susceptibility as a function of the temperature of (a) $Li_{0.5-\delta}CoPO_4$ (*Cmcm*), and (b) $Li_{1-\gamma}CoPO_4$ (*Cmcm*) at zero-field-cooled (ZFC) and field-cooled (FC) conditions under a constant applied field of 1 kOe. The insets show the inverse magnetic susceptibility and the Curie–Weiss fitting from $T = 50$ K to 300 K under ZFC conditions. The temperature dependence of the magnetic susceptibility indicates an antiferromagnetic order below the Néel-temperatures of $T_N = 10.5$ K and 11 K for $Li_{0.5-\delta}CoPO_4$ (*Cmcm*) and $Li_{1-\gamma}CoPO_4$ (*Cmcm*), respectively. In the high-temperature region, the inverse magnetic susceptibility is well described by the Curie–Weiss law. The fit to the data delivers effective magnetic moments of $\mu_{eff} = (5.20 \pm 0.02)\ \mu_B$ for $Li_{0.5-\delta}CoPO_4$ and $(5.08 \pm 0.02)\ \mu_B$ for $Li_{1-\gamma}CoPO_4$, respectively.

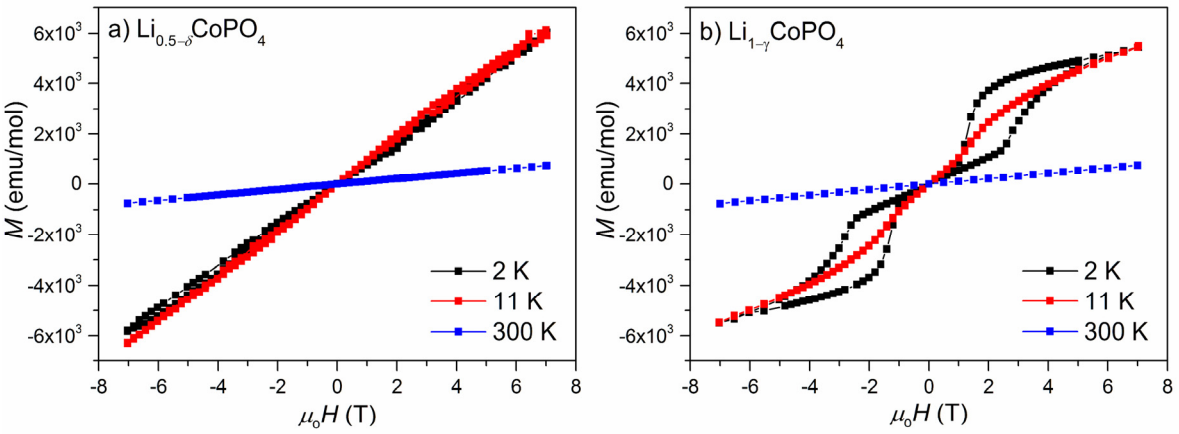

Figure S8 Magnetization as a function of the applied magnetic field between 7 and −7 T of (a) $Li_{0.5-\delta}CoPO_4$ (*Cmcm*), and (b) $Li_{1-\gamma}CoPO_4$ (*Cmcm*) recorded at temperatures of 2 K, 11 K, and 300 K, respectively. In contrast to the $Li_{1-\gamma}CoPO_4$ compound, no spin-flip transitions indicated by the double-hysteresis loop could be observed at low temperature in the Li-deficient $Li_{0.5-\delta}CoPO_4$ phase. Furthermore, no indication of a weak ferromagnetic component due to the mixed-valence state of the Co ions could be found in the magnetic hysteresis loops.

9 Rietveld refinement of the sample obtained after the TGA/DSC measurement of $Li_{0.5-\delta}CoPO_4$ (*Cmcm*) under synthetic air

Table S7 Crystallographic details and phase fractions of the phases observed in the X-ray powder diffraction pattern (T = 298 K) of the post-TGA/DSC (temperature range: 30–900 °C, atmosphere: synthetic air; *cf.* Fig. 6) sample of $Li_{0.5-\delta}CoPO_4$ (*Cmcm*) [a]

Phase	$LiCoPO_4$	α-$Co_2P_2O_7$
Space group	***Pnma***	***P*2$_1$/*c***
Phase fraction (wt%)	**44.9(6)**	**55.1(6)**
Z	4	4
a (Å)	10.2073(5)	7.0065(4)
b (Å)	5.9227(3)	8.3631(5)
c (Å)	4.7008(3)	9.0096(5)
α (°)	90	90
β (°)	90	113.648(3)
γ (°)	90	90
V (Å^3)	284.18(3)	483.60(5)
F(000)	560	
ρ (calcd.) (g·cm^{-3})	3.759(1)	4.008(1)
R_p	0.0411	
R_{wp}	0.0595	
R_{exp}	0.0328	
R_F	0.0374	0.0367
R_B	0.0565	0.0565
χ^2	1.82	
Data/restraints/parameter	3808/0/118	

[a] The estimated standard deviations were calculated by the Berar's procedure and are indicated in parentheses.

Table S8 Fractional atomic coordinates and isotropic thermal displacement parameters of $LiCoPO_4$ (*Pnma*, *Z* = 4) as refined from X-ray powder diffraction data (*T* = 298 K) of the post-TGA/DSC (temperature range: 30–900 °C, atmosphere: synthetic air) sample of $Li_{0.5-\delta}CoPO_4$ (*Cmcm*) [a]

Atom	Wyckoff position	Occupancy	*x*/a	*y*/b	*z*/c	U_{iso} (Å^2)
Li1	4*a*	1	0	0	0	0.0139 [b]
Co1	4*c*	1	0.2214(3)	¼	0.5212(9)	0.0109(15)
P1	4*c*	1	0.4046(8)	¼	0.0808(16)	0.013(2)
O1	4*c*	1	0.4052(19)	¼	0.761(3)	0.007(3)
O2	4*c*	1	0.048(2)	¼	0.298(3)	0.008(2)
O3	8*d*	1	0.3345(15)	0.047(2)	0.218(2)	0.007(2)

[a] The estimated standard deviations were calculated by the Berar's procedure and are indicated in parentheses. [b] Li positions and thermal displacement parameters have been fixed as they cannot be deduced by means of X-ray diffraction due to the low atomic scattering factor of Li.

Table S9 Selected interatomic distances of $LiCoPO_4$ (*Pnma*, *Z* = 4) as refined from X-ray powder diffraction data (*T* = 298 K) of the post-TGA/DSC (temperature range: 30–900 °C, atmosphere: synthetic air) sample of $Li_{0.5-\delta}CoPO_4$ (*Cmcm*) [a]

Atom pair			*d* (Å)
Li1	O1	×2	2.152(12)
	O2	×2	2.095(11)
	O3	×2	2.165(14)
	Li1–O average		2.137
Co1	O1	×1	2.189(19)
	O2	×1	2.06(2)
	O3	×2	2.068(12)
	O3	×2	2.192(13)
	Co1–O average		2.128
P1	O1	×1	1.504(16)
	O2	×1	1.57(2)
	O3	×2	1.541(14)
	P1–O average		1.539

[a] The estimated standard deviations were calculated by the Berar's procedure and are indicated in parentheses.

Table S10 Fractional atomic coordinates and isotropic thermal displacement parameters of α-$Co_2P_2O_7$ ($P2_1/c$, $Z = 4$) as refined from X-ray powder diffraction data ($T = 298$ K) of post-TGA/DSC (temperature range: 30–900 °C, atmosphere: synthetic air) sample of $Li_{0.5-\delta}CoPO_4$ (*Cmcm*) [a]

Atom	Wyckoff position	Occupancy	*x*/a	*y*/b	*z*/c	U_{iso} (Å^2)
Co1	4*e*	1	0.2329(16)	0.9293(9)	0.1088(13)	0.012(2)
Co2	4*e*	1	0.7001(12)	0.4421(11)	0.8248(9)	0.014(3)
P1	4*e*	1	0.942(3)	0.7656(19)	0.758(2)	0.011(5)
P2	4*e*	1	0.534(3)	0.7744(19)	0.468(2)	0.010(5)
O1	4*e*	1	0.751(7)	0.830(3)	0.605(5)	0.010(4)
O2	4*e*	1	0.378(6)	0.766(4)	0.549(4)	0.006(4)
O3	4*e*	1	1.120(5)	0.755(3)	0.705(4)	0.005(5)
O4	4*e*	1	0.979(7)	0.906(5)	0.880(4)	0.009(4)
O5	4*e*	1	0.886(5)	0.607(5)	0.816(4)	0.008(5)
O6	4*e*	1	0.486(5)	0.908(4)	0.340(4)	0.007(4)
O7	4*e*	1	0.555(6)	0.615(4)	0.397(4)	0.006(5)

[a] The estimated standard deviations were calculated by the Berar's procedure and are indicated in parentheses.

Table S11 Selected interatomic distances of α-$Co_2P_2O_7$ ($P2_1/c$, $Z = 4$) as refined from X-ray powder diffraction data ($T = 298$ K) of the post-TGA/DSC (temperature range: 30–900 °C, atmosphere: synthetic air) sample of $Li_{0.5-\delta}CoPO_4$ (*Cmcm*) [a]

Atom pair			*d* (Å)
Co1	O2	×1	2.11(4)
	O3	×1	2.08(4)
	O4	×1	2.06(5)
	O4	×1	2.13(3)
	O6	×1	2.14(3)
	O7	×1	2.17(4)
	Co1–O average		2.12
Co2	O2	×1	2.06(4)
	O3	×1	2.09(4)
	O5	×1	1.92(4)
	O6	×1	2.00(4)
	O7	×1	2.13(3)
	Co2–O average		2.04
P1	O1	×1	1.58(4)
	O3	×1	1.51(5)
	O4	×1	1.55(5)
	O5	×1	1.53(4)
	P1–O average		1.54
P2	O1	×1	1.59(4)
	O2	×1	1.54(5)
	O6	×1	1.54(4)
	O7	×1	1.51(4)
	P2–O average		1.55

[a] The estimated standard deviations were calculated by the Berar's procedure and are indicated in parentheses.

10 Thermal stability of $Li_{0.5-\delta}CoPO_4$ (*Cmcm*) under Ar

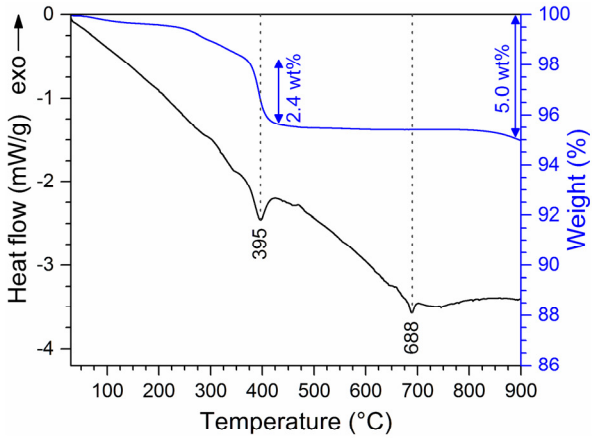

Figure S9 DSC (black) and TGA (blue) curves of $Li_{0.5-\delta}CoPO_4$ (*Cmcm*) measured in a temperature range of 30–900 °C (heating rate: 10 °C·min^{-1}) under Ar. Two endothermic signals are observed in the DSC curve at 395 °C (accompanied by a weight loss step of ~2.4 wt%) and 688 °C, respectively. The data are in good agreement with the TGA/DSC measurement performed under synthetic air (*cf.* Fig. 6 in the main article).

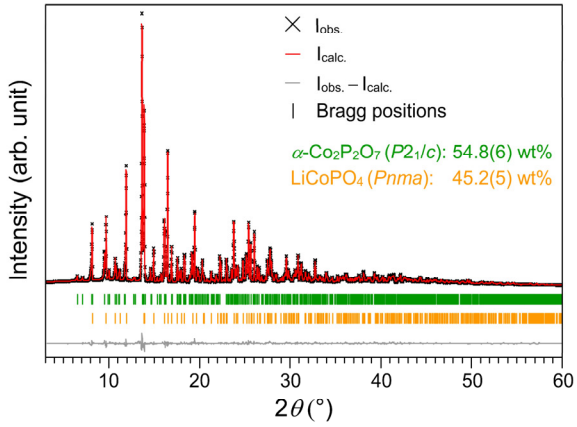

Figure S10 Rietveld fit of the X-ray powder diffraction data (transmission geometry, Mo $K_{\alpha1}$ radiation) of the dark violet material obtained after the TGA/DSC measurement of $Li_{0.5-\delta}CoPO_4$ (*Cmcm*) under Ar (T = 30–900 °C, heating rate: 10 °C·min^{-1}; *cf.* Fig. S9). Similar to the material obtained from the TGA/DSC measurement under synthetic air (*cf.* Fig. 6 in the main article), a mixture of olivine-type $LiCoPO_4$ (*Pnma*) and α-$Co_2P_2O_7$ ($P2_1/c$) was formed upon heating.

Table S12 Crystallographic details and phase fractions of the phases observed in the X-ray powder diffraction pattern (T = 298 K) of the post-TGA/DSC (temperature range: 30–900 °C, atmosphere: Ar; *cf.* Fig. S9) sample of $Li_{0.5-\delta}CoPO_4$ (*Cmcm*) [a]

Phase	**$LiCoPO_4$**	**α-$Co_2P_2O_7$**
Space group	***Pnma***	***$P2_1/c$***
Phase fraction (wt%)	**45.2(5)**	**54.8(6)**
Z	4	4
a (Å)	10.2108(5)	7.0089(4)
b (Å)	5.9247(3)	8.3659(5)
c (Å)	4.7025(2)	9.0127(5)
α (°)	90	90
β (°)	90	113.647(3)
γ (°)	90	90
V (Å^3)	284.48(3)	484.10(5)
F(000)	560	
ρ (calcd.) (g·cm^{-3})	3.756(1)	4.004(1)
R_p	0.0414	
R_{wp}	0.0599	
R_{exp}	0.0330	
R_F	0.0362	0.0347
R_B	0.0557	0.0534
χ^2	1.82	
Data/restraints/parameter	3803/0/118	

[a] The estimated standard deviations were calculated by the Berar's procedure and are indicated in parentheses.

Table S13 Fractional atomic coordinates and isotropic thermal displacement parameters of $LiCoPO_4$ (*Pnma*, $Z = 4$) as refined from X-ray powder diffraction data ($T = 298$ K) of the post-TGA/DSC (temperature range: 30–900 °C, atmosphere: Ar) sample of $Li_{0.5-\delta}CoPO_4$ (*Cmcm*) [a]

Atom	Wyckoff position	Occupancy	*x*/a	*y*/b	*z*/c	U_{iso} (Å^2)
Li1	4*a*	1	0	0	0	0.0139 [b]
Co1	4*c*	1	0.2215(3)	¼	0.5209(9)	0.0113(15)
P1	4*c*	1	0.4048(8)	¼	0.0806(15)	0.012(2)
O1	4*c*	1	0.4046(19)	¼	0.760(3)	0.005(3)
O2	4*c*	1	0.048(2)	¼	0.297(3)	0.008(2)
O3	8*d*	1	0.3344(15)	0.046(2)	0.217(2)	0.006(2)

[a] The estimated standard deviations were calculated by the Berar's procedure and are indicated in parentheses. [b] The Li position and thermal displacement parameter have been fixed as they cannot be deduced by means of X-ray diffraction due to the low atomic scattering factor of Li.

Table S14 Selected interatomic distances of $LiCoPO_4$ (*Pnma*, $Z = 4$) as refined from X-ray powder diffraction data ($T = 298$ K) of the post-TGA/DSC (temperature range: 30–900 °C, atmosphere: Ar) sample of $Li_{0.5-\delta}CoPO_4$ (*Cmcm*) [a]

Atom pair			*d* (Å)
Li1	O1	×2	2.154(12)
	O2	×2	2.097(11)
	O3	×2	2.166(13)
	Li1–O average		2.14
Co1	O1	×1	2.182(18)
	O2	×1	2.06(2)
	O3	×2	2.067(12)
	O3	×2	2.194(12)
	Co1–O average		2.13
P1	O1	×1	1.507(16)
	O2	×1	1.57(2)
	O3	×2	1.545(13)
	P1–O average		1.54

[a] The estimated standard deviations were calculated by the Berar's procedure and are indicated in parentheses.

Table S15 Fractional atomic coordinates and isotropic thermal displacement parameters of α-$Co_2P_2O_7$ ($P2_1/c$, $Z = 4$) as refined from X-ray powder diffraction data ($T = 298$ K) of the post-TGA/DSC (temperature range: 30–900 °C, atmosphere: Ar) sample of $Li_{0.5-\delta}CoPO_4$ (*Cmcm*) [a]

Atom	Wyckoff position	Occupancy	*x*/a	*y*/b	*z*/c	U_{iso} (Å^2)
Co1	4*e*	1	0.2334(16)	0.9295(8)	0.1091(13)	0.010(2)
Co2	4*e*	1	0.6998(12)	0.4418(10)	0.8248(9)	0.013(3)
P1	4*e*	1	0.943(3)	0.7666(19)	0.759(2)	0.012(5)
P2	4*e*	1	0.536(3)	0.7742(19)	0.469(2)	0.010(5)
O1	4*e*	1	0.750(7)	0.831(3)	0.606(5)	0.013(5)
O2	4*e*	1	0.377(5)	0.767(4)	0.549(4)	0.009(4)
O3	4*e*	1	1.119(5)	0.754(3)	0.704(4)	0.011(3)
O4	4*e*	1	0.980(7)	0.907(5)	0.880(4)	0.010(3)
O5	4*e*	1	0.884(5)	0.607(5)	0.815(4)	0.009(3)
O6	4*e*	1	0.487(5)	0.907(4)	0.340(3)	0.005(2)
O7	4*e*	1	0.555(5)	0.616(4)	0.398(3)	0.006(2)

[a] The estimated standard deviations were calculated by the Berar's procedure and are indicated in parentheses.

Table S16 Selected interatomic distances of α-$Co_2P_2O_7$ ($P2_1/c$, $Z = 4$) as refined from X-ray powder diffraction data ($T = 298$ K) of the post-TGA/DSC (temperature range: 30–900 °C, atmosphere: Ar) sample of $Li_{0.5-\delta}CoPO_4$ (*Cmcm*) [a]

Atom pair			***d* (Å)**
Co1	O2	×1	2.11(4)
	O3	×1	2.07(4)
	O4	×1	2.06(5)
	O4	×1	2.12(3)
	O6	×1	2.14(3)
	O7	×1	2.17(4)
	Co1–O average		2.11
Co2	O2	×1	2.05(4)
	O3	×1	2.10(3)
	O5	×1	1.92(4)
	O6	×1	2.01(4)
	O7	×1	2.14(3)
	Co2–O average		2.04
P1	O1	×1	1.59(4)
	O3	×1	1.51(5)
	O4	×1	1.55(5)
	O5	×1	1.54(4)
	P1–O average		1.55
P2	O1	×1	1.58(4)
	O2	×1	1.55(5)
	O6	×1	1.54(3)
	O7	×1	1.50(4)
	P2–O average		1.54

[a] The estimated standard deviations were calculated by the Berar's procedure and are indicated in parentheses.

11 Rietveld refinements of the *in situ* X-ray powder diffraction patterns upon heating of $Li_{0.5-\delta}CoPO_4$ (*Cmcm*) under air in the temperature range of 30–700 °C

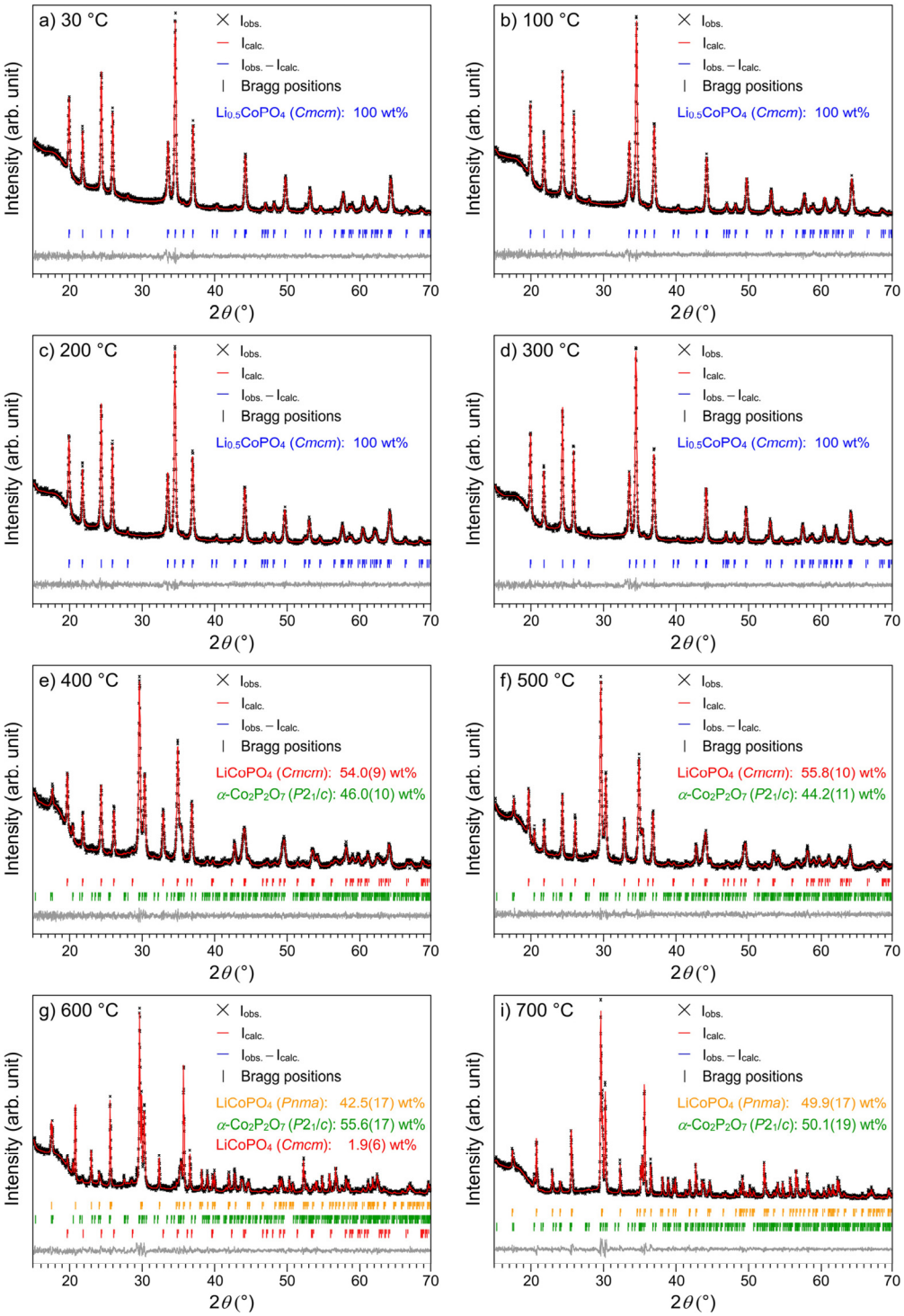

Figure S11 Rietveld fits of the *in situ* X-ray powder diffraction patterns (Bragg-Brentano geometry, Cu K_α radiation) of $Li_{0.5-\delta}CoPO_4$ (*Cmcm*; with $\delta = 0$) between 30 °C and 700 °C under air. The data at 800 °C, 900 °C, and after cooling to 25 °C are not shown because mainly reflections caused by the corundum sample holder were observed, which did not allow for a refinement of the phase fractions (*cf.* Fig. S12). Note that the Bragg reflections indicate the $K_{\alpha1}$ and $K_{\alpha2}$ peaks.

Table S17 Crystallographic details and phase fractions of the phases observed in the *in situ* X-ray powder diffraction patterns of $Li_{0.5-\delta}CoPO_4$ (*Cmcm*) between 30 °C and 700 °C under air [a]

Temperature	a) 30 °C	b) 100 °C	c) 200 °C	d) 300 °C	e) 400 °C		f) 500 °C		g) 600 °C [d]		h) 700 °C	
Phase	$Li_{0.5}CoPO_4$ [b]	$Li_{0.5}CoPO_4$ [b]	$Li_{0.5}CoPO_4$ [b]	$Li_{0.5}CoPO_4$ [b]	$LiCoPO_4$ [c]	α-$Co_2P_2O_7$	$LiCoPO_4$ [c]	α-$Co_2P_2O_7$	$LiCoPO_4$	α-$Co_2P_2O_7$	$LiCoPO_4$	α-$Co_2P_2O_7$
Space group	*Cmcm*	*Cmcm*	*Cmcm*	*Cmcm*	*Cmcm*	$P2_1/c$	*Cmcm*	$P2_1/c$	*Pnma*	$P2_1/c$	*Pnma*	$P2_1/c$
Phase fraction (wt%)	100	100	100	100	54.0(9)	46.0(10)	55.8(10)	44.2(11)	42.5(17)	55.6(17)	49.9(17)	50.1(19)
Z	4	4	4	4	4	4	4	4	4	4	4	4
a (Å)	5.3378(4)	5.3416(3)	5.3496(4)	5.3505(4)	5.4612(6)	7.0109(13)	5.4695(6)	7.0163(12)	10.2763(8)	7.0239(16)	10.2952(10)	7.0238(9)
b (Å)	8.1746(5)	8.1812(5)	8.1956(5)	8.2057(6)	8.2012(8)	8.3650(16)	8.2142(9)	8.3706(15)	6.0031(5)	8.3702(18)	6.0191(5)	8.3836(10)
c (Å)	6.3694(4)	6.3751(3)	6.3842(4)	6.4050(4)	6.2569(6)	9.0391(16)	6.2645(6)	9.0462(16)	4.7528(5)	9.0543(19)	4.7624(5)	9.0593(12)
α (°)	90	90	90	90	90	90	90	90	90	90	90	90
β (°)	90	90	90	90	90	114.218(8)	90	114.137(8)	90	114.067(12)	90	113.997(7)
γ (°)	90	90	90	90	90	90	90	90	90	90	90	90
V (Å^3)	277.93(3)	278.60(3)	279.90(3)	281.21(3)	280.24(5)	483.45(16)	281.44(5)	484.84(15)	293.19(5)	486.04(19)	295.11(5)	487.35(11)
F(000)	302	302	302	302	560		560		308		560	
ρ (calcd.) (g·cm^{-3})	3.761(1)	3.752(1)	3.735(1)	3.717(1)	3.812(1)	4.009(1)	3.796(1)	3.998(1)	3.644(1)	3.988(1)	3.620(1)	3.977(1)
R_p	0.0326	0.0333	0.0340	0.0357	0.0342		0.0349		0.0469		0.0525	
R_{wp}	0.0425	0.0431	0.0445	0.0462	0.0437		0.0458		0.0618		0.0709	
R_{exp}	0.0377	0.0383	0.0388	0.0392	0.0393		0.0396		0.0396		0.0407	
R_F	0.0187	0.0164	0.0186	0.0220	0.0155	0.0251	0.0207	0.0250	0.0371	0.0489	0.0600	0.0406
R_B	0.0456	0.0456	0.0456	0.0456	0.0264	0.0325	0.0320	0.0380	0.0614	0.0716	0.1013	0.0550
χ^2	1.13	1.12	1.15	1.18	1.11		1.16		1.56		1.74	
Data/restraints/ parameter	3291/0/52	3291/0/52	3291/0/52	3291/0/52	3291/0/104		3291/0/104		3291/0/111		3291/0/111	

[a] The estimated standard deviations were calculated by the Berar's procedure and are indicated in parentheses. [b] $Li_{0.5-\delta}CoPO_4$ with $\delta = 0$ for simplicity. [c] $Li_{1-\gamma}CoPO_4$ with $\gamma = 0$ for simplicity. [d] The cell parameters of the third phase $LiCoPO_4$ (*Cmcm*) were not refined as the phase fraction accounted for only 1.9(6) wt% (*cf.* Fig. S11).

Table S18 Fractional atomic coordinates and isotropic thermal displacement parameters of $Li_{0.5}CoPO_4$ ($Li_{0.5-\delta}CoPO_4$ with δ = 0, *Cmcm*, *Z* = 4) as refined from temperature-dependent *in situ* X-ray powder diffraction data at 30 °C, 100 °C, 200 °C, and 300 °C [a]

Temperature	Atom	Wyck. position	Occupancy	*x*/a	*y*/b	*z*/c	U_{iso} (Å^2)
a) 30 °C	Li1	4*c*	0.5 [b]	0	0.675 [c]	¼	0.019 [c]
	Co1	4*a*	1	0	0	0	0.0136(17)
	P1	4*c*	1	0	0.3578(8)	¼	0.0053(15)
	O1	8*f*	1	0	0.2540(6)	0.0555(12)	0.0048(13)
	O2	8*g*	1	0.2427(10)	0.4631(8)	¼	0.0052(13)
b) 100 °C	Li1	4*c*	0.5 [b]	0	0.675 [c]	¼	0.019 [c]
	Co1	4*a*	1	0	0	0	0.0136(15)
	P1	4*c*	1	0	0.3587(7)	¼	0.0040(18)
	O1	8*f*	1	0	0.2544(5)	0.0580(11)	0.0046(12)
	O2	8*g*	1	0.2416(9)	0.4625(7)	¼	0.0048(12)
c) 200 °C	Li1	4*c*	0.5 [b]	0	0.675 [c]	¼	0.019 [c]
	Co1	4*a*	1	0	0	0	0.0142(18)
	P1	4*c*	1	0	0.3582(8)	¼	0.0056(12)
	O1	8*f*	1	0	0.2539(6)	0.0575(12)	0.0053(13)
	O2	8*g*	1	0.2430(10)	0.4614(8)	¼	0.0055(13)
d) 300 °C	Li1	4*c*	0.5 [b]	0	0.675 [c]	¼	0.019 [c]
	Co1	4*a*	1	0	0	0	0.0149(20)
	P1	4*c*	1	0	0.3565(9)	¼	0.0058(12)
	O1	8*f*	1	0	0.2528(7)	0.0564(15)	0.0055(13)
	O2	8*g*	1	0.2447(12)	0.4637(9)	¼	0.0059(13)

[a] The estimated standard deviations were calculated by the Berar's procedure and are indicated in parentheses. [b] The Li occupancy factors were kept fixed at 50% (δ = 0). [c] Li positions and thermal displacement parameters have been fixed as they cannot be deduced by means of X-ray diffraction due to the low atomic scattering factor of Li.

Table S19 Selected interatomic distances of $Li_{0.5}CoPO_4$ ($Li_{0.5-\delta}CoPO_4$ with $\delta = 0$, *Cmcm*, $Z = 4$) as refined from temperature-dependent *in situ* X-ray powder diffraction data at 30 °C, 100 °C, 200 °C, and 300 °C [a]

	Atom pair		*d* (Å)			
			a) 30 °C	**b) 100 °C**	**c) 200 °C**	**d) 300 °C**
Li1	O1	×2	2.031(8)	2.047(7)	2.048(8)	2.050(9)
	O2	×2	2.163(6)	2.165(5)	2.180(6)	2.172(7)
	Li1–O average		2.097	2.106	2.114	2.111
Co1	O1	×2	2.106(5)	2.114(4)	2.113(5)	2.106(6)
	O2	×4	2.124(4)	2.131(3)	2.130(4)	2.126(4)
	Co1–O average		2.118	2.125	2.124	2.119
P1	O1	×2	1.502(8)	1.492(7)	1.497(8)	1.504(9)
	O2	×2	1.555(7)	1.545(6)	1.551(7)	1.577(8)
	P1–O average		1.529	1.519	1.524	1.541

[a] The estimated standard deviations were calculated by the Berar's procedure and are indicated in parentheses.

Table S20 Fractional atomic coordinates and isotropic thermal displacement parameters of $LiCoPO_4$ ($Li_{1-y}CoPO_4$ with $y = 0$, *Cmcm*, $Z = 4$) as refined from temperature-dependent *in situ* X-ray powder diffraction data at 400 °C and 500 °C [a]

Temperature	Atom	Wyck. position	Occupancy	*x*/a	*y*/b	*z*/c	U_{iso} (Å^2)
a) 400 °C	Li1	4*c*	1 [b]	0	0.675 [c]	¼	0.019 [c]
	Co1	4*a*	1	0	0	0	0.015(5)
	P1	4*c*	1	0	0.3506(16)	¼	0.007(7)
	O1	8*f*	1	0	0.2517(11)	0.046(2)	0.008(6)
	O2	8*g*	1	0.2343(17)	0.4625(13)	¼	0.009(6)
b) 500 °C	Li1	4*c*	1 [b]	0	0.675 [c]	¼	0.019 [c]
	Co1	4*a*	1	0	0	0	0.017(4)
	P1	4*c*	1	0	0.3525(16)	¼	0.012(6)
	O1	8*f*	1	0	0.2522(11)	0.047(2)	0.014(6)
	O2	8*g*	1	0.239(2)	0.4675(13)	¼	0.013(6)

[a] The estimated standard deviations were calculated by the Berar's procedure and are indicated in parentheses. [b] The Li occupancy factors were kept fixed at 100% ($y = 0$). [c] Li positions and thermal displacement parameters have been fixed as they cannot be deduced by means of X-ray diffraction due to the low atomic scattering factor of Li.

Table S21 Selected interatomic distances of $LiCoPO_4$ ($Li_{1-y}CoPO_4$ with $y = 0$, *Cmcm*, $Z = 4$) as refined from temperature-dependent *in situ* X-ray powder diffraction data at 400 °C and 500 °C [a]

Atom pair			*d* (Å)	
			a) 400 °C	**b) 500 °C**
Li1	O1	×2	1.947(15)	1.957(14)
	O2	×2	2.162(10)	2.147(11)
	Li1–O average		2.055	2.052
Co1	O1	×2	2.084(9)	2.093(9)
	O2	×4	2.156(6)	2.137(7)
	Co1–O average		2.132	2.122
P1	O1	×2	1.512(15)	1.513(15)
	O2	×2	1.574(12)	1.612(13)
	P1–O average		1.543	1.563

[a] The estimated standard deviations were calculated by the Berar's procedure and are indicated in parentheses.

Table S22 Fractional atomic coordinates and isotropic thermal displacement parameters of $LiCoPO_4$ (*Pnma*, $Z = 4$) as refined from temperature-dependent *in situ* X-ray powder diffraction data at 600 °C and 700 °C [a]

Temperature	Atom	Wyck. position	Occupancy	*x*/a	*y*/b	*z*/c	U_{iso} (Å^2)
a) 600 °C	Li1	4*a*	1	0	0	0	0.0139 [b]
	Co1	4*c*	1	0.2206(9)	¼	0.527(3)	0.015(7)
	P1	4*c*	1	0.4028(17)	¼	0.070(5)	0.010(9)
	O1	4*c*	1	0.407(4)	¼	0.756(8)	0.009(16)
	O2	4*c*	1	0.046(5)	¼	0.285(6)	0.008(14)
	O3	8*d*	1	0.343(3)	0.059(5)	0.225(5)	0.010(14)
b) 700 °C	Li1	4*a*	1	0	0	0	0.0139 [b]
	Co1	4*c*	1	0.2192(10)	¼	0.533(3)	0.016(8)
	P1	4*c*	1	0.401(2)	¼	0.083(6)	0.012(10)
	O1	4*c*	1	0.417(5)	¼	0.773(11)	0.012(12)
	O2	4*c*	1	0.050(4)	¼	0.263(6)	0.013(13)
	O3	8*d*	1	0.350(3)	0.057(6)	0.228(5)	0.014(14)

[a] The estimated standard deviations were calculated by the Berar's procedure and are indicated in parentheses. [b] The thermal displacement parameters of Li have been fixed as they cannot be deduced by means of X-ray diffraction due to the low atomic scattering factor of Li.

Table S23 Selected interatomic distances of $LiCoPO_4$ (*Pnma*, $Z = 4$) as refined from temperature-dependent *in situ* X-ray powder diffraction data at 600 °C and 700 °C [a]

Atom pair			*d* (Å)	
			a) 600 °C	**b) 700 °C**
Li1	O1	×2	2.16(3)	2.16(4)
	O2	×2	2.08(2)	2.03(2)
	O3	×2	2.11(3)	2.04(3)
	Li1–O average		2.12	2.08
Co1	O1	×1	2.20(4)	2.34(5)
	O2	×1	2.13(5)	2.16(4)
	O3	×2	2.18(3)	2.19(3)
	O3	×2	2.23(3)	2.29(3)
	Co1–O average		2.19	2.24
P1	O1	×1	1.49(5)	1.48(6)
	O2	×1	1.63(5)	1.70(5)
	O3	×2	1.49(3)	1.45(3)
	P1–O average		1.53	1.52

[a] The estimated standard deviations were calculated by the Berar's procedure and are indicated in parentheses.

Table S24 Fractional atomic coordinates and isotropic thermal displacement parameters of α-$Co_2P_2O_7$ ($P2_1/c$, $Z = 4$) as refined from temperature-dependent *in situ* X-ray powder diffraction data at 400–700 °C [a]

Temperature	Atom	Wyck. position	Occupancy	*x*/a	*y*/b	*z*/c	U_{iso} (Å^2)
a) 400 °C	Co1	4*e*	1	0.241(6)	0.947(4)	0.864(5)	0.016(12)
	Co2	4*e*	1	0.235(6)	0.563(4)	0.871(6)	0.019(12)
	P1	4*e*	1	0.435(7)	0.266(6)	0.763(5)	0.008(18)
	P2	4*e*	1	0.006(5)	0.239(6)	0.460(3)	0.007(13)
	O1	4*e*	1	0.234(14)	0.180(7)	0.589(9)	0.008(12)
	O2	4*e*	1	−0.115(11)	0.314(9)	0.567(10)	0.005(13)
	O3	4*e*	1	0.625(14)	0.252(13)	0.722(9)	0.006(13)
	O4	4*e*	1	0.497(14)	0.086(15)	0.911(13)	0.007(14)
	O5	4*e*	1	0.427(12)	0.415(12)	0.870(10)	0.007(13)
	O6	4*e*	1	0.053(11)	0.076(10)	0.421(8)	0.006(13)
	O7	4*e*	1	−0.011(12)	0.388(11)	0.349(12)	0.008(14)
b) 500 °C	Co1	4*e*	1	0.254(7)	0.944(3)	0.867(5)	0.022(11)
	Co2	4*e*	1	0.261(8)	0.562(4)	0.877(5)	0.028(14)
	P1	4*e*	1	0.488(5)	0.255(6)	0.255(6)	0.014(17)
	P2	4*e*	1	0.063(7)	0.234(8)	0.496(7)	0.016(18)
	O1	4*e*	1	0.25(2)	0.203(10)	0.650(14)	0.013(14)
	O2	4*e*	1	−0.129(18)	0.300(10)	0.527(13)	0.010(14)
	O3	4*e*	1	0.627(13)	0.253(13)	0.694(13)	0.012(14)
	O4	4*e*	1	0.520(12)	0.097(13)	0.945(11)	0.012(14)
	O5	4*e*	1	0.442(12)	0.406(12)	0.826(10)	0.013(13)
	O6	4*e*	1	0.058(10)	0.077(10)	0.390(9)	0.014(12)
	O7	4*e*	1	0.031(14)	0.371(12)	0.375(11)	0.012(13)
c) 600 °C	Co1	4*e*	1	0.262(13)	0.925(8)	0.880(8)	0.04(3)
	Co2	4*e*	1	0.257(13)	0.556(7)	0.868(7)	0.04(3)
	P1	4*e*	1	0.490(9)	0.259(18)	0.790(8)	0.02(3)
	P2	4*e*	1	0.043(11)	0.261(18)	0.474(10)	0.03(3)
	O1	4*e*	1	0.24(4)	0.21(3)	0.64(3)	0.02(5)
	O2	4*e*	1	−0.04(2)	0.22(3)	0.589(18)	0.01(5)
	O3	4*e*	1	0.661(17)	0.23(3)	0.703(11)	0.01(4)
	O4	4*e*	1	0.42(4)	0.09(3)	0.86(3)	0.02(9)
	O5	4*e*	1	0.42(4)	0.44(2)	0.82(2)	0.01(8)
	O6	4*e*	1	−0.020(18)	0.09(2)	0.344(15)	0.01(7)
	O7	4*e*	1	0.03(2)	0.42(2)	0.391(19)	0.02(6)

[*Continuing Table S24*]

Temperature	Atom	Wyck. position	Occupancy	*x*/a	*y*/b	*z*/c	U_{iso} (Å^2)
d) 700 °C	Co1	4*e*	1	0.251(10)	0.944(6)	0.872(7)	0.06(2)
	Co2	4*e*	1	0.237(11)	0.561(7)	0.870(8)	0.05(2)
	P1	4*e*	1	0.456(15)	0.272(13)	0.756(11)	0.03(4)
	P2	4*e*	1	0.039(12)	0.244(12)	0.468(8)	0.04(2)
	O1	4*e*	1	0.26(3)	0.215(15)	0.611(19)	0.04(4)
	O2	4*e*	1	−0.12(2)	0.25(2)	0.510(13)	0.02(5)
	O3	4*e*	1	0.622(13)	0.282(13)	0.685(9)	0.01(3)
	O4	4*e*	1	0.48(3)	0.10(2)	0.830(17)	0.02(6)
	O5	4*e*	1	0.41(2)	0.395(15)	0.868(16)	0.02(5)
	O6	4*e*	1	0.04(3)	0.09(3)	0.37(2)	0.02(8)
	O7	4*e*	1	0.01(2)	0.401(17)	0.360(15)	0.02(4)

[a] The estimated standard deviations were calculated by the Berar's procedure and are indicated in parentheses.

Table S25 Selected interatomic distances of α-$Co_2P_2O_7$ ($P2_1/c$, $Z = 4$) as refined from temperature-dependent *in situ* X-ray powder diffraction data at 400–700 °C [a]

	Atom pair		*d* (Å)			
			a) 400 °C	b) 500 °C	c) 600 °C	d) 700 °C
Co1	O2	×1	1.69(10)	1.95(13)	2.4(2)	2.31(19)
	O3	×1	2.17(12)	1.98(12)	2.0(2)	1.81(12)
	O4	×1	2.03(12)	1.82(8)	1.8(3)	2.2(2)
	O4	×1	2.13(9)	2.13(10)	2.5(2)	2.62(14)
	O6	×1	2.56(7)	2.46(7)	2.05(12)	2.33(18)
	O7	×1	2.21(10)	2.23(11)	2.1(2)	2.11(16)
	Co1–O average		2.13	2.10	2.14	2.2
Co2	O2	×1	2.42(9)	2.50(12)	2.2(2)	2.24(19)
	O3	×1	2.20(12)	2.00(12)	1.8(2)	2.25(13)
	O5	×1	1.83(10)	2.00(11)	1.7(3)	1.85(16)
	O6	×1	1.92(10)	1.87(9)	2.23(17)	1.9(3)
	O7	×1	2.01(9)	2.43(9)	2.41(15)	2.12(12)
	Co2–O average		2.08	2.16	2.1	2.1
P1	O1	×1	1.78(8)	1.71(11)	1.8(2)	1.53(18)
	O3	×1	1.53(12)	1.56(13)	1.71(16)	1.55(16)
	O4	×1	1.94(13)	1.87(11)	1.7(3)	1.6(2)
	O5	×1	1.59(11)	1.37(12)	1.6(3)	1.58(19)
	P1–O average		1.71	1.63	1.7	1.6
P2	O1	×1	1.62(8)	1.48(11)	1.6(2)	1.60(18)
	O2	×1	1.65(10)	1.59(15)	1.4(2)	1.35(19)
	O6	×1	1.47(9)	1.62(11)	1.8(2)	1.6(3)
	O7	×1	1.57(11)	1.54(12)	1.5(2)	1.60(17)
	P2–O average		1.58	1.56	1.6	1.5

[a] The estimated standard deviations were calculated by the Berar's procedure and are indicated in parentheses.

12 *In situ* X-ray powder diffraction patterns upon heating of $Li_{0.5-\delta}CoPO_4$ (*Cmcm*) under air at 800 °C, 900 °C, and after cooling down to room temperature (25 °C)

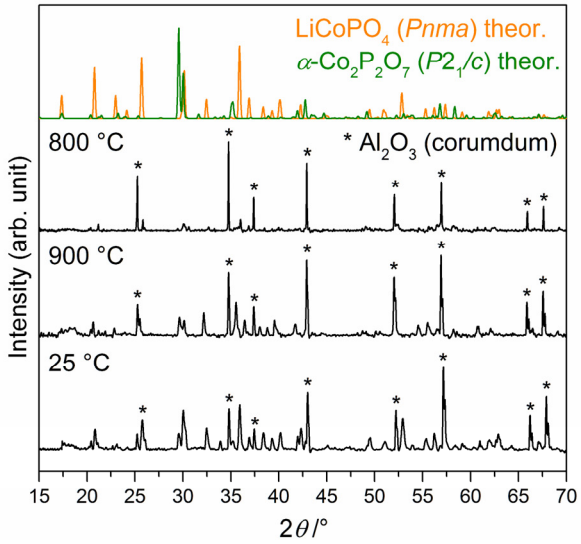

Figure S12 *In situ* X-ray powder diffraction patterns (Bragg-Brentano geometry, Cu K_α radiation) of $Li_{0.5-\delta}CoPO_4$ (*Cmcm*) measured at 800 °C and 900 °C under air (heating rate: 5 °C·min^{-1}) and after cooling to ambient temperature (25 °C). The theoretical patterns of the involved phases $LiCoPO_4$ (*Pnma*, orange, ICSD no. 431999)[2] and α-$Co_2P_2O_7$ ($P2_1/c$, green, ICSD no. 280959),[3] which were calculated from room temperature data, are displayed in color. Compared to the pattern at 700 °C (*cf.* Fig. 7 in the main article or Fig. S11i), no changes of the main phases $LiCoPO_4$ (*Pnma*) and α-$Co_2P_2O_7$ (green) is observed except for the fact that at 800 °C, strong additional reflections (marked with an asterisk *) of the corundum flat plate sample holder appear. (Since the voluminous powder showed massive shrinkage/volume reduction upon heating, the surface of the sample holder was no longer fully covered with substance at this point.)

References

1. Alarcón-Suesca, C.; Ludwig, J.; Hlukhyy, V.; Stinner, C.; Nilges, T., *Inorganics* **2016,** *4*, 35.
2. Ludwig, J.; Marino, C.; Haering, D.; Stinner, C.; Gasteiger, H. A.; Nilges, T., *J. Power Sources* **2017,** *342*, 214-223.
3. El Bali, B.; Bolte, M., *Acta Crystallogr., Sect. E: Struct. Rep. Online* **2002,** *58*, i32-i33.
4. Bramnik, N. N.; Nikolowski, K.; Baehtz, C.; Bramnik, K. G.; Ehrenberg, H., *Chem. Mater.* **2007,** *19*, 908-915.
5. Kaus, M.; Issac, I.; Heinzmann, R.; Doyle, S.; Mangold, S.; Hahn, H.; Chakravadhanula, V. S. K.; Kuebel, C.; Ehrenberg, H.; Indris, S., *J. Phys. Chem. C* **2014,** *118*, 17279-17290.
6. Kreder, K. J.; Assat, G.; Manthiram, A., *Chem. Mater.* **2015,** *27*, 5543-5549.
7. Markevich, E.; Sharabi, R.; Gottlieb, H.; Borgel, V.; Fridman, K.; Salitra, G.; Aurbach, D.; Semrau, G.; Schmidt, M. A.; Schall, N.; Bruenig, C., *Electrochem. Commun.* **2012,** *15*, 22-25.
8. Mathew, V.; Alfaruqi, M. H.; Gim, J.; Song, J.; Kim, S.; Ahn, D.; Kim, J., *Mater. Charact.* **2014,** *89*, 93-101.

The olivine-type high-voltage cathode material $LiCoPO_4$ is a promising candidate for next-generation lithium-ion batteries, but generally exhibits low capacities and poor cycle life. This thesis presents simple and fast microwave-assisted solvothermal synthesis pathways towards particle size- and morphology-tuned $LiCoPO_4$ materials with cutting-edge electrochemical performances. In addition, the structure–property relationships of metastable, non-olivine $LiCoPO_4$ polymorphs and two novel mixed-valent Co(II,III) phases are investigated.